



BEHAVIOUR OF FIRE EXPOSED REINFORCED CONCRETE COLUMNS

Assist. Prof. Dr. Nada M. Fawzi
University of Baghdad

Prof. Dr. Mahdi S. Essa
University of Babylon

Dr. Mohammed M. Kadhun
University of Babylon

ABSTRACT

This research is devoted to investigate the behaviour and load carrying capacity of reinforced concrete columns exposed to fire flame.

The experimental program consisted of casting and testing of 128 column specimens divided into two series A and B with target compressive strength (30 and 40 MPa) and named series A and B respectively. Each series was divided into three main groups loaded eccentrically with eccentricities 30mm and 80mm.

It was found that the predicted load carrying capacity of reinforced concrete columns by three codes (ACI-318/08, BS-8110/97 and Canadian/84), was unconservative after burning. The BS Code equation was found to predict load capacity after exposure to high fire temperature levels better than other codes.

Load-deflection curves indicate deleterious response to the fire exposure. Also, it was noticed that the maximum crack width increases with increasing fire temperature and amount of spacing between lateral steel ties.

(40 30)

128

. 80 30

()

(750 600 400)

(40 30)

INTRODUCTION

Concrete columns are considered to be an important structural elements in reinforced concrete structures because they support the structure and transfer the loads to the supports or foundation, so any failure or damage occurs in the column may cause a partial or complete failure of the structure by perhaps chain action (Sakai and Sheikh, 1989).

High temperatures due to fire have a significant effect on the strength and deformation characteristics of various structural components, such as columns, beams, slabs, shear walls, etc. Therefore, a good understanding of the structural behavior and response of reinforced concrete exposed to fire is important towards the saving of human lives and avoiding costly damage of structures (Book Ng et al., 1990). Human safety is one of the considerations in the design of residential, public and industrial buildings.

RESEARCH SIGNIFICANCE

There are indeed little research about temperature gradient and exposure time of concrete in direct contact with fire flames.

In order to simulate this problem to practical site conditions, reduced scale column models were cast and they were as close as possible to practical circumstances. This research is sought to cover the limited area of research about this problem. This will guide and facilitate the suggestion of rehabilitation of such members exposed to fires under loading of different degrees.

The current research proposes a reinforced concrete column model which resemble the simulation of the state of stress which reinforced concrete columns are subjected to during fire in laboratory.

Simulation of real fires in laboratory using a set of methane burners exposed the column specimens to real fire flame.

LITERATURE REVIEW

-The Effect of Fire on Reinforced Concrete Columns

Kodur et al., 2005 investigated the behaviour of fibre reinforced polymer (FRP) wrapped (confined) reinforced concrete columns under exposure to standard fire. Three full-scale reinforced concrete columns, two of these columns were circular and the third column was square in cross-section. The circular columns were 400 mm in diameter, while the square column was 406 mm in width. All three columns were 3810 mm long. The longitudinal reinforcement in the circular columns was comprised of eight 19.5mm diameter bars, with 40mm clear cover to the spiral reinforcement and 10mm for lateral reinforcement. The square column had four 25mm diameter longitudinal reinforcing bars with 40mm cover to the ties, and 10mm diameter for ties spaced at 406mm. These specimens were heated in furnace chamber by 32 propane gas burners, arranged in eight columns containing four burners each. The test results showed that the FRP materials used as externally bonded reinforcement for concrete structures were sensitive to the effects of elevated temperatures. They also noticed that providing proper fire insulation (5 and 4) hours fire endurance rating can be achieved for loaded circular and square reinforced concrete columns strengthened with FRP wraps respectively.

Wu and Li, 2008 studied the behavior of four concentrically loaded L-shaped reinforced concrete columns subjected to ISO834 fire. All columns have a nominal height of 2340mm and only the center portion of 1650mm was exposed to fire on all sides. Each column was reinforced with 12Ø10mm as the longitudinal reinforcement, and Ø6mm were used for ties, which are spaced at 100mm within the central fire exposed portion. They investigated the effect of axial restraint on columns during both expanding and contracting phases. The fire tests, which consist of four combinations of two levels of axial load with two degrees of axial restraint, were conducted at the fire laboratory of South China University of Technology. The boundary conditions of the

columns were considered as fixed-fixed for all tests. Moreover, the finite element program, SAFIR, was employed to conduct a numerical analysis of the tests. The authors concluded that columns subjected to same load ratio, the axial restraint ratio seems to have little effect on the development of column axial load during contracting and cooling phases. They also found that the maximum additional axial forces induced in axially restrained columns with axial restraint ratios of 0.0578 and 0.0875 are, respectively, around 34% and 53% of the design load for the load ratio of 0.25. For the load ratio of 0.35, the additional forces were 26% and 30% of the design load.

-Effect of Fire on Load Eccentricity of Reinforced Concrete Columns

The fire resistance of reinforced concrete columns is the time it takes for strength to be reduced to the level of the applied load. Figure (1) shows strength interaction curves during fire for a typical column, fire resistance being of the order of 2.0 hours. The fire resistance in this figure is greater in compression than in bending because the concrete core heats more slowly than the reinforcing (Allen and Lie, 1977).

Jae-Hoon and Hyeok-Soo, 2000, verified the basic design rules of high strength concrete columns. A total of 32 column specimens were tested to investigate structural behavior and strength of eccentrically loaded reinforced concrete tied columns. The main variables included in this test program were concrete compressive strength, amount of steel, and load eccentricity. In this work, concrete compressive strength varied from 34.9 to 93.2 MPa, and the longitudinal steel ratios ranged between 1.13% and 5.51%. Test results of column sectional strength were compared with the result of analysis by using the American Concrete Institute (Building Code requirements for structural concrete) rectangular stress block, trapezoidal stress block, and modified rectangular stress block. Axial force-moment-curvature analysis was also performed for predicting axial load-moment strength and compared with test results. It was found that the ACI (318-95)

code rectangular stress block provides overestimated column strengths for the lightly reinforced high strength column specimens.

EXPERIMENTAL WORK

Reinforced Concrete Column Specimens

The column specimens were divided into two series A and B with two target compressive strengths (30 and 40) MPa respectively. The specimens of each series were tested by applying compressive axial loads and divided to three groups depending on the way of load application. The specimens of the first group were concentrically loaded, whereas, the specimens of the second and third group were eccentrically loaded by eccentricity of (30mm) and (80mm) respectively. The details of the reinforced concrete column specimens are shown in Table (1). Each column is identified by three symbols. The first is a letter that refers to concrete strength series. The letters (A) and (B) refer to target compressive strength (30 and 40 MPa) respectively. The second symbol is a number that refers to the eccentricity of applied load; (1) refers to axially concentrically loaded columns, while (2) and (3) refer to the columns that were loaded at eccentricities of 30 and 80 mm respectively. The third symbol refers to the tie spacing; (0) for no ties, (1), (2) and (3) for 250, 150 and 50 mm tie spacing, respectively.

After greasing the moulds of the column specimens, reinforcement bars were held carefully in their position inside these moulds. In order to get a cover, small pieces of steel were placed at sides of the column reinforcement.

The reinforcement used is deformed steel bars of Ø8 mm and Ø10 mm respectively. Figure (2) shows the details of the reinforcement of column specimens.

Materials and Mixes

Introduction

The properties of materials used in any structure are of considerable importance (Neville, 1995, and ACI Committee 211, 1997). The properties of materials used in the current study are presented in this chapter.

Assist. Prof. Dr. Nada M. Fawzi Prof. Dr. Mahdi S. Essa Dr. Mohammed M. Kadhum	Behaviour of Fire Exposed Reinforced Concrete Columns
---	--

Standard tests according to the American Society for Testing and Materials (ASTM) and Iraqi specifications IQS were conducted to determine the properties of materials.

Cement

Tasluga-Bazian Ordinary Portland cement (O.P.C) (ASTM Type I) manufactured in Iraq was used for concrete mixes throughout the present work. The cement was properly stored in a dry place to avoid the exposure to the atmosphere. This cement complied with the Iraqi specification (IQS, No.5:1984). Testing of cement was conducted in the laboratories of Consultant Engineering Bureau in Babylon University. The physical properties and chemical analysis of the cement used are given in Tables (2) and (3). Also, the compounds of cement calculated according to Bogue equations are listed in Table (3).

Fine Aggregate

Well-graded natural sand from Al-Akhaidher region in Iraq was used for concrete mixes. The fine aggregate was sieved at sieve size (9.5 mm) to separate the aggregate particles of diameter greater than 9.5 mm. The sand was then washed and cleaned with water several times, then it was spread out and left to dry in air, after which it was ready for use. The physical and chemical properties of the sand are listed in Table (4). Its grading conformed to the Iraqi specification (IQS, No.45:1984), Zone(3).

Coarse Aggregate

The gravel used was brought from Al-Nibaii area in Iraq with a maximum size of (20 mm). The gravel was sieved at sieve size of (20 mm). The gravel was washed and cleaned by water several times, later it was speared out and left in air to dry before use. The gravel used conforms to the Iraqi specification (IQS, No.45:1984). The grading and other properties of this type of aggregate are shown in Table (5).

Mixing Water

Ordinary clean tap water was used throughout this work for both making and curing of specimens.

Reinforcing Steel Bars

Deformed steel bars of diameters ($\varnothing 8$ mm) and ($\varnothing 10$ mm) were used as reinforcement. Their mechanical properties were obtained from a digital computer complementary with the testing machine. Table (6) gives the results of testing three 1000 mm long samples from each size of bars (8 and 10 mm).

Mix Design and Proportions

Two target compressive strengths of 30 and 40 MPa were denoted as series A and B respectively. The concrete mix was designed according to American mix design method (ACI 211.1-91) specification. The proportions of the concrete mix are summarized in Table (7).

Reinforced Concrete Columns Testing Procedure

The column specimens were tested using a load cell of maximum capacity of (150 Tons) at the age of (60 days). The load was applied through a bearing plate for the axially loaded columns, and through a cylindrical roller to simulate line load, attached to the top of bearing plates. The load was applied in small increments and the readings were taken every 10.0 kN load until failure occurs. For each increment, the load was kept constant until the required measurements were recorded. Cracks were detected and drawn on the faces of the test column specimens. The positions of the visual cracks in the concrete and the loads at which these cracks were formed, were recorded. The reading of the lateral deflections versus loads were recorded simultaneously for each load increment. Testing continued until the reinforced concrete column shows a drop in load capacity with increasing deformation. The axial deformation of the columns was measured using vertical dial gauges having a minimum graduation of 0.001 mm and a maximum needle length of 50 mm mounted at the bottom face of the specimens.

For the column specimens which were subjected to fire flame under loading as shown in Plate (1). The specified (target) fire temperature was reached by mounting the fire subjecting burners by a sliding arm to control the fire distance to the surface of the column specimens, and also by monitoring the fire intensity through controlling the methane gas pressure in the burners. The temperature was measured by the digital thermometer and infrared rays thermometer continuously till reaching the specified (target) fire temperature. Then, the sliding arm and gas pressure were kept at this position along the period of burning (1.5 hour). The lateral deflection of the column specimens exposed to fire are resulting from loading to 15% of ultimate load before burning, loading 15% and applied fire flame, and loading after burning until failure. While, for column specimens without burning the lateral deflection resulted from applied load only.

RESULTS AND DISCUSSION

Comparison Between Residual Compressive Strength Results and Recommended Design Curves (CEB & CEN)

In the present study some of the test results of residual compressive strength were found to lie between CEB and CEN curves, while other results diverged from the CEB curve and converged to the CEN curve especially at 400°C of fire exposure. At 600°C and 750°C, the test results were found to be near the CEN curve only. From the figure (3), it can be concluded that the test results of the current study have better agreement with CEN design curve than with CEB curve.

Effect of Burning on Load Versus Deflection Results

The load versus midheight lateral deflection relationship of reinforced concrete column specimens loaded at eccentricity of (30 and 80mm) for series A and B are presented in Figures (4) to (7).

Deflection of these column specimens, which occurred immediately when they were loaded and subjected to fire flame, this deflection is

called immediate deflection or instantaneous deflection. Deflection measurement was taken continually during the test and the rate of increase in deflection was controlled to provide warning of impending collapse of the column specimens.

From these Figures, it can be seen that the increase in the fire temperature has a significant effect on midheight lateral deflection of column specimens for series A and B. In addition, it can be noted that the increase in the fire temperature decreases the load carrying capacity and increases lateral deflection in column specimens. This can be attributed to the fact that heating causes a reduction in column stiffness, which is essentially due to the reduction in the modulus of elasticity of concrete and the reduction in the effective section due to cracking, which means that load-deflection curves for series A are more sensitive to high temperatures compared with series B. These Figures reveal that the load-deflection relation of the column specimens is almost linearly proportional for the two eccentricities (30 and 80mm) and for temperature exposure (600°C and 750°C).

General Behavior and Verification of Building Code Provisions of Axially Loaded Column Specimens

Several existing equations are available to predict the axial load capacity of reinforced concrete columns. These equations are selected and used in this study for comparison with the results of the experimental work. These equations are outlined in the Table (8). From the results, it is clear that the predicted ultimate axial load capacity obtained from ACI Code provisions is lower than that obtained in the experimental work at burning temperature up to (400°C). While, at burning above (400°C) the predicted ultimate axial load capacity obtained from ACI Code provisions is greater than that obtained from the experimental work. This can be attributed to the precracking which happens upon burning. While, B.S-8110 gave results lower than that obtained from experimental results at burning temperatures up to 750°C. The predicted ultimate axial load capacity obtained from

Assist. Prof. Dr. Nada M. Fawzi Prof. Dr. Mahdi S. Essa Dr. Mohammed M. Kadhum	Behaviour of Fire Exposed Reinforced Concrete Columns
---	--

Canadian Code provisions is lower than that obtained in the experimental work at burning temperature up to (600°C), while at burning above (600°C) the Canadian Code provisions slightly overestimate ultimate axial load capacity.

Crack Pattern and Mode of Failure

The development of cracks and the time at which they appeared and propagated in the reinforced concrete column specimens were detected throughout testing to assess the behavior of the column specimens exposed to fire flame and the control column specimens. The cracks were marked with a blue marking pen, then photographs were taken to the crack pattern. When the load was increased, cracks appeared on the columns loaded at eccentricity 30 and 80mm on the surface from the tension zone towards the compression zone. Further, flexural cracks were formed progressively and widened as the loading increased. However some of short nearly vertical, hairline cracks were detected on the middle third of the columns. For concentric column specimens nearly vertical, hairline cracks appeared at the middle portion of columns. More cracks (mostly vertical) continued to appear on the column faces. Scabbing occurred prior to the column failure due to the crushing of the concrete and subsequent buckling of the main reinforcement at later stage.

Types of failure combined flexural and compression failure for eccentric loaded column specimens and compression failure for concentric loaded column specimens. The columns burned at 400°C, the type of failure for concentric and eccentric loaded specimens stayed without changes. For columns burned at 600 and 750 °C, the type of failure also remained constant but scabbing in the concrete cover occurred. This can be attributed to the vapor pressure of the runoff water which exerts internal pressure stresses on the surface layers of concrete which are unconfined by the tie reinforcement resulting in scabbing of these layers. Also, the cracking appeared earlier when the fire flame temperature increased.

COCLUSIONS

1. For the studied temperature range in this study, the compressive strength-reduction curve, recommended by the Euro codes CEN (1993, 1994) is in better agreement with the test results rather than CEB (1991) strength-reduction curve.
2. In this study, it is noticed that the load-midheight lateral deflection relation of column specimens exposed to fire flame temperature around 750°C are flatter and reveals softer stiffness response than that of the control column specimens. This behavior can be attributed to the continual decrease in specimens stiffness with the increase cracking due to fire flame exposure.
3. The Canadian/84 and B.S-8110/97 Codes predict ultimate load carrying capacity after exposure to (600 and 750 °C) fire flame temperature conservatively.
4. ACI Code give conservative results to predict ultimate load carrying capacity after exposure to 400°C fire flame temperature.

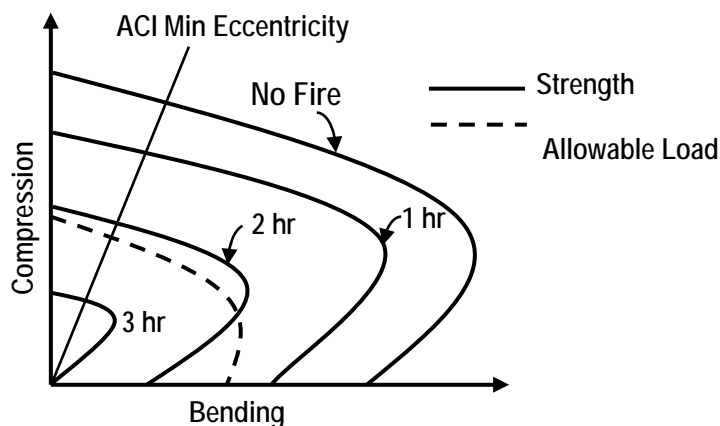
REFERENCE

- **Sakai, K., and Sheikh, S.A., 1989**, "What Do We Know About Confinement in Reinforced Concrete Columns", ACI Structural Journal, Vol.86, No.2, March-April, PP.192-207.
- **Book Ng, A.H., Mirza, S.M., Lie, T.T., 1990** "Response of Direct Models of Reinforced Concrete Columns Subjected to Fire", ACI Structural Journal, Vol. 87, No.3, May-June, pp.313-325.
- **Kodur, V.R.K., Bisby, L.A., Green, M.F., and Chowdhury, E., 2005**, "Fire Endurance Experiments on FRP-Strengthened Reinforced Concrete Columns", National Research Council of Canada, Institute for Research in Construction, Research Report No.185, March, 41pp.
- **Wu, B.O., and Li, Y.H., 2008**, "Experimental Research on Fire Performance of Axially Restrained RC Columns With L-Shaped Cross Section",

Proceedings of the Fifth International Conference on Structures in Fire, pp. 451-462.

- **Allen, D.E., and Lie, T.T., 1977**, "Fire Resistance of Reinforced Concrete Columns and Walls", National Research Council of Canada, Division of Building Research, Technical Paper No.784 Ottawa, June, pp. 17-33.

- **Jae-Hoon, L. and Hyeok-Soo, S., 2000**, "Failure and Strength of High Strength Concrete Columns Subjected to Eccentric Loads", ACI, Structural Journal, Vol. 97, No. 1, January, pp. 664-674.
- **Iraqi Organization of Standards, IOS 45: 1984**; for Aggregate.
- **Iraqi Organization of Standards, IOS 5: 1984**, for Portland Cement.



Figure(1): Typical column interaction curves (*Allen and Lie, 1977*).

Table (1): Summary of column test specimens.

Number	Series	Group	Temperature Stage (°C)	Column No.	Concrete Compressive Strength (MPa)	Eccentricity of Applied Load (mm)	Spacing of Lateral Ties (mm)
1			25 °C	A10	30	0	No ties
2				A11	30	0	250
3				A12	30	0	150
4				A13	30	0	50
5				A12*	30	0	150
6			400 °C	A10	30	0	No ties
7				A11	30	0	250
8				A12	30	0	150
9				A13	30	0	50

Assist. Prof. Dr. Nada M. Fawzi Prof. Dr. Mahdi S. Essa Dr. Mohammed M. Kadhum	Behaviour of Fire Exposed Reinforced Concrete Columns
---	--

10	A	1		A12*	30	0	150
11			600 °C	A10	30	0	No ties
12				A11	30	0	250
13				A12	30	0	150
14				A13	30	0	50
15				A12*	30	0	150
16			750 °C	A10	30	0	No ties
17				A11	30	0	250
18				A12	30	0	150
19				A13	30	0	50
20				A12*	30	0	150
21		2	25 °C	A20	30	30	No ties
22				A21	30	30	250
23				A22	30	30	150
24				A23	30	30	50
25				A22*	30	30	150
26			400 °C	A20	30	30	No ties
27				A21	30	30	250
28				A22	30	30	150
29				A23	30	30	50
30				A22*	30	30	150
31			600 °C	A20	30	30	No ties
32				A21	30	30	250
33				A22	30	30	150
34				A23	30	30	50
35				A22*	30	30	150
36				A20	30	30	No ties



37				A21	30	30	250
38			750 °C	A22	30	30	150
39				A23	30	30	50
40				A22*	30	30	150
41				A30	30	80	No ties
42			25 °C	A31	30	80	250
43				A32	30	80	150
44				A33	30	80	50
45				A32*	30	80	150
46				A30	30	80	No ties
47			400 °C	A31	30	80	250
48				A32	30	80	150
49				A33	30	80	50
50				A32*	30	80	150
51				A30	30	80	No ties
52			600 °C	A31	30	80	250
53				A32	30	80	150
54				A33	30	80	50
55				A32*	30	80	150
56				A30	30	80	No ties
57			750 °C	A31	30	80	250
58				A32	30	80	150
59				A33	30	80	50
60				A32*	30	80	150
61			25 °C	B10	40	0	No ties
62				B11	40	0	250
63				B12	40	0	150
64				B13	40	0	50

Assist. Prof. Dr. Nada M. Fawzi Prof. Dr. Mahdi S. Essa Dr. Mohammed M. Kadhun	Behaviour of Fire Exposed Reinforced Concrete Columns
---	--

65	B	1		B12*	40	0	150
66			400 °C	B10	40	0	No ties
67				B11	40	0	250
68				B12	40	0	150
69				B13	40	0	50
70				B12*	40	0	150
71			600 °C	B10	40	0	No ties
72				B11	40	0	250
73				B12	40	0	150
74				B13	40	0	50
75				B12*	40	0	150
76			750 °C	B10	40	0	No ties
77				B11	40	0	250
78				B12	40	0	150
79				B13	40	0	50
80				B12*	40	0	150
81		2	25 °C	B20	40	30	No ties
82				B21	40	30	250
83				B22	40	30	150
84				B23	40	30	50
85				B22*	40	30	150
86			400 °C	B20	40	30	No ties
87				B21	40	30	250
88				B22	40	30	150
89				B23	40	30	50
90				B22*	40	30	150
91				B20	40	30	No ties



92	3	600 °C	B21	40	30	250
93			B22	40	30	150
94			B23	40	30	50
95			B22*	40	30	150
96		750 °C	B20	40	30	No ties
97			B21	40	30	250
98			B22	40	30	150
99			B23	40	30	50
100			B22*	40	30	150
101		25 °C	B30	40	80	No ties
102			B31	40	80	250
103			B32	40	80	150
104			B33	40	80	50
105			B32*	40	80	150
106		400 °C	B30	40	80	No ties
107			B31	40	80	250
108			B32	40	80	150
109			B33	40	80	50
110			B32*	40	80	150
111		600 °C	B30	40	80	No ties
112			B31	40	80	250
113			B32	40	80	150
114			B33	40	80	50
115			B32*	40	80	150
116		750 °C	B30	40	80	No ties
117			B31	40	80	250
118			B32	40	80	150
119			B34	40	80	50

120				B32*	40	80	150
-----	--	--	--	------	----	----	-----

Concrete cover=15mm, except (* =30mm)

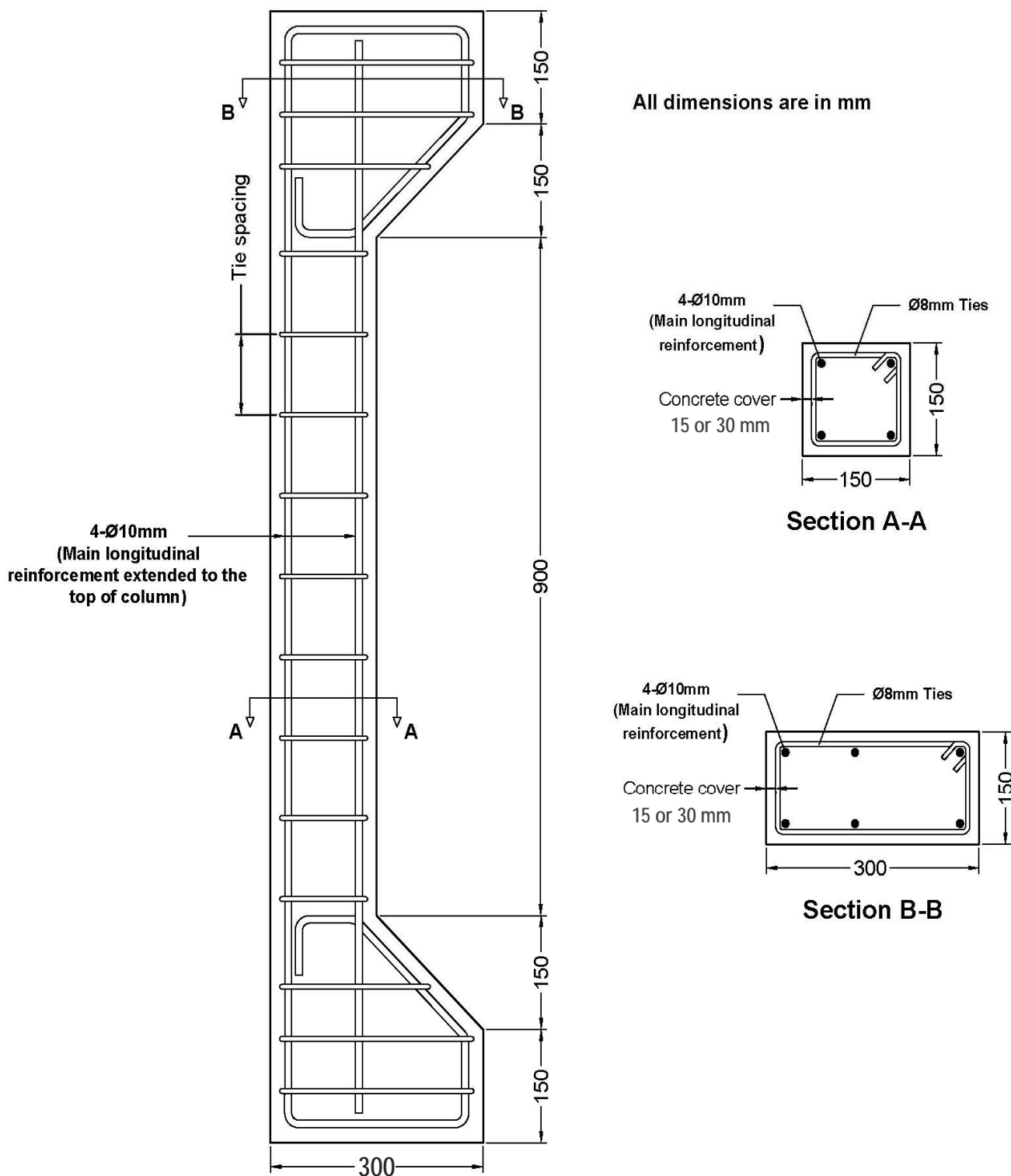


Figure (2): Reinforcement details of reinforced concrete column specimens.

**Table (2): Physical properties of the cement.**

Physical Properties	Test results	IQS (No.5: 1984) Limits
Fineness, Blaine, cm ² /gm	3105	≥ 2300
Setting time, Vicat's method		
Initial hrs: min.	1:54	≥ 0: 45
Final hrs: min.	4:25	≤ 10: 00
Compressive strength of 70.7 mm cube, MPa		
3 days	22.5	≥ 15
7 days	31.5	≥ 23

Table (3): Chemical composition of the cement.

Oxide	Percentage (%)	IQS (No.5: 1984) Limits
CaO	61.49	-----
SiO ₂	21.18	-----
Fe ₂ O ₃	3.68	-----
Al ₂ O ₃	5.16	-----
MgO	2.35	≤ 5.0
SO ₃	2.42	≤ 2.8
L.O.I.	2.27	≤ 4.0
I.R.	0.95	≤ 1.5
Compound composition	Percentage (%)	IQS (No.5: 1984) Limits
C ₃ S	41.59	-----
C ₂ S	29.59	-----
C ₃ A	7.45	-----
C ₄ AF	11.20	-----
L.S.F.	0.81	0.66-1.02

Assist. Prof. Dr. Nada M. Fawzi Prof. Dr. Mahdi S. Essa Dr. Mohammed M. Kadhum	Behaviour of Fire Exposed Reinforced Concrete Columns
---	--

Table (4): Properties of fine aggregate.

Sieve size (mm)	Percentage passing (%)	IQS (No.45: 1984) Limits, Zone 3
9.5	100	100
4.75	94	90-100
2.36	93	85-100
1.18	81	75-100
0.6	62	60-79
0.3	27	12-40
0.15	0	0-10
Properties	Test results	IQS (No.45 : 1984) Limits
Sulphate content, SO ₃ (%)	0.28	≤ 0.5
Specific gravity	2.60	-----
Absorption (%)	1.6	-----

Table (5): Properties of coarse aggregate.

Sieve size (mm)	Percentage passing (%)	IQS (No.45 : 1984) Limits size 20-5mm
37.5	100	100
20	100	95-100
9.5	53	30-60
4.75	5	0-10
Properties	Test results	IQS (No.45 : 1984) Limits
Sulphate content, SO ₃ (%)	0.08	≤ 0.1
Specific gravity	2.64	-----
Absorption (%)	0.8	-----

Table (6): Strength properties of the used steel reinforcement.(*)

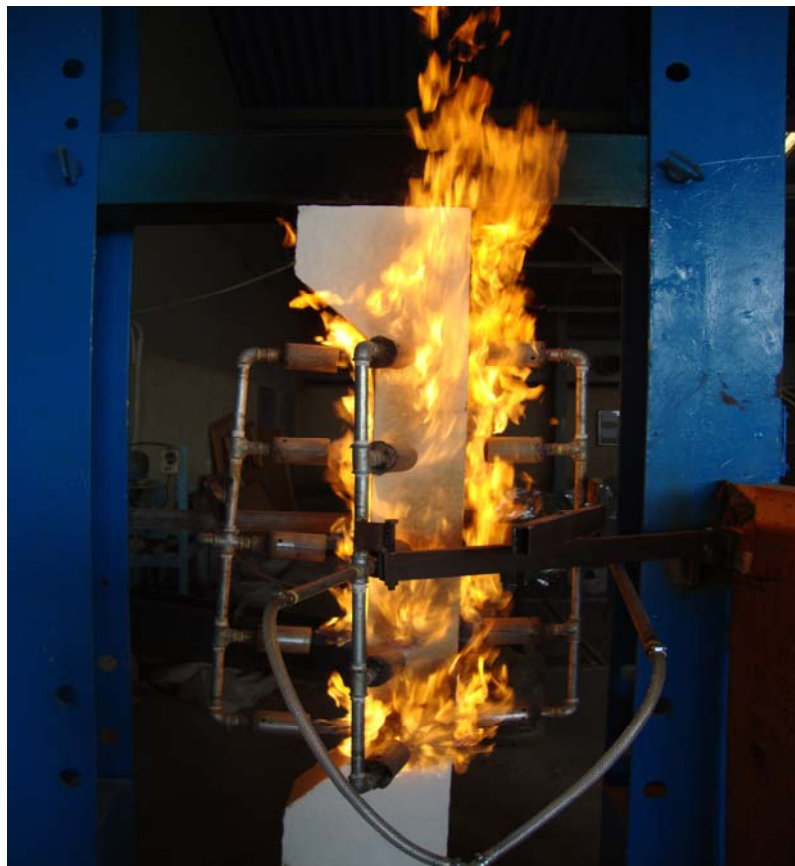
Approximate Diameter (mm)	Measured Diameter (mm)	Area (mm ²)	Yield stress F_y (MPa)	Ultimate Strength F_u (MPa)	** Modulus of Elasticity (GPa)	Uses
10	10.01	78.69	585	745	200	Main Reinforcement
8	8.00	50.26	523.5	694.4	200	Ties

*Testing of steel bars was carried out in Strength of Materials laboratory at the College of Materials Engineering / University of Babylon.

** Assumed

Table (7): Mix Proportions.

Series	W/c ratio	Mix Proportion kg/m ³				Slump (mm)
		Water	Cement	Sand	Gravel	
A	0.52	205	394	717	1024	80
B	0.45	193	429	733	1024	60

**Plate (1): Testing of column specimens under 15% of ultimate load with exposure to fire flame.**

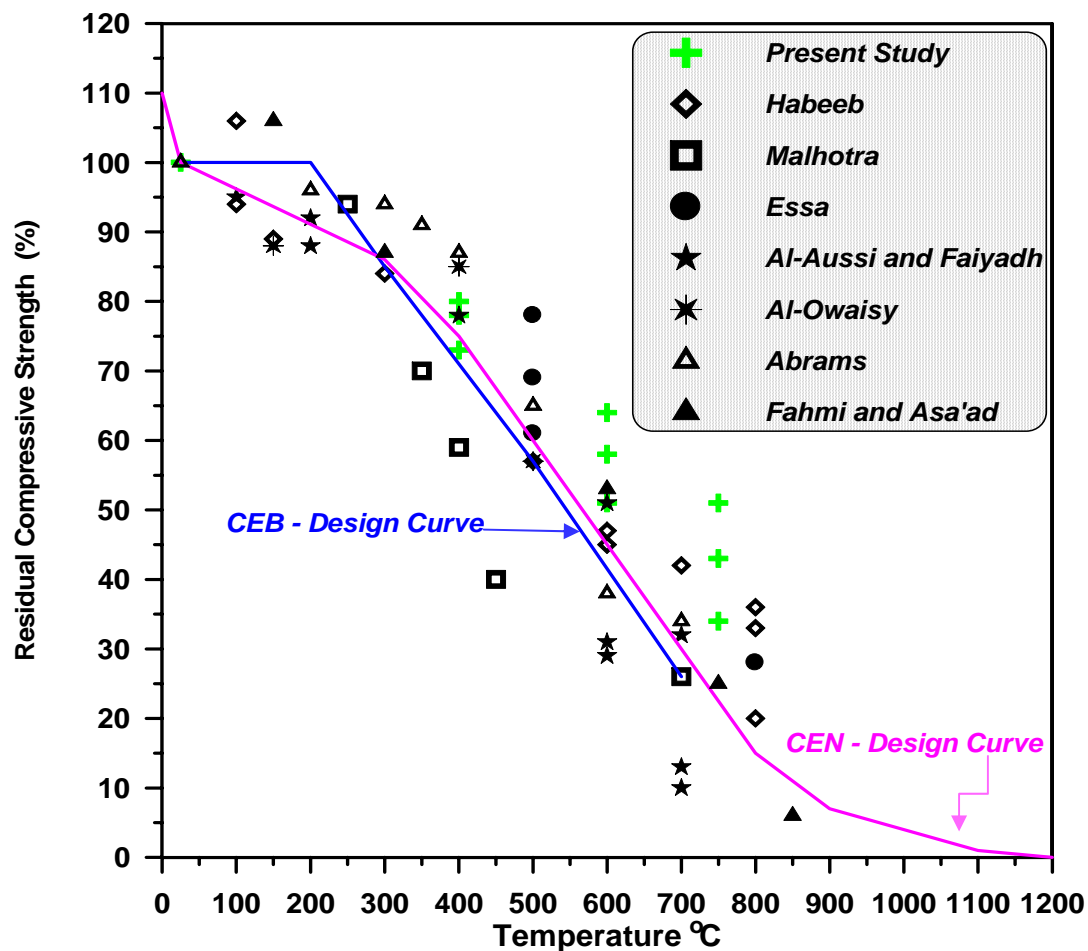


Figure (3): Comparison of residual compressive strength results and the recommended design curves of CEB and CEN.

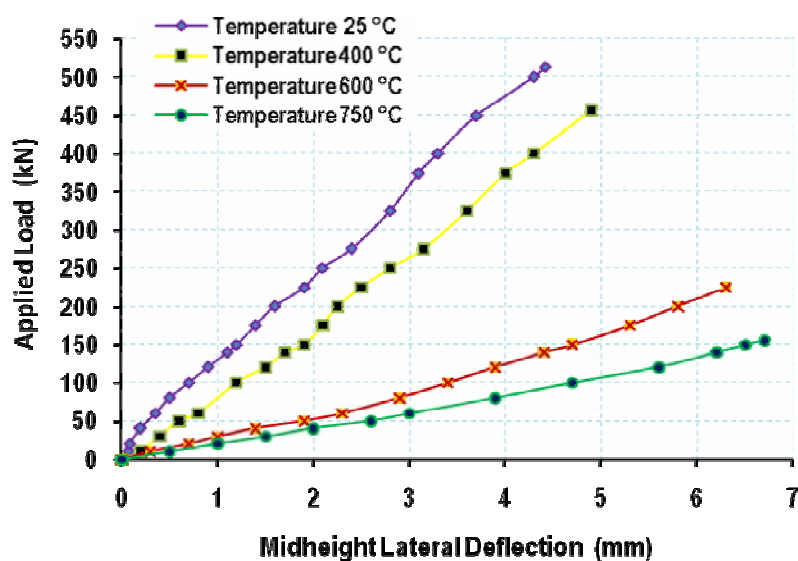


Figure (4): Load versus midheight lateral deflection curve of column specimen A22 at eccentricity ($e=30\text{mm}$).

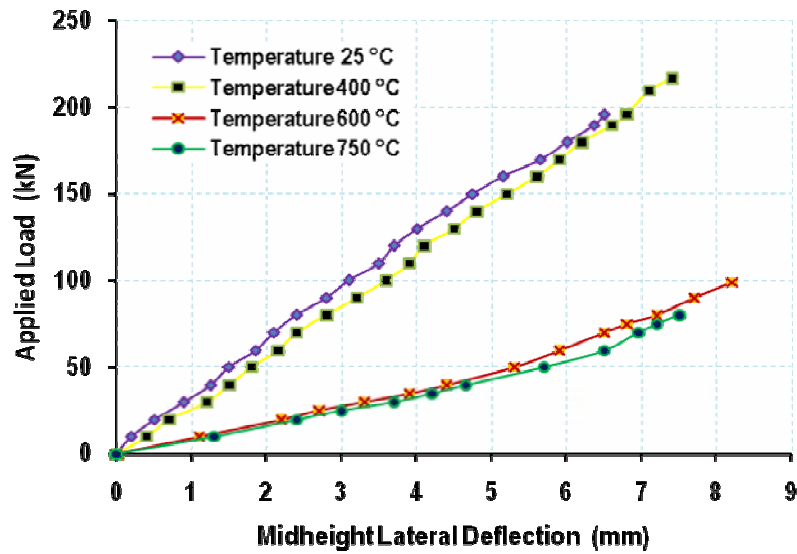


Figure (5): Load versus midheight lateral deflection curve of column specimen A₃₂ at eccentricity (e=80mm).

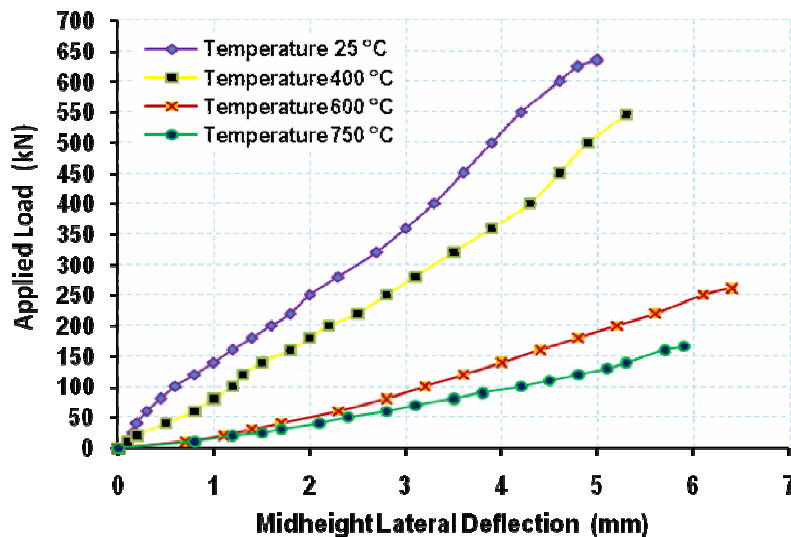


Figure (6): Load versus midheight lateral deflection curve of column specimen B₂₂ at eccentricity (e=30mm).

Table (8): Summary of formulas for predicting axial load column capacity.

Method	Equation	EQ. NO.
ACI-318M-08 Code	$P_n = 0.85f'_c \times A_n + f_y \times A_{st}$	1
B.S 8110-97 Code	$P_n = 0.4f_{cu} \times A_n + 0.75f_y \times A_{st}$	2
Canadian Code-1984	$P_n = 0.51f'_c \times A_n + 0.85f_y \times A_{st}$	3

Where :

A_n = Net concrete area = A_g-A_{st}, mm²

A_{st} = Total area of longitudinal steel reinforcement, mm².

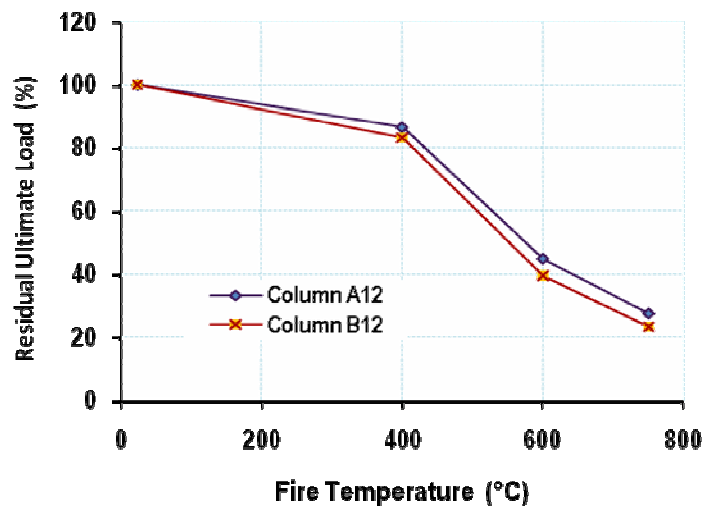


Figure (8): Effect of fire temperature on the residual axial load capacity of column specimens for series A and B.

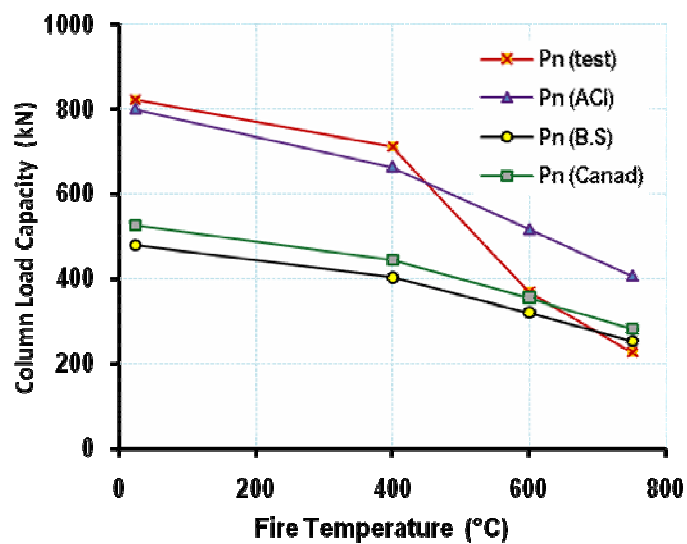


Figure (9): Effect of fire temperature on the axial load capacity of column specimens A12.

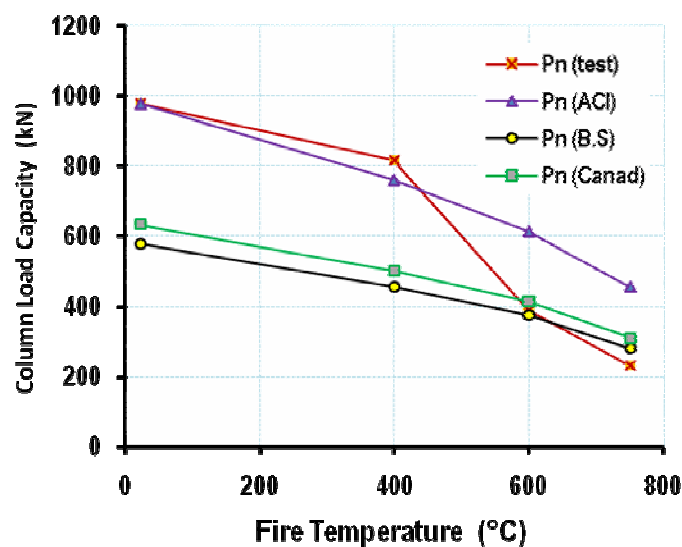


Figure (10): Effect of fire temperature on the axial load capacity of column specimens B₁₂.



1

()

Dr. Saba Jabbar Neama
Dr .Shaimaa Hameed Al- Ahbabi

:_____

) (. ()

) : . (

.(

. (- -) :

)

(

()

Mechanisms of Achieving the Social Sustainability in the Traditional Urban Structure

ABSTRACT

Sustainability as a concept has become one of the basic terms which should be taken in consideration in urban design and urban planning .There is an deficiency in knowledge covering the importance of the social approach and its mechanisims to achieve a contemporary urban structure . Therefore, the main goal of the research is to detect the elements of social sustainability

in the traditional urban structure, using the indicators derived from the theoretical argument to analyze the traditional features of Al Kadhimiya City as a case study.

The research hypothesis is: (The traditional urban structure embraces the elements of social sustainability , Traditional Islamic architecture for example is a sustainable architecture because it has adopted the intellectual aspects of Islam and reflected the cultural, civil and economic aspects of Arab Islamic communities. The research has examined a number of components of social sustainability: (sustainability of kinship system - sustainability of the waqf system - sustainability of the religious factor). Thereby it has determined the conceptual framework for research in three axes. First axis clarify the concept of social sustainability and disclosure of components in the traditional urban structure. The second axis at the general framework of indicators and mechanisms for achieving social sustainability in the traditional urban structure, third axis (the study of applied) and analyze the results of the application.

الكلمات المفتاحية: الاستدامة الاجتماعية - البنية الحضرية التقليدية - الاستدامة الحضرية .

_____ :

(

_____ :

1-1 _____ :

()

)

.(

. (Choucri, 1996, P.3)



(Ibid, P.5) .

):

()

)

(Chen . (

,2008,P.30)

(OISD)

. (

²

(OISD, 2007 ,P.3)

Triple Bottom Line

)

²

(TBL

John)

1997

.(Elkington

Elkington

) :

Elkington,) (

.(1999, P. 75

.(4 1989)

2-1

3-1

_____:

. (Hancock,2008,P.5)

(Hancock-2008)

() Stren, 2005) (Polèse &
(Social Sustainability of
cities)
)

(Polèse & Stren, . (2005, P.2)

(2010 113).

. وجعل المحدّات الثقافية والاجتماعية
اساسا لعملية الاستدامة . (2007 32)



(1977 192)

(2008 7-5).

(1988 73) .

- -

1-3-1

:()

)

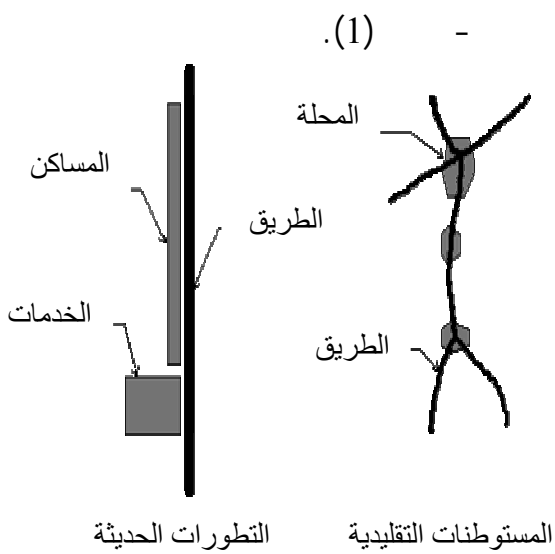
.(118 2010

) :

(16 2001) .(

2-3-1

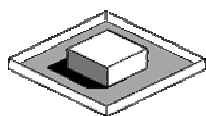
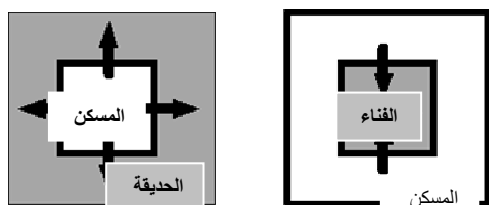
:



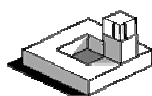
:(1)

(Mahgoub,1997,p.15) :

-(2).
!Error



تصميم المسكن الحديث



تصميم المسكن التقليدي

(Mahgoub, 1997, P.3)

3-3-1

:

:(2)

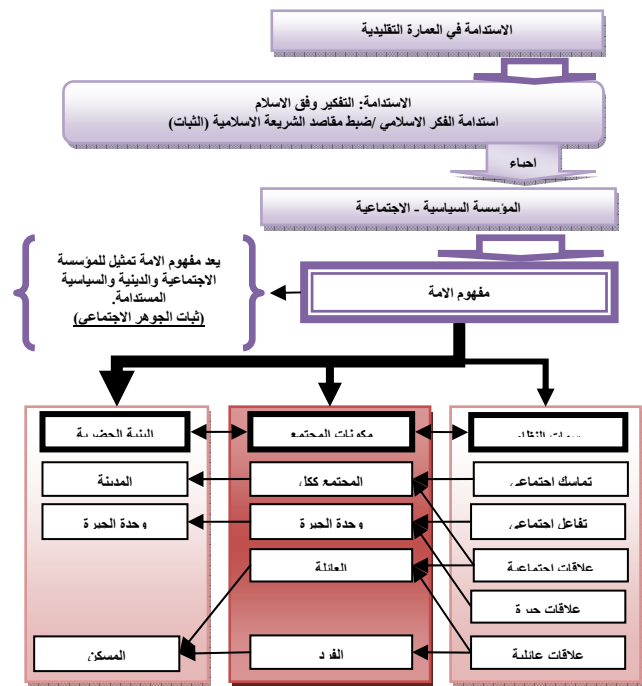
(Mahgoub,1997,p.14) :

-(3)

-(1)

:

1-2



(3) :

المصدر: (الاحبابي، 2010، ص121)



.) - :
-
-
-
) .(
(Hakim, 1991, P.22 :
-
2-2

1-2-2 :
.

.) :
-
-
-
2006) .
(15 - -()
(-
(53)

(1984 51)

(132)

:

-) :

) .(-

(2010 129)

2-2-2 : ()

()



Hamouche, 2007, .

(P.30)

(Mahgoub, 1997, .(5)

P.17)

(Ibid , P.32)

(8 2008) .

3-2-2

. Al-Tassan ,

(Bahobail &2008, P.1)

) ()

)

)

(

(

(

•



2-3

: 1-2-3



Vernacular Settlements

تخطيط حدیث

تخطيط تقليدي

:(5)

(Mahgoub,1997,P.18) :

: 2-2-3

_____ :
: **1-3**

— — —)



(

)

(28)

: 3-2-3

(2) -

-1

(Y1)

:

: 4-2-3

(X1,X2,X3,X4)

()

:

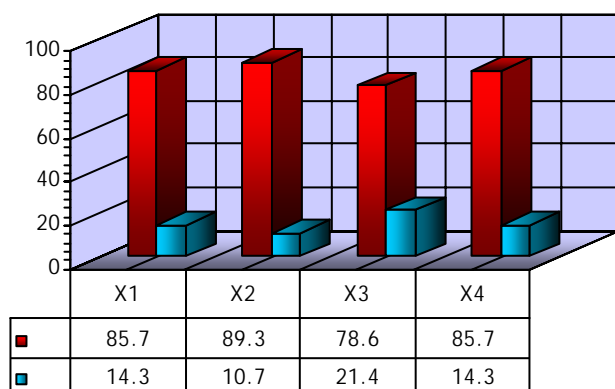
:

■

(%89,3-%78,7)

:

■



(Principle Component (PCA)

Analysis)

-2

(Y2)

:(()

: -

(%89,3)

()

(%60,7)

(X15)

()

(%78,6)

(X16)

(%75)

(X5)

(%75)

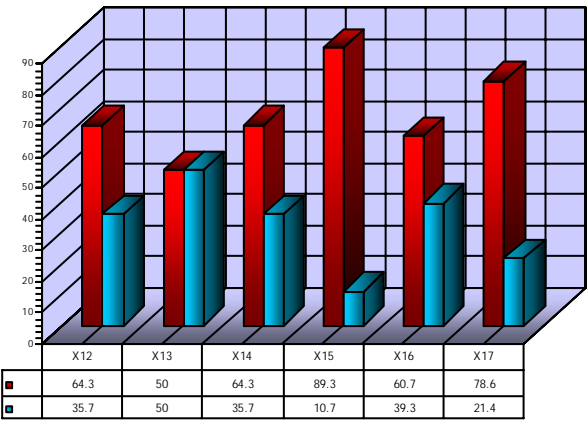
(X6)

(X7)

(X8)

(%78,6)

(%75)



:() (Y4)

-4

()

(X18,X19,X20)

(%42,9 - %35,7)

(%71,4)

(%57,1)

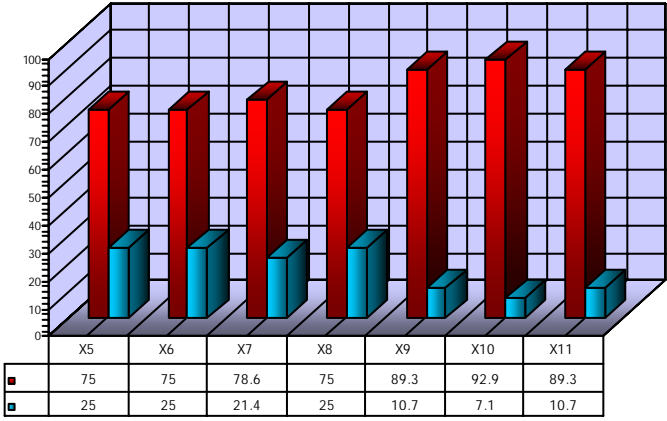
(X21)

(X22)

(X9,X10,X11)

%89,3)

(%92,9 -



:() (Y3)

-3

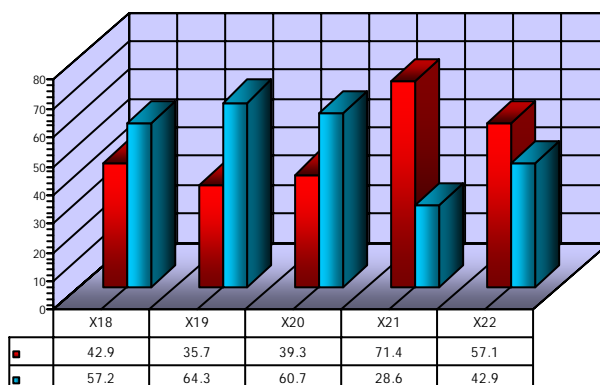
(%64,3)

(X12)

(%64,3)

(X14)

(Principle Component Analysis) (PCA)



(SPSS.10)

(Y5)

-5

:(

:(Y1) -1

(3)

(%85,7-%75)

(X2) (X1)

)

:(Y2) -2

(

(X23,X24,X25,X26)

(%50

(X5)

(4) (4)

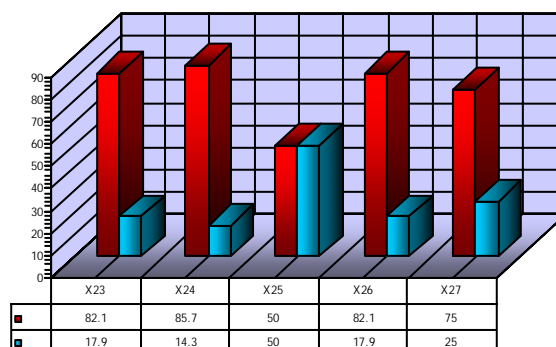
(X27)

(X10)

:(Y3) -3

(5)

(X12) (X17)



:(Y4) -4

(X18)

(6)

.

:

.

-5 (Y5) :

-

(X24) (7)

.

-

_____ :

-

.

.

.

-

-

.

-

()

.

-

_____ :

-

1. Al-Tassan and Bahobail ,MOSQUES AND SUSTAINABILITY, College of Architecture and Planning- King Saud University , Saudi Arabia , **2008**.

Change, UNIVERSITY OF TORONTO PRESS. 2005.

_____) .12

- _____ (_____
_____ / 2010 .

_____ .13

98 - _____
_____ 1989 - .51-35

_____ .14

_____ :36 : [/http://www.ulum.nl](http://www.ulum.nl)
_____ . 2008

_____ .15

_____ 1 (_____)
_____ .2006

_____ .16

_____ .2001

2 _____ .17

_____ .1988

_____ : _____ .18

_____ .1984

_____) : _____ .19

_____ - _____
_____ .2007 (_____

2. Chen, Haiyan, (Sustainable urban form for Chinese compact cities: Challenges of a rapid urbanized economy), Habitat International Vo. 32 (2008), pp.28-40. www.elsevier.com/locate/habitatint

3. Choucri ,Nazli, Sustainability Defined, Massachusetts Institute of Technology, November 1996.

4. Elkington, J, Triple Bottom Line Revolution: Reporting for the Third Millennium, Australian CPA, Vol. 69. p 75. 1999.

5. Hakim, Basim Selim ; Arabic Islamic Cities ; London, England ;1986..

6. Hakim, Basim, Urban Design in Traditional Islamic Culture: Recycling Its Success, Cities, Vol. 8, No. 4, PP. 274-277, 1991.

7. Hamouche ,Mustapha, Sustainability & Urban Management in Old Muslim Cities: The Role of Pious Foundations, J. King Saud Univ., Vol. 19, Arch. & Plann. (2), pp. 27-48, Riyadh (1427H./2007).

8. Hancock ,Trevor, Social Sustainability ,2008

9. Mahgoub, Yasser, Sustainable Architecture In The United Arab Emirates, CAA-IIA International Conference On Urbanism & Housing, GOA, India, October, 1997.

10. Oxford Institute for Sustainable Development (OISD), Social dimensions of sustainable development. 'Measuring Social Sustainability: Best Practice from Urban Renewal in the EU' , Oxford Institute for Sustainable Development, Oxford Brookes University, UK,2007.

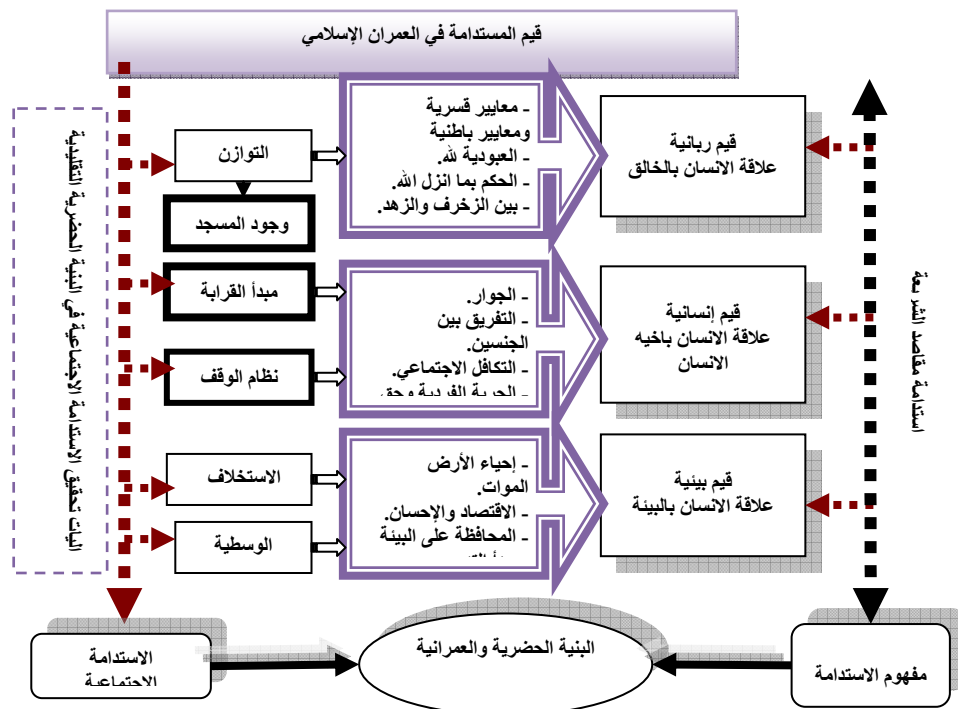
11. Polèse , Mario and Stren ,Richard, THE SOCIAL SUSTAINABILITY OF CITIES- Diversity and the Management of

: (1)

(120 2010):

:	1
()	
()	
()	
:	2

() - ()	
:	
3	
()	
() - ()	



(4):

(127 2010) :

(2)

():

X1				Y1	1
X2					
X3					



X4					
X5		Y21		Y2	2
X6				()	
X7					
X8					
X9		Y22			
X10					
X11					
X12		Y31		Y3	3
X13					
X14		Y32			
X15					
X16					
X17					
X18		Y41		Y4	4
X19					
X20					
X21		Y42			
X22					
X23				Y5	5
X24					
X25					
X26					
X27					

(Y1)

: (3)

(Y1)								
0.2-	0.893	%38.165	%38.165	1.527	1.663	0.799	X1	1
-	0.835	%70.667	%32.502	1.300	1.164	0.732	X2	2
0.185								
0.845	-				0.752	0.716	X3	3
	02.0							
0.742	-				0.421	0.580	X4	4
	0.173							

() - (Y2) :

() - (Y3)							
0.696	%67.948	%67.948	2.718	2.718	0.484	X5	1
0.901				0.787	0.812	X6	2
0.895				0.275	0.801	X7	3
0.788				0.219	0.621	X8	4

() - (Y2) :

() - (Y3)								
-	0.937	%53.033	%53.033	1.607	1.681	0.911	X9	1
0.183								
0.981	-	%92.089	%38.526	1.156	1.082	0.963	X10	2
	2.834							
0.400	0.854				0.237	0.889	X11	3

(Y3) :

(Y4)									
0.229	0.864	0.262	%29.883	%29.883	1.793	2.408	0.867	X12	1
-	0.565	0.638	%56.101	%26.217	1.573	1.278	0.744	X13	2
0.135									
-	-	0.589	%79.577	%23.477	1.409	1.088	0.737	X14	3
0.624	1.204								
0.217	-	0.795				0.632	0.778	X15	4
	0.314								
0.744	-	0.487				0.342	0.813	X16	5
	0.150								
-	-	0.846				0.251	0.836	X17	6
0.167	0.303								

(Y4) :

(Y5)									
0.129-	0.938	%49.021	%49.021	2.451	2.543	0.896	X18	1	
0.133	0.856	%81.530	%32.510	1.625	1.533	0.751	X19	2	
0.192	0.882				0.416	0.816	X20	3	
0.867	0.231				0.368	0.805	X21	4	
896 0	7.994-				0.140	0.809	X22	5	

: (7)

: (8)

.	
.	
.	.
.	.
.) .(
.()	.

ملحق (1) : استمارة استبيان

معلومات عامة عن المبحوث:	
المستوى العلمي:	بكلوريوس () ماجستير () دكتوراه ()
الاختصاص:	معماري () تخطيط حضري () اجتماع () اختصاصات اخرى ()
عدد سنوات السكن في الكاظمية:	منذ الولادة () اكثر من 30 سنة () اكثر من 20 سنة ()
	اكثر من 10 سنوات () اكثر من 5 سنوات ()

التسلسل	الاسئلة	الاجابة
الحالة الاجتماعية للمنطقة		
اولا:	هل يحقق مسكنك العوامل الاتية:	
1	حالة التماسك الاجتماعي مع السكان	لا نعم
2	حالة التفاعل الاجتماعي والمشاركة الاجتماعية	لا نعم
3	حالة التواصل مع اكبر عدد من السكان	لا نعم
4	حالة الشعور بالانتماء للمنطقة	لا نعم

اثر العامل الديني(العقيدة) في السلوك الاجتماعي		
ثانيا:أ-	هل تجد للعامل الديني اثر في:	
1	ضبط السلوك الاجتماعي في المنطقة	لا نعم
2	قوة العلاقات الاجتماعية في المنطقة	لا نعم
3	تعزيز التماسك الاجتماعي بين اجزاء المدينة	لا نعم
4	التفاعل مع فضاءات المدينة	
- ب-	هل وجود الابنية الدينية (المساجد - الحسينيات - الاضرحة وغيرها) اثر في:	
1	تعزيز العلاقات الاجتماعية والمشاركة الاجتماعية	لا نعم
2	تعزيز الشعور بالانتماء للمنطقة	لا نعم
3	زيادة التواصل والتفاعل الاجتماعي من خلال حركتك (اليومية - الاسبوعية - الشهرية) للابنية الدينية	لا نعم

اثر نظام القرباة		
ثالثا:	نظام القرباة و لتشكيل الهيئة الحضرية التقليدية	
1	هل تعتقد ان ان نظام القرباة ما يزال مؤثرا في تشكيل الهيئة الحضرية	لا نعم
2	هل تعتقد بضرورة نظام القرباة لزيادة تماسك اجزاء المدينة	لا نعم
3	هل يوفر وجود اقاربك في منطقتك دعما اجتماعيا لك	لا نعم
4	هل يسكن احد اقاربك في منطقتك السكنية	لا نعم
5	هل كان احدكما سببا في سكن الاخر في المنطقة	لا نعم
6	هل علاقتك الاجتماعية مع اقاربك في المنطقة قوية	لا نعم

نظام الوقف في الاسلام		
رابعاً:	عرفت المدن الاسلامية منذ نشأتها الاولى نظام الوقف	
1	هل تسهم الاوقاف في تحقيق التكافل الاجتماعي	لا نعم
2	هل تسهم الاوقاف في تحقيق العدالة الاجتماعية	لا نعم
3	هل تعمل على تعزيز الروابط الاجتماعية والانسانية	لا نعم
4	هل توجد اوقاف في منطقتك	لا نعم
5	هل مازال بحالة جيدة ومستغلة	لا نعم

خامساً:	هل تعتقد بتحقيق النسيج العضوي المتضام لمد	
	النسيج العضوي للمدينة	



				بنة الكاظمية للحالات الاجتماعية الاتية:	
	لا		نعم	قوة التماسك الاجتماعي لاجزاء المدينة	1
	لا		نعم	قوة العلاقات الاجتماعية بين السكان	2
	لا		نعم	المساواة الاجتماعية والتكافل الاجتماعي	3
	لا		نعم	التفاعل والتواصل الاجتماعي بين السكان	4
	لا		نعم	الحفاظ على الامن الاجتماعي	5



/

/

_____:

)

(

()

Parameters of Safe Environment in High Density Residential Complexes in City Centers

ABSTRACT

Crime is considered one of the important phenomena which was studied on the world level. The interested (planners and architects) tried hard on this phenomenon to establish security. The study of city centers is very important especially those of high population density because of the effect of this phenomenon on human behavior and his sense of security. The research is diagnosed as special

cognitive problem dealing with ingenerality of scientific knowledge about the parameters of safe environment in high density residential complexes in city centers and the effect of crime phenomenon in its different types and the absence of a clear image of what the housing environment had to be in order to be more safe and secure for living. As a result the aim of this research is specified as an attempt to establish general knowledge over planning, designing and social indicators to attain safe environment. The research used the terms (territoriality, surveillance, privacy and social interaction) as supports in investigation of the solution to the research problem enlightened by a hypothetical image that the level of the residents' sense of security in residential complexes increases with the increase in organization at the planning , designing levels within the social parameters. Accordingly, a theoretical base on (crime) phenomenon is established through defining the main concepts, patterns, factors and theories related to it. The results of the research, in its theoretical aspect, led to clear mechanism in achieving the safety phenomenon. This mechanism is formed by applying the planning and designing indicators within the social limitations in high density residential complexes in city centers in order to innovate solutions to attain “ Safe Environments” .

الكلمات المفتاحية:

_____:

_____)

)

(

.(

_____:

:

)

.(



:

:

.1

1

.2

)

. (

. (p.21 2000) .

:

:_____

)

. (Jeffry,1972, p.31) .

.2.1.1.2.1

.(

.1.1.1

)

. (p.8 1990) . (

:

:

.2.2.1

(crime)

. (1990) .

. (p.10

¹ دوركهام (والذي يعد من رواد المدخل البنبي والوظيفي للمدرسة الاجتماعية)

)

. (snatches break-ins burglary

(Violence) . 3

. (p.176 1997) .

3.1 (Urban Crime)

)

. (Pick-Pocketing

.4

. (p.53 ,1999) .

. (Boggs, 1975, P. 450-453).

2.

1.3.1 Types of)

(urban crime

) .

(Vandalism) . 1

(Property Damage

"

. (174 1997

-:

1.2.

) : . 2

(



_____:

(p.17 1997).

_____2.2

:

_____1.2.2

.

.

.

()

(Clinard,1968 , p.53-54.)

_____:

()

(p.15 2007).

_____2.2.2

:

-

(p.68 1981).

_____3.2.2

-

-

:

.(Ethology Approach)

. (p.67 1997) .

.4.2.2

. (Lang, 1987,p. 98) .

.

-)

.5.2.2

(

.(Porteous, 1975,p. 19-21)

(p.21 2002) .

.2.3

.6.2.2

:

Spatial Organization of Urban Land
(Use)
(Jacobs)

. (p.65 2000) .

.3

.1.3

(Territory theory) :



)

.(

:

Ardery, 1966,p. 40-) .

.(44

: 4.3(Environmental Organization Theory)

(Angel)

.(Jacobs,1962,p.168-171).

3.3 (Negative).Space Theory

(Ardery)

(Jacobs)

()

(Ardery)

-1

-3

Angel,) .()

.(1968,p. 50-65

:(Territoriality) :

.5.3 :

(Zones)

(Defensible Space Theory)

(Territorial Influence)

The) .1.5.3

(Defensible Space

1980 Brower

-(Newman)
(Model) "

:(Occupancy) -1

:

:(Defence) 2

:(Attachment) -3

(Identity)

.(Newman, 1972,P.3)."

-(Newman)

"

.(Brower, 1980,p. 186-192)

Natural) :

:(Surveillance

Natural)

(Territoriality)

(Surveillance

.(Ibid,P.4)."

The) .2.5.3

:(Defensible Space Elements



() .(Ibid, 1972,p. 52) .

:

3.5.3

.(Heirarchy in Defensible Space)

(Newman)

:

.(Environmental Image)

(Technique)

(Isolation)

(Stigma)

.(Ibid, 1972,p. 10) .

.(Milieu) :

(Safe Zones)

.(Newman, 1972,p. 80) .

(Newman)

()

- 1 " good Lobby "
- 2 " poor Lobby "

4.

:

1.4.

1.1.4.

3.1.4.

)

(

:

cul-

•
de-sac

2.1.4.



(Hot Spots)

•

(Semi – Public Spaces)

•

.6.1.4 :

.4.1.4 :

.7.1.4

)

.(

(Al Haboubi)

.5.1.4 :

:

-1

-2

-3

(Easy Access)
(Image) (Surveillance
(Newman
(Al Haboubi,1982, p.52-55).

8.1.4

)

(

-1

- 2

2000).

(p.80

2.4 : ()

- 3

1.2.4 :

:



2000) .

. (p.80

. (Wilson,s & Hunter , 1978 ,p. 52-62) .

(Mawby)

.3.2.4

_____ Mawby,) .

Franck

. (1977 ,p. 178

90

.4.2.4

Newman & Franck , 1980, p.83-) .

. (84

: .2.2.4

.5.2.4

)

(

3

12

(2-4)

6.2.4

:

3.4

)

:

(

1.3.4

7.2.4

:

2.3.4

:

8.2.4

:

3.3.4

:



– (peepholes):

:

-
-
-

– :

.2.4.4

.4.3.4 :

(John & Jean)

:

-1

-2

.4.4 :

.1.4.4

. ()

(120m)

(Community Territorial Model)

)

(24 m

(14m)

3.4.4

(1-3m)

:
 •
) (15-30m)

(

• John &) .
 • (Jean ,1989,p.255-295
 -3

4.4.4

)

(

Occupied During the Day)

:

(Time

-
-
-

.5

.1.5

(Guid book,2003,p16)

-



()

2.5

(5-2)

()

)

.(....

3.5

•

•

•

•

•

)

•

(

)

•

(

•

.7

.1.7 :

- Al-Haboubi, Raad, "Planning Out Crime " Montreal, 1982.
- Angle , S., "Discouraging Crime Throuh City Planning " Berkeley: Institute of Urban & Regional Development , University of California , 1968.

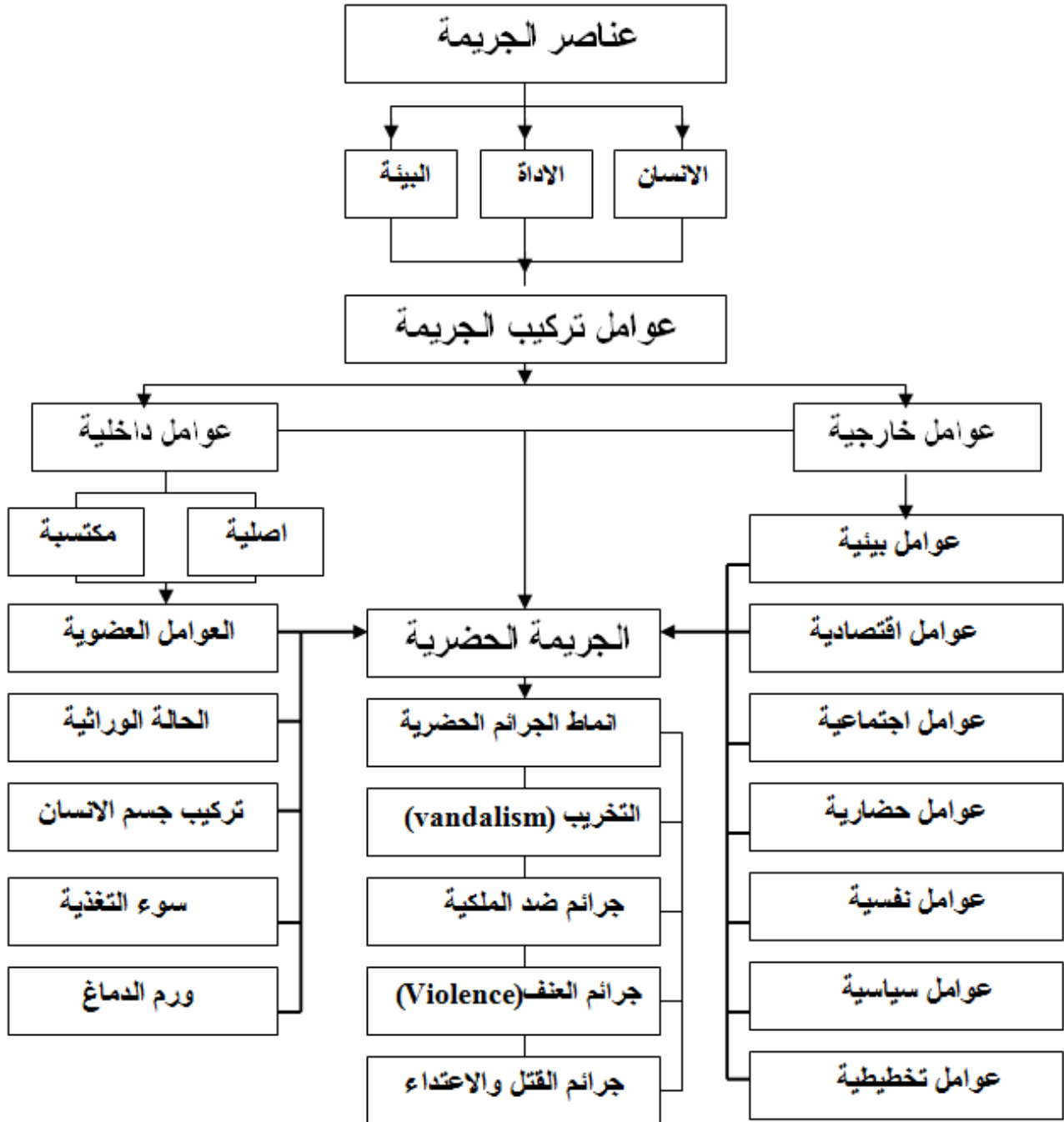
.6 :

•

(Environmental Psychology)

- Mawby, J.B. " **Crime and Urban Pattern**" Sociological Review 16 ,1977.
 - Newman, O. & Franck, K. " **Factors Influencing Crime & Instability in Urban Housing Developments** ", Washington , DC , GPO , 1980.
 - Newman ,O." **Defensible Space: People and Design in the Violent City**, "Architectural Press , London , 1977.
 - Porteous, J. " **Microspace Behaviour: Home Range** " in **Environment and Behavior : Plsnnng and Everyday Life** , 1977 .
 - Reppetto .T.A. " **Residential Crime** " Cambridge , Mass ,Ballinger ,1974.
 - Rubenstein, H. & Murray, C. & Motoyama ,T. & Rouse, W.V. & Titus ,R.M." **The Link Between Crime & the Built Environment** " The Current State of Knowledge .I, National Institute of Tustice , Washington , DC, GPO, 1980.
 - Wilson, S. & Hunter, J." **Updating Defensible Space**" Architects Journal , October 11, 1978.
 - Zahm, Diane, " **Security by Design** ", John Wiley& sons, Ltd ,U.K.,2008.
 - Ardery, R. " **The Territorial Imperative** " New York: Dell Publishers Co ,1966.
 - Boggs , Sarahl . " **Urban Crime Patterns**" American sociological Rev. .30, (A).1975.
 - Clark ,R. " **Crime in America** " . Third printing seman and shuster , N.Y. 1970
 - Clinard, Msrshall B. " **Sociology of Deviant Behavoir 3d edition** " , Rinhart and Winston, N.Y. 1968.
 - Guide book, " **National Crime Prevention Council**" national institute of justice .Washington , D.C. 2003 .
 - Goss, John " **Utopia Versus Dystopia** " , John Wiley& sons, Ltd ,U.K.,2006.
 - Jacobs , Jane " **The Death and Life of Great American Cities**, New York : Mintage Books , 1962.
 - Jeffery , C. Ray " **Crime Prevention Through Environmental Design** " Sage Publications Inc. Beverly Hill – London , 1972 .
 - John, A. & Jean, F.O. " **Neighbourhood Withen the United States** " European and North American Conference on Urban Safety and Crime Prevention , Canada , Montreal , 1989.
 - Lang, " **Creating Architectural Theory : The Role of the Behavioral Sciences in Environmental Design** " Van Nostrand Company, New York, 1987.
- .2.7
- "
- "
- .1999 .

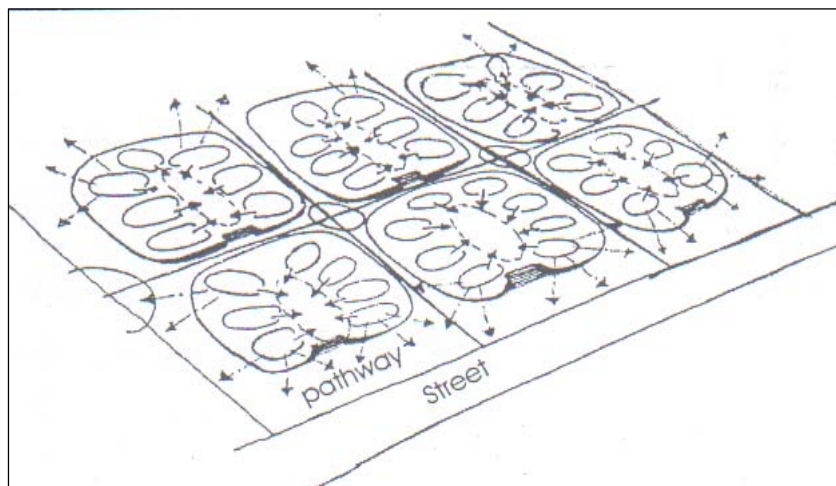
٢٠٠٥	17	—	"	•
		١٥-	"	•
	"		"	•
	"			
	—		2001.	
	2002/		"	•
	"		"	•
—	"			
	—		1996.	
	1997/		"	•
	"		"	•
(405)	"		—	
	1997.			2007.
	"		—	•
	—		—	
			1981)	
—	—	"	(•
2000/		"		•
"		"	"	
		"	"	
		—		
1990				



(1)

(p.67 1997) - /

(p.65 2000) -



(2)

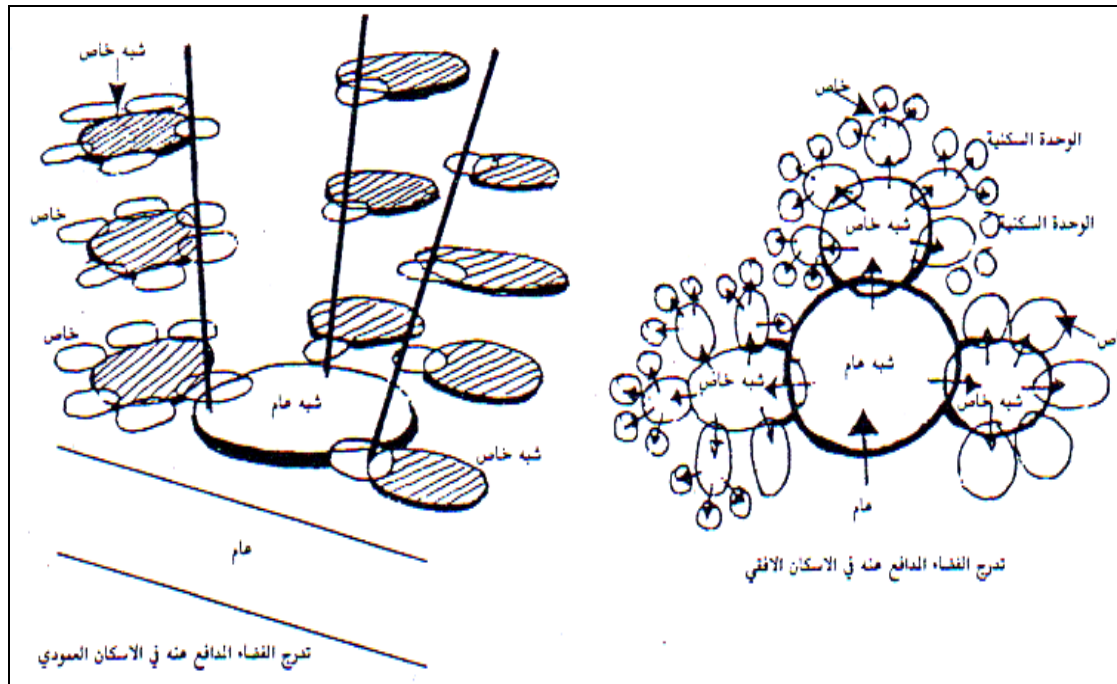
(Newman, 1972, p. 9)

(1)

Newman

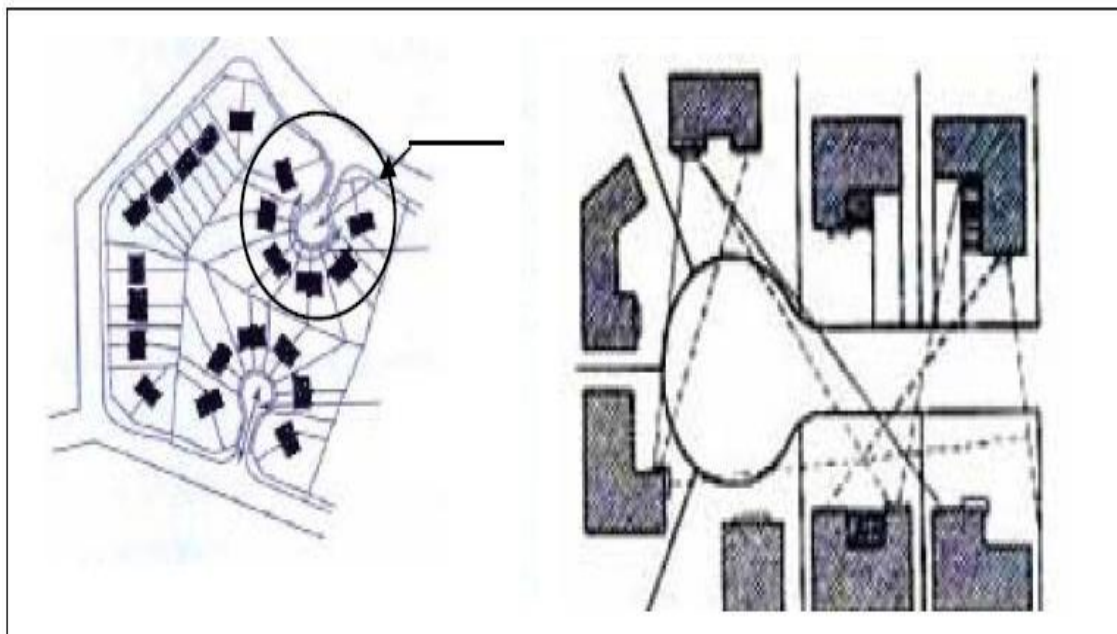
(Newman, 1972, p. 10)

المستويات	نوع الفعالية	فضاء عام	فضاء شبه عام	فضاء شبه خاص	فضاء خاص
اسكان افقي		الفعاليات والخدمات العامة في المحلة السكنية	الشارع السكني والفضاءات المشتركة لسكان الشارع	الحديقة الخاصة والرصيف امام الدار	فضاءات الوحدة السكنية
		الفضاءات والفعاليات الرئيسية في المشروع والشوارع الرئيسية	مدخل العمارة وفضاء المصاعد الرئيسي ومدخل المشروع	الدرج \ المصعد والممرات التي تربط الشقق السكنية	فضاءات الشقة السكنية



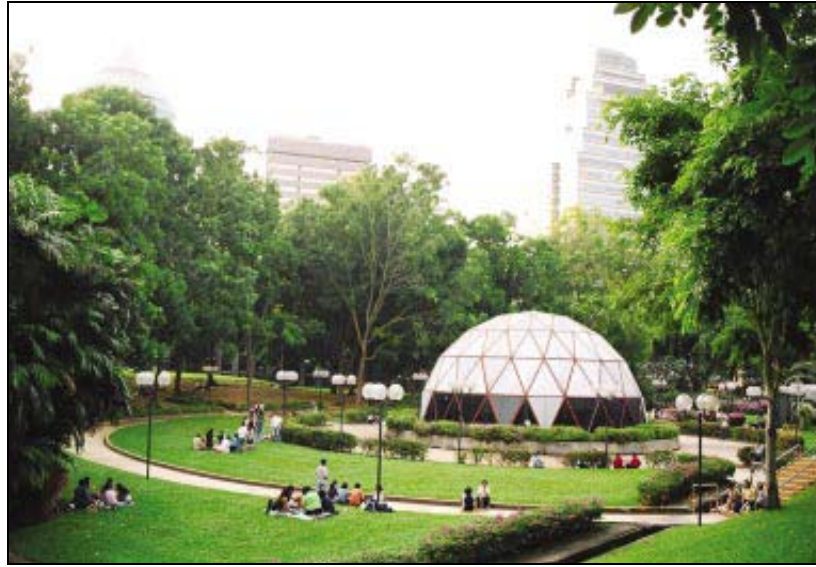
(3)

(Newman, 1972,p.9)



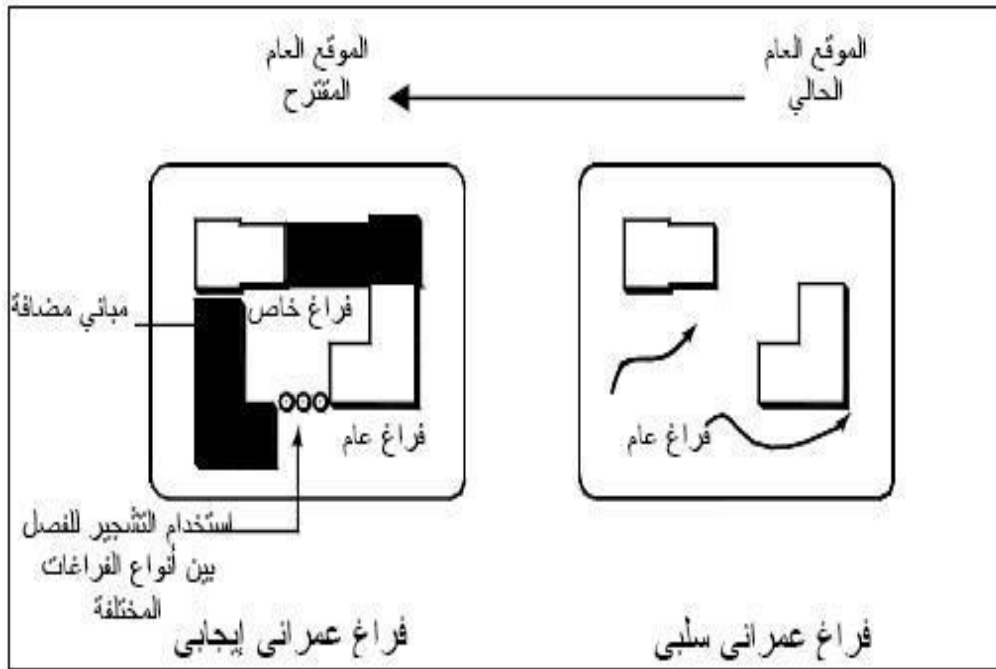
(4)

. p.8 , 2005 ,) .



(5)

المصدر / (Guid book, 2003, p11)



(6)

(12 2005)



(7)

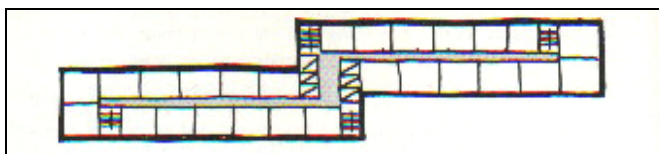
المصدر / (Guid book,2003,p15)



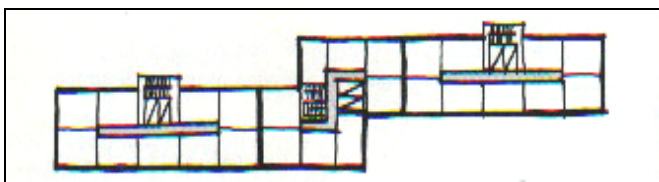
(8)

. المصدر / (Guid

(book,2003,p18



A



B

:

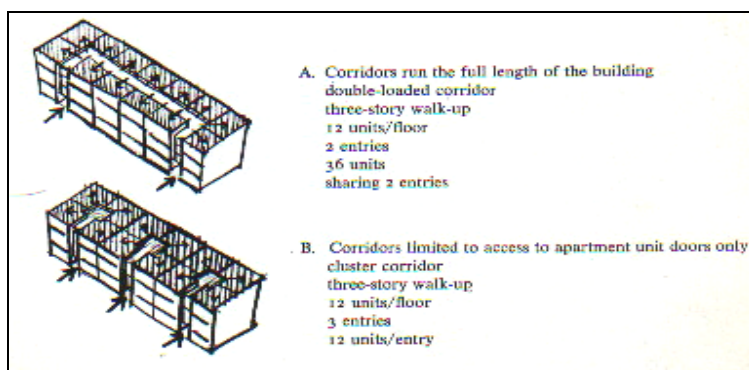
(9)

: A

3

: B

(Newman,1972,p.74) /



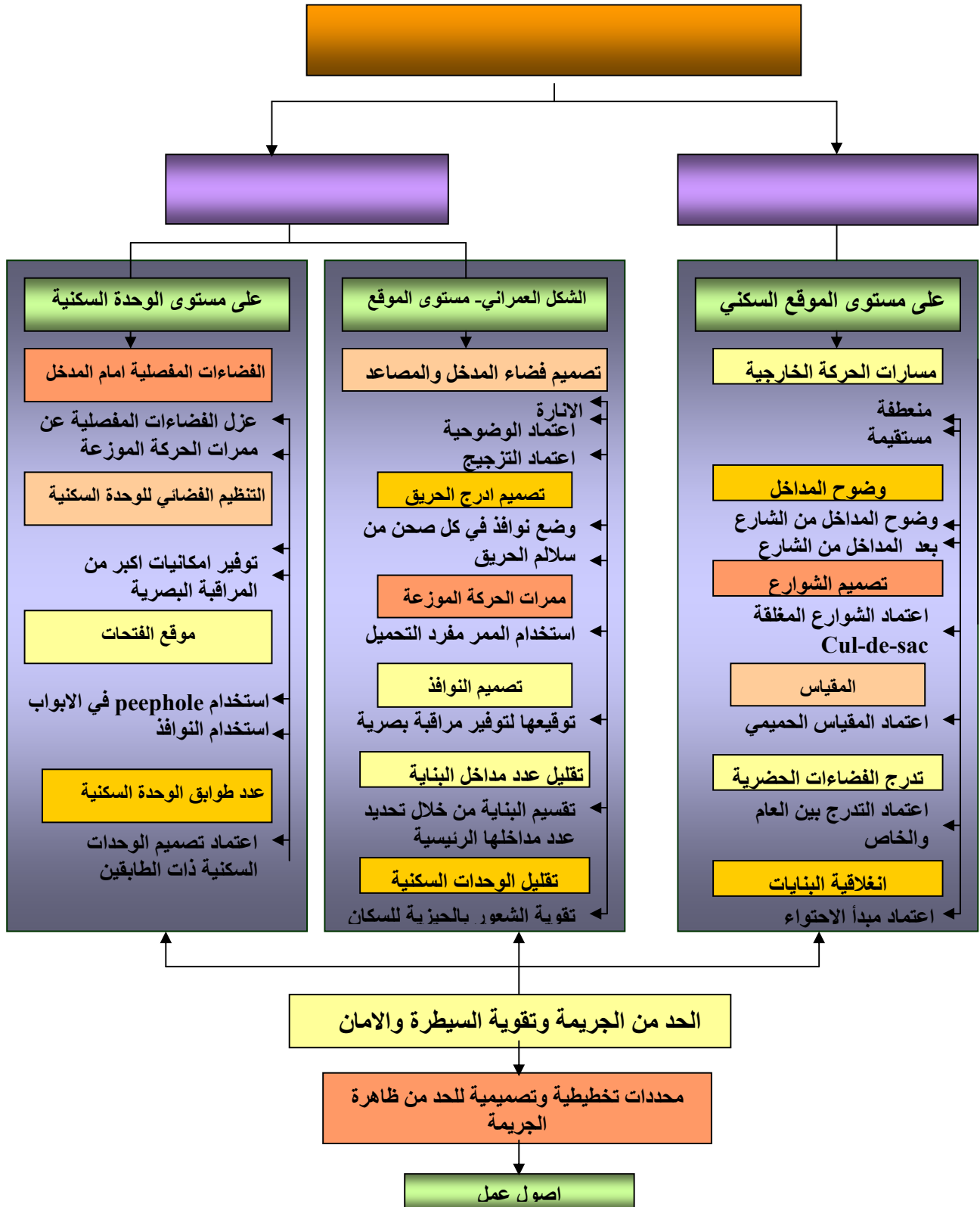
(10)

:

: A

: B

(Newman,1972,p.71) / . ()



في مناطق حدوثها (اعداد

مخطط رقم (1) يوضح

(البحث)



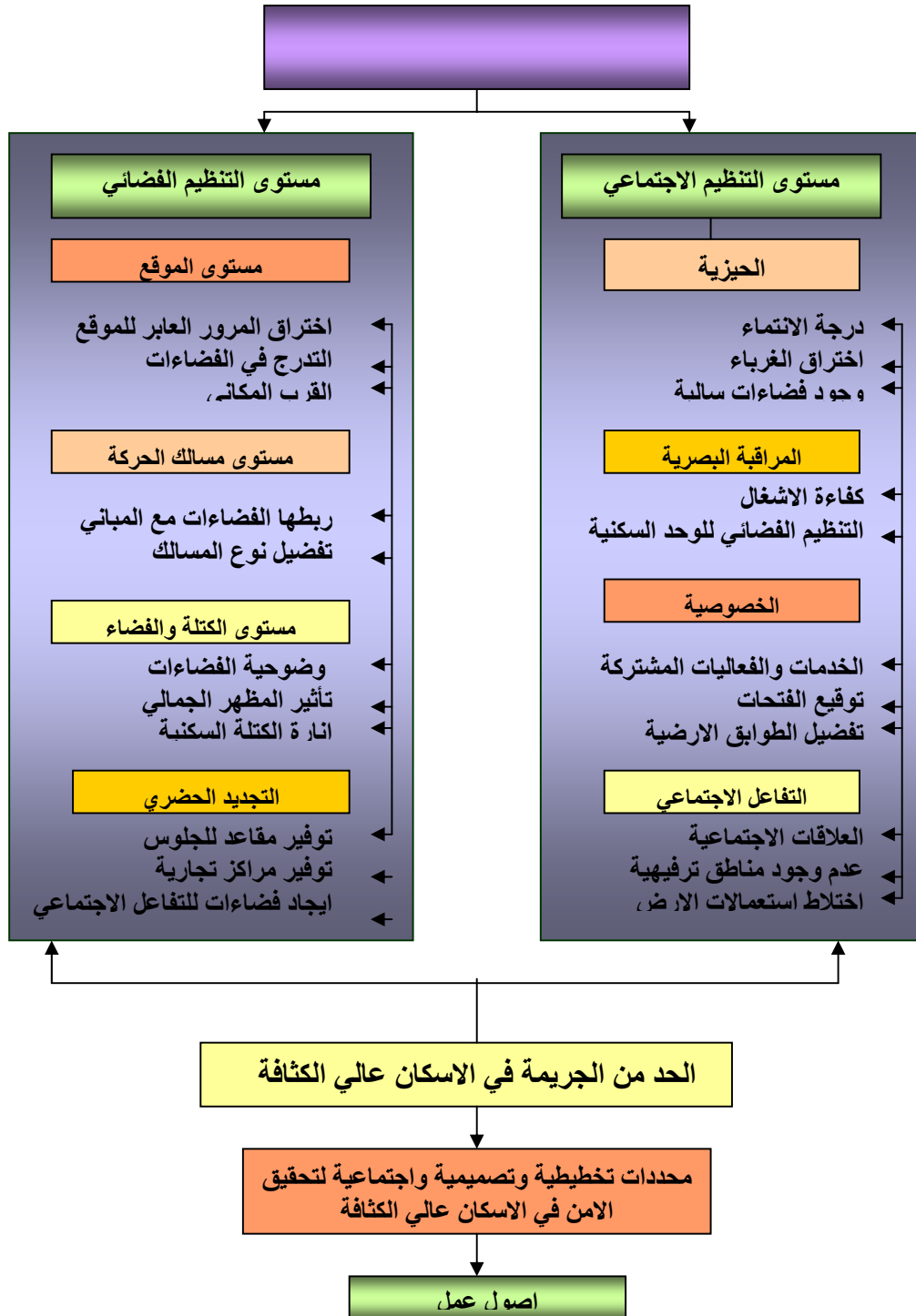
(11)

المصدر / (Guid book,2003,p23)



(12)

المصدر / (Guid book,2003,p29)



مخطط رقم (2) يوضح



ESTIMATION OF RELATIONSHIP BETWEEN COEFFICIENT OF CONSOLIDATION AND LIQUID LIMIT OF MIDDLE AND SOUTH IRAQI SOILS

Asma Y. Al- Tae'e

Lecturer, Civil Eng. Dept.

College of Eng./ University of Baghdad

Email: Asmayounis2004@yahoo.com

Abbas F. Al- Ameri

Assistant Lecturer, Civil Eng. Dept.

College of Eng./ University of Baghdad

Email: Abfcivil@yahoo.com

ABSTRACT

In this paper, a relationship between the liquid limit and the coefficient of consolidation of Iraqi soils are studied. The samples of soil used in study are undisturbed silty clay. These samples are taken from different locations and depths of Middle and South of Iraq by cooperation with Consulting Engineering Bureau- University of Baghdad- College of Engineering. The depth reached about 20 meters. The experimental work is made to calculate the liquid limit and the coefficient of consolidation. From these sites, 280 points are obtained. The relationship between the liquid limit and the coefficient of consolidation is drawn as a curve. This curve is studied and compared with the curve that obtained from other studies.

From these curves, it can be noticed that the curves are close to each other when the liquid limit is equal to 60 while they diverge when the liquid limit is less or greater than 60. Therefore, the coefficient of consolidation of Iraqi soils can be obtained when the liquid limit is given.

:

20

280

.60

60

Keywords: Liquid limit, Coefficient of consolidation, clay, Iraq, relationship.

INTRODUCTION

Attention was first drawn to the problem of the long term consolidation of clays by Terzaghi (1925), with the publication in Vienna of "Erdbaumechanik". Terzaghi proposed a theoretical approach to the consolidation process, and he had already designed the first

consolidation apparatus which he had named an "oedometer". (Head, 1988)

In the field, when the stress on a saturated clay layer is increased – for example, by the construction of a foundation- the pore water pressure in the clay will increase. Because the hydraulic conductivity of clays is very small,

sometimes will be required for the excess pore water pressure to dissipate and the increase in stress to be transferred to the soil skeleton. (Das,2007), (Head, 1986).

Sometimes consolidation is called *primary consolidation* to distinguish it from the other time- dependent component of total settlement, *secondary compression* occur after essentially all of the excess pore water pressure has dissipated, that is, it occurs at constant effective stress. In some soils, especially inorganic clay, primary consolidation is the largest component of total settlement, whereas secondary compression constitutes a major part of the total settlement of peats and other highly organic soils (Holts and Kovacs, 1981).

DETERMINATION OF THE COEFFICIENT OF CONSOLIDATION C_v :

(a) Casagrande's Logarithm of Time Fitting Method:

In this method, the deformation dial readings are plotted versus the logarithm of time, as shown in **Fig.(1)**. The idea is to find R_{50} and thus t_{50} , which is the time for 50% consolidation, by approximating R_{100} , the dial reading corresponding to the time for 100% primary consolidation, t_{100} . Refer to **Fig.(1)**, the intersection of the tangent and the asymptote to the theoretical curve defines $U_{ave} = 100\%$. The time for 100% consolidation, of course, occurs at $t = \infty$. Casagrande (1938) suggested that R_{100} could be approximated rather arbitrarily by the intersection of the two corresponding tangents to the laboratory consolidation curve. Later research (for example, Leonards Girault, 1961) has shown this procedure defines to a good approximation the dial reading at which the excess pore water pressure approaches zero, especially when the LIR is large and the preconsolidation stress is exceeded by the applied load increment. Once R_{100} is defined, then it is fairly easy to determine R_{50} and t_{50} , once we find R_0 ,

the initial dial reading. Therefore, the coefficient of consolidation is:

$$C_v = 0.197 * H^2 / t_{50}$$

Where:

H= the average height of specimen during the increment (for one way drainage)

H= the average height of specimen during the increment/2 (for two way drainage)

(b) Taylor's Square root of Time Fitting Method:

Taylor (1948) also developed a procedure for evaluating c_v , using the square root of time. It will be used the same data as before in Casarande's method to illustrate the square root of time t fitting method. These data are plotted in **Fig.(2)**. Usually a straight line can be drawn through the data points in the initial part of the compression curve. The line is projected backward to zero time to define R_0 . The common point at R_0 may be slightly lower than the initial dial reading (at zero time) observed in the laboratory due to immediate compression of the 1.15 times as large as corresponding values on the first line. The intersection of this second line and the laboratory curve defines R_{90} and is the point of 90% consolidation. Its time is t_{90} . The coefficient of consolidation is (Holts and Kovacs,1981):

TYPICAL VALUES OF C_v :

Typical values of the coefficient of consolidation c_v for a variety of soils are listed in **Table(1)**. Approximate correlation of c_v with the liquid limit are presented in **Fig.(3)** (Holtz and Kovacs, 1981).

ATTERBERG LIMITS:

The condition of a clay soil can be altered by changing the moisture content; the softening of clay by the addition of water is a well- known example. For every clay soil there is a range of moisture contents within which the clay is of a plastic consistency, and the Atterberg limits provide a means of measuring and describing the plasticity range in numerical terms.

If sufficient water is mixed with clay, it can be made into slurry, which behaves as a viscous

liquid. This is known as the 'liquid' state. If the moisture content is gradually reduced by allowing it to dry out slowly, the clay eventually begins to hold together and to offer some resistance to deformation; this is the 'plastic' state. With further loss of water the clay shrinks and the stiffness increases until there is little plasticity left, and the clay becomes brittle; this is the 'semi-solid' state. As drying continues, the clay continues to shrink in proportion to the amount of water lost, until it reaches the minimum volume attainable by this process. Beyond that point further drying results in no further decrease in volume, and this is called the 'solid' state.

These four states, or phases, are shown in diagrammatically in **Fig.4**. The change from one phase to the next is not observable as a precise boundary, but takes place as a gradual transition. Nevertheless three arbitrary but specific boundaries have been established empirically, as indicated in **Fig. 4**, and are universally recognized. The moisture contents at these boundaries are known as the

Liquid limit (LL)

Plastic limit (PL)

Shrinkage limit (SL)

The moisture content range between the PL and LL is known as the plasticity index (PI) and is a measure of the plasticity of the clay. Cohesionless soils have no plasticity phase, so their PI is zero (Head, 1984)

Liquid Limit- Casgarande One Point Method:

This method provides a quick means of determining the liquid limit of a soil, because only one moisture content measurement is needed (Head, 1984).

The one- point liquid limit test is based on research conducted on a large number of soil sample by the U. S. waterway experiment station, Vicksburg Mississippi. It was determined that the liquid limit could be established from single test using the following equation:

$$LL = w_N \left(\frac{N}{25} \right)^{0.121}$$

N is the number of drops required to close the standard groove at water content w_N . N should be between 20 and 30 and preferably close to 25, otherwise the test should be repeated. This test is dependent on the accuracy of the one point. It is more difficult to run than the multipoint test, because one must be confident that the groove will close within the range of drops specified. This requires the sample be mixed at water content close to its liquid limit. The one- point test may be conducted on dry or wet samples using the sample preparation procedure described earlier (Al- Khafaji and Andersland, 1992).

EXPERIMENTAL WORK

Many locations in Middle and South of Iraq are studied. These studies are made to determine the liquid limit and the coefficient of consolidation. The liquid limit is determined by using Casgarande one point method. The coefficient of consolidation is determined by using Taylor's square root of time method and under normal stress equal to 200 kpa. The samples are silty clay soils. These samples are undisturbed and they are taken from different depth by cooperation with Consulting Engineering Bureau-University of Baghdad- College of Engineering.

RESULTS AND DISCUSION

The number of sites for each Governorate is shown in **Table (2)**, **Fig.(5)** (State Company of Geological Survey and Mining) and **Fig.(6)** .

From these samples, 280 points are obtained. According to these points, the relationship between the liquid limit and the coefficient of consolidation for silty clay soils of Iraqi soil can be drawn as shown in **Fig. (6)**.

Table (3) shows the correlation coefficients and statistical information for the data used in this paper.

From **Fig.(6)** and **Table (3)**, the following statements can be concluded:

1. For cohesive soils, the physical properties must be found. The first experimental work is the Atterberg Limit so the coefficient of consolidation of Iraqi soil can be directly

evaluated if the liquid value of the soil is given.

2. The relationship can be expressed by the following equation:

$$C_v = 4258 X^{(-1.75)}$$

Comparing the data that obtained from Iraqi soil (**Fig.6**) and the data that obtained from other studies (Navy study) (**Fig. 3**), it can be noticed that the curves are approach one another when the liquid limit is equal to 60 while they are diverge when the liquid limit is less or greater than 60. The comparison is cleared in **Fig.7**

The frequency histograms for coefficient of consolidation and liquid limit are shown in **Fig. 8**. From the frequency histograms, it appears realistic to assume a normal distribution.

CONCLUSIONS

Based on the results, the following conclusion can be drawn:

- 1- For Middle and South Iraqi soils the relation between liquid limit and coefficient of consolidation is established. So, the coefficient of consolidation can be obtained when the liquid is given.
- 2- The two curves are (the curve is obtained from Iraqi soils and the curve is obtained from Navy study) approach one another when the liquid limit is equal to 60 while the two curves are diverge when the liquid limit is less or greater than 60.
- 3- The relationship can be expressed by the following equation:
 $C_v = 4258 X^{(-1.75)}$
- 4- For experimented soils, the liquid limit is changed from 25- 65 %.
- 5- For experimented soils, the coefficient of consolidation is changed from 2.3- 12.3 m²/yr.

REFERENCES

- Al- Kafaji, A. W., and Adersland, O., B., "Geotechnical Engineering and Soil Testing", 1992.
- Casagrande, A., "Note on Soil Mechanics-First Semester", Harvard University (Unpublished), 1938.
- Consulting Engineering Bureau- University of Baghdad- College of Engineering.
- Das, B., M., "Principles of Foundation Engineering", Sixth Edition, 2007.
- Head, K. H., "Manual of Soil Laboratory Testing", Volume 1, 1984.
- Head, K. H., "Manual of Soil Laboratory Testing", Volume 2, 1988.
- Head, K. H., "Manual of Soil Laboratory Testing", Volume 3, 1986.
- Holtz, R., D., and Kovacs, W., D., "An Introduction to Geotechnical Engineering", 1981.
- Leonards, G. A., and Girault, P., "A Study of the One- Dimensional Consolidation Test", Proceedings of the Fifth International Conference on Soil Mechanics and Foundation Engineering, Paris, Volume 1, pp- 116- 130, 1961.
- Navy, U. S., "Soil Mechanics, Foundations, and Earth Structures", NAVFAC Design Manual DM- 7, Washington, D.C., 1971.
- Terzaghi, K., "Erdbaumechanik auf bodenphysikalischer Grundlage, Deuticke, Wien", 1925.
- Taylor, D. W., "Fundamental of Soil Mechanics", John Wiley and sons, Inc., New York, 700 pp, 1948.

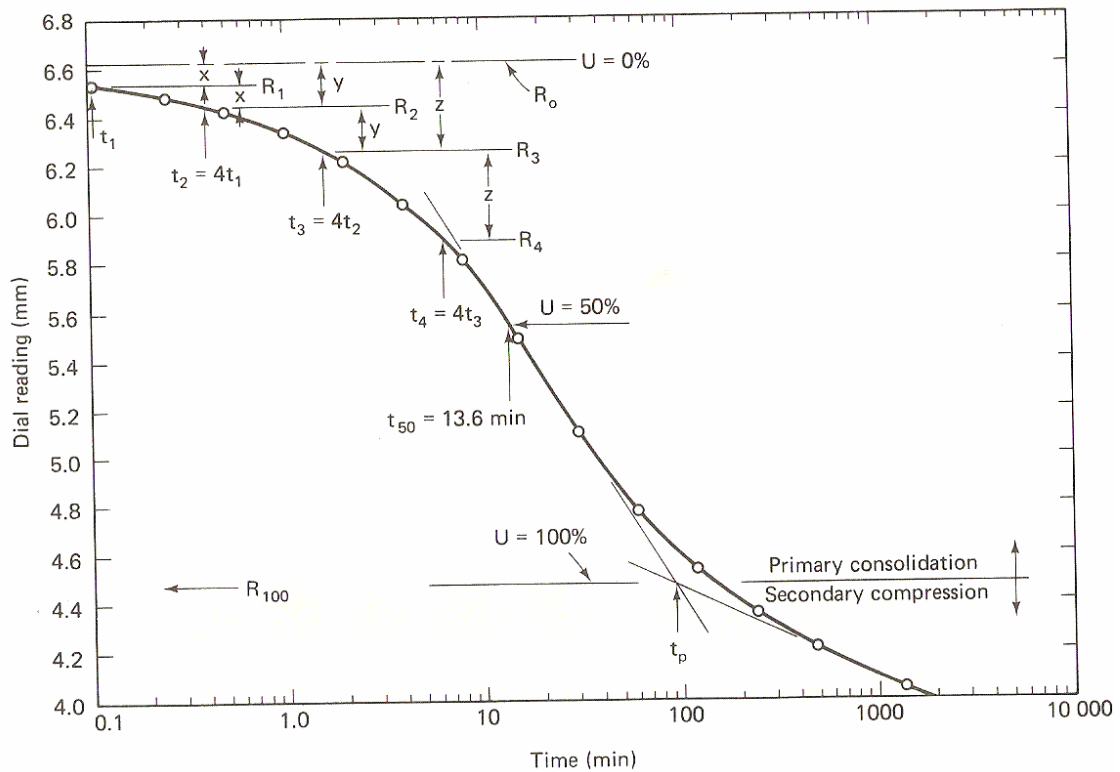


Figure (1) Determination of t_{50} by the Casagrande method (Holts and Kovacs,1981).

$$C_v = 0.848 H^2 / t_{90}$$

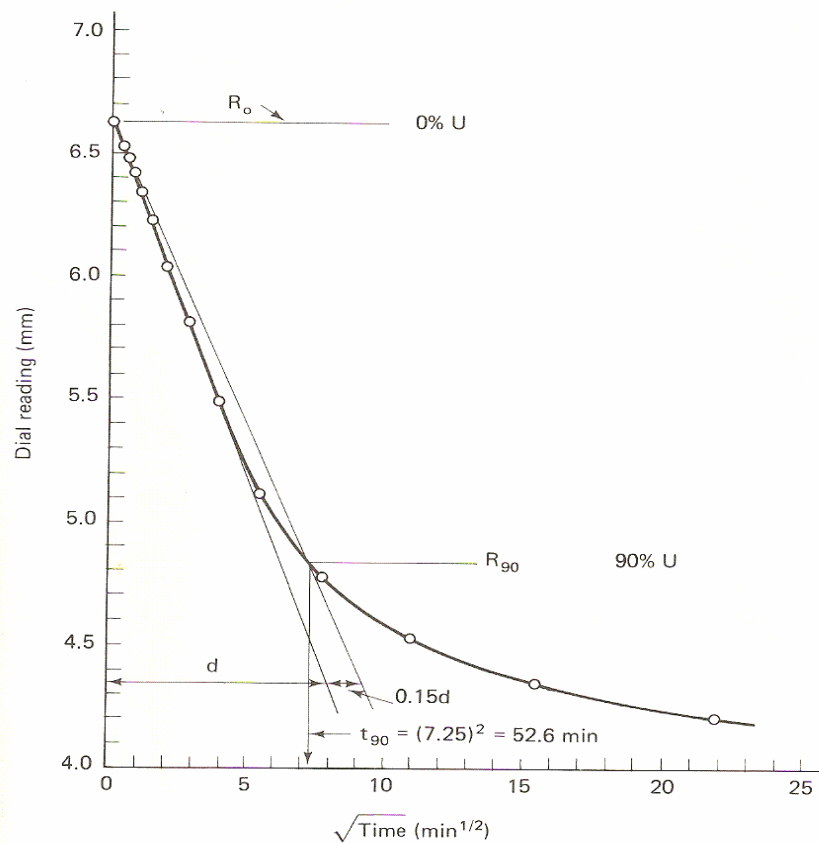


Figure (2) Determination of c_v using Taylor's square root of time method (Holts and Kovacs,1981)

Table(1) Typical values of the coefficient of consolidation c_v (from Holtz and Kovacs, 1981).

Soil	C_v ($m^2/year$)
Boston blue clay (CL) (Ladd and Luscher, 1965)	12 + 6
Organic silt (OH) (Lowe, Zaccheo, and Feldman, 1964)	0.6 -3
Glacial lake clays (CL) (Wallace and Otto, 1964)	2 – 2.7
Chicago silty clay (CL) (Terzaghi and Peck, 1967)	2.7
Swedish medium sensitive clays (CL-CH) (Holtz and Broms, 1972)	
1- Laboratory	0.1 – 0.2
2- field	0.2 - 1.0
San Francisco Bay Mud (CL)	0.6 – 1.2
Mexico City clay (MH) (Leonards and Girault, 1961)	0.3 – 0.5

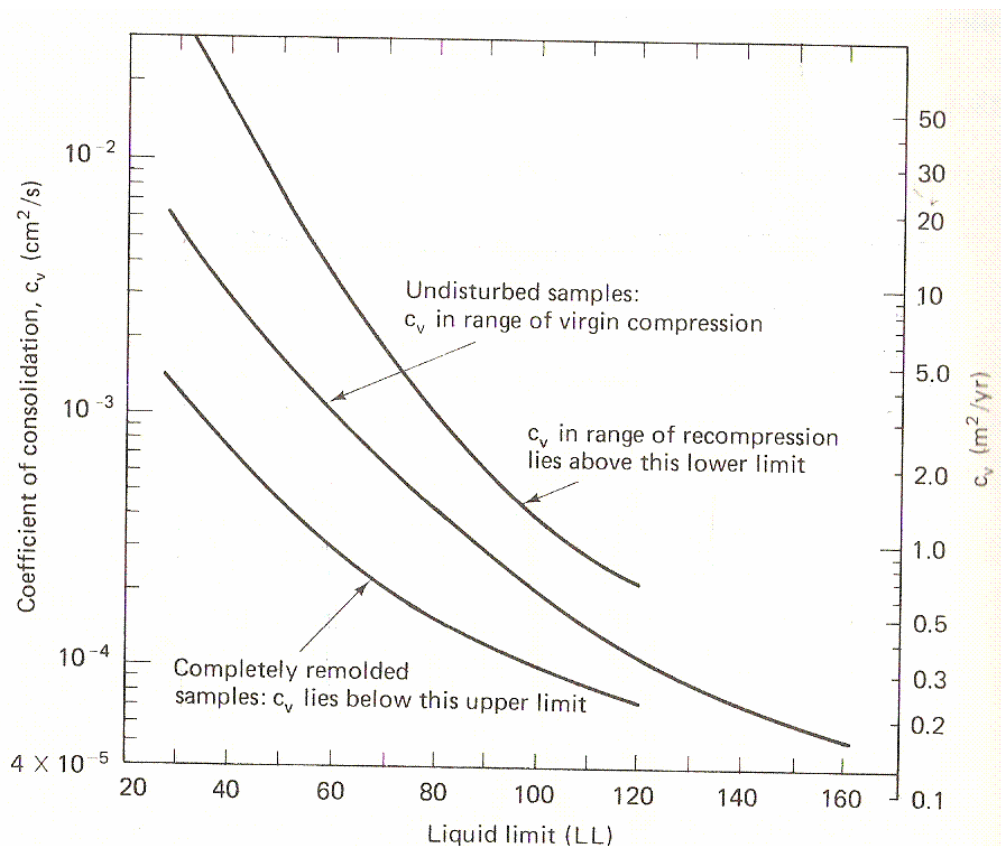


Figure (3) Approximate correlations of the coefficient of consolidation c_v with the liquid limit (after U. S. Navy, 1971).



Phase	Solid State	Semi-Solid State	Plastic State	Liquid Limit	Suspension
Water	Water content decreasing				
Limits	Dry soil	Shrinkage Limit SL	Plastic Limit PL	Liquid Limit LL	
Shrinkage	Volume constant	Volume decreasing			
Condition	Hard to stiff	Workable	sticky	Slurry	Water-held suspension
Shear Strength (kN/m ²)	Shear strength increasing (≈ 170) (1.7)			Negligible to nil	
Moisture content	SL	PL	LL		

Figure 4 Phases of soil and the Atterberg limits (Head, 1984)

Table 2 Number of sites for each Governorate in Iraq.

Governorate	Number of locations
Baghdad	26
Babil	2
Wassite	6
Karbala	4
Anbar	1
Missan	10
Qadissiya	3
Najaf	1
Thi- Qar	5
Muthanna	0
Basrah	2

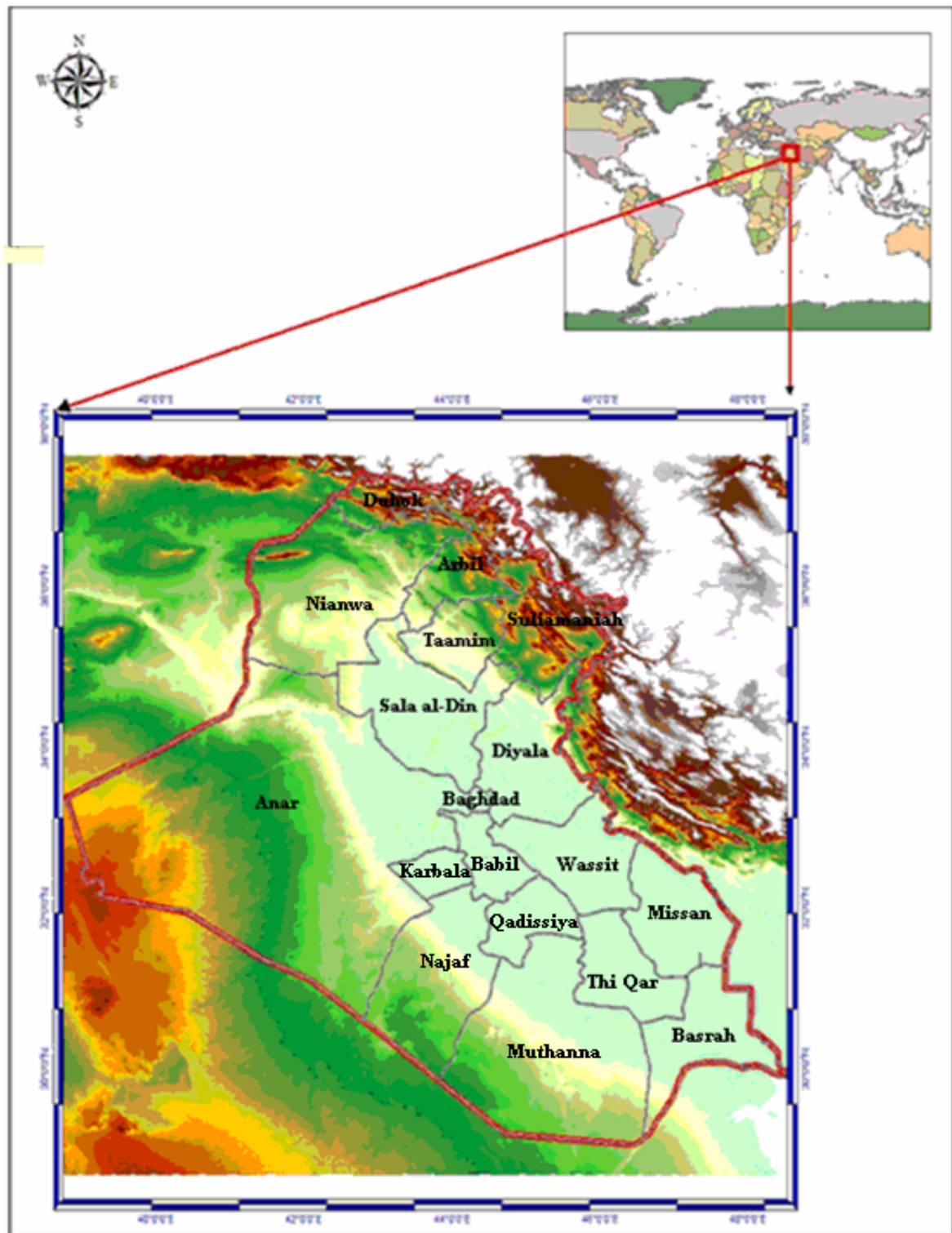


Figure (5) Map of Iraq (State Company of Geological Survey and Mining)

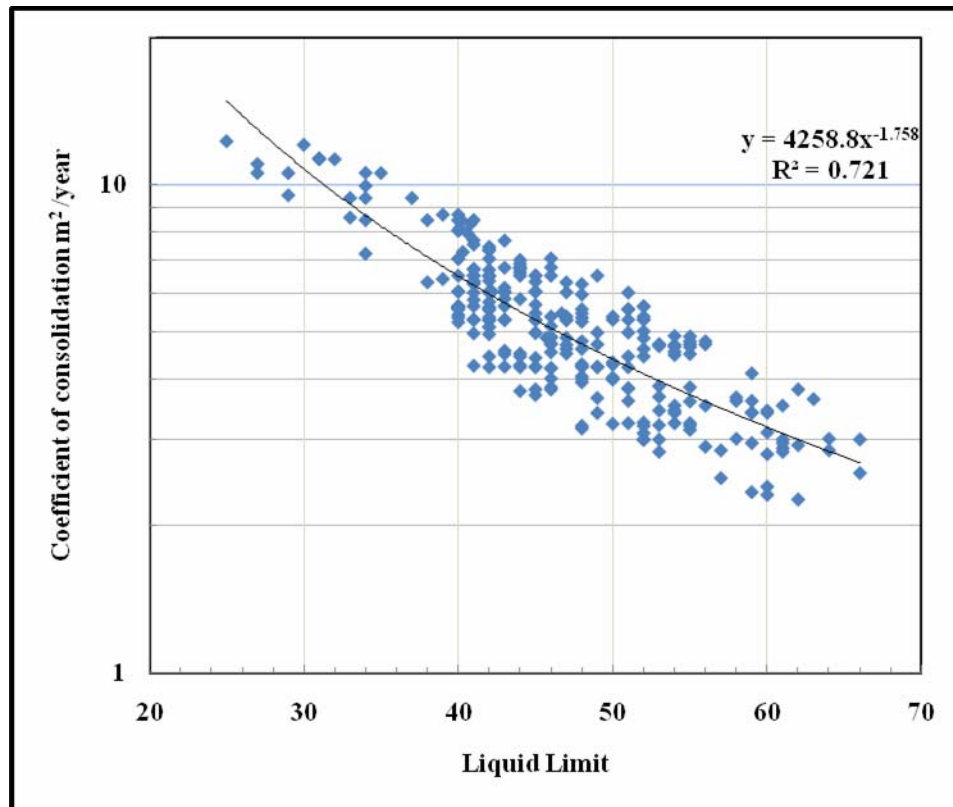


Figure 6 The relationship between the liquid limit and the coefficient of consolidation for Iraqi soils

Table (3) statistical information for the database of liquid limit and coefficient of consolidation

Power fitting used (general expression)	$Y = A X^B + C$
Resulting equation	$C_v = 4258 X^{(-1.75)}$
Number of data	280
Maximum liquid limit value (LL)	25
Minimum liquid limit value (LL)	68
Maximum coefficient of consolidation (C_v)	2.3
Minimum coefficient of consolidation (C_v)	12.3
Coefficient of determination, R^2	0.721

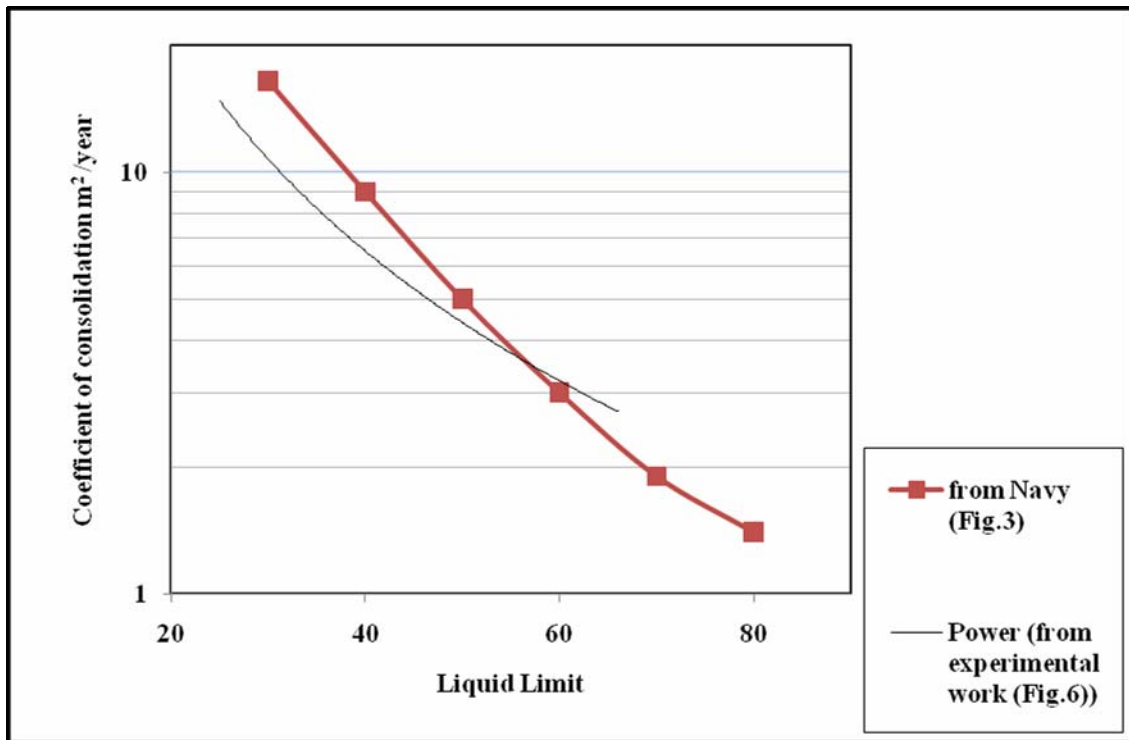
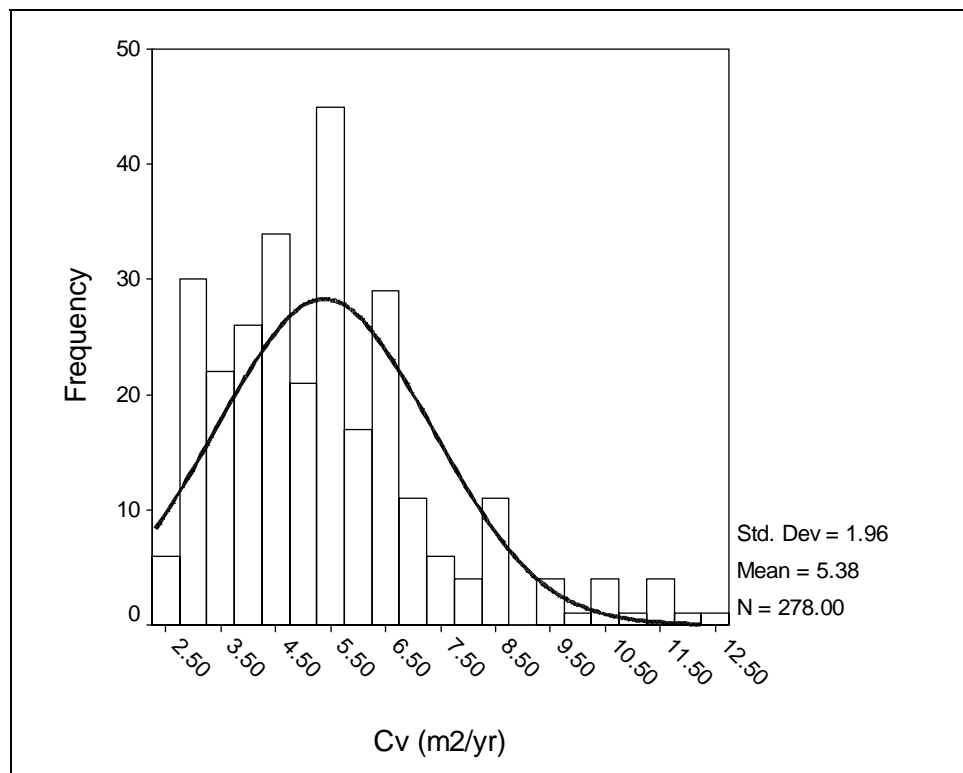
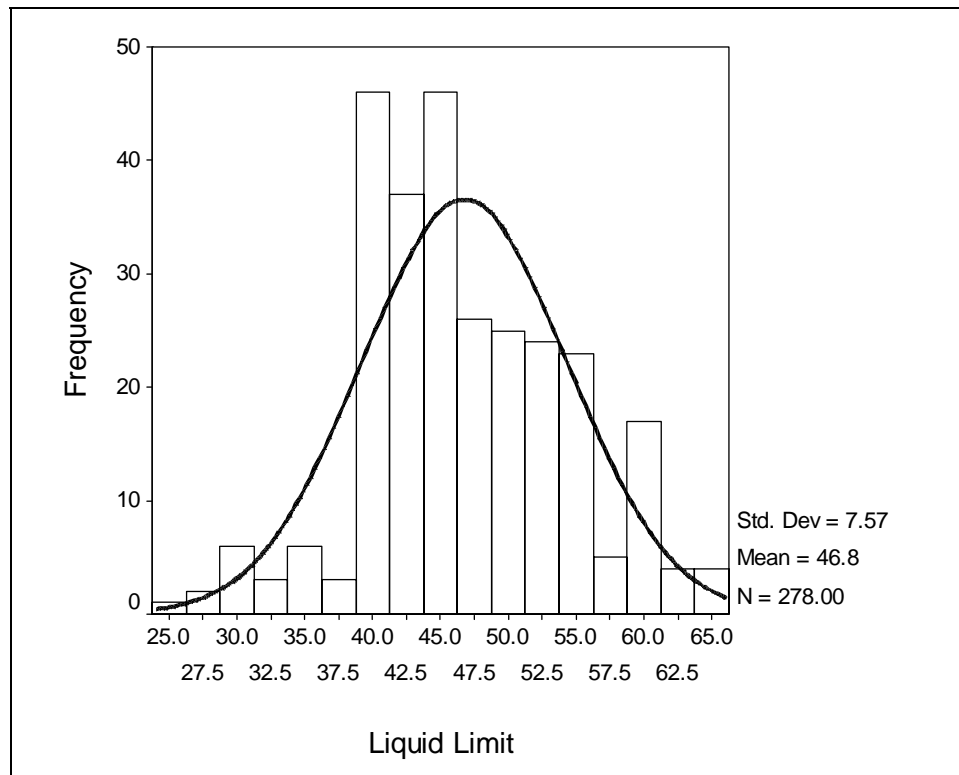


Figure 7 the comparison between experimental work and Navy study



(a)



(b)

Figure 8 (a) Frequency histogram for coefficient of consolidation (b) Frequency histogram for liquid limit.



THE GEOTECHNICAL MAPS FOR THE SOILOF THE GOVERNORATES BAGHDAD, DIYALA, WASIT AND BABYLON

_____:

(15 m) ("... 7,5,3,1 " m)

()

)

() (

(64)

(138)

.(1 : 100000)

(74) (1 : 1500000)

ABSTRACT

This study dealt with the geotechnical properties of soil of the governorates (Baghdad, Diyala, Wasit And Babylon), depending on the induction & comparison & analysis of soil properties .The study involved collecting data, tabulating the information & analyzing them, then maps were drawn for each property at depths ("1, 3, 5, 7....15" m).

The selected properties were Atterberg limits (liquid limit & plasticity index), dry unit weight, initial void ratio, fine particle percent, strength of soil in term of (number of blows in S.P.T and unconfined compressive strength), compression index, organic matter percent, sulphate content, Water table level was also taking into account for Baghdad city.

With the aid of computer program, (138) geotechnical maps was drawn , (64) of them were devoted for the study case area with scale of (1 : 1500000) & (74) maps were drawn for Baghdad city.

_____:

(Surfer / Version 7)

(Surfer /

Version 7)

)

(

_____:

"

(Bakir, 1998)

"

(Al-Naimi, 1996)

(Charts)

Reconnaissance)

(2001)

(Phase

(2002)

_____:



(Grain Size Analysis)	1" m)	(15 13 11 9 7 5 3
Engineering	.2	
:Properties of Soil	(64)	
(Standard Penetration Test " S.P.T ")	(1 : 1500000)	(74)
	(5 km × 5 km)	
(Unconfined Compressive Strength " qu ")		(1 : 100000)
(Compression Index " cc ")		
Chemical	.3	
:Properties of Soil		
(Sulphate Ions " SO3 % ")	(Low)	(L)
(Organic Matter " ORG % ")		H)
		(High)
.4		
.(Water Table Level " W.T.L ")		
:		
(1 : 1500000)	Physical	.1
—	:Properties of Soil	
1990	.(Atterberg Limits)	
	Dry " γ_{dry} ")	
)	.(Unit Weight	
(Initial Void Ratio)	
.(1-1)	.("e _o "	
(1 : 50000)		

1.)

() .

(—

1977 2. - :)

.(.

3. - :)

(1: 100000)

(5 km × 5 km)

.(1-2)

.(: _____

:

:

)

(

(7 m) (36-58 %)

(17 %) ()

.(LL₇₋₄)

(17-81%)

() (17 %)

¹(LL₇₋₄) (7 m)

() (81 %)

.(LL₁₁₋₆) (11 m)

(5 m)

(LL₅₋₃) () (30 %)

% (15 m) :

-6) (LL₉₋₅) (LL₇₋₄) (43

.(LL₁₅₋₈) (LL₁₃₋₇) (LL₁₁

.1



.(LL_{15-8})
 () ()
 (LL_{3-2}) (23 %) (3 m) (40-65 %)

-6) (11 m) (69 %)

(LL_{11})

.(LL_{13-7}) (13 m) (24 %)

(37-46 %)

9) :

(53 %) (m)

.(LL_{9-5})) (

.(

) (37-68 %)

(

(38-68 %) (32 %) (7 m)

(15 m) .(44 %)

.(LL_{15-8}) (38 %)

(43-67 %)

(11 m)

. (81 %)

.

(24-70 %) (LL) :

(24 %))

(LL_{5-3}) (5 m)

(13 m) (70 %) (33-64 %) (

.(LL_{13-7})

(LL_{11-6}) (11 m)

: (15 m) (47 %)

1.)
() 7 .(
2.) (42-62 %)
() (32-42 %)
(LL₅₋₃) (7 m) (5 m)
(LL₇₋₄)
(11 m) (9 m) .(
3.) (63-66 %)
(LL₉₋₆) (7)
(LL₁₁)
:
(31-70 %)
() :
:
(28-66 %) (9m) (LL₉₋₅)
(11 m) (31-48 (54-62 %) ()
(LL₁₁₋₆) (9 m)
(43 %) (55-62 %) ()
(LL₉₋₅)
(28-40 %) (49-70 %) m)
(9 m) (11 (31 %) (6)
(56 %) (LL₉₋₅) (15 m) (LL₁₁))
(62 %) (8)
(LL₁₅) ()
(47-62 %) (11 m) ()
(33 %) (6) (34-62 (7 m)
(LL₁₁) (7) (LL₇₋₄) (15 m) (8)
(47-57 %) (LL₁₅) ()
(13 m) -43 %)
(38 %) (LL₁₃₋₇) (33 (11 m) (5 m)
() () (58 %)



(5 m) (24 %) (LL₁₋₁) () .(LL₅₋₃)
(LL₅₋₃) -39 %)
-1) (1 m) (50 %) (11 m) (9 m) (32
.(LL₁ (69 %) (58 %)
. (40-61 %) .(LL₁₁₋₆) (LL₉₋₅)
(42-65 %) ()
(1-1) %) ()
(11 m) (50-65
(LL₁₁₋₆) (37 %)
(LL₁₃₋₇) (36 %) (13m)
()
. (38-60 %)
-50 %) ()
() () (34
(32-44 %)
(7 m)
.
:
(24-61 %)
(50-58 %) ()
. (5 m)
: (42-49 %) ()
: (5 m)
.
- : (LL₅₋₃) (5 m)
(9 m) (55 %)
(LL₉₋₅) (59 %)
. (34-55 %)
(1 m) (31 %)

:Conclusions

(0.12-0.61)

:

(0.3)

-70 %)

.(0.61)

(0.3)

(24

:

(9-63 %)

%)

(13.8-19 KN/m³)

.(0.03-17.36

(2 %)

(0.523-1.051)

(2 %)

.

هـ.

[USCS]

(0.8-6.43 m)

)

(

:

(N)

(4-80)

(SPT)

(Liquid Limit)

(Plasticity Index)

(N)

(32-536 kN/m²)



.(0.2 %)

(13.7-17.8 kN/m³)

(0.03-3.56 %)

(0.55-0.895)

(9-99 %)

.(9 m)

(50 %)

.(2 %)

.[USCS]

⋮

⋮

⋮

(N)

(9-88)

(SPT)

(38-466 KN/m²)

(15.4-16.5 KN/m³)

(0.573-0.76)

(57-94 %)

(50 %)

(0.08-0.254)

.[USCS]

⋮

⋮

(N)

(21-36)

(SPT)

(0.07-7.5%)

(N)
(5-93) (SPT) (129-366 KN/m²)

(0.15-0.235)

(38-458 KN/m²)

:

(0.14-0.33) (0.25-3.86 %)

.(0.2 %)

-1.08 %)

:

(0.06

(2 %)

(0.04-12.3 %)

_____:

)

:

(

.(0.2 %)

%)

(0.2-7.55

(2 %)

()

(4.92-7.55 %)

(13.7-15.5 KN/m³)

(0.61-0.98)

:Recommendations

(25-98 %)

.1

.[USCS]

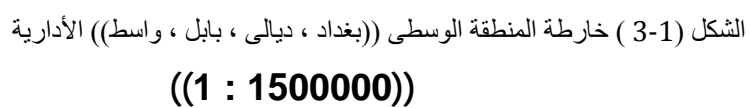
:



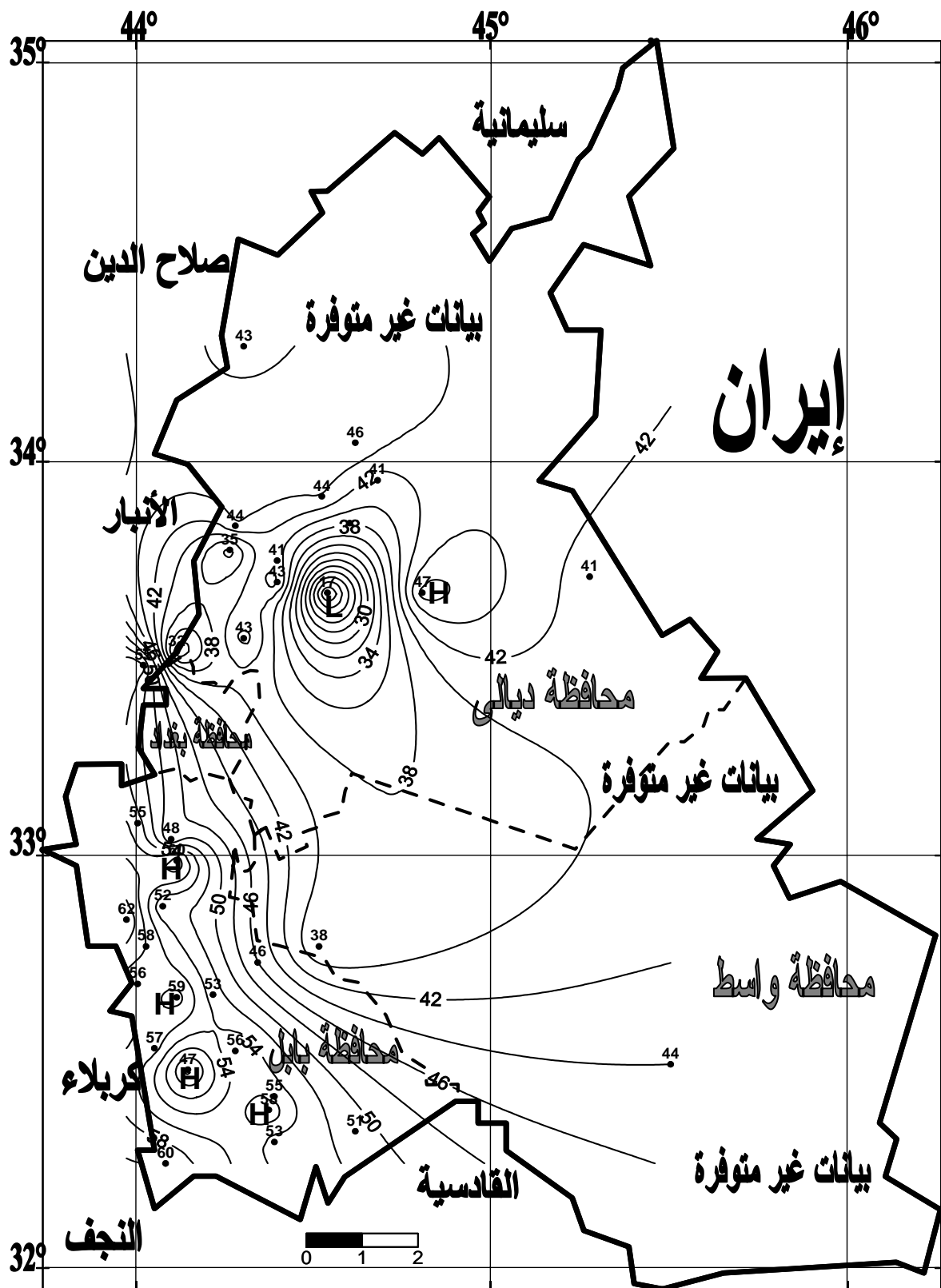
- .2
- Al-naimi, Ghaidaa A. 1996, (Evaluation Of Shear Strength Parameters Of Baghdad Soil) M. Sc. Thesis, University of Technology, Baghdad. .3
- Bakir, A. M., 1998, (The Geotechnical Maps Of Iraq [Southern Region]), M. Sc. Thesis, University Of Baghdad – College of Engineering.
-) 2002 -
- (. - .4
- 1990 -
- . -
- 1977 -
- . -
-) 2001
- (.5
- . -

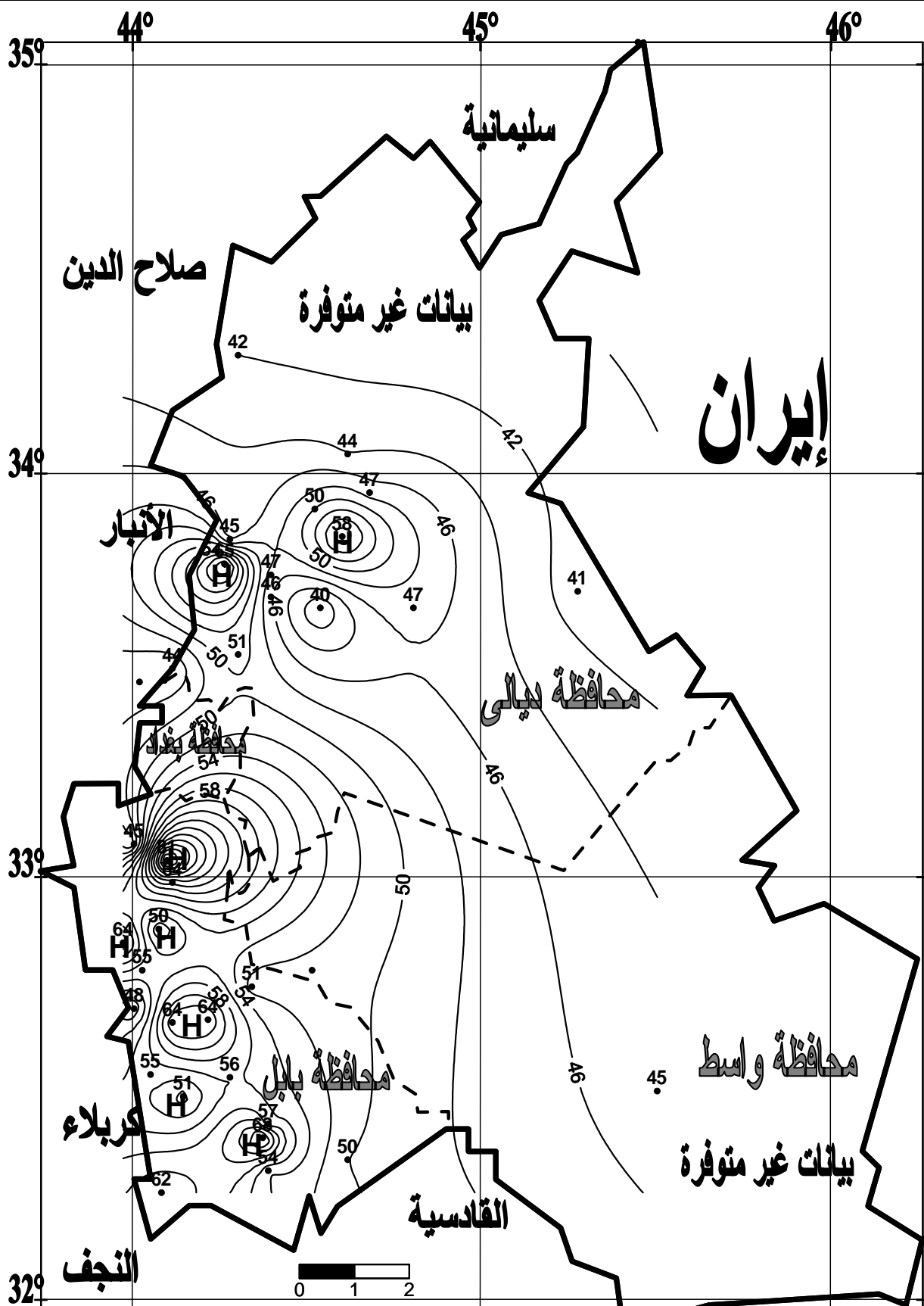
(1-1)

24	70	17	81	%		1
9	63	10	43	%		2
13.8	19	13.7	18.8	kN/m3		3
0.523	1.051	0.5	1.07	---		4
7	99	9	99	%		5
4	80	5	93			6
32	536	24	498	kN/m2		7
0.12	0.61	0.08	0.33	---		8
0.03	17.36	0.04	12.3	%		9
0.12	7.7	0.03	7.55	%		10
0.8	6.43	---	---	m		11







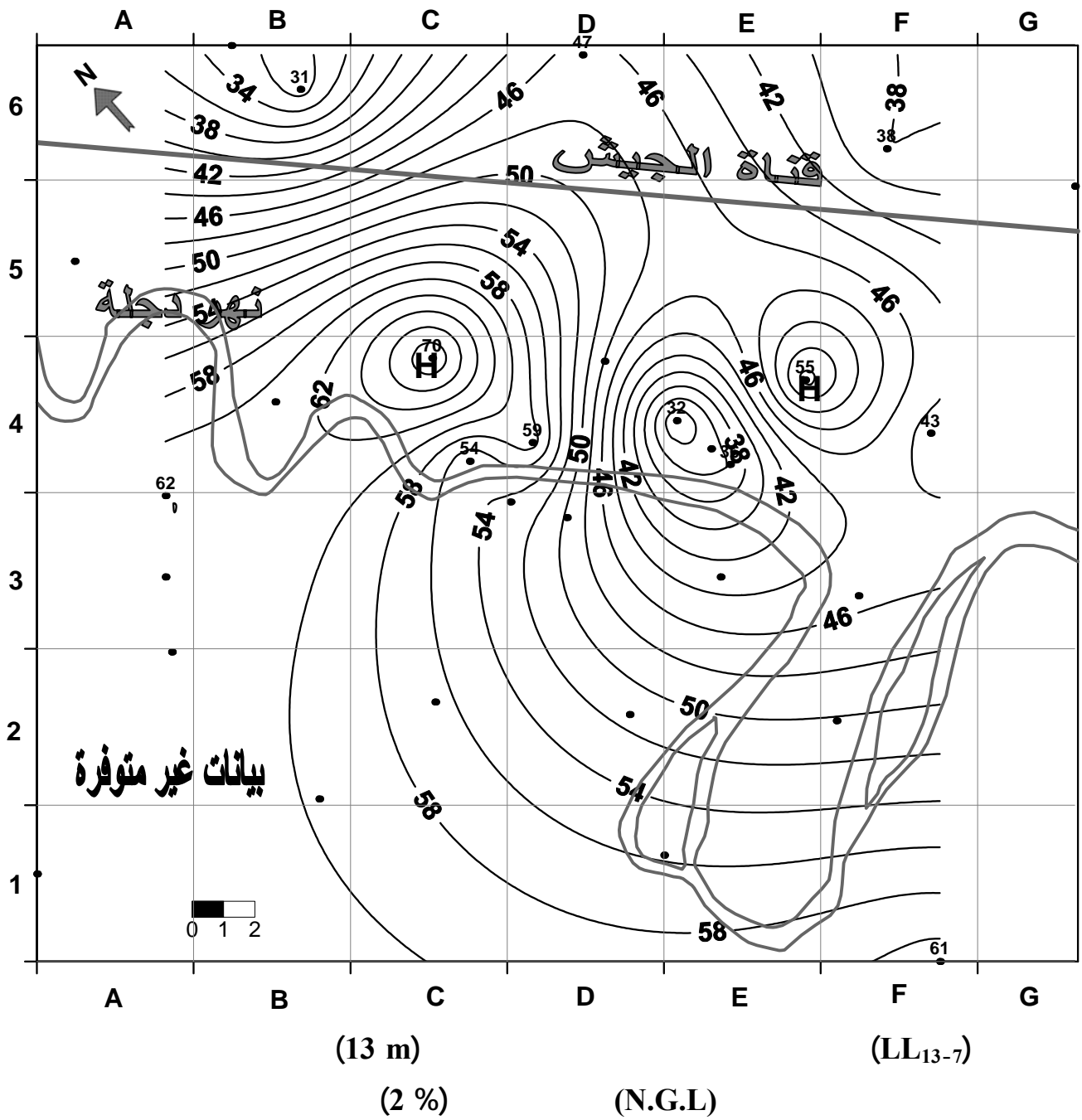


(11 m)

(2 %)

(N.G.L)

(LL₁₁₋₆)





ELECTROCHEMICAL DECOLORIZATION OF DIRECT BLACK TEXTILE DYE WASTEWATER

Baseem H. Fadhil and Atheer M. Ghalib

Chemical Engineering Department – College of Engineering – University of Baghdad – Iraq

ABSTRACT

Electrochemical decolorization of direct black textile dye was studied in the presence of sodium hydroxide (NaCl). Electrochemical cell occupy about 1 liter of working electrolyte supplied with graphite electrodes for both anode and cathode was constructed for this purpose. Decolorization percent, treatment time, power consumption, and pH were studied as a function of the applied voltage and salt concentration. Results show that decolorization increase with increasing salt concentration and applied voltage. Best decolorization of 86% can be achieved after 17 min at 7 volt and 5 g/l salt concentration. Further decolorization can be achieved but this will be accompanied with a sharp increase in power consumption. No significant decrease in pH value was observed at the end of each experiment.

KEYWORDS: Dye removal, decolonization, direct black, electrochemical, wastewater.

7

%86

17

\ 5

INTRODUCTION

Dyes used in textile industries were considered to be one of pollution sources, not because the color of thrown wastewater only but because that these dyes contain usually toxic compound that can effect the environment. The removal of dyes is therefore was considered to be a challenge for both the textile industry and the wastewater treatment.

There are many methods used to treat wastewaters containing dyes. Such methods classified as biological methods, physicochemical methods, adsorption, membrane filtration and ozonation. However, in recent years, attention was increased to the use of electrochemical techniques for the treatment of wastewater. Electrochemical technologies such as electrooxidation, electrocoagulation, and electrofloatation have been

widely used in water and wastewater treatment and several applications have been studied (Christos Comninellis and Guohua Chem, 2010). The electrochemical degradation of some synthetic and actual dye effluents over some electrodes had been studied by many authors (Efthalia Chatzisyneon *et al*, 2006, M. Fatima Esteves, 2004). Electrocoagulation includes the electrochemical formation of coagulants usually using aluminum and iron electrodes, adsorption of soluble or colloidal pollutants on coagulants, and removal by sedimentation and floatation (Peter K. Holt *et al*, 2004; Fatih Ilhan *et al*, 2008). In each of the methods there is some degree of removal and combining with other treating methods, high decolorization and oxidation of some dyes can be achieved (Tak-Hyun Kim *et al*, 2002).

Pollutants destruction in the presence of NaCl was studied by many authors (Comninellis and Nerini, 1995) and seems to be attractive in the destruction of different dyes in many types of electrochemical reactors (Karuppan Muthukumar *et al*, 2004; Raghu and Ahmed, 2008; Raghu and Ahmed, 2007) since it is of low cost, availability, easy to handle without problems. The purpose of this study is to investigate the electrochemical removal efficiency (decolorization) of Direct Black dye from textile wastewater in the presence of NaCl in an electrochemical reactor.

EXPERIMENTAL WORK

Electrochemical Cell and Equipment

Electrochemical experiments were conducted in electrochemical cell made of glass material with dimensions of 10 cm height x 15 cm width x 10 cm depth, filled by 1 liter of working electrolyte (dye solution containing NaCl) during each run. Graphite electrodes were mounted at the long side ends and magnetic stirring was applied to maintain the pH constant along the cell. Farnell stabilized power supply (model L30E, UK) was used to apply the electric current and two digital multimeters (model DT9205A, China) were used to measure voltage and current. pH measurements was achieved using Thermo Fisher Scientific portable pH meter (model Orion 3 star, USA) and Dye concentration was measured

spectrophotometrically using Labomed Inc. spectrophotometer (model Spectro SC, USA).

Dye Preparation

Direct black textile dye solution of 10 mg/liter (10 ppm) concentration was prepared in simulation to that effluent discharged by the State Company for Textile Industries (Kadhmia, Baghdad). This was suggested to be the normal effluent dye concentration discharged by the company (Rasha H. Salman, 2010).

Decolorization Measurement

NaCl up to 10 g/l was added to the reaction cell to improve decolorization efficiency. Samples were taken from the reaction cell during the experiment for spectrophotometrically measurement at wavelength of 566 nm and expressed in terms of concentration. pH was taken at the beginning and end of the experiment. All measurement and experiments were conducted at 28-30°C temperature range.

RESULTS AND DISCUSSION

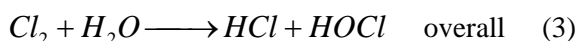
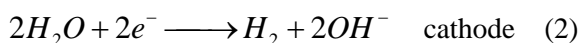
Effect of Applied Voltage on Decolorization Percentage

Figs. 1-3 show the effect of increasing the applied voltage on the decolorization percent, treatment time, and the power consumed at different salt concentrations. Samples were taken for analysis and the effective treatment time was taken just when there is no significant improvement in removal efficiency. It is clear that there is a direct relationship between the applied voltage and decolorization percent and power consumed; as the potential increases, power consumption and decolorization also increases for a given salt concentration. Also, decolorization can be achieved at reduced effective treatment times as the potential increases which may give the attention to work at some optimum point (Maria A. Sanroman *et al*, 2004).

From **Figs. 1-3**, the best operating point was suggested to be at 7 volt and 5 g/l salt concentration (maximum possible dye removal with low power consumption). This gives about 86% decolorization percent in 17 min. It is

possible to achieve higher decolorization in lower times (100% decolorization can be achieved virtually) but this should be accomplished at high power consumption rates. Power consumption start to increase gradually and linearly at 3 g/l salt concentration at all voltage ranges but it increases exponentially at higher salt concentrations and especially in the region when the voltages move from 7 to 10 volt.

The use of NaCl in the reaction cell will generate chlorine gas from the chloride ions at the anode electrode surface as indicated by equations 1-3. Chlorine gas then will react with the OH^- generated from the hydrolysis of water at the cathode surface to give hypochlorate. In this process, mixing is required to increase the reaction extent. This will enables the hypochlorate to spread along the cell and not to reside near the anode which will cause long treatment time and more power consumption as compared if mixing exists.



The role of hypochlorate was reported by Vlyssides (Vlyssides et al, 1999) and it seems to be responsible for the oxidation of dye and the rate of decolorization was affected directly by the rate of production of hypochlorate. This was also confirmed in this study.

Effect of Salt Concentration

The effect of different salt concentrations up to 10 g/l on decolorization percent were shown in **Figs. 4-7**. Normalized concentrations were used in these plots which give the dye concentration divided by the initial concentration. It should be noted that no decolorization was detected in the absence of NaCl in all applied voltage ranges. The decolorization percent increases as NaCl concentration increases. It seems that decolorization starts after the addition of NaCl and this was achieved after 7 min at 3 volt. This time were reduced with increasing the applied voltage for a given amount of salt.

The profiles obtained indicate that a minimum amount of NaCl was needed to start decolorization and there an optimum amount of NaCl which should be selected to overcome the problem of increasing the salinity of the treated wastewater. Also, the study indicates that there is no need to add salt continuously to the working solution since NaCl was not consumed during the electrochemical process as shown in equation (1).

Effect of Electrodecolorization Process on pH

As the reaction proceeds, generation of gas bubbles was observed at the surface of the electrodes due to the electrolysis of water in which oxygen gas was generated at the anode and hydrogen gas and hydroxyl ions were generated at the cathode. Therefore the pH increases near the anode and decreased near the cathode. So that, mixing is important to make the pH of the cell constant. pH was measured at the beginning and at the end of the experiment. Recorded values indicates that pH does not affected significantly during the experiments and it just moves to a lower values (acidic direction) with a maximum of 0.5 from that value at the beginning of the experiment. This is evident that production of H^+ ions is greater than OH^- ions resulting in a shift of pH to the acidic region.

CONCLUSIONS

1. Electrochemical decolorization of Direct Black dye can be effectively performed in electrochemical techniques to treat effluents containing this dye such that found in textile industry with high percentage of decolorization.
2. The use of salt in the process relies on the formation hypochlorate which seems to be a good oxidant for this type of dye.
3. Cell applied voltage affect the decolorization percent and treatment time, but power consumption should be taken in consideration in order to achieve lower cost treatment.
4. Electrochemical decolorization process of Direct Black dye does not affect the pH significantly.

REFERENCES

- Christos Comninellis and Guohua Chem, *Electrochemistry for the environment*, Springer Science+Business Media, LLC (2010).
- Coninelliis Ch., and Nerini A., *Anodic treatment of phenol in presence of NaCl for wastewater treatment*, Journal of Applied Electrochemistry, Vol. 25 (1995), pp. 23-28.
- Efthalia Chatzisyneon, Nikolas P. Xekoukoulotakis, Alberto Coz, Nicolas Kalogerakis, and Dionissios Mantzavinos, *Electrochemical treatment of textile and dyehouse effluents*, Journal of Hazardous Materials, Vol. 136, Issue 2 (2006).
- Fatih Ilhan, Ugur Kurt, Omer Apaydin, and M. Talha Gonullu, *Treatment of leachate by electrocoagulation using aluminum and iron electrodes*, Journal of Hazardous Materials, Vol. 154 (2008), pp. 381-389.
- Karuppan Muthukumar, P Shunmuga Sundaram, N Anantharaman, and C Ahmed Basha, *Treatment of textile dye wastewater by using an electrochemical bipolar disk stack reactor*, Journal of Chemical Technology and Biotechnology, Vol. 79 (2004), pp. 1135-1141.
- M. Fatima Exteves and J. Dinis Silva, *Electrochemical degradation of reactive blue 19 dye in textile wastewater*, World Textile Conference – 4th AUTEX Conference (2004).
- Maria Angeles Sanroman, Marta Pazos, and Claudio Cameselle, *Optimization of Electrochemical Decolorization Process of an Azo Dye Methyl Orange*, Journal of Chemical Technology and Biotechnology, Vol. 79 (2004), pp. 1349-1353.
- Peter K. Holt, Geoffery W. Barton, and Cynthia A. Mitchell, *The future for relctrocoagulation as a localized water treatment technology*, Chemosphere, Vol. 59 (2005), pp. 355-367.
- Raghu S. and Ahmed Basha, *Dye destruction and simultaneous generation of sodium hydroxide using a divided electrochemical reactor*, Ind. Eng. Chem. Res., Vol. 47 (2008), pp. 5277-5283.
- Raghu S. and Ahmed Basha, *Electrochemical treatment of procion black 5B using cylindrical flow reactor – a pilot plant study*, Journal of Hazardous Materials, Vol. 139 (2007), pp. 381-390.
- Rasha H. Salman, *Removal of Dyes from Textile Effluent by Adsorption onto Oven Dried Alum Sludge*, Journal of Engineering, Vol. 16, No. 2 (2010), pp. 5249-5262.
- Tak-Hyun Kim, Chulhwan Park, Jinwon Lee, Eung-Bai Shin, and Sangyong Kim, *Pilot scale treatment of textile wastewater by combined pocess (fluidized biofilm process – chemical coagulation – electrochemical oxidation)*, Water Research, Vol. 36 (2002), pp. 3979-3988.
- Vlyssides AG, M. Loizidou, P.K. Karlis, A.A. Zorpas, and D. Papaioannou, *Electrochemical Oxidation of a textile dye wastewater using a Pt/Ti electrode*. Journal of Hazardous Materials, Vol. 70 (1999), pp. 41-52.

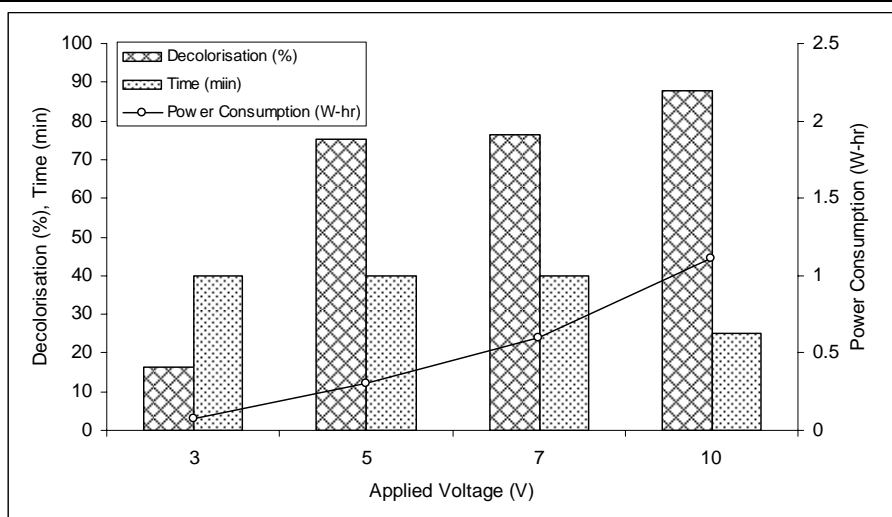


Fig.1 Effect of the applied voltage on removal percentage, treatment time, and power consumed with NaCl concentration of 3 g/l

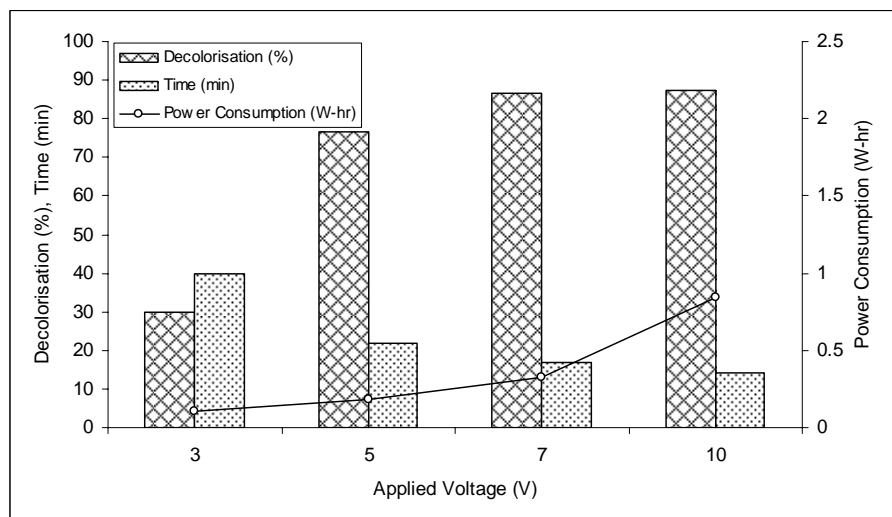


Fig.2 Effect of the applied voltage on removal percentage, treatment time, and power consumed with NaCl concentration of 5 g/l

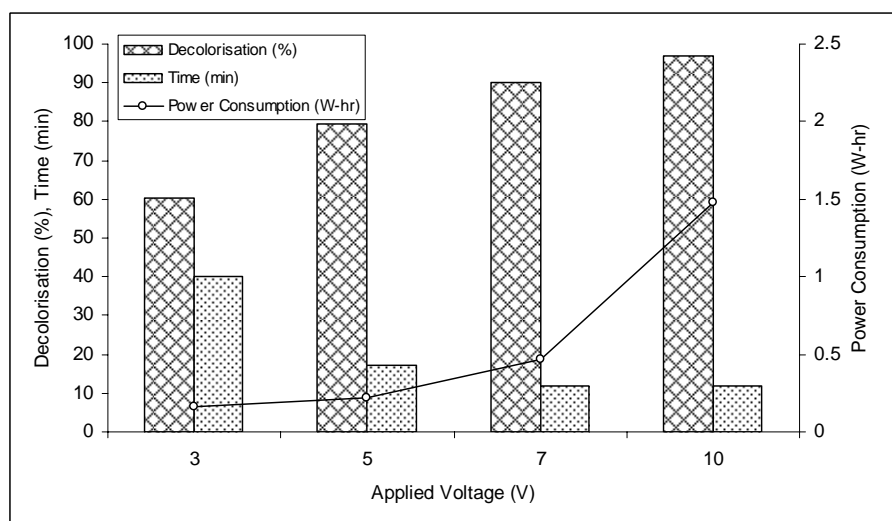


Fig.3 Effect of the applied voltage on removal percentage, treatment time, and power consumed with NaCl concentration of 10 g/l

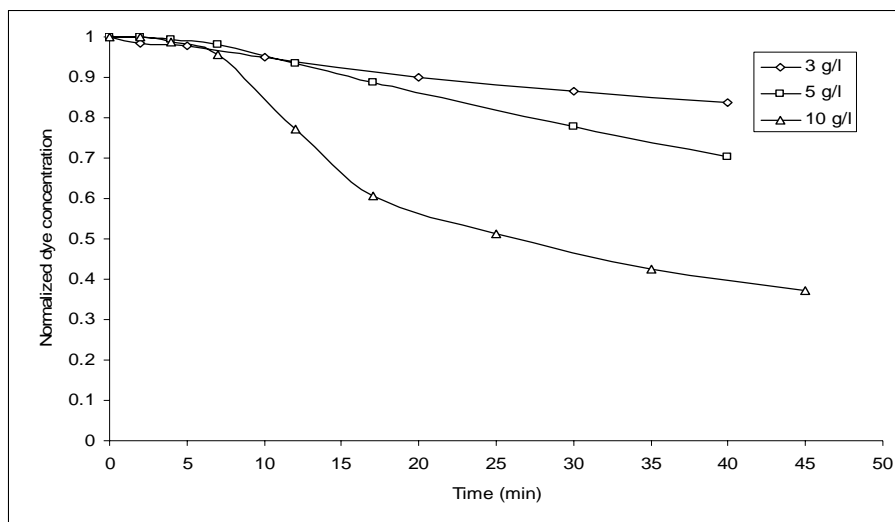


Fig. 4 Normalized concentration of Direct Black dye versus the treatment time at cell voltage of 3 V with different salt concentration

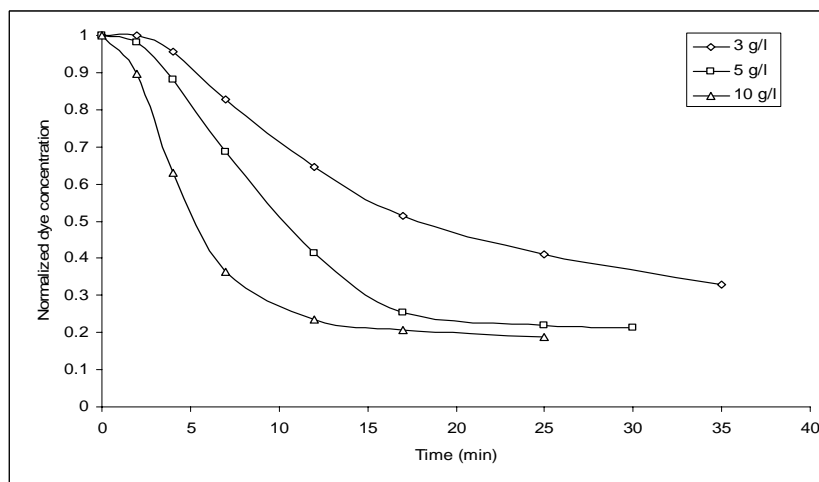


Fig. 5 Normalized concentration of Direct Black dye versus the treatment time at cell voltage of 5 V with different salt concentration

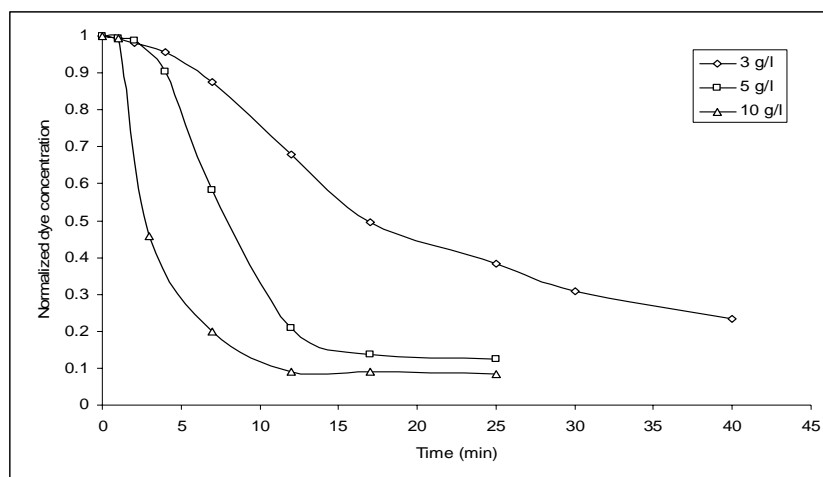


Fig. 6 Normalized concentration of Direct Black dye versus the treatment time at cell voltage of 7 V with different salt concentration

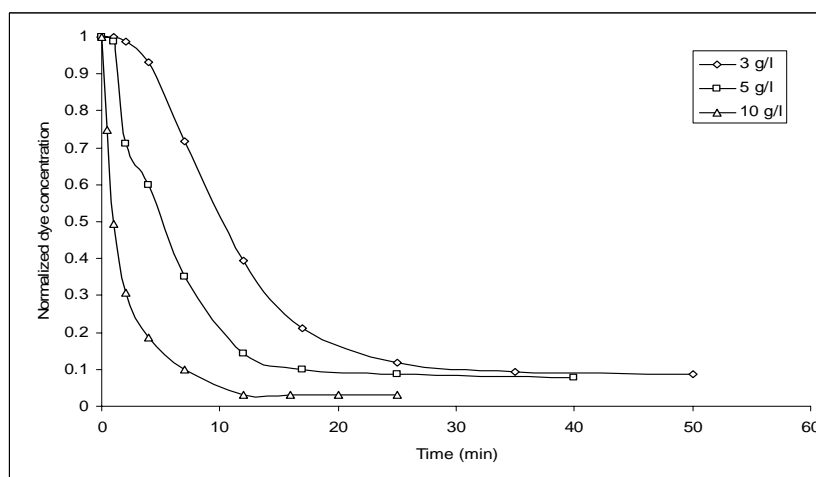


Fig. 7 Normalized concentration of Direct Black dye versus the treatment time at cell voltage of 10 V with different salt concentration



Romantic Thought in Architecture

Assis. Prof. Dr. Areage Karim Al-Sadkhan
Reem Nihad Abdul-Karim Al-Ubidi

ABSTRACT

The contemporary world had seen lately, series of disputes, crisis and wars, in addition to the drastic life, and the technological hastening. Therefore, the romanticism must be brought back to reactivate the life once again, because the romanticism: represents the internal world of human and the hidden emotional life, and it is the origin of human aspiration, in his attempt to satisfy the superior patterns.

This research is interested in studying the romantic thought and its effect in architecture. Due to the fact that most of the studies and literary thesis had dealt with the concept of romanticism as a trend subtended the classicism and as one of the architectural trends that appeared in the nineteen century, and these studies ignored the idea of romanticism continuity through the eras. Therefore, **the main problem of this research represented in: the absence of accurate understanding of the nature of the romantic thought in architecture, and sustaining in architecture and specially the contemporary architecture.** Therefore the aim of this research is to demonstrate the various aspects of the romanticism in architecture and the contemporary architectural movements, exploring the role that this thought play in the defining features of architecture and its

various movements. To fulfill this request, it required building the theoretical framework for the research, and concluded the components of the romanticism, and to apply them on the selected sample to verify its credibility, and then to apply them on contemporary architectural projects.

.1

.2

)

.(

.3

.1

.2

.4

.1

.2



.5 :

(15) . :

1-5

)

(

:1-1-5

:

) (Gelernter,1996,p30) :

Romanticism

:

((Ibid,p34)

" "

: 2-1-1-5

:

(46 1989) .

(Liberalism)

(-)

)

(11 2004) (Renaissance)

(

.

(14 2004)

(181 1982) .

•

.

() ()

() ()

(19-17 2007) .

(Kant) •

(1800-1724) (15-14 1980) .

3-1-1-5

:

() •

(1813-1770) () ()

.

(...<http://hamohd99.maktoobblog>)

(Shakespeare) •

)

(

(182 1982) .



:

).

-

-

.

-

-

)

.(

.(

:

.

A. Hauser, "The Social History of Art" V3, 1973

Hauser

"The Social History of Art"

()

2-1-5

:

Friedrich)

(Schegel

P. Collins, "Changing Ideals in Modern Architecture", 1971

Collins

)

(

Addison

:

Collins

Hauser

.

:) .

(

: _____ **

:

()
M. Gelernter, "The 3-2-1-5
Sources of Architectural Form", 1996
Gelernter

)

()

(

2-5

Gelernter

: _____

()

-700) : 1-2-5

(. 500

()



")
 .(Kimball & E.,1977,P8)

(1986 43)

.()

(1) .

)

: **2-2-5**

-5000) **1-2-2-5**

(. 500

()

)

()

()

(Kimball .

(3)

& E.,1977,P29)

(. 300-800) : **3-2-2-5**

)

(

)

.(

(2)

(. 3000) : **2-2-2-5**

) .

(

•

•

.(

)

(

•

()

•

)

3-2-5

.(

•

•

(4)

) : 1-3-2-5

(. 300) : 4-2-2-5

 $\cdot ($
$$(\quad)$$

(Schulz,1986,p74) .

•

$$\cdot (\quad)$$

:

(47 2000)

(Allsopp1971,p55)

(41 2001) •



(122 2007)
 ()
 () : 2-3-2-5
 ** (

:

() 1972) () .
 () (385-384
)
 (6) . (4-3-2-5
) :
 • (16-12 () ()

(5) .
 (Schulz,1986,p111)) : 3-3-2-5
 (:
)
) (3-3-2-5
 (Saarinen,1985,p250). (

" (13)
(70) "

_____ .
1989). _____
(79-78

)
(

_____ .
_____ .
()
((7) .
: 5-3-2-5
()
: 3-2-5 622
) : 1-3-2-5
•(

(Schulz,1986,p128)

2003) " :
(12-11 .
(18) "
" "
_____ .
(17 2003)



) (160 2001).

(

(165 2001)

1603 1558

()

()

(Gelernter,1996,p156). (35 2003)

.

..

.

.()

(9) (8) .

) : 2-3-2-5

...(1750

1800 1750

.

)

(10) .(

Perrault

Blondel

(81 2003) .

.

..

()

(163 2001)

(Gelernter,1996,p153)

...

()

4-2-5

:

: 1-4-2-5

"Exoticism"

:_____

(Collins,1971,p41)

(Gelernter,1996,p185)

()

()

(Electical Architecture)

.Orient

(12) .

(11) (Allsopp,1971,p192)

"Art Nouveau"

:_____

:

Art and

:_____

•(1880) "Crafts"

Beaux Art classicism

(Curtis,1996,pp53-54)

(Curtis)

(Curtis,1996,p23) .



: 1-2-4-2-5

1900

"Art Deco"

:_____

(23 1989)

Le Corbusier

N.Foster

.J.Stirling

R.Rogers

(280 2008) .

:

:_____

"Expressionism"

)

(

)

Stallybrass &).

) (

،(Bullock,1988,p301

(

(13) .

()

)

(

:

2-4-2-5

.()

.

(134 1999).

(172 1999)

.

(Eric Mendelsohn)

(Conrads&Sperlich,1963,p20).

(14) .

"Organism"

:_____

.

"De Stijl"

:_____

.

Purists

(231 2003)

Expressionists

.

De Stijl

.

"Futurism"

:_____

.



Hitchcock &) :

(Johnson,1966,p32

(Curtis,1996,p156)

) :

De Stijl

(

:

:

_____:

"International Style"

(International Style

(31 1996)

(Hitchcock)

.Zeitgeist

(Ph.Johnson)

(15)

) : 2-2-4-2-5

) : 1-2-2-4-2-5

(138 1997).

Meaning in " Schulz

"Western Architecture

(Jencks,1997,p109)

Not

Dam-Ronchamp

(16) (Schulz,1986,p221)

(17)

:self conscious

Beaus-Art

(Jencks,1973,p46) .(Perret)



3-2-4-2-5 :) . (1966

.(

)

)

: (

(

:)

(1997 187)

(

.

()

()

.

(18) .

(Gelernter,1996,p284)

(W.Darby)

:(194 1997)

()

.

:

)

)

(

(

(Gelernter,1996,p7)

.(

)

(1)

:

()
(<http://www.asharqalawsat.com>).

:
: 3-5

()

" () :
: 1-3-5
" : 1-1-3-5
1630

(Stevenson,1997,p54) : 2 -1-3-5
: 3-1-3-5

**

24.4 17.1 (2)
61 2-3-5

:
1-2-3-5

(Ibid,p55) .

" ()
(

« »



()

)

<http://www.asharqalawsat.com>).

) (

() (

.

4-5

:

: **1-4-5**

(Michell,1978,p133) .

22

)

(

.(

):

(20) (19) <http://www.aladala.com>**2-2-3-5**

(

:

2-4-5

:

()

:

.1

.

.2

- (Ibid,p69))
- Guggenheim Museum - 1997 :** .(
B...(22) in Bilbao, Spain .3
4. ()
- Gehry Jencks
- :
- Bilbao :
- Parc de la - 1982-1991 :**
A...(21) Villette in Paris
- (Jencks,1997,p184).
- Pearman
- Gehry
- Pearman
- () Gehry
(Pearman,1998,p11)
-) (Broadbent,1991,p67)
(Tschumi
- (Ibid,p64) .
- City Hall in - 1998-2003 :**)
C...(23) London (
- Foster City Hall



10

185.000

45

.

)

.(Walt Diseny

(Huxtable,1997,p117)

:

.()

E..(25) 1998-1992 -

/

.

.

) .

(2009

100

22000

.

<http://www.fosterandpartners.com>)

)

The Swan Hotels - 1990-2008 :**D...(24) in Florida**

.(

Michael Graves

)

Swan

(Swan Hotels

12

Hotels

7

)

()

www.luxury-) .hotels-resorts.com/.../swan-pic1

.(

) .

(.)

-

.5

-

(2009/5/4

3-4-5

)

:

(

(3)

.

.6

:

.6 _____ :

•

:

.1

.

•

)

•

(

.

.

)

.7

_____ :

.2

(

)

(

.

.3

.()

.

.4



.8

○

1

"

.1997

:

"

○

1

"

.1999

"

"

○

.1972

.

.9

"

○

"

.1989 39

:

"

○

"

:

"

:

"

○

.2000

:

"

"

○

.1989

(6)

:

"

○

.1982

:

"

"

"

○

.2007

.1989

:

"

"

○

2

"

"

○

.2001

.2003

:

"

"

○

-

-

"

○

(10)

"

.1980

.2004

"

"

○

:

.2007

"

○

"

.1996

"

"

○

.1986

English Reference:

-Allsopp, Bruce, "A General History of Architecture", Pitman Publishing, London, 1971.

- Broadbent, Geoffery, "Deconstruction, A student guide", London, 1991

-Collins, Peter, "Changing Ideals in Modern Architecture ", Faber and Faber, London, 1971.

-Conrads, Ulrich& Sperlich, Hans,G., "Fantastic Architecture", The Architecture Press,London,1963.

- Stallybrass, Oliver, and Bullock, Alan, "**The Fontana Dictionary of Modern Thought**", Fontana Press, 1988.

- Stevenson, Neil, "**Annotated Guides: Architecture**", Dorling Kindersley, London, 1997.

Internet Sites references:

"
2007
<http://hamohd99.maktoobblog>
"
"
<http://www.alsharqalawsat.com>
"
545
)
2005/ /31
(
<http://www.aladala.com>
<http://www.fosterandpartners.com>
www.luxury-hotels-resorts.com/.../sawn-pic1

- Curtis, William, "**Modern Architecture since 1900**", 3rd edition, Phaidon Press, London, 1996.

-Gelernter, Mark, "**Source of Architectural Form**", Manchester University Press, New York, 1996.

-Hauser, Arnold, "**The Social History of Art: Rococo, Classicism and Romanticism**", V3, Routledge and Kegan Paul, London, 1973.

- Hitchcock, H. Russell and Johnson, Philip, "**The International style**", W.W. Norton, 1996.

- Huxtable, Ada Louise, "the Unreal America: Architecture and Illusion", 1st edition, The New Press, New York, 1997.

- Jencks, Charles, "**Modern Movement in Architecture**", Penguin Books, London, 1973.

-Jencks, Charles, "**The Architecture of the Jumping Universe**", Academy Editions, London, 1997.

- Kimball, Fiske & Edgell, George Harold, "**A History of Architecture**", Greenwood press, United States of America, 1977.

-Michelle, George, "**Architecture of Islamic world: It is History and social meaning**", Thames and Hudson, LTD, London, 1978.

- Pearman, Hug, "**Contemporary World Architecture**", Phaidon Press Limited, London, 1988.

- Saarinen, Eliel, "**The Search for Form in Art and Architecture**", Dover Publications, INC, New York, 1985.

- Schulz, Norberg, "**Meaning in Western Architecture**", Studio Vista, London, 1986.

()

(1)

()	()			
	()			
	()			
	()			
	()			
	()			
	()			
	()			
	()			
	()			

(2)

()							
()							
:							

()						
	()					

()

(3)

	E	D	C	B	A							
2				1	1	/	1.1.1	1				
4	1	2			1	/	1.2.1					
1	1					/	1.2.2					
6		2	3	1		/	1.2.3					
1	1					/	1.2.4					
3		2	1			/	2.1.1.2	2				
						()						

1		1				/	2.2.1				
6	1			3	2		3.1	3			
4	1		3				4.1.1	4			
9		3	2	2	2		4.1.2				
7		1	2	1	3	/	5.1.1	5			
8	2	1	2	1	2	/	5.1.2				
2			1	1		/	5.1.3				
14	3	2	3	2	4		5.2				
6		1	2	1	2		6.1	6			
8	1	2	2	1	2		6.2				
1	1						6.3				
2	1				1		6.4				
5	1	1	1	1	1		6.5				
6		2	1	2	1		7.1	7			
13	3	5	3	1	1		7.2				
6	1			3	2		8.2	8			



DESIGN AND IMPLEMENTATION OF FAST THREE STAGES SLA BATTERY CHARGER FOR PLC SYSTEMS

Anas W. Ata'a

¹University of Baghdad Computer Engineering Department

Assistant teacher / email: anaswasill@gmail.com

ABSTRACT

New fast sealed lead acid (SLA) battery chargers must be able to charge the fully discharged batteries in a short time. In the same time, the charger must monitor the battery state of health in order to prevent over charge and to extend the battery life time.

In this paper a Fast charger was presented to charge SLA batteries in short time and monitor the battery voltage to prevent over charge. The design was implemented practically. And 150 charger of similar type was produced for commercial use. They are now in service in different Mobile base station sites around Baghdad. It can charge a fully discharged 12V, 4.5Ah battery in less than 5 hours. To supply PLC control system on DC power to about 24 hour of continuous operation during main electricity faults.

During one and half year of continuous operation three faults have been recorded in the 150 chargers. All of the three cases were because of bad components manufacturing.

150

150

12V, 4.5Ah

24

150

Keywords: SLA, VRLA, SoC, SoH, Battery Chargers, three mode charger, Fast charger, DC PLC backup system.

1. INTRODUCTION

In the introduction a brief discussion about the SLA batteries and charging algorithms will be presented.

1.1.VRLA Batteries

Lead-acid batteries, invented in 1859 by French physicist Gaston Planté[1]. VRLA stands for valve-regulated lead-acid and is the designation for low-maintenance lead-acid sealed rechargeable batteries. Because of their construction, VRLA batteries do not require regular addition of water to the cells.

These batteries are often called sealed lead-acid batteries, but they always include a safety pressure relief valve. As opposed to vented (also called flooded) batteries, a VRLA cannot spill its electrolyte if it is inverted.

The name "valve regulated" does not wholly describe the technology; these are really "recombinant" batteries, which means that the oxygen evolved at the positive plates will largely recombine with the hydrogen ready to evolve on the negative plates, creating water thus preventing water loss. The valve is strictly a safety feature in case the rate of hydrogen evolution becomes dangerously high.

Since VRLA batteries do not require (and make impossible) regular checking of the electrolyte level, they have been called Maintenance Free (MF) batteries. However, this is somewhat of a misnomer. VRLA cells do require maintenance. As electrolyte is lost, VRLA cells may experience "dry-out" and lose capacity. This can be detected by taking regular internal resistance, conductance or impedance measurements of cells.

1.2.Charging the lead-acid battery [2]

The charging algorithm for lead-acid batteries is to use voltage rather than current limiting. The charge time of a sealed lead-acid battery is 12-16 hours (up to 36 hours for larger capacity batteries). With higher charge currents and multi-stage charge methods, the charge time can be reduced to 10 hours or less.

It takes about 5 times as long to recharge a lead-acid battery to the same level as it does to discharge. A multi-stage charger first applies a constant current charge, raising the cell voltage to

a preset voltage (Stage 1 in Figure 1). Stage 1 takes about 5 hours and the battery is charged to 70%. During the topping charge in Stage 2 that follows, the charge current is gradually reduced as the cell is being saturated. The topping charge takes another 5 hours and is essential for the well being of the battery. If omitted, the battery would eventually lose the ability to accept a full charge. Full charge is attained after the voltage has reached the threshold and the current has dropped to 3% of the rated current or has levelled off. The final Stage 3 is the float charge, which compensates for the self-discharge.

Correct settings of the voltage limits are critical and range from 2.30V to 2.45V. Setting the voltage limit is a compromise. On one end, the battery wants to be fully charged to get maximum capacity and avoid sulfation on the negative plate. A continually over-saturated condition at the other end, however, would cause grid corrosion on the positive plate. It also promotes gassing, which results in venting and loss of electrolyte.

The voltage limit shifts with temperature. A higher temperature requires slightly lower voltages and vice versa. Chargers that are exposed to large temperature fluctuations should be equipped with temperature sensors to adjust the charge voltage for optimum charge.

The battery cannot remain at the peak voltage for too long; the maximum allowable time is 48 hours. When reaching full charge, the voltage must be lowered to maintain the battery at between 2.25 and 2.27V/cell. Manufacturers of large lead-acid batteries recommend a float charge of 2.25V at 25°C.

Car batteries and valve-regulated-lead-acid batteries (VRLA) are typically charged to between 2.26 and 2.36V/cell. At 2.37V, most lead-acid batteries start to gas, causing loss of electrolyte and possible temperature increases.

Large VRLA batteries are often charged with a float-charge current to 2.25V/cell. A full charge may take several days. It is interesting to observe that the current in float charge mode gradually increases as the battery ages in standby mode. The reasons may be electrical cell leakages and a reduction in chemical efficiency.

Aging affects each cell differently. Since the cells are connected in series, controlling the individual

cell voltages during charge is virtually impossible. Even if the correct overall voltage is applied, a weak cell will generate its own voltage level and intensify the condition further.

Lead-acid batteries must always be stored in a charged state. A topping charge should be applied every six months to avoid the voltage from dropping below 2.10V/cell on an SLA. Prolonged storage below the critical voltage causes sulfation, a condition that is difficult to reverse.

1.3.State-of-charge (SoC) reading based on terminal voltage

The state-of-charge of a lead-acid battery can, to a certain extent, be estimated by measuring the open terminal voltage[4] . Prior to measuring, the battery must have rested for 4-8 hours after charge or discharge and resided at a steady room temperature[4] . A cold battery would show slightly higher voltages and a hot battery would be lower. Due to surface charge, a brief charge will raise the terminal voltage and provide inflated state-of-charge reading. For example, a 30 minute charge could wrongly indicate 100% SoC if no rest is applied.

With sufficient rest and stable temperature, voltage measurements provide an amazingly accurate State of Charge (SoC) estimation for lead acid batteries. It is important that the battery is free of polarization. If connected in a system, such as in a car, there are steady auxiliary loads, not to mention frequent starting and driving.

Table 1 BCI standard for SoC estimation of a 12V flooded lead acid car battery [2]

Open circuit voltage	State-of-Charge in %
12.65V	100%
12.45V	75%
12.24V	50%
12.06V	25%
11.89V or less	Discharged

Proposed charger and backup system

A simplified block diagram of the system is shown in Fig. 2. This block diagram represents the functional blocks of the system. The first block is the SMPS, which is a standard SMPS. The output of the SMPS is DC voltage about 19V. This DC

voltage is transferred to the second block which is charging control and output conditioning circuit. This block is the main block of the system and the design of this block is the state of art, which contains the charging algorithms and output control circuits and contains all the protections.

2. DESIGN AND IMPLEMENTATION

In this section, the design and implementation of each block of Fig. 2 will be demonstrated.

2.1.SMPS

The first block is the SMPS. To implement this block a standard SMPS that is available commercially was used. Fig.4 shows the circuit diagram and Fig.3 shows the PCB picture of similar SMPS. The output of this power supply is set to 19V DC through the voltage divider R4 and R5. This value is limited by the MOSFET used. For the IRF3205, the max threshold voltage is 4V[13] . Since the max battery voltage during charging is 14.75, the total power supply voltage must be $14.75 + 4 = 18.75V$. 19V was used for safe circuit operation. The TL431 is an Adjustable Precision Shunt Regulator. It is responsible for keeping the output voltage fixed by controlling the feedback loop. The max current that can be drawn from similar supply is 1A.

The operation of the SMPS can be summarized as follows:

- The 220V AC is converted to about 311V DC through the diode bridge D1 and high voltage chemical capacitor C₃.
- The TOP224 is a Three-terminal Off-line PWM MOSFET switch. It chops the 311VDC at frequency of about 100 kHz. The chopping frequency is set by the internal oscillator of the TOP224. This high voltage signal will be reduced to low voltage through the ferrite step-down transformer TP.
- The high speed rectifier Diode D₄ will rectify the output of the transformer into DC voltage. This DC voltage will pass through low pass power filter to reduce switching noise.
- The TL431 regulator is responsible of keeping the output voltage constant. The TL431 compare the voltage at the middle terminal with the internal Precision Reference Voltage of 2.495V. This voltage is the R₄ and R₅ divider voltage. If the voltage is less than the reference voltage, the TL431 will conduct and the optocoupler will pass current to the C terminal of TOP224. This current will increase the duty cycle of the

PWM signal generated and more power will be transferred to the output. If the divider voltage is larger than the reference voltage, the TL431 will not conduct and the optocoupler will not pass current to the C terminal of TOP224. This will decrease the duty cycle of the PWM signal generated and less power will be transferred to the output. For farther details on the operation please refer to the datasheet of TOP224[9] and TL431[10] ICs. The output voltage of this power supply is set to 19V DC through choosing appropriate values of the divider R_4 and R_5 .

2.2.Charge Control

The charge control circuit consists of the following parts:

- Constant current charge circuit.
- Constant voltage charge circuit.
- Float charge circuit.
- Under voltage alarm circuit. This circuit will turn ON red LED when battery voltage is reduced under 10V. This indication means the battery is damage and must be replaced. Also there is an output control signal that will be activated with the red LED. This signal could be used to generate Battery LOW ALARM and to indicate that battery is completely discharged. The circuit will never disconnect the battery even if the battery is fully discharged.

These circuits are interconnected such that at each power ON of the supply voltage the charge controller will do the following sequence:

1. Start the constant current charging mode first. This represents the fast charge mode. During this mode the circuit will supply a constant current of about 0.7A to the battery and will continue supplying this current until the battery voltage reaches 14.5V.
2. When the battery voltage reaches 14.5V, the second charging stage is started. This stage is the constant voltage stage. In this stage, the circuit will behaves like a constant voltage source of 14.5V. This stage represents the slow charge mode. During this stage, the voltage will stay constant at 14.5V and the charging current will decrease gradually as the battery charge. When the charging current reduced to a specified value, the float charge stage is started.
3. The float charge stage is the final charging stage. In this stage the charger will provide a very small charging current. This small current will account for self discharge in the battery cells after the battery get fully charged. The

float charging is neither constant voltage nor constant current it is simple charging through resistor. The battery voltage and the exact charging current will depend on the battery state and battery rest.

Fig. 5 shows the complete circuit diagram of the three charging modes and the low battery indication circuits. The Battery charging current will be designated by I_{BAT} and the Battery Charging voltage will be designated V_{BAT} in the next sections.

2.3.Constant Current Charging Circuit:

The circuit below (**Fig.6b**) is the constant current charging circuit. The OPAMP U_{1A} is the core of this circuit. It always compares the SENS2 voltage with the 0.7V reference voltage. The voltage SENS2 is the voltage across the 1 ohm resistor R_1 connected in series with the Battery to monitor the charging current (see **Fig.6a**).

$$SENS2 = I_{BAT} \times 1\Omega \quad (1)$$

When the charging current drop below 0.7A, SENS2 voltage will be less than 0.7V and the comparator output will be low this will turn off D5 which in turn, turns ON the power MOSFET to supply more power to the Battery.

When the charging current rise above 0.7A, SENS2 voltage will be greater than 0.7V and the comparator output will be high. This will turn ON Q5 and D5 which in turn, turns OFF the power MOSFET to reduce the Battery charging current. This negative feedback operation will maintain the Battery Charging current $I_{BAT@CC}$ constant at 0.7A. If it is required to increase this current for larger batteries, the value of R_1 must be reduced. The power dissipated inside R_1 is:

$$\begin{aligned} P_{R1} &= (I_{BAT})^2 \times R_1 \\ P_{R1} &= 0.49 \times 1 = 0.49 \text{ W}, \end{aligned} \quad (2)$$

Choosing 1W resistor gives 50% safety margin.

The resistor R_4 is used to limit the base current for Q_2 to about 225 μ A:

$$I_{B2} = (3.65 - 1.4) / 10k = 225\mu A \quad (3)$$

Since the minimum value of β in the transistor datasheet is 100 for collector currents less than 100mA[6]. This I_{B2} will results in collector current of about 22.5mA, but since R_8 is 4.7k then max I_{C2} will not exceed $19/4700=4mA$. Then Q_2 will be heavily in saturation and the MOSFET gate voltage is zero. Also the resistor R_{22} is used to limit

I_{B5} to $70\mu A$ which will give about $7mA$ at the collector to turn the LED_1 ON.

$$I_{B5} = (1.4 - 0.7) / 10k = 70\mu A \quad (4)$$

The other function of R_4 is to protect the OPAMP output stage when the output is high. D_5 and Q_2 will clipdown the opamp output voltage to about $1.4V$. This will provide low resistance path to the OPAMP output stage. R_4 will prevent this short circuit.

The Capacitor C_2 compensates the feedback control loop by adding integration function to the error amplifier output ($U_{1:A}$).

2.4.Constant Voltage Charging Circuit

Fig.7 is the constant voltage charging circuit. The OPAMP $U_{1:C}$ is the core of this circuit.

It always compares the precisely adjusted reference voltage of RV_1 with the battery voltage. The OPAMP $U_{1:B}$ is subtraction circuit. It subtracts the voltage drop across the 1Ω resister ($SENS2$) from the Battery positive terminal voltage ($SENS1$) to get accurate Battery voltage (see **Fig.6a**). The output of $U_{1:B}$ is fraction of battery voltage.

$$V_{BAT} = SENS1 - SENS2 \quad (5)$$

$$V_{O U1:B} = SENS1 \times R_3 / (R_2 + R_3) \times (1 + R_6 / R_7) - SENS2 \times R_6 / R_7 \quad (6)$$

$$V_{O U1:B} = (SENS1 - SENS2) \times R_6 / R_7$$

Then:

$$V_{O U1:B} = V_{BAT} \times R_6 / R_7 \quad (7)$$

When the voltage $V_{O U1:B}$ drop below the voltage at the moving terminal of RV_1 , the comparator output will be low this will turn off D_4 which in turn, turns ON the power MOSFET to supply more current to the Battery. When the Battery voltage rise above the voltage at the moving terminal of RV_1 , the comparator output will be high. This will turn ON Q_6 and D_4 which in turn, turns OFF the power MOSFET to reduce the Battery charging current. This process will continue till the battery get fully charged and the charging current reduced greatly. At this point, the float charging will start.

The two fixed resistors R_9 and R_{10} are added to RV_1 to limit the max and min voltage at the moving terminal (terminal 3) of RV_1 . The values are selected such that the voltage at terminal 2 of RV_1 is:

$$\begin{aligned} V_{terminal 2} &= 5 \times R_{10} / (R_{10} + R_9 + RV_1) \\ &= 5 \times (10/35) = 1.4285V \end{aligned} \quad (8)$$

Similarly, the voltage at terminal 1 of RV_1 is:

$$V_{terminal 1} = 5 \times (R_{10} + RV_1) / (R_{10} + R_9 + RV_1) = 5 \times (20/35) = 2.8571V \quad (9)$$

From Eq. (7), these voltages correspond to battery voltages of

$$1.4285V \times R_7 / R_6 = 9.7397V \text{ and} \quad (10)$$

$$2.8571V \times R_7 / R_6 = 19.4802V \quad (11)$$

It is required to set the value of constant Voltage to $14.75V$. This value will be in the middle range of the trimming pot. The trimming pot must be adjusted such that the charging voltage in this stage is near $V_{BAT@CV} = 14.75V$.

The resister R_{13} is used to limit the base current for Q_3 to about $478.723\mu A$, for $+5V$ supply of the LM324, the comparator high level will be $3.65V$ [8] :

$$I_{B3} = (3.65 - 1.4) / 4.7k = 478.723\mu A \quad (12)$$

Since the minimum value of β in the transistor datasheet is 100 for collector currents less than $100mA$ [6] . This I_{B3} will results in collector current of about $47.872mA$, but since R_8 is $4.7k$ then max I_{C3} will not exceed $19/4700 = 4mA$. Then Q_3 will be heavily in saturation and the MOSFET gate voltage is zero. Also the resister R_{24} is used to limit I_{B6} to $70\mu A$ which will give about $7mA$ at the collector to turn the LED_3 ON.

$$I_{B6} = (1.4 - 0.7) / 10k = 70\mu A \quad (13)$$

The other function of R_{13} is to protect the OPAMP output stage when the output is high. D_4 and Q_3 will clipdown the opamp output voltage to about $1.4V$. This will provide low resistance path to the OPAMP output stage. R_{13} will prevent this short circuit.

The function of Capacitor C_3 is similar to C_2 in the last section, it compensates the feedback control loop.

2.5.Float Charging Circuit

The next figure (**Fig.8**) is the float charging circuit. The OPAMP $U_{1:D}$ is the core of this circuit. It always compares the battery charging current with reference value. When the charging current

reduced below 167mA (see eq.14 below), the comparator output will be high to turn ON LED2 and Q3 which will turn off the Power MOSFET. This reference value is determined by R15 and R16, in this case with the resistor values shown in the Fig., the voltage at pin12 will be:

$$V_{12} = 0.7 \times R_{16} / (R_{16} + R_{15}) = 0.7 \times (4.7 / 19.7) = 0.167V \quad (14)$$

The resistor R₁₁ (in Fig.5) is used to limit the base current for Q₃ to about 478.723μA:

$$I_{B3} = (3.65 - 1.4) / 4.7k = 478.723\mu A \quad (15)$$

Since the minimum value of β in the transistor datasheet is 100 for collector currents less than 100mA[6]. This I_{B3} will results in collector current of about 47.872mA, but since R8 is 4.7k then max IC3 will not exceed 19/4700 = 4mA. Then Q3 will be heavily in saturation and the MOSFET gate voltage is zero.

The circuit of Q4, C5, R18 and R20 is to turn off the comparator (make the output low) when there is no AC power. When the AC power is OFF, the base of Q4 is connected to ground through R19 and R18. Q4 will be ON and I_{B4} is -215μA:

$$I_{B4} = (-5 + 0.7) / (10k + 10k) = -215\mu A \quad (16)$$

Since the minimum value of β in the transistor datasheet is 100 for collector currents less than 100mA[7]. This I_{B4} will results in collector current of about -21.5mA, but since R₁₇ is 2.2k, then max I_{C4} will not exceed 5/2200 = -2.2727mA. Then Q4 will be heavily in saturation and the voltage at pin13 is +5V. When the AC power is ON, the transistor Q4 will be OFF because the base of Q4 will be connected to equivalent voltage of about +9.5V through equivalent base resistor of about 3.333k. This operation will not happen fast because of the charging time of C₅. The initial value of C₅ voltage is:

$$V_{C5initial} = (5 - 0.7) \times R_{18} / (R_{18} + R_{19}) = 2.15V \quad (17)$$

The final value of C₅ is:

$$V_{C5final} = 19V / 2 = 9.5V \quad (18)$$

The transistor will turn OFF when the capacitor value reaches 4.3V. The charging time constant is:

$$\tau = C_5 \times 5k \quad (19)$$

Using the capacitor charging equation to find the estimated time for the transistor Q₄ to turn OFF.

$$V_{C5} = V_{C5final} - (V_{C5final} - V_{C5initial}) \cdot e^{-\frac{t}{\tau}} \quad (20)$$

Solving for C₅ yield:

$$t = R_{eq} \cdot C_5 \cdot \ln\left(\frac{V_{C5final} - V_{C5initial}}{V_{C5final} - V_{C5}}\right) = 5k \cdot C_5 \cdot 0.346 \quad (21)$$

$$C_5 = \frac{t}{5k \cdot 0.346}$$

For 100ms delay, C₅ must be 57μF. Select 47 μF as the nearest standard value. This delay is important at start-up, because the charging current initially rises from zero to its constant value gradually. This delay will disable the comparison circuit till the charging current exceeds the 167mA. This will insure that the constant charging will start first. The capacitor discharge when the power is off will be through the resistor R18, R19 and the base of transistor Q4. This discharge time has no effect on the circuit operation.

2.6.Low Battery indication Circuit

Fig.9 shows the Low Battery indication and alarm circuit. The OPAMP U_{3A} is the core of this circuit. It always compares the battery voltage with the reference voltage. The circuit is Schmitt Trigger circuit to prevent LED and alarm fluctuation. When the battery voltage drops under 10 volt the LED will be ON and it will stay ON until the voltage become larger than 11V. Consider the output of the OPAMP is low then the voltage at pin3 is:

$$V_3 = 5 \times R_{30} / (R_{26} + R_{30} + R_{31}) = 5 \times (4.7 / 15.7) = 1.4968V = V_{TL} \quad (22)$$

This voltage corresponds to battery voltage of:

$$1.4968V \times R_7 / R_6 = 10.2054V \quad (23)$$

The output of the comparator will stay low unless the battery voltage reduced below the 11.7V. If the battery voltage reduced below this value, the comparator output will be high (about 5V-1.35V=3.65V [11]) and the current in D9 is about

$$I_{D9} = (3.65 - 0.7) / (100k) = 29.5\mu A \quad (24)$$

Referring to the diode Datasheet [12], V_{D9} will be about 440mV. Then the reference voltage will be:

$$V_3 = 5 \times (R_{30} || R_{29}) / (R_{26} + R_{30} || R_{29} + R_{31}) +$$

$$\begin{aligned} & \frac{(3.65V - V_{D9})}{(R_{30} \parallel (R_{26} + R_{31}) + R_{29})} \times \frac{(R_{30} \parallel (R_{26} + R_{31}))}{(R_{30} \parallel (R_{26} + R_{31}) + R_{29})} \quad (25) \\ & = 5 \times (4.489/15.7) + 3.21 \times \\ & 3.29299/(3.29299 + 100) = 1.449V + 0.10233V = \\ & 1.55133V = V_{TH} \end{aligned}$$

This voltage corresponds to battery voltage of:

$$1.55133V \times R_7/R_6 = 10.5772V \quad (26)$$

At the same time the red LED of the bicolour LED will be ON to indicate Low Battery ALARM. The comparator output will stay high till the Battery voltage exceeds the V_{TH} value. Practically the measured values are $V_{TH}=1.573V$ and $V_{TL}=1.518V$ and the transitions are at $V_{BAT} = 11V$ and $10.6V$ respectively.

This difference between the measured and the calculated voltages is due to the subtract circuit of U1:B non exact gain.

2.7. Output Power MOSFET Circuit

The Power MOSFET Q_1 is the main power transistor in the circuit. It was fixed on heat sink to dissipate extra heat generated inside it.

Q_3 and Q_2 are the driving transistors. Both of them must be OFF in order to make the MOSFET ON. If any one of them is ON, the gate of the MOSFET will be about zero and the MOSFET will be turned OFF see Fig.10.

R_{12} will provide the float charging current to the Battery. Changing this value will change the float charge current. For steady battery voltage of $12.8V$ and supply voltage of $19V$, the current will be:

$$\begin{aligned} I_{BAT@float} &= (19 - 12.8)/(220) \\ &= 28.1818mA \end{aligned} \quad (27)$$

This small current will count for the self discharge inside the battery cells and will prevent the battery from being over charged.

D_1 is the diode that supplies the DC voltage from the Battery to the system when the power is turned OFF. Therefore the output voltage will be $0.7V$ less than the battery voltage in case of AC power failure.

2.8. The Voltage regulator circuit

In order to make the circuit operation and reference voltages independent of battery voltage, 7805 voltage regulator was used to supply the OPAMP circuit. As shown in Fig.11.

2.9. The PCB

After passing all the primary tests, the circuit has been sent to PCB factory to produce the mass production. The circuit was printed on $10cm \times 13cm$ double layer PCB to fit inside the plastic enclosure. See the figure below.

2.10. The enclosure

A standard industrial plastic enclosure was selected for the case. See the figure below. It has standard DIN rail fixing accessories and high current barrier terminal block.

3. Test and results

In the following sections a typical data taken from one of the chargers, it was charging a $12V$ $4.5Ah$ Battery. The Battery was about 75% discharged when connected to the charger. The max charging current for the battery is $1.3A$ in the battery Datasheets[3]. All charging current in the following figures was normalized to this max value. All voltage readings also normalized to the max allowable voltage of $15V$.

3.1. Constant Current stage

Fig. 14 shows the change in battery voltage during the constant current charging stage. As seen in the figure, the voltage change is non-linear.

In Fig. 15, the charging current is approximately constant. However there is a small change in the value of the charging current as the battery voltage increases. This small change represents the accuracy of the constant current source circuit that was implemented. The change is $0.69A - 0.64A = 0.05A$. This is about 4%.

3.2. Constant Voltage stage

Fig. 16 shows the charging current variations during the constant voltage stage. It is clear that the charging current in this stage is reduced in exponential form.

Fig. 17 shows the charging voltage in this stage. It is clear that the voltage is approximately constant. However there is also a small change in the battery voltage. This change is clearer in the first 1000 points of the curve. This small change represents the limit of the constant voltage source circuit used. It is $14.42V - 14.53V = 0.11V$. This is about 1%.

3.3. Float charge stage

Fig. 18 and 19 show the charging current and voltage variations during the float charge stage

respectively. At the start point of this stage, the charging current reduced sharply to about few milli amperes. The battery voltage will drops gradually until reaches the battery steady state voltage. The charge current will increase for decreasing battery voltage.

4. CONCLUSION

Fast three stages SLA battery charger was designed, implemented and tested. This charger was able to charge 12V, 4.5A/h SLA Battery in about 2 hours and 23minutes. The three stages charger can charge the SLA batteries in short time while protecting the battery from over charge and self discharge. In the Constant Current Source the deviation was about 4% while the deviation for the constant voltage source is about 1% as seen in the results section. The control circuit is completely analogue electronic circuit. No digital parts were used. This will reduce time to fault and the system will be less sensitive to noise.

The main disadvantage of this design is that we need power supply of about 19V to supply the required power. It is about 4V above the maximum Charging voltage (15V). This is because of the MOSFT gate threshold voltage.

Better designs could use a supply voltage that is slightly above 15V to perform the same tasks without reducing the charging performance. The ambient temperature could be used to make the transition voltages between the stages more precise, also the Battery temperature could be used to monitor the Battery health and preventing over charge.

5. ACKNOWLEDGEMENT

This work was under the supervision and funding of Integrated Engineering Services Company. It was done under the project of installing 128 mobile Base transceiver station (BTS) around Baghdad.

6. REFERENCES

- [1] "Lead-acid battery", Wikipedia, the free encyclopedia, http://en.wikipedia.org/wiki/Lead-acid_battery, last modified on 5 March 2010.
- [2] Buchmann, "Charging the lead-acid battery" (BU13), batteryuniversity.com, <http://www.batteryuniversity.com/partone-13.htm>, April 2003.
- [3] "GP 1245 12V 4.5Ah Battery Datasheet", CSB BATTERY TECHNOLOGIES INC. (U.S.A), <http://www.csb-battery.com>, 2005.
- [4] Chiasson, J. Vairamohan, B, "Estimating the State of Charge of a Battery", Control Systems Technology, IEEE Transactions, Volume: 13 Issue: 3, pp. 465 – 470, May 2005.
- [5] Jiang Yong, Xie Ye, "TOPSwitch-based flyback converter optimal design of feedback circuit", Zhejiang University, Hangzhou 310027, <http://www.cp315.com/mdc/news/view.asp?id=3033>, 9 Oct. 2005.
- [6] "BC337, BC337-16, BC337-25, BC337-40, BC338-25 Amplifier Transistors NPN Silicon", Datasheet, Semiconductor Components Industries, LLC, http://www.onsemi.com/pub_link/Collateral/BC337-D.PDF, Rev. 2, October 2001.
- [7] "BC327, BC327-16, BC327-25, BC327-40 Amplifier Transistors PNP Silicon", Datasheet, Semiconductor Components Industries, LLC, http://www.onsemi.com/pub_link/Collateral/BC327-D.PDF, Rev. 5, March, 2007.
- [8] "LM124/LM224/LM324/LM2902 Low Power Quad Operational Amplifiers", Datasheet, <http://www.national.com/ds/LM/LM124.pdf>, August 2000.
- [9] "TOPSwitch-II Family Three-terminal Off-line PWM Switch", Datasheet, Power Integrations, Inc., <http://www.powerint.com/sites/default/files/product-docs/top221-227.pdf>, 2001.
- [10] "TL431/TL431A Programmable Shunt Regulator", Fairchild Semiconductor Corporation, <http://www.fairchildsemi.com/ds/TL/TL431A.pdf>, Rev. 1.0.3, 2003.
- [11] "LM158/LM258/LM358/LM2904 Low Power Dual Operational Amplifiers", Datasheet, <http://www.national.com/ds/LM/LM158.pdf>, October 2005.
- [12] "1N/FD1L 914/A/B / 916/A/B / 4148 / 4448 Small Signal Diode", Fairchild Semiconductor Corporation <http://www.fairchildsemi.com/ds/1N/1N4148.pdf>, Rev. B2, January 2007.
- [13] "IRF3205 HEXFET® Power MOSFET", International Rectifier, PD-91279E, <http://www.irf.com/product-info/datasheets/data/irf3205.pdf>, 25 Jan 2001.

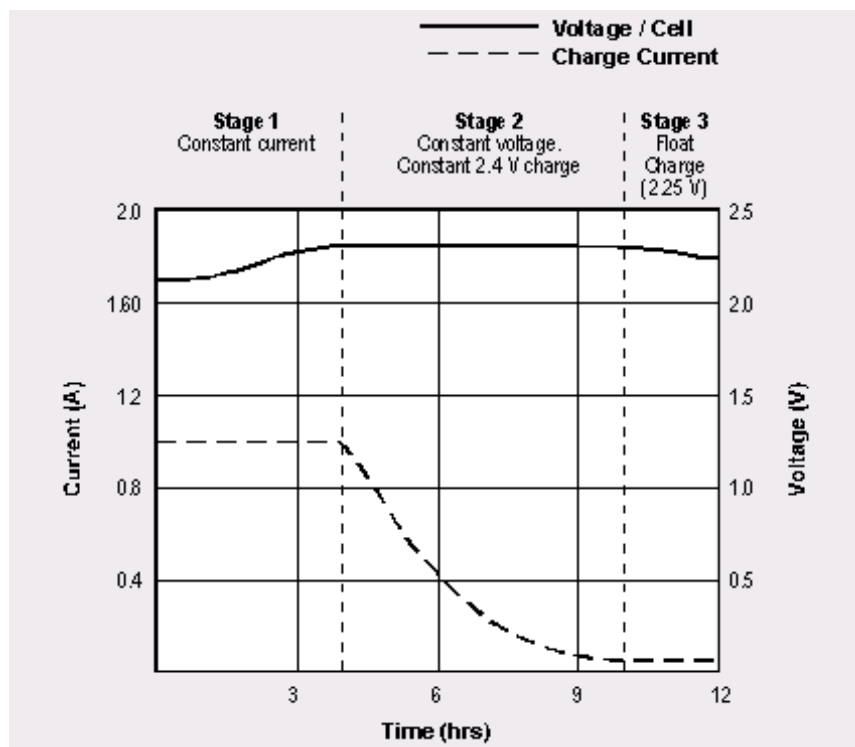


Figure 1: Charge stages of a lead-acid battery. The battery charges at a constant current to a set voltage threshold (Stage 1). As the battery saturates, the current drops (Stage 2). The float charge compensates for the self-discharge (Stage 3).

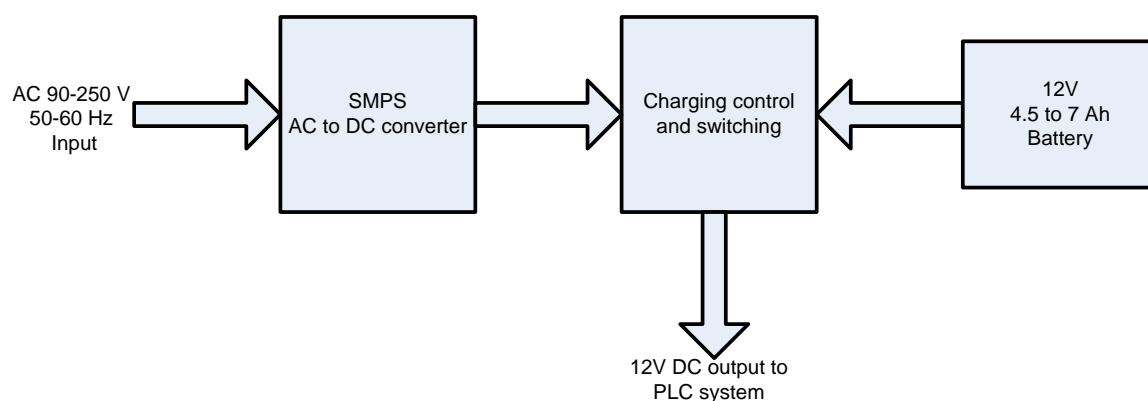


Figure. 2 simplified block diagram of the system

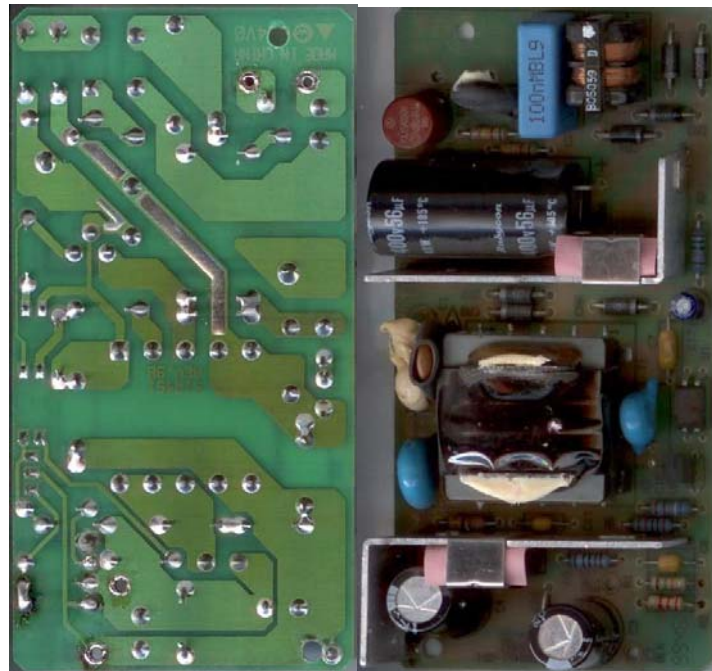


Figure. 3 SMPS board component side and solder side

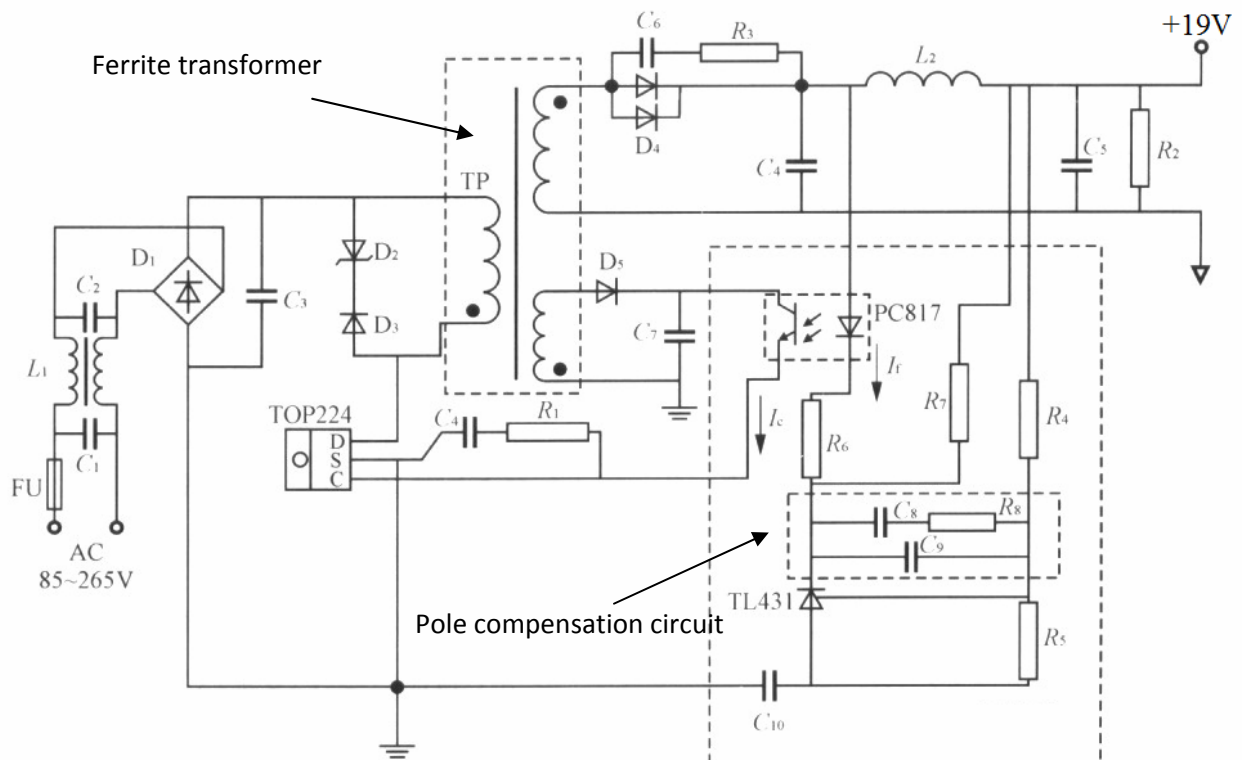


Figure. 4 Standard SMPS circuit diagram [5]



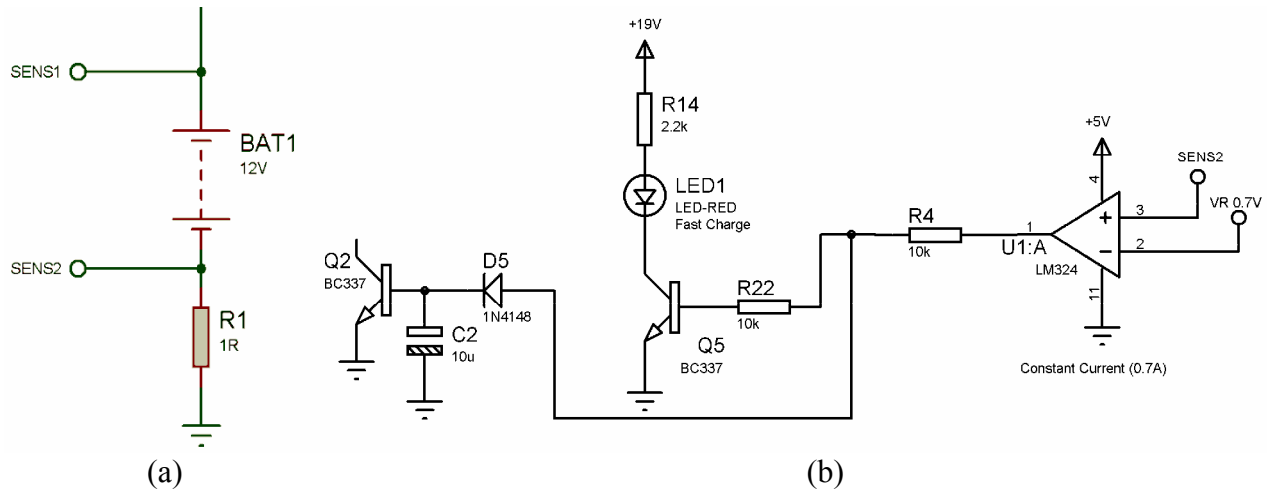


Figure. 6 (a) SENS1 and SENS2, (b) Constant Current Charging Circuit

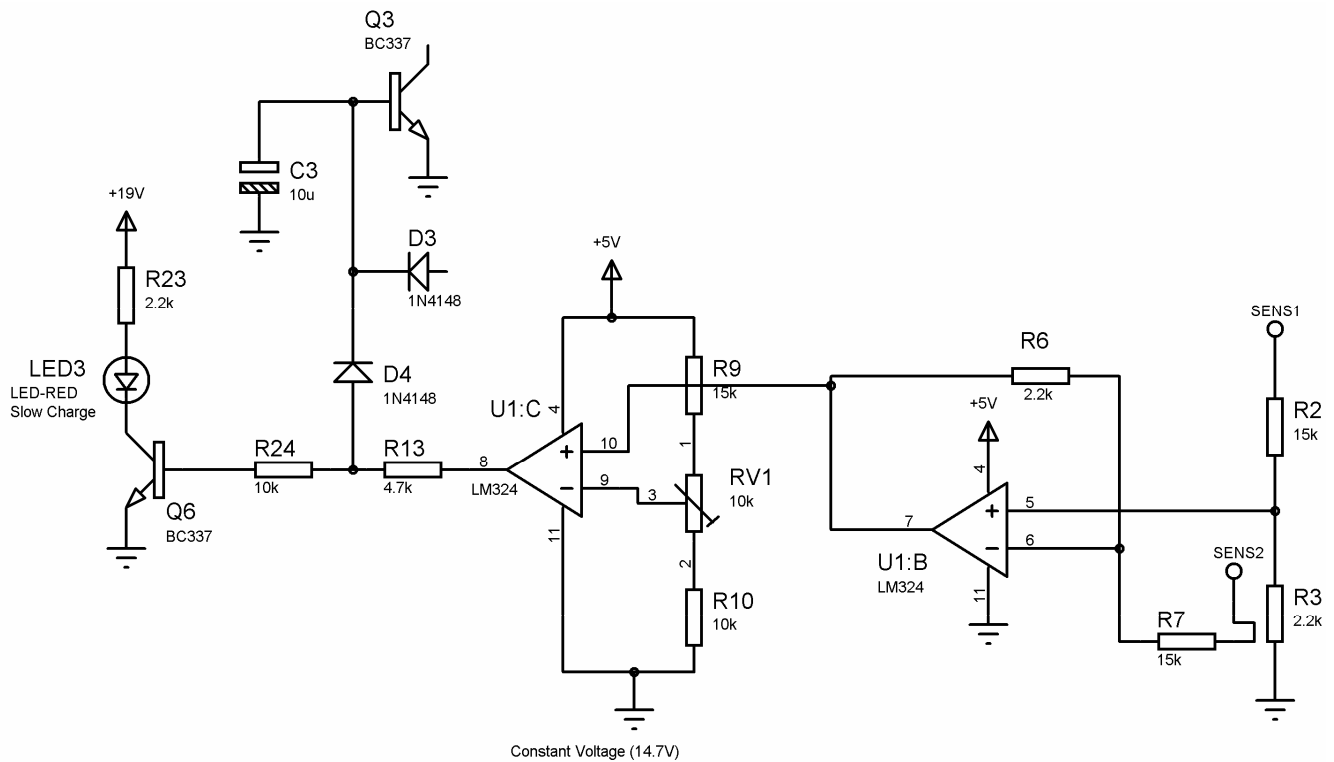
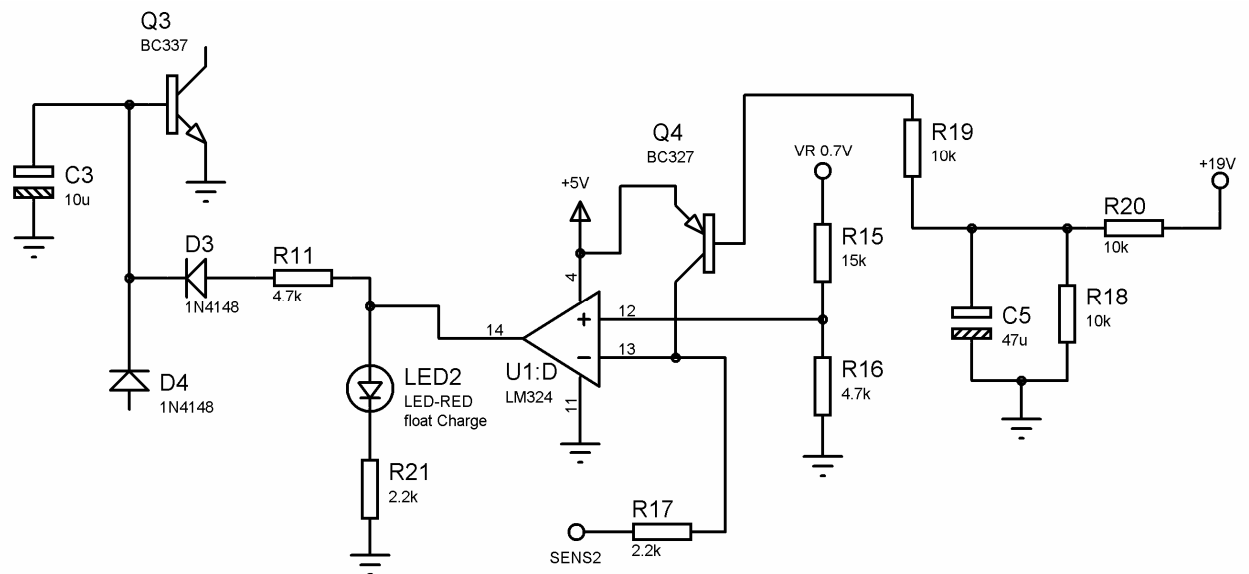
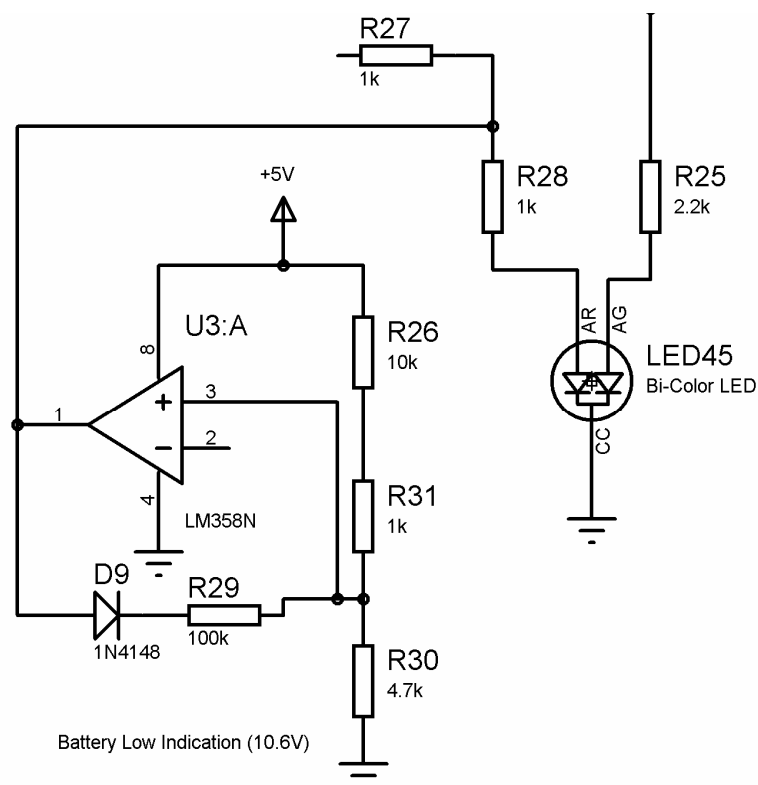


Figure. 7 Constant Voltage Charging Circuit

**Figure. 8 Float Charging Circuit****Figure. 9 Low Battery indication Circuit**

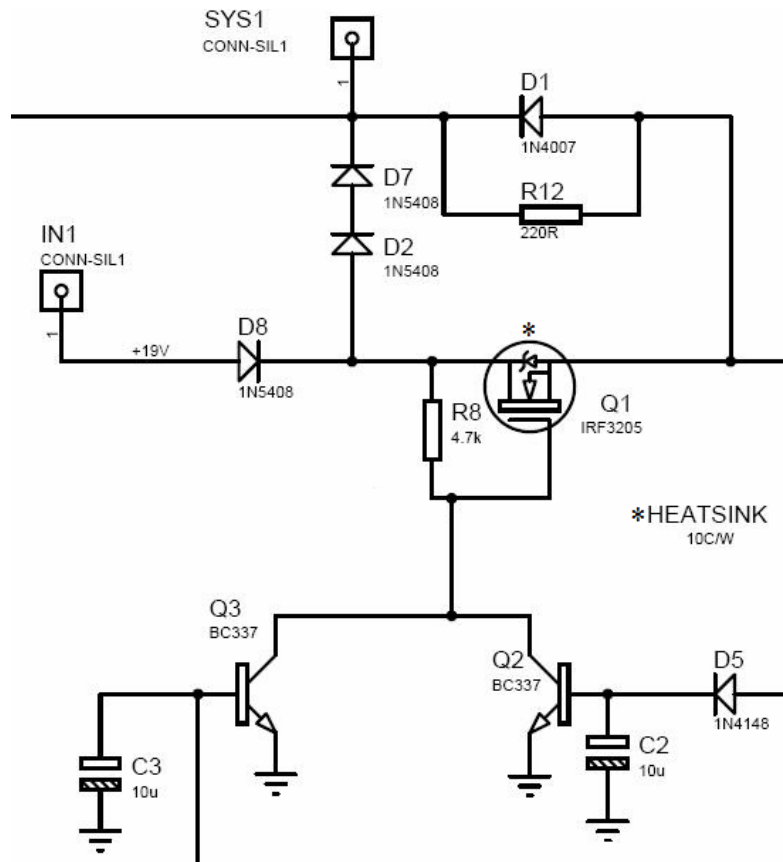


Figure. 10 Output Power MOSFET Circuit

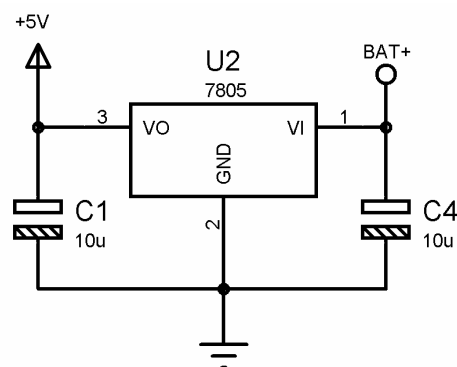


Figure. 11 Voltage Regulator Circuit

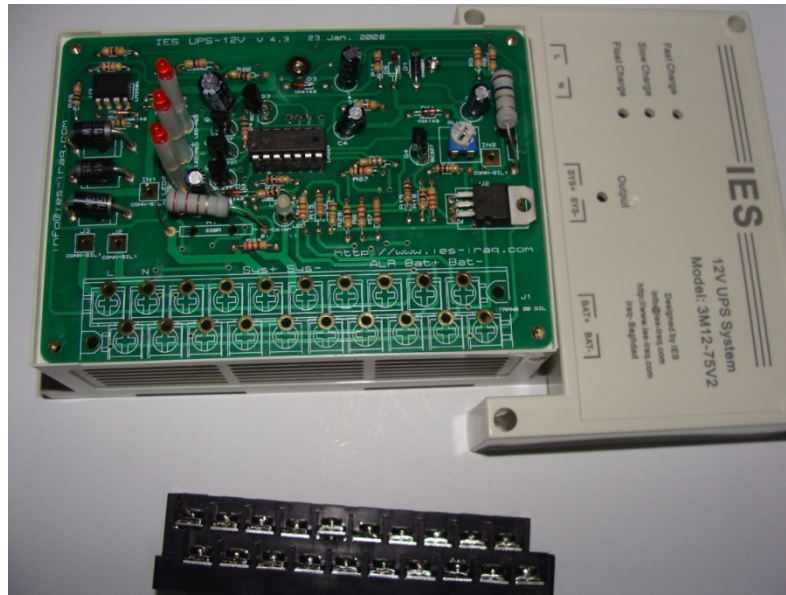


Figure. 12 PCB inside the enclosure

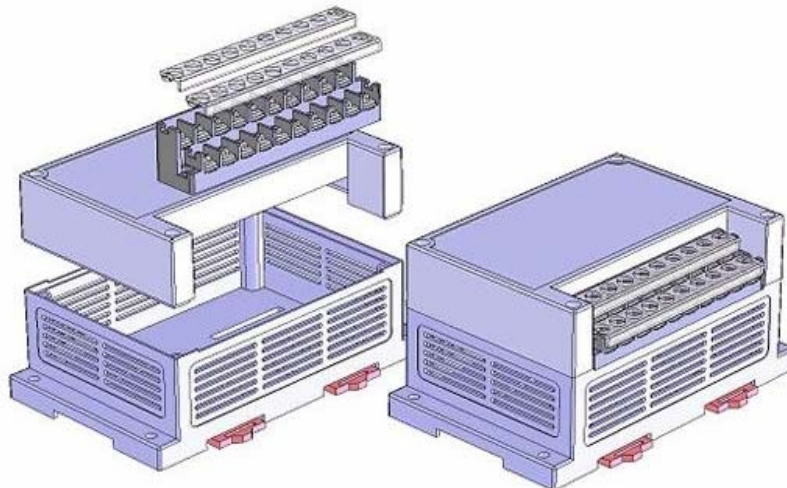


Figure. 13 the enclosure

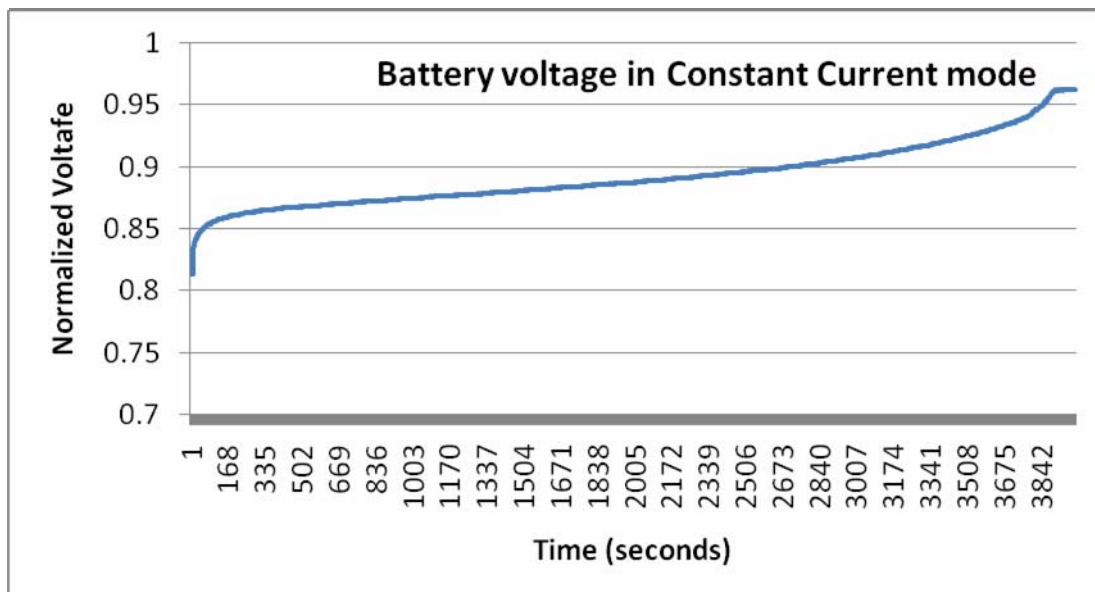


Figure.14 Battery voltage change during constant current stage

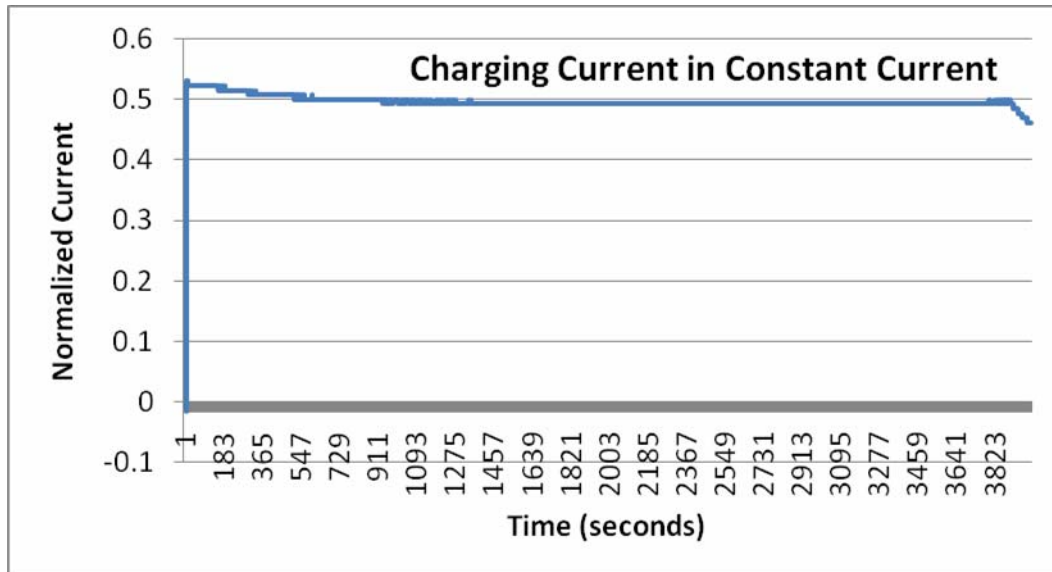


Figure.15 Battery Current change during constant current stage.

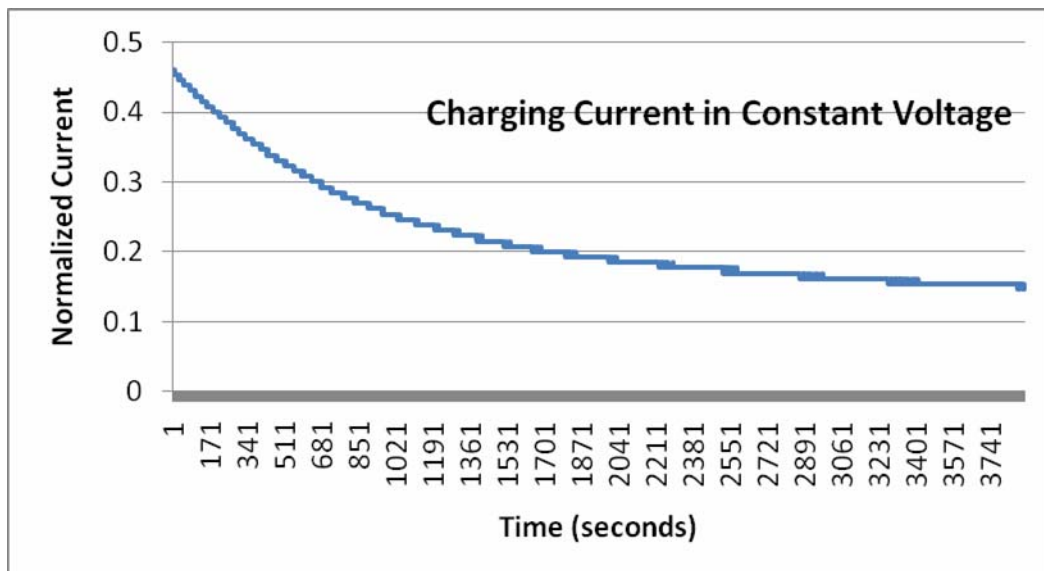


Figure.16 Battery Current change during constant voltage stage

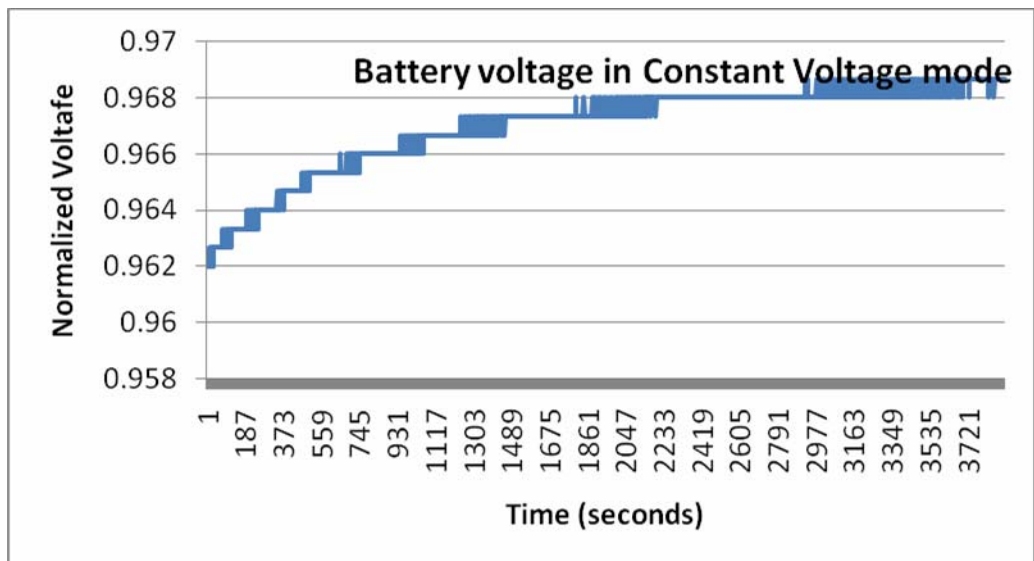


Figure.17 Battery Voltage change during constant voltage stage

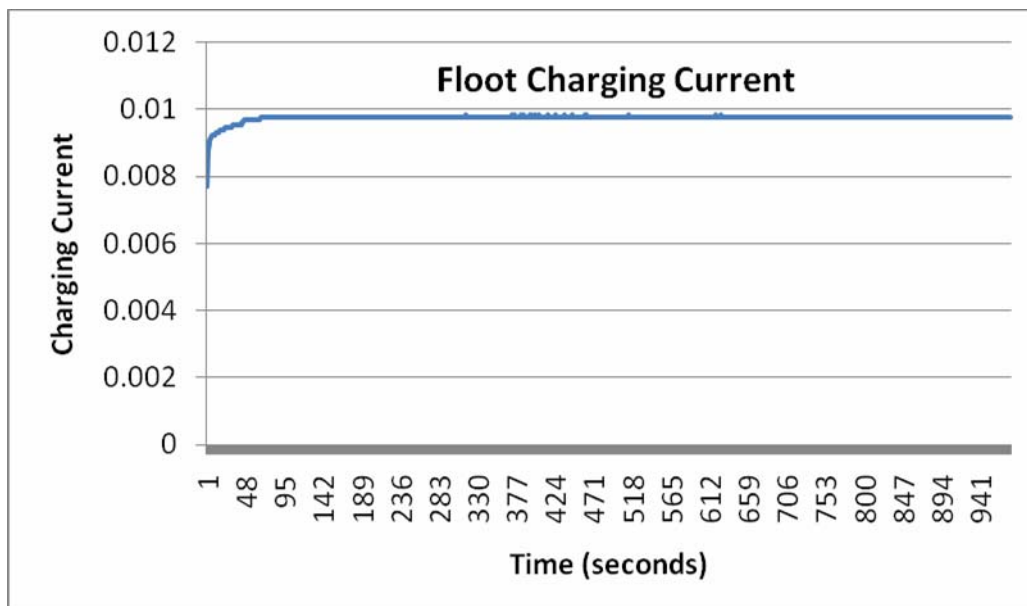


Figure.18 Battery Current change during float charge

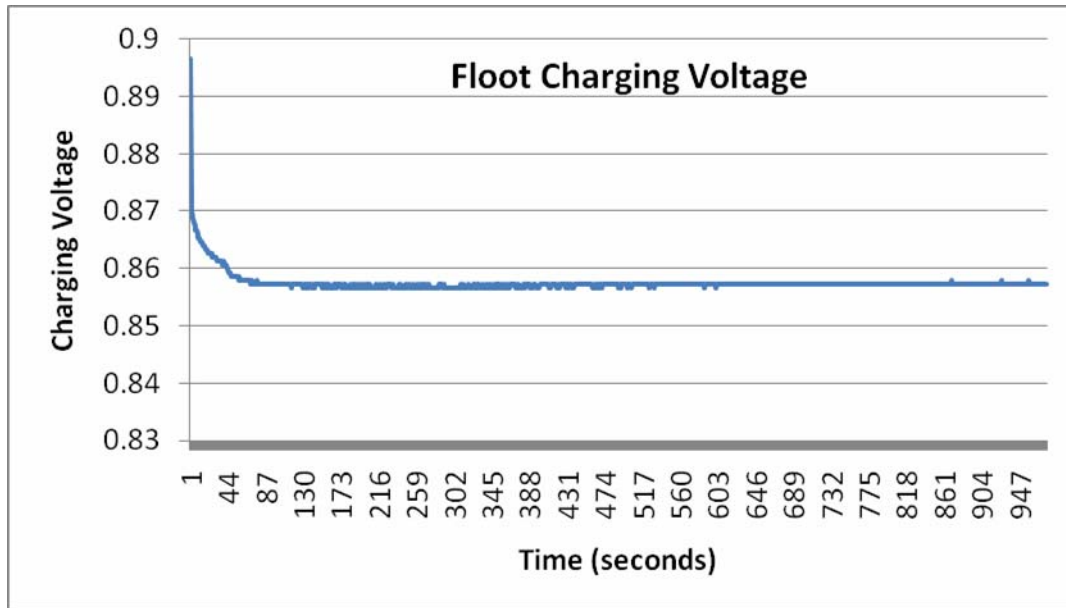


Figure.19 Battery Voltage change during float charge



DC MOTOR SPEED CONTROLLER DESIGN USING POLE ASSIGNMENT TECHNIQUE FOR INDUSTRIAL APPLICATION

Prof. Dr. Kais S. Ismail
Computer Engineering Dept.
University of Baghdad

Dr. Firas Mohammed Tuaimah
Electrical Engineering Dept.
University of Baghdad

Ruba Al-Mulla Hummadi
Mechanical Engineering Dept.
University of Baghdad

ABSTRACT

This paper describes DC motor speed control based on pole assignment feedback control technique. The present pole assignment technique specifies all closed-loop poles. Such a system where the reference input always zero is called a regulator system. The problem of shifting the regulator poles (closed-loop poles) at the desired location is called pole assignment problem, and this can be done if and only if the system is completely state controllable. Controller's objective is to maintain the speed of rotation of the motor shaft with a particular step response.

Results obtained were compared with another controller applied to the DC motor based on Proportional Integral Derivative (PID) control. The controller was designed and tested using MATLAB 7 programming language.

:

PID

MATLAB 7

KEYWORDS: DC motor, Speed control, PID controllers, Pole assignment technique

INTRODUCTION:

An electric motor is an electromechanical device that converts electrical energy into mechanical energy. This mechanical energy is used, for example, for rotating a pump impeller, fan or blower, driving a compressor, lifting materials etc. Electric motors are used at home (mixer, drill, fan) and in industry.

The purpose of a motor speed controller is to take a signal representing the demanded speed, and to drive

a motor at that speed. The controller may or may not actually measure the speed of the motor. If it does, it is called a Feedback Speed Controller or Closed Loop Speed Controller, if not it is called an Open Loop Speed Controller. Feedback speed control is better, but more complicated.

In modern intelligent motion applications especially in industry, the demand to the accurate speed and position control is increasing. In the mean time, it is also expected that control systems should be reliable,

cost effective, robust and, having with low volume weight and maintenance requirement. [Ayasun and Karbyaz, 2007]

Because of the improvements in computers software packages for modeling and simulations, many authors tried to build controllers to control the speed of a DC motor.

[Ayasun and Karbyaz, 2007] describe the MATLAB/SIMULINK realization of a DC motor speed control methods, namely field resistance, armature voltage and armature resistance control methods, and feedback control system for DC motor drives. They studied the torque/speed characteristics for different field resistance, armature voltage and different armature resistance, showing how the speed of the motor vary for different PI gain values.

[Sharaf, Elbakush and Altas, 2007] present a novel PID dual loop controller for a solar photovoltaic (PV) powered industrial permanent magnet DC (PMD) motor drive. MATLAB /SIMULINK was used in the analysis.

[Silva, Carvalho, Vasconcelos and Soares, 2007] present a remote experiment for controlling a DC motor. The experiment is controlled using a PID algorithm programmed in LabView environment.

[Roubal, Augusta, and Havlena, 2005] present the procedure of the control design, including a description of a system, an identification of its parameters, a simple and an advanced controller design based on optimal control.

[Aung, 2007] gave an analyze how to choose DC motor to be balance with their applications of especially for Wheeled Mobile Robots (WMR). Specification of DC Motor that can be used with desire WMR is to be determined by using MATLAB Simulink model.

MOTOR MODEL

Generally, the rotational speed of a DC motor is proportional to the voltage applied to it, and the torque is proportional to the current. Speed control can be achieved by variable battery tappings, variable supply voltage, resistors or electronic controls.[speed controller,2008]

A simple motor model is shown in Fig. 1. The armature is modeled as a circuit with resistance R_a

connected in series with an inductance L_a , e_a and e_b represent a voltage source and the back emf (electromotive force) in the armature when the rotor rotates respectively. [Ogata-1998, Ogata-2002, Dorf and Bishop-2005].

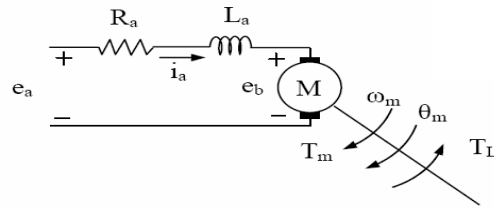


Fig. 1 DC Motor Model.

The motor torque T_m is related to the armature current, i_a , by a torque constant K_i ;

$$T_m = K_i i_a \quad (1)$$

The back emf, e_b , is relative to angular velocity by;

$$e_b = K_b \omega_m = K_b \frac{d\theta_m}{dt} \quad (2)$$

From Fig. 1 we can write the following equations based on the Newton's law combined with the Kirchhoff's law. [Ogata, 1998]

$$L_a \frac{di_a}{dt} + R_a i_a = e_a - K_b \frac{d\theta_m}{dt} \quad (3)$$

$$J_m \frac{d^2\theta_m}{dt^2} + B_m \frac{d\theta_m}{dt} = K_i i_a \quad (4)$$

There are several different ways to describe a system of linear differential equations. The plant model will be introduced in the form of **state-space representation** and given by the equations:

$$\begin{aligned} \dot{x} &= Ax + Bu \\ y &= Cx + Du \end{aligned} \quad (5)$$

According to equations from (2) to (4), the state space model will be:

$$\begin{bmatrix} \dot{i}_a \\ \dot{\omega}_m \\ \dot{\theta}_m \end{bmatrix} = \begin{bmatrix} -R_a/L_a & -K_b/L_a & 0 \\ K_t/J_m & -B_m/J_m & 0 \\ 1 & 1 & 0 \end{bmatrix} \begin{bmatrix} i_a \\ \omega_m \\ \theta_m \end{bmatrix} + \begin{bmatrix} 1/L_a \\ 0 \\ 0 \end{bmatrix} e_a \quad (6)$$

$$\omega_m = [0 \quad 1 \quad 0] \begin{bmatrix} i_a \\ \omega_m \\ \theta_m \end{bmatrix} \quad (7)$$

Fig.2 shows the closed loop control system for the DC motor in the form of a block diagram. [Aung,2007].

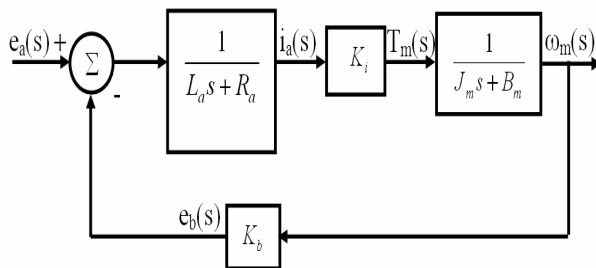


Fig. 2 DC-Motor System Block Diagram

POLE ASSIGNMENT TECHNIQUE:

In this section a design of a commonly called Pole-Placement or Pole-assignment technique will be presented. All state variables are assumed to be measurable and available for feedback. If the system is considered completely state controllable, then poles of the closed-loop system may be placed at any desired locations by means of state feedback through an appropriate state feedback gain matrix.

In the conventional approach to the design of a single-input-single-output control system a designed controller (compensator) such that the dominant closed-loop poles have a desired damping ratio ζ and an undamped natural frequency ω_n . In this approach, the order of the system may be raised by 1 or 2 unless pole-zero cancellation takes place.

In brief the pole assignment technique is somewhat similar to the root locus method in that a closed loop poles are placed at desired locations. The basic difference is that in root locus design only the dominant closed loop poles are placed at the desired locations, while in the pole assignment technique all the closed loop poles are placed at the desired locations. [Ogata-1998, Ogata-2002, Dorf and Bishop-2005].

For a control system of eq. (5) and depending on the pole assignment the control signal will be:

$$u = -Kx \quad (8)$$

Fig.3 shows the control model that is based on the pole assignment.

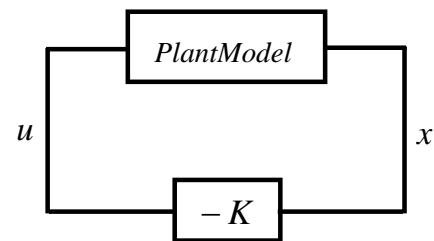


Fig. 3 Closed Loop Control System

This means that the control signal u is determined by the instantaneous state, Substituting eq. (8) into eq. (5) gives

$$\dot{x}(t) = (A - BK)x(t) \quad (9)$$

The solution of this equation is given by

$$x(t) = e^{(A-BK)t}x(0)$$

Where $x(0)$ is the initial state caused by external disturbances. The stability and transient response characteristics are determined by the eigenvalues of matrix $(A - BK)$. The eigenvalues of matrix $(A - BK)$ are called regulator poles. If these regulator poles are placed in the left-half s -plane, then $x(t)$ approaches 0 as t approaches infinity. The problem of placing the regulator poles (closed-loop poles) at the desired location is called a pole assignment problem. [Ogata-1998, Ogata-2002, Dorf and Bishop-2005].

CHOOSING THE LOCATION OF DESIRED CLOSED LOOP POLES:

The first step in the pole assignment technique is to choose the location of the desired closed loop poles. The most frequently used approach is to choose such

poles based on experience in the root locus design, placing a dominant pair of closed loop poles and choosing other poles so that they are far to the left of the dominant closed loop poles.

Note that if the dominant closed loop poles are placed far from the $j\omega$ axis, so that the system response becomes very fast, the signals in the system become very large, with the result that the system may become nonlinear. This should be avoided. [Ogata,2002]

PID TECHNIQUE:

The Proportional Integral Derivative (PID) controller calculation (algorithm) involves three separate parameters; the proportional, the integral and derivative values. The proportional value determines the reaction to the current error, the integral value determines the reaction based on the sum of recent errors, and the derivative value determines the reaction based on the rate at which the error has been changing, as shown in Fig. 4.

By tuning the three constants in the PID controller algorithm, the controller can provide control action designed for specific process requirements. The response of the controller can be described in terms of the responsiveness of the controller to an error, the degree to which the controller overshoots the set point and the degree of system oscillation. [Ogata-1998, Ogata-2002, Dorf and Bishop-2005].

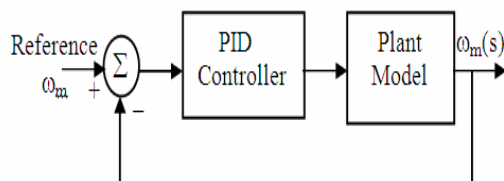


Fig. 4 PID Controller System Block Diagram

SIMULATION RESULTS:

This section presents simulation results for the speed control of a DC motor given in Appendix (A) using pole assignment technique through feedback control system. The steps of the PID controller and pole

assignment design and comparison between them based on time domain is given in the flowchart of Fig. 5.

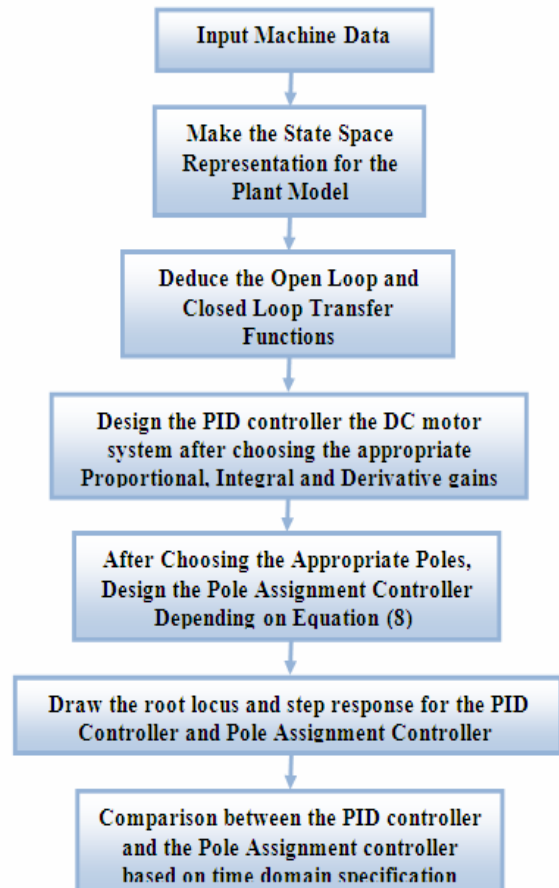


Fig.5 Flowchart for the Controller Design
Procedure

In many practical cases, the desired performance characteristics of control systems can be given in terms of transient-response characteristics.

The open loop transfer function of the DC motor according to the selected data can be given as in eq. (10), with two poles $(-0.0575+j0)$ and $(-1.95+j0)$:

$$TF_{open-loop} = \frac{0.23}{0.0055s^2 + 0.010025s + 0.000559} \quad (10)$$

To examine the accurate speed and position control, the time domain specifications (Settling time; Peak amplitude, Maximum overshoot) the close loop control system should be studied.

The closed loop transfer function of the DC motor according to the selected data can be given as in eq.(11), with two poles $(-1+j1.96)$ and $(-1-j1.96)$:

$$TF_{\text{closed-loop}} = \frac{0.23}{0.0035s^2 + 0.010025s + 0.02356} \quad (11)$$

The closed loop step response (with unity feedback control) is shown in Fig. 6, which shows that the settling time of 3.83second and peak amplitude of 1.17.

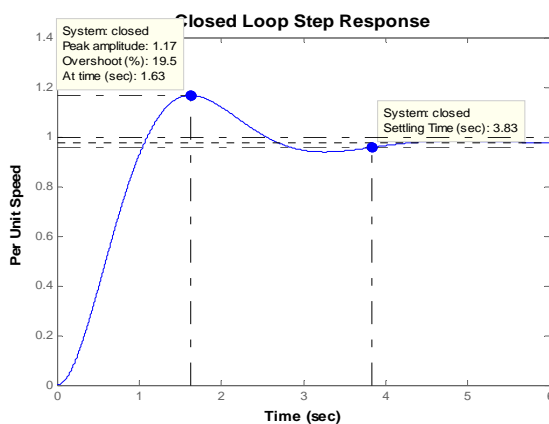


Fig. 6 Closed Loop Speed Step Response

Fig. 7 shows the step response for the PID controller which gives settling time of 2.76 sec and the peak amplitude of 1.85.

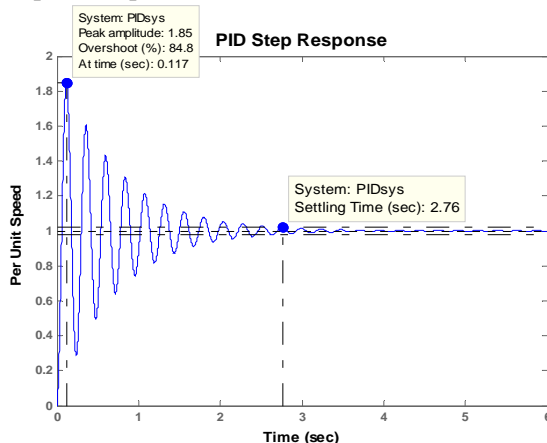


Fig. 7 PID Speed Step Response

Fig. 8 shows the root locus for the pole assignment technique where the closed loop roots $(-1+j1.96)$ and $(-1-j1.96)$ are shifted to $(-2.025 + j0.7)$ and $(-2.025 - j0.7)$, this shift was done by tray and error to give more stability for the system.

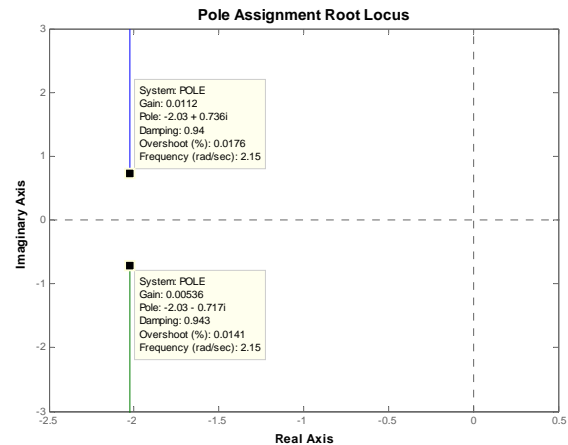


Fig. 8 Pole Assignment Root Locus

Fig. 9 shows the step response for the Pole Assignment controller which gives settling time of 2.43 sec and peak amplitude of 1.

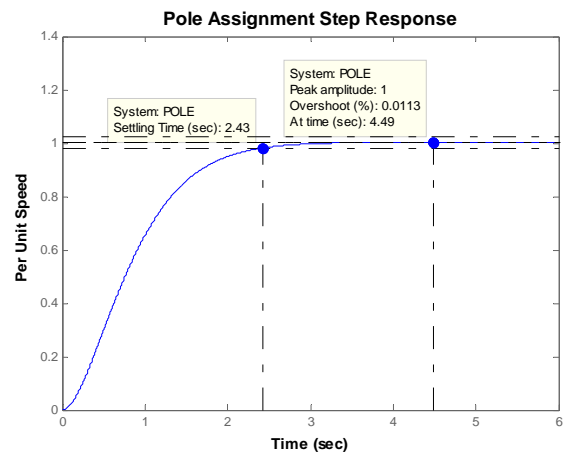


Fig. 9 Pole Assignment Speed Step response

Table 1 summarizes the values of settling time, peak amplitude and overshoot for the three different control systems, which are given previously, it is clear that the pole assignment controller is better.

Table 1: Time response specification for three speed control systems

	Settling Time	Per Unit Speed	Over shoot
Closed Loop With Unity Feedback	3.83 sec	1.17	19.5%
PID Controller	2.76 sec	1.85	84.8%
Pole Assignment Controller	2.43 sec	1	0.0113%

Drawing the plots of the closed loop with unity feedback and with PID controller and with Pole Assignment are clear indicated in Fig.10

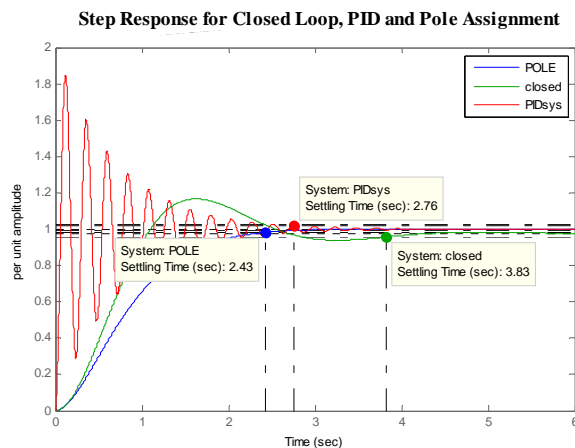


Fig. 10 Closed Loop, PID and Pole Assignment Speed Step responses

CONCLUSION

The paper presents a controller design for a dc motor speed control based on Pole Assignment technique which has been compared with another type of controller like the PID controller and with only closed loop unity feedback (no controller).

Table 1 and Fig. 10 above shows the time response specifications which indicates clearly that using the Pole Assignment Technique as a speed controller for the DC motor is a very efficient, since it shifts the left hand poles to a stable region far away from the critical area.

REFERENCES:

- A.M. Sharaf, E. Elbakush and I. H. Altas: "Novel Control Strategies for Photovoltaic Powered PMDC Motor Drives", IEEE, 2007, pp.1-6.
- Jirka Roubal, Petr Augusta, and Vladimír Havlena: "A Brief Introduction to Control Design Demonstrated on Laboratory Model servo DR300-amira, Acta Electrotechnica et Informatica No. 4, Vol. 5, 2005, pp.1-6
- Katsuhiko Ogata: "System Dynamics"; Pren-tice Hall International, Inc. Third Edition 1998.
- Katsuhiko Ogata: "Modern Control Engineering"; Prentice Hall International, Inc. Fourth Edition 2002.
- Richard C. Dorf and Robert H. Bishop: "Modern Control Systems"; Pearson Prentice Hall, 2005.
- S. Ayasun & G. Karbeyaz: DC motor speed control methods using MATLAB/Integration into undergraduate electric machinery courses, Wiley Periodicals Inc., 2007
- Speed Controllers,
- <http://homepages.which.net/~paul.hills/SpeedControl/SpeedControllersBody.html> ,2008
- V. Silva, V. Carvalho, R.M. Vasconcelos and F. Soares: "Remote PID Control of a DC Motor", International Journal of on line Engineering-www.i-joe.org,REV2007 conference, Porto, Portugal, June 2007, pp.1-3
- Wai Phyo Aung: Analysis on Modeling and Simulink of DC Motor and its Driving System Used for Wheeled Mobile Robot, proceedings of world academy of science, engineering and technology vol. 26 dec. 2007, pp.299-306

**LIST OF SYMBOLS**

A = $n \times n$ constant matrix
 B = $n \times 1$ constant matrix
 B_m = viscous friction coefficient (kgm²/s)
 C = $1 \times n$ constant matrix
 D = constant
 $e_a(t)$ = applied voltage (V)
 $e_b(t)$ = back emf (V)
 $i_a(t)$ = armature current (A)
 J_m = moment of inertia of rotor (kgm²)
 K_i = torque constant (Nm/A)
 K_b = back emf constant (V/rad/s) ($K_b = K_i$)
 L_a = armature inductance (H)
 R_a = armature resistance (Ω)
 $T_L(t)$ = load torque (Nm)
 $T_m(t)$ = motor torque (Nm)

u = control signal
 x = state vector
 y = output signal
 ϕ = magnetic flux in the air gap (Weber, Wb = Vs)
 $\theta_m(t)$ = rotor displacement (rad)
 $\omega_m(t)$ = rotor angular velocity (rad/s)
 ω_n = undamped natural frequency
 ζ = damping ratio

APPENDIX A

DC motor data are: $E = 12$ Volt
 $J_m = 0.01$ kgm², $B_m = 0.00003$ kgm²
 $K_i = 0.023$ Nm/A, $K_b = 0.023$ Nm/A
 $R_a = 1\Omega$, $L_a = 0.5$ H



ESTIMATING THE SEDIMENT TRANSPORT CAPACITY OF TIGRIS RIVER WITHIN AL MOSUL CITY.

Ala Hassan Nama
University of Baghdad, Baghdad – Iraq.

ABSTRACT

The capacity of Tigris River to transport the sediment within Al Mosul City is one of the most important characteristics of the river. Establishment of islands within this reach of the river because of decreasing the discharge of Tigris River can be controlled through studying this characteristic. Establishment of these islands and increase of the sediment deposition in the river reach affect the water treatment plants and the urban and industrial activities that are located on the banks of this reach.

A steady one dimensional mathematical model for simulating the flow and estimating the sediment transport capacity of the studied reach was implemented and run by using the HEC-RAS (Version 3.1.3) software and making use of recorded field measurements for running and carrying out the calibration and verification processes.

Flow velocity and sediment transport capacity were estimated for a range of discharge from 50 to 1500m³/sec. Locations of the low flow velocity were specified. The comparison between sediment capacity rating curves of these locations showed that the sediment transport capacity of the reach cross sections at 13000 and 4500m from the end of the reach, before and after Al Khosar River, is less than that of the other cross sections of this reach.

The comparison between the sediment transport capacity and the inflow sediment quantity into the river reach before and after Al Khosar River with discharge and sediment concentration of 425m³/sec and 600ppm from Al Mosul Dam and 5m³/sec and 3150ppm from Al Khosar River showed that the deposited sediment in the river reach before and after Al Khosar River was 21900 and 15000tonnes/day, respectively.

To avoid deposition of sediment before Al Khosar River and then along the studied reach the inflow discharge into the reach from Al Mosul Dam must be not less than 1500m³/sec. While, to avoid deposition of sediment after Al Khosar River the total discharge must be not less than 780m³/sec. The river reach cross section of low flow velocity must be developed to increase the sediment transport capacity.

Keywords: Sediment Transport Capacity, Establishment of islands, Al Khosar River

HEC-RAS (Version 3.1.3)

50

. /³ 1500

4500 13000

3150 /³ 5600 /³ 425

/ 15000 / 21900

. /³ 1500. /³ 780

1- Introduction

The reach of Tigris River from the north side of Al Mosul City to the southern end of this city, 21km, is important because it divides the city into two parts which are the Right bank and the Left bank, Figure 1. Most of the water treatment plants intakes are placed on this reach in addition to the existence of different industrial and urban activities.

There are two bends in this reach. The first at the beginning and the second at the end of this reach. However, it is straight through the city and contains a number of big and small islands.

Al Khosar River, which is a small seasonal tributary, discharged in this reach of Tigris River at the beginning of the last third of the reach.

The decrease in the discharge of Tigris River because of the decrease in the water resources causes a decrease in flow velocity, Establishment of islands and changing the morphological characteristics of this reach.

Capacity of the river to transport the sediment is one of the most important characteristics of the river and plays the major role in the establishment of islands and changing the morphological characteristics of this reach.

Integration of steady one dimensional mathematical model and field observation data and utilizing the HEC-RAS software (Version 3.1.3) was used to implement and run a simulation model to estimate the flow velocity and the capacity of the river to transport the sediment.

2- River Data

Seventy seven cross sections were surveyed along the studied reach, by using the Echo Sounder instrument [1]. These cross sections were selected to represent the geometry of each part of the reach, Figure 1. The distance between the surveyed cross sections ranged between 71 to 606m.

The water surface elevation was measured at 16 cross sections [2]. These measured water surface elevations are listed in Table 1.

The upstream inflow discharges into this reach were approximately constant during the period of measurements, 60 days, because they depend on the operation requirements of Al Mosul Dam. This discharge was 425m³/sec. The maximum, average and minimum recorded discharges at Al Huriah station in Al Mosul City for the period from the year 1986 to 2009 were 3180, 500, and 41 m³/sec, respectively[3].

The measured discharge of Al Khosar River at its outfall in Tigris River was $5\text{m}^3/\text{sec}$ [2], while the range of its discharges is between 5 to $150\text{m}^3/\text{sec}$ [4].

The velocities of flow were measured at 40 cross sections by using the Current Meter instrument [2]. The mean velocities of flow at these 40 cross sections are listed in Table 2.

The suspended and bed sediment load of Tigris River are trapped at the upstream of Al Mosul Dam. The source of the suspended and bed sediment transported in the studied reach, 60km downstream of the dam, is the catchment area of the river between Al Mosul Dam and Al Mosul City and the catchment area of Al Khosar River which transports this load into Tigris River.

The concentration and grain size distribution of the suspended sediment along this reach were measured by using the Turbidity Meter and Hydrometer instruments [2]. These measurements were carried out at different flow and rainfall conditions. Concentration of the suspended sediment when there is no rainfall, the water flows in the studied reach is only that released from Al Mosul Dam, was between 6 to 30ppm. When there is rainfall, this concentration becomes 600ppm in the reach before Al Khosar River and 3150ppm in the reach after Al Khosar River. Analysis of the collected samples shows that the grain size distribution of the suspended sediment was as shown in Figure 2.

3- Flow Routing Model

A steady one dimensional flow mathematical model was used to simulate the flow in this reach in order to obtain the water surface elevation, flow velocity, and sediment transport capacity along the reach under a set of steady flow conditions.

The HEC-RAS software (Version 3.1.3) [5] was used to accomplish this target.

3-1 Geometrical Data

The surveyed river cross sections [1], left and right banks, downstream reach length, proposed initial Manning's roughness coefficient, n , of the main channel, and other reaches' information where the geometrical data are

required to run the model were input to the model through the menu of cross sectional geometrical data.

All hydraulic structures, five bridges, on the river were specified and their details were involved to the model using bridge or culvert geometrical data menu.

3-2 Upstream Boundary Condition

The HEC-RAS model deals with the boundary conditions depending on the flow regime. In a subcritical flow regime, which is the flow regime in the river under consideration, boundary condition is only necessary at the D/S end of the river system and deals with its data in a separated window.

The measured discharge, $425\text{m}^3/\text{sec}$, and a range of discharges from 50 to $1500\text{m}^3/\text{sec}$, Table 3, were adopted as the upstream boundary required to run the model, one value is used at each time.

Flow-change locations, Al Khosar River outfall, were specified and the net flow through the river reaches was input to the model using the steady data menu.

3-3 Downstream Boundary conditions

A known constant stage type boundary condition was adopted to run the hydraulic model for the case of measured discharge, $425\text{m}^3/\text{sec}$. This stage was 211.7 m.a.s.l at cross section no. (77). Normal flow type boundary condition was adopted for running the model for the other cases, (the discharge range listed in Table 3). The adopted normal flow slope was 0.000035. These data were input to the model through the menu of steady flow data.

3-4 Model Calibration

A calibration process was carried out using stage measurements along the reach, Table 1, and the measured discharge at the upstream end of this reach, $425\text{m}^3/\text{sec}$, and the discharge of Al Khosar River into this reach, $5\text{m}^3/\text{sec}$.

The calibrated Manning's n values along the main channel and its left and right banks are 0.038 and 0.05, respectively.

An acceptable agreement was achieved between the estimated stage values using the

calibrated data and the measured stage values as shown in Figure 3.

3-5 Model Verification

The measured velocities at the 40 cross section, Table 2, were used for the verification process. The comparison between those estimated by using the model and measured mean velocities at these cross sections is shown in Figure 4. This comparison shows an acceptable agreement.

3-6 Sediment Transport Capacity

The sediment transport capacity computations can only be run once steady flow computations have been run. Sediment Transport Capacity for any cross section can be computed using Ackers-White, Meyer-Peter Müller, Laursen, Toffaletti, or Yang sediment transport functions.

The morphological characteristics of the studied reach are compatible with the criteria of Toffaletti (modified-Einstein) sediment-transport function [6] which are:

Toffaleti (field):

$0.062 < d < 4 \text{ mm}$; $0.095 < d_m < 0.76 \text{ mm}$;
 $0.21 < V < 2.36 \text{ m/s}$; $0.021 < R < 17.18 \text{ m}$;
 $0.000002 < S < 0.0011$; $19.1 < W < 1103.03 \text{ m}$;
 $40 < T < 93 \text{ degrees F}$

Toffaleti (flume):

$0.062 < d < 4 \text{ mm}$; $0.45 < d_m < 0.91 \text{ mm}$;
 $0.21 < V < 1.9 \text{ m/s}$; $0.0021 < R < 0.33 \text{ m}$;
 $0.00014 < S < 0.019$; $0.24 < W < 2.42 \text{ m}$;
 $32 < T < 94 \text{ degrees F}$

A modified-Einstein total load function that breaks the suspended load distribution into vertical zones, replicates two-dimensional sediment movement. Four zones are used to define the sediment distribution. They are the upper zone, the middle zone, the lower zone, and the bed zone. Sediment transport is calculated independently for each zone and summed up to arrive at total sediment transport. This method was developed using an exhaustive collection of both flume and field data. The flume experiments used sediment particles with mean diameters ranging from 0.45 to 0.91 mm; however, successful applications of the Toffaletti method suggests that mean particle diameters as low as 0.095 mm are acceptable.

The sediment transport capacity was estimated for the measured discharge, $425 \text{ m}^3/\text{sec}$, and a range of discharges from 50 to $1500 \text{ m}^3/\text{sec}$, Table 3.

4- Results

Results of applying the implemented model for the adopted range of discharges revealed that the water surface elevations and velocity along the studied reach were as shown in Figures 5 and 6. The mean flow velocity at main channel distances 2000 and 4500m, after Al Khosar River outfall and 9500, 13000, and 19000 m, before Al Khosar River outfall, at cross sections number 71, 62, 40, 28 and 9, respectively, was less than 0.5 m/sec for most of the adopted discharges. These low flow velocities occurred at the constituted islands at the reaches of high bed elevation and wide cross sections. These cross sections can be considered as critical sections.

The estimated sediment transport capacities, by using Toffaletti function, along the studied reach for the adopted range of discharges are shown in Figures 7 to 14.

The sediment transport capacity rating curves at the critical sections, cross sections number 71, 62, 40, 28 and 9, are shown in Figure 15. These rating curves show that the sediment transport capacity at the channel distance 4500 and 13000 m, cross sections no. 62 and 28, is less than that of other cross sections along the reach.

For the measured inflow discharge and suspended sediment concentrations from Al Mosul Dam and that from Al Khosar River, during a rainy duration, were $425 \text{ m}^3/\text{sec}$, 600ppm, $5 \text{ m}^3/\text{sec}$ and 3150 ppm, respectively. The quantity of inflow sediment into the studied reach before Al Khosar River is 22032 and that from Al Khosar River is 3160.8 tons/day, respectively and the total sediment quantity inflow into the river reach after Al Khosar River is 25192.8 tons/day. Accordingly, the quantity of deposited sediment at cross sections no. 28 and 62, which is the difference between the inflow sediment and sediment transport capacity for the adopted discharge range, is as shown in Figure 16. This figure shows that the quantity of deposited sediment at these cross sections with total inflow discharge of $430 \text{ m}^3/\text{sec}$, $425 \text{ m}^3/\text{sec}$ from

Al Mosul Dam, was 21900tons/day before Al Khosar River and 15000tons/day after Al Khosar River.

To avoid deposition of sediment before Al Khosar River and then along the studied reach, the inflow discharge into the reach from Al Mosul Dam must not be less than 1500 m³/sec. While, to avoid deposition of sediment after Al Khosar River, the total discharge through this river reach must not be less than 780m³/sec.

5- Conclusions

The following conclusions were achieved:

- 1- The main channel distances at which the mean flow velocity is less than 0.5m/sec are 2000 and 4500m, after Al Khosar River, and 9500, 13000, and 19000 m, before Al Khosar River, at cross sections number 71, 62, 40, 28 and 9, respectively. These low flow velocities occur at the established islands at the reaches of high bed elevation and wide cross sections.
- 2- Sediment Transport Capacity at the channel distance 4500 and 13000 m, cross sections no. 62 and 28, is less than that of other cross sections along the reach.
- 3- The quantity of inflow sediment during the rainy period from the catchment area of the reach between Al Mosul Dam and Al Mosul City was 22032 tons/day, while from that of Al Khosar River was 3160.8 tons/day.
- 4- The quantity of deposited sediment at main channel distances 13000 and 4500m, before and after Al Khosar River, with total inflow discharge of 430m³/sec, 425m³/sec from Al Mosul Dam and 5m³/sec from Al Khosar River, was 21900 and 15000 tons/day, respectively.
- 5- To avoid deposition of sediment before Al Khosar River and along the studied reach the inflow discharge into the reach from Al Mosul Dam must not be less than 1500m³/sec.
- 6- To avoid deposition of sediment after Al Khosar River the total discharge must be not less than 780m³/sec.
- 7- The Established islands must be removed and the wide and shallow cross sections

must be modified to prevent their occurrence during very low flow velocities.

- 8- The inflow discharges into this reach from Al Mosul Dam must be increased during the rainy period to increase the sediment transport capacity of this reach.
- 9- The sediment transport rating curve of Al Khosar River must be constructed and the discharges that must be released from Al Mosul Dam during the rainy period must be estimated for the whole discharges range of Al Khosar River.

6- References

- 1- Ministry of Water Resources, 2009; "Recorded Data of the Surveyed Cross Sections Along the Reach of Tigris River within Al Mosul City" General Directorate of Survey, Baghdad -Iraq, unpublished report.
- 2- Ministry of Water Resources and Mosul University - Dam and Water Resources Research Center 2009; "Records of Field Observations" International Center of Water Resources, Baghdad -Iraq, unpublished Data.
- 3- Ministry of Water Resources, 2009, "Recorded Discharges at Al Huriah Station in Al Mosul City for the Period from the Year 1986 to 2009" State Commission for Operation of Irrigation and Drainage Projects – DEP, Baghdad -Iraq, unpublished Data.
- 4- Mohammad E. Mohammad, 2005, "A Conceptual Model for Flow and Sediment Routing for A Watershed Northern Iraq" Ph. D. Thesis, Water Resources Dept. College of Engineering – Mosul University, Mosul - Iraq.
- 5- U.S. Army Corps of Engineers, 2005, "River Analysis System", Version 3.1.3, Hydrologic Engineering Center, Davis CA 95616.
- 6- Yang C. T, 1996, "Sediment Transport" Mc Graw-Hill Series in Water Resources and Environment Engineering.

Table 1. Measured water surface elevations along the studied reach. (After Ministry of Water Resources and Mosul University – DWRRC, 2009).

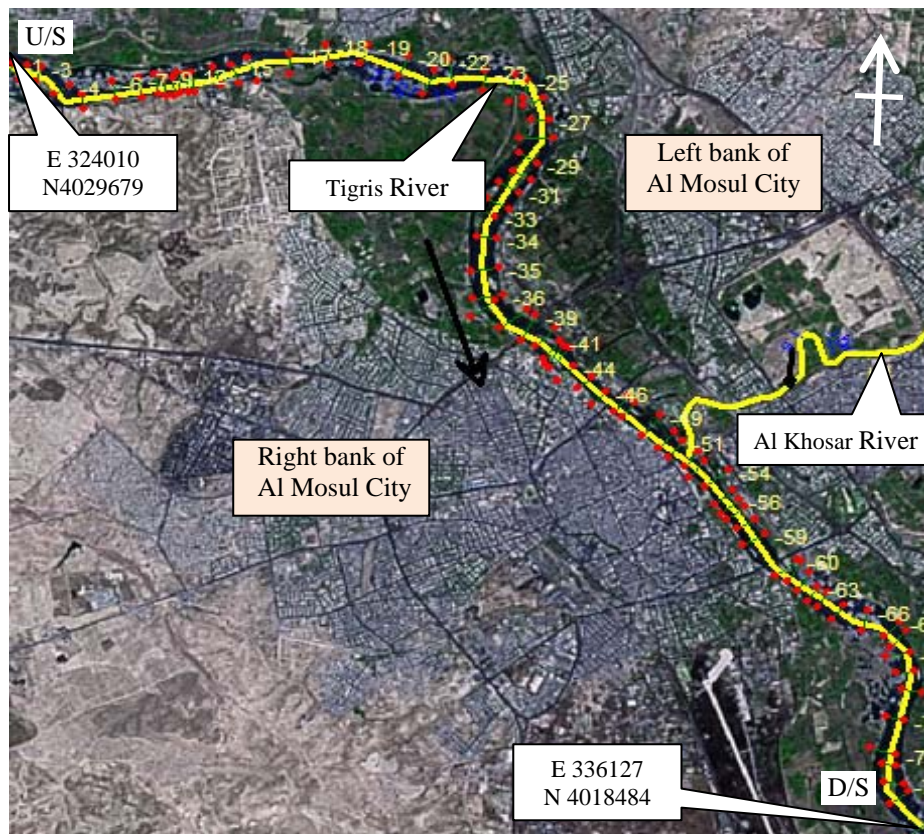
Cross section No.	Water surface elevation (m.a.m.s.l)
1	221.5
5	220.6
10	220.0
15	219.6
20	218.5
25	217.8
30	217.6
35	217.0
40	216.1
45	215.5
50	215.0
55	214.4
60	213.9
65	213.5
70	212.6
75	211.9

Table 2. Average velocity along the studied reach. (After Ministry of Water Resources and Mosul University – DWRRC, 2009).

Cross section No.	Flow velocity (m/sec)	Cross section No.	Flow velocity (m/sec)
1	0.60	39	0.40
3	0.85	41	0.60
4	0.80	44	1.00
5	1.00	46	1.00
7	0.85	48	0.75
9	0.60	51	0.70
10	0.60	54	1.20
13	0.60	55	0.90
14	0.90	56	0.80
17	1.00	57	0.70
19	1.00	60	0.80
21	1.00	61	0.90
24	0.75	62	1.25
27	0.90	65	0.90
28	0.80	67	0.90
29	0.75	69	0.90
31	0.85	70	1.00
33	0.70	72	0.90
36	0.45	74	0.80
37	0.65	77	0.45

Table 3. Adopted inflow discharges into the studied reach.

Case No.	Discharge (m ³ /sec)
1	50
2	100
3	250
4	425
5	500
6	750
7	1000
8	1500

**Figure 1. Layout of the studied reach and Al Mosul City.**

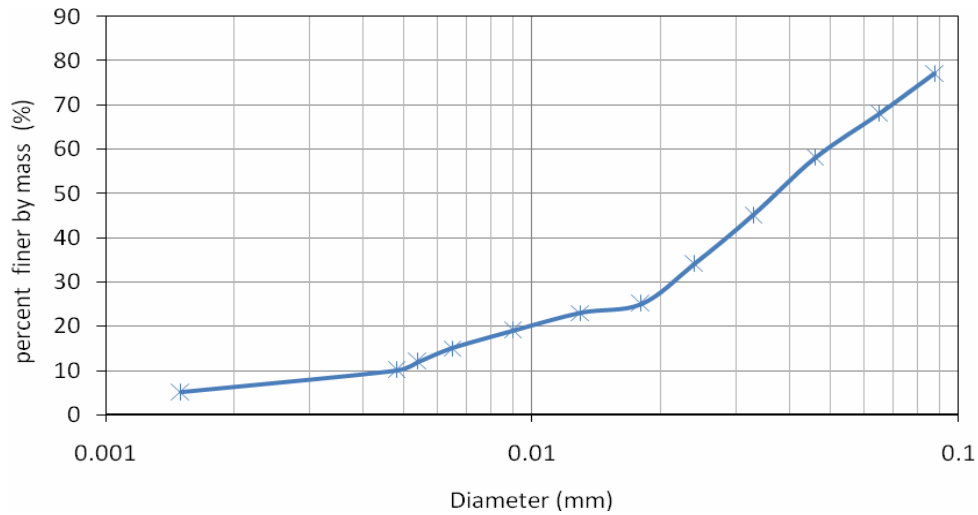


Figure 2. Grain size distribution of the suspended sediment.

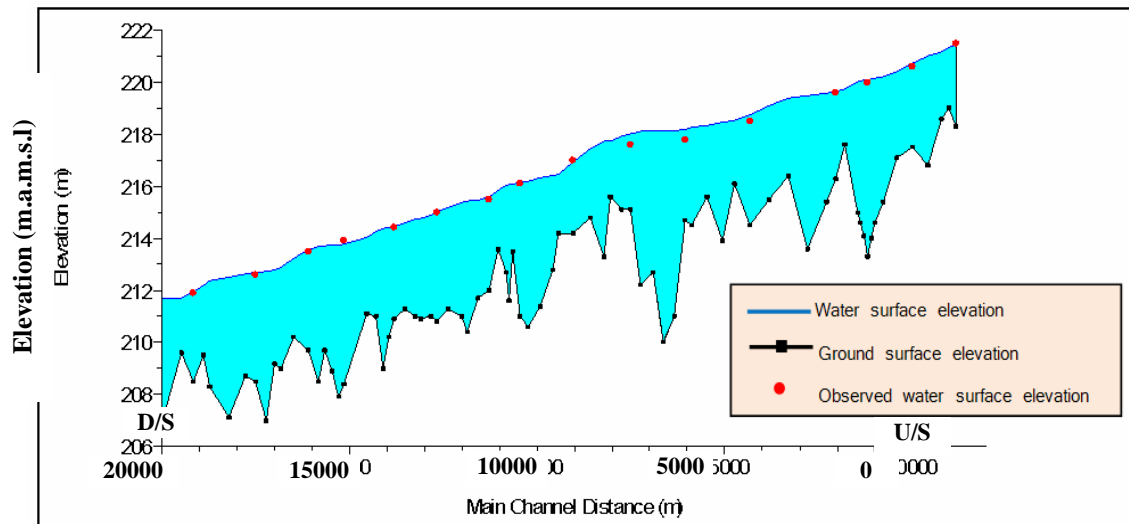


Figure 3. Comparison between estimated stage values using the calibrated data and the measured stage values.

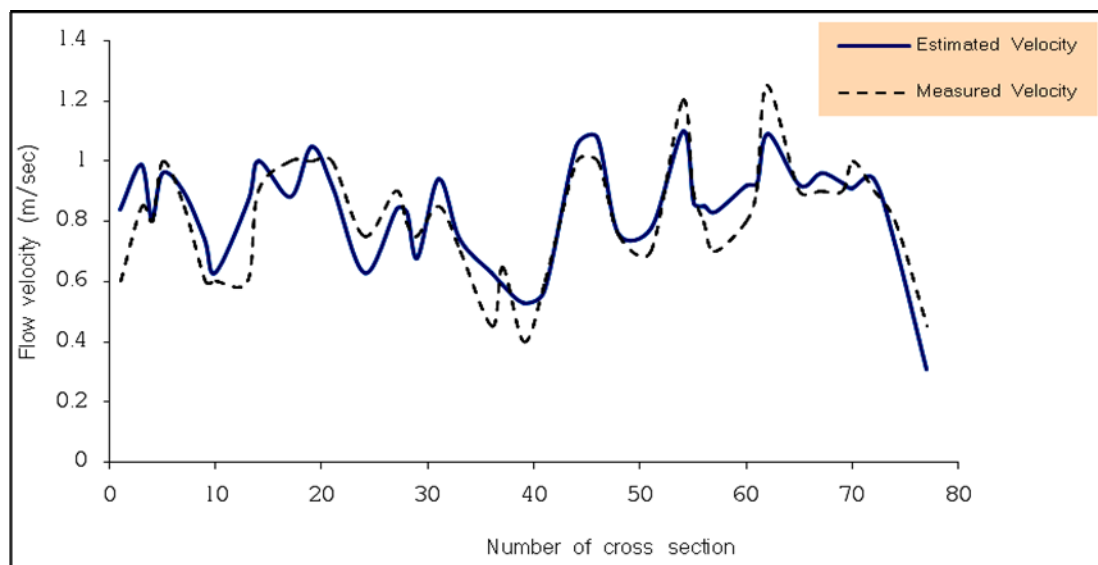


Figure 4. Comparison between estimated and measured mean velocities.

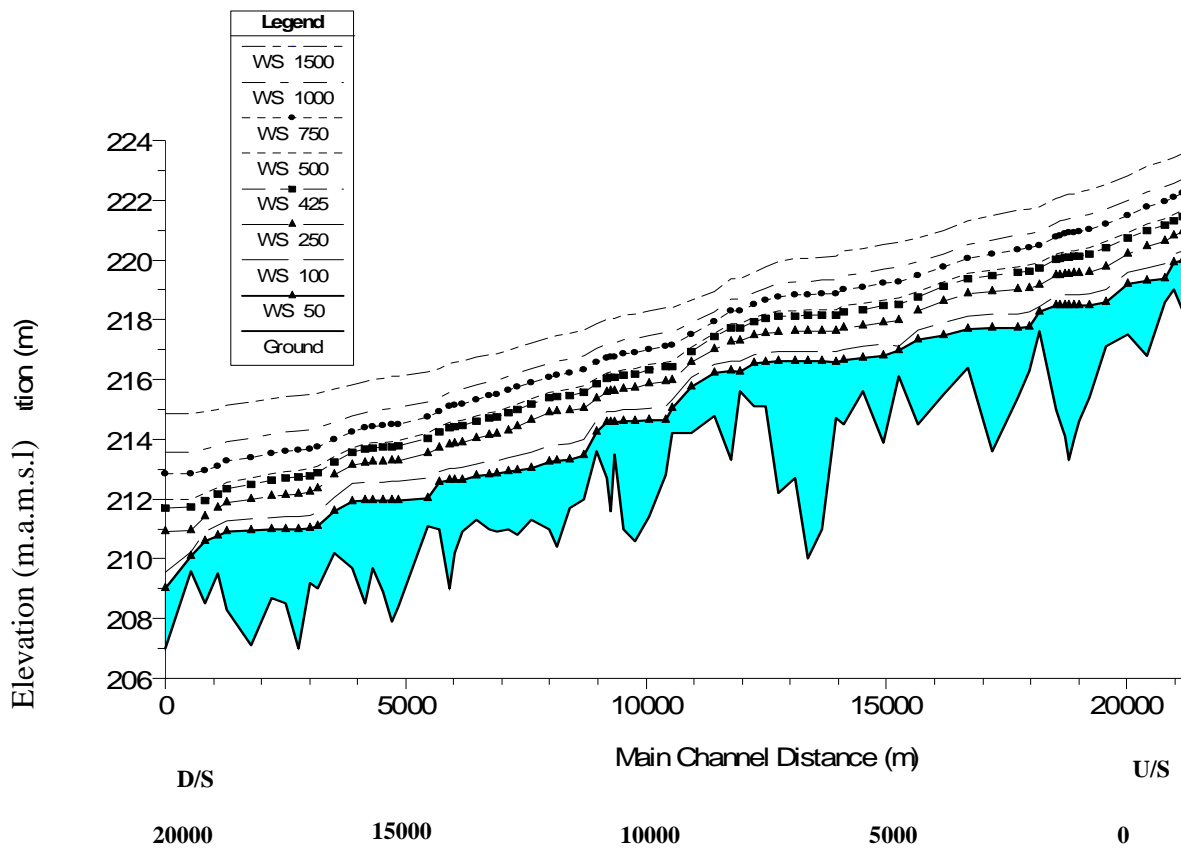


Figure 5. Estimated water surface elevation along the studied reach.

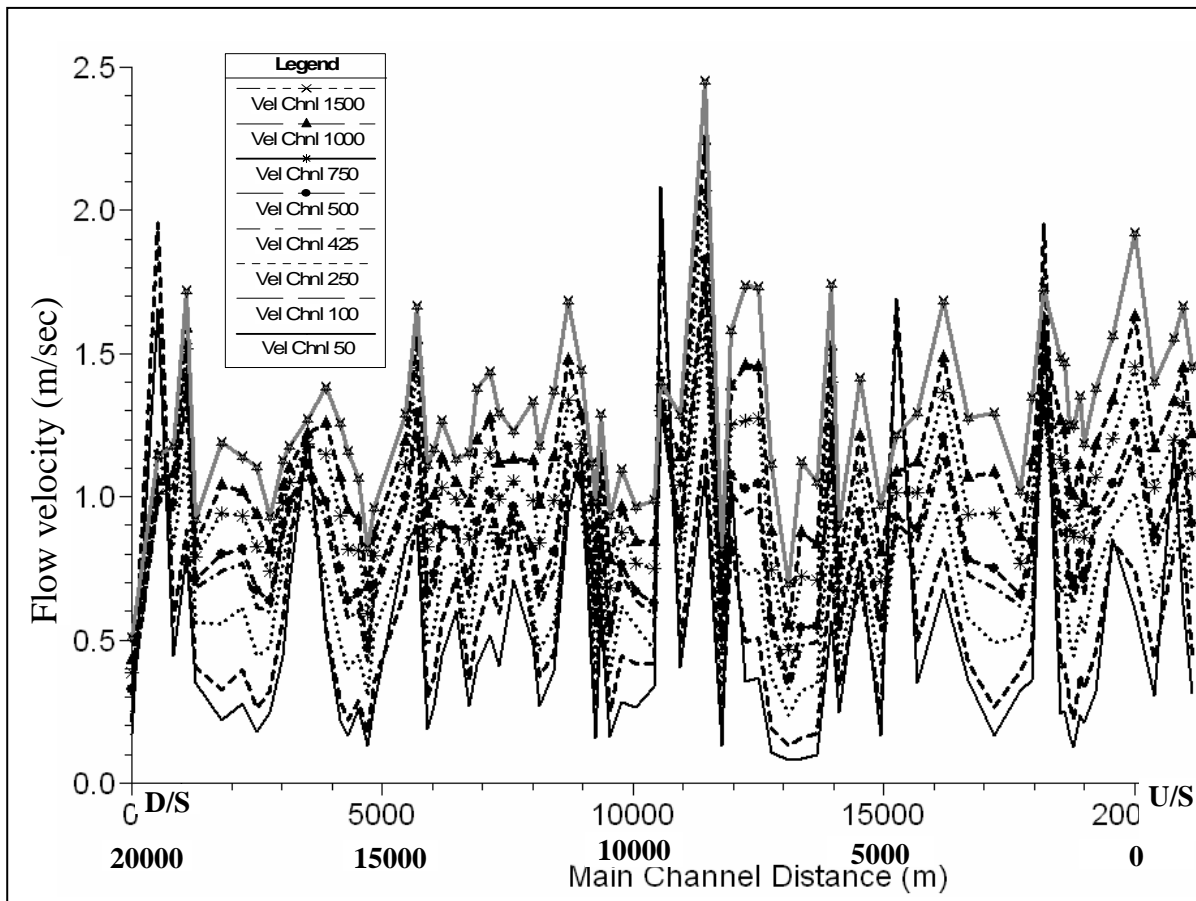


Figure 6. Estimated mean flow velocity along the studied reach.

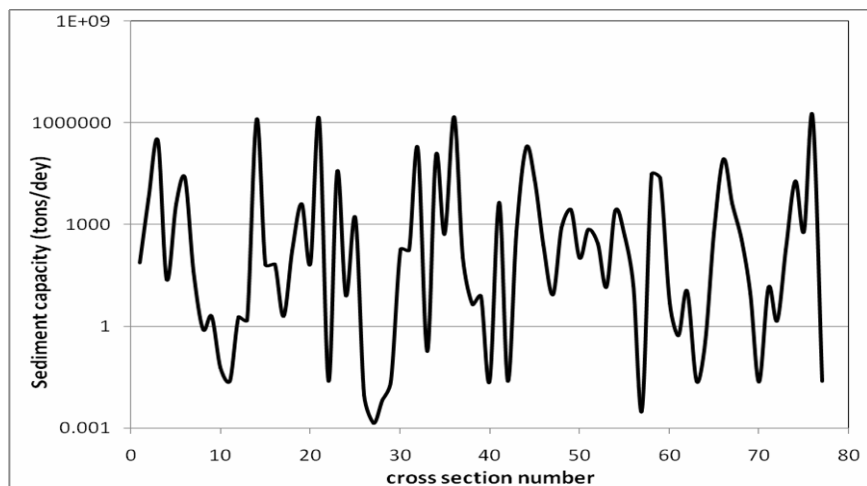


Figure 7. Estimated Sediment Transport Capacity along the studied reach with a discharge of 50 m³/sec.

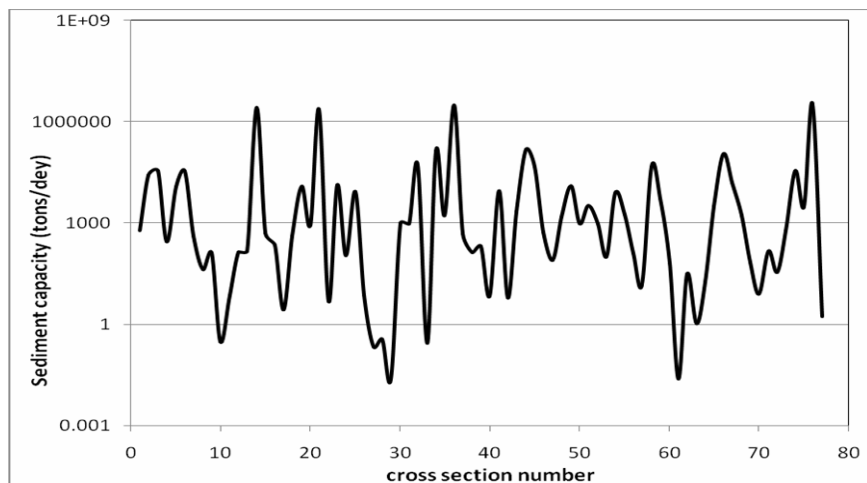


Figure 8. Estimated Sediment Transport Capacity along the studied reach with a discharge of 100 m³/sec.

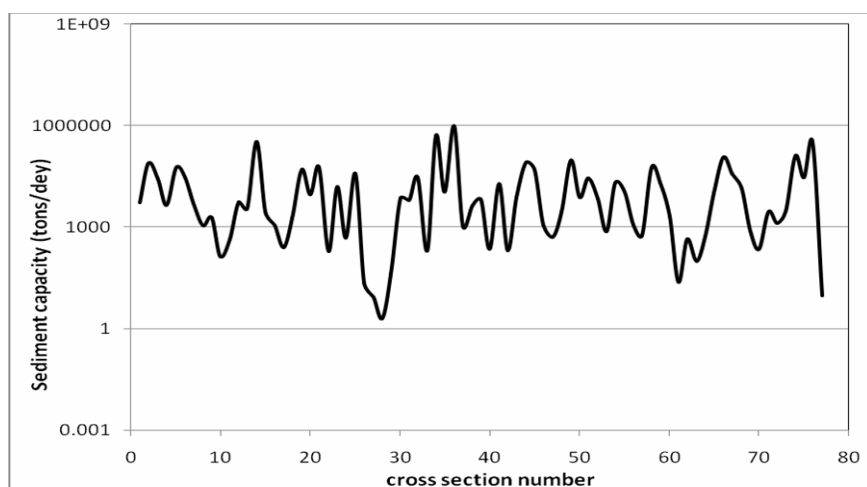


Figure 9. Estimated Sediment Transport Capacity along the studied reach with a discharge of 250 m³/sec.

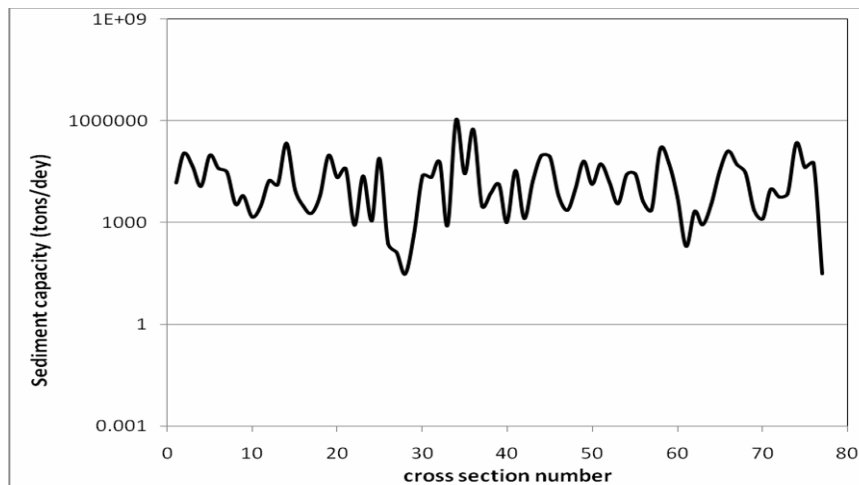


Figure 10. Estimated Sediment Transport Capacity along the studied reach with a discharge of 425 m³/sec.

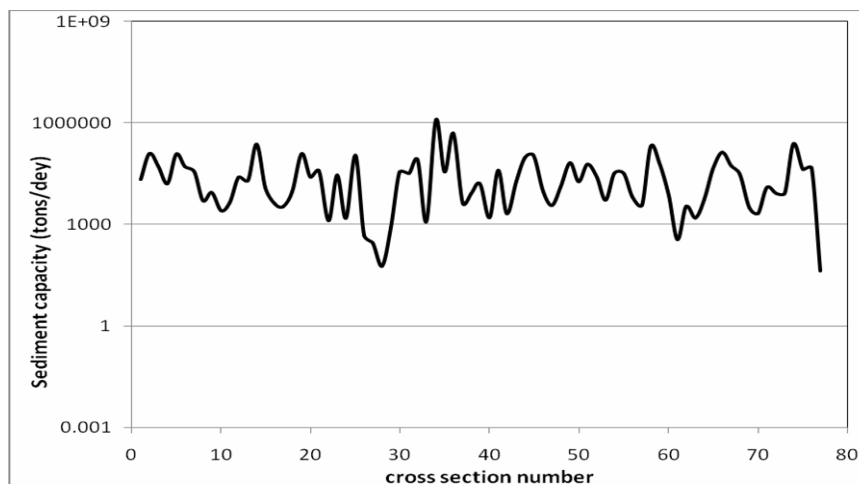


Figure 11. Estimated Sediment Transport Capacity along the studied reach with a discharge of 500 m³/sec.

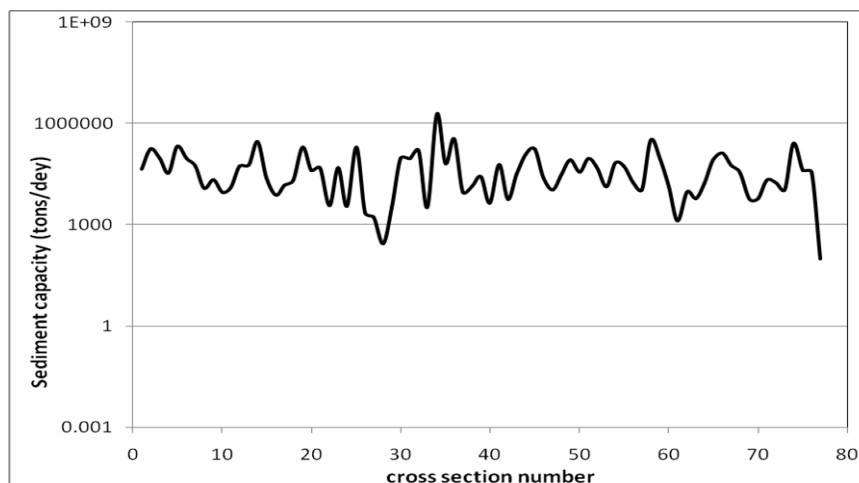


Figure 12. Estimated Sediment Transport Capacity along the studied reach with a discharge of 750 m³/sec.

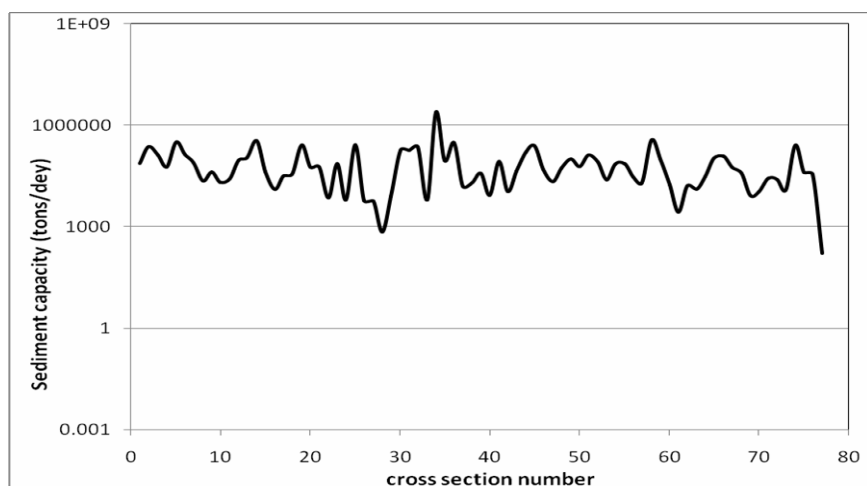


Figure 13. Estimated Sediment Transport Capacity along the studied reach with a discharge of $1000 \text{ m}^3/\text{sec}$.

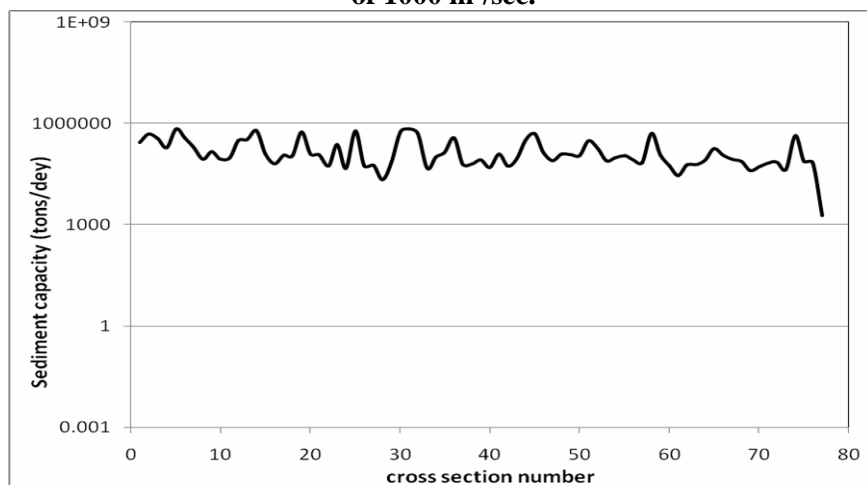


Figure 14. Estimated Sediment Transport Capacity along the studied reach with a discharge of $1500 \text{ m}^3/\text{sec}$.

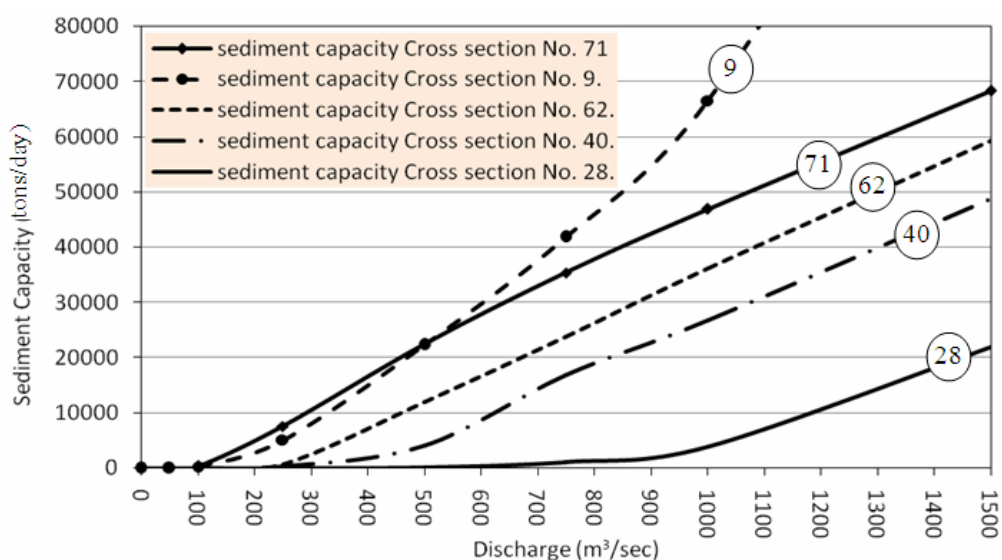


Figure 15. Estimated sediment rating curves at the critical cross sections, cross sections no. 71, 62, 40, 28, and 9.

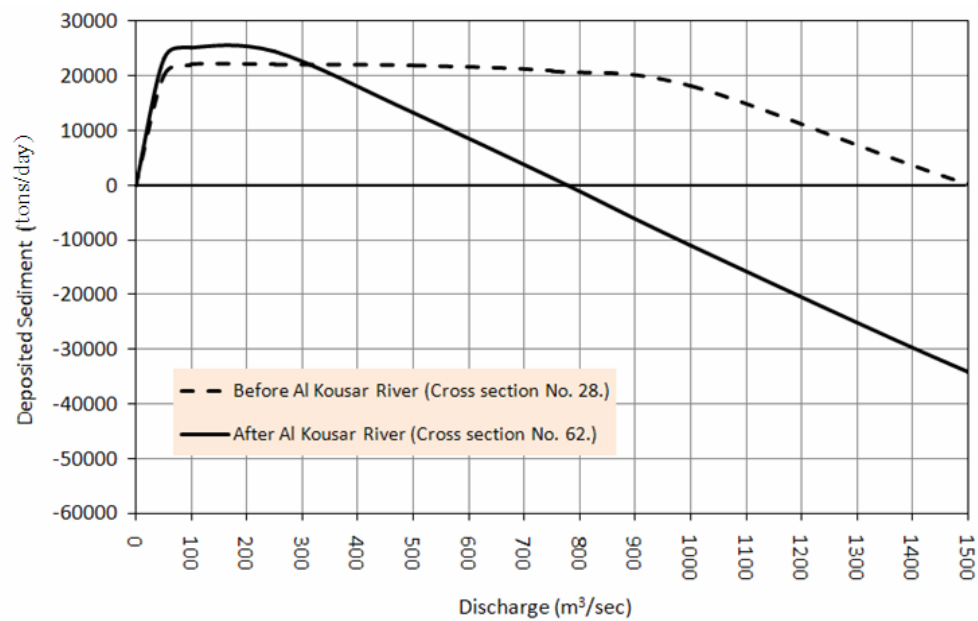


Figure 15. Quantity of deposited sediment before and after Al Khosar River for the adopted discharge range.



IMAGE BASED MULTI-LENGTH RANDOM KEY GENERATOR

Dr. Firas Ali Sabir
University of Baghdad
College of Engineering
Computer Engineering Department

Sadiq Habeeb Abdalhussain
University of Baghdad
College of Engineering
Computer Engineering Department

ABSTRACT

Random Number Generators (RNGs) are an important building block for algorithms and protocols in cryptography. They are dominant in the construction of encryption keys and other cryptographic algorithm parameters. In practice, statistical testing is employed to gather evidence that a generator indeed produces numbers that appear to be random. In this paper a new algorithm is proposed to generate variable length random binary sequence. The random sequence is generated by selecting different point from hashed digital images; the selecting process is organized in such a way to ensure randomness and to avoid regeneration of same sequence within a year. The generated sequences are tested to meet the National Institute of Standard and Technology (NIST) criteria. In proposed algorithm the traditional key exchange is not needed which gives advantage to the system from the security point of view. This proposed algorithm is capable of generating random binary sequences that can meet security requirements of cryptographic algorithms.

(RNG)

.(NIST)

Keywords: Key Generator, Randomness, NIST, Hypothesis, Hash Function.

1. INTRODUCTION

Randomness and random numbers have traditionally been used for a variety of purposes in many applications such as statistical sampling, experimental simulation, cryptography and etcetera. Computer Algorithm introduces randomness in the form of pseudo-random number generators. As the name suggests, pseudorandom numbers are not truly random. Rather, they are computed from a mathematical formula Pseudorandom numbers have the characteristic that they are predictable, meaning

they can be regenerated if you know where in the sequence the first number is starting from [Nur and Sharin, 2010]. Traditionally, the concern in the generation of a sequence of allegedly random numbers has been that the sequence of numbers be random in some well-defined statistical sense [Nur and Sharin, 2010][Nur et al, 2010]. The following two criteria are used to validate that a sequence of numbers is random [William, 2006]:

1. **Uniform distribution:** the distribution of numbers in the sequence should be uniform; that is; the frequency of occurrence of each of

the numbers should be approximately the same.

- 2. Independence:** no one value in the sequence can be inferred from the others.

This paper will go through design criteria random key generation in next sections.

2. KEY GENERATION TECHNIQUES

There are several ways to generate keys which are widely used in cryptography. Keys are considered the secret part of any cryptographic system. Its robustness and characteristic specifies the security of any cryptographic system. Some of these techniques are [Bruce, 2006][Menezes, 1997]:

2.1. Pseudorandom Number Generator (PRNGs):

Cryptographic applications typically make use of algorithmic techniques for random number generation. These algorithms are deterministic and therefore produce sequences of numbers that are not statistically random. However, if the algorithm is good, the resulting sequence will pass many reasonable tests of randomness. Such numbers are referred to as *Pseudo-random numbers*.

A **Feedback shift register** is made up of two parts: a **shift register** and a **feedback function**. The simplest kind of feedback shift register is a linear feedback shift register, or LFSR (see **Fig. 1**). The feedback function is simply the XOR of certain bits in the register; the list of these bits is called a **tap sequence**.

An n -bit LFSR can be in one of $2^n - 1$ internal states. This means that it can, in theory, generate a $2^n - 1$ bit long pseudo-random sequence before repeating. Only LFSRs with certain tap sequences will cycle through all $2^n - 1$ internal states, these are the maximal-period LFSRs. The resulting output sequence is called an **m-sequence**.

The maximal length sequence has the following properties:

- The number of ones in a sequence approximately equals the number of zeros.
- The statistical distribution of ones and zeros is well defined and always the same.

The number of ones and zeros in any linear maximal code is [Bruce, 2006][Menezes, 1997]:

$$\frac{2^n}{2} = \text{number of ones}$$

$$\frac{2^n}{2} - 1 = \text{number of zeros}$$

In order for a particular LFSR to be a maximal-period LFSR, the polynomial formed from a tap sequence plus the constant 1 must be a primitive polynomial mod 2. The *degree* of the polynomial is the length of the shift register. The easiest way is to choose a random polynomial and test whether it is primitive.

2.2. Linear Congruential Generator:

By far, the most widely used technique for pseudo-random number generation is the linear congruential method. The algorithm is parameterized with four numbers, as follows:

m	<i>the modulus</i>	$m > 0$
a	<i>the multiplier</i>	$0 < a < m$
c	<i>the increment</i>	$0 \leq c < m$
X_o	<i>the starting value, or seed</i>	$0 \leq X_o < m$

The sequence of random numbers $\{X_n\}$ is obtained via the following iterative equation:

$$X_{n+1} = (aX_n + c) \bmod m$$

If m, a, c , and X_o are integers, then this technique will produce a sequence of integers with each integer in the range $0 \leq X_n < m$.

The selection of values for a, c , and m is critical in developing a good random number generator. For example, consider $a=c=1$. The sequence produced is obviously not satisfactory. Now consider the values $a=7, c=0, m=32$, and $X_o=1$. This generates the sequence $\{7, 17, 23, 1, 7, \text{etc.}\}$, which is also clearly unsatisfactory. Of the 32 possible values, only 4 are used; thus, the sequence is said to have a period of 4. if, instead, we change the value of a to 5, then the sequence is $\{5, 25, 29, 17, 21, 9, 13, 1, 5, \text{etc.}\}$, which increases the period to 8.

We would like m to be very large, so that there is the potential for producing a long series of distinct random numbers.

Unfortunately, linear congruential generators cannot be used for cryptography; they are

predictable. Linear congruential generators were broken. Quadratic generators denoted by the following equation were also broken [Bruce, 2006][Menezes, 1997].

$$X_{n+1} = (aX_n^2 + bX_n + c) \bmod m \quad \dots(1)$$

And cubic generator:

$$X_{n+1} = (aX_n^3 + bX_n^2 + cX_n + d) \bmod m \quad \dots(2)$$

Linear congruential generators remain useful for non-cryptographic applications, however, such as simulations. They are efficient and show good statistical behavior with respect to most reasonable empirical tests.

2.3. Blum Blum Shub Generator:

A popular approach to generate secure pseudorandom is known as Blum, Blum, Shub (BBS) generator, named for its developers. It has perhaps the strongest public proof of its cryptographic strength. The procedure is as follows. First, choose two large prime numbers, p and q , that both have a remainder of 3 when divided by 4. That is, $p \equiv q \equiv 3 \pmod{4}$.

For example, the prime numbers 7 and 11 satisfy $7 \equiv 11 \equiv 3 \pmod{4}$. Let $n = p \times q$. Next, choose a random number s , such that s is relatively prime to n ; this is equivalent to say that neither p nor q is a factor of s . then the BBS generator produces a sequence of bits according to the following algorithm. Thus, the least significant bit is taken at each iteration.

start

$$X_0 = s^2 \bmod n$$

for $i = 1$ *to* ∞

$$X_i = (X_{i-1})^2 \bmod n$$

$$\text{Generated Key}_i = X_i \bmod 2$$

end

3. STATISTICAL TEST SUITE FOR RNG AND PRNG

The focus of this paragraph is on the way to examine whether the generated sequence has randomness for cryptographic purposes. A set of statistical tests for randomness is described in this paragraph. The National Institute of Standards and Technology (NIST) believe that these procedures are useful in detecting deviations of a

binary sequence from randomness. Various statistical tests can be applied to a sequence in attempt to compare and evaluate the sequence to a truly random sequence. Randomness is a probabilistic property; that is, the properties of a random sequence can be characterized and described in terms of probability. The likely outcome of statistical tests, when applied to a truly random sequence, is known a priori and can be described in probabilistic terms. There are an infinite number of possible statistical tests, each assessing the presence or absence of a "pattern" which, if detected, would indicate that the sequence is nonrandom. Because there are so many tests for judging whether a sequence is random or not, no specific finite set of tests is deemed "complete." In addition, the results of statistical testing must be interpreted with some care and caution to avoid incorrect conclusions about a specific generator and the purpose of each test is given [Andrew *et al*, 2008][Andrew and Walter, 2003]:

3.1. Frequency (Monobit) Test

The focus of the test is the proportion of zeroes and ones for the entire sequence. The purpose of this test is to determine whether the number of ones and zeros in a sequence are approximately the same as would be expected for a truly random sequence [Andrew *et al*, 2008].

3.2. Frequency Test within a Block

The focus of the test is the proportion of one's within M -bit blocks. The purpose of this test is to determine whether the frequency of ones in an M -bit block is approximately $M/2$, as would be expected under an assumption of randomness [Andrew *et al*, 2008].

3.3. Runs Test

The focus of this test is the total number of runs in the sequence, where a run is an uninterrupted sequence of identical bits. A run of length k consists of exactly k identical bits and is bounded before and after with a bit of the opposite value. The purpose of the runs test is to determine whether the number of runs of ones and zeros of various lengths is as expected for a random sequence. In particular, this test determines whether the oscillation between such zeros and ones is too fast or too slow [Andrew *et al*, 2008].

3.4. Test for the Longest Run of Ones in a Block

The focus of the test is the longest run of ones within M -bit blocks. The purpose of this test is to

determine whether the length of the longest run of ones within the tested sequence is consistent with the length of the longest run of ones that would be expected in a random sequence [Andrew *et al*, 2008].

3.5. Discrete Fourier Transform (Spectral) Test

The focus of this test is the peak heights in the Discrete Fourier Transform of the sequence. The purpose of this test is to detect periodic features (i.e., repetitive patterns that are near each other) in the tested sequence that would indicate a deviation from the assumption of randomness. The intention is to detect whether the number of peaks exceeding the 95 % threshold is significantly different than 5 % [Andrew *et al*, 2008].

3.6. Serial Test

The focus of this test is the frequency of all possible overlapping m -bit patterns across the entire sequence. The purpose of this test is to determine whether the number of occurrences of the 2^m m -bit overlapping patterns is approximately the same as would be expected for a random sequence. Random sequences have uniformity; that is, every m -bit pattern has the same chance of appearing as every other m -bit pattern [Andrew *et al*, 2008].

3.7. Approximate Entropy Test

The focus of this test is the frequency of all possible overlapping m -bit patterns across the entire sequence. The purpose of the test is to compare the frequency of overlapping blocks of two consecutive/adjacent lengths (m and $m+1$) against the expected result for a random sequence [Andrew *et al*, 2008].

3.8. Cumulative Sums (Cusum) Test

The focus of this test is the maximal excursion (from zero) of the random walk defined by the cumulative sum of adjusted (-1, +1) digits in the sequence. The purpose of the test is to determine whether the cumulative sum of the partial sequences occurring in the tested sequence is too large or too small relative to the expected behavior of that cumulative sum for random sequences. This cumulative sum may be considered as a random walk. For a random sequence, the excursions of the random walk should be near zero. For certain types of non-random sequences, the excursions of this random

walk from zero will be large [Andrew *et al*, 2008].

4. RANDOM HYPOTHESIS TESTING

A statistical test is formulated to test a specific null hypothesis (H_0). For the purpose of this study, the null hypothesis under test is that the sequence being tested is random against the alternative hypothesis (H_1) for which the sequence is not random [Andrew *et al*, 2008][Nur and Sharin, 2010][Nur *et al*, 2010].

For each statistical test, a set of p-values (corresponding to the set of sequences) is produced. For a fixed significant level, a certain percentage of p-values are expected to indicate failure. For example, if the significant level is chosen to be 0.01 (i.e. $\alpha=0.01$), then about 1% of the sequences are expected to fail. A sequence passes a statistical test whenever the p-values $\geq \alpha$ and fails otherwise [Wong *et al*, 2009][Nur and Sharin, 2010][Nur *et al*, 2010].

The parameter denotes the significance level that determines the critical region of acceptance and rejection. NIST recommended that α be in the range (0.001, 0.01) [Andrew *et al*, 2008][Nur and Sharin, 2010][Nur *et al*, 2010][Wong *et al*, 2009].

Only 8 tests are particularly suitable for practical cryptographic keys size here. The selected NIST random tests for short keys are listed in the **Table (1)**. This set of random test shall be called upon to check on the validity of short random for proposed method. The 8 selected tests are basically relies heavily on the randomness of the binary sequence. **Fig. (2)** shows the hierarchy of the tests. Once a particular block key set fails one test it is considered non-random and will certainly fail the next test in lower hierarchy [Wong *et al*, 2009][Nur and Sharin, 2010].

Additional numerical experiments should be conducted on different samples of the generator to determine whether the phenomenon was a statistical anomaly or a clear evidence of non-randomness.

For the interpretation of test results, NIST adopts following two approaches, the examination of the proportion of success-sequences (Success Rate). The range of acceptable proportions is determined using the confidence interval defined as [Charmaine, 2005][Andrew *et al*, 2008][Juan, 1999][R. B. P. Dept., 2003]:

$$P' - Value = P' \mp 3 \sqrt{\frac{P'(1-P')}{n}} \quad \dots(3)$$

Where $p' = 1-\alpha$, and n is the sample size.

If the proportion falls outside of this interval, then there is evidence that the data is nonrandom.

5. PROPOSED ALGORITHM

The idea of proposed model which is shown in **Fig. (3)** is to generate multi length random binary sequences suitable for use in cryptography and other applications. The seeds of the proposed model are selective images and the date. In this model four lengths of key are possible to be generated which are 128, 256, 512, and 1024 bits. Visual Basic 6.0 is used for model implementation. The function of blocks is illustrated in the coming paragraphs.

5.1 Input : In this block the end user enters date or could use the auto dating option which leads to current date. User also should enter number of bits to be taken from the selected pixel (1, 2, 4 or 8) in order to specify the key length.

5.2 Generating X,Y,S: In this phase, three carefully selected equations are used to obtain one-to-one system that there are no duplicate in(X,Y,S) values within a year. These values are then used as initial value (X_0, Y_0, S_0) of the seven bit PN- generator (7 Xor 6 for maximum-length LFSR [Peter, 1996]) resulting in 127 different states. The PN generator denoted by (S) is used to select one of the 43 generated images for each state according to the equation $[Integer(S/3) + 1]$ and also it has been used to determine which byte to be deal with (Red, Green, or Blue). This is done through the use of the following equation $[Round(S/3 - Image Number)*3+3]$ which must give [0, 1 or 2] indicating red, green or blue respectively.

The other PN generators marked (X and Y) are used to coordinate the pixel position by intersecting the x-axis and y-axis on the selected image. This process goes on for all states of PN generator resulting in 127 pixels randomly generated.

5.3 Main Module: The inputs to this phase are 127 bytes which are randomly chosen and number of bits (LSBs) to be taken from these bytes which is determined by user to specify how long the key is. The keys are then padded according to certain rules to reach predefined key lengths. The

resulting keys are then examined by NIST test to evaluate its randomness and to check whether it is valid for cryptographic application or not.

6. RESULTS AND DISCUSSION

As previously mentioned, the proposed algorithm generates multi-length keys. These keys are examined for randomness issue under the NIST tests. The obtained results for 10 key sequences of different lengths are shown in **Tables (2, 3, 4, and 5)** as all p-values of the test are larger than required value ($\alpha=0.01$) in order to reject the null hypothesis as random sequence.

Fig. (4, 5, 6, and 7) show the average value for 128, 256, 512 and 1024 bits key length respectively the tests with 10 generated sequences pass the threshold value (α) [Nur and Sharin, 2010].

For long sequences more than 10 sequences another tests will be taken into account which gives an indication for sequence randomness. It has been shown that as long as the sequence length increases, the possibility of fail mark may appear, so success rate test should be done to validate sequences for use in cryptographic application with respect to their randomness. **Table (6)** clearly illustrates the success rate test for multi-length keys according to equation (3)

$$\begin{aligned} P' - Value &= 0.99 \mp 3 \sqrt{\frac{0.99 * 0.01}{365}} \\ &= 0.99 \mp 0.015624 = \begin{cases} 1.005625 \\ 0.974376 \end{cases} \quad \dots(4) \end{aligned}$$

Tables (7,8 and 9) shows the proportion test for Linear Feedback Shift Register (LFSR), Blum Blum Shub (BBS) and Linear Congruential Generator (LCG) respectively, and show that these techniques fail in some of the tests. From **Table (10)** its obvious that the proposed algorithm show better results when compared with other techniques.

7. SOFTWARE IMPLEMENTATION

The proposed method is implemented using Visual Basic 6.0 as shown in **Fig. (8)** and **Fig. (9)**. It can be seen from these two figures the flexibility and the reliability taken in software design. It is very easy to the interested people in cryptographic field use this application and generate the random multi-length keys by

specifying the input parameters by pressing *generate* button and *Select No. of Bits* button and then follow the procedure.

8. CONCLUSION

In this paper, a new method of key generation is proposed and modeled depending on hashed images and date-dependent algorithm. The proposed method of key generation is examined and tested for different cases and different key lengths and compared with classical techniques and it is well proven that this method is very suitable for applications used in cryptography as it has random nature and has all properties of randomness.

9. REFERENCES

- Andrew Rukhin, *et al* "A Statistical Test Suite for Random and Pseudorandom Number Generators for Cryptographic Applications", National Institute of Standard and Technology, 2008.
- Andrew W, Walter A., "Hardware comparison of seven random number generators for smart cards", In: ITG-GI-GMM Workshop of Test Methods and Reliability of Circuits and Systems, Timmendorfer Beach, pp. 55–58, 2003.
- Bruce Schneier, "Applied Cryptography", John Wiley and Sons, 2nd Edition, 1996.
- Charmaine Kenny, "Random Number Generators: An Evaluation and Comparison of Random.org and Some Commonly Used Generators" the distributed systems group, Computer Science Department, TCD, 2005.
- Juan Soto, "Statistical Testing of Random Number Generators", Proceedings of the 22nd National Information Systems Security Conference, 1999.
- Menezes A., van Oorschot P., and Vanstone S., "Handbook of Applied Cryptography", CRC Press, 1997.
- Nur A. Abu, and Sharin Sahib, "Random ambience key generation live_on demand", Signal Processing Systems (ICSPS), 2010 2nd International Conference on 2010, Vol. 1, pp. 110-114.
- Nur A. Abu, Nanna S. Herman, and Sharin Sahib, "An Enhancement of the statistical test for randomness", Networking and Information Technology (ICNIT), 2010 International Conference 2010, pp. 521-525.
- Peter Alfke, "Efficient Shift Registers, LFSR Counters, and Long Pseudo-Random Sequence Generators", Xilinx application note, 1996.
- R. B. P. Dept. "The Evaluation of Randomness of RPG100 by Using NIST and DIEHARD Tests". Technical report, FDK Corporation, 2003.
- William Stallings, "Cryptography and Network Security", Perntice Hall, Fourth Edition, 2006.
- Wong Siaw Lang, Nur Azman Abu, Shahrin Sahib, "Cryptographic Key From Webcam Image", International Journal of Cryptology Research 2009, vol. 1, pp. 115-127.

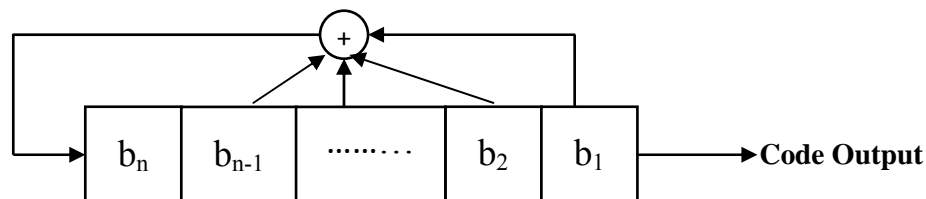


Fig. (1): Typical linear sequence generator using LFSR.

Table(1). List of suitable tests for short keys.

<i>Test Code</i>	<i>Statistical Test</i>	<i>Test Parameters</i>
1	Frequency Test	No Parameter
2	Block Frequency	M=8
3a	Cumulative Sum (Forward)	No Parameter
3b	Cumulative Sum (Backward)	No Parameter
4	Runs	No Parameter
5	Longest Run of Ones	M=8
6	Spectral DFT	No Parameter
7	Approximate Entropy	m=7
8a	Serial P-Value1	m=7
8b	Serial P-Value2	m=7

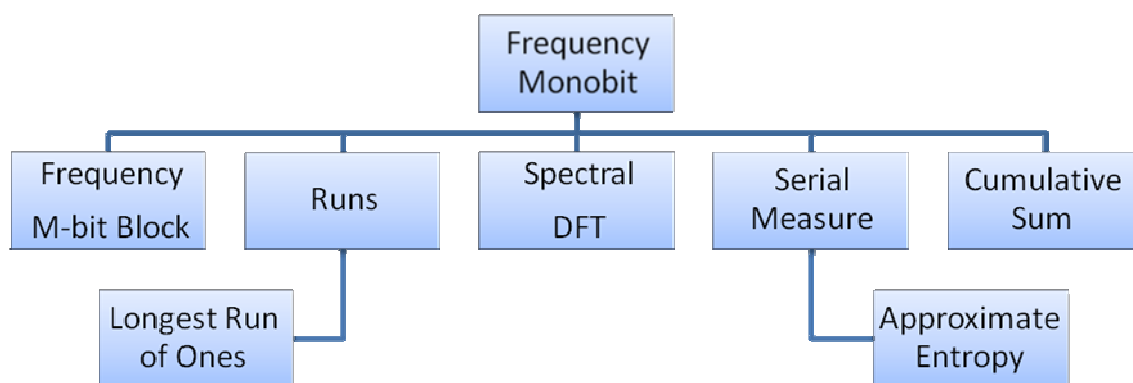


Fig. (2). The hierarchy of Random tests

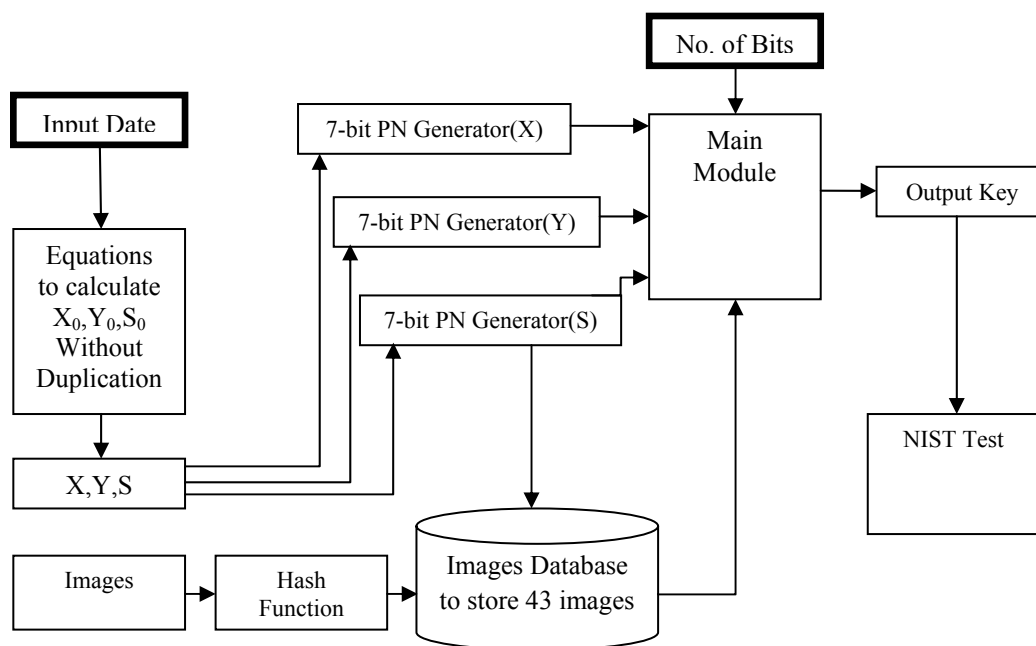


Fig. (3) The proposed Model

Table (2) 128 bit Key p-values for 10 sequence test result

Test / Sequence	1	2	3	4	5	6	7	8	9	10
Frequency	0.3768	1.0000	0.8597	0.4795	0.7237	0.0339	0.2159	0.2159	0.0771	0.5959
Block Frequency	0.3540	0.8095	0.2436	0.7440	0.1432	0.0110	0.5615	0.8392	0.1432	0.1010
Cusum (Forward)	0.0841	0.9842	0.8188	0.5748	0.7375	0.0543	0.3697	0.3697	0.1037	0.8188
Cusum (Backward)	0.4999	0.9842	0.8920	0.6548	0.8920	0.0207	0.3146	0.4314	0.1542	0.4999
Runs	0.9137	0.3768	0.7257	0.4507	0.6032	0.8189	0.3939	0.8252	0.9368	0.7418
Longest Run	0.5837	0.0788	0.7632	0.4360	0.4749	0.0371	0.8569	0.1068	0.3374	0.9936
Spectral DFT	0.5164	0.5164	0.5164	0.5164	0.5164	0.5164	0.3304	0.1443	0.0231	0.5164
Approx. Entropy	0.9456	0.9445	0.9623	0.8460	0.9025	0.7680	0.6176	0.7601	0.9155	0.6912
Serial 1	0.1121	0.7202	0.3427	0.2063	0.1636	0.0149	0.5119	0.1841	0.0743	0.3745
Serial 2	0.0382	0.9513	0.3944	0.7411	0.6192	0.2490	0.6694	0.2867	0.5937	0.0278
Minimum	0.0382	0.0788	0.2436	0.2063	0.1432	0.0110	0.2159	0.1068	0.0231	0.0278
Maximum	0.9456	1.0000	0.9623	0.8460	0.9025	0.8189	0.8569	0.8392	0.9368	0.9936

Table (3) 256 bit Key p-values for 10 sequence test result

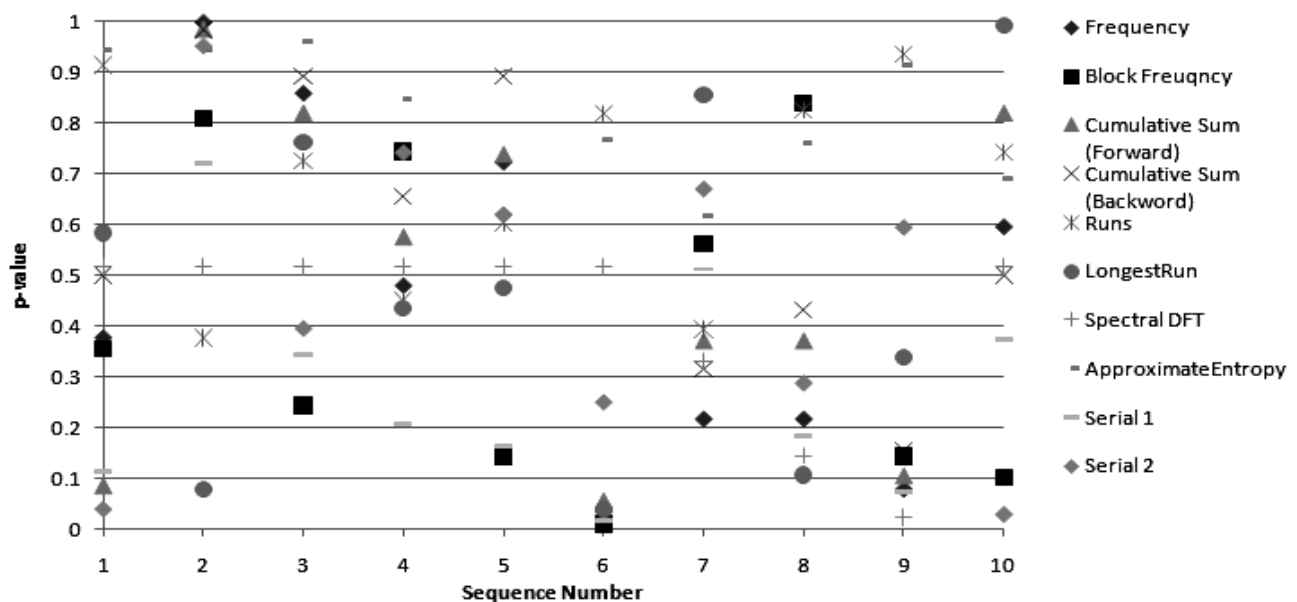
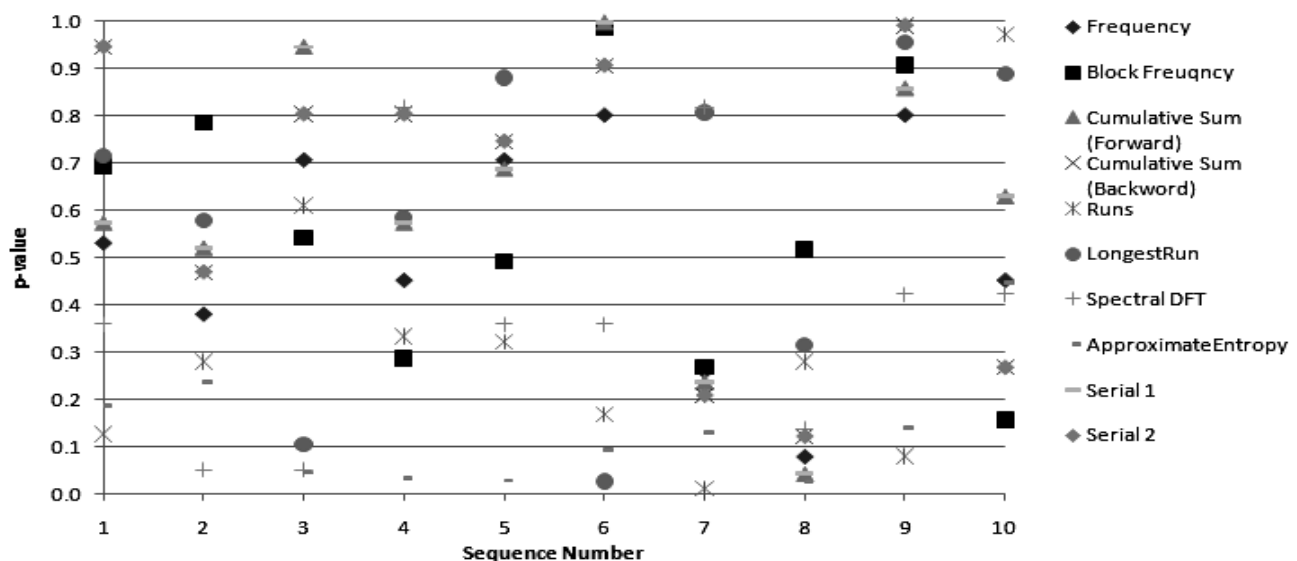
Test / Sequence	1	2	3	4	5	6	7	8	9	10
Frequency	0.5320	0.3816	0.7077	0.4533	0.7077	0.8026	0.2606	0.0801	0.8026	0.4533
Block Frequency	0.6939	0.7853	0.5425	0.2867	0.4917	0.9862	0.2674	0.5170	0.9074	0.1565
Cusum (Forward)	0.5731	0.5197	0.9459	0.5731	0.6872	0.9980	0.2363	0.0415	0.8580	0.6292
Cusum (Backward)	0.9459	0.4693	0.8035	0.8035	0.7458	0.9064	0.2083	0.1216	0.9908	0.2672
Runs	0.1268	0.2800	0.6107	0.3336	0.3213	0.1678	0.0113	0.2804	0.0794	0.9719
Longest Run	0.7165	0.5793	0.1040	0.5855	0.8809	0.0260	0.8077	0.3157	0.9560	0.8894
Spectral DFT	0.3588	0.0512	0.0512	0.8185	0.3588	0.3588	0.8185	0.1359	0.4220	0.4220
Approx. Entropy	0.1871	0.2364	0.0447	0.0330	0.0280	0.0921	0.1294	0.0255	0.1405	0.4462
Serial 1	0.5731	0.5197	0.9459	0.5731	0.6872	0.9980	0.2363	0.0415	0.8580	0.6292
Serial 2	0.9459	0.4693	0.8035	0.8035	0.7458	0.9064	0.2083	0.1216	0.9908	0.2672
Minimum	0.1268	0.0512	0.0447	0.0330	0.0280	0.0260	0.0113	0.0255	0.0794	0.1565
Maximum	0.9459	0.7853	0.9459	0.8185	0.8809	0.9980	0.8185	0.5170	0.9908	0.9719

Table (4) 512 bit Key p-values for 10 sequence test result

Test / Sequence	1	2	3	4	5	6	7	8	9	10
Frequency	0.3768	0.9296	0.7909	0.1116	0.2888	0.2505	0.8597	0.1573	0.0421	0.1849
Block Frequency	0.3273	0.0797	0.7666	0.3427	0.7360	0.6361	0.2063	0.0407	0.0916	0.2063
Cusum (Forward)	0.0196	0.6960	0.8188	0.8188	0.2040	0.2040	0.5748	0.8920	0.8188	0.4999
Cusum (Backward)	0.2348	0.9231	0.7375	0.8188	0.4649	0.1542	0.2438	0.8920	0.6548	0.4999
Runs	0.5756	0.3750	0.4797	0.9296	0.2848	0.3595	0.9724	0.2159	0.1582	0.1329
Longest Run	0.2471	0.7019	0.2690	0.7971	0.7815	0.8187	0.7650	0.4566	0.7111	0.1910
Spectral DFT	0.7456	0.3723	0.0885	0.7456	0.4654	0.1233	0.1233	0.1233	0.4654	0.4654
Approx. Entropy	0.5159	0.6769	0.1723	0.2719	0.4572	0.4396	0.4846	0.7793	0.7802	0.3599
Serial 1	0.0261	0.4245	0.5565	0.7740	0.8953	0.2559	0.8092	0.4416	0.3197	0.3427
Serial 2	0.0927	0.2068	0.3170	0.8935	0.8258	0.0435	0.7691	0.4792	0.4792	0.1111
Minimum	0.0196	0.0797	0.0885	0.1116	0.2040	0.0435	0.1233	0.0407	0.0421	0.1111
Maximum	0.7456	0.9296	0.8188	0.9296	0.8953	0.8187	0.9724	0.8920	0.8188	0.4999

**Table (5) 1024 bit Key p-values for 10 sequence test result**

Test / Sequence	1	2	3	4	5	6	7	8	9	10
Frequency	0.0244	0.2880	0.4918	0.3485	0.5320	0.4165	0.2606	0.9005	1.0000	0.5320
Block Frequency	0.1319	0.2298	0.7367	0.2298	0.9625	0.1259	0.7881	0.0807	0.0585	0.0726
Cusum (Forward)	0.0108	0.2220	0.3193	0.3785	0.6580	0.3382	0.3382	0.9742	0.7458	0.4693
Cusum (Backward)	0.0351	0.3579	0.7458	0.2220	0.4941	0.3382	0.1713	0.9064	0.7458	0.3785
Runs	0.0964	0.7752	0.6274	0.9720	0.2301	0.5877	0.1567	0.2115	0.0699	0.1539
Longest Run	0.0618	0.6673	0.4714	0.8769	0.2426	0.9741	0.1676	0.9077	0.4156	0.0299
Spectral DFT	0.3296	0.6881	0.3296	0.3019	0.6881	0.3296	0.4559	0.4559	0.1871	0.1871
Approx. Entropy	0.0977	0.1775	0.0125	0.3482	0.1919	0.4139	0.2546	0.8374	0.0098	0.0448
Serial 1	0.2461	0.4034	0.4546	0.2151	0.4076	0.8753	0.2798	0.8024	0.1277	0.0586
Serial 2	0.5329	0.2722	0.1990	0.2148	0.6632	0.9631	0.5075	0.7853	0.0413	0.0501
Minimum	0.0108	0.1775	0.0125	0.2148	0.1919	0.1259	0.1567	0.0807	0.0098	0.0299
Maximum	0.5329	0.7752	0.7458	0.9720	0.9625	0.9741	0.7881	0.9742	1.0000	0.5320

**Fig. (4) 128 bit Key p-values and average of p-values****Fig. (5) 256 bit Key p-values and average of p-values**

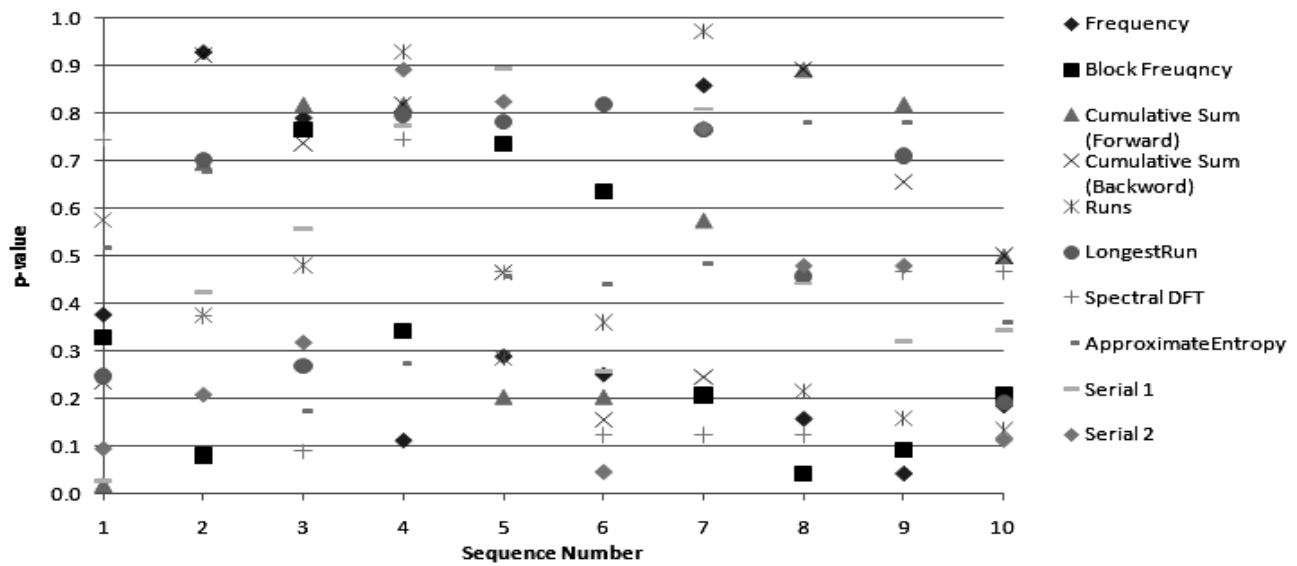


Fig. (6) 512 bit Key p-values and average of p-values

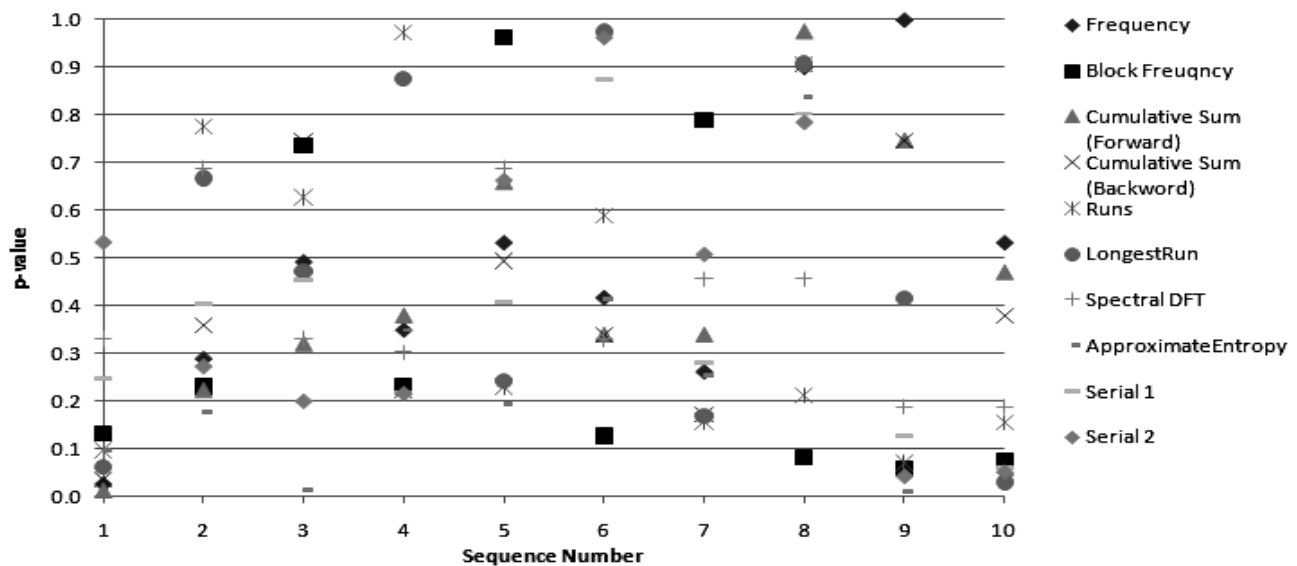


Fig. (7) 1024 bit Key p-values and average of p-values

Table (6) p-value proportion test for 365 (one year) sequences

Test Code	p-value proportion of 128 bit	p-value proportion of 256 bit	p-value proportion of 512 bit	p-value proportion of 1024 bit
1	0.98904	0.99178	0.99178	1.00000
2	0.98904	0.99726	0.99178	0.98630
3a	0.98630	0.98904	0.98356	0.99726
3b	0.99178	0.99726	0.99452	0.99452
4	0.99452	0.98630	0.99726	0.99178
5	0.99452	0.98904	0.99178	0.98904
6	0.97808	0.98904	0.98904	0.98630
7	1.00000	0.97534	0.97808	0.99452
8a	0.98904	0.98356	0.99452	0.99726
8b	0.99178	0.97808	0.99726	1.00000

**Table (7) p-value proportion test for 365 (one year) sequences for LFSR**

Test Code	p-value proportion of 128 bit	p-value proportion of 256 bit	p-value proportion of 512 bit	p-value proportion of 1024 bit
1	1.00000	1.00000	1.00000	1.00000
2	1.00000	1.00000	1.00000	1.00000
3a	1.00000	1.00000	1.00000	1.00000
3b	1.00000	1.00000	1.00000	1.00000
4	1.00000	1.00000	1.00000	1.00000
5	1.00000	1.00000	1.00000	1.00000
6	0.30136	0.20273	0	0
7	0.21917	1.00000	1.00000	1.00000
8a	1.00000	1.00000	1.00000	1.00000
8b	1.00000	1.00000	1.00000	1.00000

Table (8) p-value proportion test for 365 (one year) sequences for BBS

Test Code	p-value proportion of 128 bit	p-value proportion of 256 bit	p-value proportion of 512 bit	p-value proportion of 1024 bit
1	0.99452	1.00000	0.99452	0.98904
2	0.99178	0.98630	1.00000	0.99726
3a	0.99452	1.00000	0.99178	0.99178
3b	0.98630	1.00000	0.99452	0.98904
4	0.98630	0.98630	0.98630	0.98904
5	0.99452	0.99452	0.99726	0.98356
6	0.98630	0.99178	0.99452	0.98904
7	1.00000	0.93698	0.81369	0.92602
8a	0.98356	0.98356	0.98904	0.98082
8b	0.98904	0.98904	0.99178	0.98904

Table (9) p-value proportion test for 365 (one year) sequences for LCG

Test Code	p-value proportion of 128 bit	p-value proportion of 256 bit	p-value proportion of 512 bit	p-value proportion of 1024 bit
1	0.98082	0.99178	0.99726	0.98630
2	0.99178	1.00000	1.00000	0.99452
3a	0.98904	0.98630	1.00000	0.98356
3b	0.98082	0.99178	0.99452	0.98356
4	0.98904	0.99178	0.98356	0.98630
5	0.99452	0.99726	0.99726	0.98082
6	0.98904	0.99452	0.99726	0.98082
7	1.00000	0.95616	0.75068	0.92602
8a	0.97260	0.97808	0.99452	0.98630
8b	0.98904	0.99452	0.99726	0.99452

Table (10) the Pass / Fail for the proposed algorithm (TPA), LFSR, BBS, and LCG

Test Code	p-value Pass/Fail for 128 bit				p-value Pass/Fail for 256 bit				p-value Pass/Fail for 512 bit				p-value Pass/Fail for 1024 bit			
	TPA	LFSR	BBS	LCG	TPA	LFSR	BBS	LCG	TPA	LFSR	BBS	LCG	TPA	LFSR	BBS	LCG
1	P	P	P	P	P	P	P	P	P	P	P	P	P	P	P	P
2	P	P	P	P	P	P	P	P	P	P	P	P	P	P	P	P
3a	P	P	P	P	P	P	P	P	P	P	P	P	P	P	P	P
3b	P	P	P	P	P	P	P	P	P	P	P	P	P	P	P	P
4	P	P	P	P	P	P	P	P	P	P	P	P	P	P	P	P
5	P	P	P	P	P	P	P	P	P	P	P	P	P	P	P	P
6	P	F	P	P	P	F	P	P	P	F	P	P	P	F	P	P
7	P	F	P	P	P	P	F	F	P	P	F	F	P	P	F	F
8a	P	P	P	F	P	P	P	P	P	P	P	P	P	P	P	P
8b	P	P	P	P	P	P	P	P	P	P	P	P	P	P	P	P
	(P = Pass) (F = Fail)															

The screenshot displays a software interface for generating a 128-bit key. It is divided into five main sections:

- 1- Generate Numbers:** Includes a 'Generate' button with input fields for 21, 69, and 101. Below are 'Bit For X, Y and S' (7, 6, 5, 4, 3, 2, 1) and 'Generate All Numbers' buttons. A list of generated numbers is shown in a grid.
- 2- Selecting Bit Per Pixel:** Features a 'Select No. of Bits' field set to 1 and a 'Key Length' field set to 128.
- 3- Generate Key:** Contains a 'Start Generate' button and a large window displaying a noisy, multi-colored image representing the generated key.
- 4- Data Acquired From Images:** A table with columns: Image No, X, Y, Pixel, Pixel Value, and Bit(s) Value. It lists data for images 25, 8, 15, 29, 15, 30, 16, 32, and 22.
- 5- Build the Key:** Shows a 'Build' button and a large text area containing a long binary string (101000111110000010110010110110011010101110110101010011111001111001101011000101010110000011001010101010000111011000). An arrow points from the 'Output Key' label to this binary string.

At the bottom, there are buttons for 'Auto Build Key' and 'Build Keys for Year'.

Fig. (8) 128 Bit Generation



Form1

1- Generate Numbers

Generate **50** **18** **74**

Bit For X, Y and S

7 6 5 4 3 2 1

Generate All Numbers

110	14	57
92	28	115
57	56	102
115	113	76
102	98	25
76	68	50
25	9	101
50	18	74

2- Selecting Bit Per Pixel

Select No. of Bits

Bits	Key Length
8	1024

3- Generate Key

Start Generate

4- Data Acquired From Images

Image No	X	Y	Pixel	Pixel Value	Bit(s) Value
8	101	36	Red	51	00110011
15	74	73	Red	227	11100011
29	21	19	Green	232	11101000
15	42	38	Green	165	10100101
30	85	77	Red	234	11101010
16	43	27	Blue	26	00011010
32	87	54	Blue	192	11000000
22	47	109	Red	246	11110110
43	95	90	Green	47	00101111

5- Build the Key

Build

```
0011001111100011111010001010010111101010000110101000000111011000101111000
0111001010101110001010011010110011011100111110110000111000000111111000111
00010000010011000011100010100100110111111010111110011010100010001001110
000000110101001010001100100110000100101000000010110010000111101001010010010
01100010000011011110010100101010100010100011000010110111100011110111010
10000011111001000110100000100110000111101010101000001011001100000101000001
100011010000110001111101100110100111010001100011110111110011110111101010
11110000011111110010100001001011100010011110110101001001001010110111101
110000001000100001001001111110101110010110000101100110111000111010011
0011111011100011111011010010111011010001010001010101111000010101001011001
01001000101010000100001000100000000010110011100001010111101100011111010
00111011000110111000010000100110100011110100111100110000101011101101100110
1010011101110000011111101001111000110011001111010001001011111100011010101
1111001101100110001111101100010101110011100000000
```

Auto Build Key Build Keys for Year

Fig. (9) 1024 Bit Generation



SIMULATION OF INDIRECT EVAPORATIVE COOLER HEAT EXCHANGER AT IRAQI CONDITIONS

Khalid A. Joudi¹, Khawla N. Hmood²

Department of Mechanical Engineering

College of Engineering, University of Baghdad, Baghdad, Iraq

ABSTRACT

The investigation included PHE performance variation with heat exchanger dimensions, plate spacing, inlet air velocities and inlet air temperatures. The momentum and energy equations were solved in 3-dimensions by using FLUENT 5.3 software and heat exchanger performance parameters were extracted from the post processing of the numerical data. In addition, a 2-dimensional fluid flow and heat transfer numerical analysis for the crossflow PHE was carried out. A numerical code based on the finite difference method and the SIMPLE algorithm was developed to solve the governing equations. The result of the numerical study for PHE performance shows that for both air streams the maximum thermal gradient occurs at 0.5 m/s inlet air velocity while the minimum occurs at 5 m/s velocity. Furthermore; the greater thermal gradient for the both air streams occurs at 3 mm plate spacing and decrease progressively to the lowest gradient at 10 mm spacing. Also, the results indicated that indirect evaporative cooling could be applied to obtain suitable outlet air temperatures for low and medium values of wet-bulb temperatures in arid climates.

1000x1000 mm 300x300 mm

5 m/s 0.3 m/s

15 mm 3 mm

(FLUENT 5.3)

(Finite Difference)

(SAMPLE Algorithm)

. FORTRAN

¹ Prof. of Mech. Eng., Corresponding author

² Graduate student

Keywords: plate heat exchanger; wet crossflow; convective heat mass transfer; air coolers.

INTRODUCTION

Indirect evaporative cooling (IEC) involves sensibly cooling a process air stream and keeping its water content unchanged. Cross flow plate heat exchangers are widely used in IEC (Mazza 1984).

A cross-flow heat exchanger was used sheets only 0.18 mm thick, such that their thermal resistance was very low. Pescod 1974 proposed an idealized minimum supply temperature from an IEC unit as equal to the wet bulb temperature of room air.

Said and Khassaf 1984 evaluated the use of direct and indirect methods of evaporative cooling for residential comfort in Iraq using a heat exchanger. They concluded that the IEC is superior to direct evaporative cooling (DEC) in Mousl and Baghdad where it is usually dry; and that the use of IEC may be extended to the humid southern part of the country around Basrah where DEC would perform poorly. Yellott and Gamero 1984 described different types of indirect evaporative cooling units and the psychrometric analysis related to these various IEC system types. Kettleborough and Hsieh 1983 described a counter flow indirect evaporative cooler with configuration of upward flow of the primary air, downward flows of secondary air and water. Numerical analysis was utilized to study the thermal performance of the unit.

Awishalim and Al-Shawi 1986 and Enwia 1986 introduced a crossflow plate heat exchanger for use as an indirect evaporative cooler for Iraq. The heat exchanger was alternate passages of Aluminum plates. Both workers carried out tests on a number of heat exchanger geometries and plate spacing of 6 mm and 3.5 mm.

The performance of IEC is affected by changes in primary and secondary air velocities and mass flow rates, wet-bulb temperature, altitude, and other factors (Peterson 1993). Joudi and Mehdi 2000 carried out a theoretical study into the application of indirect-direct evaporative cooling systems in fulfillment of the variable cooling load of a typical Iraqi dwelling. This study was based on a mathematical model given by Pescod for a plate-type heat exchanger to simulate the indirect evaporative cooler.

Abdul Jabar 2000 conducted a study into the evaluation of indirect evaporative-desiccant cooling system performance. The study used a computer simulation for the evaluation of four systems. These systems employed a plate heat exchanger for the indirect evaporative cooler. The results showed that the best of the suggested systems was the indirect evaporative-desiccant cooling system.

Adhikari 2004 investigated alternatives to vapour compression technology by using polymer plates in crossflow heat exchanger as indirect evaporative cooling, which he claimed, provided a cost effective and efficient system for all climates.

The present study consists of two parts. The first part used the FLUENT software, to evaluate the performance of crossflow PHE upon the variation in the inlet velocities, and inlet temperatures for the two air streams. The temperature and velocity distributions for the two air streams inside the PHE were obtained and would be used as input data in a developed 2-dimensional analysis. The second part, involved a numerical scheme in 2-dimensions for the wet surface plate heat exchanger. The scheme was developed by a FORTRAN program based on the finite difference method. The calculation included distribution of temperature and velocity for the two air streams for various exchanger dimensions, inlet air velocities and varying inlet air conditions.

FLUENT SOFTWARE ANALYSIS

Physically, a PHE in Fig. 1 is a set of parallel metal plates, which separate hot and cold fluid streams from each other by using a crossflow mode. Heat transfer resistance through the plates is small compared to the air stream boundary layer resistance on each side of the plates. The basic system is a heat exchanger where both fluid flows remain in the gaseous phase and no condensation occurs over the exchanger surfaces.

The full numerical solution of heat exchangers is computationally prohibitive because the flow and temperature fields must be simultaneously determined in two fluids and making full simulation of heat exchangers is practically

nonexistent (Patankar 1980). Heat transfer and fluid flow in enclosed channels is usually analyzed in 3-dimensions. Therefore, it was suggested to employ the FLUENT package to carry out the 3-dimensional analysis.

The steady state governing equations for continuity, momentum and energy are solved using a segregated solver, which means that temperature and flow fields are segregated from each other and were solved by using FLUENT 5.3 software. The initial guesses for velocity and temperature fields were set to constant values over the entire computational domain. To obtain the flow and heat transfer solutions, the solver undertakes iteration until the convergence criterion is satisfied, which employed scaled residuals of the modified variables in the governing equations as the measure. In addition, the averaged fluid temperature was examined implicitly for convergence (to less than a 0.01% variation between iterations).

The physical model of the present work was simulated as flow in 3D geometry using quadrilateral/hexahedral grids. The assumptions made were as follows:

- Incompressible laminar flow.
- Steady state conditions.
- Newtonian fluids.
- Forced convection heat transfer.
- Coupled conduction/convection heat transfer.

The calculation domain consisted of six rectangular channels stacked one over the other to form the crossflow plate heat exchanger. The limitation to six channels depended on the CPU of the computer and the number of nodes that could be solved at the same time. Various dimensions for a square plate heat exchanger were employed. These included 300x300, 500x500, 700x700, 800x800, and 1000x1000 mm. Also, the spacing between plates for each dimension was varied and included 3, 4, 5, 7, 8, 10, and 15 mm. The hot air was set at 320 K and the cold air at 302 K. Aluminum was selected for the plate heat exchanger material. Also, several inlet velocities were used for the hot and cold fluids. Namely, 0.3, 0.5, 0.7, 1, 1.5, 2, 2.5, 3, 4, and 5 m/s.

Fig. 2 is a typical case for demonstrating the effect of plate dimensions on the hot air temperature distribution. It is clear that the thermal gradient increased progressively with increasing heat exchanger dimensions. Larger area means higher heat exchanger effectiveness. The effect of

various plate spacing on the hot air temperature distribution is shown in Fig. 3. It is observed that the thermal gradient increased with decreasing plate spacing. This is due to the two reasons. First, Re number is decreasing. Second, heat transfer coefficient is increasing. Fig. 4 illustrates the effect of the various inlet air velocities on the hot air temperature distribution. It clearly shows that the thermal gradient increases with decreasing inlet velocity for the hot air. As a result the thermal gradient increased progressively with decreasing plate spacing, lower velocity and larger dimensions. As a result of, it is increasing in heat transfer between two streams.

It is intended to find a suitable IEC heat exchanger for domestic use at Iraqi houses. The most commonly used evaporative coolers are 2500, 3500, 4500 cfm (1179.875, 1651.825, 2123.775 l/s) air coolers. Dimensions of a suitable IEC heat exchanger and other conditions for such flow rates are sought after. The Fluent results would be used for this purpose in a 2-D analysis. It is observed from the results in Fig. 5, that the values of ΔT_h and ΔT_c for 700x700, 800x800, and 1000x1000 mm are comparable. The 800x800 mm is selected as representative of the three. Thus, the 300x300, 500x500 and 800x800 mm dimensions will be used for the purposes of this study in the 2-D analysis.

From Figs. 6, and 7, the 3 mm plate spacing gives the maximum values as a consequence of ΔT_h and ΔT_c . The 7 and 8 mm spacing give approximately the same results for ΔT_h and ΔT_c . Hence, 8 mm plate spacing may be selected as representative of both. The maximum value of plate spacing in heat exchangers used in air conditioning does not usually exceed 12.5 mm (ASHRAE 2000 equipment and applications). Therefore, the 15 mm plate spacing will be neglected in the 2-dimensional analysis. Thus, the representative plate spacings that will be used in the 2-dimensional analysis will be 3, 5, 8, and 10 mm. Also, from these Figures, it can be observed that velocities of 1.5 and 2 m/s give approximately the same value of ΔT_h and ΔT_c and the velocities of 2.5 and 3 m/s give the same results. Thus, the representative velocities that will be used in the 2-dimensional analysis will be 0.5, 1, 2, 3, 4, and 5 m/s.

TWO DIMENSIONAL SIMULATION MODEL FOR THE HEAT EXCHANGER

To simulate a plate heat exchanger, the velocity field is uncoupled from the temperature field and determined first before solving the energy

equation. The continuity and momentum equations need to be solved to determine the velocity field. Since the momentum equations are nonlinear and coupled to the continuity equation, they have to be solved iteratively (Albakhit and Fakheri 2005).

The general assumptions for the problem solution used by Mishra, et al. 2004 which will be adopted here are as follows:-

1. Incompressible fluids and hydrodynamically developing flows.
2. Both fluids are single phase, unmixed and do not contain any volumetric source of heat generation.
3. The exchanger shell is adiabatic and the effects of the asymmetry in the top and bottom layers are neglected. Therefore, the heat exchanger may be assumed to comprise of a number of symmetric sections.
4. Variation of temperature in the fluid streams in a direction normal to the separating plate (z-direction) is neglected.
5. Conduction along the walls is negligible.

FLOW GOVERNING EQUATIONS IN TWO DIMENSIONS

The incompressible Navier-Stokes equations in 2-dimensions are in the following form:

- Continuity Equation:

$$\frac{\partial u}{\partial x} + \frac{\partial v}{\partial y} = 0 \quad (1)$$

- Momentum Equations:

$$\frac{\partial(\rho u^2)}{\partial x} + \frac{\partial(\rho uv)}{\partial y} = -\frac{\partial p}{\partial x} + \mu \left(\frac{\partial^2 u}{\partial x^2} + \frac{\partial^2 u}{\partial y^2} \right) \quad (2)$$

$$\frac{\partial(\rho vu)}{\partial x} + \frac{\partial(\rho v^2)}{\partial y} = -\frac{\partial p}{\partial y} + \mu \left(\frac{\partial^2 v}{\partial x^2} + \frac{\partial^2 v}{\partial y^2} \right) \quad (3)$$

One type of numerical solution for the above equations is an iterative process called the pressure correction technique. This technique is embodied in an algorithm called SIMPLE (semi-implicit method for pressure-linked equations) (Patankar 1980). The above equations are applied for the two fluids to find the velocity distribution along the flow direction, by non-dimensionalizing as follows (Albakhit and Fakheri 2005), (Incropera and DeWitt 1996);

- For the hot fluid,

$$\left. \begin{aligned} U &= \frac{u}{u_{in}}, & V &= \frac{v}{u_{in}}, & X &= \frac{x}{L}, \\ Y &= \frac{y}{L}, & P &= \frac{P - P_{in}}{\rho u_{in}^2} \end{aligned} \right\} \quad (4)$$

These terms are substituted in eqs. (2) and (3). The resulting equations take the following form;

$$\frac{\partial U^2}{\partial X} + \frac{\partial UV}{\partial Y} = -\frac{\partial P}{\partial X} + \frac{1}{\text{Re}} \left(\frac{\partial^2 U}{\partial X^2} + \frac{\partial^2 U}{\partial Y^2} \right) \quad (5)$$

$$\frac{\partial VU}{\partial X} + \frac{\partial V^2}{\partial Y} = -\frac{\partial P}{\partial Y} + \frac{1}{\text{Re}} \left(\frac{\partial^2 V}{\partial X^2} + \frac{\partial^2 V}{\partial Y^2} \right) \quad (6)$$

- For the cold fluid,

$$\left. \begin{aligned} U &= \frac{u}{v_{in}}, & V &= \frac{v}{v_{in}}, & X &= \frac{x}{L}, \\ Y &= \frac{y}{L}, & P &= \frac{P - P_{in}}{\rho v_{in}^2} \end{aligned} \right\} \quad (7)$$

These equations will be used in the iterative solution.

TWO DIMENSIONAL WET HEAT EXCHANGER ANALYSIS

Evaporatively cooled heat exchangers (Fig. 8) can achieve heat transfer rates higher than dry heat exchangers. Heat transfer takes place from hot dry air, flowing inside channels, to wet air in alternate channels, through a water film which is formed by spraying water onto the heat exchanger surface. Spray water is circulated in a closed circuit. Heat transfer to air is in sensible and latent forms. The latent heat transfer makes up a major part and is produced by the evaporation of a small amount of the spray water into the air stream. When compared with dry heat exchangers, wet heat exchangers can achieve lower temperatures because the air wet-bulb temperature is, theoretically, the ultimate limit of the air-water direct contact process.

Essentially, the water on the plate is "excessive water" in the wet passage. Because the thickness of the water film is small, it is assumed that the temperature difference across the water film on the plate is negligible, and, hence, the local temperature of water on the plate can be taken to be the same as the local temperature of the plate (Kettleborough and Hsieh 1983). For a steady state condition, it is assumed that spray water flow rate is sufficient to wet the whole surface of the plate. The analysis of the energy balance is as follows:-

Heat is transferred from the hot air to the spray water film through the plate thickness as a result of the temperature gradient between the hot air temperature T_h and the spray water temperature T_s . The rate of heat lost by the hot air dq_h is

$$dq_h = \dot{m}_h c_{ph} dT_h = -U_o (T_h - T_s) dA \quad (8)$$

Where, U_o is the overall heat transfer coefficient between the hot air through the separating plate to the water film on the other surface. It is given as,

$$U_o = \frac{1}{1/h_h + s/k} \quad (9)$$

To find the heat transfer coefficients for the two air streams the Nusselt number must be specified. For laminar, developed conditions with constant wall temperature and Reynolds number less than 2300, the Nusselt number is given as (Incropera and DeWitt 1996);

$$Nu = 7.542 + 7.542 * \left(0.003 + 0.039 * \frac{a}{b} \right) * \frac{Pe}{L/d_h} \quad (10)$$

Where, Pe is the Peclet number, and for turbulent flow, where the Reynolds number is higher than 2300, it is given as,

$$Nu = 0.036 Re^{0.8} Pr^{\frac{1}{3}} \left(\frac{L}{d_h} \right)^{-0.054} \quad (11)$$

After the calculation of the Nusselt number, the value for local convection coefficient h can be determined from,

$$h = \frac{Nu k}{d_h} \quad (12)$$

Heat transfer from the cold air–water interface region to the cold air stream dq_c consists of a sensible part dq_s and a latent part dq_l ;

$$dq_c = \dot{m}_c dH_c = dq_s + dq_l \quad (13)$$

Substituting for the sensible and latent heats gives,

$$dq_c = \dot{m}_c dH_c = h_i (T_i - T_c) + k_m (w_i - w_c) h_{fg} dA \quad (14)$$

The enthalpy of air and water vapor mixtures is given as (Joudi 1990);

$$H = (1.005 T_d - 0.026) + w(2501 + 1.84 T_d) \quad (15)$$

Then, the temperature of moist air can be written as

$$T_c = \frac{H_c + 0.026 - 2501 w}{1.005 + 1.84 w} \quad (16)$$

The specific heat for humid air c_{pu} is equal to $(1.005 + 1.84w)$. Substituting for T_c and T_i from Eq. (16) and taken into consideration that for air and water mixtures the Lewis number could be taken as unity (ASHRAE fundamentals 1997) the Eq. (14) is reduced to :

$$dq_c = \dot{m}_c dH_c = k_m (H_i - H_c) dA \quad (17)$$

The liquid side of the interface offers a negligible resistance to heat transfer, so that the interface enthalpy H_i in Eq. (17) could be considered equal to the saturated air enthalpy H_s at the spray water temperature T_s . Therefore, Eq. (17) is rewritten as;

$$dq_c = \dot{m}_c dH_c = k_m (H_s - H_c) dA \quad (18)$$

Eq. (18) is called the Merkel equation (Hasan and Siren 2002). It shows that the energy transfer could be represented by an overall process based on enthalpy potential difference, between air–water interface and bulk air, as the driving force.

But, for the DEC the enthalpy is essentially constant. Therefore, the sensible heat transfer from cold air to the air–water interface, can be written as,

$$-\dot{m}_c c_{pu} dT_c = h_i (T_c - T_s) dA \quad (19)$$

Also, $h_i = c_{pu} k_m$ then;

$$-\dot{m}_c c_{pu} dT_c = c_{pu} k_m (T_c - T_s) dA \quad (20)$$

$$\dot{m}_c dT_c = k_m (T_s - T_c) dA \quad (21)$$

In problems where both convection and mass transfer are important, the dimensionless ratio v/D_{ab} is important and is called the Schmidt

number Sc . Thus, the Schmidt number plays a role similar to that of the Prandtl number in convection heat transfer problems. The functional dependence of the heat transfer coefficient is;

$$\frac{h d_h}{k} = f(Re, Pr) \quad (22)$$

In convection mass transfer problems, the functional dependence of the mass transfer coefficient is;

$$\frac{k_m d_h}{D_{ab}} = f(Re, Sc) \quad (23)$$

The similarities between the governing equations for heat, mass, and momentum transfer suggest that empirical correlations for mass transfer coefficient would be similar to those for the heat transfer coefficient. The grouping of terms $k_m d_h / D_{ab}$ is called the Sherwood number Sh .

The mass transfer coefficient for the humid air could be found from the Sherwood number for laminar flow at constant wall temperature by the following Equation (Incropera and DeWitt 1996);

$$Sh = 7.542 + 7.542 * \left(0.003 + 0.039 * \frac{a}{b} \right) * \frac{Re * Sc}{L/d_h} \quad (24)$$

For turbulent flow the Sherwood number is (Incropera and DeWitt 1996);

$$Sh = 0.036 Re^{0.8} Sc^{\frac{1}{3}} \left(\frac{L}{d_h} \right)^{-0.054} \quad (25)$$

$$k_m = \frac{Sh * D_{ab}}{d_h} \quad (26)$$

Where, the value of the diffusion coefficient D_{ab} at one atmosphere is equal to $0.26 * 10^{-4} m^2 / s$ (Table A-8, Incropera and DeWitt 1996). Also, the value of Sc , for water vapor and air, is equal to 0.6 (Table A-18, Kays and Crawford 1993).

The solution to the above equations is in two parts. The first part solves the flow equations (continuity and momentum) and the second part solves the energy equation.

COMPUTATIONAL MODEL FOR THE WET CROSSFLOW HEAT EXCHANGER (IEC)

The surface area of the heat exchanger is divided into a number of two-dimensional small regions. Thus, the flow in the X-direction is divided into (N_x) sections and flow in the Y-direction into (N_y) sections. The reference points form a nodal network, in which the value of a new point is calculated from the results of its adjacent points where, the properties of hot air, spray water and cold air are defined on the surface boundaries. The numerical solution was based on a finite difference representation for the eqs. (8) and (21).

The variation of spray water temperature along a channel is small. Therefore, it could be assumed that the spray water temperature is constant and equal to T_s . For the above equations the forward finite difference approach will be applied and the average at $(i + \frac{1}{2}, j)$ and $(i, j + \frac{1}{2})$ will be in the following form;

By using the finite difference method and the average of T_s , heat transfer from the hot air to the spray water in eq. (8) becomes;

$$\frac{1}{2} u_h \rho c_{ph} a_h dx (T_h(i, j) - T_h(i-1, j)) = U_o dx dy \left(\frac{T_s + T_s}{2} - \frac{T_h(i, j) + T_h(i-1, j)}{2} \right) \quad (27)$$

After some rearrangement the above equation. can be written as;

$$T_h(i, j) = \frac{2 U_o dy}{u_h \rho c_{ph} a_h + U_o dy} T_s + \frac{u_h \rho c_{ph} a_h - U_o dy}{u_h \rho c_{ph} a_h + U_o dy} T_h(i-1, j) \quad (28)$$

The heat transfer from air- water interface to the cold air in eq. (26) becomes;

$$\frac{1}{2} v_c \rho a_c dy (T_c(i, j+1) - T_c(i, j)) = k_m dx dy \left(\frac{T_s + T_s}{2} - \frac{T_c(i, j+1) + T_c(i, j)}{2} \right) \quad (29)$$

After some rearrangement the above equation. can be written as;

$$T_c(i, j) = \frac{v_c \rho a_c - k_m dx}{v_c \rho a_c + k_m dx} T_c(i, j-1) + \frac{2 k_m dx}{v_c \rho a_c + k_m dx} T_s \quad (30)$$

The FORTRAN code for solving the energy equation was composed of two parts. The first part reads the velocity field which was found from the

solution of the flow equations for the hot and cold fluids. The second part of the code solved the energy equation for the entire heat exchanger and determined the temperature distribution. Also, the wet bulb temperature T_w was obtained from dry bulb temperature T_d and moisture content w for the outlet air from the heat exchanger by using the empirical relation given by Said and Khassaf 1984 as;

$$T_w = 2.265 \left(1.97 + 4.3 T_d + 10^4 w \right)^{\frac{1}{2}} - 14.85 \quad (31)$$

RESULTS AND DISCUSSION

The result for the present work for the following conditions, the inlet temperature for hot air equal to 45 °C and the cold air temperature equal to 29 °C while the spray water temperature was set equal to the wet bulb temperature at a value of 22 °C. Figs. 9, 10, and 11 are taken as typical of the results. Fig. 9 shows that the thermal gradient increases with decreasing inlet velocity for the process air. It is important to note that, the inlet velocity affects the Re number, Nu number, the heat transfer coefficient and consequently the rate of heat transfer. However, the maximum thermal gradient occurs at 0.5 m/s inlet air velocity and the minimum thermal gradient occurs at 5 m/s velocity. As a result of, the lower velocity improves the heat transfer between the two air streams. This result is similar to that for the wet air passage but with opposite direction as shown in Fig. 10. Fig. 11 is typical for other results and shows that the thermal gradient increases with decreasing plate spacing. The definition of Re number in this work is based on the plate spacing ($d_h = 2a$). Nu number is a function of the Re number and renders a heat transfer coefficient, for the smaller spacing, higher in value than that for the larger plate spacing. Analysis of this result shows that the heat capacity rate is decreased using narrower passages because a lower air flow rate is obtained at any given velocity. Thereby, the greater thermal gradient occurs at 3 mm plate spacing and decreases progressively to the lowest gradient at 10 mm spacing. Also, these Figures show a uniform outflow temperature for the two air streams from the outflow port. This is because of the effect of assumed constant plate surface temperature. The quantitative effects of inlet air velocity and plate spacing on the wet heat exchanger performance are further shown in Figs.

12 to 15. These figures represent the temperature difference between the inlet and average outlet process air temperatures, the difference between the inlet and average outlet wet passage air temperatures and the difference between the inlet and average outlet wet bulb temperature for the process air with the inlet velocity of the two air streams. These figures are typical of the results for other plate heat exchanger dimensions. It is clear that ΔT_d , for the two air streams, and ΔT_w , for the process air, for any plate spacing, decrease with increasing inlet air velocity. The maximum value of temperature difference for each stream occurs for 3 mm plate spacing and at 0.5 m/s inlet velocity. The minimum value of temperature difference occurs for 10 mm plate spacing and at 5 m/s inlet velocity. This may be due to the larger number of plates used for the 3 mm spacing case where, the number of plates is obtained by dividing the dimension of plate on the spacing between plates. Also, ΔT_d for the two air streams is equal for any one specific condition because of the thermal balance between the two air streams. Moreover, ΔT for both streams becomes more pronounced as the plate heat exchanger dimensions increases from 300x300 to 800x800 mm as shown in Figs. 12 to 15.

Figs. 12 and 13 show that for 5 mm spacing, ΔT at 5 m/s velocity is larger its value at 4 m/s velocity and the curve changes direction. This may be due to turbulence setting in at 5 m/s velocity, which raises the rate of heat transfer between the two air streams. For 8 and 10 mm plate spacing, the slope of the curves is steep at low velocity and becomes nearly horizontal and steady after a velocity of 3 m/s. Figs. 14 and 15 show similar results for 800x800 mm heat exchanger dimensions. Change in direction of the curves is more pronounced in this case.

The previous results were for a specified dry-bulb and wet-bulb temperature test program. They were carried out at restricted Re numbers for each spacing by restricting the inlet air velocity. If Re number is less than 2300 the flow is laminar, if greater or equal to 2300 the flow is turbulent (Incropera and DeWitt 1996). Further tests were carried out at velocities ranging from 0.5 to 9 m/s to find out when turbulence sets in. The values of such velocities, as obtained for 800x800 mm PHE dimension from Fig. 16, for each plate spacing are listed in Table (1);

Table 1. Inlet air velocity at which turbulence occurs

Spacing mm	Inlet air velocity m/s
------------	------------------------

3	7
5	5
8	3
10	3

The effect of heat exchanger dimensions on the process air and the wet air passage temperature is shown in Fig. 17 for an inlet air velocity of 2 m/s and 5 mm plate spacing. The maximum thermal gradient occurs in the 800x800 mm heat exchanger because of the increased heat transfer area. Fig. 19 shows a comparison between experimental results for a 200x200 mm IEC heat exchanged obtained by Enwia 1986 and the results of the present model. Dimensions and parameter values employed by Joudi and Mehdi 2000 Ref. were used in the present model. Namely 3.5 mm plate spacing and an inlet velocity for the two streams varying from 1.1 to 6.7 m/s. Good agreement is observed in Fig. 18A. This comparison is repeated for 6 mm plate spacing and an inlet air velocity range from 0.77 to 7.6 m/s in Fig. 18B. Fig. 19 compares the present results with that of a parallel flow plate heat exchanger by Kettleborough and Hsieh 1983. The crossflow is difference from the parallel flow. Where, the temperature in outlet crossflow is variable along the outlet while, in the parallel flow the outlet temperature is equality.

CONCLUSIONS

1. The process air outlet temperature from PHE is lower with increased heat exchanger dimensions, lower inlet air velocity and smaller plate spacing.
2. The present finite difference model is in good agreement with other experimental works and the errors in the results not exceeded 15%.
3. The indirect evaporative cooler PHE rendered substantial reductions in dry bulb temperature and can be used effectively in hot arid climates as in Iraq.

REFERENCES

- ASHREA Handbook of Fundamentals, 1997.
- ASHRAE 2000 equipment and applications.
- Awishalim, J., and Al-Shawi, I.M., 1986, "Development and assessment of a plate heat exchanger for indirect evaporative", 4th conference of the Scientific Research Council, Iraq.
- Abdul Jabar, M., 2000, "Simulation of Indirect Evaporative Desiccant Cooling System", M.Sc. Thesis, Mechanical Engineering Department, University of Baghdad.

- Adhikari, A.K., 2004, "Improving energy efficiency using indirect evaporative cooling with vapour compression assistance", M.Sc. Thesis, The Australian Institute of Energy, Sydney Branch. 2004.
- Albakhit, H., and Fakheri, A., 2005, "A Hybrid Approach for Full Numerical Simulation of Heat Exchangers", ASME Heat Transfer Summer Conference, July 17-22, 2005, San Francisco, CA, USA.
- Enwia, J.A., 1986, "Development and Assessment of a Crossflow Plate Heat Exchanger for Use in Indirect Evaporative Cooling", M. Sc. Thesis, Mechanical Engineering Department, University of Baghdad.
- Hasan, A., and Siren, K., 2002, "Theoretical and Computational Analysis of Closed Wet Cooling Towers and Its Applications in Cooling of Buildings", Energy and Buildings, Vol. 34, No. 5, pp. 477-486.
- Incropera, P.F., and DeWitt, D.P., 1996, "Fundamentals of heat and mass transfer", 4th Ed.: John Wiley & Sons, Inc. Pp. 886. ISBN 0-471-30460-3
- Joudi, K.A., 1990, "Principles of Air-conditioning and Refrigeration", Basrah, University Press, 2nd printing, 1990, In Arabic.
- Joudi, K.A., and Mehdi, S.M., 2000, "Application of Indirect Evaporative Cooling to a Variable Domestic Cooling Load", Energy conversion and Management, Volume 41, Issue 17, 1 November 2000, Pages 1931-1951.
- Kays, W.M., and Crawford, M.E., 1993, "Convective Heat and Mass Transfer", Third Edition, McGraw-Hill Book Co.-Singapore.
- Kettleborough, C.F., and Hsieh, C.S., 1983, "The Thermal Performance of the Wet Surface Plastic Plate Heat Exchanger Used As an Indirect Evaporative Cooler", Trans. Of the ASME, J. of Heat Transfer, Vol. 105, pp. 366-372, May 1983.
- Mazza, V. 1984, "Plate heat exchangers for HVAC applications", Heating /Piping /Air Conditioning, Vol. 56, No. 8, pp. 59-63, August 1984.
- Mishra, M., Das, P.K., and Sarangi, S., 2004, "Transient Behaviour of Crossflow Heat Exchangers with Longitudinal Conduction and Axial Dispersion", J. of Heat Transfer, Vol. 126, No. 3, pp. 425-433.
- Pescod, D., 1979, "A Heat Exchanger for Energy Saving in an Air-Conditioning Plant", ASHRAE Trans., Vol. 85, No. 2, pp. 238-251.

- Pescod, D., 1968, "Unit Air Cooler Using Plastic Heat Exchanger with Evaporatively Cooled Plates", Australian Refrigeration, Air-conditioning and Heating, V.22, pp.22, September 1968.
- Pescod, D., 1974, "An Evaporative Air Cooler Using a Plate Heat Exchanger", CSIRO Technical, Report No.TR2, Victoria, Australia
- Peterson, J.L., 1993, "An effectiveness model for indirect evaporative coolers", ASHRAE Transactions, Vol. 99, Pt.2, pp.392-399.
- Patankar, S.V., 1980, "Numerical Heat Transfer and Fluid Flow", McGraw-Hill, New York
- Said, W.K., and Khassaf, F.H., 1984, "Indirect Evaporative Cooling for Residential Comfort", Al-Muhandis, No. 85, PP. 36-46, Des. 1984.
- Wooldridge, M.J., Chapman, H.L., and Pescod, D., 1976, "Indirect Evaporative Cooling Systems", ASHRAE Trans. pp. 146-153.
- Yellott, J.I., and Gamero, J., 1984, "Indirect Evaporative Air Coolers for Hot, Dry Climates", ASHRAE Trans., Vol.90, Pt.1B, pp.139-147.

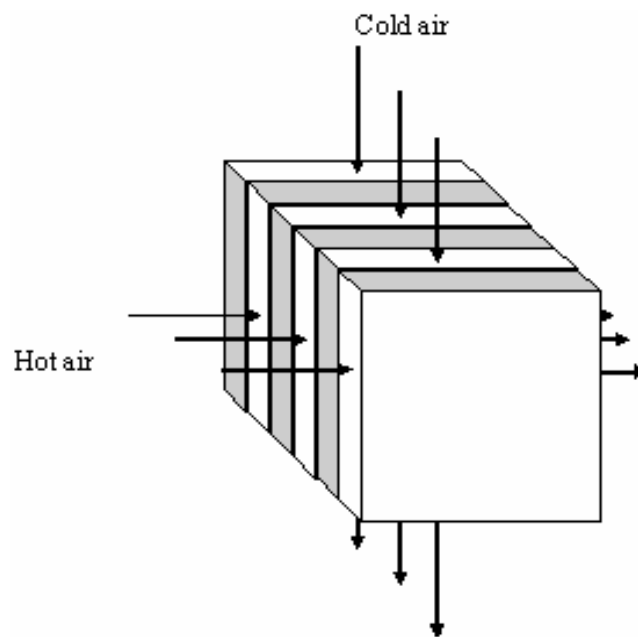


Figure. 1. Crossflow plate heat exchanger



a) 300X300 mm



c) 700X700 mm

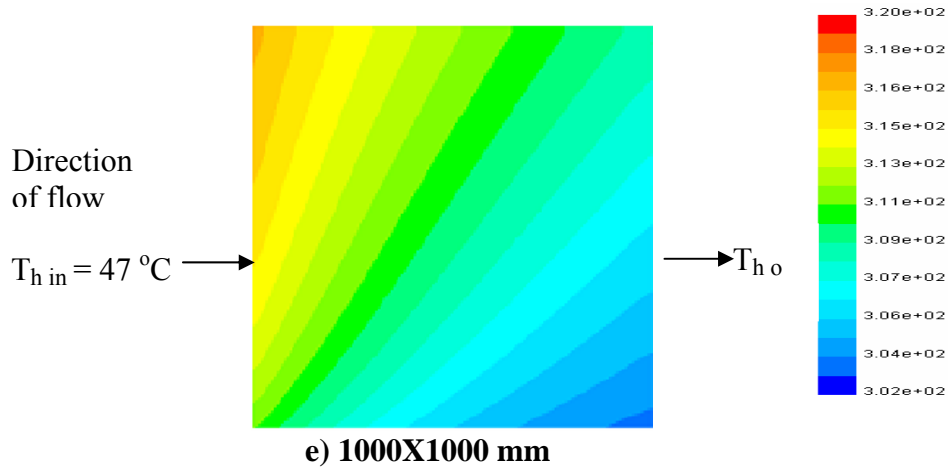
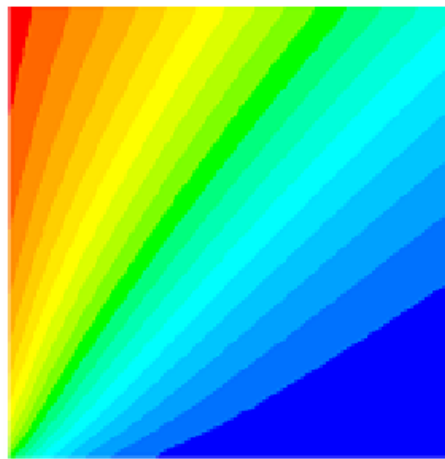
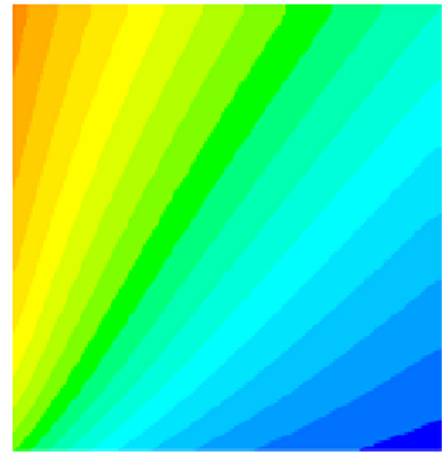


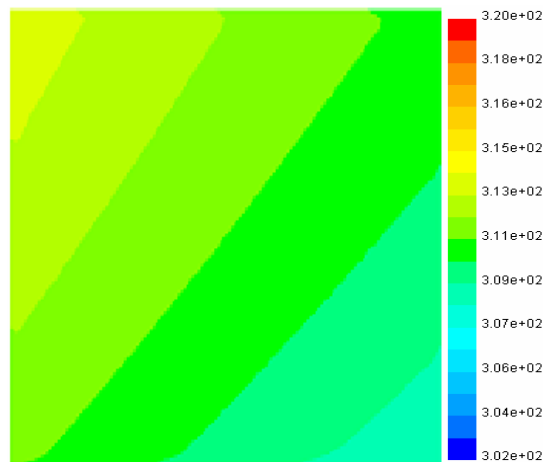
Figure. 2. The effect of PHE dimensions on hot air temperature distribution for 5 mm spacing and 2 m/s inlet air velocity



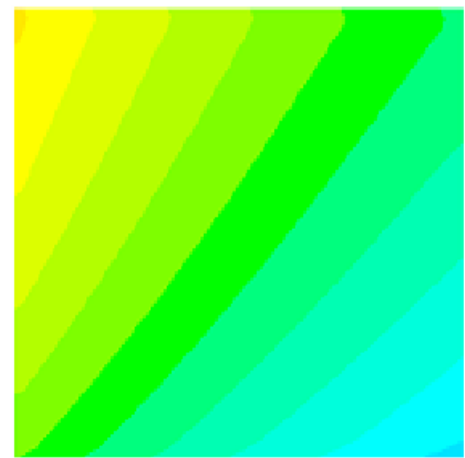
a) Spacing = 3 mm



b) Spacing = 5 mm



c) Spacing = 10 mm



d) Spacing = 15 mm

Figure. 3. The effect of plate spacing on the hot air temperature distribution for an 800X800 mm PHE at inlet air velocity of 1 m/s

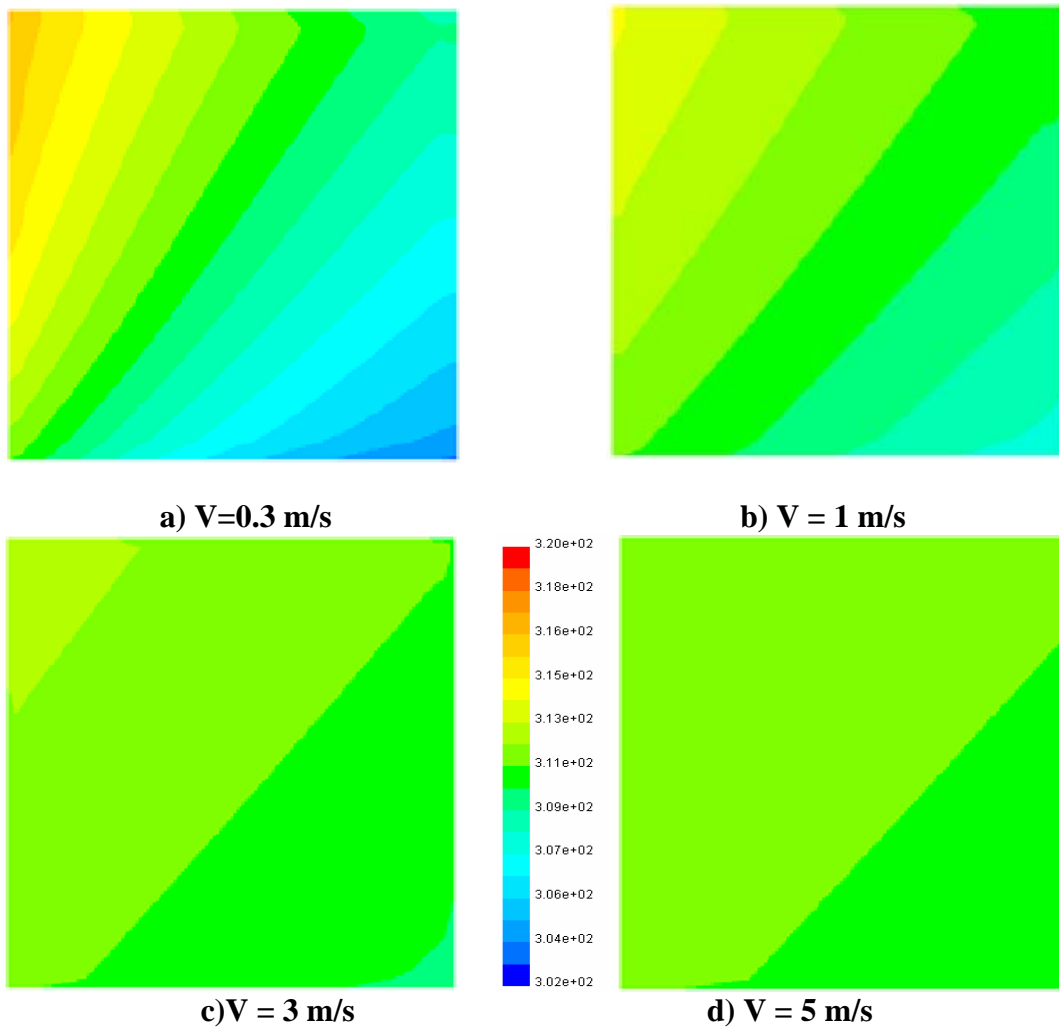


Figure. 4. The effect of inlet air velocity on hot air temperature distribution for the 300X300 mm PHE and 8 mm plate spacing

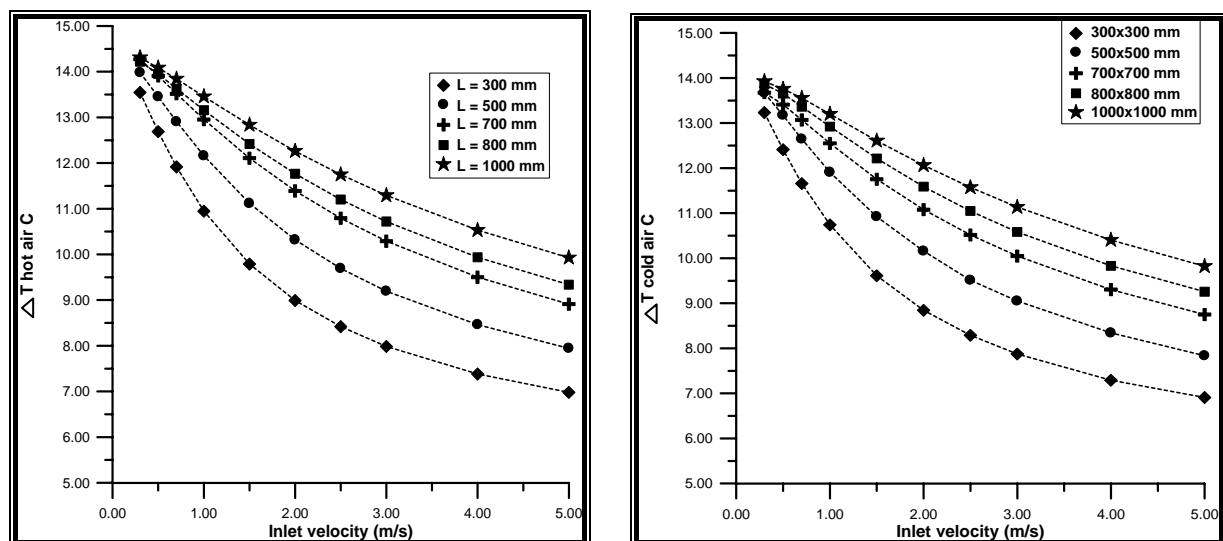


Figure. 5. The temperature difference for the two air streams at 5 mm spacing

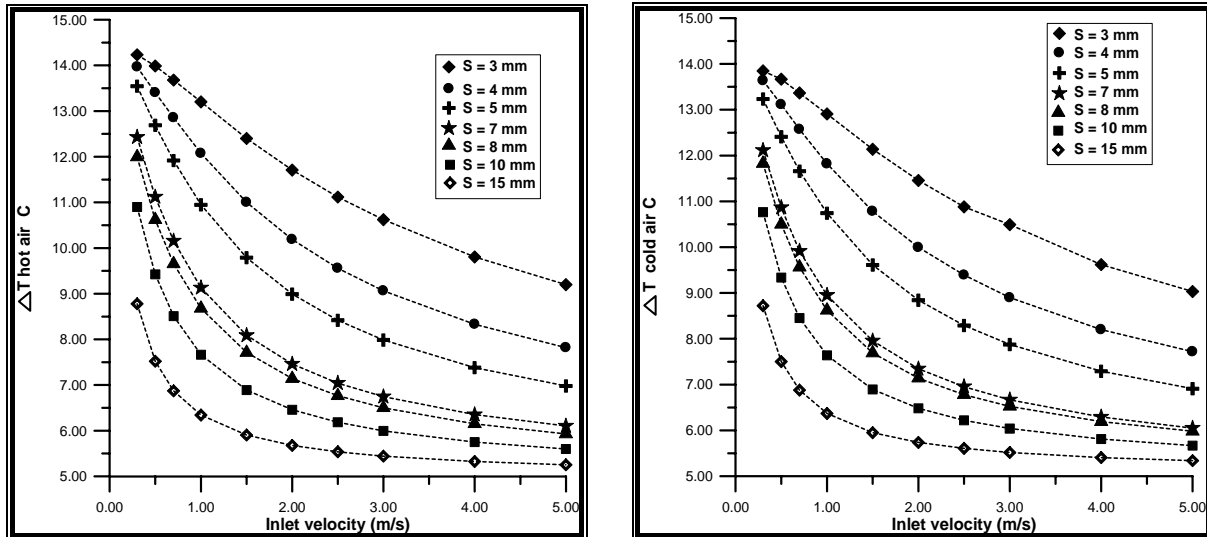


Figure. 6. The temperature difference for the two air streams at 300x300 mm PHE dimension

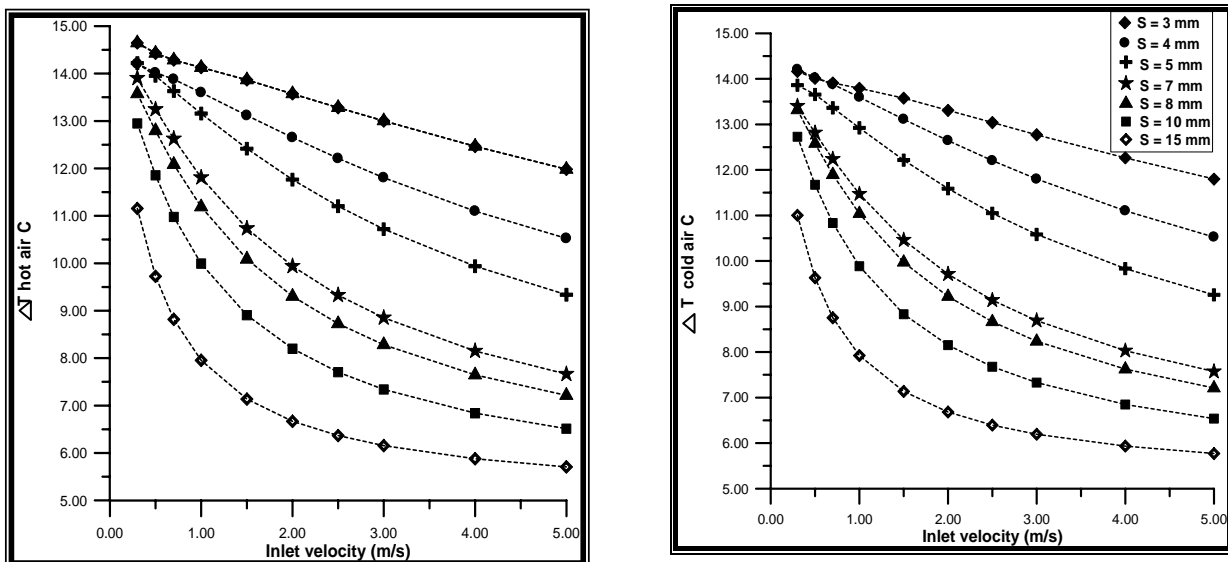


Figure. 7. The temperature difference for the two air streams at 800x800 mm PHE dimension

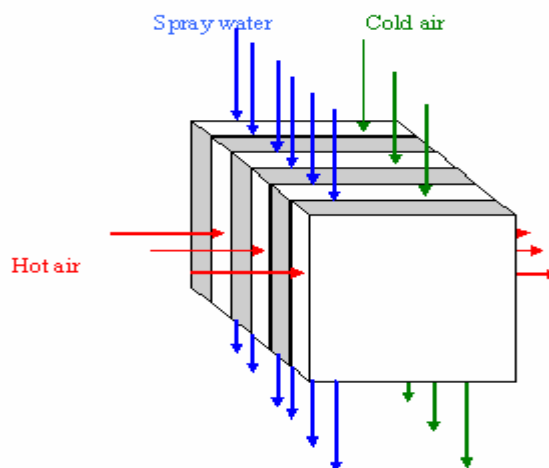


Figure. 8. Evaporatively plate heat exchanger

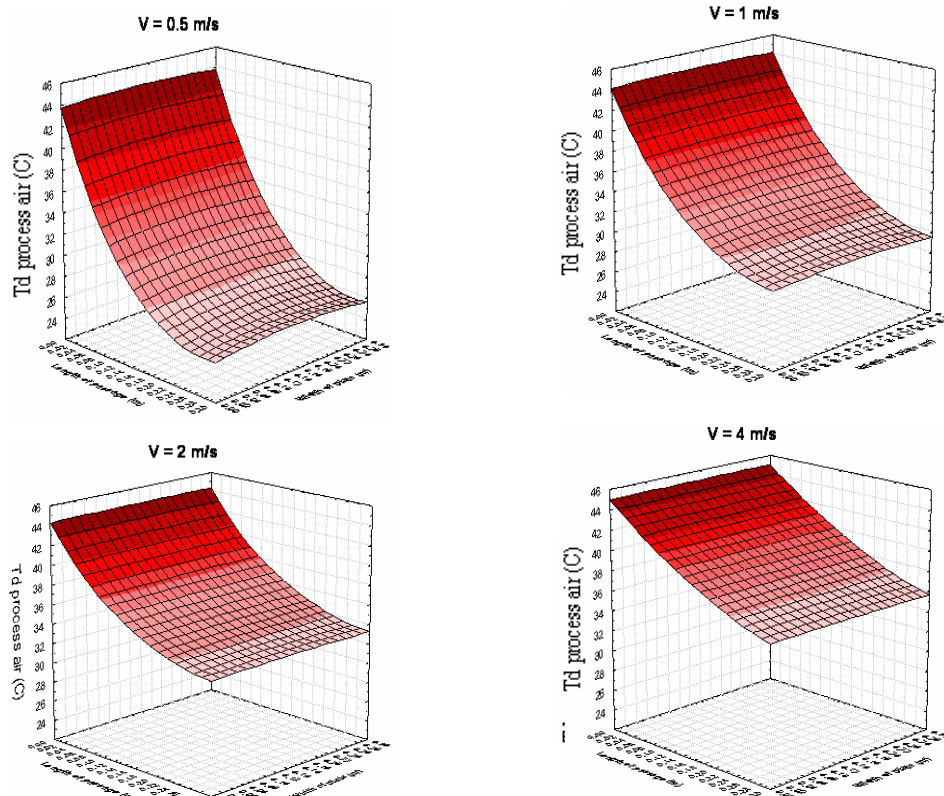


Figure. 9. The effect of inlet air velocity on the process air temperature distribution for the dimensions 300x300 mm and 8 mm plate spacing

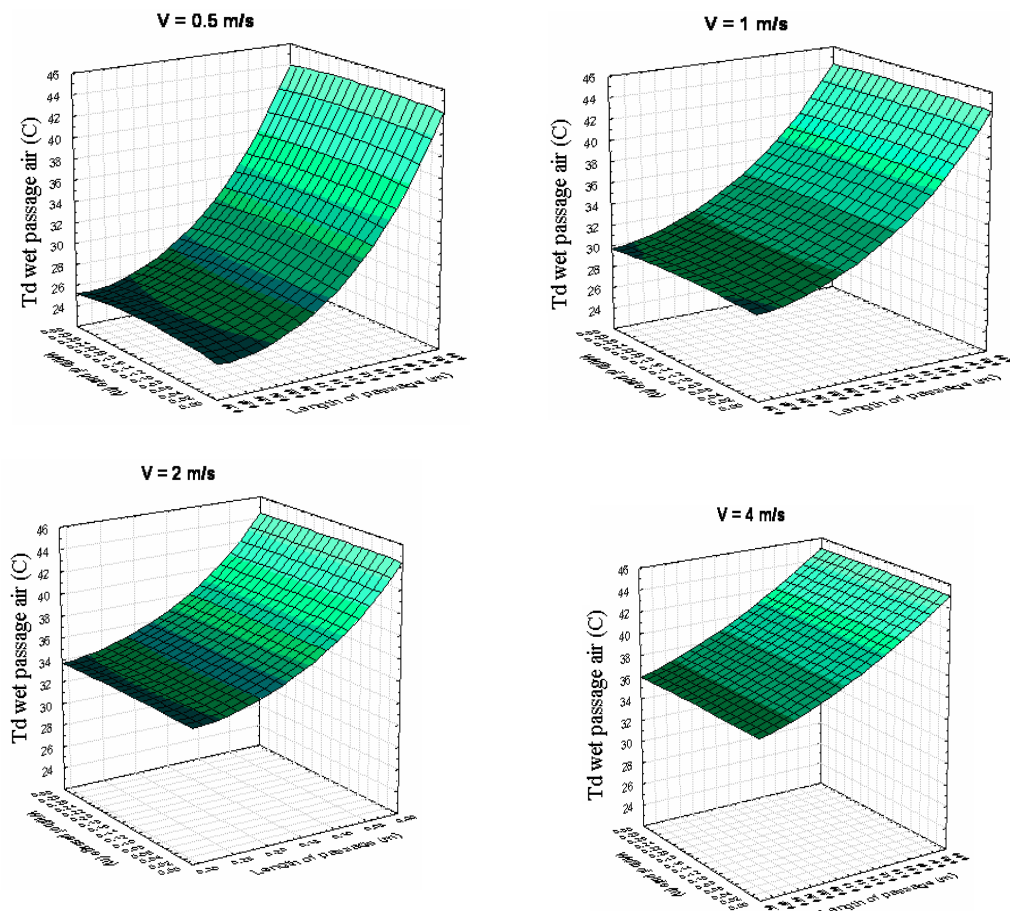


Figure. 10. The effect of inlet air velocity on the distribution of the wet passage air temperature for the dimensions 300x300 mm and 8 mm plate spacing

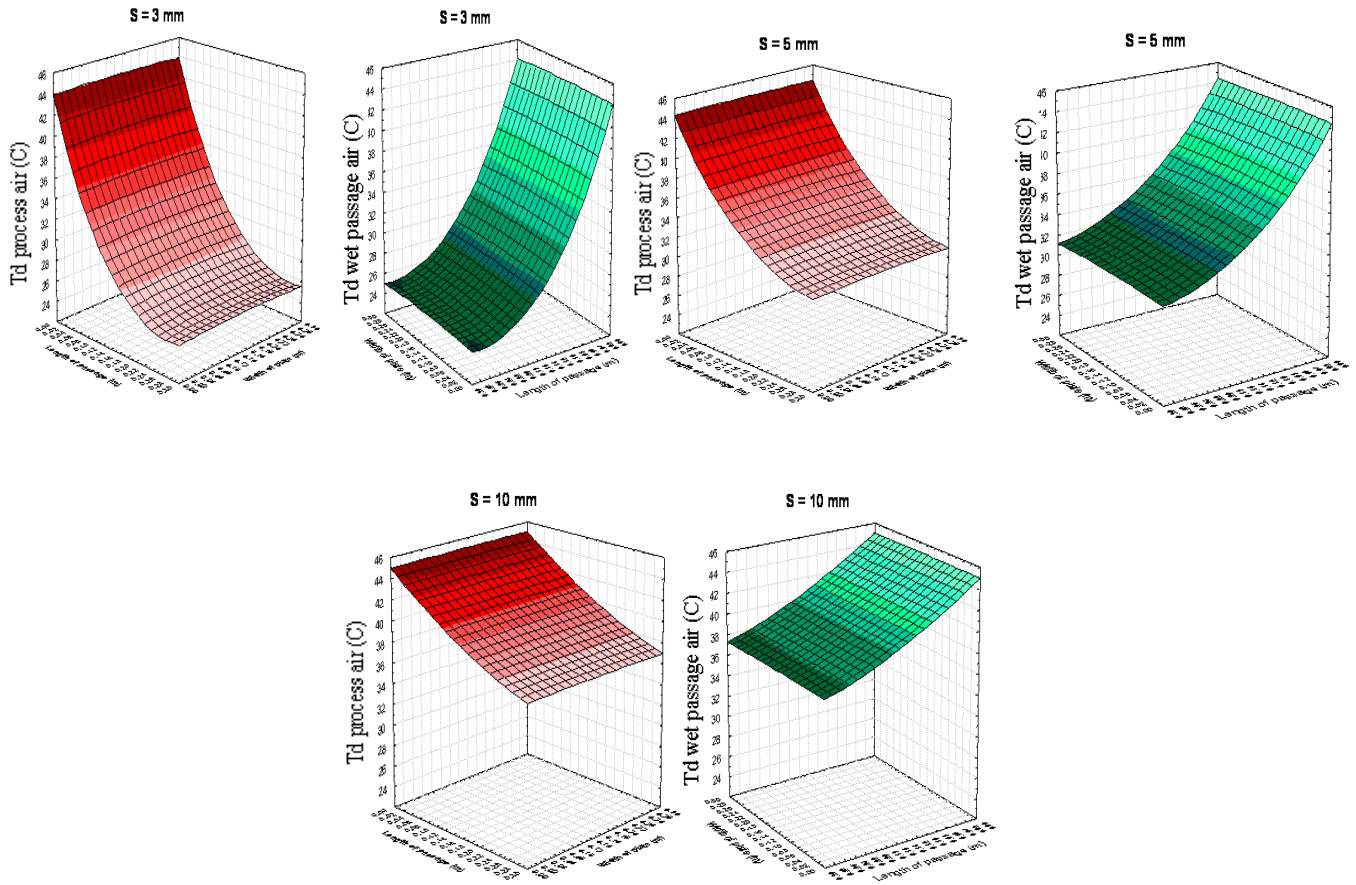


Figure. 11. The effect of plate spacing on the process air and the wet passage air temperature distribution for the dimensions 300x300 mm and 3 m/s inlet air velocity

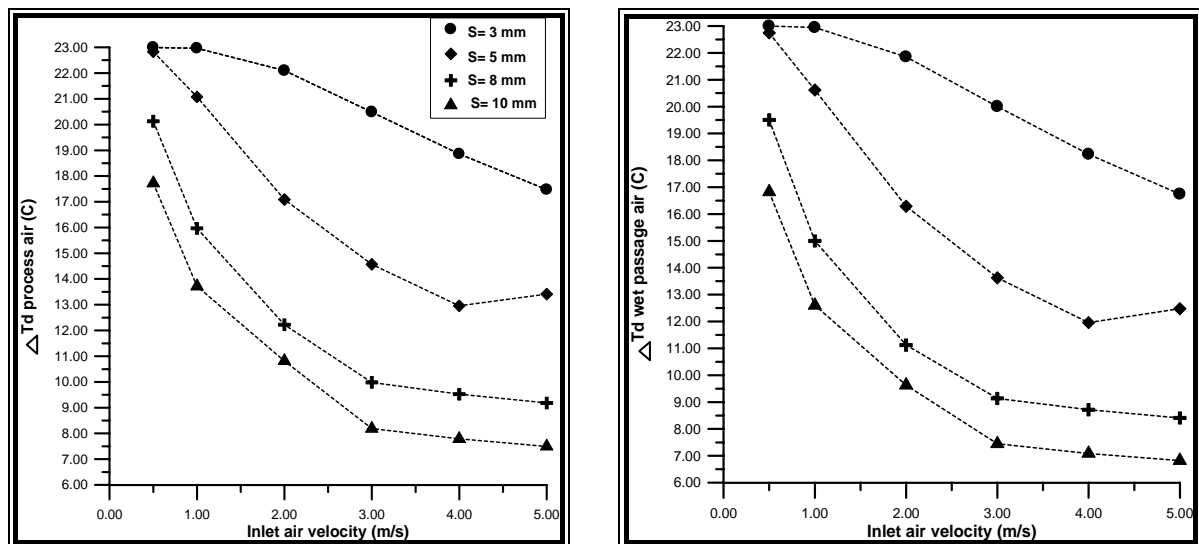


Figure. 12. The dry bulb temperature drop for the process air stream and for the wet passage air for 300x300 mm dimensions

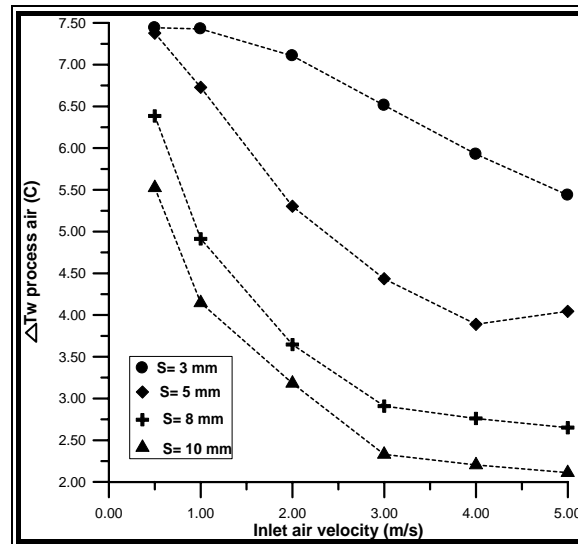


Figure. 13. The wet bulb temperature drop in the process air for 300x300 mm dimension

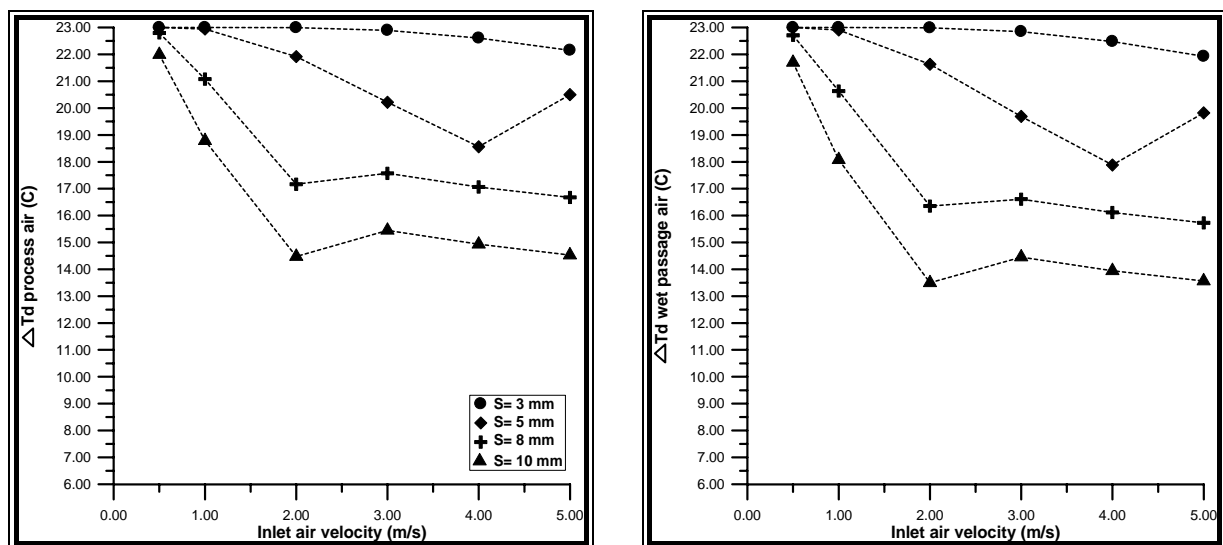


Figure. 14. The dry bulb temperature drop for the process air stream and for the wet passage air for 800x800 mm dimensions

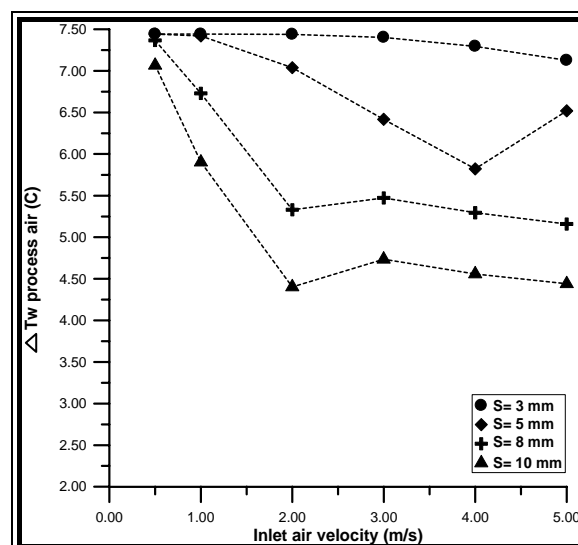


Figure. 15. The wet bulb temperature drop in the process air for 800x800 mm dimensions

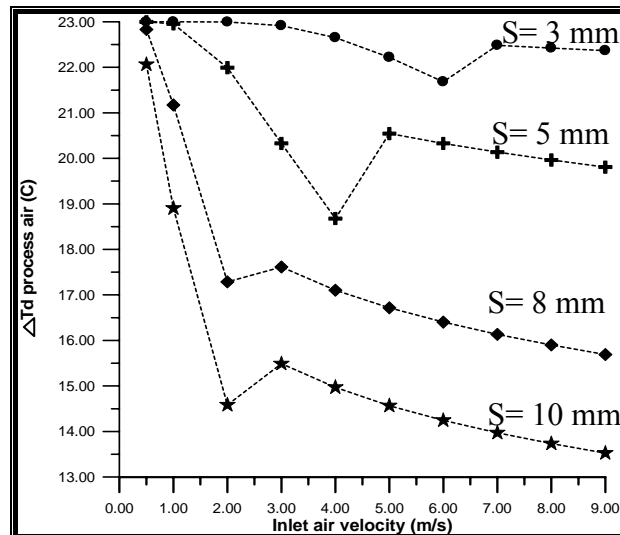


Figure. 16. Occurrence of turbulence at different plate spacing

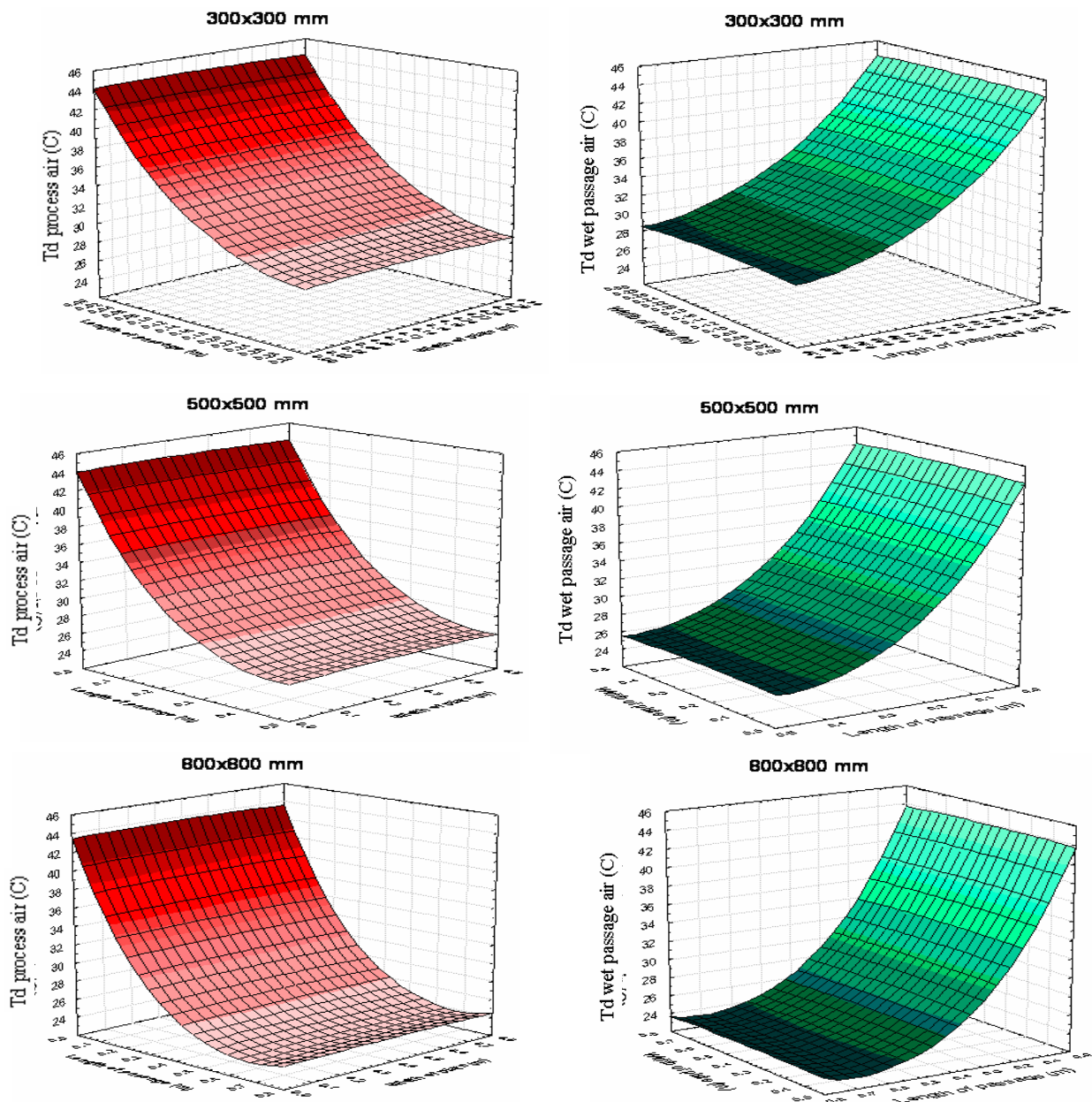
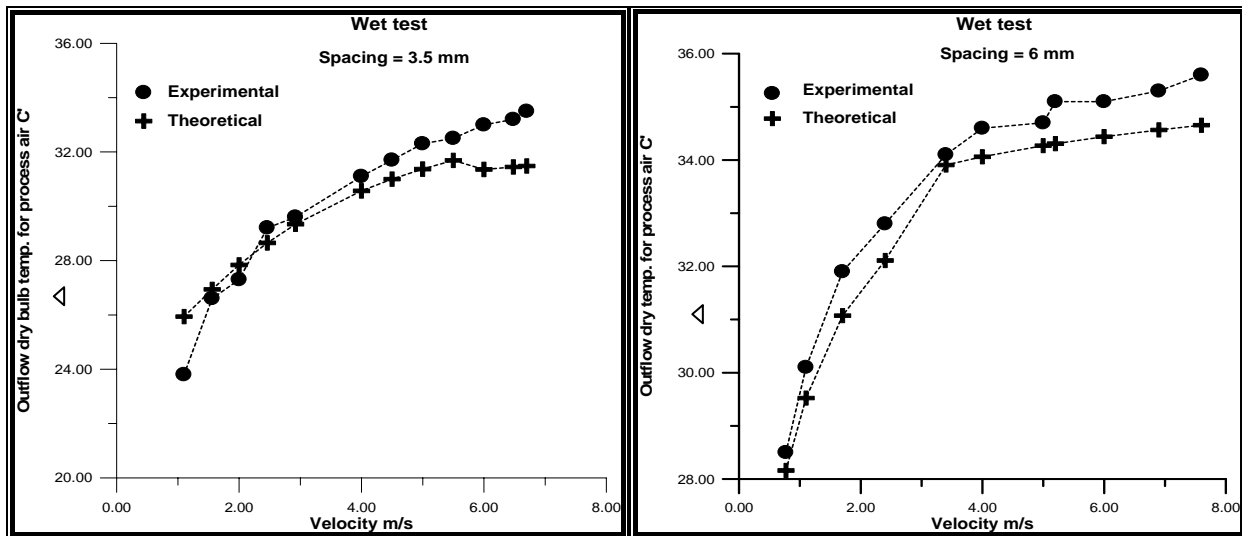


Figure. 17. The effect of various heat exchanger dimensions on the process air and the wet passage air temperature distribution for 5 mm plate spacing at 2 m/s inlet air velocity



(A) 3.5 mm plate spacing

(B) 6 mm plate spacing

Figure 18. Comparison between present theoretical results with experimental results of Enwia (1986)

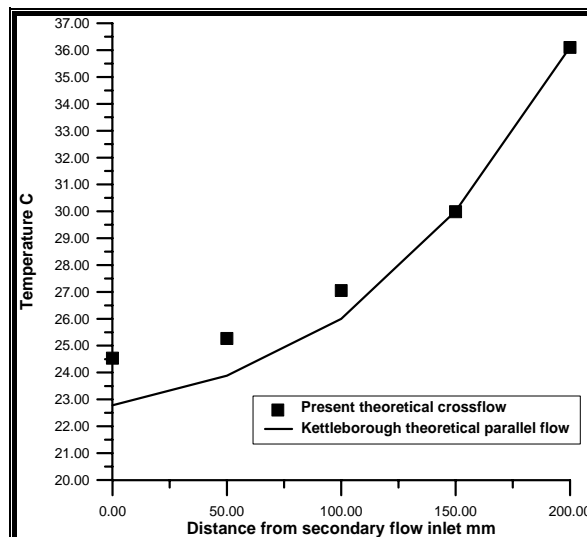


Figure 19. Comparison of wet PHE between theoretical work for parallel flow by Kettleborough and Hsieh 1983 and the present theoretical work for crossflow PHE

NOMENCLATURE

Symbol	Description	units
A	Heat transfer area	m^2
a	Plate spacing in a heat exchanger	m
b	Width of plate	m
c_p	Specific heat at constant pressure	$kJ/(kg.K)$
c_{pu}	Specific heat for humid air	$kJ/(kg.K)$
D	Diameter	m
D_{ab}	Diffusion coefficient between two substances	m^2/s
d_h	Hydraulic diameter	m
H	Specific enthalpy	kJ/kg
h	Heat-transfer coefficient;	$W/(m^2.K)$

Khalid A. Joudi Khawla N. Hmood	Simulation of Indirect Evaporative Cooler Heat Exchanger at Iraqi Conditions
--	---

<u>Symbol</u>	<u>Description</u>	<u>units</u>
h_{fg}	Latent heat of evaporation	kJ/kg
k	Thermal conductivity	W/ (m.K)
k_m	Mass transfer coefficient	m/s
L	Length	m
Le	Lewis number = $h_i/k_m c_{pu}$	-
\dot{m}	Mass-flow rate	kg/s
Nu	Nusselt number = $h d_h/k$	-
P	Dimensionless pressure	-
p	Pressure	N/m ²
Pe	Peclet number = $Pr * Re$	-
Pr	Prandtl number = $c_p \mu / k$	-
q	Heat	kJ
Re	Reynolds number = $\rho v d_h / \mu$	-
s	Plate thickness	m
Sc	Schmidt number = ν / D_{ab}	-
Sh	Sherwood number = $k_m d_h / D_{ab}$	-
T	Temperature	K, °C
U	Dimensionless velocity component in the x-direction	-
U_o	Overall heat transfer coefficient	W/(m ² .K)
u	Velocity component in the x-direction	m/s
V	Dimensionless velocity component in the y-direction	-
v	Velocity component in the y-direction	m/s
w	Moisture content	kg/kg _{d.a}
X	Nondimensional distance in x-coordinate (x/L)	-
Y	Nondimensional distance in y-coordinate (y/L)	-

Greek symbols

ρ	Fluid density	kg/m ³
μ	Dynamic viscosity	kg/(s.m)
ν	Kinematic viscosity	m ² /s

Subscripts

c	cold fluid
ci	cold air-water interface region
d	dry-bulb
h	hot fluid
i	interface
in	inlet
l	latent
s	saturated; sensible; spray water temperature
w	wet-bulb



THEORETICAL ANALYSIS OF TEMPERATURE DISTRIBUTION IN FRICTION STIR WELDING

Prof. Dr.
*Qasim M. Doos

Ass. Prof. Dr.
Ahmad Zaidan

M.Sc Eng.
Hassan R. Hassan

ABSTRACT

Friction stir welding (FSW) is a relatively new welding process that may have significant advantages compared to the fusion processes as follow: joining of conventionally non-fusion weldable alloys, reduced distortion and improved mechanical properties of weldable alloys joints due to the pure solid-state joining of metals. In this paper, a two-dimensional model based on finite element analysis is used to study the thermal history and thermomechanical process in the butt-welding of aluminum alloys. The model incorporates the mechanical reaction of the tool and thermomechanical process of the welded material. The heat source incorporated in the model involves the friction between the material and the probe and the shoulder. The calculation result also shows that preheat to the workpiece before process is beneficial to FSW. The effects of welding parameters such as preheating (100, 200) °C, rotational speed (960, 1200) rpm and linear speed (110, 155, 195) mm/min on the distribution of temperature of Al Alloy will be studied.

80 200) (1435)
) .(4
\\ (1200,960)() (100,200)(
\\ (110,155,195)()

Keywords: Friction stir welding; Finite element method; Thermomechanical process; Temperature distribution.

* University of Baghdad, college of Eng. Mechanical Dep.

Kasim_Daws@yahoo.com

INTRODACTION

Friction stir welding (FSW) is a recently emerged solid-state joining technology patented by The Welding Institute (TWI) in 1991 [Thomas, et. al 1991]. The process is illustrated in Fig.1, where a rotating cylindrical shouldered tool plunges into the butted plates and locally plasticizes the joint region during its movement along the joint line that causes a join between the work pieces.

In this process, the heat is originally derived from the friction between the welding tool (including the shoulder and the probe) and the welded material, which causes the welded material to soften at a temperature less than its melting point. The softened material underneath the shoulder is further subjected to extrusion by the tool rotational and transverse movements. It is expected that this process will inherently produce a weld with less residual stress and distortion as compared to the fusion welding methods, since no melting of the material occurs during the welding [Thomas, et. al 1991].

Despite significant advances in the application of FSW as a relatively new welding technique for welding aluminum alloys, the fundamental knowledge of such thermal impact and thermomechanical processes are still not completely understood [Thomas, et. al 1991].

published a three-dimensional heat transfer model in 1998, in their paper, a constant heat generation input from the tool shoulder/workpiece interface was assumed, a trial-and-error procedure was used to adjust the heat input until the all the calculated temperatures matches with the measured ones [Chao and Qi.1998]. Developed a process model for FSW, the heat input from the tool shoulder is assumed to be the frictional heat, and the coefficient of friction or the calculated temperature during the welding is adjusted to keep the calculated temperature from exceeding the material melting point [Frigaard, et. al 1998 and Frigaard, et. al 2001]. The Rosenthal equation for

modeling heat-transfer for thin plates has also been applied in modeling the heat transfer in FSW [Gould and Feng 1998 and Russell and Shercliff 1999]. The heat transfer for overlap friction stir welding with the finite element method; a moving heat source is used [Zahedul, et. al 2001]. Applied the CFD method in modeling the heat and material flow process for FSW, where the material is assumed to be a kind of non-Newtonian fluid in their modeling [Bendzsak et. al 2000 and Smith, et. al 2000]. In the above-mentioned models, the heat input from the tool shoulder is the only heat input, the heat generated at the tool pin workpiece interface has not been included. Heat generated by the pin was estimated to be only 2% of the total heat generation during the FSW [Russell and Shercliff 1999]; however, this ration was estimated to be up to 20% by some researchers [Kohn 2002]. In order to model the heat transfer process accurately, it is necessary to include the heat generated by the tool pin in the modeling. The heat transfer process during the tool penetration period cannot be modeled if the heat input from the pin is not included. Moreover, the initial field is very important in a transient heat transfer model, especially for modeling the preheat effects of laser-assisted preheated FSW [Song and Kovacevic 2002]. For this purpose, the heat transfer during the tool penetration period cannot be neglected. During the FSW process the tool penetrates into the workpiece, then moves along the joint line at a constant speed (see Fig. 2). The material in front of the rotating tool pin is plastically deformed and stirred back to the trail edge of the tool pin in the welding. This continuous “stir” process makes it difficult to model the heat input from the pin. First, the material plastic flow process is very complicated, making it almost impossible to determine the temperature distribution of the relocated material that is stirred from the front edge to the aft edge of the tool pin. Secondly, the tool pin is non-consumable in the welding, and modeling a moving tool pin in the workpiece is also not easy. The heat input from the tool pin is simplified as a moving heat source [Song

and R. Kovacevic 2004]; however, this assumption is not helpful in modeling the coupled heat transfer for both the tool and the workpiece. In this paper, a moving coordinate has been introduced to model the transient two-dimensional heat transfer process for FSW. The coordinate is chosen stationary with the moving tool. Therefore, the difficulty of modeling the complicated stir process can be greatly reduced, thus making this model more accurate.

THERMAL MODELING OF FRICTION STIR WELDING(CFD ANALYSIS):

In this paper, the application of computational fluid dynamics (CFD) method in modeling the heat transfer during FSW process has been used.

The following assumptions are introduced to simplify the model:

1. FSW produces high temperature metal flow.
2. It is a transient analysis model.
3. In thermal modeling, the main heat input comes from the tool shoulder/workpiece interface; therefore heat generation at the tool pin/workpiece interface is negligible.
4. Homogeneous material.
5. Constant properties.
6. Isotropic material.
7. Two dimensional heat transfer model due to a thin plate.
8. The radiation heat loss can be neglected.[Song and R. Kovacevic 2003].
9. Constant heat input from the tool shoulder / workpiece interface was assumed.

Mathematical model

The FSW process is divided into the following three periods: the penetration period, the weld period, and the tool pulling out period [Song and R. Kovacevic 2002], as shown in Fig. 3 The following assumptions are introduced in the model:

1. The heat generated at the tool shoulder/workpiece interface is frictional heat;
2. The tool pin is a cylinder; the thread of the pin can be neglected;
3. No heat flows into the workpiece if the local temperature reaches the material melting temperature.

➤ Heat Transfer Equation for the Workpiece:

The heat transfer equation for the workpiece in a moving coordinate system with a positive X-direction moving tool can be written as [Song and R. Kovacevic 2003]:

$$\rho c \frac{\partial T}{\partial t} = K \left(\frac{\partial^2 T}{\partial x^2} + \frac{\partial^2 T}{\partial y^2} \right) + v_w \rho c \frac{\partial T}{\partial x} \quad \dots (1)$$

Where (T) is the temperature, (c) is the specific heat, (ρ) is the density, (k) is the thermal conductivity and (v_w) is the welding speed.

➤ Heat Generation:

In FSW, there are two main heat inputs: heat generated at the tool pin/workpiece interface and heat generated at the tool shoulder/workpiece interface.

➤ Heat Generated at The Tool Shoulder / Workpiece Interface:

The heat generated at the tool shoulder / workpiece interface is assumed frictional heat. The local friction force at every point can be calculated from:

$$F_f = \mu F_n \quad \dots (2)$$

Where:

(F_f) : Friction force.

(F_n) : Normal force applied to the workpiece.

(μ) : Coefficient of friction.

Therefore, heat generation rate can be calculated as:

$$q = F_f \cdot v \quad \dots (3)$$

Where (q) is heat generation rate and (v) is the linear speed. Because $v=R\omega$ and $\omega=2\pi n$ therefore:

$$q=2\pi\mu FnRn \quad \dots (4)$$

Where (R) is the distance from the calculated point to the axis of the rotating tool and (n) is the number of rotation [Mohanad 2007].

The coefficient of friction is believed to vary during FSW, but the details of the variation of the friction coefficient are not clear so far. In this modeling constant coefficient of friction is assumed.

Boundary Conditions and Initial Condition for CFD Modeling:

1. Plate surface:

$$q=h(T-T_{\infty}) \quad \text{for } r > R_{sh} \text{ and}$$

$$q=qi \quad (\text{Heat input}) \text{ for } r < R_{sh}$$

2. For incoming side and out coming side of plate :

$$V_x = V \text{ (Welding speed)}$$

$$V_y = 0$$

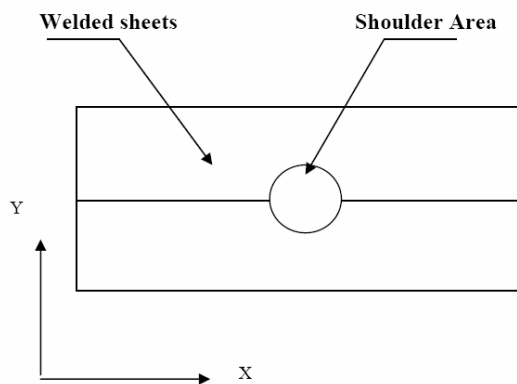
$$q=h(T-T_{\infty})$$

3. For two vertical sides:

$$V_x=V, \quad V_y=0$$

$$q=h(T-T_{\infty})$$

4. Initial Temperature = T_i



Boundary Restriction:

The heat generation input condition is applied only to the points within the tool

shoulder covered surface, i.e. when $r < R_{sh}$, while the convection boundary condition is applied to all other points in the plate surface i.e. $r > R_{sh}$.

Finite element model

The general purpose finite element code ANSYS is used for solving the energy equations and carrying out analysis. In this study a, 2-D transient model based on a finite element proposed to study the thermal history in the welded plates. Ansys/FLOTTRAN as a finite element software used to carry out the numerical simulation.

In the present study, it is assumed a reference framework fixed to the welding tool, in such a way that, the plate moves towards it with different welding speed.

In the finite element modeling the convection heat transfer coefficient at the welded plates used is ($30 \text{ W/m}^2 \cdot \text{C}$), which is typical for natural convection between aluminum and air [Song and R. Kovacevic 2002].

A right-handed X-Y coordinate system was used throughout. The X-axis is parallel to the welding direction. The mesh used is also illustrated in Fig. 3; FLUID 141 two-dimensional element type was used with refined element around the welding tool shoulder.

REESULTS AND DISCUSSION

Curves Discussion

In general, the figures represent the relationship between the temperature and time, from Fig. 4, it was concluded that the revolution speed and linear speed and preheating process had a strong effect on the temperature distribution along the welded plates.

Also, it was noticed that in each curve the peak temperature at A ((20 mm) from the edge of the plate), B ((20 mm) from the edge of the plate), and C (in the center of the plate) is affected by the location of welding tool which turning in its limited speed.

The temperature at point (A) begins about (100 or 200) depend on preheating, then increased when the welding tool being in the points of testing, after that the temperatures begins to decrease gradually while the welding tool leave the testing point.

From the increase and decrease of temperature at the testing points it was noticed that the welded plates takes more time to dissipate heat that for its gain.

The temperature at this point decreases continuously until the end of welding process.

This is coincide with point (B) which reach about (300 °C) where it's temperature increased as the temperature of point (A) reach about (293 °C) decreased because welding tool passing through point (B) while it leaves point (A).

The highest temperature at point (B) was recorded as the welding tool reaches the point, while it begins to decrease when the welding tool leave it.

The process of increasing and decreasing the temperature is also true for point (C), but at this point the decreasing of temperature becomes lower than the previous points because the welding process was on its end according to the position of the testing point.

In all figures, it was noticed that the temperature of point (C) reach about (314 °C) was higher than that of point (B) which reach about (300 °C), while the temperature of point (B) was higher than that of point (A), this is because of the nature of the process, which begins at point (A) (the beginning of heat input), so that point (A) was the lowest one. While point (B) was higher than (A) because of heat build in the welded plates. Also, the temperature of point (C) was higher than the temperature of point (B) for the same reason.

The heat building process at point (B) and (C) was very effective factor on the welding process which gives more homogenous, smooth and clean welding.

This is very clear when comparing the welding at points A, B, and C with

theoretical analyses as shown in Fig. (5) to (7) when rotation speed 1200 RPM, translational speed of 110 mm/min, preheating 100 °C.

Discussion of the parameters effect on the welding.

1. The preheating effect.

Case one:

With working conditions as follows:-

Preheating 100 °C
Revolution speed 1200 RPM
Linear velocity 155 mm/min

Fig. (8 - 10) represent the temperature distribution for point A, B, and C respectively.

Case two:

With working conditions as follows:-

Preheating 200 °C
Revolution speed 1200 RPM
Linear velocity 155 mm/min

Fig. (11 - 13) represent the temperature distribution for point A, B, and C respectively.

According to the two cases above it was noticed that the increasing of the preheating with constant revolution speed and linear velocity, the temperature of testing points increased.

Fig. 14 represent the curves of temperature distribution in point (B) with various preheating and constant revolution speed and linear speed.

The effective of preheating on the peak temperature tested point can be show in Fig. (15).

The revolution speeds effect.

Case one:

With working conditions as follows:-

Preheating 100 °C
Revolution speed 960 RPM
Linear velocity 155 mm/min

Figures (16- 18) represent the temperature distribution for point A, B, and C respectively.

Case two:

With working conditions as follows:-

Preheating 100 °C

Revolution speed 1200 RPM
Linear velocity 155 mm/min
Figures (8-10) represent the temperature distribution for point A, B, and C respectively.

In the welding process, the heat come from the friction between the specimen and the tool shoulder as well as from the stir and plastic deformation of the specimen. The rotation speed of the tool shoulder may change all these factors. The influence of the tool shoulder rotation speed on the temperature field is shown in Fig. 20. From Fig. 20, it is clear that the rotational speed has an effect on the peak temperature.

According to the two cases above it was noticed that the increasing of the revolution speed with constant preheating and linear velocity, the temperature of testing points (A, B, C) increased. This is because (a high rotational speed, the relative velocity between the tool and workpiece is high and consequently, the heat generation rate and the temperature are also high).

Fig. 19 represents the curves of temperature distribution at point (B) with various revolution speed and constant preheating and linear speed.

The effect of revolution speeds on the peak temperature tested point can be show in Fig. 20.

The linear speed effect.

Case one:

With working conditions as follows:-
Preheating 100 °C
Revolution speed 1200 RPM
Linear velocity 195 mm/min
Figures (21-23) represent the temperature distribution for point A, B, and C respectively.

Case two:

With working conditions as follows:-
Preheating 100 °C
Revolution speed 1200 RPM
Linear velocity 155 mm/min
Figures (8-10) represent the temperature distribution for point A, B, and C respectively.

Case three:

With working conditions as follows:-
Preheating 100 °C
Revolution speed 1200RPM
Linear velocity 110 mm/min
Figures (5 - 7) represent the temperature distribution for point A, B, and C respectively.

According to the three cases above it was noticed that the linear speed had a reverse effect on the temperature distribution, so that with increasing the linear speed the temperature become lower and this is because of the fact that at high welding speed (linear speed), the heat input per unit length decreases and heat is dissipated over a large volume of the workpiece. So the points that tested had not enough time to increase the temperature.

Fig. 24 represents the curves of temperature distribution in point (B) with various welding speed and constant preheating and revolution speed.

Fig. 25 shows the effective of linear speed on the peak temperature of welded plate.

CONCLUSIONS

1- A preheat is beneficial to increase the temperature of the workpiece in front of the tool pin, making the material easy to be welded, while protecting the tool from being worn out.

2- It be select optimum welding parameters to obtain good weld, there is no necessary to use high values of revolution speed or linear Speed with preheating process.

REFERENCE

- Bendzsak G.B. et. al “ An experimentally validated 3D model for friction stir welding, Proceedings of the second International Symposium on Friction Stir Welding, Sweden, August 2000.
- Chao Y.J. and X. Qi, Thermal and thermo-mechanical modeling of friction stir welding of aluminum alloy - 6061-T6, Journal of Materials Processing & Manufacturing Science (1998).



- Colegrove P., Three dimensional flow and thermal modeling of the friction stir welding process, Proceedings of the second International Symposium on Friction Stir Welding, Sweden, August 2000.
- Frigaard, et. al "Modeling of the heat flow phenomena in friction stir welding of aluminum alloys, Proceedings of the Seventh International Conference Joints in Aluminum— INALCO '98, Cambridge, UK, April 15-17, 1998.
- Frigaard, et. al "A process model for friction stir welding of age hardening aluminum alloys, Metallurgical and Materials Transactions A 32A (2001).
- Gould J.E. and Z. Feng, "Heat flow model for friction stir welding of aluminum alloys, Journal of Material Processing and Manufacturing Science 7 (1998).
- Kohn G., Laser-assisted friction stir welding, Welding Journal Feb (2002) 46–48.
- Mohanad Okab Yousuf "Investigation of Mechanical and microstructural Characteristics of Friction Stir Welded Joints", PhD The University of Baghdad 2007.
- Russell M.J. and H.R. Shercliff, "Analytical modeling of microstructure development in friction stir welding, Proceedings of the first International Symposium on Friction Stir Welding, Thousand Oaks, CA June 1999.
- Smith C.B., et. al "Heat and material flow modeling of the friction stir welding process, Proceedings of Ninth International Conference on Computer Technology in Welding, in: T. Siewert, C. Pollock (Eds.), May 2000.
- Song M. and R. Kovacevic, "A new heat transfer model for friction stir welding, Accepted by Journal of Engineering Manufacturing 2002.
- Song M. and R. Kovacevic. "Heat transfer modeling for both workpiece and tool in the friction stir welding process: a coupled model." Proc. Of Instn. Mech. Engrs Vol.218 part B: J. Engineering Manufacture. PP 1-17, 2004.
- Song M. and R. Kovacevic. "Thermal modeling of friction stir welding in a moving coordinate system and its validation" International Journal of Machine Tools & Manufacture 43pp. 605–615, 2003.
- song M and R Kovacevic. "A new Heat Transfer model for friction stir welding" Transactions of NAMRI/SIME Volume xxx pp. 565-572, 2002.
- Thomas W.M., et. al "Friction stir butt welding" International patent application no. PCT/GB92/02203 and GB patent application no. 9125978.8, 6 December 1991.
- Zahedul M., et. al "Thermal modeling of overlap friction stir welding for Al-alloys, Journal of Material Processing and Manufacturing Science 10 (2001).

NOMENCLATURES

ρ	: Density (Kg/m^3).
μ	: Coefficient of friction.
C_p	: The specific heat (J/Kg.K)
F_f	: Friction force.
F_n	: Normal force.
k	: Heat conductivity (w/m.k)
R_p	: Radius of pin (mm).
R_{sh}	: Radius of shoulder (mm).
T	: Temperature (K or $^{\circ}\text{C}$).
t	: Welding time (sec).
T_i	: Initial or preheat temperature of the workpiece ($^{\circ}\text{C}$).
T_m	: Melting temperature (K or $^{\circ}\text{C}$).
V	: Welding speed (mm/sec).
W	: Rotational speed (rev/min).

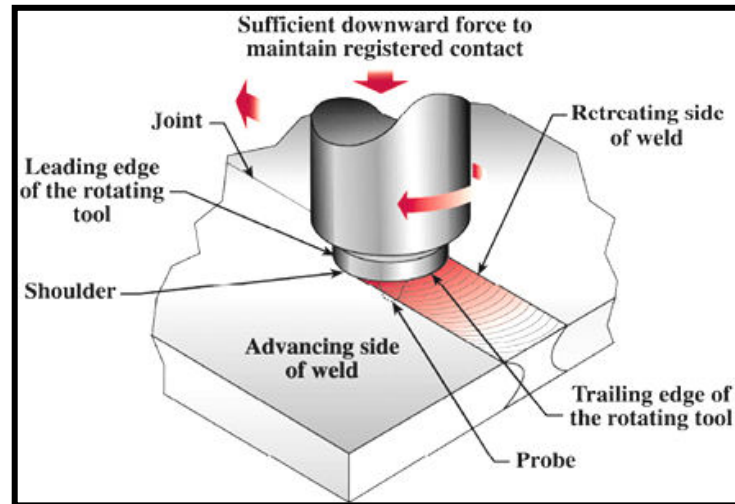


Figure. 1: Schematic representation of FSW of a butt joint.

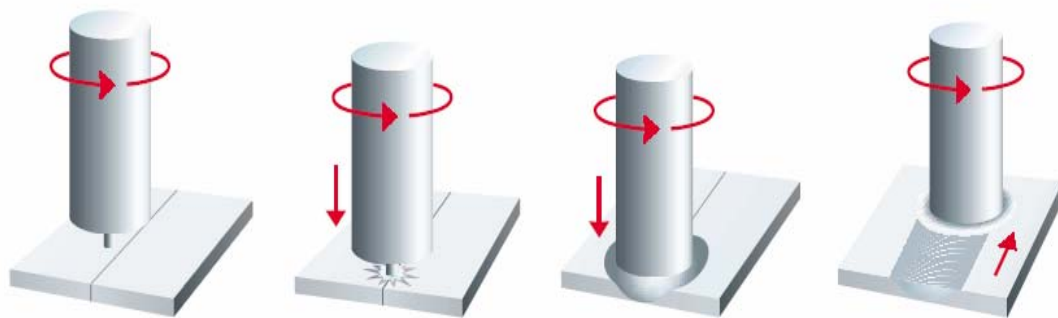


Figure. 2 Schematic diagram of FSW.

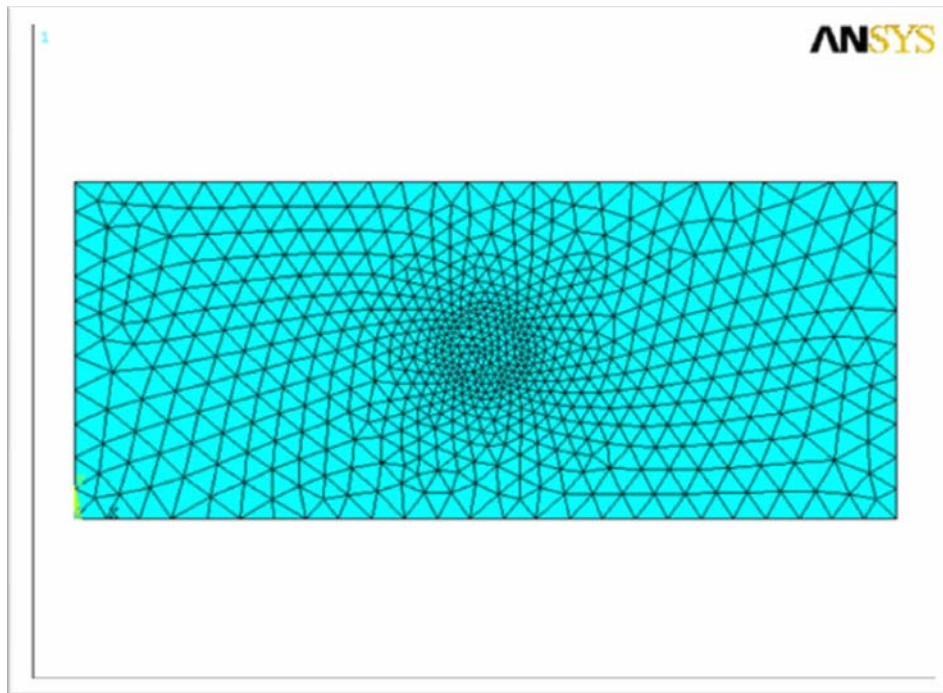


Figure. 3:2-D mesh of modeled welded plates.

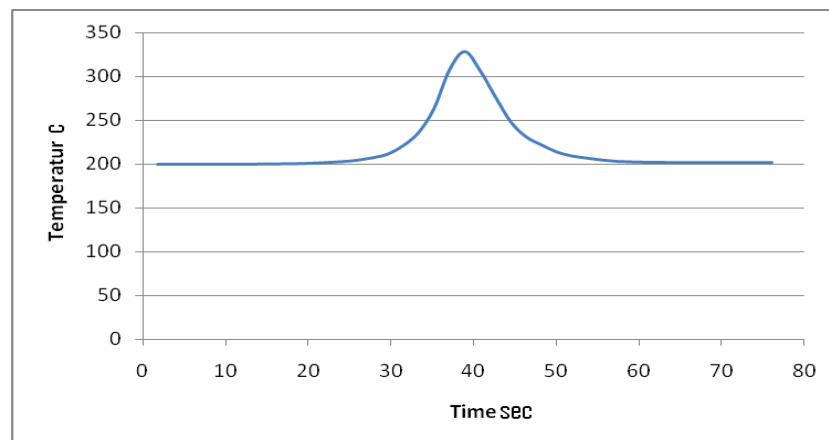


Figure. 4: Temperature distribution in points (B). 1200 RPM, 155 mm/min, preheating 200 °C.

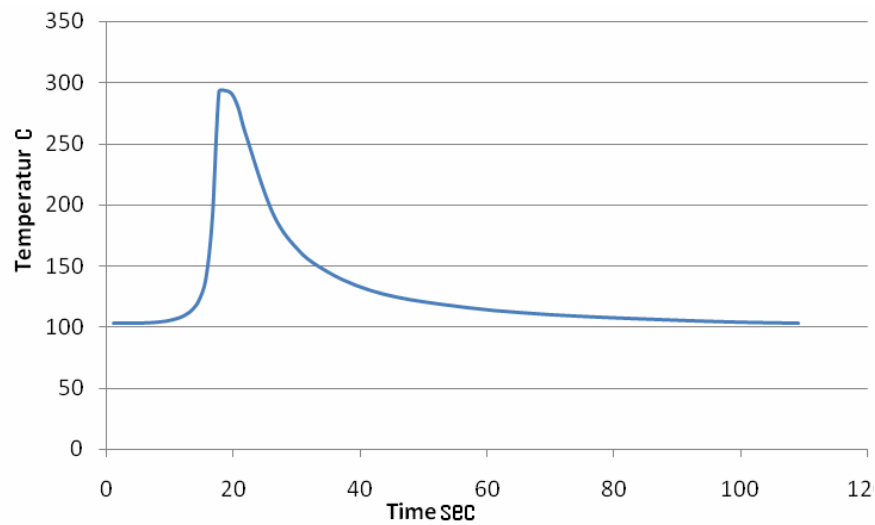


Figure. 5: Temperature distribution at point (A). 1200 RPM, 110 mm/min, preheating 100 C.

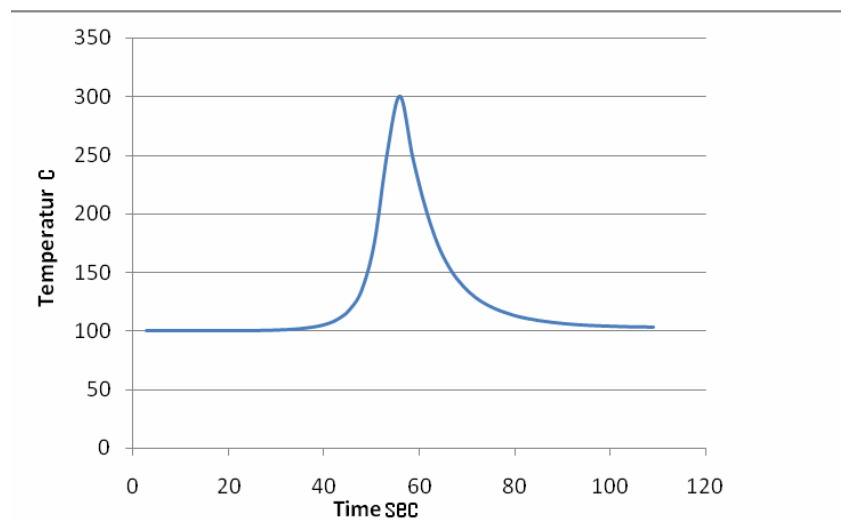


Figure. 6 : Temperature distribution in points (B). 1200 RPM, 110 mm/min, preheating 100 °C.

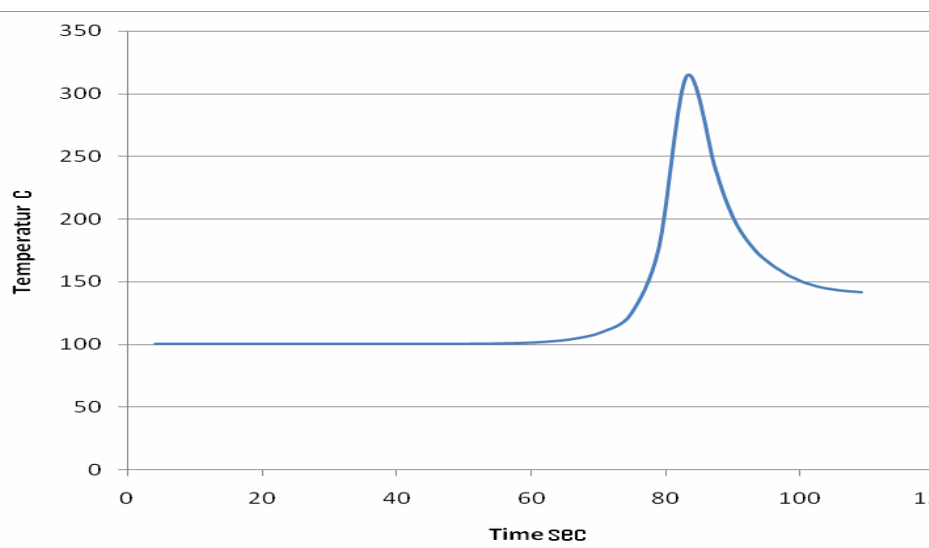


Figure. 7: Temperature distribution in points (C). 1200 RPM, 110 mm/min, preheating 100 °C.

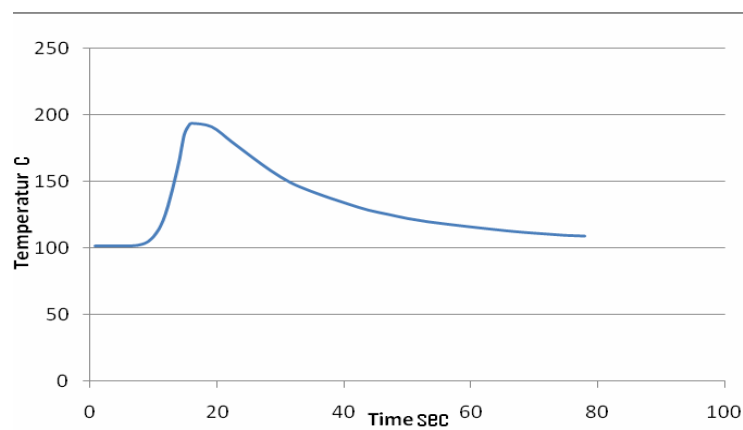


Figure. 8: Temperature distribution in points (A). 1200 RPM, 155 mm/min, preheating 100 °C.

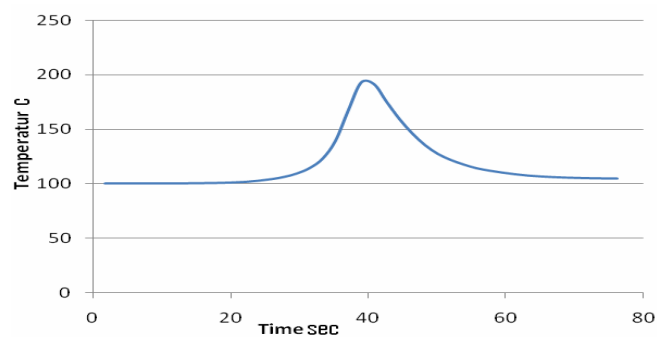


Figure. 9: Temperature distribution in points (B). 1200 RPM, 155 mm/min, preheating 100 °C.

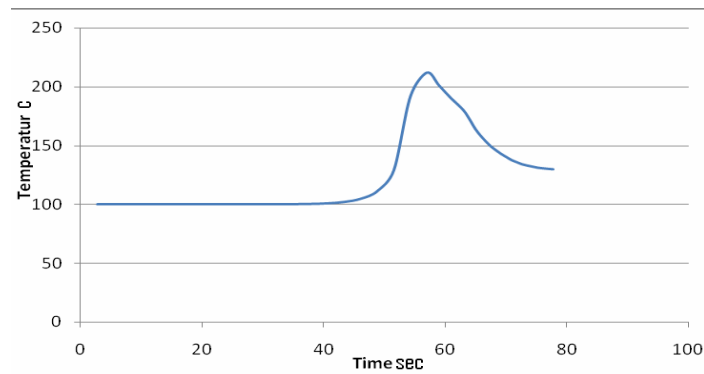


Figure. 10: Temperature distribution in points (C). 1200 RPM, 155 mm/min, preheating 100 °C.

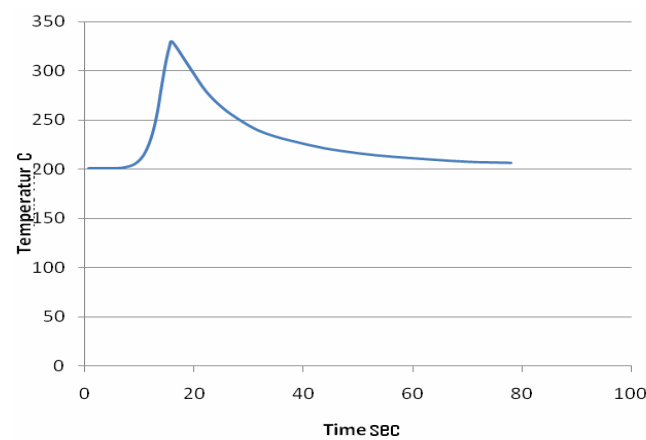


Figure. 11: Temperature distribution in points (A). 1200 RPM, 155 mm/min, preheating 200 °C.

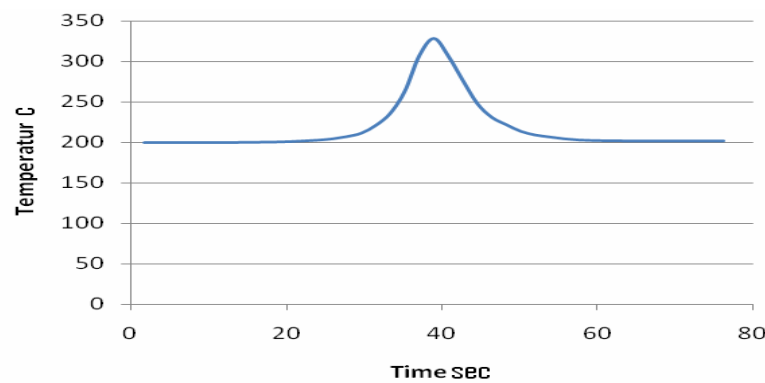


Figure. 12: Temperature distribution in points (B). 1200 RPM, 155 mm/min, preheating 200 °C.

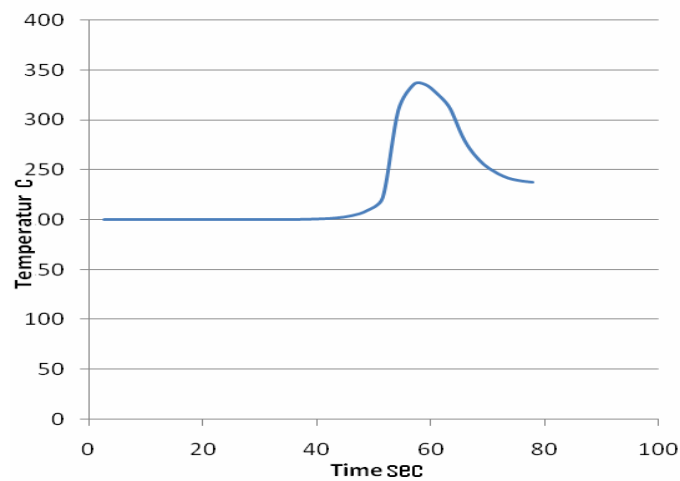


Figure. 13: Temperature distribution in points (c). 1200 RPM, 155 mm/min, preheating 200 °C.

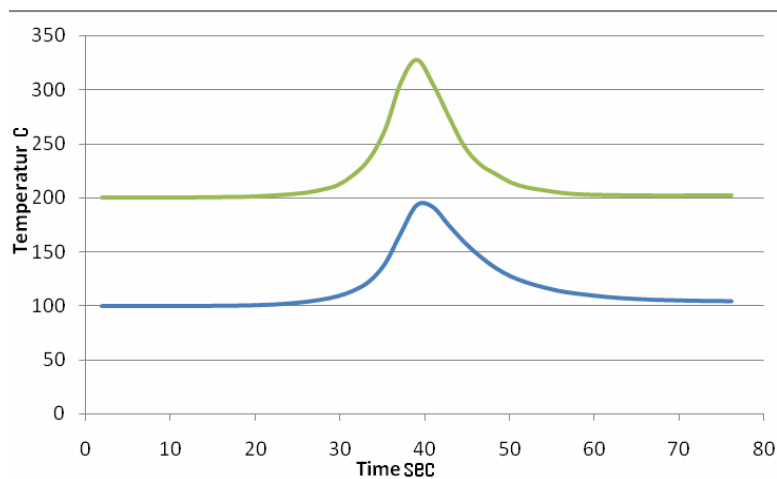


Figure. 14: Temperature distribution in point (B) with variable preheating and constant linear speed and revolution speeds.

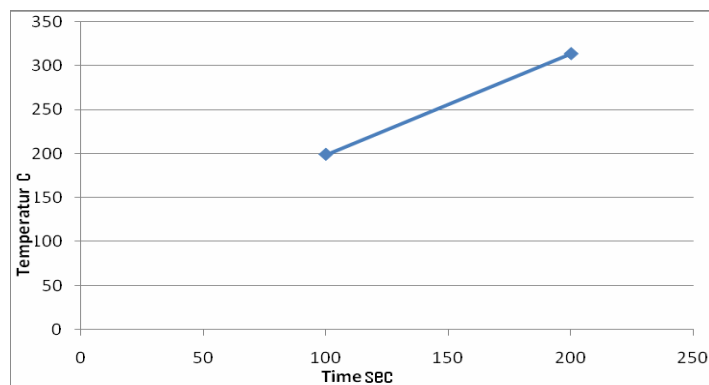


Figure. 15: The effective of preheating on the peak temperature in point (B).

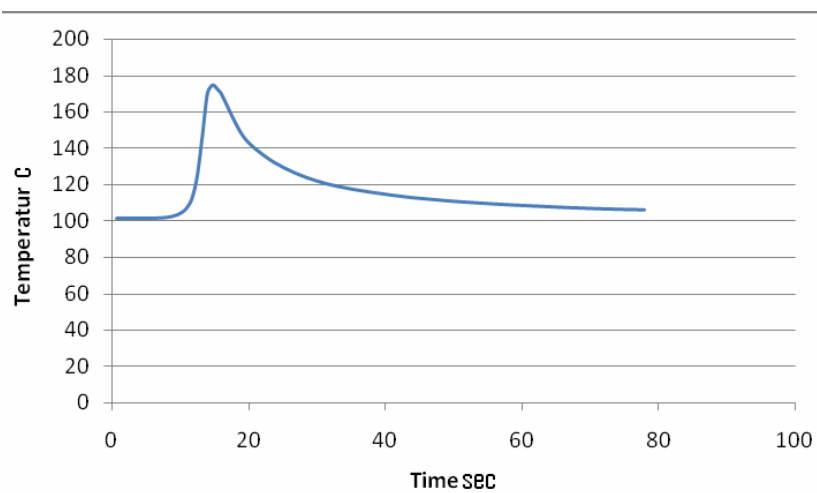


Figure.16: Temperature distribution in points (A). 960 RPM, 155 mm/min, preheating 100 °C.

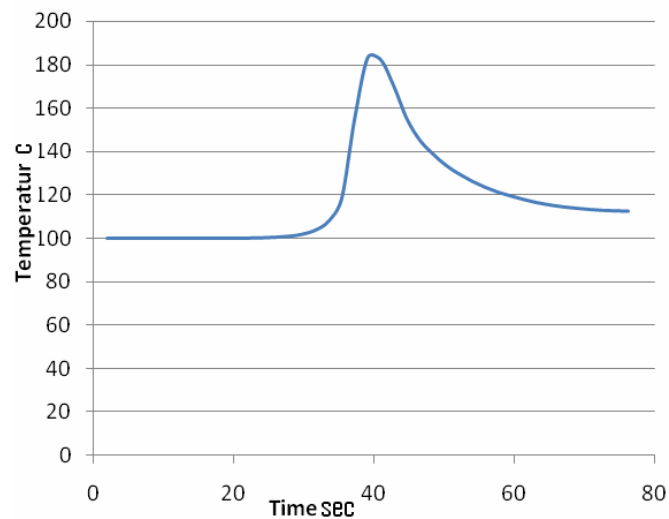


Figure. 17: Temperature distribution in points (B). 960 RPM, 155 mm/min, preheating 100 °C.

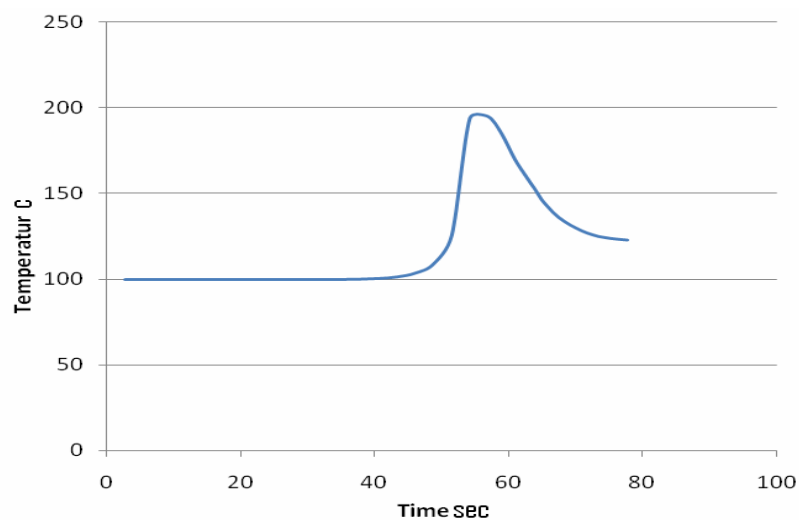


Figure. 18: Temperature distribution in points (A). 960 RPM, 155 mm/min, preheating 100 °C.

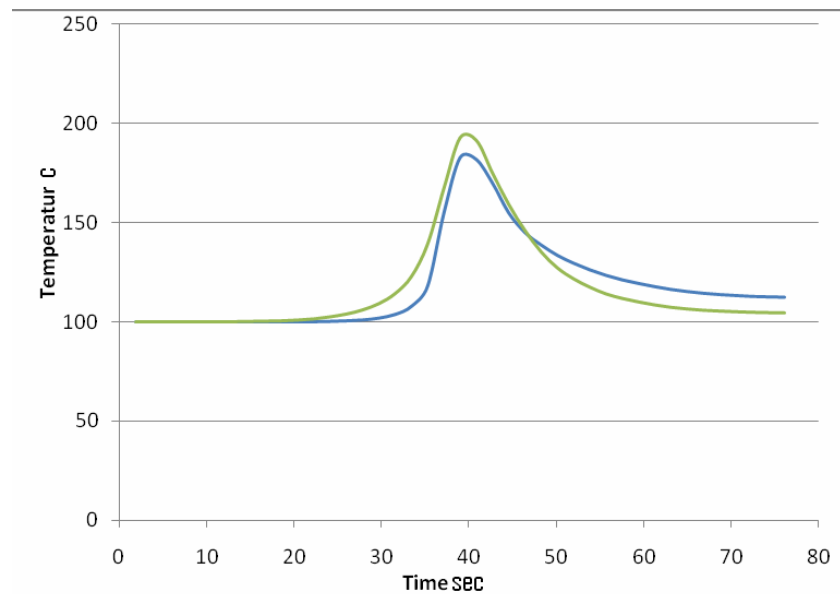


Figure.19: Temperature distribution in point (B) with variable revolution speeds and constant linear speed and preheating.

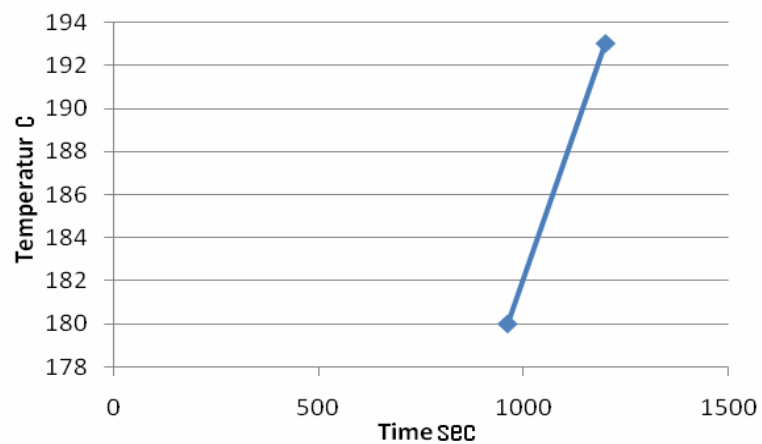


Figure. 20: The effective of revolution speeds on the peak temperature in points (B).

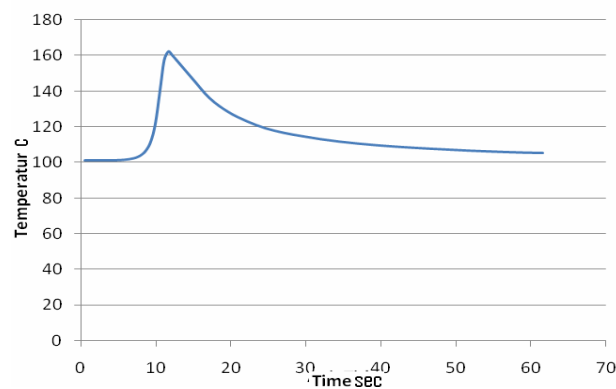


Figure. 21: Temperature distribution in points (A). 1200 RPM, 195 mm/min, preheating 100 °C.

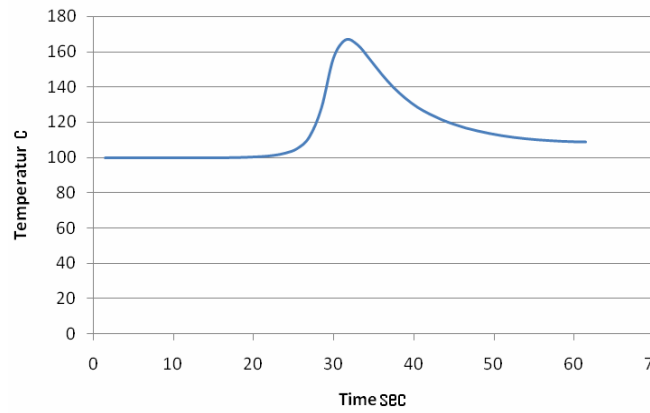


Figure. 22: Temperature distribution in points (B). 1200 RPM, 195 mm/min, preheating 100 °C.

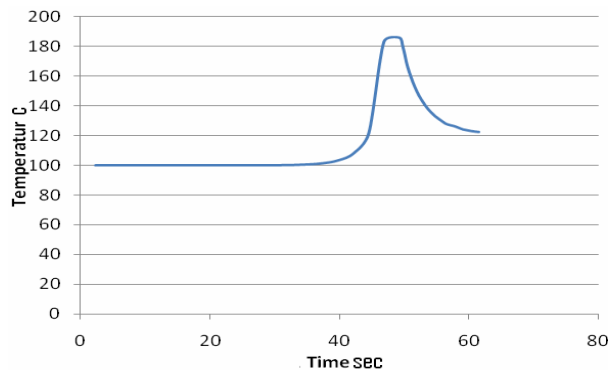


Figure. 23: Temperature distribution in points (C). 1200 RPM, 195 mm/min, preheating 100 °C.

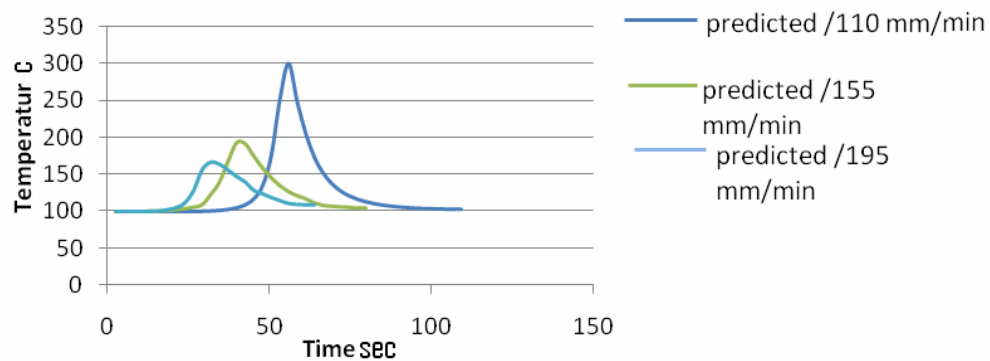


Figure. 24: Temperature distribution at the point (B) with variable welding speed and constant revolution speed (1200rpm) and preheating (100 °C).

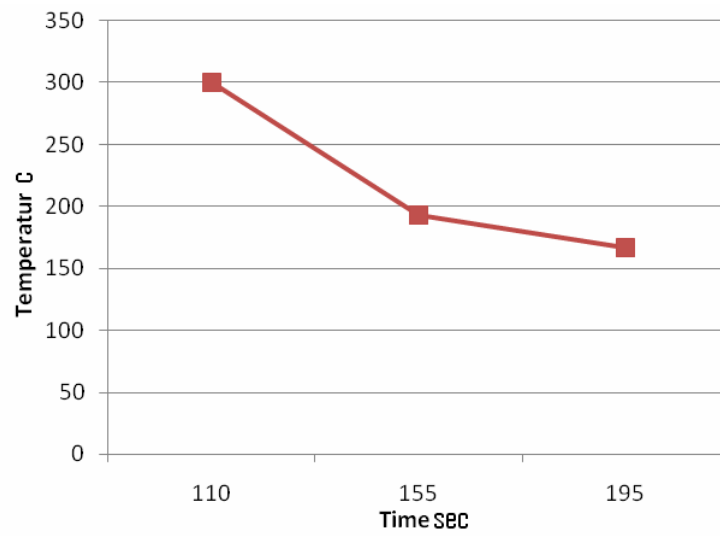


Figure. 25: The effective of linear speed on the peak temperature of welded plate in the point (B).



NUMERICAL INVESTIGATION OF TURBULENT NATURAL CONVECTION IN AN INCLINED SQUARE ENCLOSURE

Ass. Prof. Dr. Qasim S. Mehdi
College of Engineering
University of Mustansiriya

Ass. Prof. Dr. Khudheyer S. Mushatet
College of Engineering
University of Thiqr

ABSTRACT

Two dimensional turbulent natural convection heat transfer and fluid flow inside an air filled inclined square enclosure differentially heated has been numerically studied. Fully elliptic Navier-Stokes and energy equations are solved using finite volume method. The problem is simulated for different angles of inclination ($0 \leq \theta \leq 180\text{deg.}$) and Rayleigh numbers ($10^8 \leq Ra \leq 10^{16}$). The turbulence k- ϵ model is used to model the effect of turbulence. The wall function approach is used to model the regions near the walls of the enclosure. The obtained results from this study show that the rate of heat transfer is increased with the increase of Rayleigh number and decreased with the increase of angle of inclination ($0 \leq \theta \leq 90\text{deg.}$). Also the induced vortices are strongly elongated with increase of Rayleigh number. The thickness of thermal boundary layer is decreased with the increase of Ra. The validation of the present code was done by comparing the computed results with the published ones. The comparison indicated a good agreement.

:

$$(10^8 \leq Ra \leq 10^{16})$$

$$(0 \leq \theta \leq 180\text{deg.})$$

(k- ϵ)

$$.(0 \leq \theta \leq 90 \text{ deg })$$

Keywords: natural convection, heat transfer, enclosed enclosure

INTRODUCTION

Natural convection heat transfer in an enclosure is of importance in many engineering applications. These include cooling of electronic systems, double windows, air gaps in unventilated spaces and solar collectors.. However turbulent natural convection in inclined enclosures is still needs more research area to understand the complex fluid flow and heat transfer behavior. In the reviewed studies on natural convection, there is a few studies relating the turbulent natural convection inside inclined enclosures, so the present study try to facillate the challenge in understanding the flow and heat transfer behavior in this type of the problems. One of the most important bench mark studies on turbulent natural convection inside enclosed cavities was an experimental study done by[Ampofo and Karayiannis,2003]. [Corcione,2003] performed a numerical study on the natural convection in a rectangular horizontal enclosure differentially heated. He used various thermal conditions of the cavity side walls. Also laminar natural convection in enclosed cavities has been studied numerically and experimentally by [Davis to Kuper et al., 1983-1993]. [Markatos et al.,1984] and [Lankhorst et al., 1991] used a k-ε model to study the two and three dimensional turbulent flows inside a cavity. Some interesting studies for both laminar and turbulent flows in inclined cavities has been found by the authors [Zhongand Young,1985] and[Elshirbiny,1982].

In the present work a numerical investigation has been performed to study the turbulent 2D thermally driven air flows inside a square enclosure. The objective was to investigate how the enclosure tilted angle can effect on these flows which are found in a diverse engineering applications. The computations were performed for Ra ranging from 10^8 to 10^{16} and an angle of inclination from 0° to 180° . The enclosure is differentially heated as shown in Fig.1.

MATHEMATICAL MODEL

The turbulent viscous flow and temperature distribution inside an inclined square enclosure are described by the steady Navier-Stokes, energy and turbulence equations. The flow is assumed to be incompressible and Boussine approximation is valid. Employing the eddy viscosity concept, the time averaged governing equations are defined as follows[Jones and Luander,1972]:

$$\frac{\partial u}{\partial x} + \frac{\partial v}{\partial y} = 0 \quad (1)$$

$$\rho u \frac{\partial u}{\partial x} + \rho v \frac{\partial u}{\partial y} = -\frac{\partial p}{\partial x} + 2 \frac{\partial}{\partial x} \left(\mu_{eff} \frac{\partial u}{\partial x} \right) + \frac{\partial}{\partial y} \left(\mu_{eff} \frac{\partial u}{\partial y} \right) + \frac{\partial}{\partial y} \left(\mu_{eff} \frac{\partial v}{\partial x} \right) + \rho g \beta (T - T_0) \sin \theta \quad (2)$$

$$\rho u \frac{\partial v}{\partial x} + \rho v \frac{\partial v}{\partial y} = -\frac{\partial p}{\partial y} + \frac{\partial}{\partial x} \left(\mu_{eff} \frac{\partial v}{\partial x} \right) + 2 \frac{\partial}{\partial y} \left(\mu_{eff} \frac{\partial v}{\partial y} \right) + \frac{\partial}{\partial x} \left(\mu_{eff} \frac{\partial u}{\partial y} \right) + \rho g \beta (T - T_0) \cos \theta \quad (3)$$

$$\rho u \frac{\partial T}{\partial x} + \rho v \frac{\partial T}{\partial y} = \frac{\partial}{\partial x} \left(\Gamma_{eff} \frac{\partial T}{\partial x} \right) + \frac{\partial}{\partial y} \left(\Gamma_{eff} \frac{\partial T}{\partial y} \right) \quad (4)$$

$$\mu_{eff} = \mu + \mu_t, T_0 = (T_c + T_h)/2, \beta = 1/T_0 \quad (5)$$

$$\Gamma_{eff,T} = \frac{\mu}{Pr} + \frac{\mu_t}{Pr} \quad (6)$$

The turbulent kinetic energy and the rate of its dissipation for two dimensional buoyancy turbulent flow can be written as follows[Jones and Luander,1972]:

$$\rho u \frac{\partial k}{\partial x} + \rho v \frac{\partial k}{\partial y} = \frac{\partial}{\partial x} \left(\Gamma_{eff,k} \frac{\partial k}{\partial x} \right) + \frac{\partial}{\partial y} \left(\Gamma_{eff,k} \frac{\partial k}{\partial y} \right) + G - \rho \varepsilon \quad (7)$$

$$\rho u \frac{\partial \varepsilon}{\partial x} + \rho v \frac{\partial \varepsilon}{\partial y} = \frac{\partial}{\partial x} \left(\Gamma_{eff,\varepsilon} \frac{\partial \varepsilon}{\partial x} \right) + \frac{\partial}{\partial y} \left(\Gamma_{eff,\varepsilon} \frac{\partial \varepsilon}{\partial y} \right) + C_{1\varepsilon} \frac{\varepsilon}{k} G + C_{2\varepsilon} \frac{\varepsilon^2}{k} \quad (8)$$

where

$$G = \nu_t \left[2 \left(\frac{\partial u}{\partial x} \right)^2 + 2 \left(\frac{\partial v}{\partial y} \right)^2 + \left(\frac{\partial u}{\partial y} + \frac{\partial v}{\partial x} \right)^2 \right] \quad (9)$$

$$\Gamma_{eff,k} = \mu + \frac{\mu_t}{\sigma_k}, \Gamma_{eff,\varepsilon} = \mu + \frac{\mu_t}{\sigma_\varepsilon} \quad (10)$$

The eddy dynamic viscosity is obtained by the Prandtl-Kolmogorov hypothesis

$$\nu_t = C_\mu \frac{k^2}{\varepsilon} \quad (11)$$

the model coefficients are (σ_k ; σ_ε ; $C_{1\varepsilon}$; $C_{2\varepsilon}$; C_μ) = (1.0 , 1.3 , 1.44 , 1.92, 0.09) respectively [Jones and Luander,1972].

BOUNDARY CONDITIONS

In order to solve the mathematical model, the following boundary conditions are used at the walls: $u = v = 0$. and wall function approach [Versteeg and Meer,1995] is used for the near wall grid points.

For perpendicular walls on the x-axis: at $x = 0$, $T = T_h$, at $x = L$, $T = T_c$ and the parallel walls to the x-axis are insulated.

The local and average Nusselt numbers along the left vertical hot wall can be obtained from the following formulas:

$$Nu = \frac{\partial \Phi}{\partial X} = \frac{\partial T}{\partial x} \frac{L}{T_h - T_c};$$

$$Nu_{av} = \int_0^1 \left(\frac{d\Phi}{dX} \right) dy \approx \frac{1}{N} \sum_{j=1}^N \frac{\partial \Phi}{\partial X}$$

The average Nusselt number is a function of Rayleigh and grid points. The number of grid points for $10^8 \leq Ra \leq 10^{10}$ is 41×41 and for $10^{10} \leq Ra \leq 10^{16}$ is 84×82 . The increase in Ra needs more grid points and computational time to obtain a converged solutions. The large part of grid points for all the studied Ra are found near the walls in all directions.

NUMERICAL PROCEDURE

Finite volume method is used for the discretisation of the considered governing equations. This gives a system of discretization equations which means that the system of elliptic partial differential equations is transformed into a system of algebraic equations. The solution of these equations is performed by implicit line by line Gauss elimination scheme. A computer program is developed to attain the results using the pressure

velocity coupling (SIMPLEC algorithm) [Versteeg and Meer,1995]. Due to this strong coupling and non-linearity inherent in these equations, relaxation factors are needed to ensure convergence. The relaxation factors used for velocity components, temperature, pressure and turbulence quantities are 0.4, 0.5, 0.45 and 0.7 respectively. These relaxation factors have been adjusted for each case studied in order to accelerate convergence. Non uniform grid with refinements near the walls is used. The computational grids are staggered for the scalar variables and not staggered for the scalar one. The accuracy of the considered code is validated by comparing the present results with published results as shown in the table 1. The linear least square regression method is used for the correlation between Ra and Nu_{av} for the present results found in the table 1. This relation takes the form $Nu_{av} = 0.25Ra^{0.40}$

RESULTS AND DISCUSSION

The computed results are presented as follows for different Rayleigh numbers and angles of inclination.

Fig.2. demonstrates the stream function for different values of Ra and $\theta = 0^\circ$. It can be seen that at $Ra = 10^8$, there is two elongated vortices near the enclosure walls. When Ra increased to 10^{10} , the two vortices are stretched to one vorticity in the central part of the enclosure. However there is small vortices arises in the bottom right corner. As $Ra = 10^{12}$, there is small secondary vortices found in the upper part of the enclosure besides the central vorticity. At $Ra = 10^{14}$ and $Ra = 10^{16}$ the secondary vortices are distributed near the walls. The increasing of Ra due to the increment in H leads to increase the buoyancy which leads to increase the vertical and horizontal velocities consequently effect on the vorticity distribution. The effect of angle of inclination on stream function distribution for $Ra = 10^8$ is depicted in

Fig.3. As the Figure shows, when $\theta = 30^\circ$, the stretching vortices are elongated in the direction of inclination and the size of the occupied region by these vortices is less compared with the case of $\theta = 0^\circ$. When $\theta = 60^\circ$, besides to the elongated vortices, there is a small secondary vortices near the enclosure walls. The size of these vortices is larger compared with $\theta = 30^\circ$. At $\theta = 90^\circ$ there is four re-circulating secondary vorticities formed near the vertical walls and bottom surface

as a result of increasing the buoyancy force because the hot wall became at the bottom. As the angle increased to $\theta = 120^\circ$, there is elongated vortices and two secondary vortices near the walls. The occupied zone by the elongated vortices is larger. For $\theta = 150^\circ$, the distribution is nearly similar to the case of $\theta = 30^\circ$. However the boundary layer is thicker. This is demonstrated at **Fig.6** and **Fig.8**. For $\theta = 180^\circ$ there is two secondary vortices and the size of these vortices is larger compared with the case of $\theta = 0^\circ$. The temperature distribution for different Rayleigh numbers and $\theta = 0^\circ$ is shown in **Fig.4**. It is evident that the heat is transferred from the hot wall to the cold wall through a working fluid (air) by convection. This assessed when one observe that the isotherm lines are not perpendicular. Also it can be seen that the thermal boundary layer thickness as shown in b,c,d and e. is decreased with the increase of Ra and as a consequence of this the rate of heat transfer is faster with increasing the Rayleigh number. The temperature distribution for different angles of inclination and $Ra=10^8$ is shown in **Fig.5**. It can be seen that at $\theta = 30^\circ$, the isotherm lines are inclined with direction of the enclosure tilted angle and the rate of heat transfer is less compared with case of $\theta = 0^\circ$. The isotherm lines be thicker at the lower part of the hot wall and upper part of the cold one and this leads to the rate of heat transfer to be larger. This confirmed through **Fig.6**. which demonstrates the variation of the average Nusselt number with angles of inclination. As **Fig.5**. shows, the rate of heat transfer is continuous to decrease from $\theta = 60^\circ$ to $\theta = 90^\circ$. At $\theta = 120^\circ$ to $\theta = 180^\circ$, the rate of heat transfer is noticeably increased and this confirmed at **Fig.6**. Also it can be seen from **Fig.6** that the average Nusselt number is increased with the increase of Ra for all angles of inclination because when Ra is increased, the buoyancy induced flow is increased and that leads to increase the rate of heat transfer. The local nusselt number variation along the hot wall for different Ra and $\theta = 0^\circ$ is depicted in **Fig.7**. It can be seen that the the lower corner of the hot wall indicated the high value of Nu and hence the high rate of heat transfer. When the enclosure is tilted with the considered angles of inclination($0 \leq \theta \leq 90 \text{deg.}$), **Fig.8**., the local Nusselt number values is decreased. It is evident

that for $\theta = 30^\circ$ to $\theta = 90^\circ$, the lower corner($y/H=0$) of the hot wall disclosed the high values of Nu while at $\theta = 120^\circ$ to $\theta = 180^\circ$, this position is shifted to $y/H=0.95$ as a result of change of the location of hot and cold walls and hence changing the strength of buoyancy force.

CONCLUSIONS

In the present paper, the turbulent 2D natural convection inside inclined square enclosure has been successfully predicted. From the computed results, the following conclusions can be obtained.

- The rate of heat transfer is increased with the increase of Ra and decreased with the increase of angle of inclination($0 \leq \theta \leq 90 \text{deg.}$) and converse verse at($90 \leq \theta \leq 180 \text{deg.}$) .
- The local Nusselt number values along the hot tilted wall is higher at the bottom section of the wall, while for the tilted cold wall at the top section.
- The thermal boundary layer thickness is decreased with the increase of Ra
- The resulted vortices are stretched to the middle of the enclosure with the increase of Ra.

REFERENCES

- Ampofo, F., Karayiannis, T.G., “ Experimental benchmark data for turbulent natural convection in an air filled square cavity”, Int. J. Heat Mass Transfer, vol.46, 2003.
- Corcione, M., “ Effect of thermal boundary conditions at side walls upon natural convection in rectangular enclosures heated from below and cooled from a above”, Int. J. Thermal Sci. vol.42, 2003.
- El shirbiny, S.M., Hollands, G.D., Raithby, “ Nusselt number distribution in a vertical and inclined air layers”, J. heat Transfer, 1983.
- Elshirbiny, S.M., Hollands, G.D., “ Heat transfer by natural convection across vertical and inclined air layers”, J. Heat Transfer 104, 1982.
- Ganzarolli, M.M, Milane Z, L.F., “ Natural convection in rectangular enclosures heated from below and symmetrically cooled from the sides”, Int. J. Heat and Mass Transfer, 1995.



- Hart, E.J., "Stability of the flow in a differentially heated inclined box", J. Fluid Mech., 1971.
- Jones, W.P., Lunder, B.E., The prediction of laminarization with a two equation model of turbulence", J. Heat and Mass transfer, 1972
- Kuiper, R.A., Van Der Meer, C.J., Henkes, R.A., "Numerical study of laminar and turbulent natural convection in an inclined square cavity, Int.J. Heat mass Transfer, 36, 1993.
- Lankhorst, A.M., Henkes, Hoogendoorn, C.J., "Natural convection in cavities at high Rayleigh numbers", second UK national conference on heat transfer, university of Strathclyde, Glasgow, 1991
- Markatos, N.C., Pericleous, K.A., "Laminar and turbulent natural convection in an enclosed cavity", Int. J. Heat mass transfer, 1984.
- Osttrach, S., "Natural convection in enclosure", J. heat Transfer Trans., ASME, 1988.
- Vahl Davis, G.De., "Natural convection in a square cavity, a comparison exercises", Int. J. Numer. Methods Fluids, 1983.
- Versteeg, H. and Meer, W., "An introduction of computational fluid dynamics", Hemisphere Publishing Corporation, United State of America, 1995.
- Zhong, Z.Y., Yang, K.T., "Variable property natural in tilted cavities with thermal radiation", Numerical Methods in Heat Transfer, vol.3, 1985.

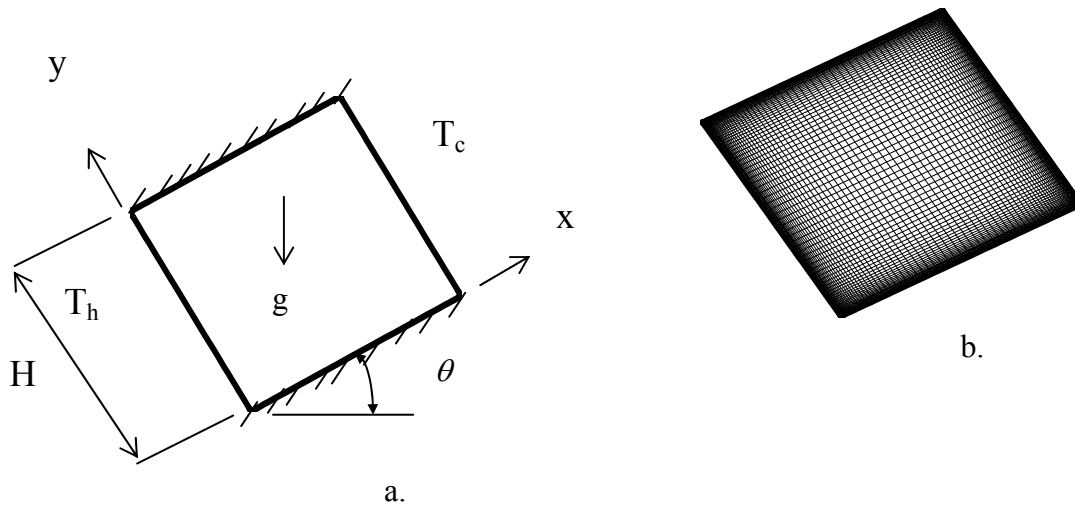


Figure.1. problem of interest; (a) physical domain , (b) computational domain

Table1. Comparison of the present results with the published results of [Marakato,1984] for
 $Pr=0.71$ and $\theta = 0^\circ$.

Ra	Nu_{av} (present results)	Nu_{av} (published results)
10^6	8.748	8.754
10^8	32.1	32.04
10^{10}	156.85	156.8
10^{12}	840.8	840.1
10^{14}	3627	3264
10^{16}	11229.9	11226

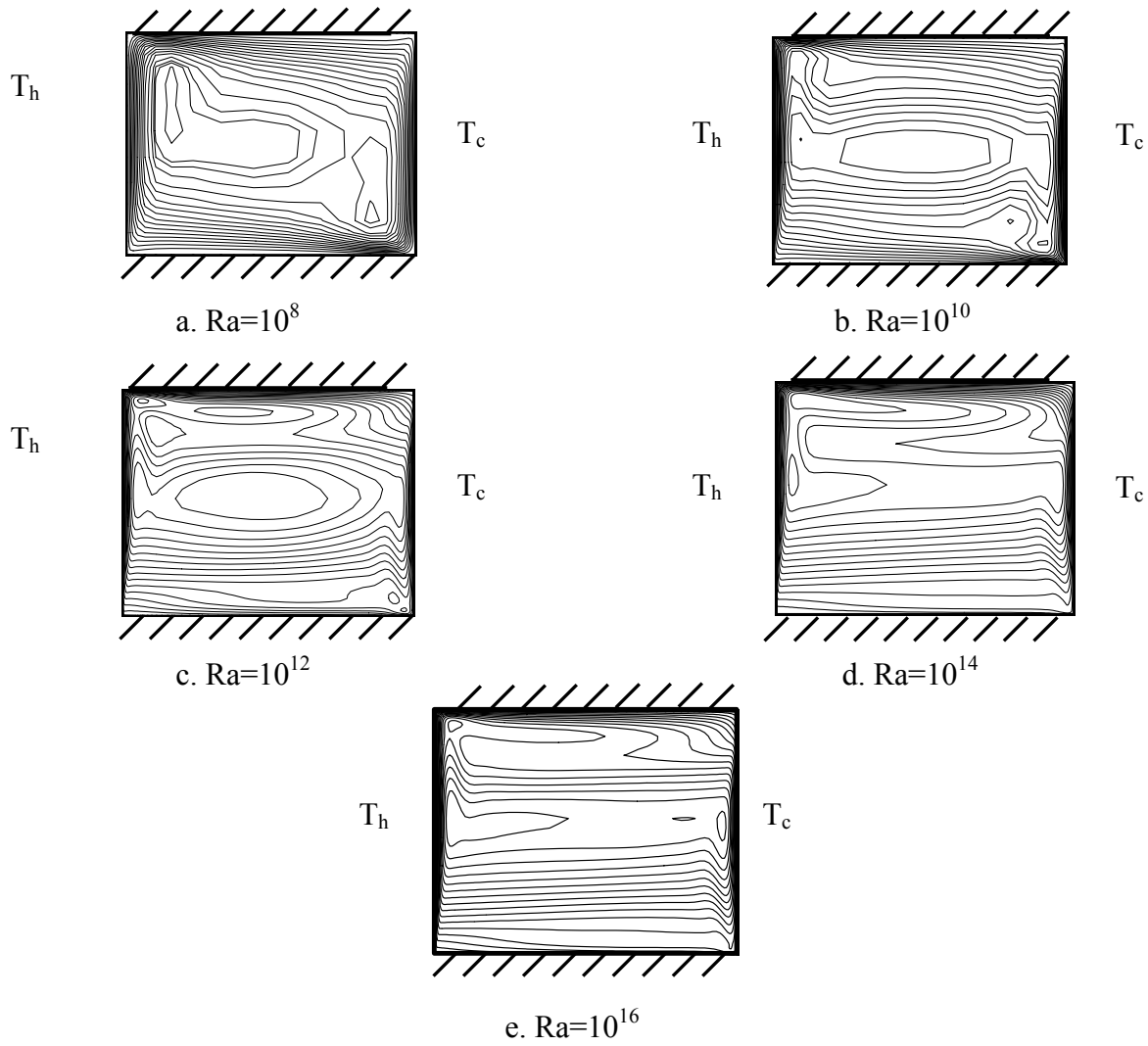
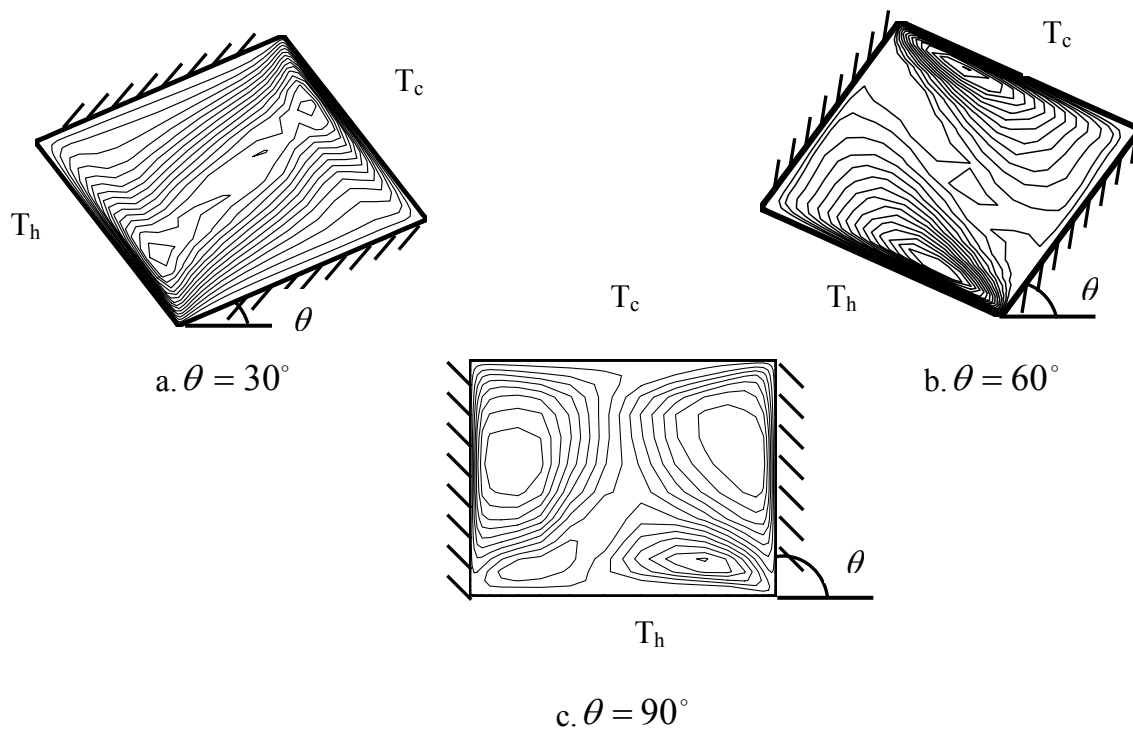


Figure.2. stream function distribution at different Ra and $\theta = 0^\circ$



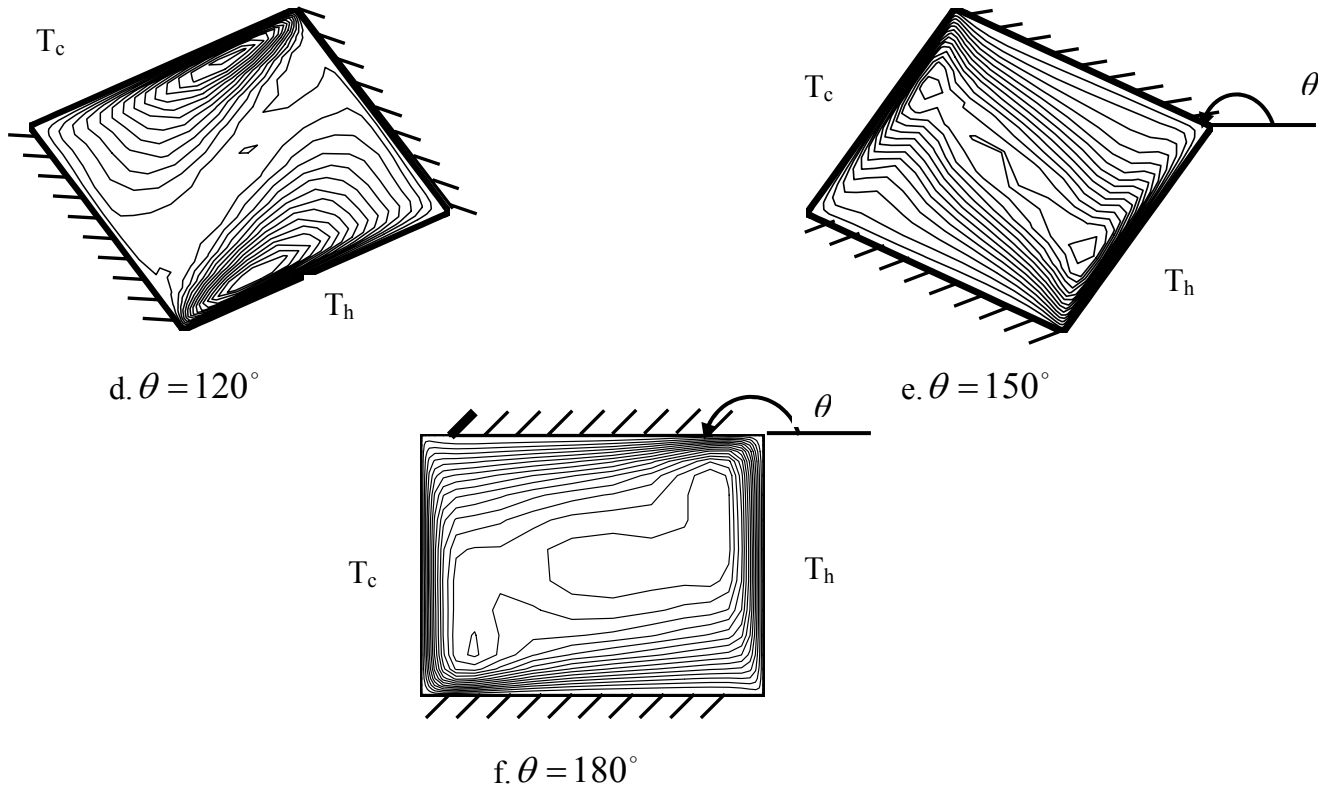


Figure.3. stream function distribution at different angles of inclination and $Ra=10^8$

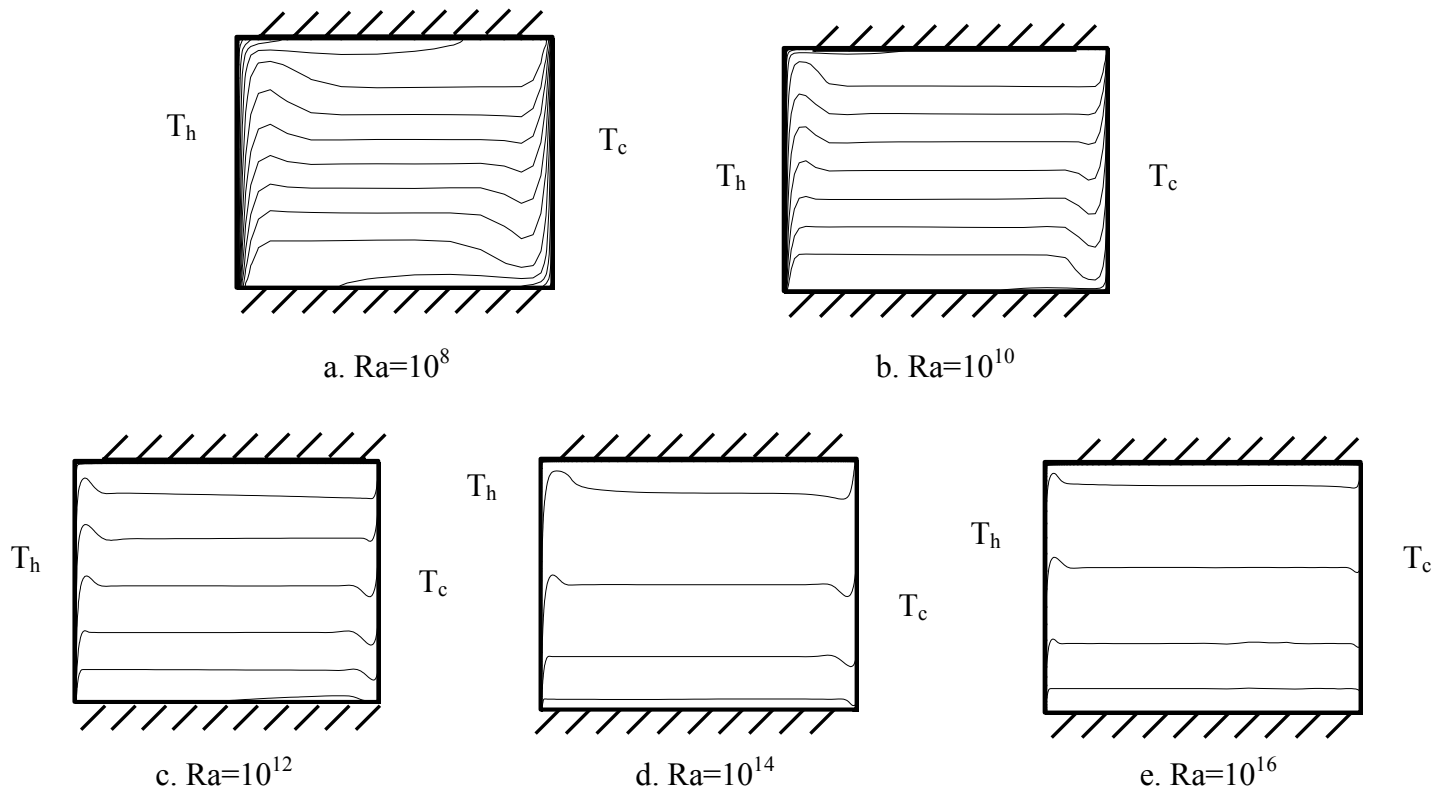


Figure.4. isotherms for different Rayleigh numbers and $\theta = 0^\circ$

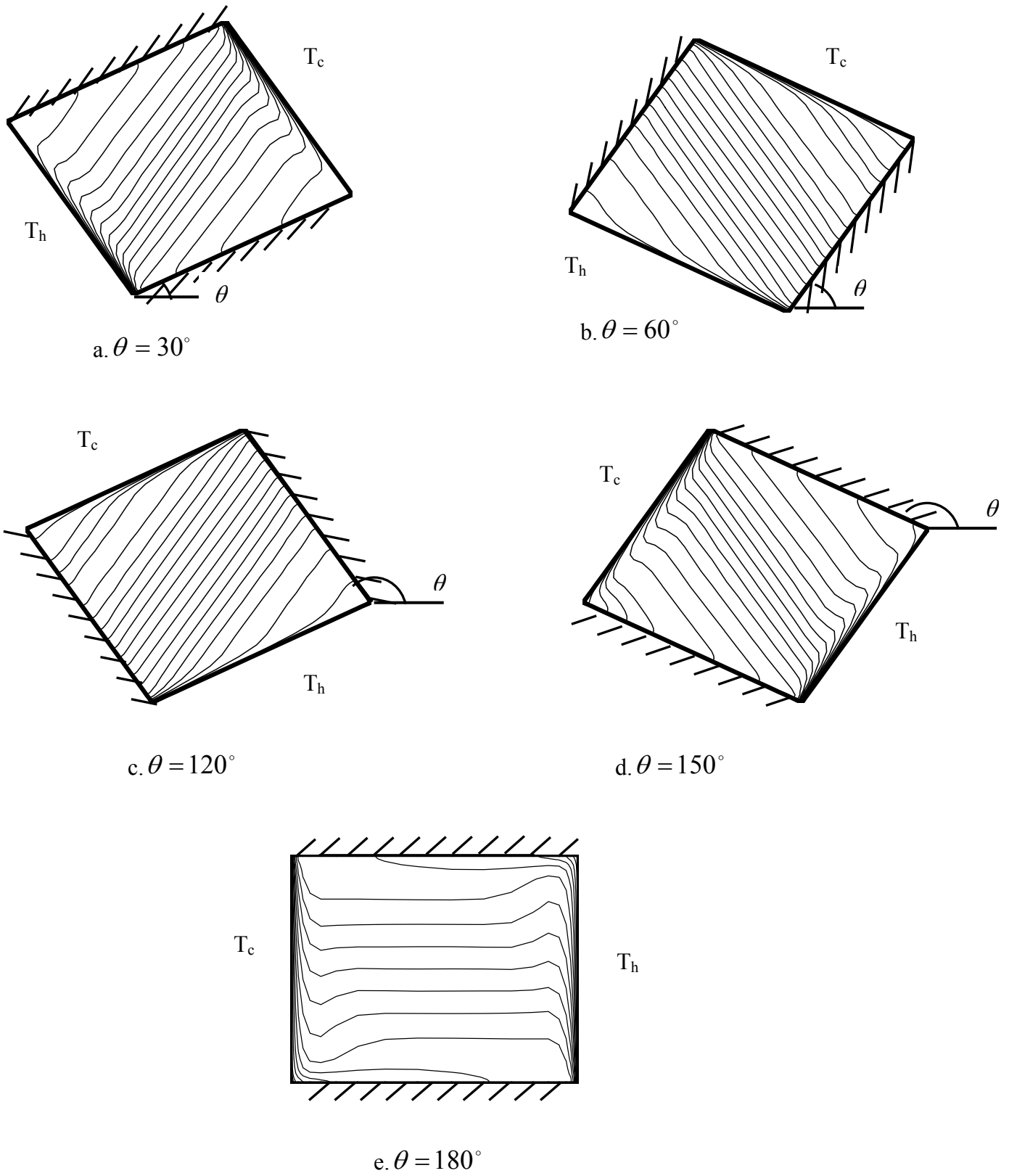
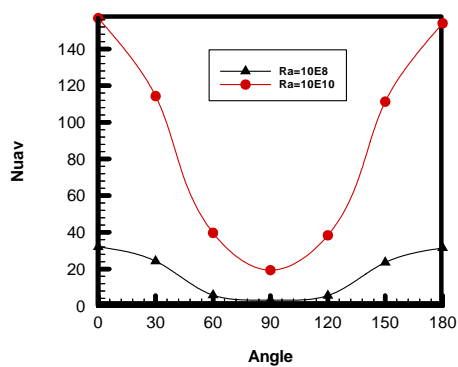
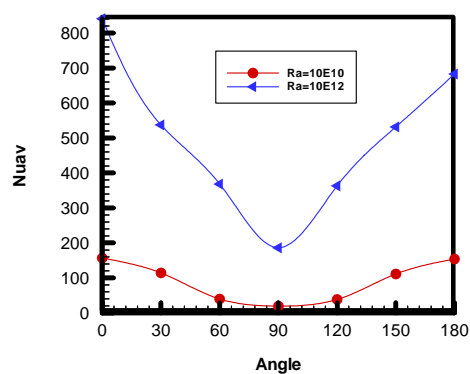


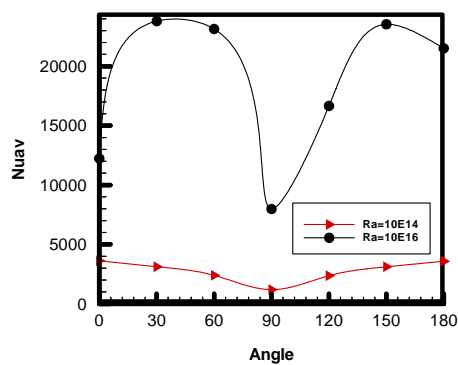
Figure.5. isotherm for different angles of inclination and $Ra = 10^8$



a

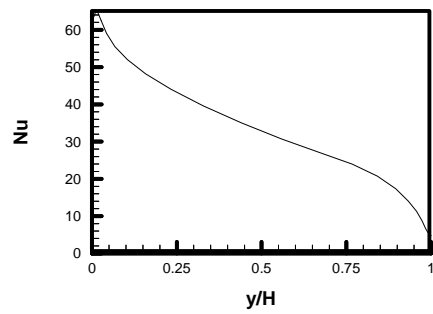


b

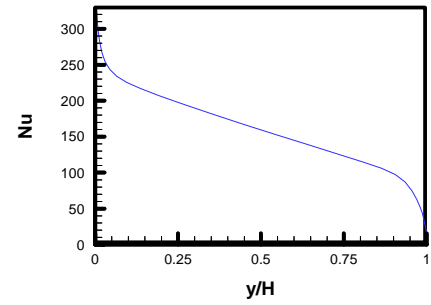


c

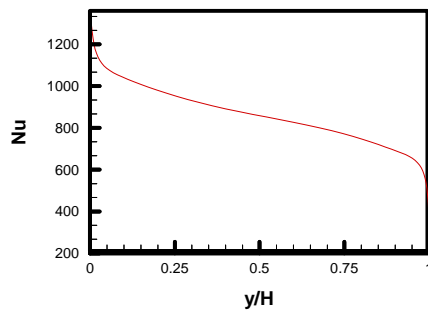
Figure. 6. variation of average Nusselt number with angles of inclination at different Rayleigh numbers



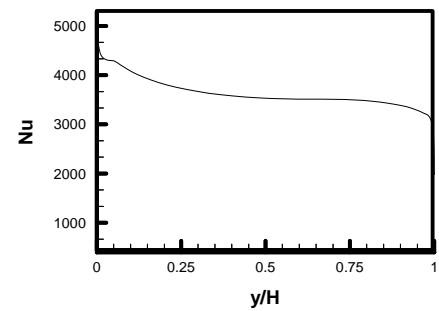
a.



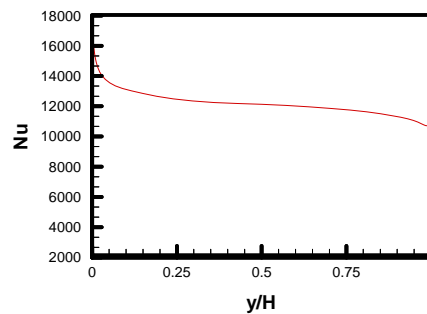
b.



c.

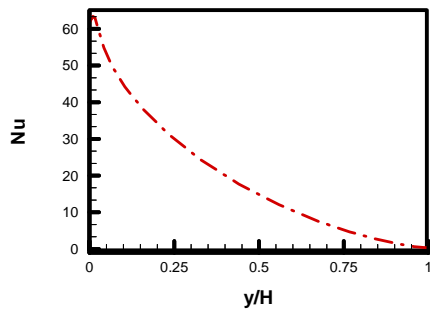


d.

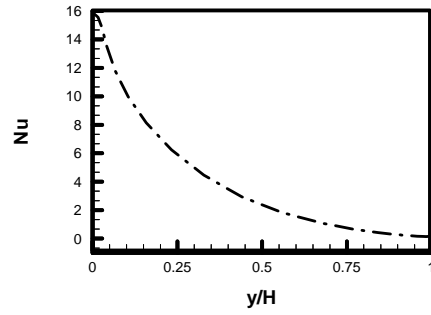


e.

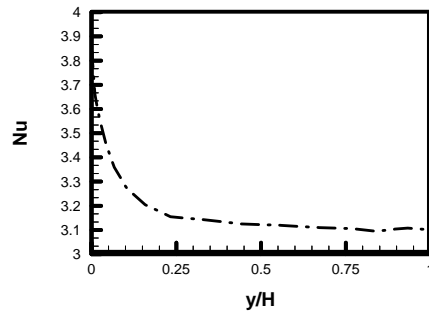
Figure.7. Local Nusselt number variation at the hot wall ($x=0$) for different Ra ;
a. $Ra=10^8$; b. $Ra=10^{10}$; c. $Ra=10^{12}$; d. $Ra=10^{14}$ e. $Ra=10^{16}$



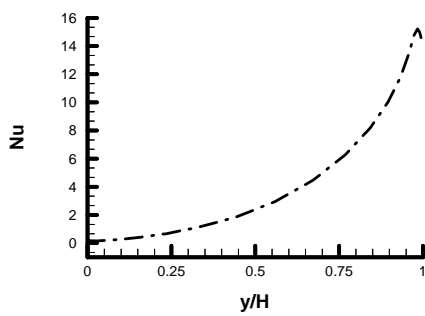
a. $\theta = 30^\circ$



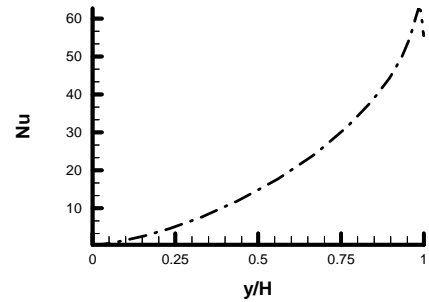
b. $\theta = 60^\circ$



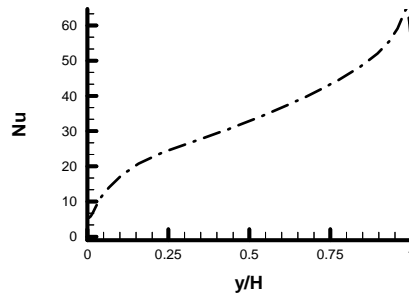
c. $\theta = 90^\circ$



d. $\theta = 120^\circ$



e. $\theta = 150^\circ$



f. $\theta = 180^\circ$

Figure.8. variation of local Nusselt number on the hot wall ($x=0$)
with angles of inclination at $Ra=10^8$

**NOMENCLATURE**

$C_u, C_{1\epsilon}, C_{2\epsilon}$	turbulence constants, -
G	generation term by shear, Kg/m.sec^3
H	height of the enclosure, m
k	turbulent kinetic energy, m^2/s^2
Nu	local Nusselt number, -
Nu_{av}	average Nusselt number, -
P	pressure, N/m^2
Pr	Prandtl number, -
Ra	Rayleigh number $\left(\frac{g\beta H^3 (T_h - T_c)}{\alpha \mu} \right)$, -
T_c	cold wall temperature, $^\circ\text{C}$
T_h	hot wall temperature, $^\circ\text{C}$
x, y	Cartesian coordinates, m
X	dimensionless Cartesian coordinate $\left(\frac{x}{H} \right)$, -

Greek symbols:

ϵ	turbulence dissipation rate, m^2/s^3
μ	dynamic viscosity, N.s/m^2
μ_t	turbulent viscosity, N.s/m^2
ν_t	eddy dynamic viscosity, m^2/s
μ_{eff}	effective turbulent viscosity, N.s/m^2
Γ_{eff}	effective exchange coefficient, kg/m.s
Φ	dimensionless temperature $\left(\frac{T - T_c}{T_h - T_c} \right)$, -
$\sigma_k, \sigma_\epsilon$	turbulent schmidt numbers, -
α	thermal diffusivity of fluid, m^2/s



LAMINAR AIDING COMBINED CONVECTION IN THE DEVELOPING REGION OF INCLINED CYLINDER

Prof. Dr. Abdulhassan A. Karamallah
University of Technology
Mechanical Eng. Dep.

Dr. Akeel A. Mohammed
University of Technology
Mechanical Eng. Dep.

Engineer. Ameer A. Jadoaa
University of Technology
Electromecanical Eng. Dep

ABSTRACT

The influence of natural convection due to buoyancy on the laminar upwards air flow in a uniformly heated inclined circular cylinder has been experimentally studied. The investigation covered a wide range of Reynolds number ($450 \leq Re \leq 2008$), heat flux ($95 \leq q \leq 898$) W/m², Rayleigh number ($1.1132 \times 10^5 \leq Ra \leq 3.6982 \times 10^5$), with different angles of cylinder inclination $\alpha = 0^\circ$ (Horizontal), $\alpha = 30^\circ$, $\alpha = 60^\circ$ (Inclined) and $\alpha = 90^\circ$ (Vertical). Results show that the heat transfer process improves as the angle of inclination moves from vertical to horizontal position. A general empirical equation for average Nusselt number Nu_m as a function of Rayleigh number Ra , Reynolds number Re and angle of inclination α was obtained.

$$(1.1132 \times 10^5 \leq Ra \leq 3.6982 \times 10^5) \quad (450 \leq Re \leq 2008) \\ (\alpha = 0^\circ \quad 30^\circ \quad 60^\circ \quad 90^\circ) \quad (95 \leq q \leq 898) \text{ W/m}^2 \\ \alpha \quad Ra \quad Re$$

Keywords: Free and Forced, Convection, Cylinder.

INTRODUCTION

The convection heat transfer coefficient and fluid flow characteristics of duct flows are often affected by the presence of gravity, particularly at low or moderate flow rates. The orientation of the duct can have a considerable influence on the velocity and temperature profiles and the associated heat transfer and friction coefficients in the duct. For horizontal cylinder, the buoyancy forces are perpendicular to the main flow direction and give rise to secondary currents in the cross section. For vertical cylinder, the gravity forces are in the main flow direction, and axial symmetry is preserved since there is no secondary flow in the cross-section. In inclined cylinder, however, buoyancy forces act in both the main flow and the cross-

stream directions. In practice, this situation is commonly encountered in heat exchanger equipment and in solar collectors. Because of important practical application, laminar combined free and forced convection in horizontal, inclined, and vertical circular duct had been studied theoretically and experimentally by many authors such as; Eckert and Diaguila [1953]; Jackson, Harrison and Boteler [1958]; Mc comas and Eckert [1966]; Zeldin and Schmidt [1972]; Morcos and Bergles [1975]; Pascal and Ralph [1985]; Choudhury and Patankar [1988]; Wang, Tsuji, and Nagano [1994]; etc. Akeel [1999], performed experiments to study the local heat transfer by mixed free and forced convection to a simultaneously developing air flow in a vertical and horizontal cylinder for $L/D=30$. The results



demonstrate an increase in the Nusselt number values along the axial distance as the heat flux increases and as the cylinder moves from vertical to the horizontal position.

Busedra and Soliman [2000], performed an experimental investigation of laminar water flow mixed convection in a uniformly heated inclined semicircular duct under buoyancy assisted and opposed conditions within $\pm 20^\circ$. The experiment was designed for determining the effect of inclination on the wall temperature, and local fully-developed Nusselt numbers at three Reynolds numbers 500, 1000, and 1500 and a wide range of Grashof numbers. They found that for the upward inclinations, the value of Nusselt number increases with Grashof number and the inclination angle up to 20° , while the effect of Reynolds Number was found to be small. For the downward inclination, Reynolds number has a strong effect on Nusselt number and the manner by which it varies with Grashof number. The purpose of this paper is to present an experimental study of the simultaneously developing laminar air flow and heat transfer in an inclined uniformly heated circular cylinder in which the heating from the cylinder wall leads to significant buoyancy effects in the upward flow. An empirical equation describes the average Nusselt number as a function of Rayleigh number, Reynolds number, and angle of inclination of cylinder has deduced.

EXPERIMENTAL APPARATUS AND PROCEDURE

The experimental apparatus shown in **Fig.(1)** consists essentially of cylinder as an open air loop test section, mounted on an iron frame (I) which can be rotated around a horizontal spindle. The inclination angle of the cylinder can thus be adjusted as required. An open air circuit was used which included a centrifugal fan (B), orifice plate section (C), settling chamber (F), test section and a flexible hose (E). The air which is driven by a centrifugal fan can be regulated accurately by using a control valve and enters the orifice pipe section and then settling chamber through a flexible hose (E). The settling chamber was carefully designed to reduce the flow fluctuation and to get a uniform flow at the test section entrance by using flow straightener (G). The air then passed through 1.2 m long test section.

A symmetric flow and a uniform velocity profile produced by a well designed Teflon bell mouth (H) which is fitted at the entrance of aluminum cylinder (N) and bolted in the other side inside the settling chamber (F). Another Teflon piece (H)

represents the cylinder exit and has the same dimensions as the inlet piece. The Teflon was chosen because its low thermal conductivity in order to reduce the heat losses from the aluminum cylinder ends. The inlet air temperature was measured by one thermocouple located in the settling chamber (F) while the outlet bulk air temperature was measured by two thermocouples located in the test section exit (R). The local bulk air temperature was calculated by using a straight line interpolation between the measured inlet and outlet bulk air temperature. The test section consists of 7.5 mm wall thickness, 59.3 mm outside diameter and 1.2m long aluminum cylinder. The cylinder is heated electrically using an electrical heater which consists of 1 mm in diameter and 60 m in length nickel-chrome wire (L) electrically isolated by ceramic beads, wounds uniformly as a coil with 10 mm pitch. The outside of the test section was then thermally insulated, covered with asbestos rope layer and fiber glass of 60 mm and 5.7 mm as thickness, respectively. To enable the calculation of heat loss through the lagging to be carried out, six thermocouples are inserted in the lagging as two thermocouples at three locations along the heated section 390 mm apart. Using the average measured temperature drop and thermal conductivity of lagging the heat losses through lagging can be calculated. The cylinder surface temperatures were measured by eighteen asbestos sheath thermocouple (type K). All the thermocouple wires and heater terminals were taken out the test section. To determine the heat loss from the test section ends, two thermocouples were fixed in each Teflon piece. Knowing the distance between these thermocouples and the thermal conductivity of the Teflon, the heat ends loss could thus be calculated. The thermocouple circuit consists of a digital electronic thermometer (type TM-200, serial no. 13528), connected in parallel to the thermocouples by leads through a selector switches. An orifice plate British Standard Unit (BSU) of diameter of (50 mm) and discharge coefficient of (0.6099) was used to compute the flow rate through the cylinder, by using the following equation.

$$\dot{V} = C_d \cdot (\pi D_o^2 / 4) \cdot \sqrt{2g\Delta h}$$

Where:

$$\dot{V} = \text{flow rate} = \text{mm}^3/\text{sec}$$

$$C_d = \text{discharge coefficient} = 0.6099$$

$$D_o = \text{diameter of orifice} = 50 \text{ mm}$$

Prof. Dr. Abdulhassan A. Karamallah Dr. Akeel A. Mohammed Engineer. Ameer A. Jadoaa	Laminar Aiding Combined Convection In The Developing Region Of Inclined Cylinder
--	---

The following steps were followed throughout the experimental procedure:

1. Adjust the required inclination angle of the cylinder.
2. Switch on the centrifugal fan to circulate the air, through the open loop. A regulating valve was used for adjusting the required mass flow rate.
3. Switch on the electrical heater then adjust the input power to give the required heat flux.
4. The apparatus was left at least three hours to establish steady state condition. The thermocouples readings were taken every half an hour by means of the digital electronic thermometer until the reading became constant, a final reading was recorded. The input power to the heater could be increased to cover another run in a shorter period of time and to obtain steady state conditions for next heat flux and same Reynolds number. Subsequent runs for other Reynolds number and cylinder inclination angle ranges were performed in the same previous procedure.
5. During each test run , the following readings were recorded:
 - a. The angle of inclination of the cylinder in degree.
 - b. The reading of the manometer (air flow rate) in mm H₂O.
 - c. The readings of the thermocouples in °C.
 - d. The heater current in Amperes.
 - e. The heater voltage in volts.

EXPERIMENTAL ANALAYSIS AND CALCULATION

Simplified steps were used to analyze the heat transfer process for the air flow in a cylinder subjected to a uniform heat flux.

a- The total input power supplied to the cylinder is obtained by,

$$Q_t = V \quad (1)$$

b-The convection and radiation heat transferred from the cylinder is given by :

$$Q_{cr} = Q_t - Q_{cond} \quad (2)$$

where Q_{cond} is the conduction heat loss expressed by,

$$Q_{cond} = \frac{\Delta T_{oi}}{\ln \frac{r_o}{r_i}} \quad (3)$$

$$2 \pi k_a L$$

where:

$$\Delta T_{oi} = T_o - T_i$$

T_o , is the average outer asbestos rope layer lagging surface temperature.

T_i , is the average cylinder surface temperature.

c-The convection and radiation heat flux can be represented by:

$$q_{cr} = Q_{cr} / A_1 \quad (4)$$

where:

$$A_1 = 2\pi r_i L$$

d-The local radiation heat flux can be calculated as follows:

$$q_r = F_{1-2} \epsilon \sigma \left[\left((T_s)_z + 273 \right)^4 - \left((\overline{T_s})_z + 273 \right)^4 \right] \quad (5)$$

where:

$(T_s)_z, (\overline{T_s})_z$ = are local and average temperature of cylinder wall, respectively .

σ = Steavan Boltzman constant = 5.66×10^{-8} W/m² K⁴

ϵ = emissivity of the polished aluminum surface = 0.09.

$F_{1-2} \approx 1$ = shape factor.

Then the convection heat flux at any position is:

$$q = q_{cr} - q_r \quad (6)$$

Since the radiation heat flux is very small and can be neglected, then

$$q_{cr} \approx q$$

e-The local heat transfer coefficient can be obtained by,

$$h_z = \frac{q}{(T_s)_z - (T_b)_z} \quad (7)$$

and the local mean film temperature:

$$(T_f)_z = \frac{(T_s)_z + (T_b)_z}{2} \quad (8)$$

where $(T_b)_z$, Local bulk air temperature.

f-The local Nusselt number (Nu_z) then can be determined as:

$$Nu_z = \frac{h_z D_h}{k} \quad (9)$$

And the average values of Nusselt number Nu_m can be calculated as follows:

$$Nu_m = \frac{1}{L} \int_0^L Nu_z dz \quad (10)$$

The average values of the other parameters can be calculated based on calculation of average cylinder surface temperature and average bulk air temperature as follows:

$$\bar{T}_s = \frac{1}{L} \int_{z=0}^{z=L} (T_s)_z dz \quad (11)$$

$$\bar{T}_b = \frac{1}{L} \int_{z=0}^{z=L} (T_b)_z dz \quad (12)$$

and the average mean film temperature is:

$$\bar{T}_f = \frac{\bar{T}_s + \bar{T}_b}{2} \quad (13)$$

All the air physical properties ρ , μ , ν , and k were evaluated at the average mean film temperature (\bar{T}_f).

RESULTS AND DISCUSSION

Temperature Variation

Generally, the variation of surface temperature along the surface cylinder may be affected by many variables such as heat flux, Reynolds number, and cylinder inclination angles.

The temperature variation in the horizontal position is plotted for selected runs in **Figs.(2, 3, 4 and 5)**. **Fig.(2)** shows the variation of the surface temperature along cylinder for $Re=450$ and various values of heat flux. The surface temperature increases at the cylinders entrance and attains a maximum point after which the surface temperature begins to decrease. The rate of surface temperature rises at early stage is directly proportional to the wall heat flux. This can be attributed to the increasing of the thermal boundary layer faster due to buoyancy effect as the heat flux increases for the same Reynolds number. The point of maximum temperature on the curve represents actually the starting of thermal boundary layer fully developed. The region before this point is called the entrance of cylinder, The same behavior seems in the **Fig.(3)** for Reynolds number 2008, but with lower temperature because of dominant forced convection in the heat transfer process.

Figs.(4 & 5) show the effect of Reynolds number variation on the cylinder surface temperature for lower and higher heat flux ($q=145 \text{ W/m}^2, q=898 \text{ W/m}^2$); respectively. It is obvious that the increasing of Reynolds number reduces the surface temperature as heat flux kept constant. It is necessary to mention that as heat flux increases the cylinder surface temperature increases because the free convection is the dominating factor in the heat transfer process. The axial temperature variation trend of cylinder surface for vertical and inclined cylinder ($\alpha=30^\circ, 60^\circ$ and 90°) is the same as that obtained in the horizontal position. The extent of mixed convection depends on the magnitude of the heat flux and Reynolds number for the same angle of inclination. When heat flux and Reynolds number are kept constant, the extent of local mixing due to the buoyancy effect in horizontal cylinder is larger than other cylinder angles of inclination. It has been proved that for the same condition of flow rate and input heat flux, the surface temperature variation along the cylinder decreases as the angle of inclination changes from vertical to horizontal position.

Angle of Inclination Effect on the Temperature Distribution

The variations of cylinder surface temperature along the axial distance for the same heat flux and Reynolds number, and for different angles of inclination ($\alpha=0^\circ, 30^\circ, 60^\circ$, and 90°) are shown in **Figs. (6 to 9)**. Figures show a reduction in surface temperature with mean approximated value 11% as the angle of cylinder inclination moves from vertical to horizontal position; this can be attributed to the large buoyancy effect in a horizontal cylinder compared with the other angles of cylinder inclination.

Fig.(6) shows the influence of the cylinder orientation on the cylinder surface temperature for ($q=115 \text{ W/m}^2$ & $Re=450$, gives $Ri=0.91$). It is observed that when the angles change from 60° to 90° at specific axial distance ($x=0.37 \text{ m}$) the cylinder surface temperature for the vertical position is lower than that in the inclined position ($\alpha=60^\circ$). Then beyond this location a reverse trend takes place and the cylinder surface temperature for the vertical position becomes higher than that in the inclined position ($\alpha=60^\circ$). This behavior can be explained that at cylinder entrance, the effect of free convection is small and forced convection is dominant in the heat transfer process causes the cylinder surface temperature in vertical position less than that in the inclined position ($\alpha=60^\circ$), but after a certain axial distance a significant reduction

in the cylinder surface temperature exists as the cylinder orientation changes from the vertical to the inclined position ($\alpha=60^\circ$) due to the effect of free convection which begins to dominant factor in the heat transfer process and reduces the cylinder surface temperature. If the Reynolds number is increased to 2008 (gives $Ri=0.051$) as shown in **Fig(7)**, the behavior of surface temperature distribution along the axial distance is relatively as same as **Fig(6)**.

Fig(8) shows the influence of the cylinder orientation on the cylinder surface temperature for ($q=816\text{W/m}^2$ & $Re=450$, gives $Ri=2.1$). It is observed that when the angle changes from ($\alpha=0^\circ$ to 30°) at a specific axial distance ($x=0.72\text{m}$) at the cylinder entrance the cylinder surface temperature for the inclined position ($\alpha=30^\circ$) is lower than that in the horizontal position ($\alpha=0^\circ$). If the Reynolds number is increased to 2008 (gives $Ri=0.11$) as shown in **Fig(9)**, the behavior of surface temperature distribution along the axial distance is relatively as same as **Fig(8)**.

Local Nusselt Number (Nu_x)

The variation of local Nusselt number (Nu_x) with a logarithmic dimensionless axial distance (inverse Graetz number, $zz = \frac{x/D_h}{Pr Re}$), for horizontal position are plotted, for a selected runs, in **Figs.(10 to 12)**.

The effect of heat flux on the Nu_x for $Re=450$ is shown in **Fig.(10)**. It is clear from this figure that at the higher heat flux, the results of the local Nusselt number are higher than the results of lower heat flux. This may be attributed to the secondary flow superimposed on the forced flow effect which increases as the heat flux increases leading to higher heat transfer coefficient.

The effects of Re on Nu_x variation with zz are shown in **Figs.(11) & (12)** for heat flux equal to 145 W/m^2 and 898 W/m^2 ; respectively. For constant heat flux, results depicted that the deviation of Nu_x value moves towards the left and increases as the Reynolds number increases because of decreasing of inverse Graetz number zz . This situation reveals the domination of forced convection on the heat transfer process which improves as Reynolds number increases. The behavior and trend of the variation of local Nusselt number (Nu_x) with a logarithmic dimensionless axial distance, for inclined and vertical position ($\alpha=30^\circ$, 60° and 90°) is the same as that obtained in the horizontal position.

Angle of Inclination Effect on the Local Nusselt Number

The local Nusselt number variation with zz for different angles of inclination and for ($q=115\text{ W/m}^2$ and $Re=450$, gives $Ri=0.91$) and ($q=816\text{ W/m}^2$ and $Re=2008$, gives $Ri=0.1$) are shown in **Fig.(13) & Fig.(14)**; respectively. This figure indicates that for all zz values, the Nu_x value for horizontal position is higher than that for inclined and vertical position (with mean approximated value 5% between $\alpha=0^\circ$ and $\alpha=90^\circ$ for **Fig.(13)** and approximated value 10% for **Fig.(14)**. As explained before the dominant free convection, for horizontal cylinder creates a longitudinal vortex along the cylinder which its intensity reduces as the angle of inclination moves from horizontal to vertical position leads to reducing of heat transfer coefficient.

Fig. (15) shows the influence of the cylinder orientation on the Nu_x for $Re=2008$ and $q=115\text{ W/m}^2$ (gives $Ri=0.051$). It is observed that when the angles changes from ($\alpha=0^\circ$ to 30°) at the specific zz value (0.001), the Nu_x value for the inclined position ($\alpha=30^\circ$) is higher than that in the horizontal position ($\alpha=0^\circ$). Then beyond this zz a reverse trend takes place and the values of Nu_x for the inclined position ($\alpha=30^\circ$) become lower than that in the horizontal position ($\alpha=0^\circ$) and closer to that ($\alpha=0^\circ$). This behavior can be attributed to the small buoyancy effect at cylinder entrance and the forced convection is being the dominating factor in the heat transfer process. But in down stream the secondary flow becomes more effective which improves the heat transfer process. Hence, the heat transfer appears to be higher at horizontal position and its effect is reduced as cylinder orientation moves towards the vertical position.

In horizontal cylinder, the effect of the secondary flow is high; hence at low Reynolds number and high heat flux, situation makes the free convection predominant. Therefore two Cells will be grown about each side of the vertical centre line of cylinder. The cellular motion behaves so as to reduce the temperature difference between the cylinder surface and the air flow, leads to increase the growth of the hydrodynamic and thermal boundary layers along the cylinder and causes an improvement in the heat transfer coefficient. But at low heat flux and high Reynolds number the situation makes forced convection predominant and decreasing of vortex strength leads to decrease the temperature difference between the heated surface and the air, hence, the Nu_x values become

close to the vertical cylinder values for the same conditions.

Correlation of Average Heat Transfer Data

The values of the average Nusselt number (Nu_m) for horizontal position ($\alpha=0^\circ$), inclined position for ($\alpha=30^\circ$, 60°), and vertical position ($\alpha=90^\circ$) are plotted in **Figs.(16 to 19)** in the form of $\log(Nu_m)$ against $\log(Ra/Re)$ for the range of Re from 450 to 2008, and Ra from 1.1132×10^5 to 3.6982×10^5 . These values of Reynolds number and Rayleigh number give a range of Richardson number between 0.0395 (Forced convection dominating) and 2.6 (mixed convection with stronger natural convection than forced convection)

$\alpha=90^\circ$ (vertical)	$Nu_m=2.993 (Ra/Re)^{-0.7941}$
$\alpha=60^\circ$	$Nu_m=2.831 (Ra/Re)^{-0.6537}$
$\alpha=30^\circ$	$Nu_m=2.982 (Ra/Re)^{-0.7823}$
$\alpha=0^\circ$ (horizontal)	$Nu_m=2.962 (Ra/Re)^{-0.6369}$

The heat transfer equation at any angle of inclination was deduced in the following from:

$$(Nu_m)_{inc.}=7.7515 \cdot (Ra)^{-0.639} \cdot (Re)^{0.6411} \cdot (\alpha)^{-0.0137} \quad (18)$$

where: α is measured in degree

CONCLUSIONS

1. Generally, the buoyancy effect is very weak at the entrance.
2. The heat transfer process improves as the heat flux increases where Reynolds number is kept constant and vice versa.
3. The horizontal position is the better position to achieve higher heat transfer coefficients which decrease as the cylinder position deviates from horizontal to vertical position.
4. Four empirical equations has been deduced for average Nusselt number as a function to Reynolds number and Rayleigh number for angles of inclination; $\alpha=0^\circ$ (horizontal), 30° , 60° , and 90° (vertical).

5. General empirical equation has been deduced for average Nusselt number at any angle of inclination {i.e., $Nu_m=f(Re, Ra, \alpha)$ }.

REFERENCES

- **Akeel Abdullah[1999]** "Combined free and forced convection in a circular cylinder" M.Sc. thesis, university of Baghdad, college of engineering, mechanical department, (1999).
- **Choudhury and Patankar[1988]** "Combined forced and free laminar convection in the entrance region of an inclined isothermal tube" J.Heat Transfer, Vol. 110, pp. 901-909, November 1988.
- **Eckert and Diaguila[1954]** "Convective heat transfer for mixed, free, and forced flow thought tubes" Transactions of the ASME, J.Heat Transfer, pp.497-504, May 1954. (15)
- **Jackson, Harrison and Boteler[1958]** "Combined free and forced convection in a constant-temperature vertical tube" Transactions of the ASME, Vol.80, pp.739-745. (17)
- **Mc comas and Eckert[1966]** "Combined free and forced convection in a horizontal circular tube" Transactions of the ASME , J.Heat Transfer, pp.147-153, May 1966.
- **Morcos and Bergles[1975]** "Experimental investigation of combined forced and free laminar convection in horizontal tubes" J.Heat Transfer, Vol.97, pp.212-219.
- **Pascal and Ralph[1985]** "An investigation of laminar mixed convection inside a horizontal tube with isothermal wall conditions' J.Heat Mass Transfer, Vol.28, No.7, pp.1293-1305.
- **Wang, Tsuji, and Nagano[1994]** "Mixed convection with flow reversal in the thermal entrance region of horizontal and vertical pipes" Int. J. Heat Mass Transfer, Vol. 37, No. 15, pp. 2305-2319, 1994
- **Zeldin and Schmidt[1972]** "Developing flow with combined forced-free convection in an isothermally vertical tube" Transactions of the ASME , J.Heat Transfer, pp. 211-220, May 1972.

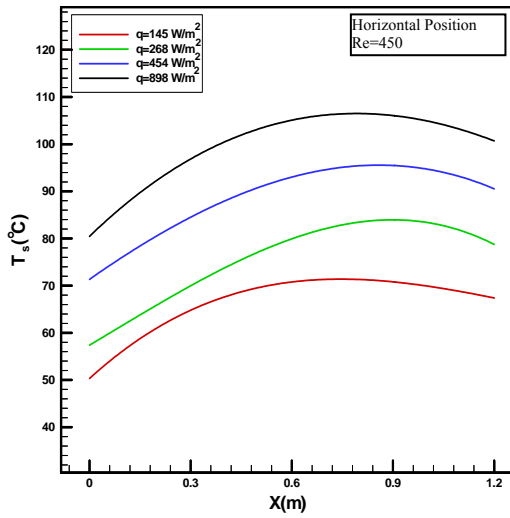


Fig.(2): Experimental Variation of the Surface Temperature with the Axial Distance, $Re=450$, $\alpha=0^\circ$ (Horizontal).

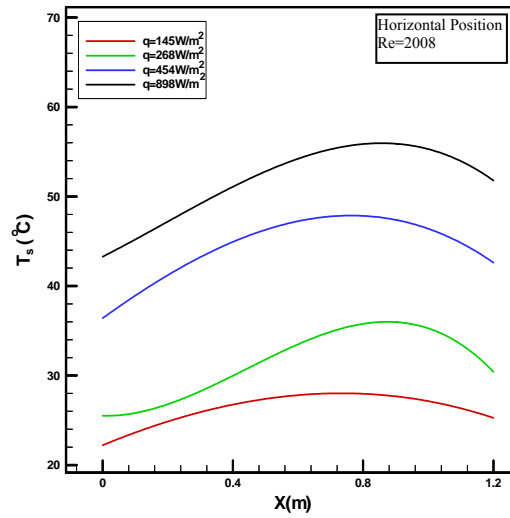


Fig.(3): Experimental Variation of the Surface Temperature with the Axial Distance, $Re=2008$, $\alpha=0^\circ$ (Horizontal).

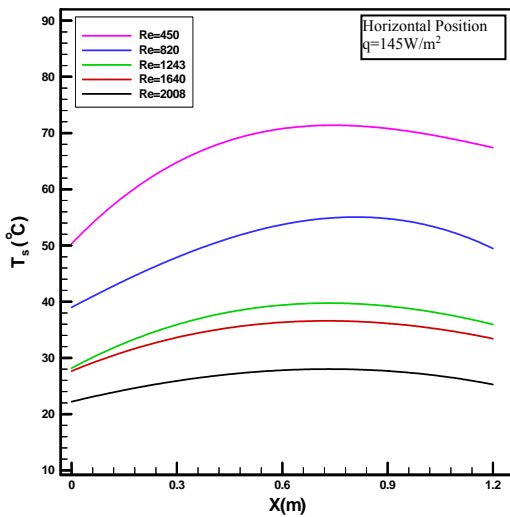


Fig.(4): Experimental Variation of the Surface Temperature with the Axial Distance, $q=145W/m^2$, $\alpha=0^\circ$ (Horizontal).

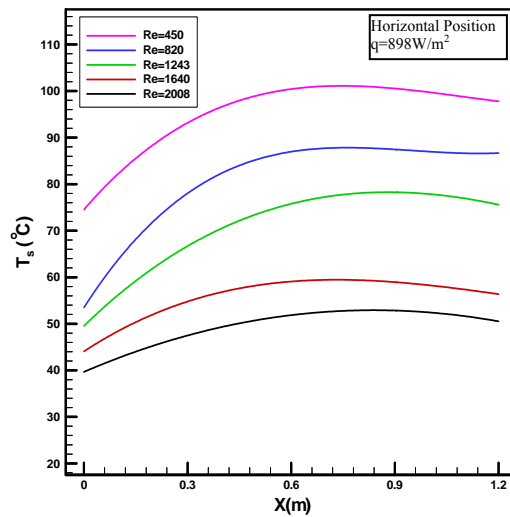


Fig.(5): Experimental Variation of the Surface Temperature with the Axial Distance, $q=898W/m^2$, $\alpha=0^\circ$ (Horizontal).

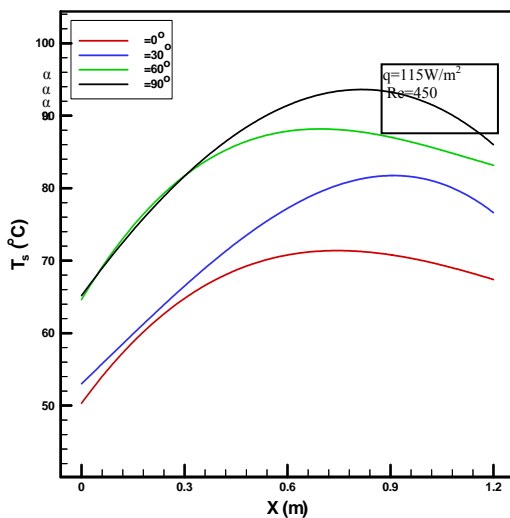


Fig.(6): Experimental Variation of the Surface Temperature with the Axial Distance for Various Angles, $q=115 W/m^2$, $Re=450$

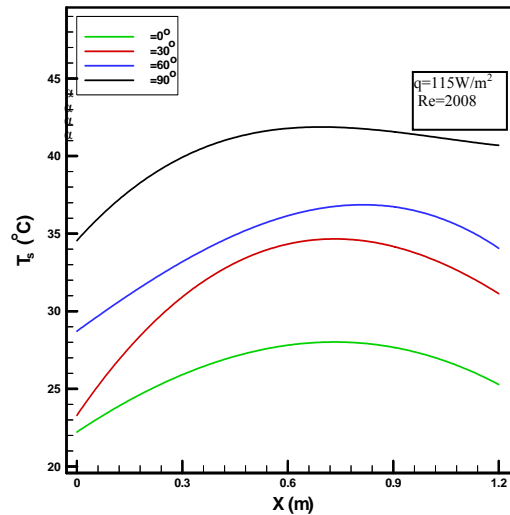


Fig.(7): Experimental Variation of the Surface Temperature with the Axial Distance for Various Angles, $q=115 W/m^2$, $Re=2008$

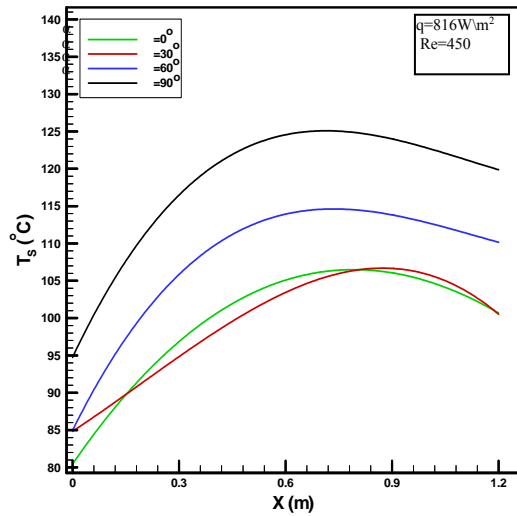


Fig.(8): Experimental Variation of the Surface Temperature with the Axial Distance for Various Angles, $q=816\text{W/m}^2$, $Re=450$

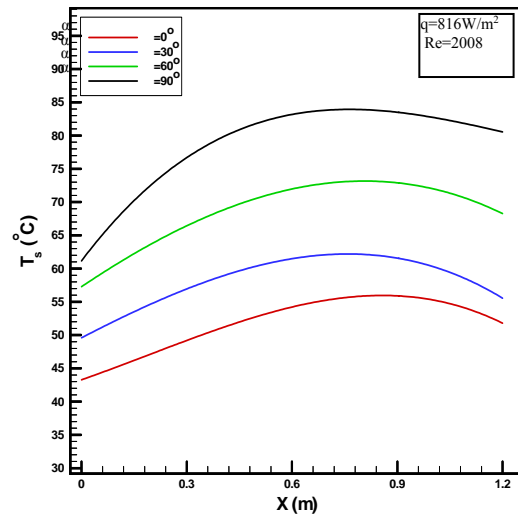


Fig.(9): Experimental Variation of the Surface Temperature with the Axial Distance for Various Angles, $q=816\text{W/m}^2$, $Re=2008$

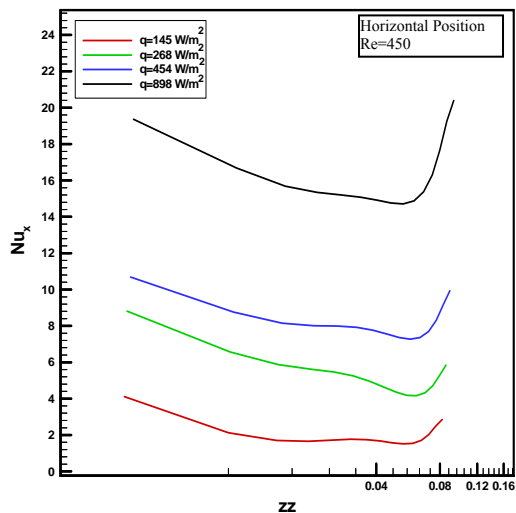


Fig.(10): Experimental Local Nusselt number Versus Dimensionless Axial Distance, $Re=450$, $\alpha=0^\circ$ (Horizontal).

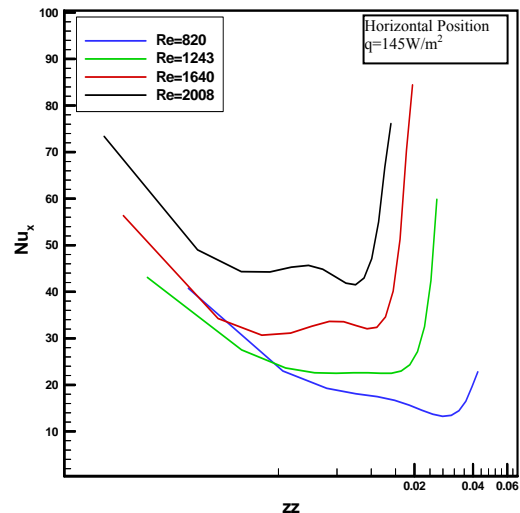


Fig.(11): Experimental Local Nusselt number Versus Dimensionless Axial Distance, $q=145\text{W/m}^2$, $\alpha=0^\circ$ (Horizontal).

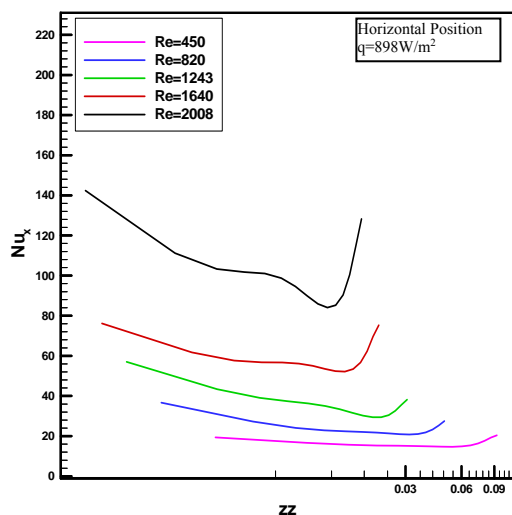


Fig.(12): Experimental Local Nusselt number Versus Dimensionless Axial Distance, $q=898\text{W/m}^2$, $\alpha=0^\circ$ (Horizontal).

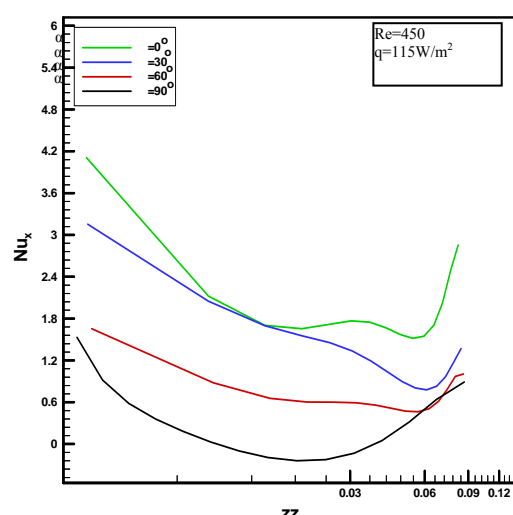


Fig.(13): Experimental Local Nusselt number Versus Dimensionless Axial Distance for Various Angles, $Re=450$, $q=115\text{W/m}^2$

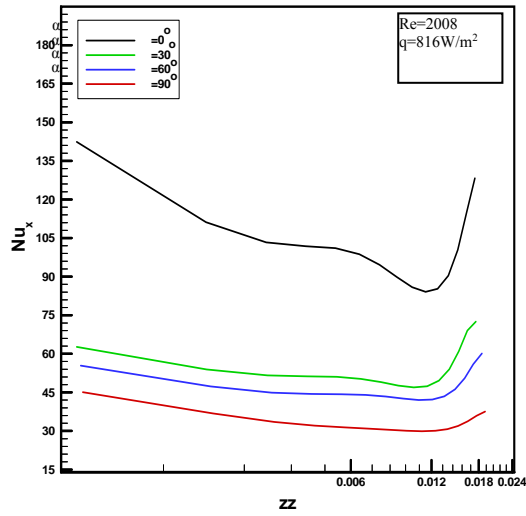


Fig.(14): Experimental Local Nusselt number Versus Dimensionless Axial Distance for Various Angles, $Re=2008$, $q=816W/m^2$

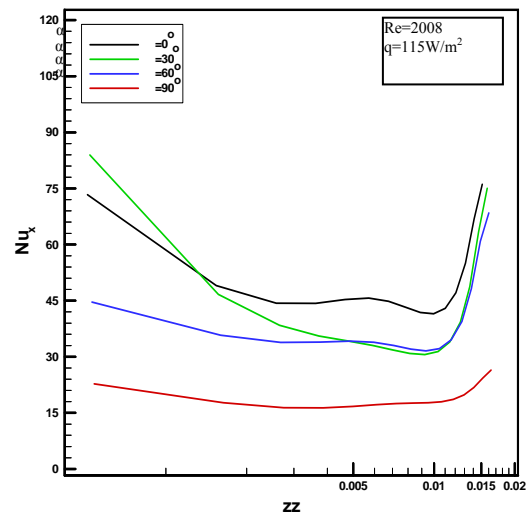


Fig.(15): Experimental Local Nusselt number Versus Dimensionless Axial Distance for Various Angles, $Re=2008$, $q=115W/m^2$

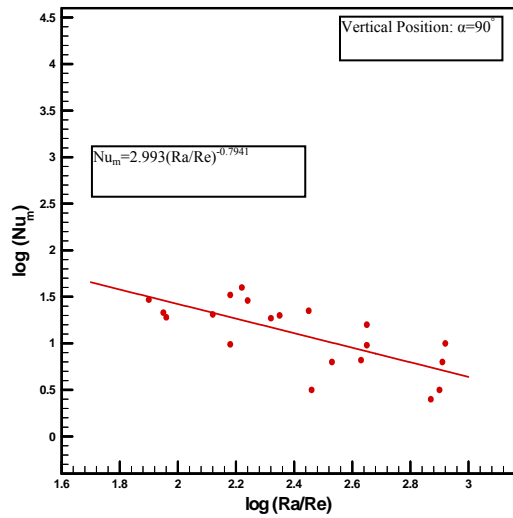


Fig.(16): Experimental Average Nusselt number Versus Ra/Re For $\alpha = 90^\circ$ (Vertical Position).

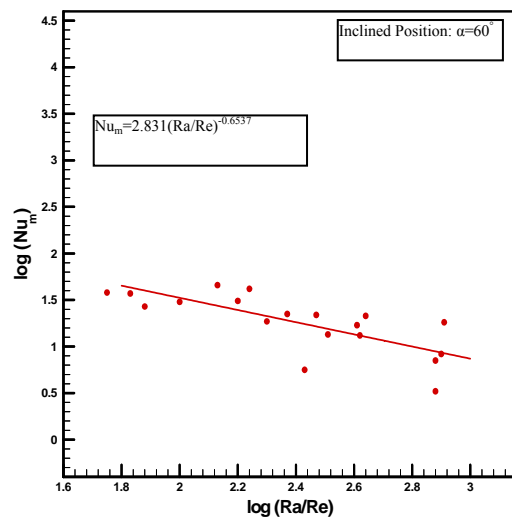


Fig.(17): Experimental Average Nusselt number Versus Ra/Re For $\alpha = 60^\circ$ (Inclined Position).

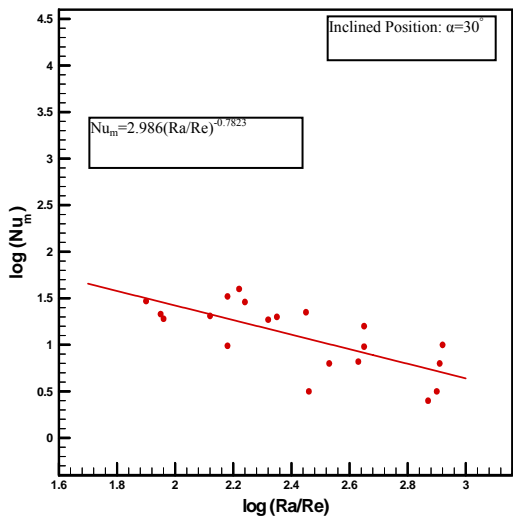


Fig.(18): Experimental Average Nusselt number Versus Ra/Re For $\alpha = 30^\circ$ (Inclined Position).

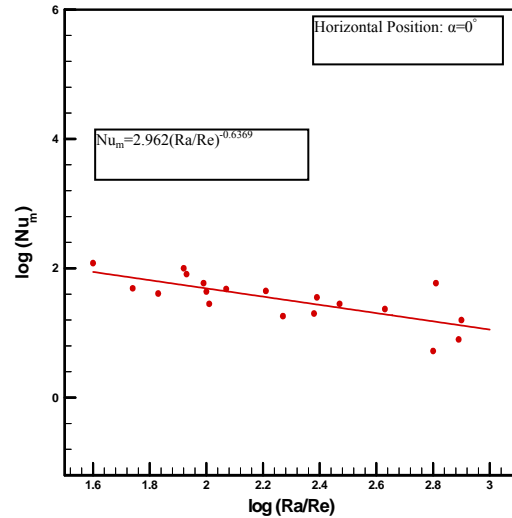


Fig.(19): Experimental Average Nusselt number Versus Ra/Re For $\alpha = 0^\circ$ (Horizontal Position).

**NOMENCLATURE****Latin Symbols:**

Symbol	Description	Unit
A_c	Cylinder cross section area	(m ²)
A_s	Cylinder surface area	(m ²)
C_p	Specific heat at constant pressure	(J/Kg.°C)
D_h	Hydraulic diameter	(m)
G	Gravitational acceleration	(m/s ²)
H	Coefficient of heat transfer	(W/m ² .°C)
I	Current	(amp)
K	Thermal conductivity	(W/m ² .°C)
K_a	Thermal conductivity of asbestos	(W/m ² .°C)
L	Cylinder length	(m)
V_i	Volumetric flow rate	(m ³ /s)
Q_c	Convection heat flux	(W/m ²)
Q_{cond}	Conduction heat loss	(W)
Q_t	Total heat given	(W)
r_i	Inner radius of cylinder	(m)
r_o	The distance from center of cylinder to the outer lagging surface	(cm)
r_{is}	The distance from center of cylinder to the beginning lagging (radius of outer cylinder surface)	(cm)
t_b	Bulk air temperature	(°C)
t_f	Mean film air temperature	(°C)
t_i	Air temperature at cylinder entrance	(°C)
t_s	Cylinder surface temperature	(°C)
v	Voltage	(Volt)
x	Axial coordinate	(m)

Creek:

α	cylinder Inclined angle	(degree)
μ	Dynamic viscosity	(Kg/m.s)
ν	Kinematics viscosity	(m ² /s)
P	Air density at any point	(Kg/m ³)

Subscript:

$^{\circ}$	Degree
x	Local
m	Average

Dimensionless Gropes:

Gr	Grashof number	$\frac{g\beta(t_s - t_b)D_h^3}{\nu^2}$
Nu	Nusselt number	$\frac{hD_h}{k}$
Pr	Prandtal number	$\frac{\mu C_p}{k}$
Ra	Rayligh number	$Gr.Pr$
Re	Reynolds number	$\frac{u_i D_h}{\nu}$
Ri	Richardson number	$\frac{Gr}{Re^2}$
ZZ	Axial distance	$x/Re.Pr.D_h$

DESIGN OPTIMIZATION OF SERIAL ROBOT MANIPULATOR

Dr. Ahmed A.A.
Univ. of Baghdad
College of Eng.

MS.c Alyaa H.A
Univ. of Baghdad
College of Eng.

ABSTRACT

Optimal design of three links and four links serial manipulator involves striking a balance between an appropriate link length, radius, link exact end effector deflection and the amount of stress induced in each link. Optimization has been applied for getting a minimum robot weight through making the robot arm section tapered while keeping the first link as cylindrical tube as it represent the robot base only. The synthesis optimization problem involves setting up guess values for links length and radius subjected to constraints of deflection, stress and geometric constraints of total robot length. The optimization process focuses on minimization of robot weight as an objective function, the guess values has taken from three links manipulator and the industrial robot as four links serial manipulator. The results of optimization has been plotted and represented through the different relations between the design parameters (Link radius, length and total robot deflection, total robot weight, stress...etc). The results shows a good agreement minimizing the total deflection to $(2 \times 10^{-5} \text{ m})$ with this degree of precision an optimum design features may be obtained that gives a robot structure with high stiffness and minimum weight that enables the robot to do its tasks with minimum inertia effect.

الخلاصة

التصميم الهندسي الأمثل لنظام الاذرع الآلية لنوعين من الروبوت ذو ثلاثة أذرع والآخر ذو أربعة أذرع يتضمن الاختيار الأمثل لطول وقطر الذراع مع السيطرة على مقدار التشوه الكلي الحاصل للروبوت ومقدار الأجهاد المتولد في كل ذراع. تم تطبيق الأمثلية للحصول على اخف وزن ممكن للروبوت من خلال جعل مقطع ذراع الروبوت مسلوب مع ابقاء الذراع الأول اسطواناني بما أنه يمثل قاعدة الروبوت فقط، تمت عملية الأمثلية من خلال اعطاء قيم أولية لكل من طول ونصف قطر الأذرع مأخوذة من نوعين من الروبوت أحدهما يمثل روبوت ذو ثلاثة أذرع أما الآخر يمثل روبوت ذو أربعة أذرع وتم تمثيل نتائج الأمثلية بيانياً من خلال العلاقات المختلفة بين الأبعاد (نصف القطر، الطول) والتشوه الكلي والوزن والأجهاد... إلخ تم تمثيلها خلال هذا العمل والتي تظهر ان الهدف من العمل قد تحقق. النتائج أظهرت نسبة توافق عند قيمة التشوه (2×10^{-5}) حيث مثلت هذه القيمة النتيجة المثلى للتصميم التي أعطت لهيكل الروبوت المتانة العالية مع الوزن الأقل مما يمكن الروبوت من تأدية مهامه بصورة مثالية.

Introduction

Optimal design of robots is important as it influences the system performance such as the cost of manufacturing, accuracy, related deflection and so on.

Ever since the robotic manipulators were introduced in the automation industry, robotic manipulators have been refined to have better energy efficiency, faster operation and higher

payload to arm weight ratio. These technical goals have been achieved up to a certain levels by designing the low inertia and stiff structure is relative to the motion speed and control accuracy. The dynamic effect of the payload is much larger in the light weight flexible manipulators than in the conventional rigid manipulators. One of the main points of designing a robust and versatile robot is to develop a solid geometry are the link shape and weight.

Shiakolas et al (2002) made a comparison of three evolutionary optimization approaches which are Simple Genetic Algorithm, Genetic Algorithm Elitism and Differential Evolution for designing serial link robotic manipulators based on task specification and constraints. The design process considered the kinematic, dynamic and structural characteristics of the manipulator links and the end effectors' payload. The objective function was minimizing the torque required to perform the defined motion subject to constraints on link parameters which are length and cross section area. Hollow square section, hollow circular section and hollow rectangular section were considered. The analysis procedure was first defining the problem, the design variables; assign values to all parameters and the constraint vector. The defined values are used in the analysis routines to obtain values for design variables, the design variables are checked for constraints violation and then used in evaluating the objective function.

These evaluations are used in optimization routine where new values for design variables are generated. Differential Evolution Method gives more accurate results than the other two methods.

Matlab Optimization Toolbox was used for simulation for the various sections.

Ceccarelli et al (2005) presented a design procedure for manipulators both of serial and parallel architectures taking into account the several aspects and behaviors for optimum solutions both in design and optimization.

The optimality criteria are focused on the well organized main aspects of workspace, singularity and stiffness. Optimality criteria and computational aspects have been elaborated by taking into account the peculiarity and constraints of each other.

Multi objective function of workspace position, workspace orientation, velocity response, static behavior and the angular compliant displacements is presented and solved by the numerical technique which is advised for solving the proposed multi objective optimization problem.

A six degree of freedom PUMA- like manipulator has been considered to test the engineering feasibility of the optimum design of manipulators as specifically applied to serial architecture.

The CaPaMan manipulator has been considered to test the engineering feasibility of the optimum design of manipulators as specifically applied to parallel architectures.

J.P.Merlet(2002) presents a dimensional synthesis approach based on the design requirements that

allows one to obtain almost all the feasible design solutions that are guaranteed to satisfy the requirements. The research presents (The Parameters Space Approach) as the design methodology consist of defining the parameters space as a n-dimensional space in which each dimension corresponds to one of the n-design parameters of the robot and a list of requirements that define minimal or maximal allowed values of some robots performances (such as accuracy, stiffness,...) or some required properties. The methodology is applied to the micro-robot MIPS for medical application and it implemented in C++ using BIAS/profil package.

Edward Mebarak (2003) addressed the optimal design of robots which are designed for minimum weight, which still withstand the highest levels of allowable stresses while carrying design payload. A commercial robot (Schilling robot) was analyzed as a case study, implementing an automated interaction between the Matlab and Pro/Engineer software packages was made that the optimization was carried out within Matlab, and the optimal design results were automatically shipped to Pro/Engineer to regenerate the three dimensions graphical representation of the final robot design.

An evaluation for optimal design of robotic manipulators to achieve high stiffness to weight ratio, this had been done through making the links of robot tapered to minimize its weight and also to make full use of the metal used in the construction of the robot links. The effect of varying the dimension of the robot structure had been addressed in this work to find its effect on the total deflection of the end point effectors. This work presents a geometric design of serial robot manipulator through optimizing link parameters which are length and radius so that the robot weight is minimized while keeping the link deflection and stress at acceptable design limits, this had been achieved through making the link cross section tapered along its length. A flow chart of optimization technique used in this work is shown in fig (1).

Theoretical Analysis

Types of robots studied in this work are three links and four links manipulator where the first link is considered as cylindrical tube while the other links are tapered cylinders, the four links manipulator is shown in fig(2), all tubes have a constant thickness.



The Load that the robot will manipulate is assumed to be a concentrated at the free end of the last manipulator link.

Manipulator's link section is circular which has radius(r) and thickness (t),

Where:

r: Distance from Neutral Axis to the Inside Surface

I: Second Moment of Area of Link's Cross Section

The second moment of area of link's cross section is shown in fig (3)

$$I_x = \int_0^{2\pi} (r^2 \sin^2 \theta) r t d\theta$$

$$I_x = \int_0^{2\pi} r^3 t \sin^2 \theta d\theta$$

$$I_x = r^3 t \int_0^{2\pi} \sin^2 \theta d\theta$$

$$I_x = \pi r^3 t \quad (1)$$

Calculation of Maximum Deflection due to Concentrate Load

$$M_{AA} = EI \frac{d^2 y}{dx^2}$$

$$M_{AA} = Px$$

$$\therefore EI \frac{d^2 y}{dx^2} = Px$$

$$I = \pi r^3 t \quad \text{See Eq(1)}$$

$$\therefore E \frac{dy}{dx} = P \int \frac{x dx}{\pi r^3 t}$$

As the relation between moment and length of the section is relation of square root of the length(x) so this function is approximated to straight line this means that the end diameter of manipulator arm section will be half of the diameter of the other end.

$$r = \frac{R}{2} \left(1 + \frac{x}{L} \right)$$

$$\therefore E \frac{dy}{dx} = \frac{8P}{\pi R^3 t} \int \frac{x dx}{\left(1 + \frac{x}{L} \right)^3}$$

$$E \frac{dy}{dx} = \frac{8P}{\pi R^3 t} \left[\frac{-x}{2 \left(1 + \frac{x}{L} \right)^2} - \frac{L^2}{2 \left(1 + \frac{x}{L} \right)} + \frac{3L^2}{8} \right]$$

$$Ey = \frac{8P}{\pi R^3 t} \int \left[\frac{-xL}{2 \left(1 + \frac{x}{L} \right)^2} - \frac{L^2}{2 \left(1 + \frac{x}{L} \right)} + \frac{3L^2}{8} \right] dx$$

$$Ey = \frac{8P}{\pi R^3 t} * \left[\frac{xL^2}{2 \left(1 + \frac{x}{L} \right)} - L^3 \ln \left| 1 + \frac{x}{L} \right| + \frac{3L^2}{8} x + 0.068147L^3 \right] \quad (2)$$

$$y = y_{\max} \quad \text{at} \quad x = 0$$

$$y_{\max} = 0.54517 \frac{PL^3}{\pi ER^3 t} \quad (3)$$

Calculations of Maximum Deflection due to Link's Weight

The center of the tapered section occurs at distance of $\left(\frac{4}{9}x \right)$ from the first end, thus the weight is centered at this distance.

$$M_{AA} = EI \frac{d^2 y}{dx^2}$$

$$M_{xx} = W \frac{4}{9} x$$

$$\therefore EI \frac{d^2 y}{dx^2} = \frac{4}{9} Wx$$

$$W = \rho Vg$$

$$V = \frac{\pi R t \sqrt{L^2 + \frac{R^2}{4}}}{2L} \left[x \left(1 + \frac{x}{L} \right) + x \right]$$

$$\therefore W = \frac{\pi \rho g R t \sqrt{L^2 + \frac{R^2}{4}}}{2L} \left[x \left(1 + \frac{x}{L} \right) + x \right]$$

$$I = \pi r^3 t$$

$$I = \frac{\pi R^3 t}{8} \left(1 + \frac{x}{L} \right)^3 \quad (4)$$

$$E \frac{d^2 y}{dx^2} = \frac{4 \pi \rho g R t \sqrt{L^2 + \frac{R^2}{4}}}{18L}$$

$$\frac{8}{\pi R^3 t \left(1 + \frac{x}{L} \right)^3} \left[x \left(1 + \frac{x}{L} \right) + x \right] x$$

$$E \frac{d^2 y}{dx^2} = \frac{16 \rho g \sqrt{L^2 + \frac{R^2}{4}}}{9 R^2 L} \left[x \left(1 + \frac{x}{L} \right) + x \right] \frac{x}{\left(1 + \frac{x}{L} \right)^3}$$

$$\text{let } \frac{16 \rho g \sqrt{L^2 + \frac{R^2}{4}}}{9 R^2 L} = \text{const.}$$

$$E \frac{dy}{dx} = \text{const.} \int \frac{x \left[x \left(1 + \frac{x}{L} \right) + x \right]}{\left(1 + \frac{x}{L} \right)^3} dx$$

$$E \frac{dy}{dx} = \text{const.} \left[\int \frac{x^2 dx}{\left(1 + \frac{x}{L} \right)^2} + \int \frac{x^2 dx}{\left(1 + \frac{x}{L} \right)^3} \right]$$

$$\therefore E \frac{dy}{dx} = \text{const.} \left[\frac{-x^2 L}{\left(1 + \frac{x}{L} \right)} + 2xL^2 - 2L^3 \ln \left| 1 + \frac{x}{L} \right| - \frac{x^2 L}{2 \left(1 + \frac{x}{L} \right)^2} + \frac{L^3}{\left(1 + \frac{x}{L} \right)} + L^3 \ln \left| 1 + \frac{x}{L} \right| - 1.18185 L^3 \right]$$

$$Ey = \text{const.} \int \left[\frac{-x^2 L}{\left(1 + \frac{x}{L} \right)} + 2xL^2 - L^3 \ln \left| 1 + \frac{x}{L} \right| - \frac{x^2 L}{2 \left(1 + \frac{x}{L} \right)^2} + \frac{L^3}{\left(1 + \frac{x}{L} \right)} - 1.18185 L^3 \right] dx$$

$$\therefore y = \frac{16 \rho g \sqrt{L^2 + \frac{R^2}{4}}}{9 E R^2 L} \left[2L^4 \left(1 + \frac{x}{L} \right) - \frac{L^4}{2} \left(1 + \frac{x}{L} \right)^2 - L^4 \ln \left| 1 + \frac{x}{L} \right| + x^2 L^2 - L^3 x \ln \left| 1 + \frac{x}{L} \right| \right]$$

$$L^3 x - L^4 \ln \left| 1 + \frac{x}{L} \right| + \frac{x^2 L^2}{2 \left(1 + \frac{x}{L} \right)} - x L^3$$

$$+ L^4 \ln \left| 1 + \frac{x}{L} \right| + L^4 \ln \left| 1 + \frac{x}{L} \right| - 1.181815 L^3 x - 1.375 L^4$$

$$y = y_{\max} \quad \text{at} \quad x=0$$

$$y_{\max} = \frac{2 \rho g L^3 \sqrt{L^2 + \frac{R^2}{4}}}{9 E R^2} \quad (5)$$

Calculation of Maximum Deflection of Robot Link due to Moment

$$M_{AA} = EI \frac{d^2 y}{dx^2}$$

$$M_{AA} = M_o$$



$$EI \frac{d^2 y}{dx^2} = M_o$$

$$E \frac{dy}{dx} = \frac{8M_o}{\pi R^3 t} \int \frac{dx}{\left(1 + \frac{x}{L}\right)^3}$$

$$E \frac{dy}{dx} = \frac{8M_o}{\pi R^3 t} \left[\frac{-L \left(1 + \frac{x}{L}\right)^{-2}}{2} + \frac{L}{8} \right]$$

$$E \frac{dy}{dx} = -\frac{4M_o L}{\pi R^3 t \left(1 + \frac{x}{L}\right)^2} + \frac{M_o L}{\pi R^3 t}$$

$$Ey = \frac{4M_o L^2}{\pi R^3 t \left(1 + \frac{x}{L}\right)} + \frac{M_o L}{\pi R^3 t} x - \frac{3M_o L^2}{\pi R^3 t}$$

$$y = y_{\max} \text{ at } x = 0$$

$$y_{\max} = \frac{M_o L^2}{\pi E R^3 t} \quad (6)$$

Robot Manipulator Links Equations

The system of forces applied on the robot Links are shown in Fig (4)

Where:

m_1, m_2, m_3, m_4 = Masses of Gear Boxes (kg)

W_1, W_2, W_3, W_4 = Weight of Each Arm (N)

L_1, L_2, L_3, L_4 = Length of Each Arm (m)

W_{Load} = Manipulated load (N)

f_1, f_2, f_3, f_4 = Reaction forces at the Joints (N)

$M_{O1}, M_{O2}, M_{O3}, M_{O4}$ = Reaction Moment at the Joints (N.m)

Fourth Arm

The Fourth arm section and its system of forces are shown in Fig (12)

$$W_4 = \rho V g$$

$$W_4 = \frac{3}{2} \pi \rho g t R_4 \sqrt{L_4^2 + \frac{R_4^2}{4}} \quad (7)$$

$$\sigma = \frac{My}{I}$$

$$\sigma \leq \sigma_{\text{allowable}}$$

$$\sigma_4 = \frac{M_{O4}(R_4 + t)}{\pi R_4^3 t} \quad (8)$$

$$M_{O4} = W_{\text{load}} L_4 + W_4 \left(\frac{4}{9} L_4 \right) + m_4 g L_4 \quad (9)$$

$$f_4 = W_4 + W_{\text{load}} + m_4 g \quad (10)$$

δ_4 = Deflection of Fourth Arm

$$\delta_4 = \delta_{\text{arm weight}} + \delta_{\text{load}}$$

$$\delta_4 = \frac{2\rho g \sqrt{L_4^2 + \frac{R_4^2}{4}}}{9ER_4^2} L_4^3 + \frac{0.54517L_4^3}{\pi ER_4^3 t} (W_{\text{Load}} + m_4 g) \quad (11)$$

Third Arm

$$W_3 = \frac{3}{2} \pi \rho g t R_3 \sqrt{L_3^2 + \frac{R_3^2}{4}} \quad (12)$$

$$\sigma_3 = \frac{M_{O3}(R_3 + t)}{\pi R_3^3 t} \quad (13)$$

$$M_{O3} = f_4 L_3 + W_3 \left(\frac{4L_3}{9} \right) + m_3 g L_3 + M_{O4} \quad (14)$$

$$f_3 = W_3 + f_4 + m_3 g \quad (15)$$

$$\delta_3 = \delta_{\text{arm weight}} + \delta_{\text{load}} + \delta_{\text{moments}}$$

$$\delta_3 = \frac{2\rho g \sqrt{L_3^2 + \frac{R_3^2}{4}}}{9ER_3^2} L_3^3 + \frac{0.54517L_3^3}{\pi ER_3^3 t} + \frac{M_{O4}L_3}{\pi ER_3^3 t} \quad (16)$$

Second Arm

$$W_2 = \frac{3}{2} \pi \rho g t R_2 \sqrt{L_2^2 + \frac{R_2^2}{4}} \quad (17)$$

$$\sigma_2 = \frac{M_{O2}(R_2 + t)}{\pi R_2^3 t} \quad (18)$$

$$M_{O2} = f_3 L_2 + W_2 \left(\frac{4L_2}{9} \right) + m_2 g L_2 + M_{O3} \quad (19)$$

$$f_2 = W_2 + f_3 + m_2 g \quad (20)$$

$$\delta_2 = \delta_{\text{arm weight}} + \delta_{\text{load}} + \delta_{\text{moments}}$$

$$\delta_2 = \frac{2\rho g \sqrt{L_2^2 + \frac{R_2^2}{4}}}{9ER_2^2} L_2^3 + \frac{0.54517(m_2 g + f_3)L_2^3}{\pi ER_2^3 t} + \frac{M_{o3} L_2^2}{\pi ER_2^3 t} \quad (21)$$

First Arm

The dimensions of the first link are calculated by equating the maximum stress induced in it with the maximum allowable stress. This maximum stress is found by the Rankin-Gordon formula which is a combination of the Euler and crushing loads for a strut.

$$\frac{1}{F_R} = \frac{1}{F_e} + \frac{1}{F_c} \quad (22)$$

Where:

F_R : Rankin Load

F_e : Euler Load

F_c : Compressive Load

σ_e : Euler Stress

For very short struts F_e is very large, $\frac{1}{F_e}$ can therefore be neglected and $F_R = F_c$, for very large struts F_e is very small and $\frac{1}{F_e}$ is very large so that $\frac{1}{F_c}$ can be neglected, thus $F_R = F_e$

The Rankin formula is therefore valid for extreme values of slenderness ratios. It is also found to be fairly accurate for the intermediate values.

For a strut with one end free and the other fixed

$$F_e = \frac{\pi^2 EI}{4L^2} \quad (23)$$

$$\sigma_e = \frac{\pi^2 EI}{4L^2 A} \quad (24)$$

The crushing load on the first arm is:

$$f_c = f_1 = f_2 + W_1 + m_1 g \quad (25)$$

$$\sigma_y = \frac{f_c}{A} = \frac{f_1}{A} \quad (26)$$

The final stress σ_1 on the first arm is the sum of direct stress calculated by Rankin formula and that due to bending generated by the exerted moment

$$\therefore \sigma_1 = \sigma_R + \sigma_{\text{bending}} = \frac{\sigma_y}{1 + \frac{\sigma_y}{\sigma_e}} + \frac{M_{o1} \cdot (R_1 + t)}{I_1} \quad (27)$$

$$\delta_1 = \frac{M_{o1} L_1^2}{2E\pi R_1^3 t} \quad (28)$$

Results and Conclusions

A geometric optimization of three and four links serial robot manipulator is addressed in this work, the goal of the optimization was reducing the robot manipulator weight through making the second, third and fourth links tapered while keeping the first link cylindrical. The objective function(robot weight) of the optimization was subjected to several constraints that keep the end effector deflection as minimum as possible and the links stresses at the allowable values, the optimization process is hold on using two software tools which are Mathcad and Matlab Optimization Toolbox, a comparison between results of each tool had been done and are shown in figures, the results shows convergence between both tools with better accuracy and smoothness in results of Matlab Optimization Toolbox. The optimization focused on the links length and radius while the thickness is considered to be constant through the whole robot length.

In the case of three links manipulator, the stress in the third link calculated by (Matlab Optimization Toolbox) is larger than that by Mathcad for the same radius. This is referred to the length of the third link which is longer in the calculated results of (Matlab Optimization Toolbox) than in Mathcad which makes the moment arm longer and therefore increasing the stress. also it is clear that the radius in both methods of calculation begins to approach one another when minimizing the limit of deflection. In the first arm, the stress calculated by (Matlab Optimization Toolbox) is bigger than that by Mathcad although the moment arms ($L_2 + L_3$) are almost equal, this is because the radius of the first link calculated by Mathcad is bigger than that calculated by (Matlab Optimization Toolbox) for



the same total deformation limit. It is clear that the stress in the second link which is calculated by both (Matlab Optimization Toolbox) and Mathcad are so close this is referred to the link radius which is so close in both programs. This can be said also for the third link stress and this referred to the third link length which is so close as calculated by both programs, this make the moment arm almost the same, those results are shown in figures (5-8). the links length effect was more than the links radii effect on the stress values this is referred to the moments values keeping in mind that the moment involves the actuators moment and as the actuator mass is bigger and the link length is long this makes the moment value larger and therefore the stress value increases even though the radius is big.

The sum of robot links length and first link length were considered as constraints in the optimization problem, we chose to fix the first link length because it represent the base in which its section is cylindrical while the optimization is focused on the tapered sections and its effect so we can see that each figure which represent the relation between total links length robot deflection is ended at the same point. We prefer the presentation of the total robot links length rather than each link separately so as to show the change in length of each link corresponding to the other, this can be seen in figures(14-15),it is obvious that the second link length(L_2) calculated by(Matlab Optimization Toolbox) is less than that calculated by Mathcad while the third link length(L_3) calculated by(Matlab Optimization Toolbox) is bigger than that calculated by Mathcad. In the case of four links manipulator, the stress in the first link calculated by(Matlab Optimization Toolbox) is larger than in Mathcad, this is referred to the length of the third and fourth links which are bigger in the calculated results of (Matlab Optimization Toolbox)while the second link length is smaller in the calculated results of (Matlab Optimization Toolbox) ,this make the moment arm bigger and therefore the stress is higher. It can seen that the first and second links radii were the same in figures(16-17) and this may referred to the first link which represent the robot base which handle the maximum part of the robot structure weight in addition to the extra components so the first link is fixed and has no degree of freedom, this makes the robot movement to be done by the other three links and as the second link is the nearest to the first link and it carries reasonable part of the robot movement and transport it to the neighbor links so its dimensions must not differ so much from the

first link. The third link radius calculated by (Matlab Optimization Toolbox) and Mathcad was also so close to each other and there was a little difference for the fourth link radius which proves that the optimization process is reaching the feasible design. This results can be seen in figures (18-19).It can be noticed that the first and fourth links act at the same manner which can be noticed also for the second and third links, even though the values of each link parameters such as (radius, stress, length,...etc.) is different. This may referred to that the first link handle the maximum part of the robot structure weight and the fourth link handle the load capacity which make them related in the weight effect issue and overcome the inertia effect and keeping the deformation at the acceptable range while the second and third links are related in transporting the movement and the power between the robot links and controlling the final robot movement, this can be seen in figures (29-30).

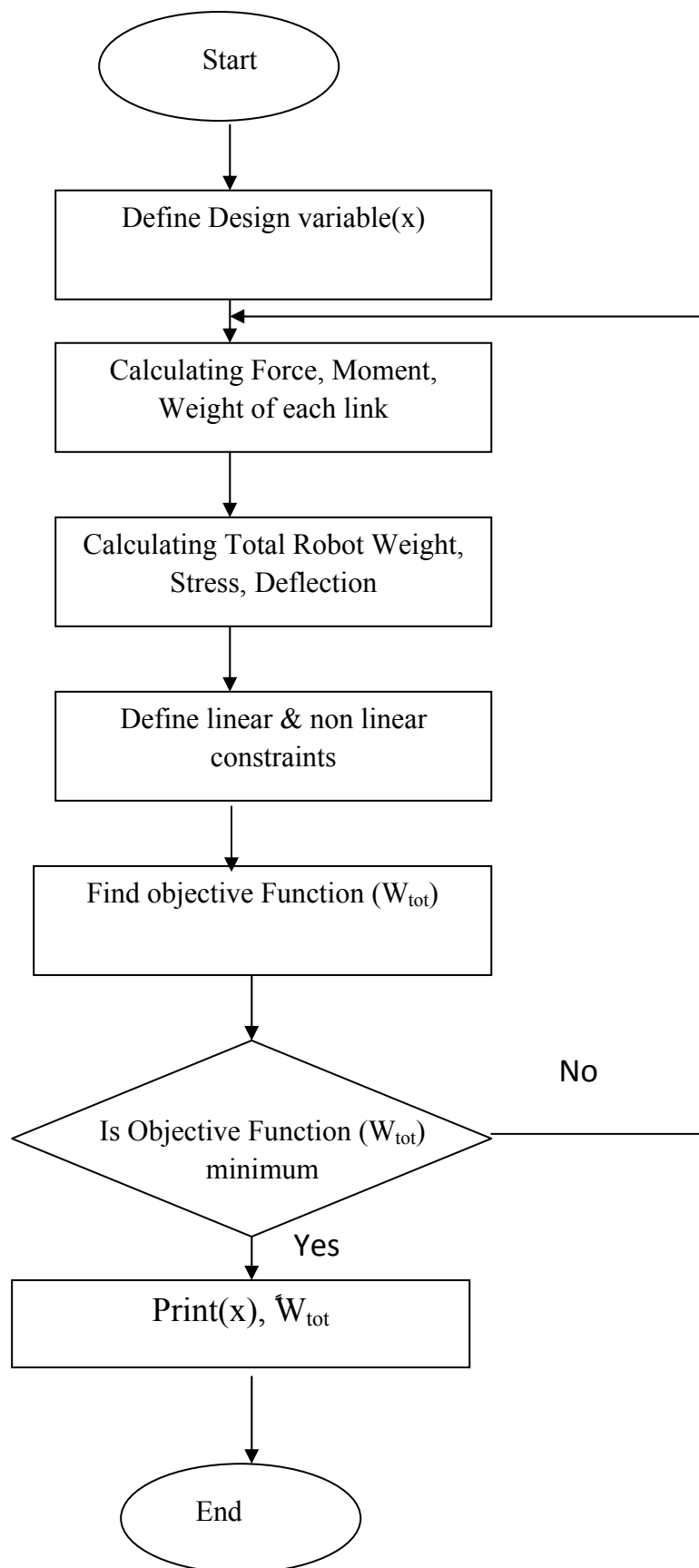
Whenever the deflection was minimized the results of both programs began to approach which shows the optimization process procedure that is having an objective design to get and constraints to keep so the program of optimization is acting like a search engine looking for the feasible area for the designer to start from to get the optimum performance and because of this it has been chosen to run the optimization process through two programs to check our results because any optimization method must lead us to the same result of the other, the difference will be in the accuracy, speed of optimization only.

References

- Chinyere Onwbiko(2000)''Introduction to Engineering Design Optimization'' Prentice-Hall,Inc.
- Ceccarelli, M., Carobone, G. and Ottaviano, E.(2005) "Multi Criteria Optimum Design of Manipulators", Bulletin Technical Sciences Vol.53, No.1, P.P.9-18.
- Edward Mebarak.(2003) "On the Development of an Automated Design Procedure to Design Optimal Robots", M.Sc.Thesis, Florida International University, Miami, Florida.
- Grace A''Optimization Toolbox Users Guide'',The Matlab Works,Inc,1992.
- John, J. Craig. (1989). "Introduction to Robotics Mechanics and Control", Addison-Wesley.

Dr. Ahmed A.A. MS.c Alyaa H.A	Design Optimization of Serial Robot Manipulator
--	--

- Merlet J.P.(2002)''Optimal Design of Robots''INRIA Sophia, Antipolis,France.Robotics and Automation Proceedings,ICRO,IEEE International Conference,Vol 2,PP1149-1154.
- Shiakolas, P. S.; Koladiya, D. and Kebrle, J.(2002) "Optimum Robot Design Based on Task Specifications Using Evolutionary Techniques and Kinematic, Dynamic, and Structural Constraints", International Journal of Inverse Problem in Engineering.Vol.10, No.4, P.P.359-375.

**Fig (1)**

Flowchart of Optimization Problem

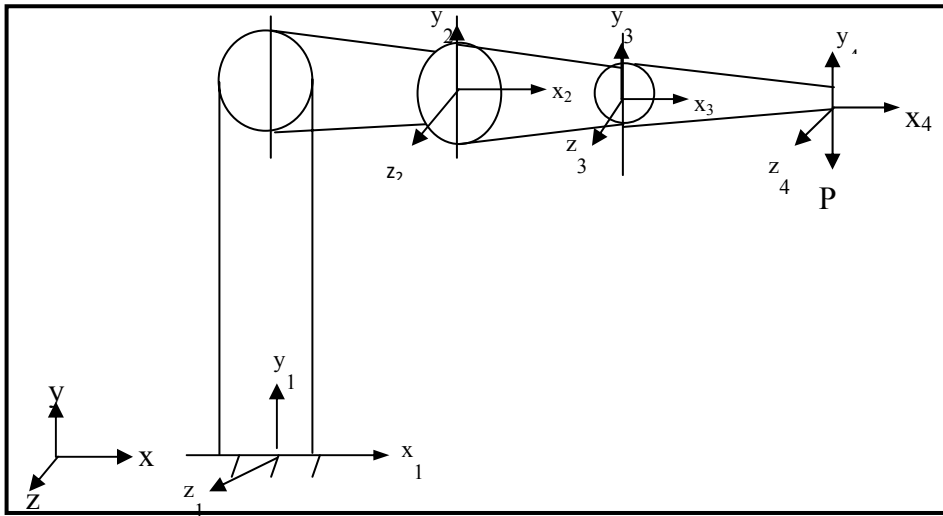


Fig (2) Four Links Manipulator Construction

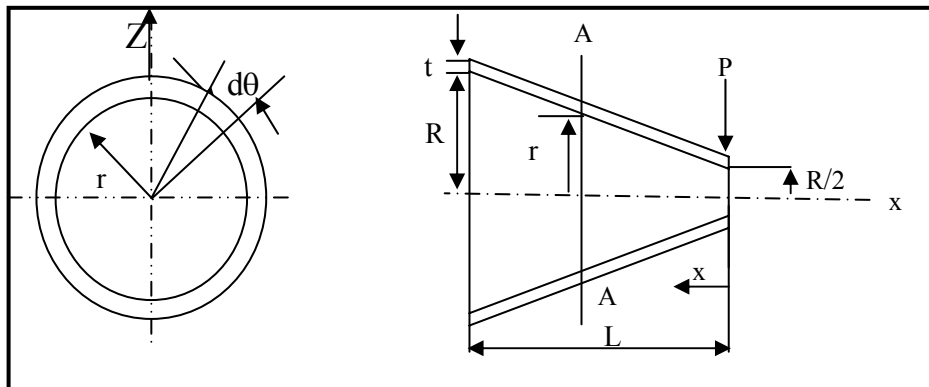


Fig (3) Link Cross Section

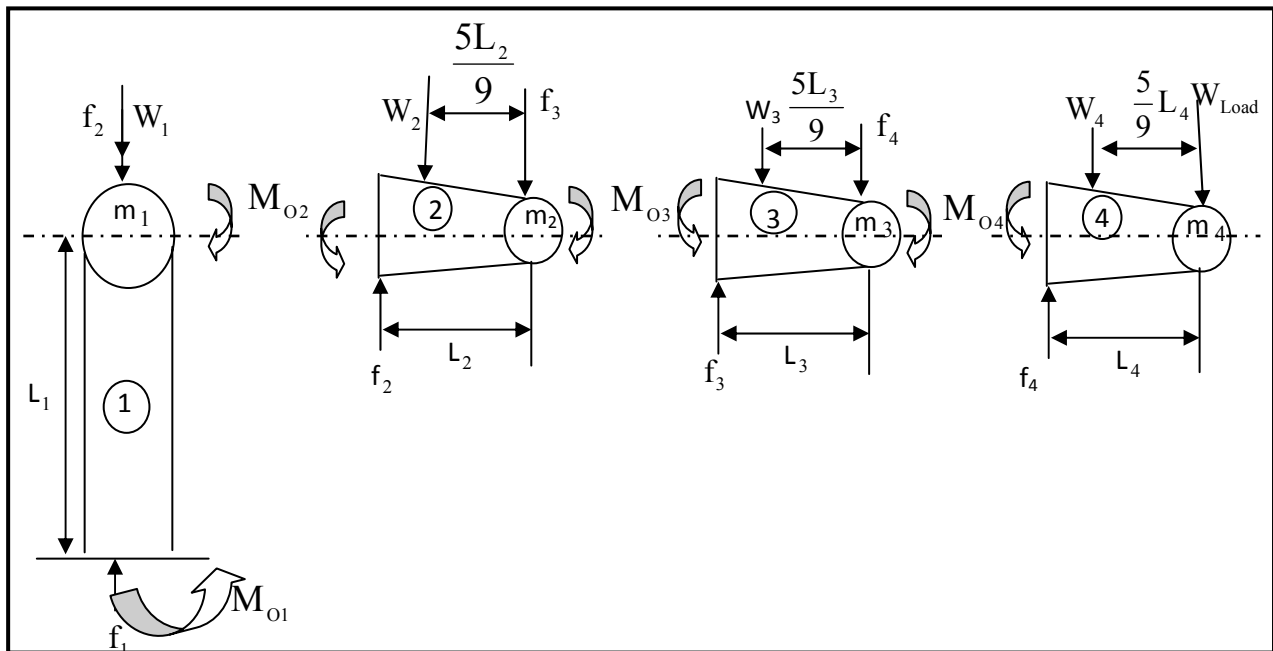
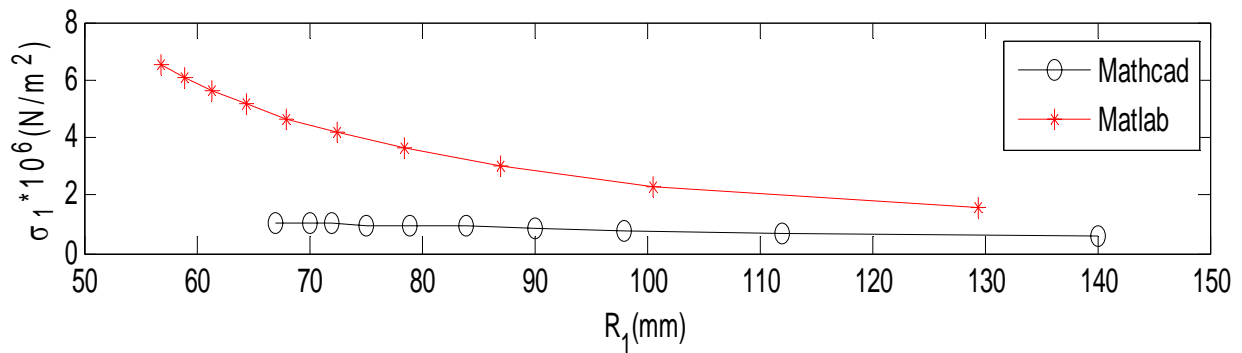
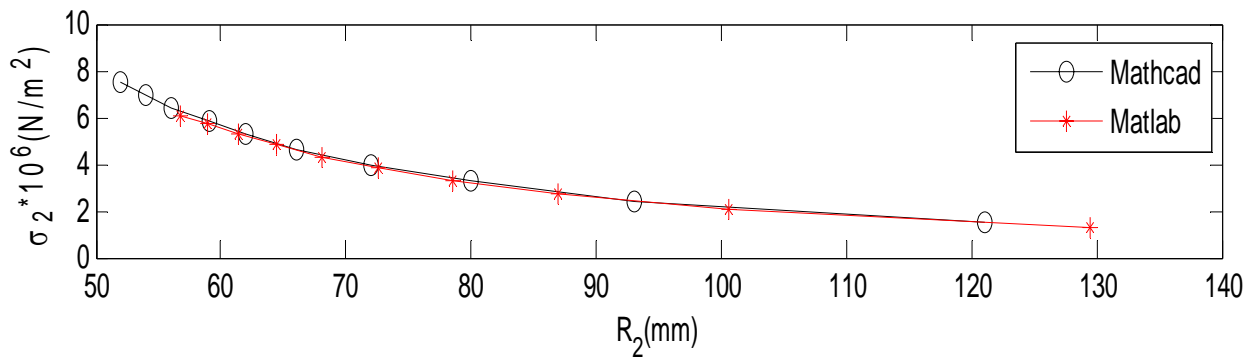


Fig (4) Robot Links Forces System

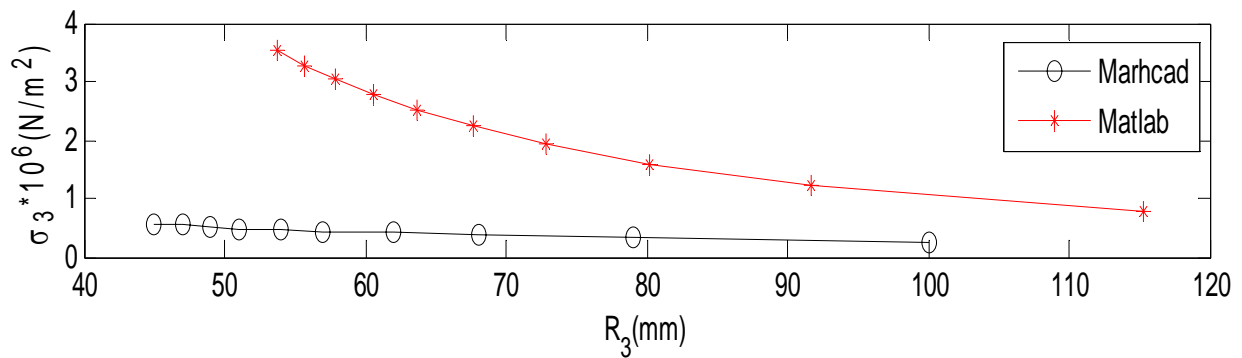
Results of Three Links Manipulator

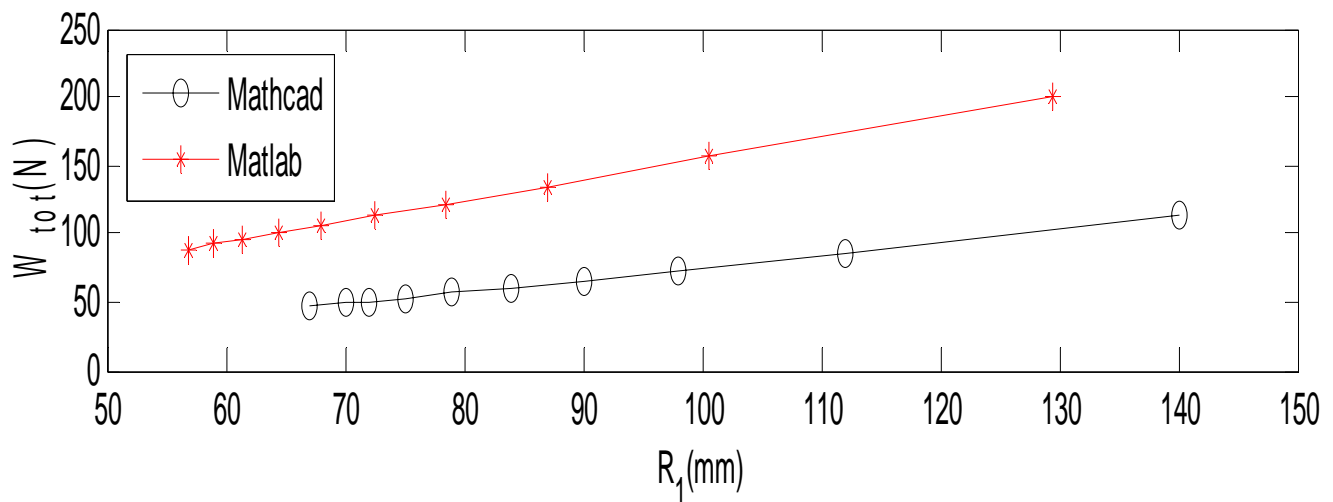
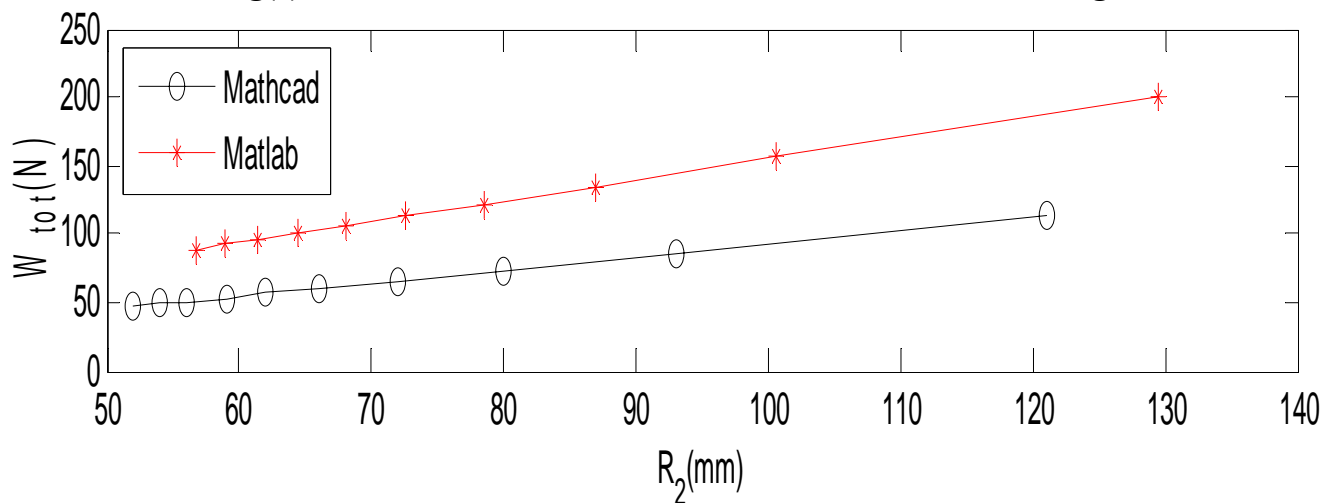
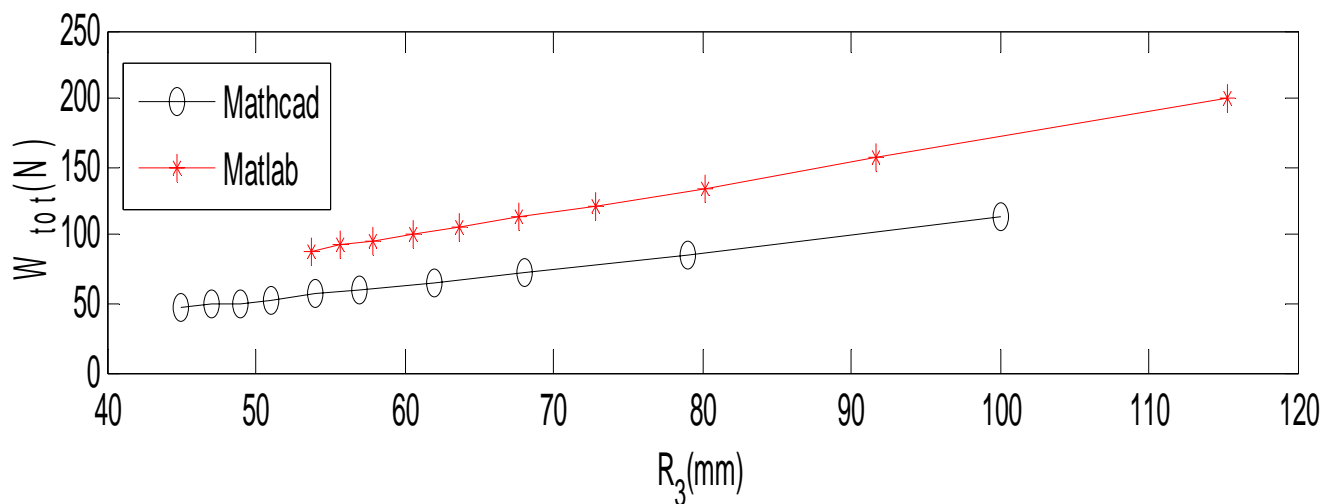


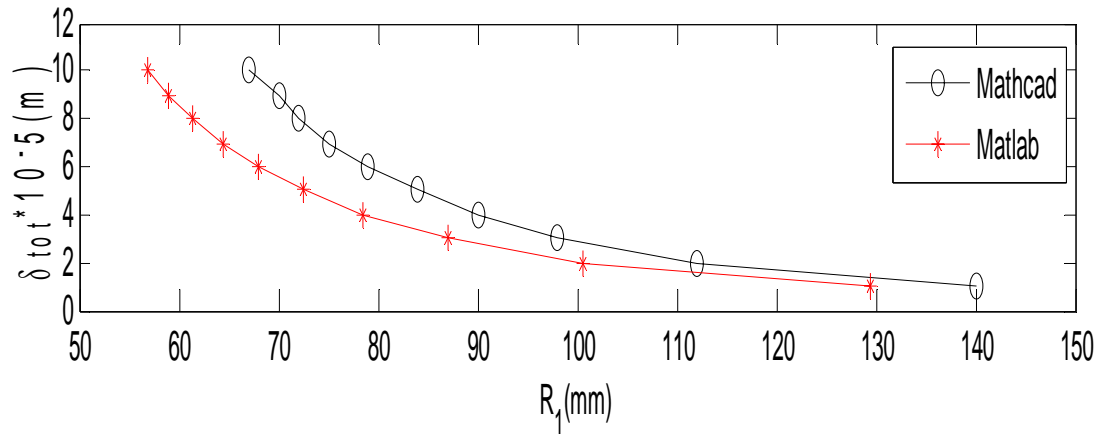
Fig(5) Relation between First Link Radius and its Bending Stress



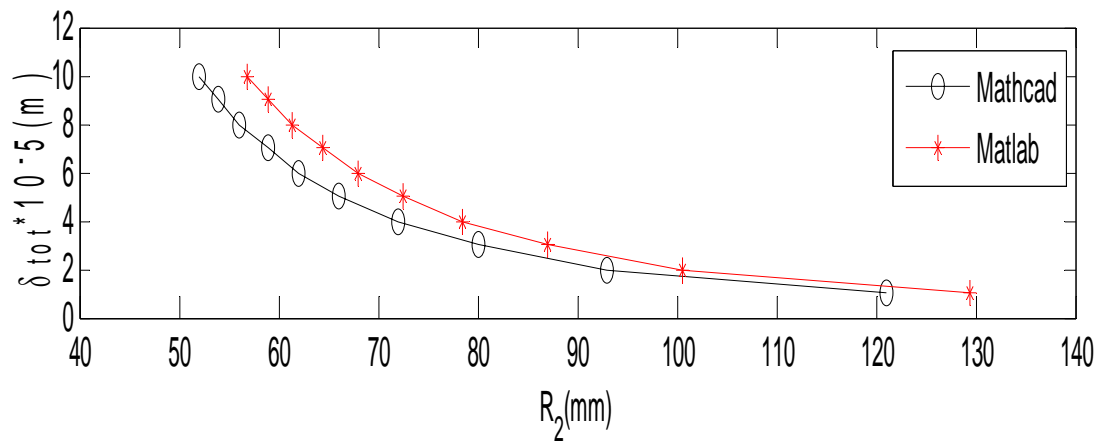
Fig(6) Relation between Second Link Radius and its Stress



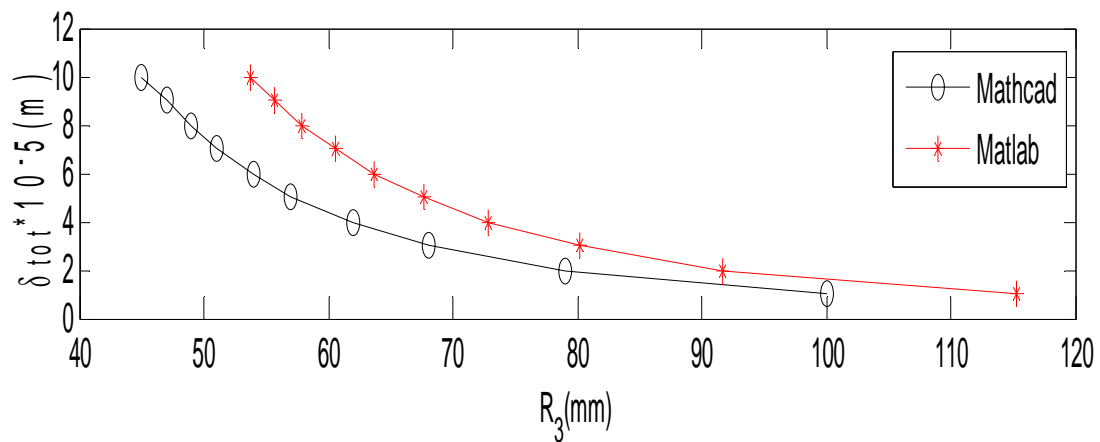
**Fig(8) Relation between First Link Radius and Total Robot Weight****Fig(9) Relation between Second Link Radius and Total Robot****Fig(10) Relation between Third Link Radius and Total Robot Weight**



Fig(11) Relation between First Link Radius and Total Robot



Fig(12) Relation between Second Link Radius and Total Robot Deflection

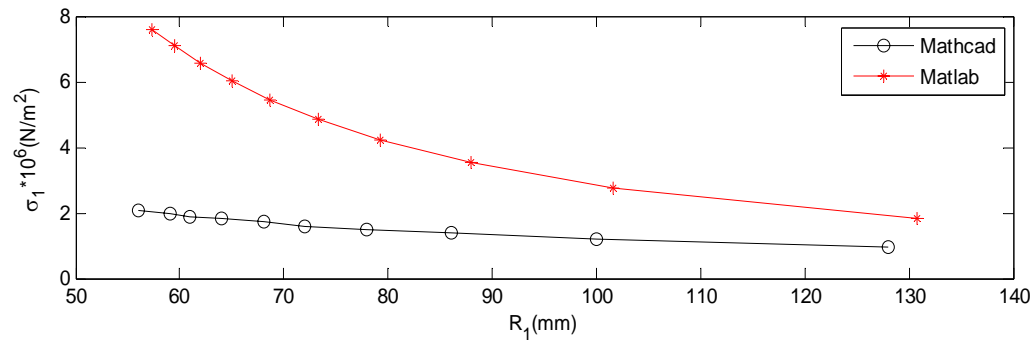


Fig(13) Relation between Third Link Radius and Total Robot

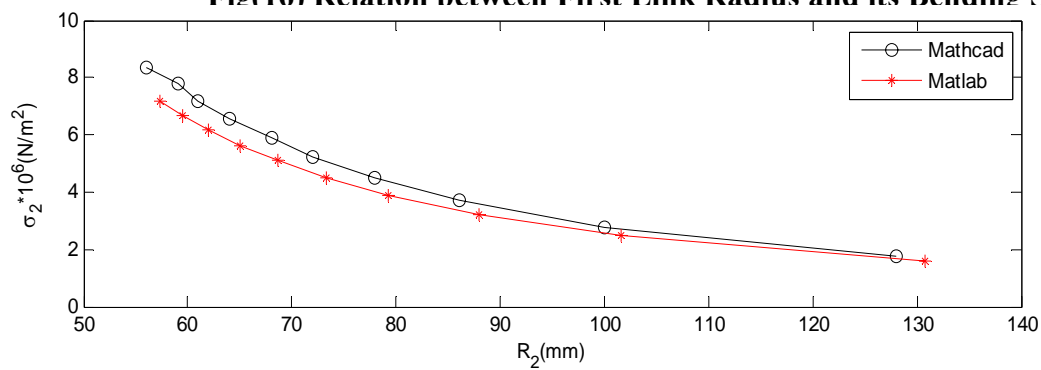
**Table (1) Comparison between Links Length using Matlab Optimization Toolbox and MathCAD for Three****Links Manipulators**

Deflections $\times 10^{-5}(\text{mm})$	Matlab and MathCAD First Link Length (mm)	Matlab Second Link Length (mm)	MathCAD Second Link Length (mm)	Difference (mm)	Matlab Third Link Length (mm)	MathCAD Third Link length (mm)	Difference (mm)
1	475	328	375	-47	502	455	47
2	475	320	373	-53	510	457	53
3	475	316.1	373	-56.9	513.9	457	56.9
4	475	313.6	372	-58.4	516.4	457	58.4
5	475	311.9	372	-60.1	518.1	458	60.1
6	475	310.6	372	-61.4	519.4	458	61.4
7	475	309.5	372	-62.5	520.5	458	62.5
8	475	308.6	371	-62.4	521.4	459	62.4
9	475	307.9	371	-63.1	522.1	459	63.1
10	475	307.2	371	-63.8	522.8	459	63.8

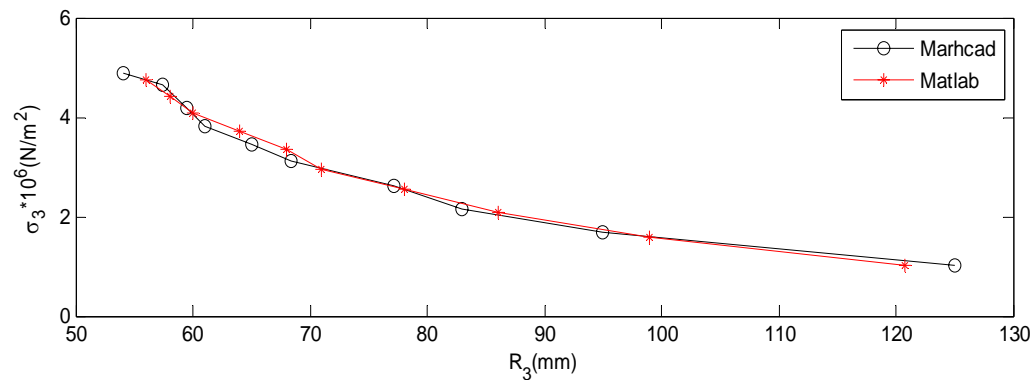
Results of Four Links Manipulator



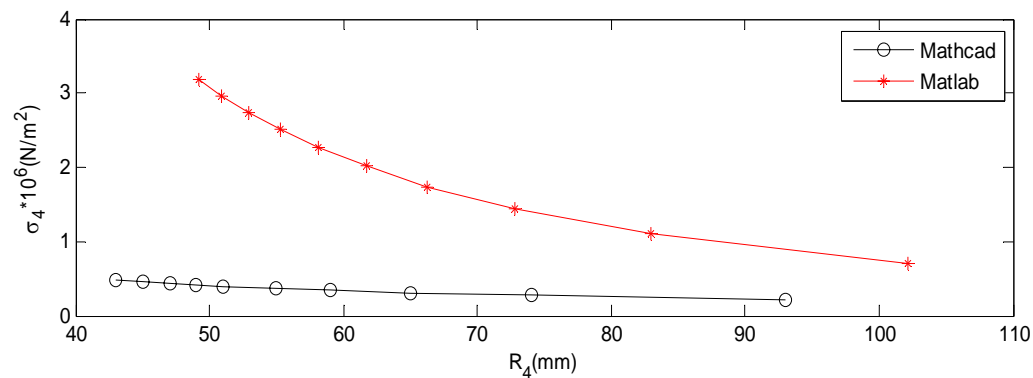
Fig(16) Relation between First Link Radius and its Bending Stress



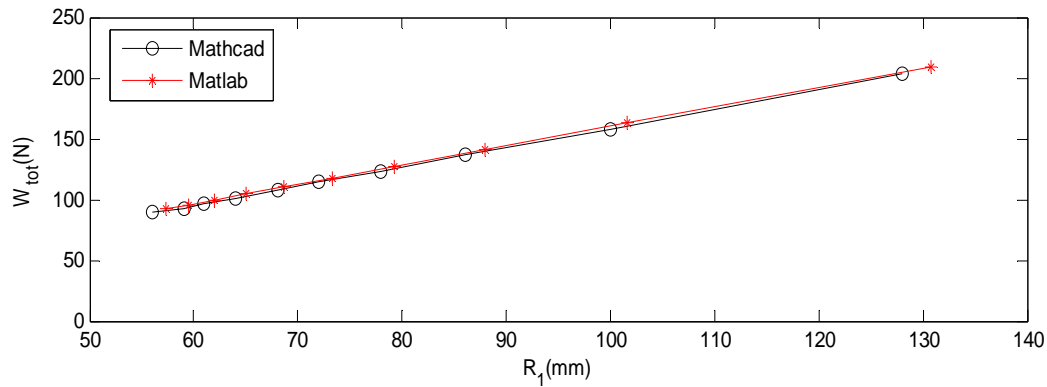
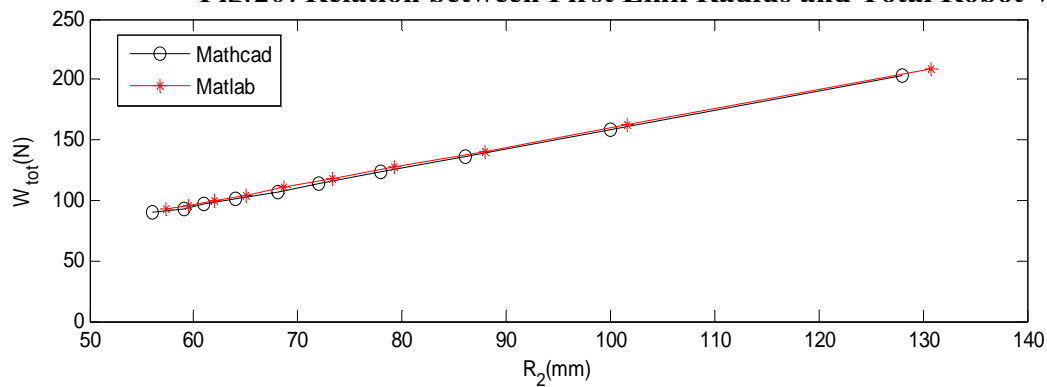
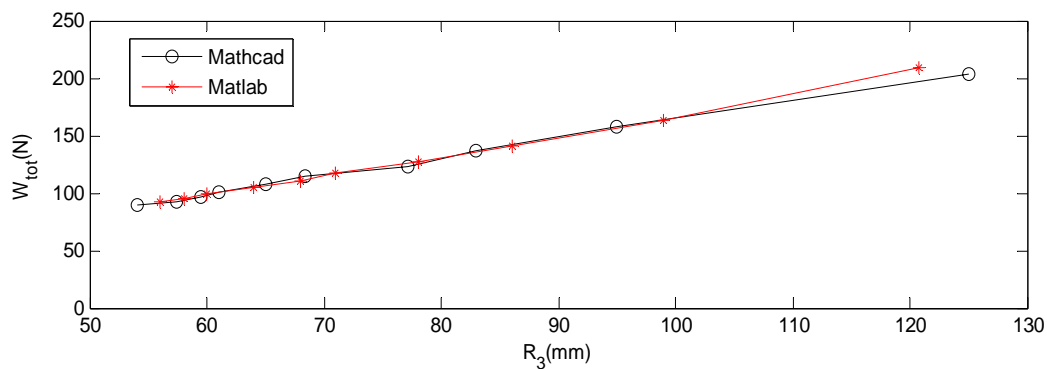
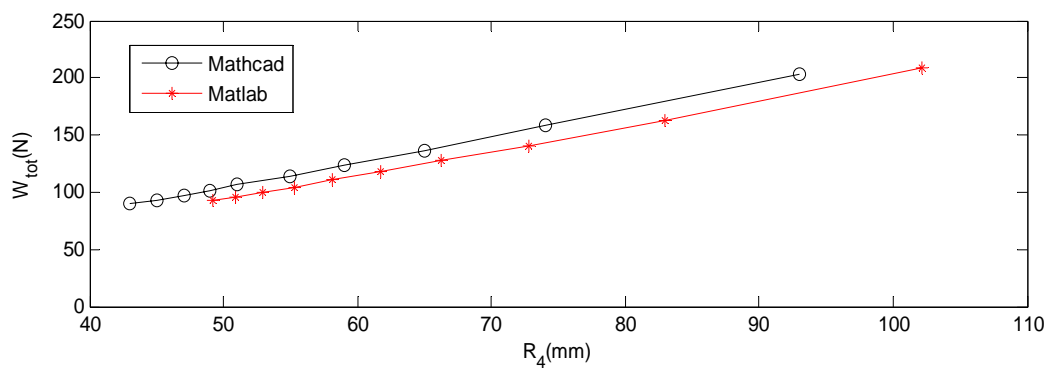
Fig(17) Relation between Second Link Radius and its Bending Stress

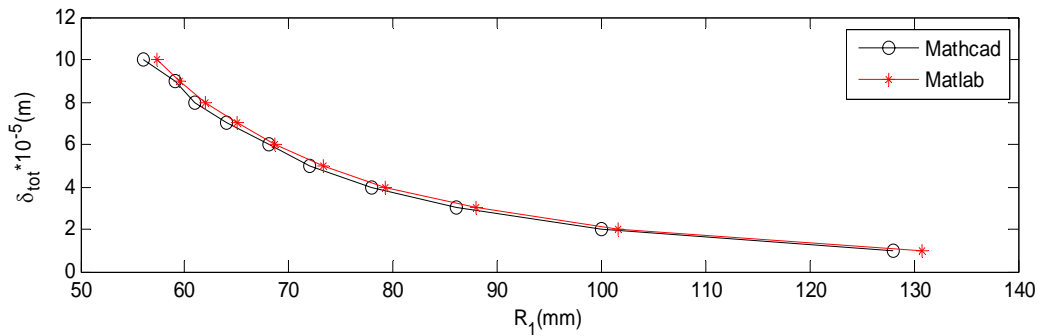


Fig(18) Relation between Third Link Radius and its Bending Stress

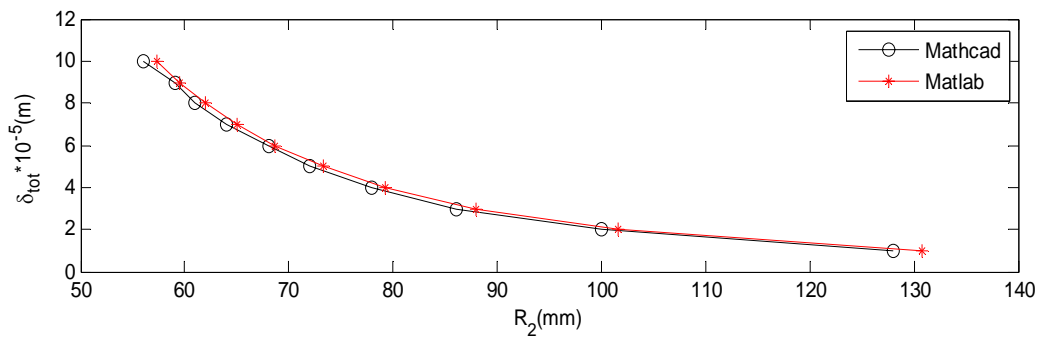


Fig(19) Relation between Fourth Link Radius and its Bending Stress

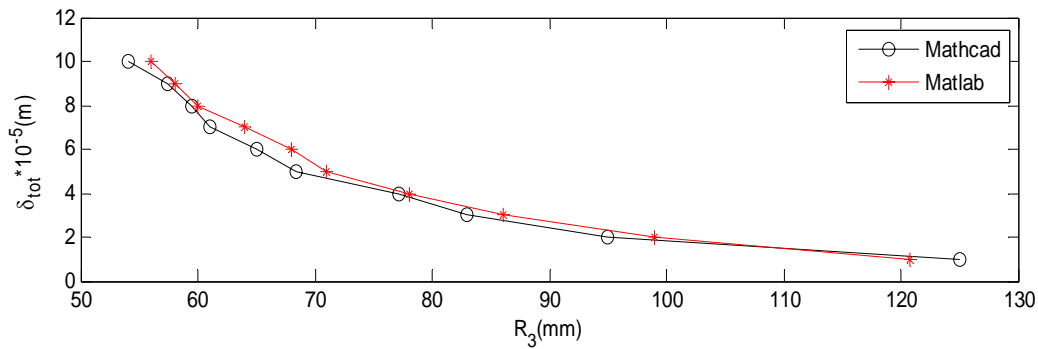
**Fig(20) Relation between First Link Radius and Total Robot Weight****Fig(21) Relation between Second Link Radius and Total Robot Weight****Fig(22) Relation between Third Link Radius and Total Robot Weight****Fig(23) Relation between Fourth Link Radius and Total Robot Weight**



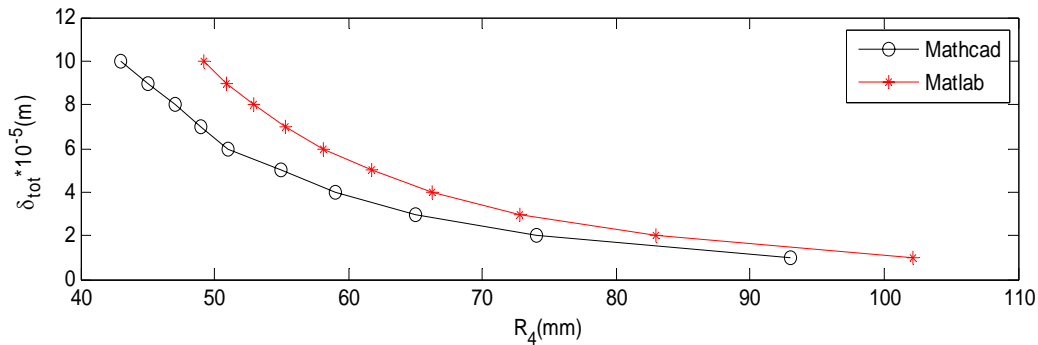
Fig(24) Relation between First Link Radius and Total Robot Deflection



Fig(25) Relation between Second Link Radius and Total Robot Deflection



Fig(26) Relation between Third Link Radius and Total Robot Deflection



Fig(27) Relation between Fourth Link Radius and Total Robot Deflection

**Table(2) Comparison between Links Lengths using Matlab and Mathcad for Four Links Manipulator**

Deflections $\times 10^{-5}$	Matlab and MathCAD First Link Length (mm)	Matlab Second Link Length (mm)	Math CAD Second Link Length (mm)	Difference (mm)	Matlab Third Link Length (mm)	MathCAD Third Link Length (mm)	Difference (mm)	Matlab Fourth Link Length (mm)	MathCAD Fourth Link Length (mm)	Difference (mm)
1	420	229.1	293	-63.9	325.3	323	2.3	425.6	364	61.6
2	420	224.7	30.2	-77.3	319.1	307	12.1	436.2	368	68.2
3	420	222.5	303	-80.5	316	308	8	441.5	369	72.5
4	420	221.2	305	--83.8	314	305	9	444.9	370	74.9
5	420	220.2	306	-85.8	312.6	303	9.6	447.3	371	76.3
6	420	219.4	307	-78.6	311.5	301	10.5	449.1	372	77.1
7	420	218.8	308	-89.2	310.6	301	9.6	450.6	371	79.6
8	420	218.3	309	-90.7	309.9	299	10.9	451.9	372	79.9
9	420	217.8	310	-92.2	309.2	298	11.2	452.9	372	80.9
10	420	217.5	310	-92.9	308.7	297	11.7	453.8	373	80.8

IMPROVEMENT OF A HYDROSTATIC TRANSMISSION CONTROL SYSTEM PERFORMANCE USING RADIAL BASIS NEURAL NETWORK

Dr. Amjad Jalil Humadi
(Lecturer)

University of Technology
Control and Systems Engineering Department

Ayad Qasim Hussein
(Assist. Lecturer)

Foundation of Technical Education
Electrical and Electronics Technical College

Mashaal Matti Farjo
(Assist. Lecturer)

Foundation of Technical Education
Electrical and Electronics Technical College

ABSTRACT

Pump-controlled motors (PCM) are the preferred power elements in most applications because of their high maximum operating efficiency. The dynamics of such hydraulic systems are highly nonlinear and the system may be subjected to non-smooth and discontinuous nonlinearities. Aside from the nonlinear nature of hydraulic dynamics, hydraulic servo systems also have large extent of model uncertainties such as uncompensated friction forces variation of system parameters and external disturbances. The conventional Proportional, Integral and Derivative (PID) controller can not cope with hydraulic system nonlinearities and could not compensate its variation of parameters. Therefore, a radial basis neural network has been suggested to control the speed response of PCM. The structure of radial basis neural network (RBNN) controller is simple and efficient in control purposes. The design of control surface based on radial basis function (RBF) controller has been considered. The performance of PID and RBF controllers has been assessed based on the improvement in speed behavior and their capabilities to compensate the changes in system parameters (load and bulk of modulus). Also, the effect of tuning of the radial basis parameters on the dynamic response has been studied. Results showed that the RBF controller is more robust and shows typical results compared to classical PID controller. Moreover, a further improvement in speed dynamic can be obtained with appropriate tuning of RBF parameters.

KEYWORDS: Hydrostatic transmission, PID controller, radial basis neural network controller.

الخلاصة:

تستخدم المحركات المسيطر عليها باستخدام الضاغط الهيدروليكي (pump-controlled hydraulic motors) في تطبيقات كثيرة وذلك لكفاءة اشتغالها العالية. تمتلك مثل هذه المنظومات خواص لاخطية عالية وكذلك تتعرض خلال الاشتغال الى تغيرات لاخطية ومتقطعة (discontinuous nonlinearities). لغرض السيطرة على سرعة المنظومة الهيدروليكية فان المسيطر التقليدي (التناسبي ، التفاضلي ، التكاملية) يفشل في توليد اشارة سيطرة تلم او تعوض (compensate) عن الطبيعة اللاخطية للمنظومة وهذا يتطلب استخدام مسيطر غير تقليدي (ذكي) لمعالجة مثل هذه المشاكل. حيث تم في هذا البحث استخدام مسيطر عصبي شبكي (neural network) وتم تصميم سطح السيطرة (control surface) الذي يشكله هذا المسيطر. علاوة على ذلك تمت دراسة تأثير متغيرات المسيطر الذكي (intelligent) controller على أداء استجابة السرعة للمنظومة الهيدروليكية. حيث تبين من النتائج الممثلة باستخدام الحاسبة بأن أداء المنظومة بوجود المسيطر العصبي الشبكي يتفوق على أدائها بوجود المسيطر المناظر (التقليدي) وكذلك تبين من النتائج بان المسيطر العصبي الشبكي له قابلية عالية في كبت تأثير التغيرات المفاجئة وتأثير التغير في معلمات المنظومة على أداء السرعة للمنظومة الهيدروليكية.

1. INTRODUCTION

Pump controlled motor are the preferred power element in applications which required considerable horsepower for control purpose because of their high maximum operating efficiency which can approach 90% in practice. However, the comparatively slow responses of these elements limit their use in high performance systems [Merrit 1967, Watton 1989].

Variable displacement piston pump is usually accomplished with a swash plate that has a variable degree of angle. As the piston barrel assembly rotates, the pistons rotate around the shaft, with the piston shoes in contact with and sliding along the swash plate surface. Since there is no reciprocating motion when the swash plate is in vertical position, no displacement occurs. As there is an increase in the swash plate angle, the pistons move in and out of the barrel as they follow the angle of the swash plate surface. The pistons move out of the cylinder barrel during one half of the cycle of rotation thereby generating an increasing volume, while during the other half of the rotating cycle, the pistons move into the cylinder barrel generating a decreasing volume. This reciprocating motion results in the drawing in and pumping out of the fluid. Pump capacity can easily be controlled by altering the swash plate angle, larger the angle, greater being the pump capacity. A cross-sectional view of this pump is shown in Fig.(1) [Ravi 2005, Noah 2001].

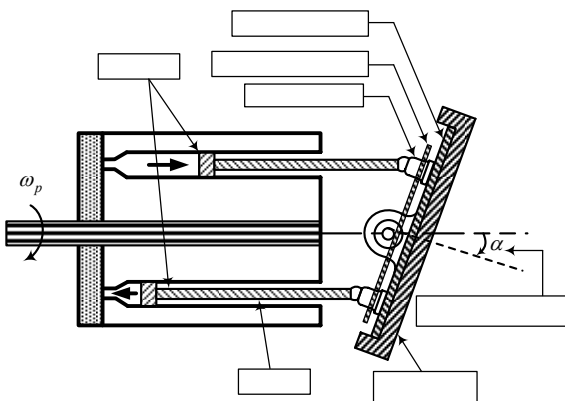


Figure (1) Variable-displacement pump

The basic pump-controlled motor, often called a hydrostatic or hydraulic transmission, is shown schematically in Fig. (2). A variable displacement pump, driven by a constant speed power source and capable of reversing the direction of the flow, is directly connected to a fixed displacement hydraulic motor. Hence, the motor speed and

direction of rotation may be controlled by varying the pump stroke [Merrit 1967, Ali 2006].

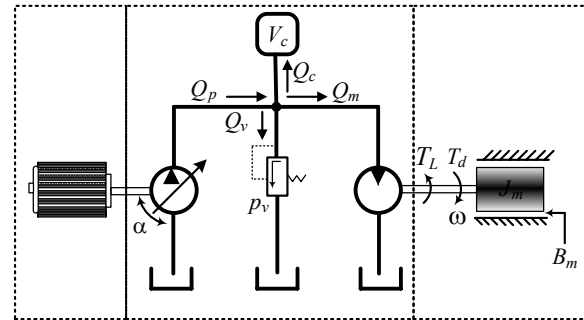


Figure (2) Pump-controlled Motor

A replenishing supply is required to replace leakage losses from each line and to establish a minimum pressure in each line. This auxiliary supply is a constant pressure type with low capacity because only leakage flows are supplied. The replenishing supply prevents cavitations and air entrainment because it pressurize each line and helps dissipate heat by providing cooler fluid to replace the leakage [Merrit 1967].

Safety relief valves are used in the lines to protect system from damage due to pressure peaks. These valves establish an upper limit to the line pressure and are set to operate above normal operating pressures. Theses valves must respond rapidly and have a large capacity because they must pass the maximum pump flow in an extreme overload. These valves should be connected across the lines so that overload flow is dumped to the other line to help prevent cavitations [Merrit 1967, Ali 2006].

2. MATHEMATICAL MODEL

It is assumed that the angular velocity of the prime mover (induction motor) and hence the angular velocity of the pump shaft ω_p is constant. Pump flow rate can be varied by adjusting the swashplate displacement angle and the flow-angle relationship can be given as [Ravi 2005, Ali 2006].

$$Q_p = (K_p \eta_{vp}) \alpha \quad (1)$$

where, Q_p is pump flow rate (m^3/s), α is displacement angle of swashplate ($^\circ$), K_p is pump coefficient (m^3/s), η_{vp} is pump volumetric efficiency which is assumed not to depend on pump rotation angle.

To simplify the analysis, pressure relief valve dynamics is not taken into consideration. Therefore, two equations are given for passing

flow rate through pressure relief valve (m^3/s) in state of opening and closing as follows:

$$Q_v = \begin{cases} K_v (P - P_v) & P > P_v \\ 0 & \text{else} \end{cases} \quad (2)$$

or,

$$Q_v = \lambda K_v (P - P_v) \quad (3)$$

where, K_v is slope coefficient of valve static characteristic ($m^5/N.s$), P is system pressure (P_a), P_v is valve opening pressure (P_a) and λ is given by:

$$\lambda = \begin{cases} 1 & P > P_v \\ 0 & P \leq P_v \end{cases} \quad (4)$$

If, it is assumed that pressure drop in the hydraulic hose is negligible:

$$Q_c = (V / \beta)(dP / dt) \quad (5)$$

$$(dP / dt) = (\beta / V)Q_c \quad (6)$$

where, Q_c is flow rate deal with fluid compressibility (m^3/s), V is the fluid volume (m^3) subjected to pressure effect, β is fixed bulk modulus (P_a). Flow rate used in the hydraulic motor can be written as in [Ravi 2005, Ali 2006];

$$Q_m = K_m \omega_m / \eta_{vm} \quad (7)$$

where, K_m is hydraulic motor coefficient (m^3), ω_m is angular velocity of hydraulic motor (rad/s) and η_{vm} is volumetric efficiency of the motor. Hydraulic motor torque (N.m) can be written as:

$$T_d = (K_{mt} \eta_{mm}) P \quad (8)$$

where T_d is the developed torque (N.m), K_{mt} is motor torque coefficient (m^3), P is the pressure drop in hydraulic motor (P_a) and η_{mm} is mechanical efficiency of hydraulic the motor. The developed torque T_d produced in the hydraulic motor is equal to the sum of the moments from the motor loads and can be given as, [Merrit 1967]

$$T_d = J_m \dot{\omega}_m + B_m \omega_m + T_L \quad (9)$$

where, J_m is the inertia of the hydraulic motor shaft ($N.m.s^2$), B_m is viscous friction coefficient of motor and its shaft ($N.s/m$). From Fig.(2), one can deduce

$$Q_p = Q_c + Q_m + Q_v \quad (10)$$

From Eqs.(1-7), one can write Eq.(10) as

$$\dot{P} = -\lambda \left(\frac{\beta K_v}{V} \right) P - \left(\frac{\beta K_m}{V \eta_{vm}} \right) \omega_m + \left(\frac{\beta K_p \eta_{vp}}{V} \right) \alpha + \lambda \left(\frac{\beta K_v}{V} \right) P_v \quad (11)$$

Similarly, from Eqs.(8-9), the following equation will result

$$\dot{\omega}_m = \left(\frac{K_m \eta_{mm}}{J_m} \right) P - \left(\frac{B_m}{J_m} \right) \omega_m - \left(\frac{1}{J_m} \right) T_L \quad (12)$$

Setting x_1 , x_2 and u as P , ω and α , respectively, the following state-space form can be obtained

$$\begin{cases} \dot{x}_1 = \lambda a_{11} x_1 + a_{12} x_2 + b_{11} u + \lambda b_{12} P_v \\ \dot{x}_2 = a_{21} x_1 + a_{22} x_2 + b_{21} T_L \end{cases} \quad (13)$$

where

$$\begin{aligned} a_{11} &= -(\beta K_v)/V, & a_{12} &= -(K_m \beta)/(V \eta_{vm}), \\ a_{21} &= (K_{mt} \eta_{mm})/J_m, & a_{22} &= -B_m/J_m \\ b_{11} &= (\beta K_p \eta_{vp})/V, & b_{12} &= (\beta K_v)/V, \end{aligned}$$

$$\lambda = \begin{cases} 1 & x_1 > P_v \\ 0 & x_1 \leq P_v \end{cases}$$

One can argue that Eq.(13) acquire its nonlinearity from the nonlinear coefficient λ and the saturation of control signal u , where it should not exceed maximum angular displacement; i.e., $u_{\max} = \alpha_{\max}$, which is equal to 16° in the present application.

3. RADIAL BASIS STRUCTURE

A radial basis function neural network is shown in Fig.(2). There, the inputs are x_i , $i = 1, 2, \dots, n$ and the output is $y = F_{rbf}(x)$ where $F_{rbf}(x)$ represents the processing by the entire radial basis function neural network. Let $x = [x_1, x_2, \dots, x_n]^T$.

The input to the i^{th} receptive field unit (sometimes called a radial basis function) is x , and its output is denoted with $R_i(x)$. The receptive field unit has what is called a "strength" which is

denoted by b_i . Assume that there are n_R receptive field units. Hence, from Fig.(3), [Dan 2001,Yu 2002]

$$y = \sum_{k=1}^{n_R} b_k R_k(x) \quad (14)$$

is the output of the radial basis function neural network. If Gaussian radial basis is chosen, then

$$R_k(x) = \exp\left(\frac{(x - c^k)^2}{(\sigma^k)^2}\right) \quad (15)$$

where $c^k = [c_1^k, c_2^k, \dots, c_n^k]$, σ^k is a scalar.

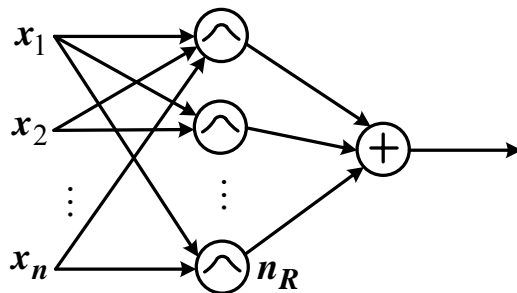


Figure (3) Radial basis function neural network model

For the case where $n=1$, $c^1=[c_1^1]=2$ and $\sigma^1=0.1$, $R_1(x)$ is shown in Fig.(4) [Kevin 2006],



Figure (4) Radial neuron activation

4. TRADITIONAL TUNNING OF PID CONTROLLER

In order to use a controller, it must first be tuned to the system. This tuning synchronizes the controller with the controlled variable, thus allowing the process to be kept at its desired operating condition. Standard methods for tuning controllers and criteria for judging the loop tuning have been used for many years. Some of them are mathematical criteria, Ziegler-Nichols Cohen-coon method, trial and error method, continuous cycling

method, relay feed-back method and Kappa-Tau tuning method. From the above mentioned methods, Ziegler-Nichols method is the most common one and will be adopted here in the present work as a traditional method of tuning PID parameters [Astrom 1995, Michael 2005].

The design based on this method is based on knowledge of the point on the Nyquist curve of the process transfer function where the Nyquist curve intersects the negative real axis. For historical reasons this point is characterized by the parameters K_u and T_u , which are called the *ultimate gain* and the *ultimate period* Fig.(5).

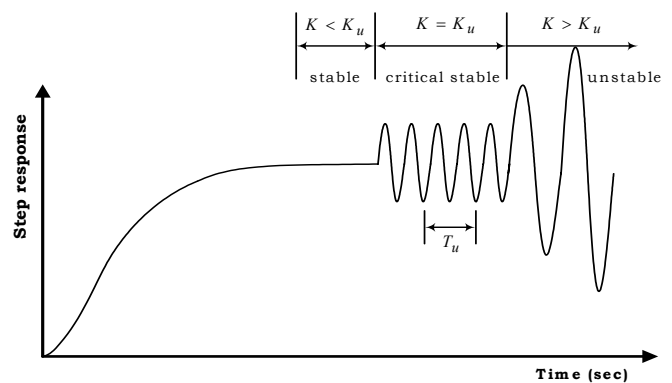


Figure (5): Characterization of a step response in the Ziegler-Nichols frequency response method.

The formulas, given by Ziegler-Nichols, which relating the parameters of the PID controller, and the ultimate gain and ultimate period are listed in Table (1). It should be noted that Table (1) applies for the design of P (proportional) and PI controllers in addition to the PID controller with the same set of experimental data from the plant.

Table (1): PID controller parameters obtained from the Ziegler- Nichols frequency response method.

Controller	k_p	k_I	k_d
P	$0.5 K_u$	---	---
PI	$0.4 K_u$	$0.8 T_u$	---
PID	$0.5 K_u$	$0.5 T_u$	$0.125 T_u$

5. DESIGN AND SYNTHESIS OF RBF CONTROL SURFACE, [Kevin 2006]

Figure (6) shows the speed control of hydrostatic transmission system based on RBF controller. The

receptive
field units

inputs to the radial basis function neural network will be the error and change of error, respectively,

$$e = \omega_r - \omega \quad (16)$$

$$\dot{e} = \dot{\omega}_r - \dot{\omega} \quad (17)$$

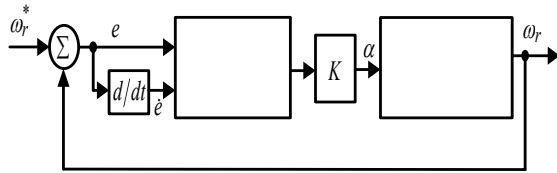


Figure (6): Hydrostatic transmission system.

Lets consider a radial basis function neural network with $n=2$ inputs, and $n_R=11$ so we will have to pick 11 strength b_i , $i=1, 2 \dots 11$. Based on simulations of step response of the PCM speed, the maximum excursions (dimensions) of the error and change of error can be estimated as

$$e(k) \in [-3000, 3000] \quad \text{Reference Speed}$$

$$c(k) \in [-6e^5, 6e^5] \quad \text{Change of Error}$$

For the respective field units we use spread σ_j^i (i.e. so that the size of the spread depends on which input dimension is used) with

$$\sigma_j^i = 0.7 \frac{espan}{\sqrt{n_R}}, \sigma_j^i = 0.7 \frac{cespan}{\sqrt{n_R}} \quad (i=1, 2 \dots 11) \quad (20)$$

where *espan* and *cespan* are the maximum excursions of error and change of error, respectively. It is worthy to note that they, *espan* and *cespan*, can be estimated via simulation. For σ_j^i , the (*espan*/11) factor makes the spread size depend on the number of grid points along the e input dimension (similarly for σ_j^i), and the 0.7 factor was chosen to get a smooth interpolation between adjacent respective field units.

To design radial basis function neural network for the angular velocity problem, we simply need to choose the b_i , $i=1, 2 \dots 11$, parameters to shape the mapping in the approximate way. Suppose that we view parameter as being loaded in a matrix,

$$\begin{bmatrix} b_1 & b_{12} & b_{23} & b_{34} & b_{45} & b_{56} & b_{67} & b_{78} & b_{89} & b_{100} & b_{111} \\ b_2 & b_{13} & b_{24} & b_{35} & b_{46} & b_{57} & b_{68} & b_{79} & b_{90} & b_{101} & b_{112} \\ \vdots & \vdots & \vdots & \vdots & \vdots & \vdots & \vdots & \vdots & \vdots & \vdots & \vdots \\ b_{11} & b_{22} & b_{33} & b_{44} & b_{55} & b_{66} & b_{77} & b_{88} & b_{99} & b_{110} & b_{121} \end{bmatrix}$$

Figure (7): Control Surface of RBNN Controller

The entries of matrix B is based on the controller action.

One can note that if $e=c=0$, the actual speed is not deviating from the reference speed hence, the controller sets the control signal $u=0$; i.e., the angular position of α is set to zero and no change of speed appears. In this case, the value of $b_{61} = 0$.

If, however, the error e is near positive maximum value and that c is positive and near a maximum positive value, then the angular speed of hydraulic motor is moving to become even worse than it currently is. In this situation, the neural network controller will produce the largest positive control signal u_{\max} to actuate the pump plate such as to counteract the effects of having a change of velocity in the wrong direction. Then the value of b_{121} is set to u_{\max} .

If the error is near negative maximum and change of error is near negative maximum value, the motor velocity would decrease from the reference angular speed ω_r . Therefore, a maximum negative actuating signal is necessary to be fed to the pump plate such that the pump would give the required pressure to pull down the velocity to reference speed in a minimum time. Consequently, the value of b_1 is given value of $-u_{\max}$.

As the error reaches maximum positive value and change of error reaches maximum negative value, then the actual speed approaches the reference with high rate. This situation is also repeated if the error reaches maximum negative value and the change of error reaches maximum positive value, the motor velocity runs quickly to reference value. At such cases, no actuating signal is fed to the pump plate, as no need to give any pressure signal to hydraulic motor. Therefore, the values of b_{11} and b_{111} are set to zero. Based on the above argument, the stimulus-response characteristic of the RBNN, we have just designed, can be depicted in the form of a control surface and is illustrated in Fig.(7). One can note that the plot summarizes the (decisions) that the neural network will make.

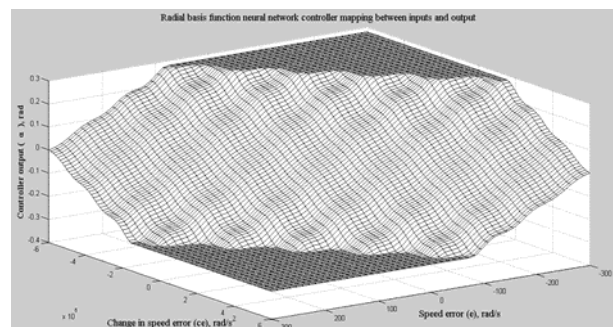


Figure (8) Speed responses of the PID controller

6. RESULTS

For simulation purposes, we have used a backward difference approximation to the derivative, i.e.,

$$\dot{e} = \frac{e(kT) - e(kT - T)}{T}$$

where T is the sampling period and k is an index for the time step (k). The step size in this work is chosen to be 5×10^{-5} and the system differential equations have been solved using fourth order Runge-Kutta. The program code used for implementing the neural network controller, solving governing differential equations of the hydrostatic transmission system (pump and hydraulic motor) and simulating different system behaviors has been written in MATLAB/m-file. The simulation time has been selected to be 0.04 seconds for most simulated results.

For setting the parameters of PID controller using Zeigler-Nichols method, one should connect the controller to the process such that the control action is proportional only, i.e., $K_i = 0$ and $K_d = 0$. The proportional gain is increased slowly until the process starts to oscillate as shown in Fig.(8). The gain when this occurs is K_u and the period of the oscillation is T_u . It is found that the value of K_u which makes the response oscillatory is equal to 2×10^{-3} . From the oscillatory response the value of T_u is equal to 0.04. Based on Table (1), one can by now determine the values of PID controller parameters:

$$K_p = 1 \times 10^{-3}, \quad K_i = 9 \times 10^{-4}, \quad K_d = 2.25 \times 10^{-4}$$

Setting these values into their corresponding parameters, the PID controller based response would be set up.

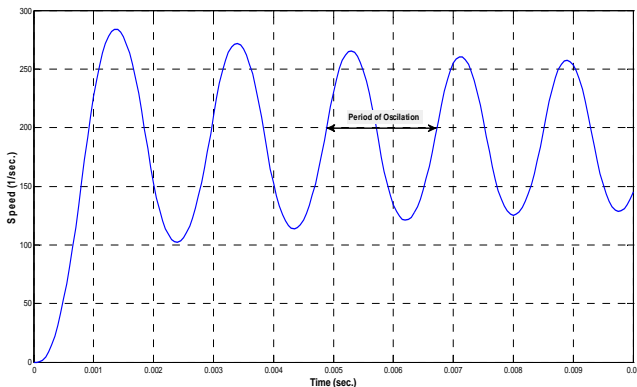


Figure (9) shows the speed dynamic behaviors based on both controllers. The comparison of the two controllers is evaluated in terms of transient parameters such as peak overshoot, rise time and

steady-state error. It is evident from Fig.(8) that the response due to RBF-based controller has an excellent dynamic; as no overshoot or oscillation is observed and the speed track the reference faster than that with PID controller case. However, the steady state value of the speed response based on RBF controller does not coincide with the reference value, but can be further reduced if sigma value, number of receptive field units and scaling gain has been increased. On the other hand, PID controller could overcome this problem by virtue of integration action; as the integrator continues integrating until zero steady-state value has been reached.

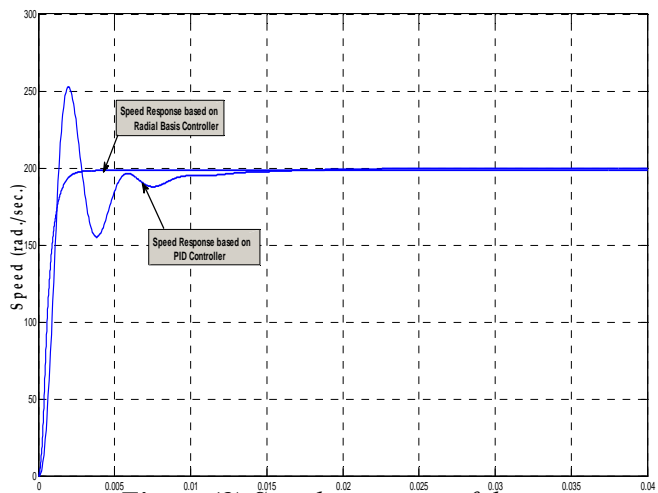


Figure (9) Speed responses of the two controllers

Upon the simulation run, the control signal would travel over the control surface like that shown in Fig.(10). This control surface has been synthesized based on all possible simulated (outcome) values of error and change of error. The equilibrium point where $\dot{e} = 0$ and $e = 0$ has been indicated in the figure.

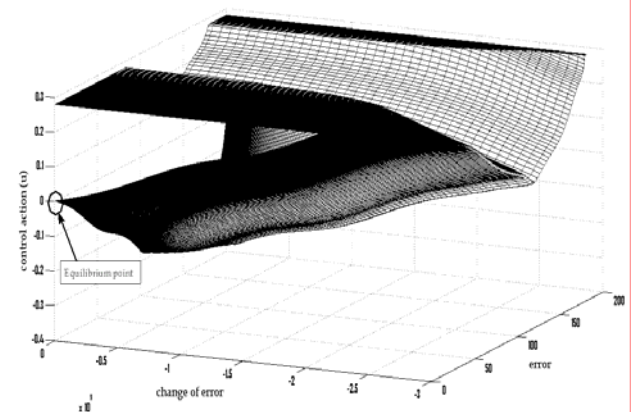


Figure (10) Instantaneous input-output mapping of RBF controllers

In Fig. (11) the effect of changing the spread values (σ) of all Gaussian functions on the speed response is considered. The spread values are set at $\sigma=0.3, 0.5$ and 0.7 . In this simulation, the number of receptive field units, over the ranges of error and its change, has been held to 121 units. One can see from the figure that setting spread value at 0.3 would show a limit cycle characteristics. With this small spread value, the Gaussian functions, responsible for synthesizing the control surface, would have high projections at their centers. This would produce a high steep hill and valleys surface, which in turn would make the solution at equilibrium point ($\dot{e} = e = 0$) to oscillated between these minima and maxima. Setting the spread values of the Gaussian functions at $\sigma = 0.7$ would better flattening the control surface and this would result in a smooth control surface near the equilibrium point. Therefore, the speed response is much improved. The decrease of steady-state error value due to increasing of spread values is attributed to the increase of control surface average value. This would boost the control signal to higher level and then decreasing the steady-state error.

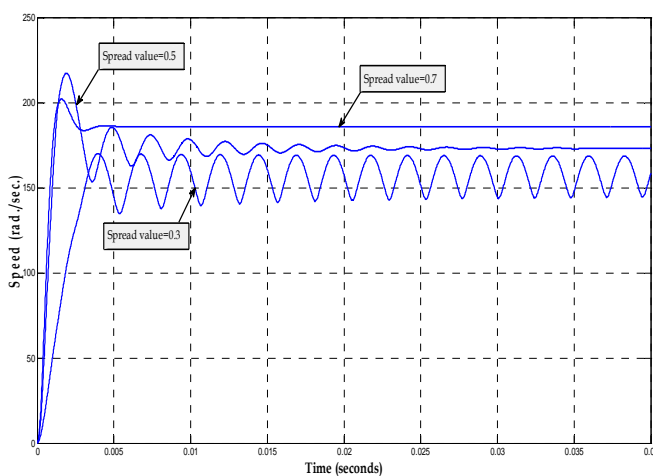


Figure (11) Speed response with different spread values

In Fig. (12-a), the number of receptive field units is changed. Three cases with 3, 5 and 6 number of units are considered. One can see clearly from the figure that the case with 3 numbers of units shows oscillatory characteristics, while the case with 9 numbers shows the best transient performance among the others. One can argue that the low number of receptive units would produce high ripple control surface, while high number of receptive units results in a smooth and monotonic control surface especially at the equilibrium points. Moreover, it is clear from the

figure that increasing the number of such units would decrease the steady state error. This is a true deduction, since the slant of the control surface would be high with high number of receptive field units, and then the boosting of control signal near the equilibrium points would be so high.

Further increasing of receptive units would not affect considerably on the envelope of the control surface and, therefore, there is a small change in the transient response. However, the steady-state error continues decreasing with the increase of such unit numbers. This is such since the slope or gradient of the control signal near equilibrium points would further increase (see Fig.(12-b)).

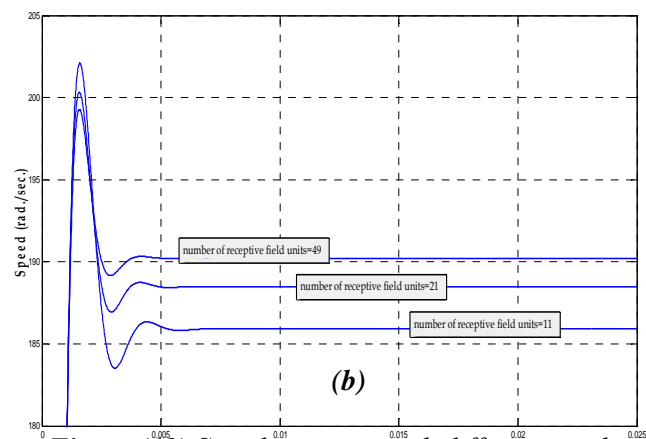
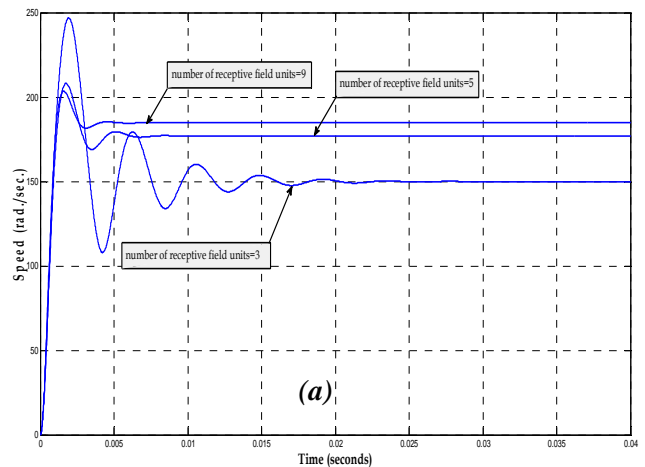


Figure (12) Speed response with different numbers of receptive field unit values

In Fig. (13), the scaling gain at the output of RBF has been varied at 0.5, 1 and 30. In this simulation, the number of receptive units is set at 11 and the spread value is fixed at a value of 0.7. The scaling gain has a large effect on the slope and envelope of the control surface. Low values of scaling gain would gives a small slant of the surface and this make the control signal to

swinging around the equilibrium points; i.e., an oscillation would arise. High value of scaling gain would make the control signal reaching the steady state in a fast fashion.

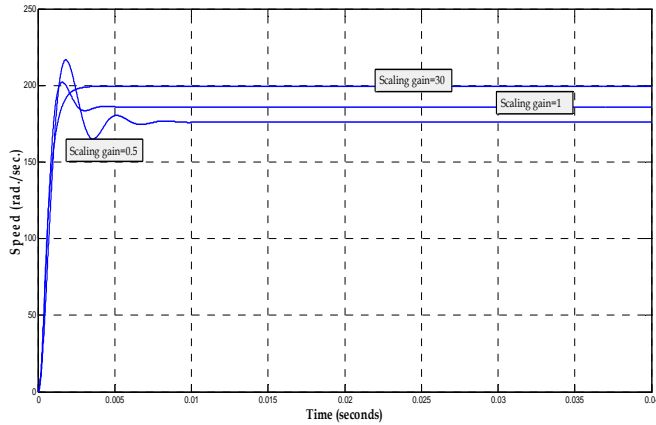


Figure (13) Speed response with different scale gains

In Fig.(14), a step load of $T_L = 25 \text{ kN}$ is exerted to the pneumatic system at time 0.03 second (to permit the transient response to come into settling condition). A comparison can be made between the speed responses based on these controllers. The height of change, due to load application, in speed response based on RBF controller is much lower than that with PID controller. Also, the speed behavior at time of load exertion shows an oscillatory characteristic before returning its steady state value, while the speed response with RBF shows a monotonic behavior and it reaches its previous value in a much lower time than its counterpart. The load rejection capability of RBF controller can be attributed to a large boost control signal to the swash-plate and then a high quantity of fluid would flow into the hydraulic motor with a low time. It is seen from the figure that the pressure latches at a specific negative value after a short time of load exertion; this is the required pressure to counteract the applied load.

In Fig.(15), the robustness of both controllers is again examined in terms of changing one of the system parameter (bulk of modulus of hydraulic fluid). Three responses has been simulated for each controller; one for fixed bulk of modulus (β), the other with 0.05% increment change in bulk of modulus ($\beta = \beta + 0.05\% \beta$) and the last plot is for 0.05% decrement change in bulk of modulus ($\beta = \beta - 0.05\% \beta$). The figure shows that there is degradation in speed response with PID controller when the value of bulk modulus has been

decreased and an improvement when this value has been lowered. On the contrary, the change in speed response with RBF controller is much less than that with PID controller. Therefore, one can conclude that RBF-based controller is more robust than its counterpart.

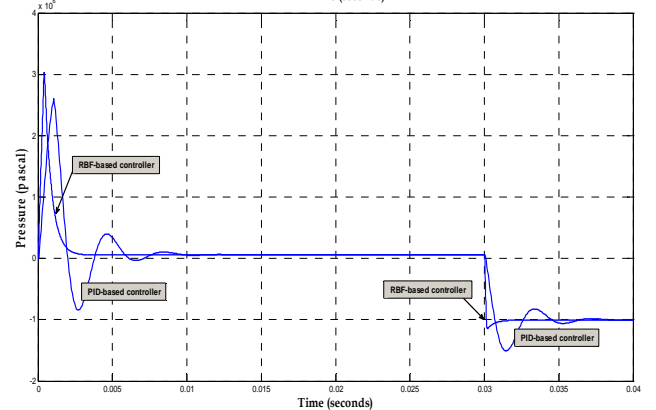
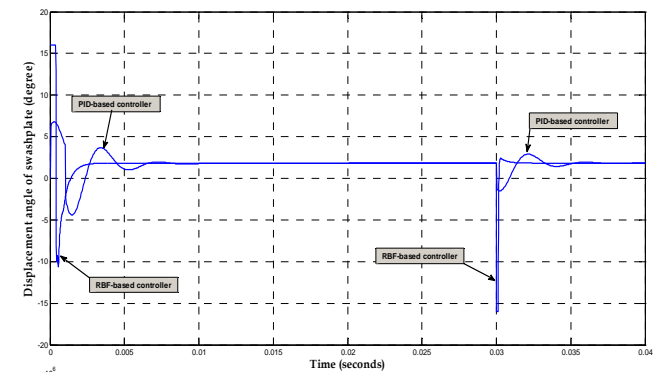
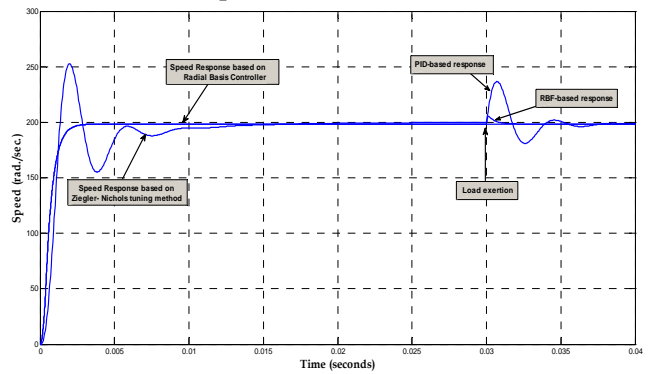


Figure (14) Load rejection capabilities of both controllers

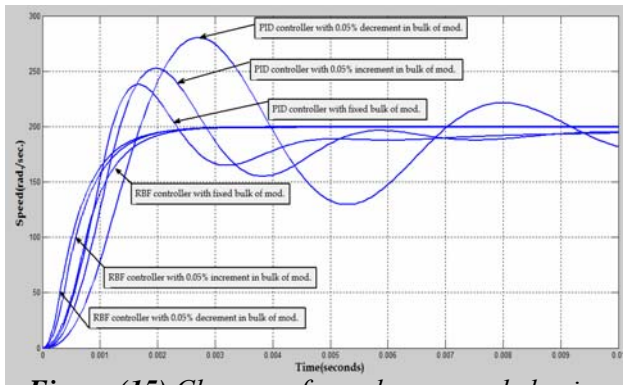


Figure (15) Changes of speed response behavior of both controllers with change in bulk of modulus parameter.

7. CONCLUSIONS

1. One can deduce from the simulated results that increasing the number of receptive field units could improve the control surface, and hence would enhance the dynamic performance of the speed response and lead to less steady state error. However, increasing the number of receptive units will increase the computation effect of executing the software program.
2. Increasing the scaling gain value could make the control surface steeper and then could bring the solution to steady state condition in a faster way with a minimum steady state error.
3. Increasing the spread value of the Gaussian function would make the controller surface flatter (i.e. become more even with fewer ripples). The solution, then, would slide on a smooth surface and no oscillation or peak-overshoot would appear.
4. If the hydraulic system is exerted to load changes or if it encounters change variation of parameters, the neural-base controller shows high load rejection capabilities and more robust characteristics than its counterpart.

REFERENCE:

Ali, V. A., "Effect of bulk modulus on performance of a hydrostatic transmission control system," Sadhana Vol. 31, pp. 543–556, Part 5, October 2006.

Astrom, K. J., Tore, H., "PID Controllers: Theory, Design and Tuning" Instrument Society of America, 1995.

Dan, J. S., "Training radial basis neural networks with the extended Kalman filter," Elsevier, 2001.

Kahaner, D., Moler, C., and Nash, S., "Numerical Methods and Software," Prentice-Hall, New Jersey, 1989.

Kevin, M. P., "Biomimicry for Optimization, Control, and Automation," Springer, 2005.

Merrit, H. E., "Hydraulic control systems," John Wiley & Sons, New York, 1967.

Michael, A. J., Mohamed, H. M., "PID Control: New Identification and Design Methods," Springer-Verlag, 2005.

Noah D. Manring, Fikreadam A. Damtew "The Control Torque on the Swash Plate of an Axial-Piston Pump Utilizing Piston-Bore Springs", Journal of Dynamic Systems, Measurement and Control, 2001, Vol. 123.

Ravi Doddannavar, Andries Barnard, "Practical Hydraulic Systems," Elsevier Science & Technology Books, 2005.

Shampine, L. F., "Numerical Solution of Ordinary Differential Equations," Chapman & Hall, New York, 1994.

Watton, J., "Fluid power systems: Modeling, simulation, analog and microcomputer control," Englewood Cliffs, Prentice-Hall, 1989.

Yu, H.H., Jenq, N.H., "Hand book of Network signal processing," CRC Press, 2002.

APPENDIX

Table (2): Parameters and coefficients

Coefficient	Values
a_{11}	-2.1068e+003
a_{12}	-4.4120e+006
a_{21}	0.0945
a_{22}	-375
b_{11}	2.7465e+010
b_{12}	2.5281e+010
b_{22}	-3750
T_L	150
P_v	12e+6



TECHNOLOGICAL ANALYSIS OF FLAT SURFACE CONDITIONS BY MAGNETIC ABRASIVE FINISHING METHOD (MAF)

Dr. Ali H. Kadhum – Baghdad University – Al-Khawarizmi College of Engineering, Manufacturing Operations Department- Al-Jadriia, Baghdad (kadhumali59@yahoo.com).

Yahya M. Hamad - Baghdad University – Al-Khawarizmi College of Engineering, Manufacturing Operations Department- Al-Jadriia, Baghdad (yahya_m_hamad@yahoo.com.au)

Nazar K. Mohammad - Baghdad University – Al-Khawarizmi College of Engineering, Manufacturing Operations Department- Al-Jadriia, Baghdad

ABSTRACT

This study introduced the effect of using magnetic abrasive finishing method (MAF) for finishing flat surfaces. The results of experiment allow considering the MAF method as a perspective for finishing flat surfaces, forming optimum physical mechanical properties of surfaces layer, removing the defective layers and decreasing the height of micro irregularities. Study the characteristics which permit judgment parameters of surface quality after MAF method then comparative with grinding.

:

(MAF)

Keywords: Magnetic abrasive finishing (MAF), characteristic of roughness, flat surface, coefficients of parabola, ferromagnetic abrasive powder, magnetic induction, running clearance, cutting speed, support curve.

INTRODUCTION

At the present time, the magnetic –abrasive finishing method (MAF) is used in cleaning, grinding and polishing of flat surfaces in manufacturing engineering. The diagram of magnetic abrasive finishing of flat surface is represented in (Fig. 1). The MAF method based on the principle that the work piece can be machined by the effect of ferromagnetic abrasive powder, this powder is densities by energy of external magnetic field; energy is supplied to running clearance between working surfaces and

electromagnetic poles. Working motion is imported to the powder; the powder is pressed by magnetic field forces against working surfaces to finish it. The most important feature of this method is that the abrasive instrument has no bond; its function is performed by a magnetic flux in a working zone. These lead to arrange the cutting forces and also controlling the degree of elasticity by change of field strength [1-8] , via varying magnitude of the magnetic field in the machining zone, running clearance and the speed of rotation poles (cutting speed) .

The MAF method gives combined effects on work piece which influence to surface layers of parts is conditioned by abrasive cutting, plastic deformation, electromagnetic adhesive effect and chemical processes [5, 8, 11, 12].

The criteria of effective use the quality of surface of the parts after MAF and grinding methods defined by the parameters of roughness determined by formula (1):

R_a : arithmetic mean of profile declination.

R_z : height of profile roughness over 10 points.

R_{max} : the biggest height of profile unevenness.

S_m : the average pitch of profile unevenness.

r_1 : radius of top of micro roughness.

r_2 : radius of bottom of micro roughness.

t_p : relative support length of profile.

$$\left. \begin{aligned} R_a &= \frac{1}{n} \sum_{i=1}^n |y_i|, \\ R_z &= \frac{1}{5} \left[\sum_{i=1}^5 |y_{pmi}| + \sum_{i=1}^5 |y_{vmi}| \right] \\ S_m &= \frac{1}{n} \sum_{i=1}^n S_{mi}, \quad t_p = \frac{1}{L} \sum_{i=1}^n l_i \\ R_{max} &= \frac{y_{max} - y_{min}}{B_y}, \quad B_y = \frac{20000}{R_a} \end{aligned} \right\} \quad (1)$$

The effectiveness of using MAF method can be determine by the effects to surface layer of parts and depend upon many technological parameters. Three technological parameters have been choose, which are magnetic induction or current force, running clearance and cutting speed (rotation of poles). They have combined effects on forming surfaces and the amount of pressure acting on work piece. Also they form the shape and nature of the brush of the ferromagnetic abrasive powder. According to experiments data obtained from references [1- 4, 7, 8, 11] the range of these parameters can be taken as following :

$B = 0.2 \dots\dots\dots 0.8$ TL (magnetic induction)

$C = 1.0 \dots\dots\dots 4.0$ mm (running clearance)

$V = 100 \dots\dots\dots 250$ mm/min (cutting speed)

The ability of guiding these parameters to get the optimum values will help for finding the parameters of roughness (R_a , R_z , R_{max} , S_m , r_1 , r_2 , t_p),, which influence for wear resistance under

conditions of bounding and fluid friction, corrosion resistance, vibration resistance, heat reflection, contact rigidity and strength of surface connections. The most complex characteristic of roughness is the support curve, the analytical expression will be determined [6, 7, 8].

The most complex characteristic of roughness is support curve **Fig. 2**. the analytical expression of which is determined by formula (2)

$$Y = B_0 + B_1 Z_1 + B_2 Z_2^2 + B_3 Z_3^3 \quad (2)$$

The mode construction of a support curve and the curve itself is represented in .Fig (2). On abscissa are laid off ration of sum of portions profile to studied length L; corresponded to distance y_i measured from over hang height H laid off as ordinate (**See Fig.(5)**). In this case the height of profile levels is measured in absolute units.

The support curve is approximated by parabola:

$$\left. \begin{aligned} Y &= B_0 + B_1 f(z) + B_2 f(z) + B_3 f(z) \\ Z &= \frac{1}{L} \sum_{i=1}^n l_i, \quad Y = y_i \end{aligned} \right\} \quad (3)$$

Coefficient of parabola B_0 , B_1 , B_2 , B_3 , are determined by formula (4-7) :

$$B_0 = [0.208y_0 + 0.196(y_1 + y_2) + 0.161(y_3 + y_4) + 0.103(y_5 + y_6) + 0.021(y_7 + y_8) - 0.084(y_9 + y_{10})] \quad (4)$$

$$B_1 = [0.065(y_1 - y_2) + 0.111(y_3 - y_4) + 0.114(y_5 - y_6) + 0.006(y_7 - y_8) - 0.074(y_9 - y_{10})] \quad (5)$$

$$B_2 = -[0.012y_0 + 0.01(y_1 + y_2) + 0.007(y_3 + y_4) + 0.001(y_5 + y_6) - 0.007(y_7 + y_8) - 0.017(y_9 + y_{10})] \quad (6)$$

$$B_3 = -[0.003(y_1 - y_2) + 0.004(y_3 - y_4) + 0.004(y_5 - y_6) + 0.001(y_7 - y_8) - 0.006(y_9 - y_{10})] \quad (7)$$

Then Z exchange within limit ± 5 and t_p in limit ± 0.5

After correction, we get:

$$\begin{aligned} B_1 &= B_1 * 10, \quad B_2 = B_2 * 10^2, \quad B_3 = B_3 * 10^3 \\ Z &= \frac{1}{L} \sum_{i=1}^n l_i - 0.5, \quad Z = t_p - 0.5 \end{aligned} \quad (8)$$

EXPERIMENTAL METHOD AND MATERIALS

An experiment was conducted using MAF laboratory machine, it contains rotating magnetic poles, inside these poles there is an iron core made from ferromagnetic material. A running clearance (C) is filled with ferromagnetic powder. Magnetic poles rotate with powder over the work piece (which is fixed on the base (Fig.1)) by using variable speed electric motor and the axis of rotation is perpendicular to the work piece axis. Magnetic coils generate magnetic field and electric current which in turn gives the magnetic inductance (B). Variable values of electric current can be obtained by using current regulator. Running clearance value can be controlled by the work piece fixing base and its feed speed obtained from other electric motor with gear box.

The experiment executed according to the following steps:

- 1- Surface roughness test executed three times for each samples by using profile meter- profilograph.. Then the mean value of ΔR_a and other parameters obtained.
- 2- The experiment conducted according to the matrix factor plan (table 1).
- 3- Repeat the steps 1, 2 for each sample.

The Following Data Used in The Experiments:

Test specimen shown in **Fig. 3** is a flat surface of dimensions : $t \times W \times L = 3,0 \times 150 \times 250$ mm. Material of the specimen :Aluminum Alloys Number 2024, Hardness120 HB ; working conditions (constant) The magnetic abrasive powder-mass composition: Al= 0,2% to 16% ; c < 4% ; P= 1,5% ; Si= 0,2% to 8% ; The rest is - Fe. Graininess of powder from 100 to 120 μm . working time= 30 sec; table feed= 340 mm/min; the volume of powder portion $V_p = 20 \text{ cm}^3$

Ideal stress concentrators have been used for finishing the Aluminum alloy [11]. To test the effect of the three technological parameters on the effectiveness of the working operation and to specify the effectiveness relationships of the operation, experiments must be executed. Because the finished surfaces have more than one parameter at same time, a plan factors must be use to obtain the multifunction relationship which explain the combination between the main three technological parameters. To execute less number of experiments, statistical practical values used as listed in **Table 1**.

RESULTS AND DESCUSSION

Table 2 shows the values of final results, for the parameters of surface quality after MAF method. An example for obtaining the curve and the calculation of coefficients of the parabola is shown in **Fig. 4**

- 1- divide axis Z into ten steps 0, 1, 2, 3, 4, 5, -1, -2, -3, -4, -5 , then we can obtain ten values for y (obtained from Fig.(5)) as listed in **Table 3**

- 2- From these values , draw **Fig. 3** for the absolute value of $y=R_a$

- 3- Calculate the values of adding and subtracting.

$$y_1 + y_2 = 0.288 \quad y_1 - y_2 = -0.038$$

$$y_3 + y_4 = 0.34 \quad y_3 - y_4 = -0.07$$

$$y_5 + y_6 = 0.34 \quad y_5 - y_6 = -0.1$$

$$y_7 + y_8 = 0.31 \quad y_7 - y_8 = -0.17$$

$$y_9 + y_{10} = 0.33 \quad y_9 - y_{10} = -0.21$$

- 4- Calculate the coefficients of equation of support curves after MAF method B_0, B_1, B_2, B_3

$$B_0 = [0.0291 + 0.0564 + 0.0547 + 0.0350 + 0.0065 - 0.0277] = 0.1541$$

$$B_1 = [-0.00247 - 0.0077 - 0.0114 - 0.00102 + 0.01554] = -0.00712$$

$$B_2 = - [0.00168 + 0.00288 + 0.00238 + 0.00034 - 0.00217 - 0.00561] = -0.00384$$

$$B_3 = - [-0.000114 - 0.00028 - 0.0004 - 0.00017 + 0.00126] = -0.000296$$

- 5- Calculate the correction :

$$B_1 = -0.00712 \times 10 = -0.0712$$

$$B_2 = -0.00384 \times 10^2 = -0.384$$

$$B_3 = -0.000296 \times 10^3 = -0.296$$

- 6- Then we get the following equation :

$$y = 0.1541 - 0.0712Z - 0.384 Z^2 - 0.296 Z^3$$

- 7- Divided by 0.4(the height of profile) to get :

$$y = 0.385 - 0.178 Z - 0.96 Z^2 - 0.74 Z^3$$

The analysis of profile roughness by studying various model, showed that the maximum value for the relative support length of profile in the level 50% $t_{p50} = 68\%$ (See **Fig. 4**). At the optimum technological parameters, from the best results of the support curve for model 10 (See **Table.2**), then:

Dr. Ali H. Kadhum Yahya M. Hamad Nazar K. Mohammad	Technological Analysis of Flat Surface Conditions by Magnetic Abrasive Finishing Method (MAF)
---	--

$B = 0.96 \text{ TL}$, $C = 2.5 \text{ mm}$, $V = 175 \text{ mm/min}$. (the optimum technological parameters)

At the best values, as following:

$R_a = 8 \text{ }\mu\text{m}$, $R_z = 0.14 \mu\text{m}$, $R_{max} = 0.2 \mu\text{m}$,
 $S_m = 15.5 \mu\text{m}$,

$r_1 = 121 \mu\text{m}$, $r_2 = 79.5 \mu\text{m}$, $t_{p50} = 68\%$

By comparing these results with those obtained by grinding method from reference [6] as shown below:

$R_a = 0.32 \text{ }\mu\text{m}$, $R_z = 1.2 \text{ }\mu\text{m}$, $R_{max} = 1.7 \text{ }\mu\text{m}$,
 $S_m = 30.1 \text{ }\mu\text{m}$

$r_1 = 36.6 \text{ }\mu\text{m}$, $r_2 = 70.4 \text{ }\mu\text{m}$, $t_{p50} = 53\%$

Topography of micro relief formed by MAF is more smoothing tops and bottoms of micro unevenness in comparison with grinding.

To assess the efficiency of the magnetic abrasive finishing method on flat surfaces and their edges, it has been a 15 technological system, by examining three parameters, affecting on the MAF method, by statistical method as **Table 1**.

To stand on the quality on surface and their edges from aluminum alloys was obtained practical results as **Table 2**, of the surface characteristics of previous of 15 technological systems, from profile of the surface (**Fig. 5**).

It can obtained an equal elevation of surface roughness in deferent ways and from deferent technological conditions, so that it have been developed by backing the equation of support curve, showing the characteristics of surface roughness, so that can comparison with other technological process .

Study shows that the MAF method can access to the largest amount of micro profile proportion to the length of any profile, that mean, $t_{p50} = 68\%$. The grinding method give the value $t_{p50} = 53\%$ (9, 10) Magnetic induction affected on the supported curve value at $B = 1 \text{ TL}$ get the best result.

CONCLUSIONS

1. The implementation of theoretical and practical test and established clear technological process for the operation of flat surfaces and their edges from aluminum alloys by MAF method.
- 2- An optimum technological system is achieved which would work to improve the roughness surface compared with grinding method. Thus obtaining practical advice to choose the most rational and technological uses of the area.

3- This method gives machining efficiency which is 1.5 to 2.5 times as great as that when using conventional grinding

4- The micro-irregularities can be reduced to 0.08mm

5- MAF method permits to increase the surface quality of machined parts

6- This method can be use to clean and polish the surface to create a situation before welding operations, without affecting the environment compared with the hazardous chemical method.

REFERENCES

- 1- Amit M. Wani , Vinod Yadava, Atul Khatri, "simulation for the prediction of surface roughness in magnetic abrasive flow finishing (MAFF)" Elsevier, Vol.190 (2007).p282-290.
- 2- O.V.Steponova, V.P. Smirnov, and others, "Effect of magnetic abrasive finishing on the chemical and phase composition of Tic coatings on VK8alloy" springer, New York.vol.44(2005)p.451-454.
- 3- Dharendra k. Singh, V.K. Jain, V.Raghuram." parametric study of magnetic abrasive finishing" Elsevier, Vol.190 (2004).
- 4- Baron Y. M. "Technology of abrasive finishing in magnetic field", Leningrad, Mashinostroenie, 1975, p128.
- 5- Baron Y. M. "Magnetic abrasive and magnetic finishing of parts and cutting tools", Leningrad, Mashinostroenie, 1986, p172.
- 6- Sakulevich F. Y. "Principles of magnetic abrasive machining", Minsk, Nauka texika, 1981.
- 7- Skrorchevski N. Y., Fedorovich E. N., and Yasscheritsin P. I., "Effectiveness of magnetic abrasive machining", Minsk, Nauka tekhnika, 1991.
- 8- Yascheritsin P. I. and Sergeev L. E. "The comparative appraisal of quality characteristics of holes after different finishing methods", Advanced performance materials manufactured in the Netherlands, Vol. 4, 1997, p337-347.
- 9- Matalen A. A. "Technology method for achine parts", 1972, p142.
- 10- Meken E. M. "Wear in condition plastic contact ", Minsk, Nauka, 1968, p31.
- 11- Ali. H. Kadhum, Chachin V. N., and Khomich M. "Magnetic abrasive machining for different materials to increase the quality of the finishing

surface technology", Moscow, Academic of Kosmonaftiki, 1993, Vol. 3, p22-23.

- 12- Shimmura T. and Wang F. H. "A new process for precision finishing of silicon nitride fine ceramics by application of magnetic abrasive

machining using chromium-oxide abrasives mixed with iron particles", International journal , Japan society processing, 1994, Vo. 28, part 3, p229-230.

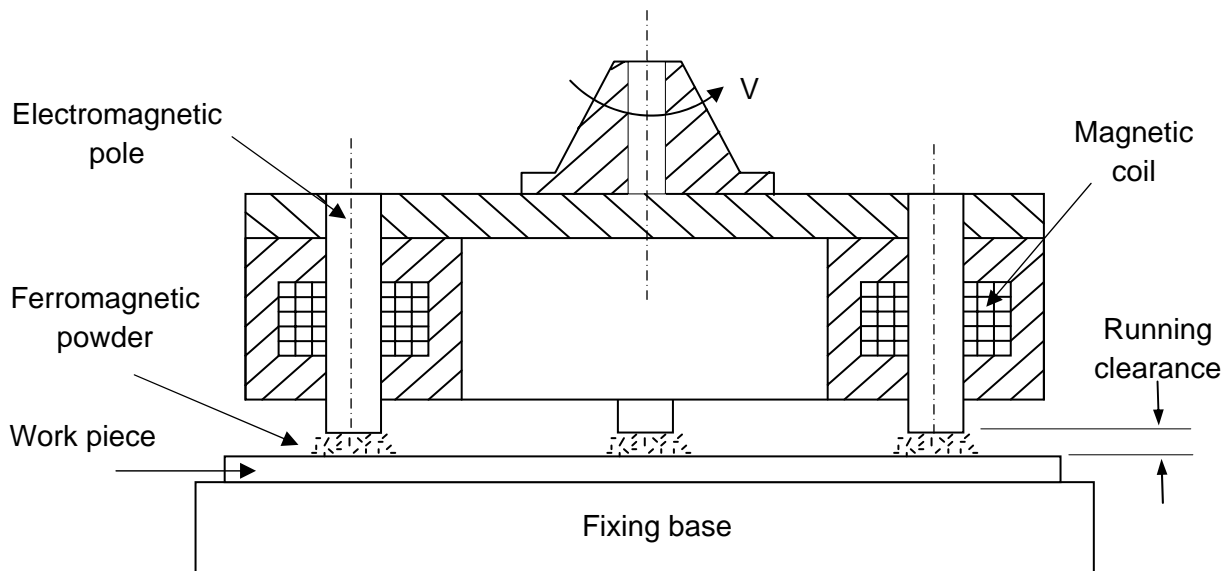


Figure. (1) Machine

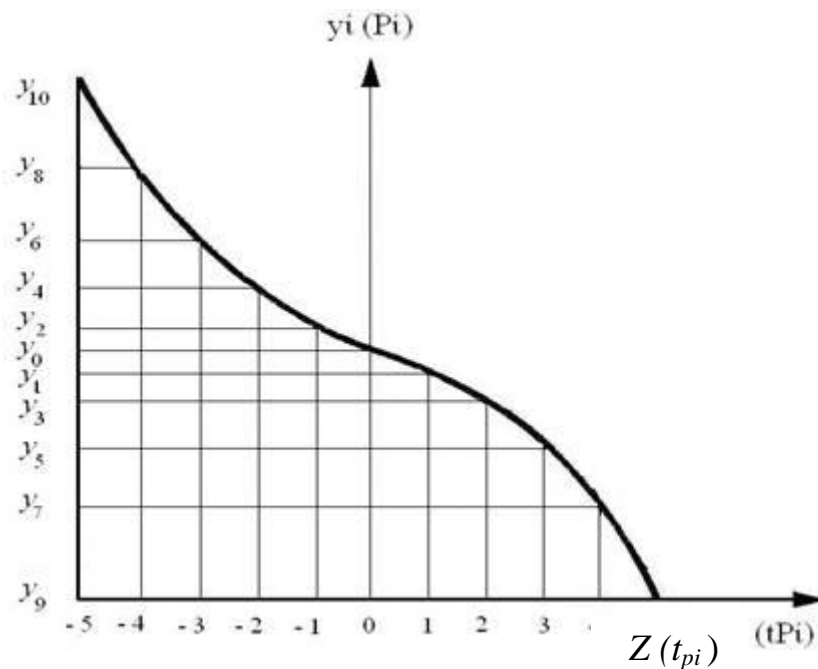


Figure. (2) Support Curve

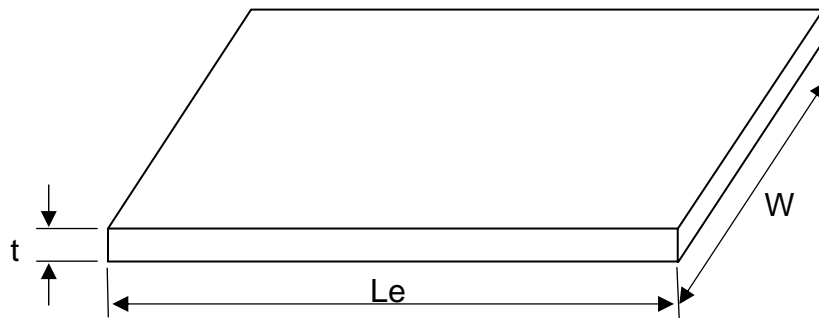


Figure. (3)

Table (1): Factor Plan Matrix

$$N=2^3+2.3+1$$

No. of experiments	Factor level					
	F.L.	(B) TL	F.L.	(C) mm	F.L.	V) mm/min
1	-1	(0.2)	-1	(1)	-1	(100)
2	+1	(0.8)	-1	(1)	-1	(100)
3	-1	(0.2)	+1	(4)	-1	(100)
4	+1	(0.8)	+1	(4)	-1	(100)
5	-1	(0.2)	-1	(1)	+1	(250)
6	+1	(0.8)	-1	(1)	+1	(250)
7	-1	(0.2)	+1	(4)	+1	(250)
8	+1	(0.8)	+1	(4)	+1	(250)
9	-1.2	(-0.96)	0	(2.5)	0	(175)
10	+1.2	(+0.96)	0	(2.5)	0	(175)
11	0	(0.5)	-1.215	(-4.86)	0	(175)
12	0	(0.5)	+1.215	(+4.86)	0	(175)
13	0	(0.5)	0	(2.5)	-1.215	(300)
14	0	(0.5)	0	(2.5)	+1.215	(300)
15	0	(0.5)	0	(2.5)	0	(175)

Note: -1 _ minimum value, +1 _ maximum value, 0 _mid value

Then we can get the relation:



$$F = f(B, C, V), \quad F\text{-The criteria } (R_a, R_z, R_{max}, S_m, r_1, r_2, t_p)$$

Table (2): Experimental Results

No. of experiments	R_a μm	R_z μm	R_{max} μm	S_m μm	r_1 μm	r_2 μm	t_p %
1	0.34	1.12	1.6	30.2	32.2	63.7	55
2	0.27	0.91	1.4	20.3	48.1	85.7	54
3	0.19	0.22	0.29	17.0	123.4	59.2	60
4	0.105	0.21	0.28	11.85	55.5	130.1	62
5	0.09	0.19	0.18	10.6	171.2	129	65
6	0.24	1.12	0.85	22.6	70.5	78.4	57
7	0.30	0.95	1.30	27.3	50.1	61.2	54
8	0.21	0.82	1.55	18.4	86	70.1	60
9	0.09	0.19	0.23	17.7	98.4	88.2	67
10	0.08	0.14	0.2	15.5	121	79.5	68
11	0.11	0.2	0.25	16.8	87	90.2	66
12	0.07	0.16	0.19	16.6	99.1	87	67
13	0.19	0.22	0.24	17.5	123	145	65
14	0.28	0.16	0.208	25.3	263.7	205	61
15	0.17	0.20	0.26	16.63	124.0	59.0	60

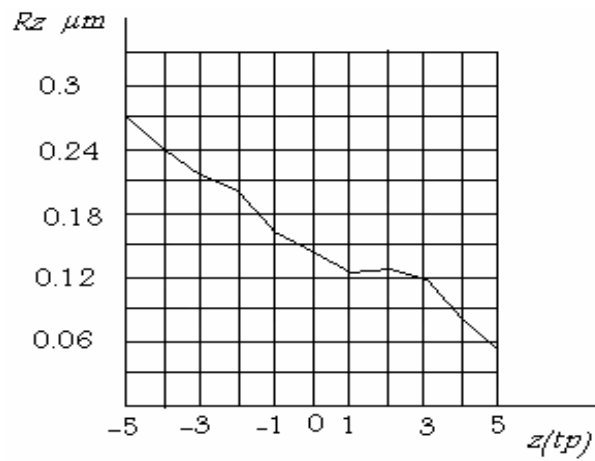


Figure.(4) Graph of Support Curve by MAF

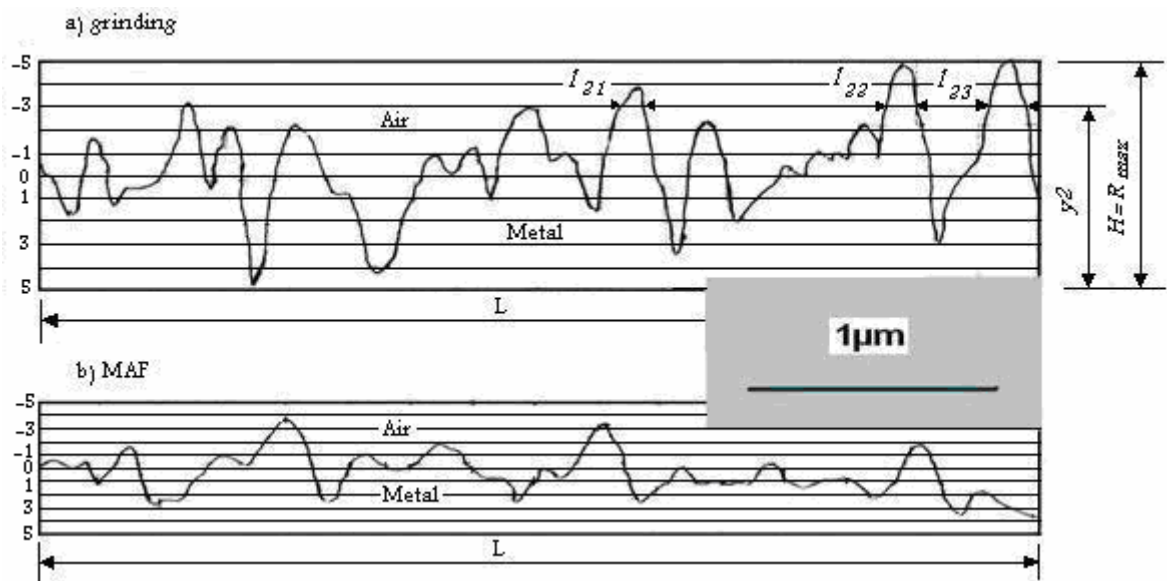


Figure.(5) Surface Profilogram Formed by MAF and Grinding.

Table (3)

	y_0	y_1	y_2	y_3	y_4	y_5	y_6	y_7	y_8	y_9	y_{10}
y (μm)	0.14	0.125	0.163	0.135	0.205	0.12	0.22	0.07	0.24	0.06	0.27
Z	0	+1	-1	+2	-2	+3	-3	+4	-4	+5	-5



EFFECT OF ROTATING CYLINDER ON THE DRAG FORCE OF A ROAD TRUCK VEHICLE

Najdat N. Abdulla
Prof.Dr./ University of Baghdad

Alaaldin A. Ismail
Mechanical Engineer

ABSTRACT

The effect on aerodynamic drag of a truck by controlling the boundary layer separation using a rotating cylinder on leading edge of the truck-trailer is investigated numerically. The flow was assumed to be steady, incompressible, turbulent, and two-dimensional passing over the top surface of the truck. The boundary condition for all the boundaries of the truck was set as well as the cylinder was treated as a moving wall with a specific rotational velocity. The developed computational algorithm is tested for the flow over a flat plate (8m) long with various free stream inlet relative velocity (U_∞) which are considered the same as truck velocity and has the values (40, 60, 90, and 120) km/h. The effect of cylinder diameter (10,20,30,and 40) , rotational speed (1000-5000 r.p.m) and free stream velocity on the aerodynamic drag and pressure distribution of the flow field were investigated. The governing equations which used are the continuity, momentum, and the (K- ϵ) turbulence model. These equations are approximated by using a finite volume method, with staggered grid and modified SIMPLE algorithm. A computer program in FORTRAN 90 is built to perform the numerical solution. The numerical results show that, the optimum cases for inlet free stream relative velocity (U_∞) values(40,60) km/h, a significant reduction of drag coefficient equal to 80% and 77% respectively was obtained by using a speed of rotation and diameter size equal to 5000 r.p.m and 40 cm , for (U_∞) value(90)km/h a reduction equal to 76%, and for (U_∞) equal to (120) km/h a reduction equal to 60% was obtained . These optimum results lade to reduce the effect of the aerodynamic drag on the vehicle by delaying the separation zone of boundary layer and enhancing the pressure gradient of the flow field. Comparison of the results with the available previous published experimental and fluent program results was investigated.

(momentum injection)

60 40) (U_∞) (8)
 (U_∞) . / (120 90
 30 20 10)
 . (5000-1000) (40
 Finite) . (K - ϵ)
 . (Simple Algorithm) (Staggered Grid) (Volume Method
 . (FORTRAN 90)
 80% / (60,40) (U_∞)

(30) (4000) 77%
. 60% / (120) 76% / (90)

(fluent)

Keywords: boundary layer control, rotating cylinder, computational fluid dynamics, road vehicles.

INTRODUCTION

Boundary layer separation takes place under adverse pressure gradient conditions when viscous effects are no longer confined to a thin layer but affect the overall flow pattern drastically, **Singh (2005)**. It can be seen that an adverse pressure gradient, ($\partial p / \partial x > 0$), is a necessary condition for separation. It does not mean that if ($\partial p / \partial x > 0$), a separation will occur, but rather it is reasoned that separation cannot occurs unless ($\partial p / \partial x > 0$). The point on the boundary where $[\partial u / \partial y]_{y=0} = 0$ is called the point of separation.

Just downstream from the point of separation, the flow direction in the separated region is actually opposite to the main flow direction. The low energy fluid in the separated region is forced back upstream by the increased pressure downstream **Robert (1973, 1978)**. The most common application to date has been the flow around an aerofoil wing of an aircraft. Flow separation takes place on the upper surface of the aerofoil at a large angle of attack resulting in a drastic fall in lift. Several methods, such as mass injection either by blowing or by suction, coating of the wall, or transition to turbulent flow etc. have been practiced with varying degrees of success. The concept of delaying boundary layer separation has also been used in road vehicles to reduce aerodynamic drag. However, the use of momentum injection using a moving wall for boundary layer control is still in its nascent stages. Momentum injection using rotating cylinders has been applied to airfoils in order to improve their lift characteristics like applied the concept of moving surface boundary layer control to a joukowski airfoil using rotating cylinders at the leading and trailing edges of the airfoil. However, the use of rotating cylinders to reduce aerodynamic drag on trucks is a new concept **Singh (2005)**. At 70 mph, a common highway speed today, overcoming aerodynamic drag represents about 65% of total energy expenditure for a typical heavy truck vehicle. Reduced fuel consumption for heavy vehicles can be achieved by altering truck shapes to decrease the aerodynamic resistance or drag. It is

conceivable that present day truck drag coefficients might be reduced by as much as 50%. This reduction in drag would represent approximately a 25% reduction in fuel use at highway speeds **Rose (2004)**.

Singh et.al {2005}, investigated aerodynamic drag effect using a model of a truck to control the boundary layer separation by the momentum injection method using a rotating cylinder. They used an experiments coupled with computational fluid dynamics (CFD) analysis to validate the theory of momentum injection. Modeling of the truck has been done on the software (GAMBIT); the best suitable turbulence model was selected by comparing the results with the experimental results. Steady state Navier Stokes equations are taken as the governing equations for the fluid motion, and appropriate boundary conditions are used. The rotational speed and radius of the cylinder are varied to establish the effect of momentum injection on aerodynamic drag. The coefficient of drag reduces by approximately 35 percent from an initial value of 0.51- 0.32 for a cylinder of radius 1cm with rotational speed of 4000 r/min. **Robson et.al {2005}**, used a generic rotating ventilator as a form of low energy drag reducer for use on bluff bodies such as transport vehicles. An experimental investigation of a rectangular bluff body was conducted to demonstrate the viability of this novel concept. The ventilator is expected to produce an effect on the flow characteristics similar to a rotating cylinder but with the added advantage that it can be operated using natural wind without the need for any power input by the engine or any auxiliary unit. The bluff body was modeled as a rectangular box; the ventilator was mounted on the front of the model with the axis of rotation parallel to the front surface and bottom edge. Open circuit open jet wind tunnel was used to conduct the experiments. The test Reynolds numbers were selected to lie between $3.5 - 6.5 \times 10^5$, measurements were taken at yaw angles of 0, 5, 10, 15 degrees. The results indicate that the device decreases drag on the body significantly by approximately 50% at Reynolds numbers of 3.5×10^5 and 6.5×10^5 . The

incorporation of this device also makes the drag of the body less Reynolds number dependent. Consequently the proposed configuration is more efficient at higher speed in comparison with the conventional configuration which did not have the device attached to it.

Salam Al-Tae {2005}, studied the separation control on the *NACA 0012 & NACA 0018* airfoils by using a rotating cylinder based on the computation of Reynolds-average Navier-Stokes equations. A numerical model based on collocated finite volume method is developed to solve the governing equations on a body-fitted grid. To ensure the accuracy of the code first, second and third order differencing schemes, with and without flux-limiters, have been implemented and tested. The systematical investigation of the rotating cylinder is conducted on the same *NACA 0012* airfoil in the range of attack angles from 10^0 up and beyond the stall angle at $Re=10^6$. the influence of some parameters associated with using rotating cylinder, such as its radius, location, and the speed ratio (U_c/U_∞) strength on the performance of the airfoils have been studied. The result shows that the rotating cylinder is affected in controlling the separation and the lift coefficient of circulation control airfoil is increased with the angle of attack.

Robert Clark {2006}, presented a combination of wind tunnel test, computational fluid dynamic modeling, and real-world testing to determine the effects of the external additions devices and systems on aerodynamic drag and fuel economy. These devices include (cab enclosure, vortex traps, side strakes, and side skirts). The results showed a reduction on the aerodynamic drag by 23% for tractor-semitrailer systems.

Johan Hoffman {2007}, considered the problem of computational simulation of flow past a wheel of a vehicle. As a model he used a rotating cylinder in contact with a flat surface moving with the same velocity as the uniform free stream. In particular he was interested in the importance of including the effect of rotation in the model to accurate compute the drag force. He compared two different models; (i) a cylinder rolling around ground, and (ii) a stationary cylinder in free stream, corresponding to a simple wind tunnel testing. He compared the drag for (i) and (ii) at Reynolds number of 10000. He used CFD method to investigate the importance of including (i)-(ii) in a model. As computational model he considered the flow about cylinder rolling along a flat surface. CFD concerns the computational solution of the Navier-Stokes equations, which are considered to model both laminar and turbulent flow. In this paper study the flow of turbulent boundary layer over a flat plate, study the effect of

a rotating cylinder (in order to inject momentum) on the aerodynamic drag, utilizes CFD method and standard $\kappa\text{-}\epsilon$ model to analyze the effect of momentum injection on the aerodynamic drag, use different values of rotation speeds to demonstrate the effect of rotation on the drag coefficient and use different values of diameter size to demonstrate the effect of diameter size on the drag coefficient.

MATHEMATICAL MODEL

The starting point of any numerical method is the mathematical model, i.e. the set of partial differential or integral-differential equations and boundary conditions. These equations are based on the conservation of mass and momentum. A finite volume method (FVM) is presented for the solution of two-dimensional Navier-Stokes equations in a Cartesian coordinate. The (k- ϵ) model is utilized to describe the turbulent flow on the upper surface of the truck. The flow was assumed to be steady, two- dimensional and incompressible over a flat plate with a rotating cylinder in the leading edge of the plate.

Geometry and Coordinate System:

The usual system of Cartesian coordinates is adopted which represents the x-axis being along the wall and the y-axis being at right angle to it, as shown in **Fig. (a)**.

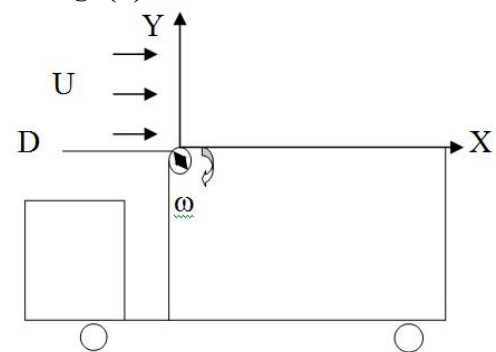


Figure.(a).

The Governing Equations:

The equations of motion for steady state, two dimensional and incompressible flows over flat plate can be written as follows ,**Robert(1973,1978):-**

(i) Continuity Equation

$$\frac{\partial}{\partial x}(\rho u) + \frac{\partial}{\partial y}(\rho v) = 0 \quad (1)$$

(ii) Momentum Equations

X- Direction (u – momentum)

$$\frac{\partial}{\partial x}(\rho u u) + \frac{\partial}{\partial y}(\rho u v) = -\frac{\partial p}{\partial x} + \mu \left[\frac{\partial^2 u}{\partial x^2} + \frac{\partial^2 u}{\partial y^2} \right] \quad (2)$$

Y-Direction (v- momentum)

$$\frac{\partial}{\partial x}(\rho u v) + \frac{\partial}{\partial y}(\rho v v) = -\frac{\partial p}{\partial y} + \mu \left[\frac{\partial^2 v}{\partial x^2} + \frac{\partial^2 v}{\partial y^2} \right] \quad (3)$$

The effects of fluctuation can be introduced by replacing the flow variable u, v, ρ and p by the sum of mean and fluctuating components. Thus, Versteeg (1995):

$$\left. \begin{aligned} u &= \bar{U} + u' \\ v &= \bar{V} + v' \\ P &= \bar{P} + p' \end{aligned} \right\} \quad (4)$$

With some simplification the momentum equations become, Awbi(1991):

$$\rho U \frac{\partial U}{\partial x} + \rho V \frac{\partial U}{\partial y} = -\frac{\partial P}{\partial x} + \frac{\partial}{\partial x} \left[\mu_e \frac{\partial U}{\partial x} \right] + \frac{\partial}{\partial y} \left[\mu_e \frac{\partial U}{\partial y} \right] + \frac{\partial}{\partial x} \left[\mu_e \frac{\partial U}{\partial x} \right] + \frac{\partial}{\partial y} \left[\mu_e \frac{\partial U}{\partial x} \right] \quad (5)$$

$$\rho U \frac{\partial V}{\partial x} + \rho V \frac{\partial V}{\partial y} = -\frac{\partial P}{\partial y} + \frac{\partial}{\partial x} \left[\mu_e \frac{\partial V}{\partial x} \right] + \frac{\partial}{\partial y} \left[\mu_e \frac{\partial V}{\partial y} \right] + \frac{\partial}{\partial x} \left[\mu_e \frac{\partial V}{\partial y} \right] + \frac{\partial}{\partial y} \left[\mu_e \frac{\partial V}{\partial x} \right] \quad (6)$$

Turbulence Model:

Standard K-ε Model

The general modified form of (K-ε) model can be written as follows, Versteeg (1995):

$$\rho U \frac{\partial K}{\partial x} + \rho V \frac{\partial K}{\partial y} = \frac{\partial}{\partial x} \left[\frac{\mu_t}{\sigma_k} \frac{\partial K}{\partial x} \right] + \frac{\partial}{\partial y} \left[\frac{\mu_t}{\sigma_k} \frac{\partial K}{\partial y} \right] + \mu_t \left[2 \left(\frac{\partial U}{\partial x} \right)^2 + 2 \left(\frac{\partial V}{\partial y} \right)^2 + \left(\frac{\partial U}{\partial y} + \frac{\partial V}{\partial x} \right)^2 \right] - \rho \epsilon \quad (7)$$

$$\rho U \frac{\partial \epsilon}{\partial x} + \rho V \frac{\partial \epsilon}{\partial y} = \frac{\partial}{\partial x} \left[\frac{\mu_t}{\sigma_\epsilon} \frac{\partial \epsilon}{\partial x} \right] + \frac{\partial}{\partial y} \left[\frac{\mu_t}{\sigma_\epsilon} \frac{\partial \epsilon}{\partial y} \right] + c_{1\epsilon} \frac{\epsilon}{K} \mu_t \left[2 \left(\frac{\partial U}{\partial x} \right)^2 + 2 \left(\frac{\partial V}{\partial y} \right)^2 + \left(\frac{\partial U}{\partial y} + \frac{\partial V}{\partial x} \right)^2 \right] - c_{2\epsilon} \rho \frac{\epsilon^2}{K} \quad (8)$$

The empirical constants appearing in the above equation have the values of, Fayadh (2004/2005):-

$$C_\mu=0.09 \quad C_{1\epsilon}=1.44 \quad C_{2\epsilon}=1.92 \quad \sigma_K=1.00 \\ \sigma_\epsilon=1.3 \quad \sigma=0.7 \quad \sigma_t=0.9$$

Further Calculation:

The most important parameters for boundary layer flow, is drag coefficient C_{Df} :

$$Drag = 1/2 \rho V^2 A C_{Df}$$

Where C_{Df} : coefficient of skin friction drag.

A: is the surface area.

ρ : is the density of the air.

V: is the speed of the vehicle relative to the air.

COMPUTATIONAL TECHNIQUE

The solution of the continuity and momentum equations was performed by using a finite volume method (FVM) to obtain the discretization form for these equations. These discretization equations are solved by using SIMPLE algorithm with hybrid scheme. A computer program based on this algorithm and uses FORTRAN 90 language was built to meet the requirements of the problem. The SIMPLE algorithm was based on the staggered grid in which the velocities staggered midway between the grid intersections is used to obtain the numerical results.

The General form of the Governing Equations, Versteeg (1995):

$$\frac{\partial}{\partial x}(\rho u \Phi) + \frac{\partial}{\partial y}(\rho v \Phi) = \frac{\partial}{\partial x} \left[\Gamma_\Phi \frac{\partial \Phi}{\partial x} \right] + \frac{\partial}{\partial y} \left[\Gamma_\Phi \frac{\partial \Phi}{\partial y} \right] + S_\Phi \quad (9)$$

Where Φ , Γ_Φ , S_Φ define in table (1) as flow

Table (1) Source terms in the transport equation.

Equation	ϕ	Γ_ϕ	S_ϕ
Continuity	1	0	0



U-momentum	U	μ_e	$-\frac{\partial P}{\partial x} + \frac{\partial}{\partial x} \left[\mu_e \frac{\partial U}{\partial x} \right] + \frac{\partial}{\partial y} \left[\mu_e \frac{\partial V}{\partial x} \right]$
V-momentum	V	μ_e	$-\frac{\partial P}{\partial y} + \frac{\partial}{\partial x} \left[\mu_e \frac{\partial U}{\partial y} \right] + \frac{\partial}{\partial y} \left[\mu_e \frac{\partial V}{\partial y} \right]$
Kinetic energy	K	Γ_K	G- $\rho \epsilon$
Dissipation rate	ϵ	Γ_ϵ	$C_{1\epsilon} \rho \frac{\epsilon}{K} G - C_{2\epsilon} \rho \frac{\epsilon^2}{K}$

Where:

$$G = \mu_t \left[2 \left(\frac{\partial U}{\partial x} \right)^2 + 2 \left(\frac{\partial V}{\partial y} \right)^2 + \left(\frac{\partial U}{\partial y} + \frac{\partial V}{\partial x} \right)^2 \right] \quad (10)$$

$$\Gamma_K = \frac{\mu_e}{\sigma_K} \quad \Gamma_\epsilon = \frac{\mu_e}{\sigma_\epsilon} \quad (11)$$

$$\Gamma_e = \frac{\mu}{\sigma} + \frac{\mu_t}{\sigma_t} \quad (12)$$

Grid Generation:

To avoid the instability in the solution, and unrealistic pressure field, the staggered grid technique has been adopted. Staggered grids imply that different dependent variables are evaluated at different grid points. The scalar variables are stored at the main grid points, while the velocity components are stored at staggered grids (the velocities are defined at the faces of control volumes). Hence, the scalar variables including pressure are stored at the main grid nodes denoted by small circles, **Versteeg (1995)**.

Discretization of the general form of Equations:

The final discretised algebraic equation, **Versteeg (1995)**:

$$A_P \phi_P = A_E \phi_E + A_W \phi_W + A_N \phi_N + A_S \phi_S + S_u \quad (13)$$

Where:

$$A_p = A_E + A_W + A_N + A_S - S_p \quad (14)$$

$$\left. \begin{aligned} A_E &= D_e - \frac{F_e}{2} \\ A_W &= D_w + \frac{F_w}{2} \\ A_N &= D_n - \frac{F_n}{2} \\ A_S &= D_s + \frac{F_s}{2} \end{aligned} \right\} \quad (15)$$

Where the above equations can be expressed in general form for different types of schemes as **Patankar (1980)**:

$$\left. \begin{aligned} A_E &= D_e A(|Pe|)_e + [[-F_e, 0]] \\ A_W &= D_w A(|Pe|)_w + [[F_w, 0]] \\ A_N &= D_n A(|Pe|)_n + [[-F_n, 0]] \\ A_S &= D_s A(|Pe|)_s + [[F_s, 0]] \end{aligned} \right\} \quad (16)$$

Here, $A(|Pe|)$ is a function concerned with various types of schemes. Expressions for $A(|Pe|)$ for different schemes are listed in Table (4-2) in which $|Pe|$ is peclet number ($Pe = Re Pr$) at the control volume faces which may be expressed as the ratio of the strength of convection term (F) to that of diffusion term (D). The operator $[[A \dots]]$ appearing in equations refers to the maximum value of the quantities contained within it.

Table (2) Function A ($|Pe|$) for different schemes, Patankar (1980).

Scheme	Formula for A($ Pe $)
Central difference	$1-0.5 Pe $
Upwind	1
Hybird	$[[0, 1-0.5 Pe]]$
Power law	$[[0, (1-0.1 Pe)^5]]$
Exponential	$ Pe / [\exp(Pe) - 1]$

RESULTS AND DISCUSSION

Fig. (1) Shows the effect of varying the mesh size on the drag coefficient at rotation speed $\omega=2000$ and cylinder diameter $D=40$ cm. A grid independency test is performed to check the validity of the numerical technique, the numbers of nodes which had been taken are (2800, 3200, 3600, 4000). It is clear that the influence of the mesh size on the drag coefficient was small, so (3200) nodes was selected for all calculations.

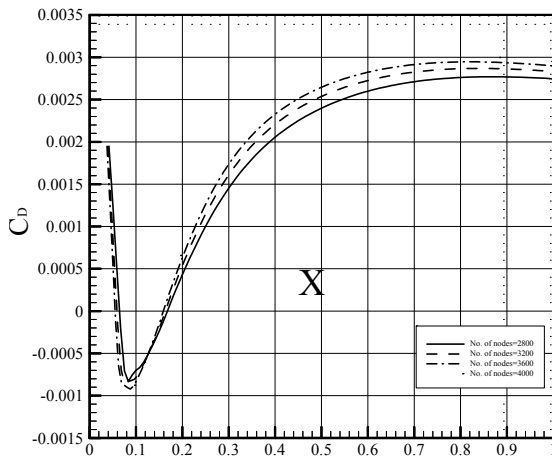


Figure. (1) Effect of mesh size on the drag coefficient.

The parameters that had a direct influence on the amount of reduction in the drag coefficient are the rotation speed (ω), and diameter size (D), thus the effect of each parameter was studied in separate cases according to the value of vehicle speed (U_∞) as will shown in the figures.

Fig. (2.a-d) show the effect of variation of cylinder rotation speeds on the drag coefficient (C_D) and wall shear stress (τ_w) with vehicle speed (U_∞) equal to 60 km/h. The cases are classifying according to diameter size. When the cylinder rotates, the fluid starts to inject over the surface, this action creates a low pressure zone directly after the cylinder and this causes an appearing of a streamwise vortices **Solberg (1989)**. This streamwise jet help the air flow to cling more closely to the upper surface {1}, and this is leading to delay the separation zone and reduce the drag coefficient. The amount of reduction depends on rotation speed as shown in the figures. For the case of D=10, 20 cm, it can be seen that the drag coefficient (C_D) increases along distance as the rotation speed increases, but for cases of D=30, and 40 cm the drag coefficient decreases as the rotation speed increases. For small cylinder diameter the momentum injected of the flow is small and will not create enough streamwise vortices to help the flow to cling closely to the surface which has a reverse influence on the flow.

Also, it can be seen in the figures that an extreme dropping in the drag coefficient, this due to the streamwise vortices zone and low pressure accompanying with it.

Fig. (3.a-d) show the effect of variation of cylinder rotation speeds on the drag coefficient (C_D) with vehicle speed (U_∞) equal to 90 km/h. The cases also classified according to diameter size. For the cases of D=10, 20 cm, it can be seen that the drag coefficient (C_D) increases along distance as the rotation speed increases, but in the other cases of D=30, 40 cm they are started to decrease after the rotation speed (ω) became 3000 r.p.m. This behavior is due to diameter size and the high vehicle speed (U_∞) velocity. For small cylinder diameter the momentum injected of the flow is small and will not create enough streamwise vortices to help the flow to cling closely to the surface which has a reverse influence on the flow.

Fig. (4.a-d) show the effect of diameter sizes on the drag coefficient (C_D) with vehicle speed of (U_∞) equal to 120 km/h. For the cases of $\omega=1000$, 2000 r.p.m the figures showed a little reduction in the drag coefficient, while the case of case of $\omega=3000$ r.p.m showed a significant reduction in the drag coefficient, Furthermore for the cases of $\omega=4000$, 5000 r.p.m it can be seen a huge reduction in the drag coefficient. The amount of reduction depends on the diameter size, as shown in the figures and the amount of reduction increases by increasing the diameter. This is due to the significant amount of injected flow, and thus the streamwise vortices significantly increases.

Fig. (5) show the predicted distribution of velocity field vector over the surface with and without rotation, $\omega=0$, 3000, 5000 r.p.m for each vehicle speed, $U_\infty=90$ to demonstrate the influence of rotation. It can be seen that at $\omega=0$ there is no vortices, but as the rotation starts, the effect of streamwise vortices appears and perform a significantly influence on the flow field.

CONCLUSIONS

For the case of vehicle speed (U_∞) equal to (40km/h), the maximum reduction in the drag coefficient obtained by using a rotation speed (ω) equal to (5000) r.p.m and a diameter equal to (40) cm. For the case of vehicle speed (U_∞) equal to (60km/h), the maximum reduction in the drag coefficient obtained by using a rotation speed (ω) equal to (5000) r.p.m and a diameter equal to (40) cm. For the case of vehicle speed (U_∞) equal to (90km/h), the maximum reduction in the drag

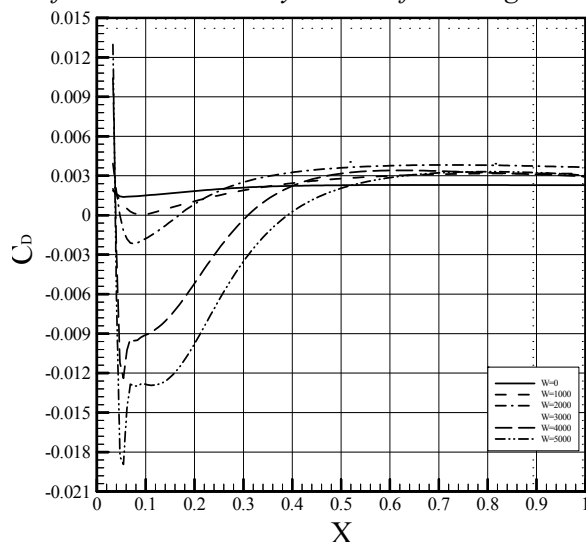


coefficient obtained by using a rotation speed (ω) equal to (5000) r.p.m and a diameter equal to (40) cm. For the case of vehicle speed (U_∞) equal to (120km/h), the maximum reduction in the drag coefficient obtained by using a rotation speed (ω) equal to (5000) r.p.m and a diameter equal to (40) cm.

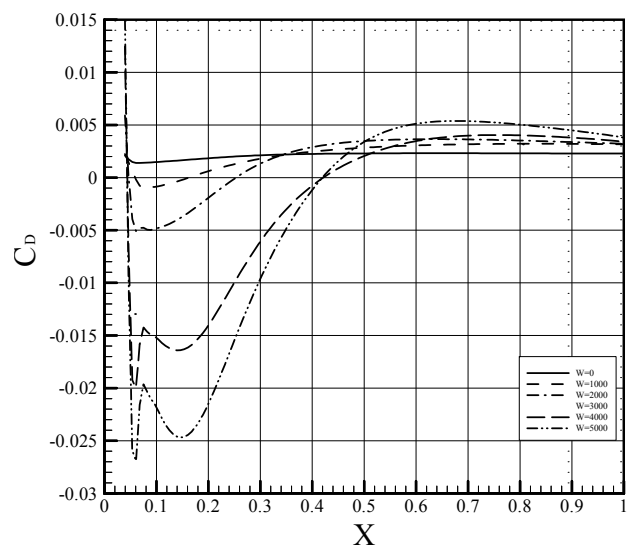
Using a rotating cylinder creates stream vortices and this helps in attachment of the flow to the wall and hence delaying the separation of boundary layer separation.

REFERENCES

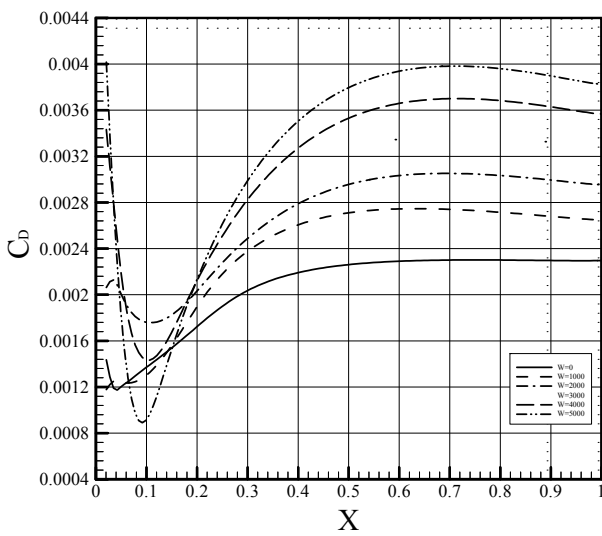
- Awbi, H.H. "Ventilation of Building", Department of Construction Management and Engineering, University of Reading, London (1991).
- Robert M. Clarke "Truck Manufacturers Program to Reduce Aerodynamic Drag ", Tam, Truck Manufacturers Association, April (2006).
- Robert W. Fox, Alan T. McDonald "Introduction to Fluid Mechanics" Second Edition, by John Wiley & Sons, Inc. (1973, 1978).
- Robonson S.E. and Ahmed, N.A. "Drag Reduction on Bluff Bodies using a Rotating Device" 15th Australasian Fluid Mechanics Conference, University of Sydney, (2004).
- Rose C. McCallen, Larry J. Dechant, and David Pointer W. "DOS's Effort to Reduce Truck Aerodynamic Drag – Joint Experiments and Computations Lead to Smart Design "34th AIAA Fluid Dynamics Conference and Exhibit, Portland, or, United States, June 28, 2004 through July 1, (2004).
- Salam H. Hussain "Numerical investigation of Airfoil Flow Control by Means of Rotating
- Fayadh, and M. Abed Al-Dulaimy, R. Cousin " A CFD Assessment to Transonic Flow Around a RAE-2822 Airfoil", Research Reports from Guest Scientists in the Faculties 07 and 09 in the Academic year (2004/2005) Issn 1612 – 9040.
- Johan Hoffman " Computational Study of the Effect of Rotation in a Model of the Turbulent Flow Due to a Cylinder Rolling", (Turbulent flow past a rolling cylinder), School of Computer Science and Communication, KTH, SE-10044 Stockholm, Sweden 1st June (2007).
- Patankar S.V. "Numerical Heat Transfer and Fluid Flow", Hemisphere Publishing Corporation, Taylor & Francis Group, (1980).
- Cylinder ", PhD. Thesis, Mechanical Engineering Department, University of Baghdad, April (2005).
- Singh S. N., Rai L, Puri P. and Bhatnagar A. "The Effect of Moving Surface On The Aerodynamic Drag of Road Vehicles", Proc. ImechE .Vol.219 Part D: J. Automobile Engineering, (2005).
- Solberg T., and Eidsvik, K. J. "Flow Over a Cylinder at a Plane Boundary-a Model Based Upon ($k-\epsilon$) Turbulence", ASME Journal Vol. 111, December (1989).
- Versteeg, H.K., and Malalasekera, W. "An Introduction to Computational Fluid Dynamics- The finite volume method", Longman group Ltd., (1995).



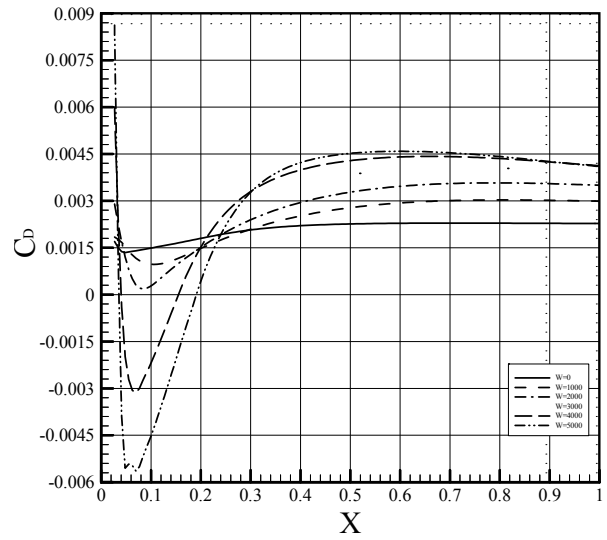
(2.a) D=10cm.



(2.b) D=20cm.

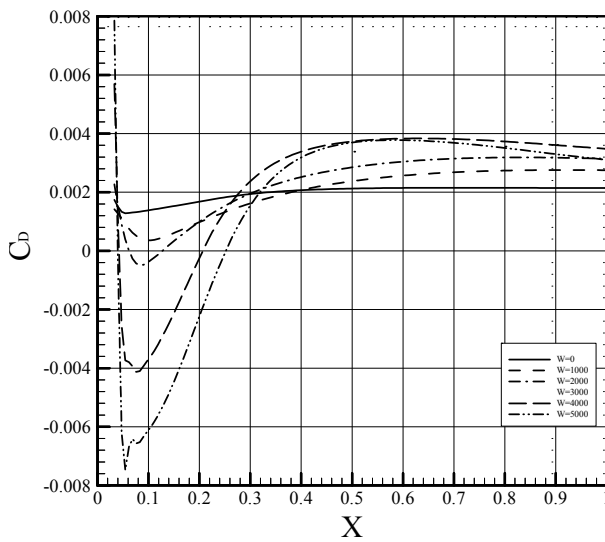


(2.c) $D=30\text{cm}$.

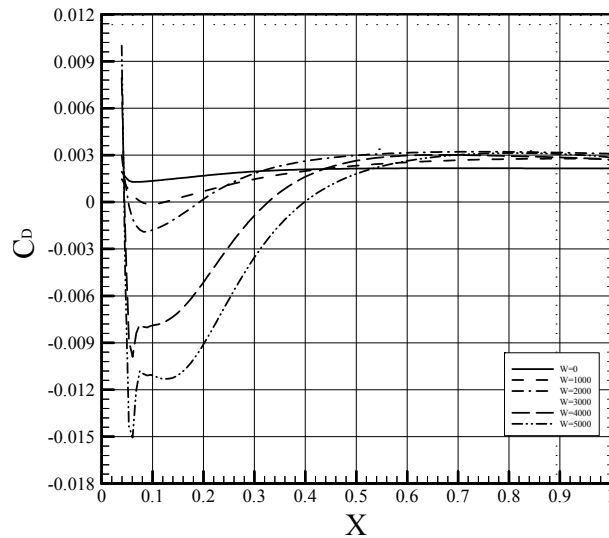


(2.d) $D=40\text{cm}$.

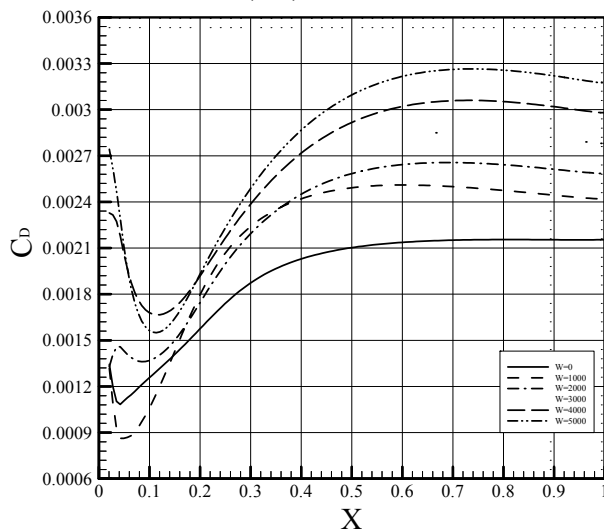
Figure. (2) Effect of cylinder rotation on drag coefficient, for vehicle speed $U_\infty=60\text{ km/h}$.



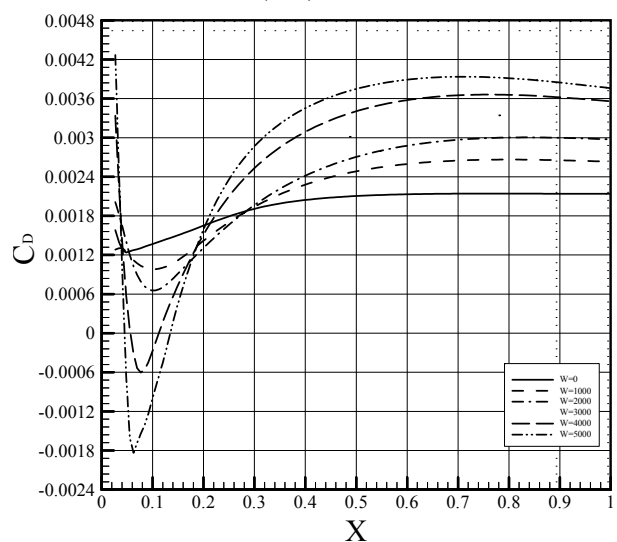
(3.a) $D=10\text{cm}$.



(3.b) $D=20\text{cm}$.

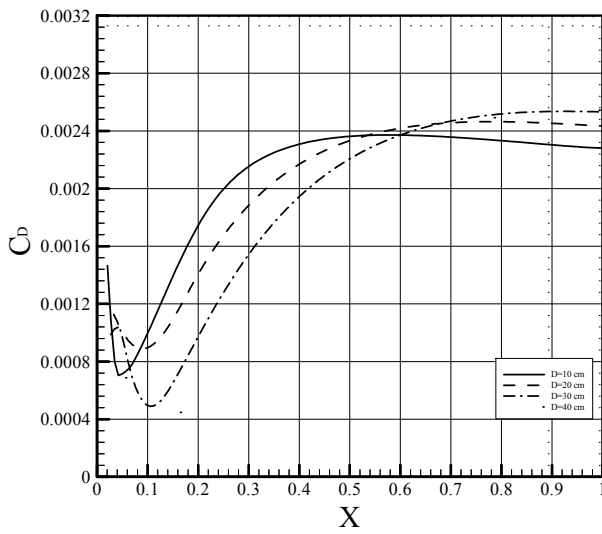


(3.c) $D=30\text{cm}$.

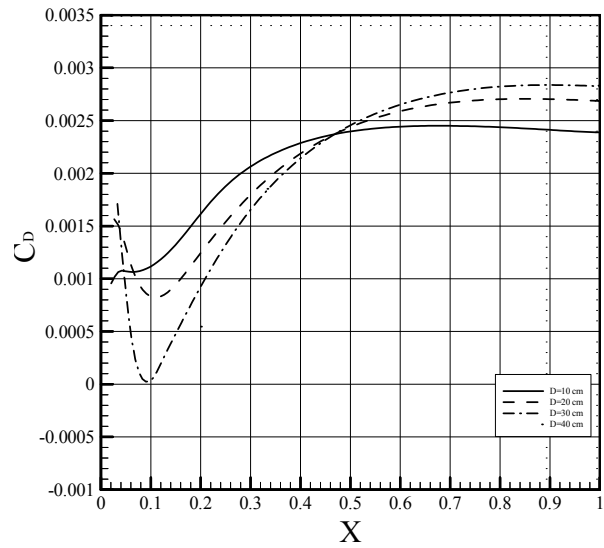


(3.d) $D=40\text{cm}$.

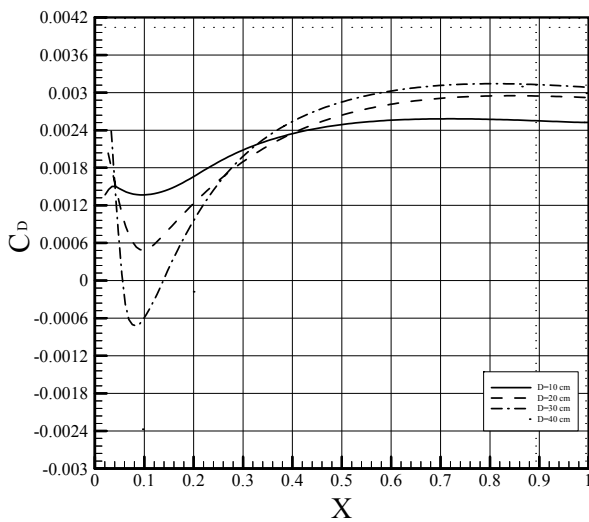
Figure. (3) Effect of cylinder rotation on drag coefficient, for vehicle speed $U_\infty=90$ km/h.



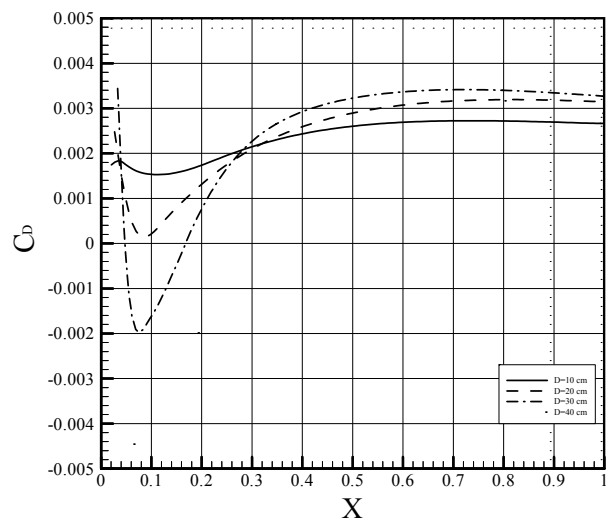
(4.a) $\omega=1000$ r.p.m.



(4.b) $\omega=2000$ r.p.m.



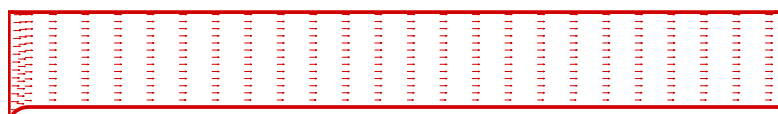
(4.c) $\omega=3000$ r.p.m.



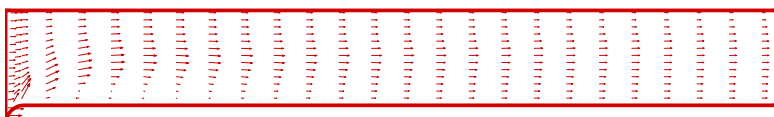
(4.d) $\omega=4000$ r.p.m.

Figure. (4.a-d) Effect of cylinder diameter on drag coefficient, for vehicle speed $U_\infty=120$ km/h.

$U=90$ Km/h
 $D=40$ Cm
 $W=0$ r.p.m



$U=90$ Km/h
 $D=40$ Cm
 $W=3000$ r.p.m



$U=90$ Km/h
 $D=40$ Cm
 $W=5000$ r.p.m

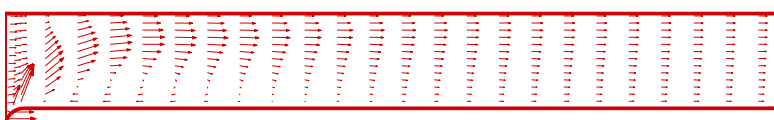


Fig. (5) Velocity field vectors over upper surface at different values of ω , for vehicle speed $U_{\infty}=90$ km/h and $D=40$ cm.

**NOMECLATUR**

A = Convection- diffusion coefficient (kg/s)

C_D = coefficient of skin friction drag

$C_\mu, C_{1\epsilon}, C_{2\epsilon}$ = Constants in turbulence model

D = Diffusion term (kg/s)

F = Convection term (kg/s)

P = Pressure (Pa)

Pe = Peclet number ($Pe=Re \cdot Pr$)

Re = Reynolds number ($Re = \rho UL / \mu$)

U_∞ = Relative Free stream velocity (m/s)

U, V = Mean velocity components in x,y directions (m/s)

X, Y = Cartesian coordinates (m)

S_ϕ = Source term

ω = Rotational speed (r.p.m)

Γ = Diffusion coefficient

ϵ = Dissipation rate of turbulent kinetic

μ = Laminar viscosity (kg/m.s)

μ_t = Turbulent or eddy viscosity (kg/m.s)

μ_e = Effective eddy viscosity (kg/m.s)

ρ = Density (kg/m³)

λ = Thermal conductivity (W/m.k)

ϕ = Dependent variable

ν = Kinematic viscosity (m²/s)

ν_t = Turbulent kinematic viscosity (m²/s)

$\sigma_K, \sigma_\epsilon$ = Constants for the K- ϵ model

σ = Laminar Prandtl number ($\sigma = \mu c_p / \lambda$)

σ_t = Turbulent Prandtl number ($\sigma_t = \mu_t c_p / \lambda$)

ABBREVIATIONS

CFD= Computational Fluid Dynamics

FVM= Finite Volume Method

SIMPLE= Semi-Implicit Method for Pressure Linked Equations

TDMA= Tri -Diagonal Matrix Algorithm



SEISMIC ANALYSIS OF LIQUID STORAGE TANKS

Dr. AbdulMuttalib I. Said

Civil Engineering Department, College of Engineering, University of Baghdad

Email: abdmusawi@yahoo.com

Ammar A. AbdulMajeed

Civil Engineering Department, College of Engineering, University of Baghdad.

ABSTRACT

This study presents an idealization scheme for the analysis of rectangular storage tanks acted upon by earthquake excitations. Above and below ground tank, uses have been considered. A linear three-dimensional finite element analysis has been used to predict the natural frequencies. Analysis parameters are the ratio of height to length of the tank, the type of soil, level of water in the tank, and also the wall thickness. The results for top displacement and axial force components for a full tank above ground case have values greater than those in half- full (31%) and empty tank cases (75%). At the opposite of that, the underground tank demonstrates that top displacement and axial force components for an empty tank case have values greater than those in half- full (19%) and full tank cases (40%). The base shear for above ground tank case has values greater than those in underground tank cases (19% to 37%). The shear base for soil type 2 is greater than those in soil type 1 (17% to 28%).

Key words: Seismic analysis, viscous dampers, rectangular tanks, finite element models, fluid-structure-soil interaction, time history, free vibration, ANSYS.

الخلاصة

تتضمن الدراسة تحليل الخزانات المستطيلة المعرضة الى هزات أرضية بحالتين، الأولى تكون فيها الخزانات مدفونة بشكل كامل تحت الارض والحالة الثانية تكون الخزانات فيها فوق مستوى سطح الارض. استخدم التحليل الخطي ثلاثي الابعاد بطريقة العناصر المحددة لغرض تحري علاقة كل من الاهتزاز الطبيعي ونسبة ارتفاع الجدران من حيث تغير نوع التربة وكمية الماء الموجودة بالخزان وكذلك علاقتة ايضا باختلاف سمك الجدران والأزاحة العليا والقوة المحورية لحالة الخزان فوق الارض وهو مملوء، لها قيم اعظم من الحالة النصف مملوءه بنسبة 31% وبنسبة 75% اعظم من الحالة الفارغة. بعكس ذلك تكون الأزاحة العليا والقوة المحورية لحالة الخزان المدفون اعظم وهو فارغ من ما هو نصف مملوء بنسبة 19% وبنسبة 40% اعظم من حاله المملوءه. قوة القص عند الاساس لحالة الخزان فوق سطح الارض لها قيم اعظم من حالة الخزان تحت الارض بنسبة (19% الى 37%). قوة القص عند الاساس في حالة التربة رقم 2 (التربة الضعيفة) تكون اعظم من حالة التربة رقم 1 بنسبة (17% الى 28%).

1. INTRODUCTION

Damages of storage tanks due to recent earthquakes have been extensively studied by (Jennings 1971, Hanson 1973, and Monos and Clough 1985). These tanks are mainly steel tanks whose failure modes are edge effects in the form of elephant foot buckling at the base. (Housner 1957) is the first who considered the hydrodynamic pressure distribution developed in rigid tanks during horizontal base excitation. He formulated a dynamic model for estimating the liquid response in seismically excited rigid, rectangular and circular tanks. The effect due to shell flexibility is later incorporated in the model by (Veletsos and Yang 1976), (Nash et al. 1978), (Haroun and Housner 1980). (Haroun and Tayel 1984) have investigated the effect of soil-structure interaction. (Veletsos and Tang 1986) and (Luft 1984) have considered the effect of vertical excitation on the hydrodynamic pressures. (Haroun and Chen 1989) have investigated the nonlinear sloshing behavior in rectangular tanks by considering large amplitude sloshing. The finite element analysis of the liquid-tank system is studied by (Haroun and Housner 1981). Several studies were also carried out to investigate that dynamic interaction between deformable wall of the tank and the liquid using finite element analysis. (ASCE 1984) comprehensively discusses the effect of fluid-structure interaction on the hydrodynamic pressures and (ASCE 1981) provides excellent guidelines for the analysis and design of liquid storage structures.

2. BASIC ASSUMPTIONS

The assumptions introduced in the present analysis are as follows:

- The tank is symmetric about x-axis and z-axis in terms of geometry.
- The material of the tank is linearly elastic, isotropic and homogeneous.
- The contained liquid is inviscid, incompressible and in a non-rotational motion, within vessels having no net flow rate
- The base is connected rigidly to the tank wall.
- The soil medium is represented as a system of closely spaced independent linear springs, masses and dashpots.
- The seismic effect is parallel to the z-axis and perpendicular to the x-axis

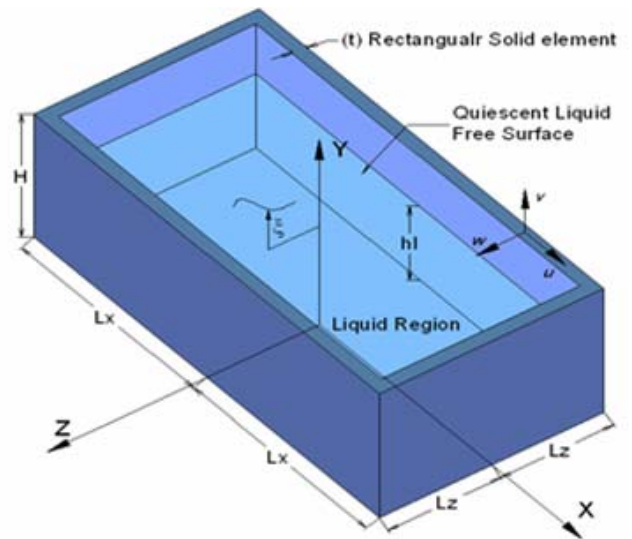


Plate (1) Rectangular storage tank and coordinate system

3. DESCRIPTION OF STRUCTURE

The structure analyzed in the present study, shown in Plate (1), is a typical rectangular storage tank with a volume of 767.6m³. The contained liquid is assumed to be water with the density of 10kN/m³, $E_w = 2.0684 \times 10^9$ kN/m² and Viscosity = 1.2379×10^{-12} kN/m.s, $\nu_w = 0.19$. The tank has a length of 12.6m, a width 6.3m, a height 12.6m and a shell thickness of 0.45m and is constructed using concrete with $E_c = 20 \times 10^6$ kN/m², $\nu_c = 0.15$ and $\rho_c = 24$ kN/m³. The damping coefficient of the overall structure has been assumed equal to 5%. The soil has been chosen, according to (Prakash 1981) classification, four different models of soil types are considered. The four types of soil are classified in Table (1).

Table (1) Parametric studies of soil type

No.	Soil type	Mass density (ρ_s) kN.s ² /m ⁴	Shear modules (G_s) kN /m ²
1	Loess at natural moisture	1.67	112892
2	Medium-sized gravel	1.8	58320
3	Medium-grained sand	1.65	42240
4	Fine-grained sand	1.65	19965

4. SEISMIC GROUND EXCITATION

The structure is assumed to be acted upon by a seismic ground motion, represented by acceleration whose duration is 31.18sec. A peak ground acceleration (PGA) of 0.318g have been used. A rectangular concrete tank has been analyzed due to north-south component El-Centro earthquake of Fig. (1), the first five seconds were considered for analyzing the tanks

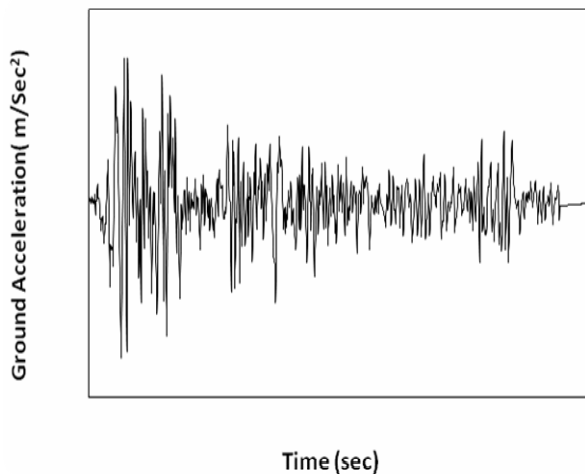


Figure (1) Accelerogram N-S El Centro earthquake, 18-May-1940

5 .SOIL-STRUCTURE INTERACTION

According to (Clough 2003), the soil-structure interaction (SSI) effects on the dynamic response of a rectangular tank can be taken into account by modeling each of the physical degrees-of-freedom, i.e .horizontal and vertical, of the surrounding soil system as discrete system with six degrees-of-freedom. The constants of all the discrete elements are computed as listed in Table(2)

Table (2) Soil properties of all concrete models considered in the analysis

Soil type		unit	soil type 1	soil type 2	soil type 3	soil type 4
Directions	r	m	0.5085	0.5085	0.5085	0.5085
	G_s	kN/m	112892	58320	42240	19965
	v_s	-	0.45	0.2	0.3	0.35
Vertical	K_s	kN/m²	417495	148278	122737	62475
	C_s	kN.s/m	542.0	335.3	305.1	208.4
	m_s	kN.s²/m	0.33	0.36	0.36	0.33
Horizontal	K_s	kN/m	346811	159921	123092	59554
	C_s	kN.s/m	298.0	210.1	184.3	122.8
	m_s	kN.s²/m	0.06	0.07	0.07	0.06

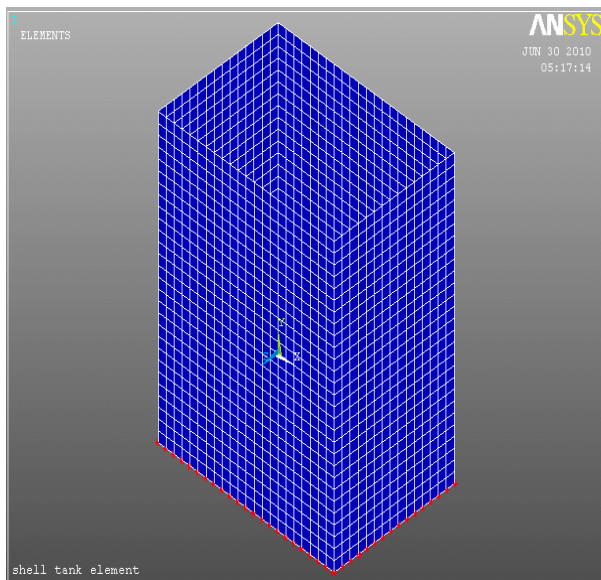
6. FINIT ELEMENT MODEL

The numerical analysis of the rectangular storage tank structure is performed on the basis of detailed FE model implemented with the help of the routines available in the ANSYS Finite Element program (ANSYS 2008), as shown in Plate (2). The rectangular storage tank is modeled using 26485 or 19093 element, for the two cases of tank considered in this work, i.e. the underground tank and the tank above ground respectively. Four-noded shell elements (SHELL63) with six DOFs per node are used. The eight node solid fluid element (FLUID80), with three DOFs per node, has been chosen to model the incompressible fluid content. A total of 4368 or 8736 FLUID80 elements are used, respectively, for the three levels of water tank is considered in this work, i.e. empty, half full and full. In order to satisfy the continuity conditions between the fluid and solid media at the rectangular tank boundary, the coincident nodes of the fluid and shell elements are constrained to be coupled in the direction normal to the interface, while relative movements are allowed to occur in the tangential directions. The uniaxial “tension only” behavior of the braces is simulated by means of the 3-D spar elements LINK10, which feature a bilinear stiffness matrix, i.e. the stiffness is removed if the element goes into compression. The viscous fluid damper devices are modeled using the 1-D non-linear damper elements COMBIN37. Finally, concentrated mass elements (MASS21) and linear spring-damper elements (COMBIN14) are used to model the discrete elements for the simulation of

soil-structure interaction. The above FEM rectangular tank model is numerically analyzed by means of a full transient linear analysis. The governing equations of motion can be expressed in matrix form as (Chopra 1996)

$$[M]\{\ddot{U}\} + [C]\{\dot{U}\} + [K]\{U\} = -[M]\{R\}\ddot{U}_g(1)$$

with $[M]$, $[C]\{\dot{U}\}$ and $[K]\{U\}$ being the mass, damping and stiffness matrices of the structure, respectively, $\{R\}$ an influence coefficient matrix, and \ddot{U}_g the ground acceleration. Eq. (1) is integrated directly in time using the Newmark- β method.



Plat (2) Finite element rectangular tank model

7. NUMERICAL STUDY

Seismic response of the rectangular liquid storage tank above ground and underground is investigated by performing two types of analyses: (i) modal analysis and (ii) time domain analysis. The problem is solved for four types of soil.

7.1 Modal Analysis

The first step in the dynamic analysis of any structural system is to determine the free vibration characteristic natural frequencies and mode shapes, which are important in calculating the seismic response of the liquid storage tanks. The Block Lanczos method is used in ANSYS for the Eigenvalue and Eigenvector extractions to calculate natural frequencies including the fluid modes (Hallquist 1998).

7.1.1 Effect of Tank Height to Length Ratio Variation

For this purpose, two cases of storage tanks are considered, above ground tank and buried tank, for each case, both empty and completely full tanks. The results of natural frequencies are given in Fig.(2) and (3) for empty and completely full tanks, resting on four different types of soil. It is observed that as the soil becomes weaker (having low shear modules (Gs)), natural frequencies become less (soil type No.4).

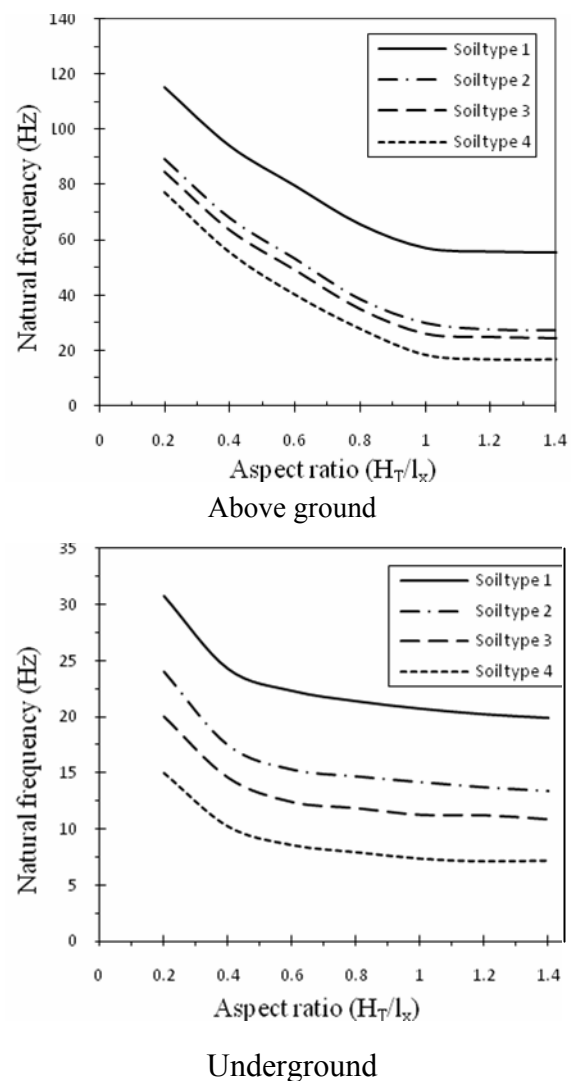
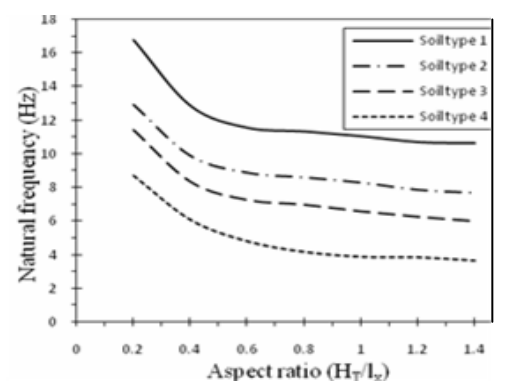
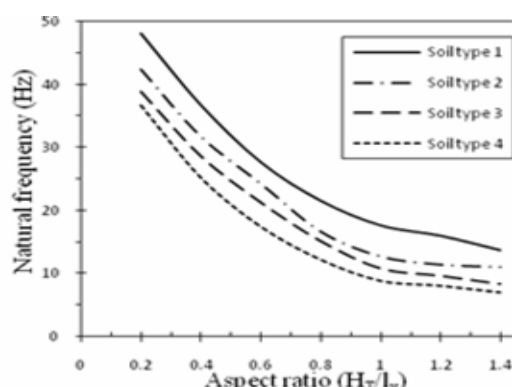


Figure (2) Fundamental natural frequencies versus aspect ratio (H_T/L_x) variation of empty tank



Above ground



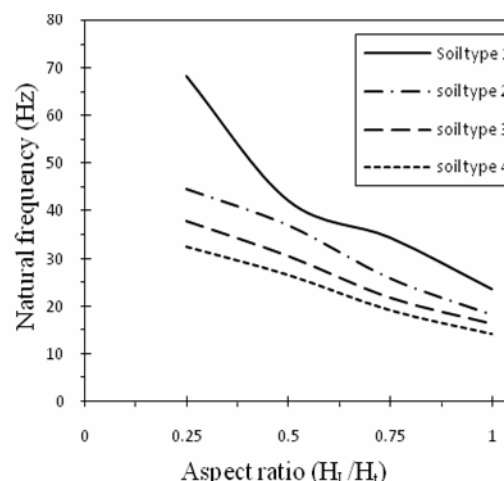
Underground

Figure (3) Fundamental natural frequencies versus aspect ratio (H_T/L_T) variation of full tank

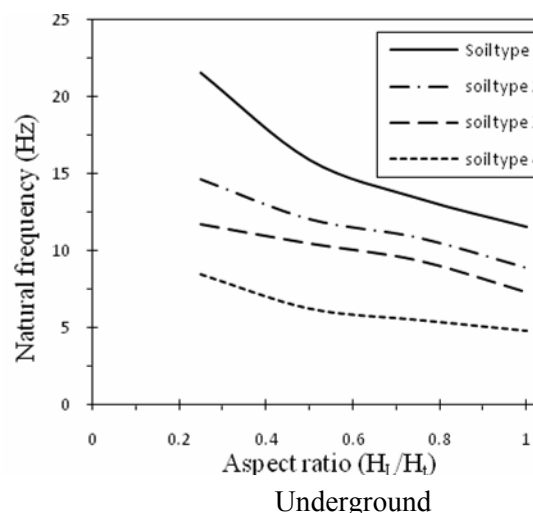
Comparing the results between the two cases of tanks (above ground and buried tank), it has been found that the buried tank has natural frequencies less than the tank above ground, because the mass of the tank will increase causing reduction in the natural frequencies. It is also noticed, that the natural frequencies of the empty tank are much larger than those of the full tanks regardless of the type of soil.

7.1.2 Effect of Liquid Height to Tank Length Ratio Variation

To demonstrate the effect of liquid height variation (H_L/H_T), two cases of the tanks (the tank above ground and buried tank) were considered for this purpose. The resulting natural frequencies are given in Fig.(4) for above ground and buried tanks respectively.



Above ground



Underground

Figure (4) Fundamental natural frequencies versus height of fluid ratio (H_L/H_T)

It can be observed from these tables and plots that, as the level of fluid in the tank increases, the natural frequencies decrease for both cases of tanks and for all four types of the soil. This behavior is obvious since the mass of the structure system increases with the level of fluid.

7.1.3 Effect of Wall Thickness Variation

To demonstrate the effect of wall thickness variation, empty tank and completely full tank, are studied for the free vibration characteristics with wall thickness varies from 450mm to 1350mm for a tank resting on soil type 1, and also for two cases (above ground and buried tank).

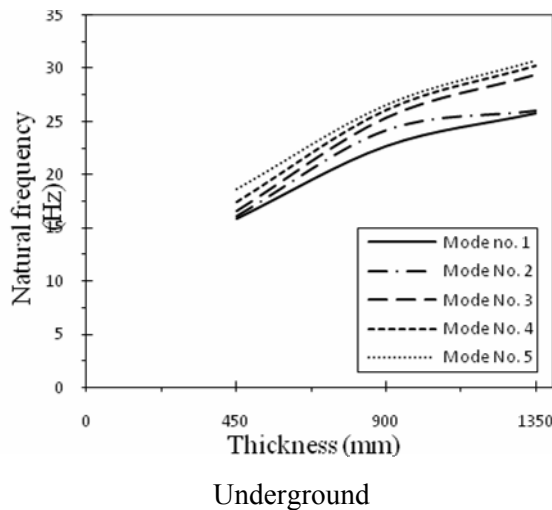
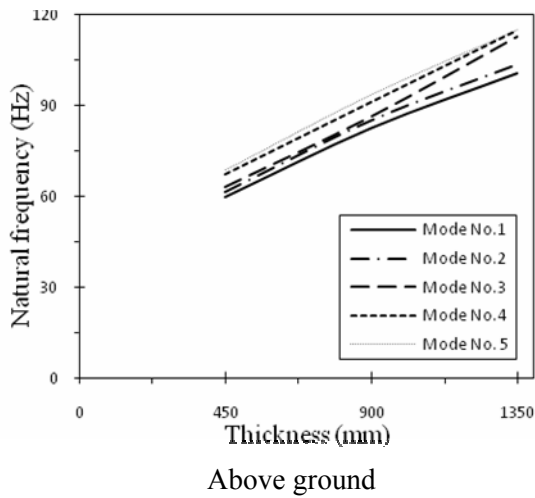


Figure (5) Effect of thickness variation on natural frequencies of empty tank

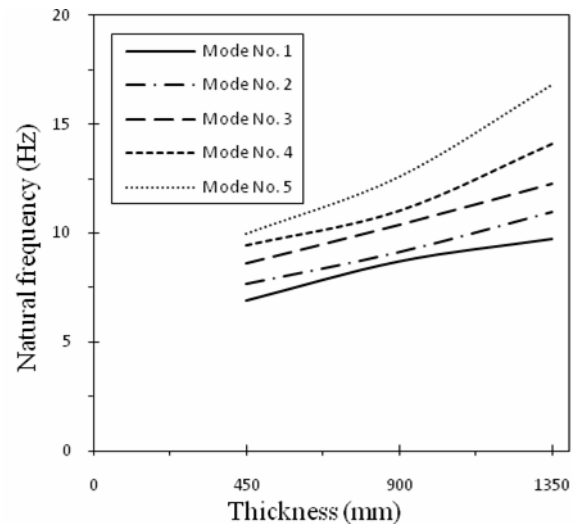
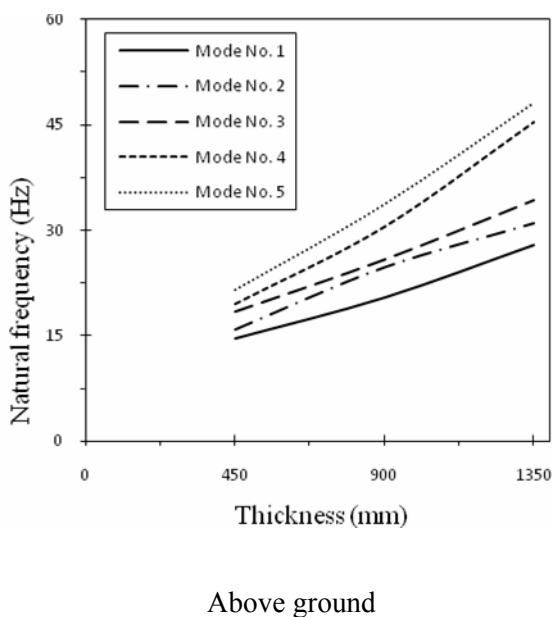


Figure (6) Effect of thickness variation on natural frequencies of full tank

The resulting natural frequencies are given in Fig.(5) and (6). It can be seen clearly from these results that, the natural frequencies increase when the thickness of the wall increases without changing the height of the tank (the wall stiffness increases with increasing its thickness)

7.2 Time Domain Analysis

A time domain analysis using the first five seconds of the north-south component of the 1940 El Centro earthquake was used for the linear elastic model. Peak ground acceleration values were adjusted to 0.318g. Model time history analysis under linear elastic, small deformation assumptions included evaluation of water surface profiles top displacements, axial force, and resulting base shear. The following sections summarize results. The four sets of figures drawn for the different two types of surrounding soil are assumed (soil type 1, and 2), with different levels of water (full, half –full, and empty tank) are considered, as shown in Figs.((7) – (10)). The plots are presented for earthquake response of the rectangular tank above ground demonstrate that top displacement and axial force components for a full tank case have values greater than those in half- full (31%) and empty tank cases (75%). While the case of underground rectangular tank demonstrate that top displacement and axial force components for an empty tank case have values

greater than those in half- full (19%) and full tank cases (40%). It is also interesting to notice that the base shear for the above the ground tank case have values greater than those in underground tank cases (19% to 37%). The shear base for soil type 2 is greater than those in soil type 1 (17% to 28%). It is found that the surrounding soil type has a significant influence on the tank response, as shown in Fig.(11) and (12).

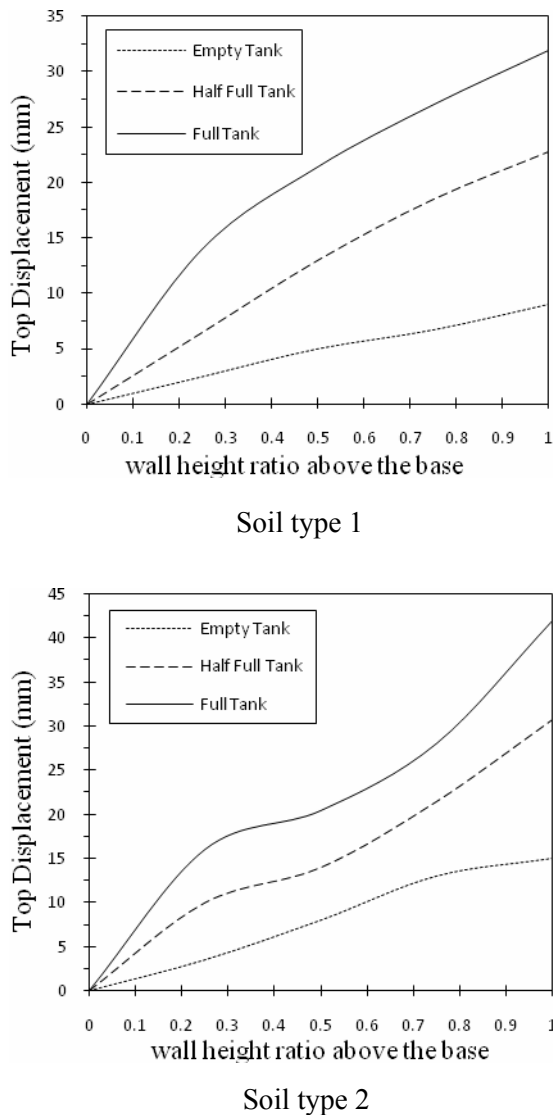


Figure (7) Plots of the top displacement-versus wall height ratio above the base (tank above ground)

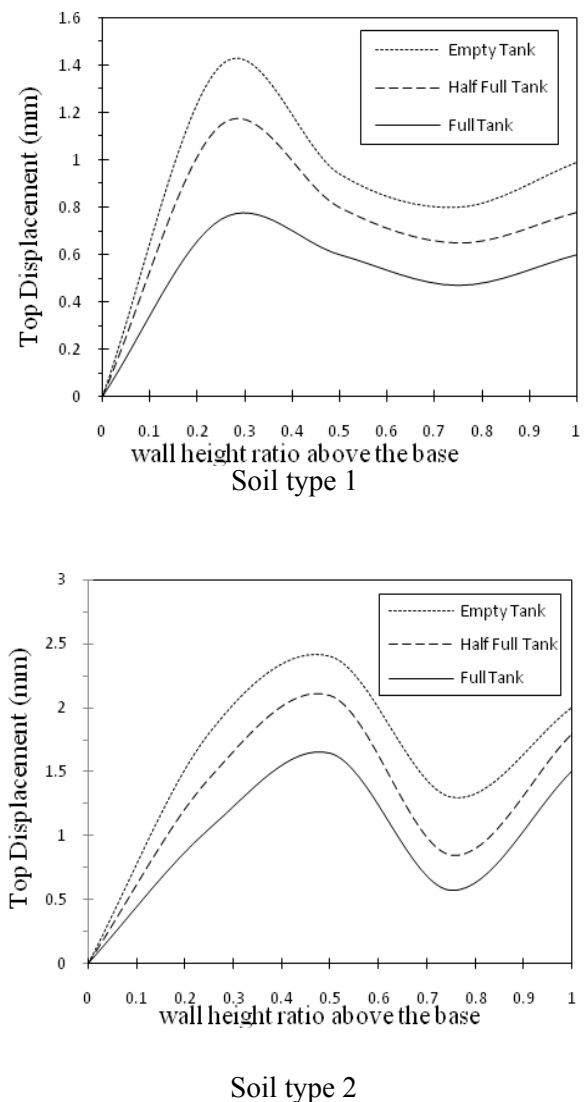


Figure (8) Plots of the top displacement-versus wall height ratio above the base (buried tank)

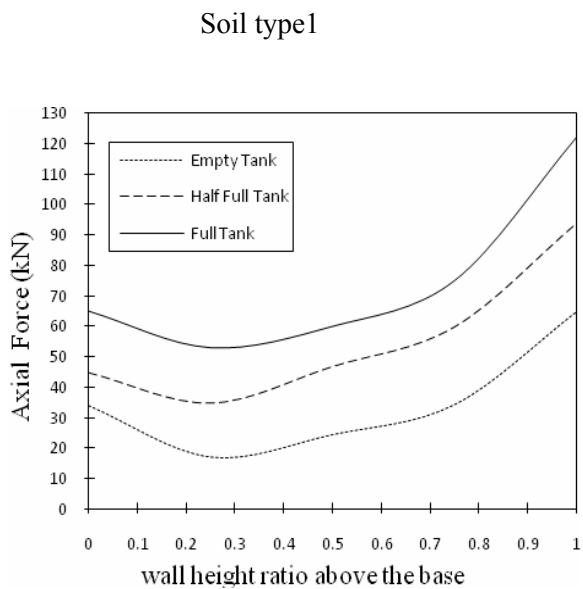
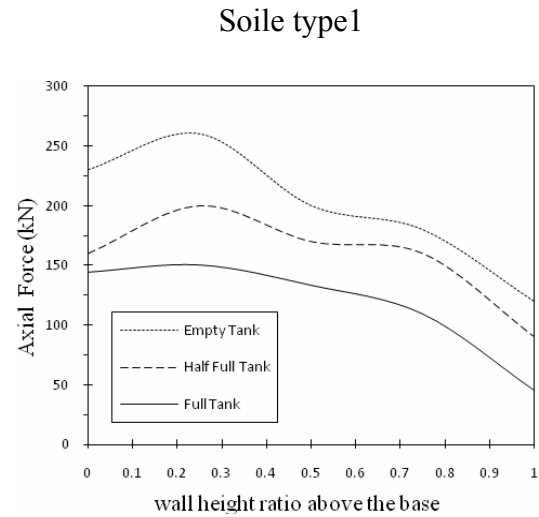
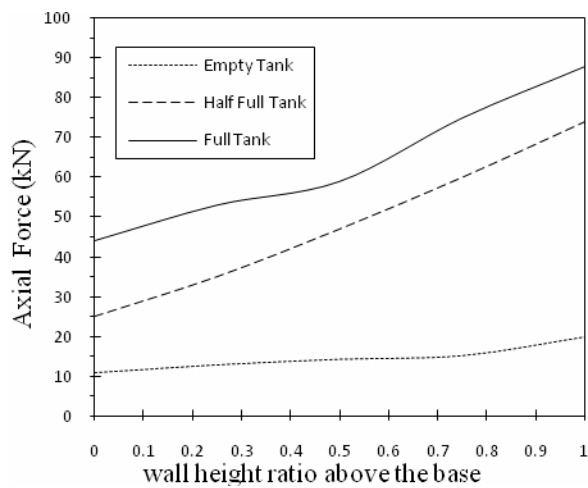


Figure (10) Axial Force- wall height ratio for relationships above the base in long wall

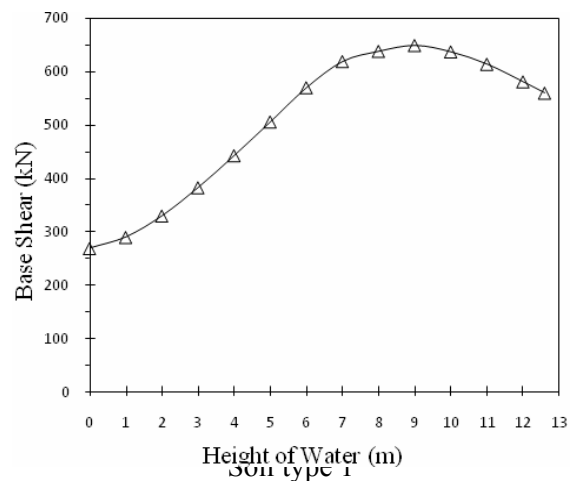


Figure (9) Axial Force- wall height ratio for relationships above the base in long wall

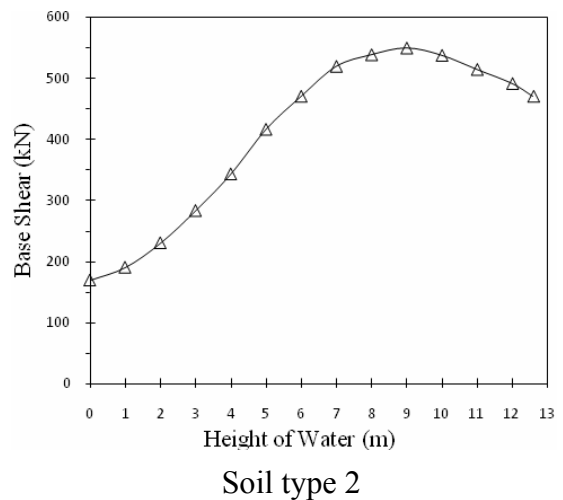
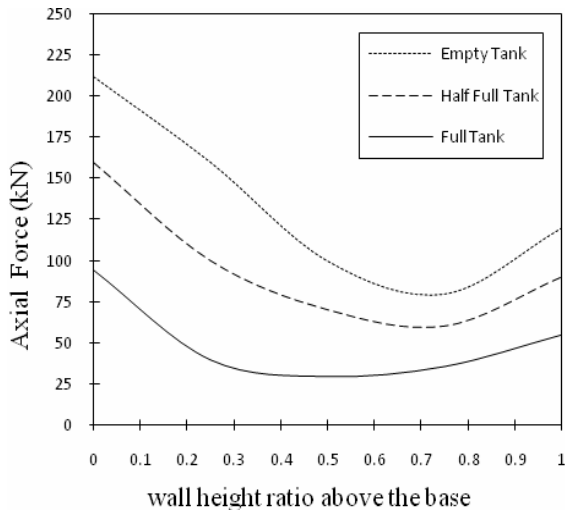
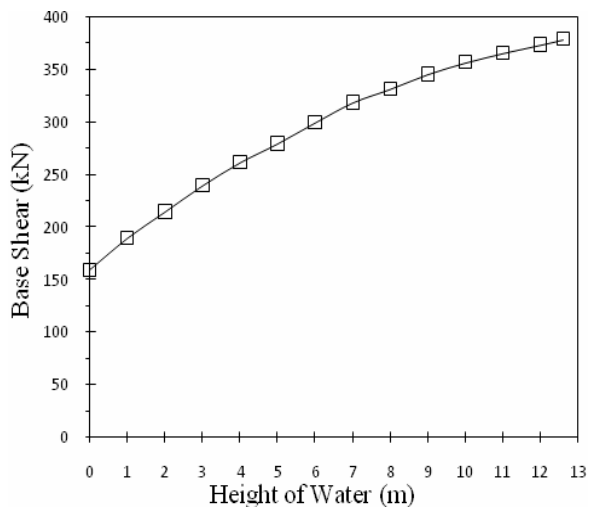
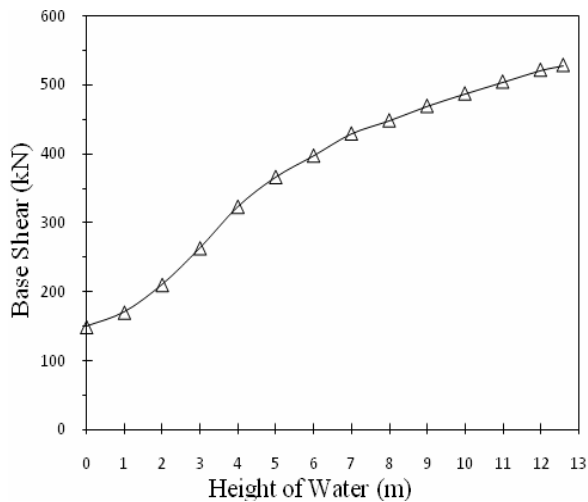


Figure (11) Plots of base shear-height of water (tank above ground)



Soil type 1



Soil type 2

Figure (12) Plots of base shear-height of water (buried tank)

8. CONCLUSIONS

- 1- Variations of the properties of surrounding soil medium are found to have an important influence on the free and forced vibrational response (seismic excitation) of the storage tanks.
- 2- The frequencies in the above ground tank are greater than those for buried tank nearly (26% to 27%), and the frequencies in soil type 1 (stiff soil) case have values greater than those in type 2 (weaker soil) nearly (29% to 31%).
- 3- The shear base for above ground tank have values greater than those in underground tank by ratio ranging between 19% and 37%, The shear base for soil type 2 is greater than those in soil type 1 by a ratio ranging between 17% and 28%. It is found that the surrounding soil type has a significant influence on the tank response. It is also found that, the natural frequency is proportional to the wall thickness of the tank. This behavior is related to the fact that the stiffness of a tank is a function of its wall thickness

Dr. AbdulMuttalib I. Said Ammar A. AbdulMajeed	Seismic Analysis Of Liquid Storage Tanks
---	--

9. REFERENCES

- ANSYS Manual, Version 11. (2008).
- ASCE, American Society of Civil Engineering, (1984), "Fluid-Structure Interaction during Seismic Excitation," Report by the Committee on Seismic Analysis.
- ASCE, American Society of Civil Engineers (1981),
- Chopra, A. K., (1996), "Dynamics of Structures (Theory and Applications to Earthquake Engineering)", Prentice-Hill.
- Clough R. W., and Penzien, J., (2003), "Dynamics of Structures", Third Edition Computers and Structures, Inc.
- Hallquist, John O., (1998), "LS-DYNA Theoretical Manual", Livermore Software Technology Corporation.
- Hanson, R.D., (1973), "Behavior of liquid storage tanks", Report No. EERL 80-04, Caltech
- Haroun, M. A. and Chen, W., (1989), "Seismic large amplitude liquid sloshing theory", Seismic Engineering Structures Congress, San Francisco, 418-427.
- Haroun, M. A. and Housner, G. W. (1980), "A Procedure for seismic design of liquid storage tanks", Earthquake Engineering Research Lab. Report, Caltech, October
- Haroun, M. A. and Housner, G. W., (1981), "Seismic design of liquid storage tanks", Journal of Technical Councils of ASCE, Vol. 107, No. TC1, 191-207.
- Haroun, M. A., and Tayel, M. A., (1985), "Axisymmetric Vibration of Tank-Analytical and Numerical", Journal of Engineering Mechanics, ASCE, vol.111, No.3, pp. 329-358.
- Housner, G. W. (1957), "Dynamic pressures on accelerated fluid containers", Bull. Seism. Soc., America, 47, 15- 35.
- Jennings, P.C. (1971), "Engineering features of the San Fernando earthquake, Report EERL 71-02, California Institute of Technology.
- Luft, R. W., (1984), "Vertical accelerations in prestressed concrete tanks", Journal of Structural Engineering, ASCE, Vol. 110, No. 4, 706-714.
- Manos, G.C. and Clough, R.W. (1985), "Tank damage during the may 1983 Coalinga earthquake", Earthquake Engineering in Structural Dynamics, 13, 449-466.
- Nash, W.A., Balendra, T., Shaaban, S.H. and Mouzakis, T. (1978), "Finite element analysis of seismic response of cylindrical tanks", ASCE Convention and Exposition, Preprint 3315, Chicago, Illinois.
- Prakash, S., (1981), "Soil Dynamics", McGraw-Hill.
- Veletsos, A.S. and Tang, Y. (1986), "Dynamics of vertically excited liquid storage tanks", Journal of Structural Engg. ASCE, 112, June, 1228-1246.
- Veletsos, A.S. and Yang, J.Y. (1976), "Dynamics of fixed-base liquid storage tanks", U.S.-Japan Seminar for Earthquake Engineering Research, Tokyo, Japan.

THE EFFECTIVE EMBEDDED LENGTH OF STEEL BARS IN SELF COMPACTED CONCRETE (SCC)

Dr. Amer F. Izzat
Lecturer in
Civil Engineering Depart.
AmerFarouk@yahoo.com

Dr. Ali I. Salahaldin
Lecturer in
Civil Engineering Depart.
ali_salahaldin@yahoo.com

ABSTRACT:

Eight reinforced concrete beams were tested in order to investigate the effective embedded length of the longitudinal reinforcement bar in self compacted concrete (SCC). All specimens were reinforced with a uni-reinforced bar, six of them embedded in self compacted concrete and the others embedded in normal concrete. The test was carried out on simply supported beams loaded at two points. At the end of the reinforcement bar slip was measured, also under the loading point slip and the bar strain were measured. The investigated variables in this study were: **The bar diameter, and the available embedded length.**

To find out how these variables influence the embedded length in case of using self compacted concrete and comparing it with the normal concrete.

The results show that, with increasing the bar diameter, bond stress slightly decreases, while with increasing the embedded length of the longitudinal bar the bond stress decreases and this improves the mode of the bond failure, especially for the specimens having small bar diameter.

Key word: SCC, Bond strength, Bond stress, Embedded length and Shear span.

الخلاصة:

دراسة عملية اجريت على ثمان عتبات خرسانية مسلحة لدراسة الطول المظمور لقضبان حديد التسليح الموضوع في الخرسانة ذاتية الرص. كل التماذج تحتوي على قضيب تسليح احادي. ست منها استعملت فيها خرسانة ذاتية الرص ونموذجين استعمل فيها الخرسانة الاعتيادية. الفحوصات اجريت على عتبات بسيطة الاسناد، حملت بنقطة تحميل. في نهاية حديد التسليح تم قياس الانسحاب، واسفل نقطة التحميل تم قياس الانسحاب لحديد التسليح مع الانفعال الحاصل في حديد التسليح.

تم بحث المتغيرات التالية في هذه الدراسة: **قطر قضيب حديد التسليح. وطول التثبيت المتاح لقضبان التسليح.** لايجاد كيفية تأثيرهما على قيم الطول المظمور في حالة استخدام خرسانة ذاتية الرص ومقارنتها بالخرسانة الاعتيادية.

اظهرت النتائج المختبرية بانه مع ازدياد قطر حديد التسليح يقل اجهاد الترابط بمقدار طفيف. ومع ازدياد الطول المظمور يقل اجهاد الترابط وهذا يحسن من نوع فشل الترابط الحاصل، وخصوصا في النماذج الحاوية على تسليح قليل.

INTRODUCTION:

Most of the researchers investigated the bond strength tests in normal or high strength concrete. All of them were concurrent in the factors that affective on the bond strength. [Ferguson et al 1954] studied the effect of concrete cover on bond strength of reinforcement. [Hribarand and Vasco1969] investigated the end anchorage and its effect on the pull out of the main reinforcement. [Lutz 1970] studied the effect of transverse reinforcement (stirrups) on bond strength, he found that, when using stirrups improve the bond strength.

Many techniques of tests were used to find the bond strength. Some researchers used the direct pull out test [Watstein 1947 and Tepfers 1973]. Others used beams technique [Ferguson et al 1954 and Ferguson 1965]. Also Eccentric pull out specimen technique were used [Ferguson1965] to simulate the actual behavior of reinforcing bars in concrete beam. Few tests were made on bond strength of self compacted concrete (SCC). [Sonebi et al 2000] and [Foroughi et al 2008] studied the bond strength by using pull-out tests on bars embedded in SCC.

Mechanism of failure:

The applied external load resisted by an internal force couple in simply supported beam, represented by the top compression force in concrete and the tensile force in steel reinforcement. The equation $dM/dX = V$ means that if there is any change in moment with respect to the beam length shear force will appear. This can happen in shear span. Where there is a variation in applied moment from maximum value at applied load to zero value at support, resulting longitudinal shear force on reinforcing bars. This shear force leads to cause shear cracks which has a bad effects on

bond strength, as shown in **Fig (1)**, this can be explained as follows [Stratford, and Burgoyne 2003]: when the shear cracks appear the longitudinal reinforcement act as a dowels and by increasing the shear force (applied load) the shear cracks propagate toward the support around the longitudinal reinforcement and the bond failure will occur by splitting the concrete in this region. So, the mechanism of bond failure is not due to pure of pull out the main reinforcement due to axial force only, but due a combination of loads which cause bond failure.

Many researches on bond strength were carried out by applying pure axial tensile force, by pulling out a reinforcement bar from a concrete block. In pull out technique the tensile stresses in the reinforcement bar are transmitted progressively from the point of applied loading throughout the reinforcement bar and by shear stress to the concrete surrounding the reinforcement bar to the concrete block. The failure will beginning at the concrete surrounding the steel bar near the top of the concrete block surface, as shown in **Fig (2)**. Due to the difference in the deformations of the two materials (steel and concrete) the cracks will start to appear at the top zone of the concrete block. Then the maximum tensile stress in the steel bar will transmit to the next adjacent part of the bar downward the concrete block. This process makes the bond failure progressive and the bond stresses is not constant along the overall embedded length (the embedded length not works together). Rather than, the manner of applying load in the pull out test makes the top concrete block surface compress and the relative slippage between the reinforcement bar and the concrete top surface will deviate slightly from the real value. In contrast [Orangen et al 1975]

assume that the bond stress was constant

along the bar reinforcement.

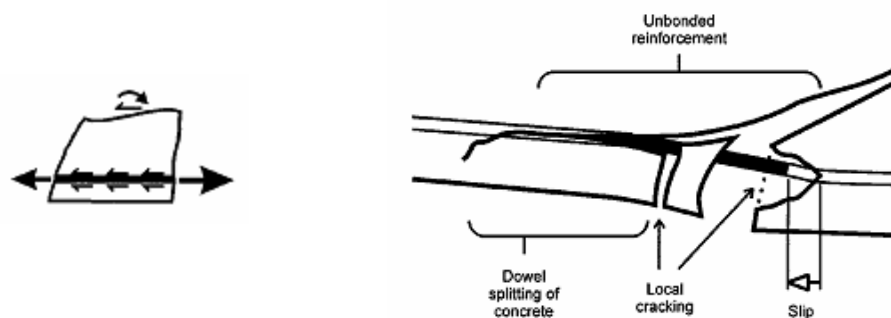


**Figure (1): Beam with no shear reinforcement
[Stratford and Burgoyne 2003]**

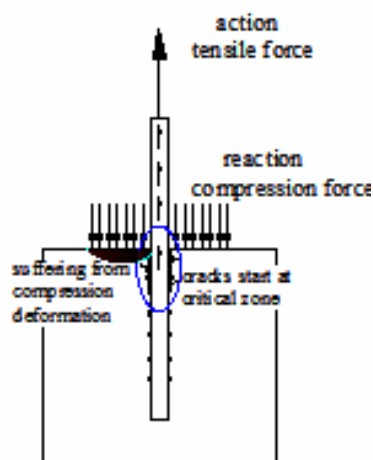


Figure (2): Mechanism failure of the pull-out test

MATERIAL PROPERTIES:

The cement used in this study was Ordinary Portland Cement complying

with ASTM C150-02. The test results are shown in **Tables (1 & 2)**

Table (1): Chemical cement test results

Chemical composition	
Composition	Quantity%
SO ₃	1.24
MgO	2.80
C ₃ A	8.60
SiO ₂	21.2
Al ₂ O ₃	5.4
L.O.I	3.34
C ₃ S	35.1
CaO	52.5

*Chemical analysis was conducted by National Center for Construction Laboratories and Researches

Table (2): physical cement test results

Physical properties	
Compressive strength, MPa (3 days) (7 days)	32.6 39.4
Setting time (Vicate apparatus), Initial setting, h:min Final setting, h:min	2:35 4:40
Specific surface area (Blaine method), m ² /kg	472
Soundness (Auto Clave) method, %	0.24

*Physical tests was conducted by National
Center for Construction Laboratories and Researches

The coarse aggregate used was natural aggregate with nominal size 4.74-19mm. The grading obtained from the results of sieve analysis of the aggregate lies within the range defined by ASTM C136-01.

The results of the sieve analysis which was carried out on fine aggregate lies within the range defined by ASTM C136-01. The chemical and physical test results for gravel and sand are shown in **Tables (3 & 4)** respectively.

Table (3): Chemical and physical test results of gravel

properties	Test results
Absorption %	0.70
Specific gravity	2.60
Dry loose-unit weight kg/m ³	1582
Sulfate content as SO ₃ %	0.42
Materials finer than 75µm%	2.80

- Tests was conducted by National Center for Construction Laboratories and Researches

Table (4): Chemical and physical test results of sand

properties	Test results
Absorption %	0.54
Specific gravity	2.54
Sulfate content	0.07

- Tests was conducted by National Center for Construction Laboratories and Researches



Glenium 51: (modified polycarboxylic ether) was used as a water reducing agent plus a stabilizing agent with a specific gravity of 1.1 at 20°C, PH = 6.5 as issued by the producer.

Silica fume mineral admixture or micro silica: composed of ultrafine, amorphous glassy spheres of silicon dioxide (SiO₂), produced by Warrington, England, Crosfield Chemicals.

CONCRETE MIX PROPORTIONS:

Several trial mixes were used. The final mix proportions used was 1:1.5:1.6 by weight with water cement ratio 0.5 plus 3 liters of glenium-51 admixture for each 100kg of cement. The mixture proportions are summarized in **Table (5)** below.

The slump flow for the self compacted concrete was 710mm (using cone test- ASTM C1611-05) and the slump test for

the normal concrete was 110mm (ASTM C143-00).

The longitudinal steel reinforcement bars were deformed. Determine their tensile properties according to ASTM 615-05a. The results are shown in **Table (6)**.

The mixing of concrete was carried out in a tilting pan type mixer of 0.1m³ capacity. In all the mixes, the aggregates and cement were first mixed dry for about 90 seconds. The water, silica fume and the superplasticizer together were mixed externally in a pan then were added to the pan mixer, after that mixing continued, for a further 90seconds.

With each beam the following specimens were cast to determine the properties of the hardened concrete:

3-150mm diam. x 300mm long cylinders for compressive strength.

3-150mm diam. x 300mm long cylinders for indirect tensile strength.

Table (5): Concrete mix proportions

		SCC	NC
Water	Kg/m ³	200	200
Super plasticizer	lit./100Kg (powder)	3	-
Cement	Kg/m ³	392	400
Silica Fume	Kg/m ³	8	-
Total Powder (Cement+ Silica Fume)	Kg/m ³	400	400
Gravel	Kg/m ³	640	640
Sand	Kg/m ³	600	600

Table (6): Properties of steel bars

Bar diameter (mm)	Modulus of elasticity (GPa)	Yield stress (MPa)	Strain at yield stress (microstrain)	Ultimate stress (MPa)
6	201	510	2537	650
12	198	500	2525	630
16	199	480	2412	580

EXPERIMENTAL PROGRAM:

Eight beams were tested as simply supported beams. The clear span was 1000mm. All beams have the same dimensions; 100mm wide and 180mm deep as shown in **Fig (3)**. Load was applied by using hydraulic jack. **Table (7)** shows the details of the beam specimens.

The bar embedded length was specified as follows: grooves were made by using filler material (cork) placed and fixed to the mold and tied to the reinforcement bar at the inner side of the shear span of the beam under the loading point. The other end of the embedded length (the free end) was rolled up by a tephlon as a spreader between the concrete and the reinforcement bar.

The slip at the free end of the reinforcement bar, is called free end slip (slip at the end of the embedded bar), as shown in the **Fig (3)**. This slip was

measured by using a dial gage fixed on a steel angle glued on the beam end.

At the groove (under the applied load), the loaded end slip which is the relative slippage between the reinforcement and the concrete of the groove side was measured, as shown in **Fig(3)**, by welding a 6mm bar diameter with 30mm long to the reinforcement bar side to fix the dial gauge. On the other side of the reinforcement bar at the groove zone two bars 6mm diameter with 30mm long welded at a space of 50mm to gluing the demec discs to measure the strain in the reinforcement bar by using the demec gauge.

All dial gauges were used to measure the slip have sensitivity of 0.002mm/division. The details of the beam reinforcement, all dimensions and details of fixing the test instruments were used are shown in **Fig (3)**. **Fig (4)** shows the beam was tested in a rig using a machine 25tons loading capacity.

Table (7): Details of the bar diameter with the embedded length

Beam designation	Bar diameter (mm)	Embedded length (mm)	Type of concrete
B1	12	150	SCC
B2	12	200	SCC
B3	12	250	SCC
B4	16	150	SCC
B5	16	200	SCC
B6	16	250	SCC
B7	12	250	NC
B8	16	250	C

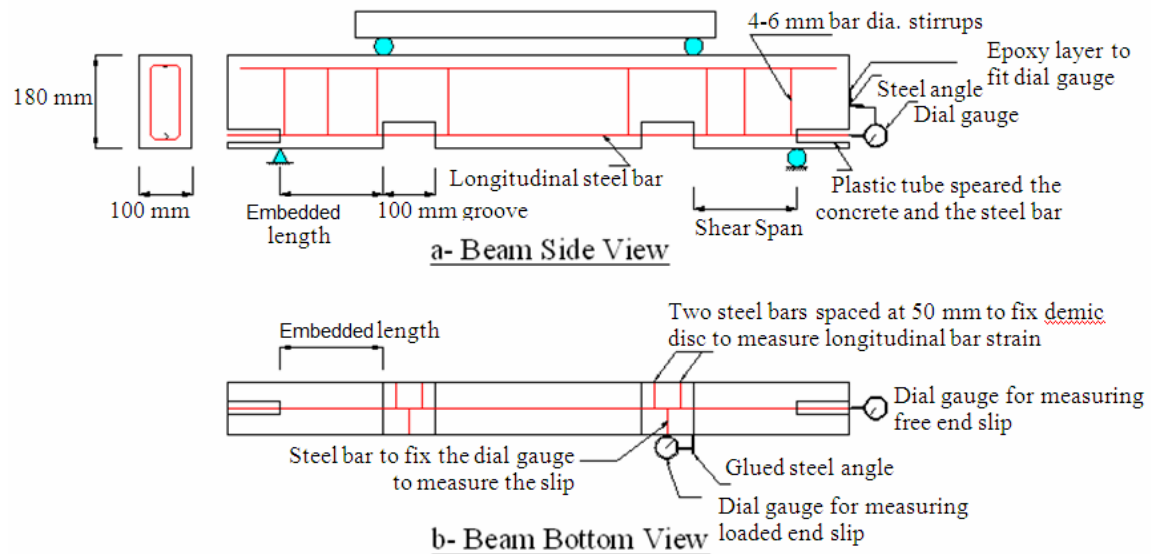


Figure (3): Details of the beam specimens



Figure (4): Test set up of beam B3

RESULTS AND DISCUSSION:

Mode of failure: All beams failed by the splitting of the concrete cover in the anchorage zone (along the embedded length or the bottom face of the shear span). As shown in **Table (8)**, three beams failed in bond after yielding of the bar reinforcement and the other five beams failed by splitting of the concrete cover before yielding of the bar reinforcement. Also, it shows that increasing the embedded length; improve the mode of failure, by delaying the pull out of the reinforcement bar and splitting of the concrete cover until the stress in

the reinforcing bar reach the yielding stress. This improvement was more than that in beams with smaller bar diameter than that of larger bar diameter. Where, for the beams with 12 mm bar diameter, increasing the embedded length 33% gives improvement in the mode of bond failure, while for beams with 16mm bar diameter, similar improvement requires 66% increasing in the embedded length.

The cracks pattern development were as follow: at the bottom face of the beam shear span, a longitudinal splitting crack started to appear from the loaded point at the end face

of the groove and developed toward the free end of the beam, along the bar reinforcement, as shown in **Fig (5)**. At the same region, with increasing the applied load flexural crack was observed (transverse crack) at a right angle to the longitudinal bar. With more applied load this main longitudinal crack gradually increased till reaching the free end of the beam, at the same time and with increasing applied load many flexural cracks were appeared and some of them changed to diagonal tension cracks to joining the flexural cracks until the concrete cover at the anchorage zone was marked with one main longitudinal splitting crack and many transverse flexural and diagonal cracks, causing bond failure. In the same time at the mid span zone many flexural cracks were observed. In spite of the beams containing shear reinforcement, but at the two side faces of the shear span some diagonal shear cracks were observed, gradually growing and propagated toward the loading point, but no shear failure were happened.

By equating the tensile force on the bar with the total bond force on the bar surface area $l_d \pi d_b u = A_b f_s$ bond

stress can be found $u = \frac{d_b f_s}{4 l_d}$, as

shown in **Table (8)**, where the bar stress can be measured experimentally by measuring the strain at the groove zone.

In this equation the quantity $\frac{d_b}{4}$ is constant for each group of beams (B1, B2 and B3) and (B4, B5 and B6), so, the calculated bond stress u will depends on $\frac{f_s}{l_d}$, this value decrease with

increasing the embedded length, because the increase in the reinforcement stress less than that of the embedded length. This means with increasing the embedded length the bond stress will

decrease; despite of that, the bond failure was observed, because this equation assume that the bond stress is constant along the embedded length, while the value f_s is measured under the loading point at the inner end of the shear span (embedded length) only and it is not constant along the embedded length. So, the value of the bond stress u which causes the failure is higher than the calculated value, because the failure is progressively propagated process, and it is not constant along the embedded length.

Table (9) shows the loaded and free ends slip of the reinforcement bar near failure. The loaded end slip is higher than that of the free end slip for all beams, this because, the cracks started to appear from the groove zone and developed to the next adjacent region toward the beam end. So, the bond failure (separation) between the concrete and the reinforcement bar started from the groove zone propagated toward the beam end (free end). **Fig (6)** shows the difference between free end slip and the loaded end slip for beam B2 at different bond stress. At the earlier loading stage the bar reinforcement slip at both loaded end and the free end no slip were recorded. With increasing applied load the loaded end started to record slip while the dial gauge at free end slip was not sensitive any slip. After that, with increasing the applied load the loaded end slip increased more than that of the free end slip. Near the bond failure the slip of the loaded end was 5 times that of the free end of the reinforcement bar. In **Fig (6)**, the difference in behavior proves that, the bond stress is not constant and the bond failure is progressively process. Also, **Table (9)** shows with increasing the embedded length the loaded end slip increase while the free end slip decrease. Because increasing the embedded length will delay the pull out of the

reinforcement bar and allowing to more slipping at the groove zone, but for each bar diameter the ratio of loaded end slip /embedded length is approximately similar, this means that increasing the embedded will increase the loaded end slip in approximately same quantity, despite of that, the mode of bond failure changed, if the bar diameter is constant. This means the loaded end slip has fewer effects on the bond failure. Also **Fig (7)** shows, with increasing the embedded length the loaded end slip increase, while **Fig (8)** shows less difference between the loaded end slip with increasing the embedded length, due to increasing in bar diameter. **Fig (9)** shows, with increasing in bar diameter the loaded end slip will decrease, because the stresses in the bar will decrease, or the bond stress will decrease. Same observation was recorded by [Sonebi et al 2000], and by [Ferguson et al 1954] but comparing the SCC beams with that which used normal concrete (NC) as shown in **Figs (7&8)**, the deference were very clearly in the bond stresses and the slip at both loaded and free end slip, this because of the enhancing the concrete properties such as the compressive strength and the concrete tensile strength which is affect on the bond strength. But, [Mindess et al 2003] they show that the compressive strength increases more than that the tensile strength.

The bond failure is specified by the free end slip, because it is the last resistance point of the embedded length. **Figs (10 & 11)** show the free end slip-bond stress curves for beams containing 12mm bar diameter and 16mm bar diameter respectively. These figures show that, with increasing embedded length the free end slip will slightly decrease, as

mentioned previously the bond stress is not uniform along the embedded length. So, the bond stress which causes the slip at the free end is less than that at the loaded end. **Table (9)** shows, increasing the embedded length will decrease the free end slip of the reinforcement bar, where, increasing the embedded length by 33% and 25% give decrease in free end slip about 14% and 26% respectively for beams with longitudinal bar diameter 12mm, and 28% and 9% for bar diameter 16mm respectively. **Fig (12)** shows, with increasing bar size the free end slip will increase, and the curves of the NC beams tend to be more flattened than the curves of the SCC beams, this because of the improvement of concrete properties. **Fig (13)** shows, with increasing the embedded length, the ratio of free end slip/embedded length decreases (for each similar bar diameter group), and the curves tend to be horizontally with increasing the embedded length, i.e. excessive increasing in embedded length has no effect on the bond strength. Theoretically if each curve in **Fig (13)** extends to the x-axis (zero end slip) point of intersecting will find the best embedded length. But this curve needs more experimental tests to get an adequate embedded length, for each type of concrete strength and bar diameter. The curve of beams with 16mm bar diameter was above that of 12mm bar diameter, this means increasing bar diameter needs to increase the embedded length. Beams with SCC, increasing the bar diameter by 33% gives increase in the free end slip by 45%, 21% and 50% for beams with 150mm, 200mm and 250mm embedded length respectively, and it was 16% in NC beam.

Table (8): Beams test results.

Beam designation	Embedded length* (mm)	Bar diameter (mm)	Compressive strength (MPa)	Steel stress (MPa)	Bond stress (MPa)	Mode of failure
B1	150	12	43	484	9.68	Bond
B2	195	12	45	535	8.23	Bond with yield
B3	245	12	44	610	7.47	Bond with yield
B4	150	16	45	362	9.25	Bond
B5	200	16	42	416	8.02	Bond
B6	255	16	44	485	7.61	Bond with yield
B7	250	12	27	354	4.25	Bond
B8	255	16	26	257	4.03	Bond

*Embedded length is for the failed side of concrete beam.

Table (9): results of loaded end and free end slips

Beam designation	Loaded end slip		Free end slip (mm)	
	slip (mm)	Slip/embedded length $\times 10^{-3}$	Slip (mm)	Slip/embedded length $\times 10^{-3}$
B1	0.87	5.8	0.22	1.47
B2	1.12	5.7	0.19	0.97
B3	1.49	6.08	0.14	0.57
B4	0.51	3.4	0.32	2.13
B5	0.59	2.95	0.23	1.15
B6	0.63	2.47	0.21	0.82
B7	0.42	1.68	0.53	2.12
B8	0.37	1.45	0.62	2.43



Figure (5): Crack pattern of beam B3 after failure

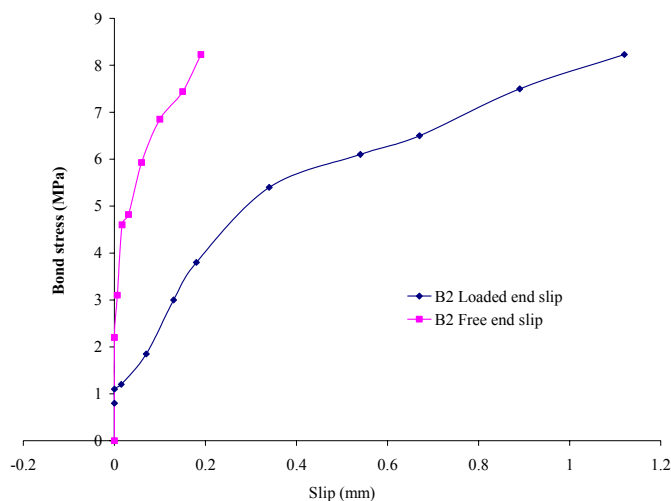


Figure (6): Bond stress versus loaded slip and free end slip for beam B2

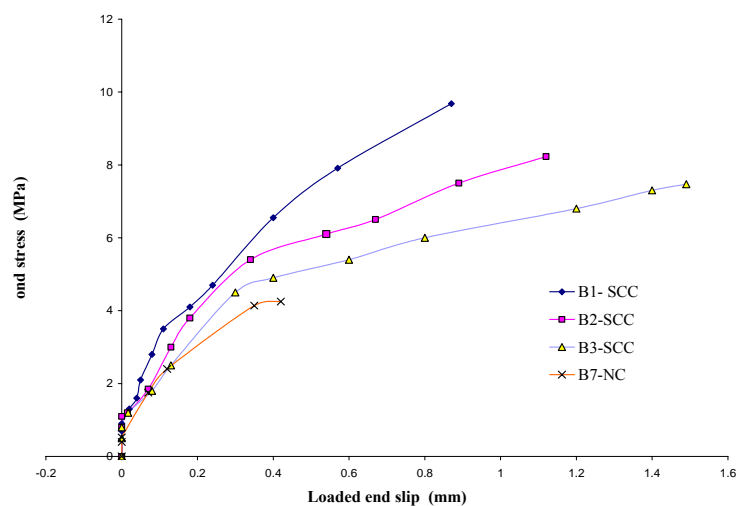


Figure (7): Bond stress versus loaded end slip for beams with 12mm bar diameter

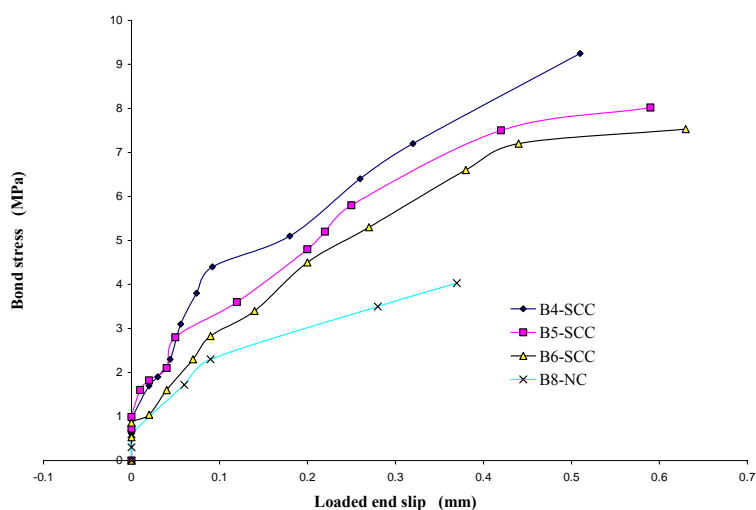


Figure (8): Bond stress versus loaded end slip for beams with 16mm bar diameter

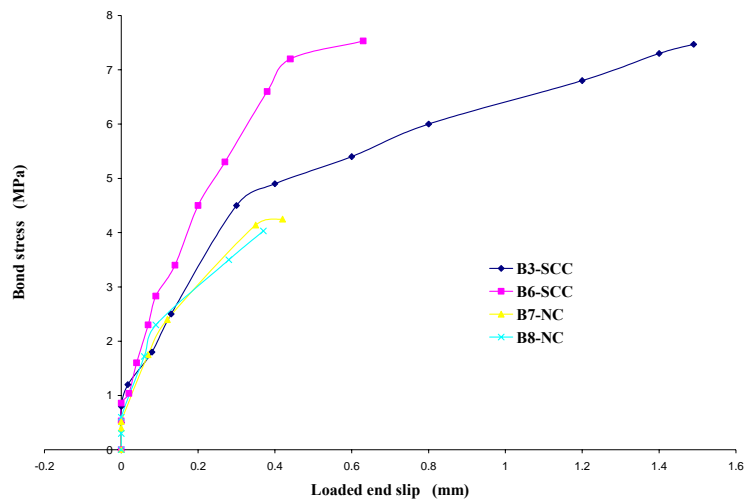


Figure (9): Bond stress versus loaded end slip for beams had same embedded length and different bar diameter

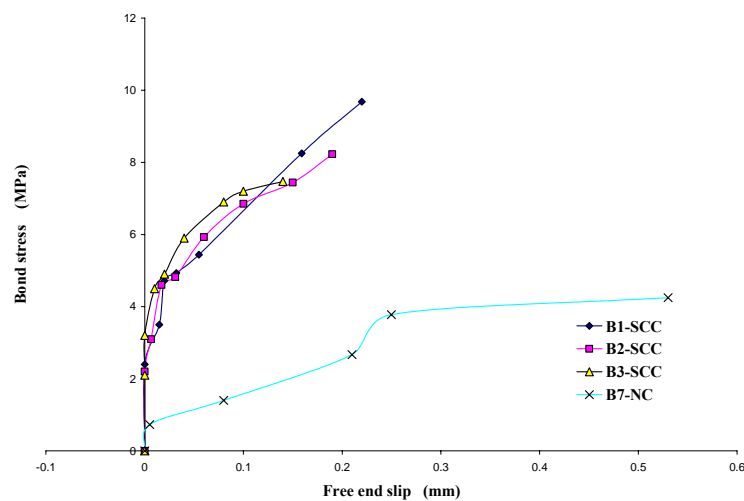


Figure (10): Bond stress versus free end slip for beams with 12mm bar diameter

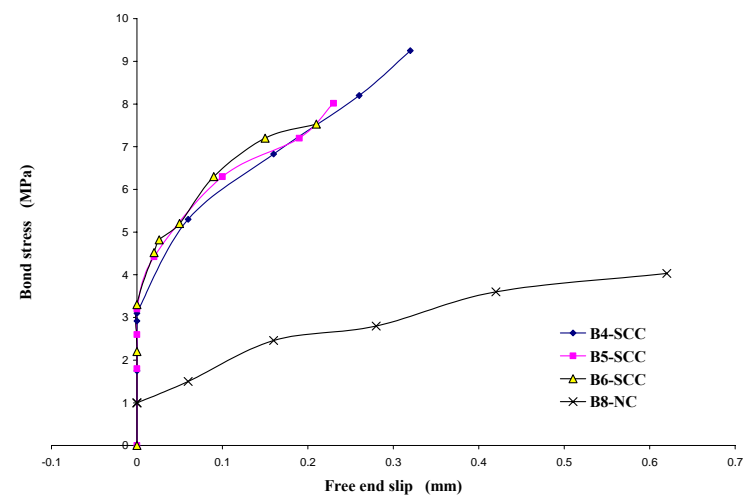


Figure (11): Bond stress versus free end slip for beams with 16mm bar diameter

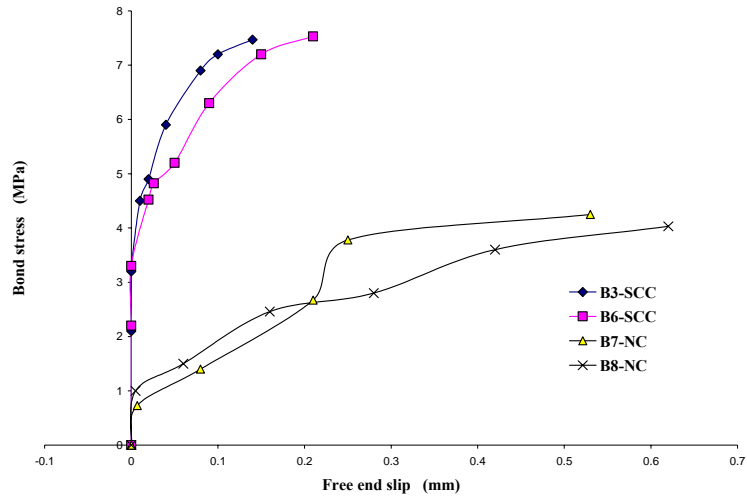


Figure (12): Bond stress versus free end slip for beams had same embedded length and different bar diameter

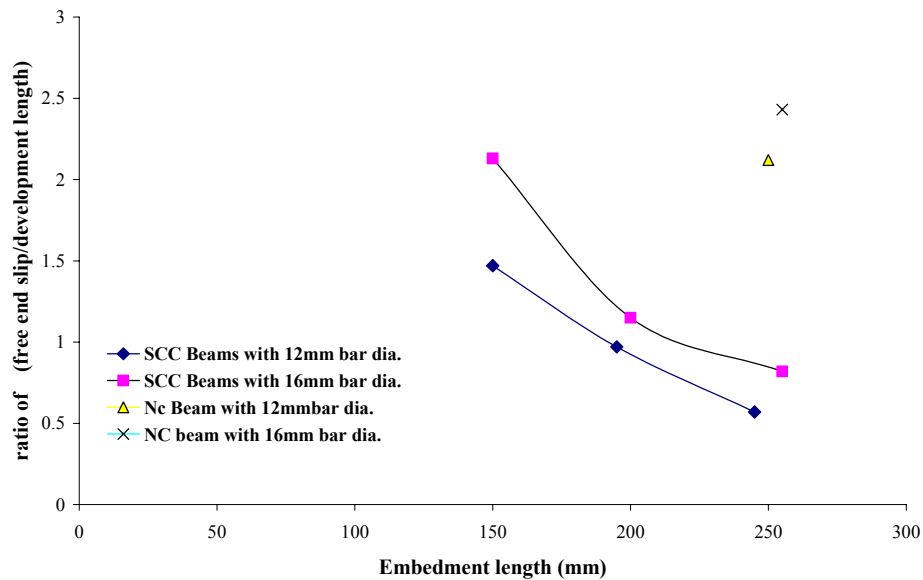


Figure (13): The ratio of $\left(\frac{\text{free end slip}}{\text{loaded end slip}} \right)$ versus with the embedded length

CONCLUSION:

- 1- Using self compacted concrete enhancing the concrete properties (compressive strength and tensile strength), which affects on bond strength of the bar embedded on it.
- 2- The bond stress is not constant along the embedded length of the reinforcement bar. It reaches the maximum value under the loading point and decreases toward the embedded length end (beam end).
- 3- Increasing embedded length 33% for beams with 12mm bar diameter give improvement in the mode of bond failure, while for beams with 16mm bar diameter similar improvement requires 66% increasing in the embedded length.
- 4- Free end slip of the reinforcement bar, specify the bond failure, which affected by the embedded length and the bar diameter.
- 5- Increasing the embedded length will decrease the free end slip of the reinforcement bar, where increasing the embedded length 33% and 25% give decrease in free end slip about 14% and 26% respectively for beams with longitudinal bar diameter 12mm, and 28% and 9% for bar diameter 16mm respectively.
- 6- Increasing bar diameter will increase the free end slip. The 33% increase in bar diameter gives 50% increase in free end slip for SCC beams and 16% for NC beams
- 7- With increasing the longitudinal bar diameter, embedded length needs increasing.
- 8- The relation curve of embedded length versus ratio of free end slip/embedded length shows a good relationship between the variables studied in this research.

**NOTATIONS:**

A : Bar cross-section area (mm^2)

d_b : Bar diameter (mm)

l_d : Actual embedded length measured from the groove at the loaded end to the free end as shown in Fig (3-a) (mm).

f_s : Steel stress (MPa)

NC: Normal concrete.

SCC: Self compacted concrete

u : Bond stress (MPa)

$\left(\frac{dM}{dx}\right) = V$: Change in moment with respect to beam length causes shear force

REFERENCES:

- A. Foroughi-Asl, S., Dilmaghani. H. Famili "Bond Strength of Reinforcement Steel in Self Compacted Concrete", International Journal of Civil Engineering, Vol.6, No. 1, March 2008. pp 24-33

- ASTM Designation C143/ C143 M-00 "Standard Test Method for Slump of Hydraulic-Cement Concrete " 2000 Annual Book of ASTM Standard, American Society for Testing and Material, Philadelphia Pennsylvania, Section4, Vol. 4.02.

- ASTM Designation C150-02 "Standard Specification for Portland Cement " 2002 Annual Book of ASTM Standard, American Society for Testing and Material, Philadelphia Pennsylvania, Section4, Vol. 4.02. pp 89-93.

- ASTM Designation C136-01 "Standard Specification for Concrete Aggregate" 2002 Annual Book of ASTM Standard, American Society for Testing and Material, Philadelphia Pennsylvania, Section4, Vol. 4.02, pp 10-16.

- ASTM Designation A370-05a "Standard Specification for Testing Method and Definitions for Mechanical Testing of Steel Products " 2002 Annual Book of ASTM Standard, American Society for Testing and Material,

Philadelphia Pennsylvania, Section4, Vol. 1.01, pp 248-287.

- ASTM Designation C1611-05 "Standard Test Method for Slump Flow of Self Consolidated Concrete" 2005 Annual Book of ASTM Standard, American Society for Testing and Material, Philadelphia Pennsylvania, Section4, Vol. 4.02.

- C. O. Orangun, J. O. Jirsa, and J. E. Breen "The Strength of Anchorage Bars: "A Reevaluation of Test Data on Embedded Length and Splices", Research Report No. 154-3F, Centre for Highway Research, the University of Texas at Austin, Jan. 1975.

- D. Watstein, "Distribution of Bond Stress in Concrete Pull-out Specimens" ACI Journal, Proceeding V. 43, No. 5, May 1947, pp1041-1052.

- R. Tepfers, " A Theory of Bond Applied to Overlapped Tensile Reinforcement Splices for Deformed Bars", Publication 73:2, division of Concrete Structures, Chalmers University of Technology, Goteborag, Sweden, 1973, p 328.

- J. A. Hribar and R. C. Vasco, "End Anchorage of High Strength Steel Reinforcing Bar", ACI Journal, Proceeding V. 66, No. 11, Nov. 1969, pp 875-883.

- L. A. Lutz, "Information on the Bond of the Deformed Bars from Special Pull-out Test", ACI journal, Proceeding V. 67, No. 11, Nov. 1970, pp 885-887

- P. M. Ferguson, R. D. Turpin, and J. N. Thompson "Minimum Bar Spacing as a Function of Bond and Shear Strength", ACI Journal, Proceedings V.50, No.10, June 1954, pp 869-887.

- P. M. Ferguson, and J. E. Breen, "Lapped Splices for High Strength Reinforcing Bars", ACI Journal, Proceeding V. 62, No. 9, Sept. 1965, pp 1063-1078.

- P. M. Ferguson, J. E. Breen, and J. N. Thompson, "Pull-out Tests on High Strength Reinforcement Bars", ACI

Journal, Proceedings V. 62, No. 8, Aug. 1965, pp 933-950.

- T. Stratford, and C. Burgoyne, "Shear Analysis of Concrete with Brittle Reinforcement", ASCE Journal of Composites for Construction, November 2003, pp 323-330.

- W. Zhu, M. Sonebi and P.J.M. Bartos "Bond and Interfacial Properties of Reinforcement in-Self Compacted Concrete", Advanced Concrete and Masonry Cement, University of Paisley, PA12BE, Scotland, UK, 2000 pp 442-448.

REMOVAL OF HEAVY METALS USING REVERSE OSMOSIS

Haider A. Aljendeel

Chemical Engineering Department – College of Engineering – University of Baghdad – Iraq.

ABSTRACT

The aim of this work is to study reverse osmosis characteristics for copper sulfate hexahydrate ($\text{CuSO}_4 \cdot 6\text{H}_2\text{O}$), nickel sulfate hexahydrate ($\text{NiSO}_4 \cdot 6\text{H}_2\text{O}$) and zinc sulfate hexahydrate ($\text{ZnSO}_4 \cdot 6\text{H}_2\text{O}$) removal from aqueous solution which discharge from some Iraqi factories such as Alnasser Company for mechanical industries. The mode of operation of reverse osmosis was permeate is removed and the concentrate of metals solution is recycled back to the feed vessel. Spiral-wound membrane is thin film composite membrane (TFC) was used to conduct this study on reverse osmosis. The variables studied are metals concentrations (50 – 150 ppm) and time (15 – 90 min). It was found that increasing the time results in an increase in concentration of metal in permeate, feed concentration in feed vessel and recovery percent. While, it was found that water flux, rejection percent and mass transfer coefficient is decreasing with increasing operating time. Also, it was found that the permeate concentration and feed concentration in feed vessel increases with increasing feed concentration, on the contrary, water flux, the percentage of recovery, rejection percent and mass transfer coefficient decreases with increasing the concentration of feed solution. The maximum rejection of copper, nickel, and zinc salts are 96.6%, 95.7% and 98.2% respectively. The maximum recovery percentage of copper, nickel, and zinc salts are 40.8%, 41.35% and 38.44% respectively. The pure water permeability constant was calculated for TFC membrane.

Key words: reverse osmosis, heavy metal, copper, nickel, zinc.

ان هدف هذا البحث هو دراسة خواص التناضح العكسي عند ازالة المعادن (سلفات النحاس المائية، سلفات النيكل المائية، سلفات الزنك المائية) من المحاليل المائية التي تطرحها بعض مصانع العراق مثل شركة النصر للصناعات الميكانيكية. ان اسلوب التشغيل للتناضح العكسي هو ازالة الماء النقي والماء المركز بالمعادن الثقيلة ليتم ارجاعه الى خزان اللقيم الرئيسي. تم استعمال غشاء اللف الحلزوني وهو غشاء رقيق لهذا النوع من الدراسة ، وان المتغيرات التي استعملت هي تراكيز المعادن (50-150 جزء بالمليون) و الزمن (15 – 90 دقيقة) . لقد وجد ان زيادة الزمن يؤدي الى زيادة تركيز المعدن في الماء النقي وزيادة التركيز في خزان اللقيم الرئيسي وزيادة نسبة الاسترجاع ، بينما لقد وجد ان معدل جريان الماء ونسبة الرفض ومعامل انتقال الكتلة يقل بزيادة الزمن. كذلك وجد ان تركيز الماء النقي وتركيز المعادن في خزان اللقيم الرئيسي يزداد بزيادة تركيز المعادن ، على العكس من ذلك فان معدل جريان الماء ونسبة الاسترجاع ونسبة الرفض ومعامل انتقال الكتلة تقل بزيادة تركيز المعادن في اللقيم. وان اكبر معدل رفض لاملاح النحاس والنيكل والزنك الخارصين هو 96,6%، 95,7% و98,2% على التوالي . ووجد ان اكبر استرجاع للنحاس والنيكل والزنك الخارصين هي 40.8%، 41.35% و 38.44% على التوالي. تم ايضا حساب معامل نفاذية الماء النقي للغشاء المستعمل.

INTRODUCTION

Heavy metals are one of the most important sources of environmental pollution. Some of them can form compounds which are toxic even in very low concentration (Srisuwan and Thongchai, 2002). Some of these compounds may suppress the immune system, leading to increase susceptibility to disease while others may be carcinogenic (Crespo et al., 2004).

Membrane technology has become increasingly promising in removing heavy metals from wastewater and improving water recovery rate due to its high efficiency and low cost (Liu et al., 2008). Huge improvements have been made in recent years, and the utilization of membrane technology has dramatically increased in potable water treatment. It is expected that membrane processes will be used more and more in the future as well as more stringent drinking water quality standards will likely become enforced. Therefore, Membrane processes such as microfiltration (MF), ultrafiltration (UF), nanofiltration (NF) and reverse osmosis (RO) are increasingly being applied for treating wastewater (Syed et al., 2000). Microfiltration and ultrafiltration used as pretreatment for nanofiltration and reverse osmosis processes. Membrane separation processes have been found greatly used in industrial applications as an alternative to thermal separation process. Some of the advantages of membrane process are low energy consumption, high product quality, and, flexible design and installation. Seawater desalination, waste reduction, food processing, biotechnology and medical applications are some of the processes where membranes are used (Cheryan., 1998).

Reverse osmosis is a hyperfiltration process which allows the removal of particles such as metals, bacteria, salts, sugars, proteins, particles, dyes, and other constituents that have a molecular weight of greater than 150-250 daltons (Ghulam, 2007). Reverse osmosis (RO) is a pressure driven process similar to conventional filtration processes but using a much tighter filter or membrane. Reverse osmosis (RO) involves separating water from a solution of dissolved solids by forcing water through a semipermeable membrane. As pressure is applied to the solution, water and other molecules with low molecular weights pass through micropores in the membrane (Sourirajan, 1970 and Fazilet, 2000). Larger molecules, such as organic dyes and metal, are retained by the membrane (Patrick, 1976 and Nes

et al., 2008). This process (RO) found a broad application in the desalination of sea and brackish water. It is applied to purify water for laboratory use and is very promising as a pre-concentration technique in trace and environmental analysis (Belkacem et al., 2008).

Howard (1973) showed that heavy metal removal increases with increasing temperature of feed solution in the reverse osmosis process. Removal percentage also increases with operation time of the system until reaching steady value. He also proved that the percentage of removal of heavy metals would vary this variation due to the metal's ability or inability to form complex ion structures which would be retained by the membranes. Oh et al., (2000) applied reverse osmosis and nanofiltration membrane processes for the treatment of arsenic contaminated water applying low pressure by using pump, they concluded that low-pressure nanofiltration with pre-oxidation or reverse osmosis with a pump device could be used for the treatment of arsenic contaminated groundwater in rural areas. Myzairah (2007) showed the importance of operating pressure in determining the permeate flux in reverse osmosis process, even for low pH and feed concentration of the feed solutions. The higher the operating pressure, the higher the permeate flux. His results showed that the feed concentration of copper chloride and pH were the most important factors in determining the significant parameters for the percentage of copper removal. It can be summarized that the higher the feed concentration of copper and pH, the higher the percentage of copper removal.

The present study includes application of reverse osmosis process to recovery of water from wastewater by heavy metals. Membrane used in this work was polyamide (thin film composite (TFC)) membrane. The effect of time and feed solution concentration on recovery percentage, water flux, product concentration of metals, rejection percentage and mass transfer coefficient have been determined.

Rejection Percentage

The measure of membrane selectivity is solute rejection, the ratio of solute rejected by a membrane to the solute in the feed. It is the most common method of evaluating a membrane's ability to separate solute, because the determination is simple and can be done as accurately in the field as in the laboratory (Hasan 2008 and Yip et al., 2010).

$$R\% = \left(\frac{C_F - C_P}{C_F} \right) \times 100 \quad (1)$$

Where C_F is the concentration of a specific component in the feed solution to the membrane process and C_P is the concentration of the same specific component in the product stream leaving the membrane system.

RECOVERY PERCENT

The recovery rate (Y%) is a measure of efficiency of reverse osmosis system and can be calculated by

$$Y\% = (\text{volume of treated water produced} / \text{total volume of feed water}) \times 100 \quad (2)$$

TRANSPORT EQUATION FOR REVERSE OSMOSIS PROCESS

Reverse osmosis models can be divided into three types: irreversible thermodynamics models (such as Kedem-Katchalsky and Spiegler-Kedem models); nonporous or homogeneous membrane models (such as the solution-diffusion, solution-diffusion-imperfection, and extended solution-diffusion models); and pore models (such as the finely-porous, preferential sorption capillary flow, and surface force-pore flow models). The transport models focus on the top thin skin of asymmetric membranes or the top thin skin layer of composite membranes since these determine fluxes and selectivities of most membranes (Bhattacharyya and Williams, 1992). Also, most of the membrane models assume equilibrium (or near equilibrium) or steady state conditions in the membrane.

The transport of solvent water (N_B) through the porous membrane is proportional to the effective pressure, and that of the solute is due to pore diffusion and hence proportional to its concentration difference across the membrane (Taha, 2000).

The solvent flux is calculated according to the following equation

$$N_B = A [P - \{\pi(X_{A2}) - \pi(X_{A3})\}] \quad (3)$$

Where N_B is the solvent flux, P is the applied pressure, $\pi(X_{A2})$ and $\pi(X_{A3})$ represent the osmotic pressure corresponding to mole fraction of solute X_{A2} at membrane surface and X_{A3} in permeate respectively. A is defined as a pure water permeability constant which is obtained

independently from the pure water permeation data with the use of the following relation

$$A = \frac{N_{BP}}{P} \quad (\Delta\pi=0) \quad (4)$$

Where N_{BP} is the pure water permeation rate with pure water as the feed as shown in figure 1.

Concerning the solute permeation rate N_A , a simple diffusion (solution-diffusion model) equation is assumed as:

$$N_A = \frac{c_m \cdot D_{AM}}{\delta} (X_{AM2} - X_{AM3}) \quad (5)$$

Where D_{AM} , X_{AM} and c_m are the diffusivity, mole fraction and molar density of solute in the membrane respectively, and δ is the effective thickness of the membrane. If the distribution ratio of solute between the aqueous solution and the membrane is assumed constant, then:

$$c \cdot X_A = K \cdot c_m \cdot X_{AM} \quad (6)$$

Where K is constant. And equation (5) becomes

$$N_A = \frac{c_m \cdot D_{AM}}{K \delta} (X_{A2} - X_{A3}) \quad (7)$$

We assume that the total molar density of the solution, c , is constant throughout the module. Further, the linear relations express osmotic pressures

$$\begin{aligned} \pi(C_{A2}) &= bC_{A2} = bcX_{A2} \\ \pi(C_{A3}) &= bC_{A3} = bcX_{A3} \end{aligned} \quad (8)$$

Where b is osmotic pressure constant
Since

$$X_{A3} = \frac{N_A}{N_A + N_B} \quad (9)$$

Substituting equation (9) in equation (7)

$$N_B = \frac{c_m \cdot D_{AM}}{K \delta} \cdot \frac{(1 - X_{A3})}{X_{A3}} \cdot (X_{A2} - X_{A3}) \quad (10)$$

Now we want to examine the concentration of solute in the near neighborhood of the membrane, on the high-pressure side figure (1).

The flux of solute (species A) in the region $0 < z < \ell$ may be written as the sum of the convective and diffusive fluxes.

$$N_A = X_A (N_A + N_B) - D_{AB} c \frac{dX_A}{dz} \quad (11)$$

Where D_{AB} is the diffusivity of solute in the aqueous feed solution. Using equation (9), and in integrated equation (11) with a boundary conditions

When $z=0$, $X_A=X_{A1}$

And $z=\ell$, $X_A=X_{A2}$

Solving the simple differential equation (11) with the above boundary conditions

$$\ln \frac{X_{A2}-X_{A3}}{X_{A1}-X_{A3}} = \frac{N_A+N_B}{c} \cdot \frac{\ell}{D_{AB}} \quad (12)$$

Defining the mass transfer coefficient k_1 , on the high pressure side of the membrane.

$$k_1 = \frac{D_{AB}}{\ell} \quad (13)$$

Equation (12) can be written as

$$\ln \frac{X_{A2}-X_{A3}}{X_{A1}-X_{A3}} = \frac{N_A+N_B}{k_1 c} \quad (14)$$

Equation (3) , (10) and (14) are combined to give the following relations

$$N_B = k_1 c (1 - X_{A3}) \ln \frac{X_{A2}-X_{A3}}{X_{A1}-X_{A3}} \quad (15)$$

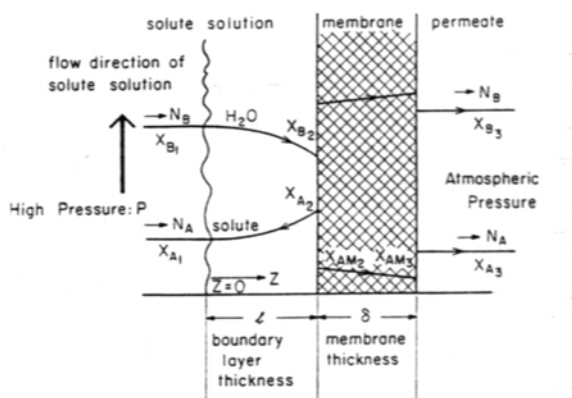


Fig.1 Concentration distribution in the boundary layer and the membrane (Ahmed ,2000)

EXPERMENTALS

Materials

The salt solution of Copper sulfide hexahydrate, Nickel sulfide hexahydrate, and Zinc sulfide hexahydrate were used as heavy metals solution in this study. The chemical analysis of the solutions are given in Table 1.

Table 1 Chemical Specification of Feed Solutions

Substance	Properties
Copper sulfide hexahydrate, $\text{CuSO}_4 \cdot 6\text{H}_2\text{O}$, M.W: 267.68 fluka,Switzerland.	Assay 96% min. Max. limits of impurities (%) Free acid: 0.2% As: 0.0005% Pb: 0.001% Fe: 0.005% CD: 0.005%

	Chloride: 0.001% Cu: 24.96% Zn: 0.001% Ni: 0.0005%
Nickel sulfide hexahydrate, $\text{NiSO}_4 \cdot 6\text{H}_2\text{O}$, M.W:262.86 fluka,Switzerland.	Assay 99.7% min. Max. limits of impurities (%) Mg 0.005% Ca 0.005 % Zn 0.0005% Pb 0.0005% Fe 0.0005% Cu 0.0005%
Zinc sulfide hexahydrate, $\text{ZnSO}_4 \cdot 6\text{H}_2\text{O}$,269.54 fluka,Switzerland.	Assay 99% min. Max. limits of impurities (%) Arsenic 0.008% Cu 0.013% Cl 0.02%

Reverse Osmosis Membrane

Commercially marketed spiral-wound membrane elements are adopted in this research. The membrane used in spiral wound module is a thin film composite membrane consisting of three layers: a polyester support web (120 μm), a microporous polysulfone interlayer (40 μm), and an ultra thin polyamide barrier layer (0.2 μm) on the top surface. Each layer is tailored to specific requirements.

Table 2 The specifications of the module

Type	SSRO50G
Membrane Type	Thin film composite (TFC)
Membrane length	115 cm
Membrane width	21cm
No. of membrane	2
Membrane active area	4830 cm^2
Metals rejection	=96 – 99 %

Experimental Procedure

Feed solution was prepared in the QVF glass vessels by dissolving each metal in 25 liter

of demineralized water (2 – 3 mg/l), and then the outlet valve of the feed vessel was opened to let the solutions fill the whole pipes of the system. The feed solution drawn from the feed vessel by means of a centrifugal pump (11.4 – 54.6 l/min, 3 – 13.7 m. H, 210 Watt, STUART TURNER LTD. HENLEY ON THAMES ENG, England) to pass through reverse osmosis pump. Then the solution is introduced into the spiral-wound RO elements by means of a high pressure pump (santoprene and polypropylene materials, maximum pressure = 120 psi, power = 220 – 240 V, and current = 1.2 A). Through reverse osmosis, water transports from the solution across the metals rejecting membrane and into the product solution as shown in figure 2.

In reverse osmosis a certain fraction of the feed passes across the membrane to produce permeate. The feed is gradually concentrated and

leaves the system at a higher concentration; the concentrate stream out of the module is directed back to the feed vessel of the module (or stage) and mixed with the feed stream. Every 15 minutes the concentrations of the feed solution, reject solution (concentrate) and product solution were measured by TDS meters (Type Waterproof TDS Test r High+, Range (0 – 1 * 10⁴ p.p.m), operating temperature (0 – 50°C), Accuracy (± 1%) power supply (6 Volt), Oakton instruments), and the flow rate of the product (permeate) solution for each run was recorded. The water flux was calculated by dividing the permeate volume by the product of effective membrane area and time. After recording the results, the solution (remaining in feed vessel), was drained by means of a drain valve. The whole system was washed by distilled water.

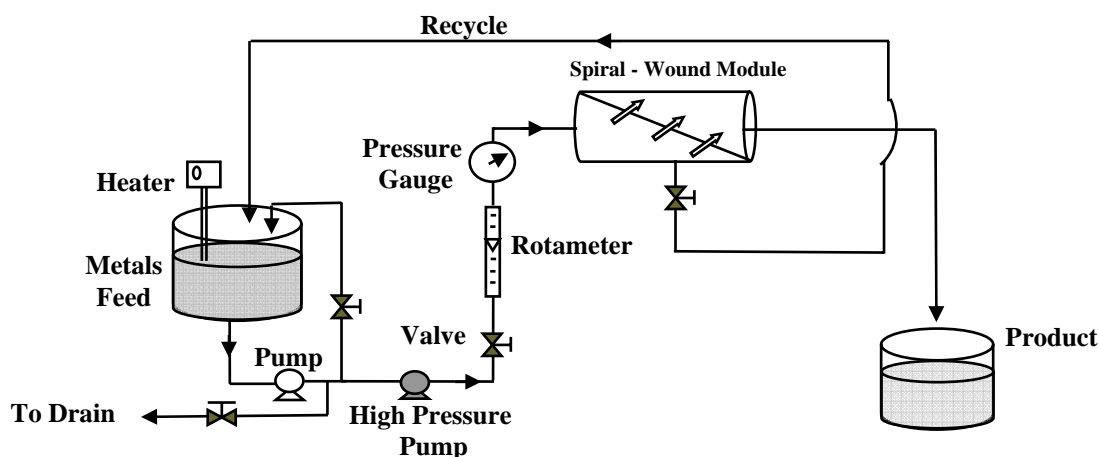


Fig .2 Schematic Diagram of Reverse Osmosis Process

RESULTS AND DISCUSSION

MEMBRANE HYDRAULIC PERMEABILITY

The pure water permeability constant (A) is a fundamental quantity; it is a measure of the overall porosity of the film. Water permeability was experimentally determined using a hydraulically pressurized reverse osmosis (RO) process. The flux of pure water through each membrane was determined under a range of pressures, according to the following equation:

$$N_{BP} = A \Delta P, \quad (\Delta\pi=0) \quad (4)$$

Where N_{BP} is the pure water permeation rate with pure water as the feed, the result of this hydraulic permeability test is shown in figure (3). As expected, the data show a linear relationship between driving force and water flux. Membrane hydraulic permeability is determined from the slope of this curve, the value of A was obtained 2.713 l.bar⁻¹ m².hr⁻¹ and this value is very closely approximate the result of Ahmed (2000).

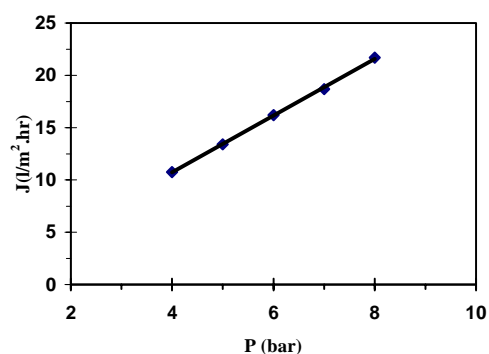


Fig.3 Water Flux vs. Operating Pressure
Effect of Operating Time

Effect of Operating Time and Feed Concentration on Product Rate

The water flux rate from reverse osmosis unit are plotted vs. time, as shown in figure (4 - 6). It can be easily observed that the flow rate from reverse osmosis unit decrease with increase in operating time.

The product rate of a reverse osmosis system decrease as fouling occurs, because the foulants on the membrane surface retard the back diffusion of the salt into the bulk solution to cause concentration polarization at the membrane surface. The increase in concentration polarization causes a decrease in the product rate. This can be explaining the decreasing of product rate with increase operating time, this observation is well agreed with the results of Mohammed and Salaheddin (2007). It can easily observed that the product rate decreases while the feed concentration is increasing and this is due to the possibility of fouling inside the pores of membrane would be larger in case of the concentrated solution flowing, this fouling could be acting in two ways. First, blockage a number of bores completely or partly, so the flow would be decreased, and the second decrease the voidage which increased the osmotic pressure across the membrane and that also would be decreased the product rate, this observation is well agreed with the results of Ahmed (2000) .

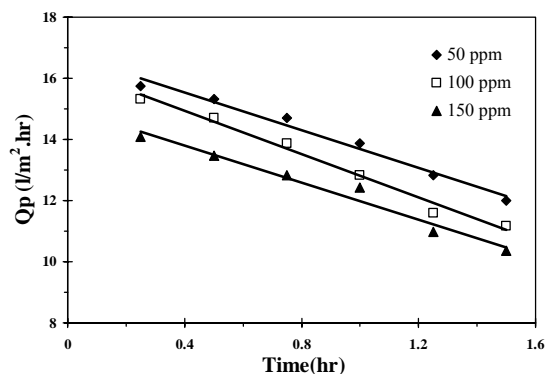


Fig. 4 Product Rate of Cu vs. Time for Reverse Osmosis Unit.

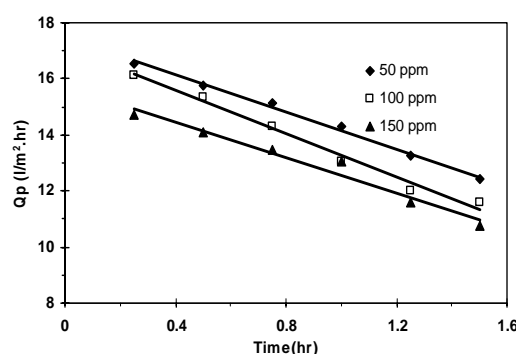


Fig. 5 Product Rate of Ni vs. Time for Reverse Osmosis Unit.

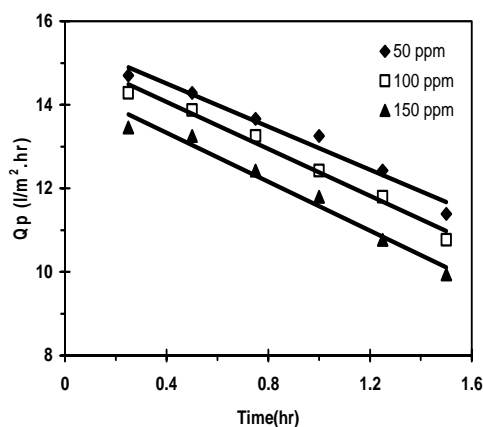


Fig. 6 Product rate of Cu vs. Time for Reverse Osmosis Unit.

Effect of Operating Time on Product Metal Concentration

Figure (7 - 9) shows the effect of operating time on product metal concentration for reverse osmosis industrial unit.

The increase in concentration polarization causes an increase in the salt passage. This reason can be explain the increase metal concentration with increase in operating time and this observation is well agreed with the result of

Kavitskaya et al. (2000). The minimum product concentration at 50 ppm, for copper, nickel and zinc were 2,2.5 and 1 mg/l respectively. While, at 100 ppm for copper, nickel and zinc were 5.3,5.5 and 4.2 mg/l respectively. At the concentration 150 ppm, for copper, nickel and zinc were 8.4,8.7 and 7.4 mg/l respectively.

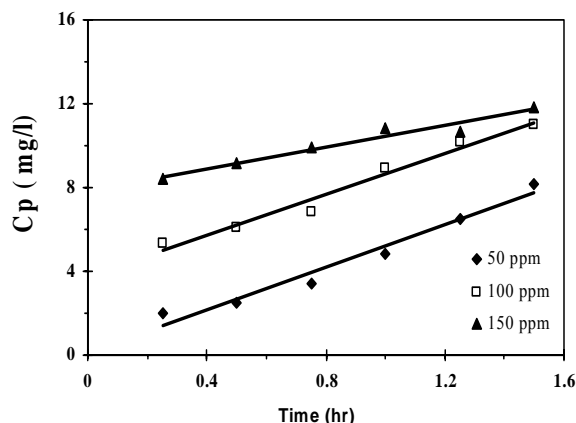


Fig. 7 Product concentration of copper vs. Time for Reverse Osmosis Unit

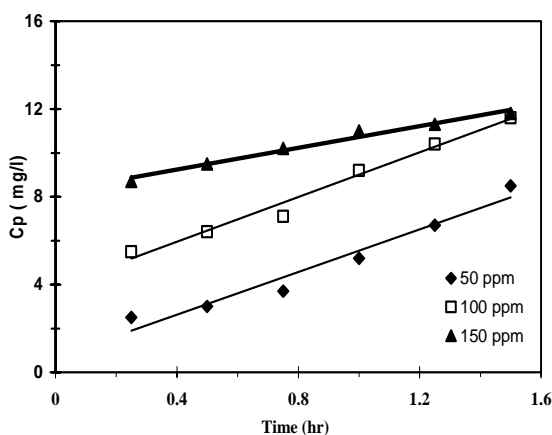


Fig.8 Product concentration of Nickel vs. Time for Reverse Osmosis Unit

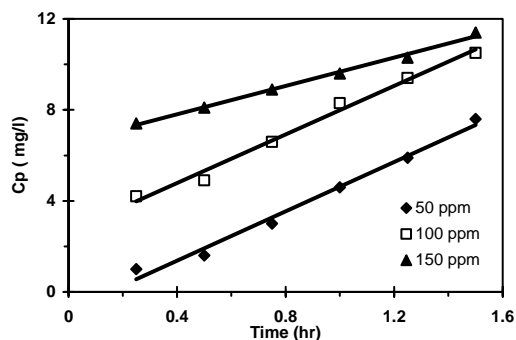


Fig.9 Product concentration of Zinc vs. Time for Reverse Osmosis Unit

Effect of Operating Time on Feed Solute Concentration

As shown in figures (10 - 12) during feed passage across the membrane to produce permeate, the feed concentrated gradually. The concentrate stream is directed back to the feed this cause an increase in feed concentration, the maximum feed solute concentration at 50 ppm, for copper, nickel and zinc were 89.2, 89.4 and 88.1 mg/L respectively. While, at 100 ppm, for copper, nickel and zinc were 139.7, 140.1 and 138.5 mg/L respectively. At the concentration 150 ppm, for copper, nickel and zinc were 182.8, 183, and 181.4 mg/L respectively.

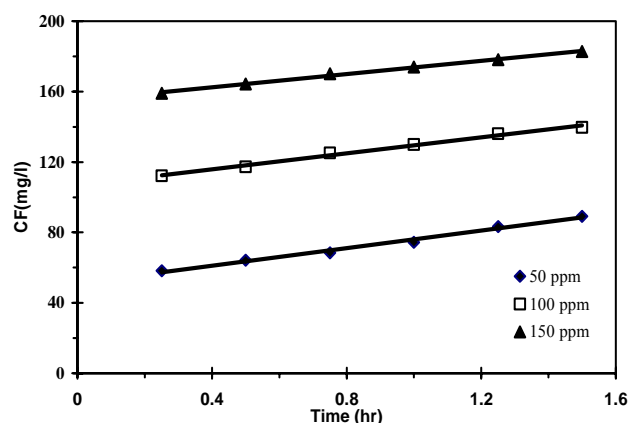


Fig. 10 Feed Concentration of Cu vs. Time for Reverse Osmosis Unit.

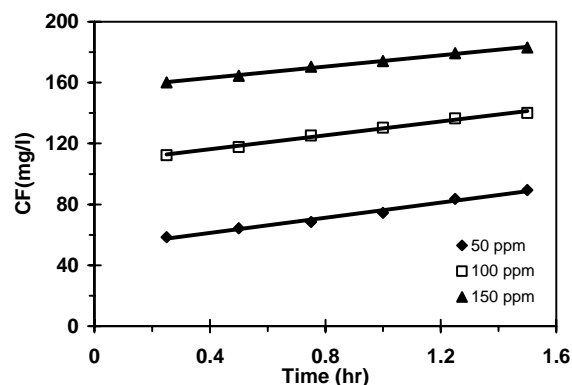


Fig. 11 Feed Concentration of Ni vs. Time for Reverse Osmosis Unit.

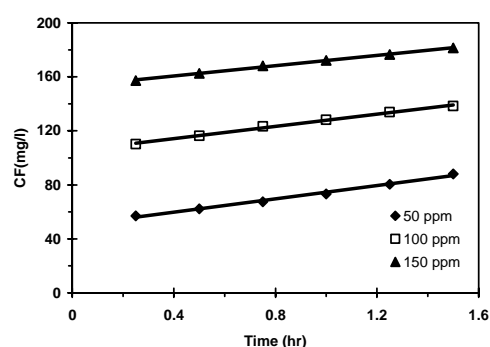


Fig. 12 Feed Concentration of Zn vs. Time for Reverse Osmosis Unit.

Effect of Operating Time on water recovery

As shown in figures (13 –15) the recovery at 50 ppm, for copper, nickel and zinc were 7.6-40.8, 7.7-41.4 and 7.1-38.4 % respectively. While, at 100 ppm, for copper, nickel and zinc were 7.4-38.4, 7.5-38.9 and 6.8-35.1% respectively. At the concentration 150 ppm, for copper, nickel and zinc were 6.8-35.8, 7.1-37.2, 6.5-34.6 % respectively. According to equation (2) the increase in percentage recovery with increase in time is due to an increase in the volume of pure water transfer from feed solution across the membrane to the permeate and this observation is well agreed with the result of Bruce., et al (2008).

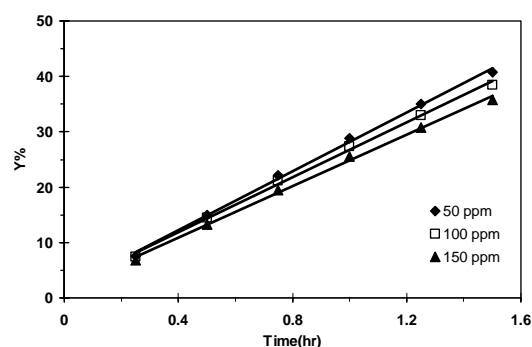


Fig. 13 Recovery percent vs. Time for Reverse Osmosis Unit for Cu.

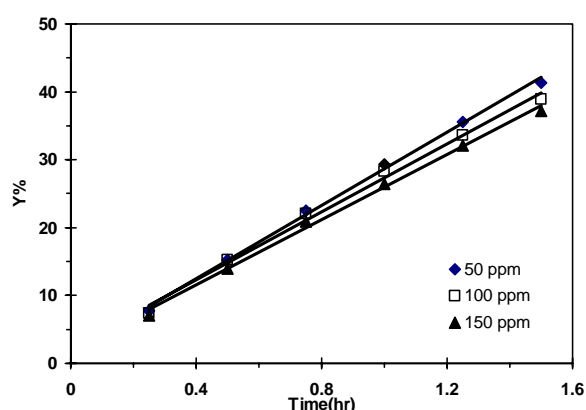


Fig. 14 Recovery percent vs. Time for Reverse Osmosis Unit for Ni.

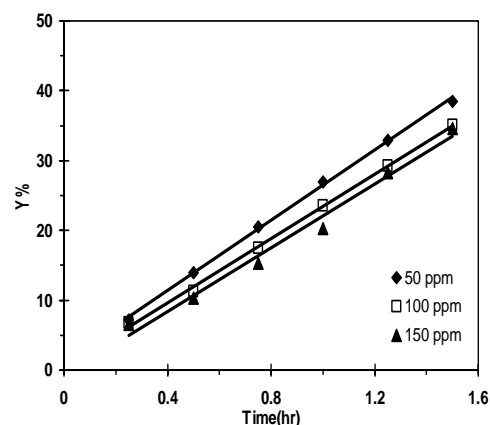


Fig. 15 Recovery percent vs. Time for Reverse Osmosis Unit for Zn.

Membrane metals rejection

Figures (16 – 18) show the influence of operating time on rejection percentage, that was studied by increasing operating time from 15, 30, 45, 60, 75 to 90 minutes with operating pressure fixed at 5.5 bar. According to equation(1) the increase in metals concentration will decrease the rejection percentage, this is due to the layer formed on the membrane surface hinders the back diffusion of the metals from the membrane surface back to the bulk solution. Consequently, created a larger concentration prepared for its diffusion across the RO membrane and this observation is well agreed with the results by How and Menachem (2004).

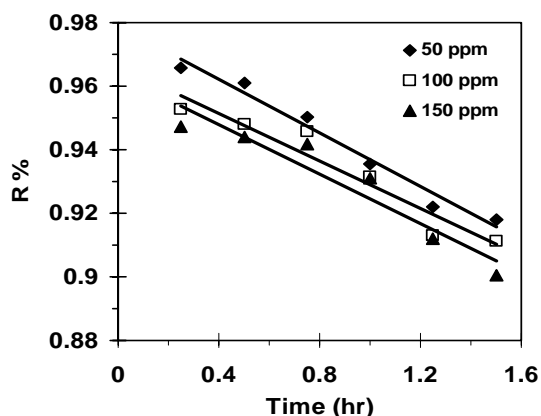


Fig. 16 Cu rejection percent vs. Time for Reverse Osmosis Unit.

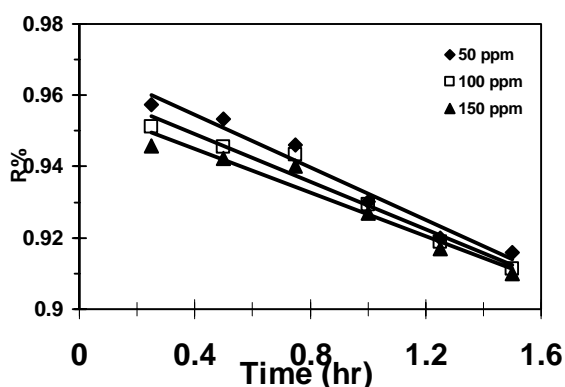


Fig. 17 Ni rejection percent vs. Time for Reverse Osmosis Unit .

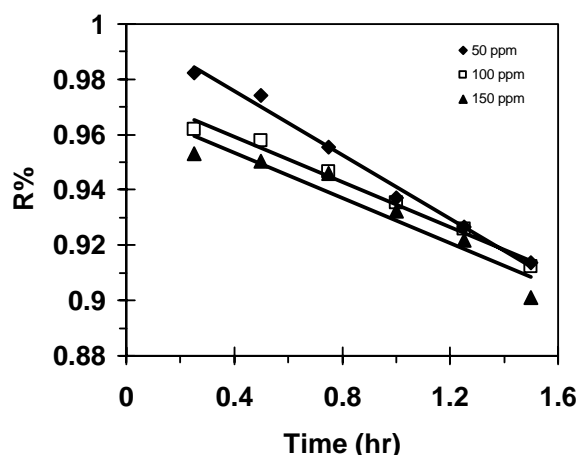


Fig. 18 Zn rejection percent vs. Time for Reverse Osmosis Unit for Zn.

Effect of Time and Feed Concentration on Mass Transfer Coefficient

The value of k_l can be obtained as function of operating pressure and feed

concentration. It is calculated according to the following equations:

$$N_B = A[P - \{\pi(X_{A2}) - \pi(X_{A3})\}] \quad (3)$$

And

$$N_B = k_l c(1 - X_{A3}) \ln \frac{X_{A2} - X_{A3}}{X_{A1} - X_{A3}} \quad (15)$$

As shown in figures (19 – 21) the metal permeability decreases with increasing the metal concentration according to the above equations, as time is increasing the feed concentration increases and this will lead to decreases in metal permeability. The mass transfer coefficient for the metals are very closely related because of their approximate molecular weight, the mass transfer coefficient at 50 ppm for copper, nickel and zinc were (11.4-4.3, 10.9-5.3 and 11-5) $\times 10^{-7}$ m/s respectively. While, at 100 ppm, for copper, nickel and zinc were (9.3-4, 9.1-4.1 and 9-3.9) $\times 10^{-7}$ m/s respectively. At the concentration 150 ppm, for copper, nickel and zinc were (8.7-3.7, 8.5-3.4 and 8.5-3.4) $\times 10^{-7}$ m/s. Water flux decreases with increasing feed solute concentration since the higher concentrations result in larger osmotic pressures (and so a smaller driving force across the membrane). This behavior is also predicted by most of the transport models and this observation agreed with results by Michael (2003).

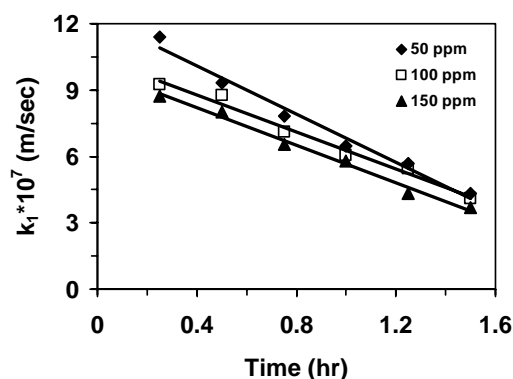


Fig.19 Mass transfer coefficient for Copper vs. time

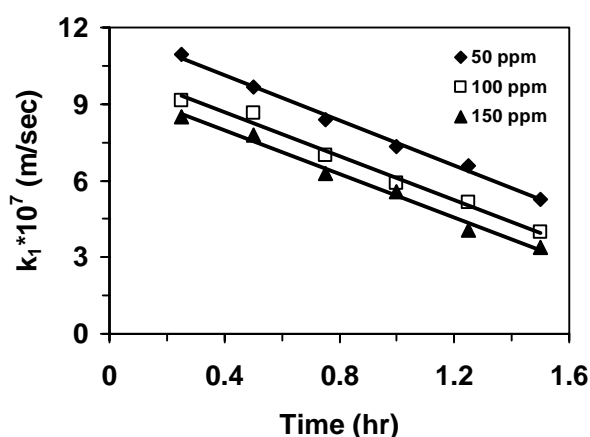


Fig.20 Mass transfer coefficient for Nickel vs. time

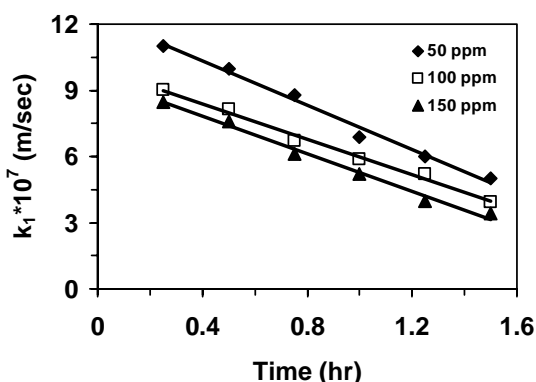


Fig.21 Mass transfer coefficient for Zinc vs. time

CONCLUSION

- The reverse osmosis process gives a high efficiency in separating metals.
- The increases in time cause an increase in metal passage.
- Flow rate of permeate from reverse osmosis unit decreases with increasing in operating time.
- The rejection of metals decreases with increasing time and also the increase in feed metals concentration will decrease the rejection percentage.

- The maximum recovery of copper, nickel, and zinc are 40.8%, 41.35% and 38.44 respectively.
- The maximum Rejection of copper, nickel, and zinc are 96.6%, 95.7% and 98.2% respectively.
- The difference in molecular weight for metals affects the water flux in RO process. Therefore, the results are closely related due to the nearest molecular weight for each metal.
- The pure water permeability constant for TFC membrane is $2.713 \text{ gmol H}_2\text{O} \cdot \text{bar}^{-1} \cdot \text{m}^{-2} \cdot \text{sec}^{-1}$
- Mass transfer of permeate decreases with the time operation.

REFERENCES:

- Ahmed, F.H., 2000, "Study of The Factors Affecting the Efficiency of Reverse Osmosis Process", M.Sc. thesis, Baghdad University.
- Belkacem Abas, Sid El Mahi Lamine Kadi and Omar Belhamiti.,2008, "Mathematical Modeling of reverse Osmosis Process by the Orthogonal Collocation of finite element method" , Asian Journal of Applied Science 1(1): 1-18.
- Bhattacharyya, D., and Williams, M.,1992, "Theory - Reverse Osmosis", in Membrane Handbook, W. Ho and K. Sirkar, eds., pp. 269-280, Van Nostrand Reinhold, New York .
- Bruce I.Dvorak ,Sharon O.Skipton., 2008 "Drinking water treatment :reverse osmosis", university of Nebraska-Lincoln. Pure & Appl Chem., Vol. 46, pp.193- 204.
- Cheryan, M., 1998, "Ultrafiltration and Microfiltration Handbook", Technomic, Lancaster, PA.
- Crespo, J.G., Velizarov, S. and Reis, M.A. 2004 "Membrane bioreactors for the removal of anionic micropollutants from drinking water." Biotechnology. 15: 463-468.
- Fazilet., 2000," Optimization of reverse osmosis membrane network",



- Ph.D.Thesis, The University of New south Wales ,Sydney, Australia.
- Ghulam M. Mustafa., 2007, " The study of pretreatment options for composite fouling of reverse osmosis membranes used in water treatment and production" , Ph.D. Thesis,University of New South Wales. Sydney, Australia.
 - Hasan, F. M., 2008, "Investigating Polyamide Membrane in Direct Osmosis Process in Cooling Towers", Ph.D. Thesis, Baghdad University.
 - How Y. Ng., Menachem Elimelech.,2004 "Influence of colloidal fouling on rejection of trace organic contaminants by reverse osmosis" Journal of Membrane Science 244, 215–226 .
 - Howard brown., 1973., "Removal of heavy metals from water by reverse osmosis", M.Sc.Thesis, Department of Civil Engineering and Applied Mechanics McGill University Montreal .
 - Kavitskaya, A.A., . Knyazkova, T.V, and Maynarovich,A.A.,2000 " Reverse osmosis of concentrated calcium sulphate solutions in the presence of iron (III) ions using composite membranes" , Desalination 132 , 281-286.
 - Kedem, O., and Katchalsky, A.,1958,, "Thermodynamic Analysis of the Permeability of Biological Membranes to Non-Electrolytes", Biochim. Biophys. Acta, 27, 229 .
 - Liu Feini , Zhang Guoliang , Meng Qin and Zhang Hongzi , 2008 "Performance of Nanofiltration and Reverse Osmosis Membranes in Metal Effluent Treatment" Chinese Journal of Chemical Engineering, 16(3) 441-445.
 - Michael E. Williams., 2003 " A Review of Reverse Osmosis Theory", Ph.D.
 - Mohamad Aboabboud., Salaheddin Elmasallati., 2007 "Potable water production from seawater by the reverse osmosis technique in Libya ",Desalination, 203,119-133.
 - Myzairah Binti Hamdzah .,2007 " low pressure reverse osmosis membrane for rejection of heavy metals", M.Sc.Thesis, University Teknologi Malaysia.
 - Nes,e Öztürk, Duygu Kavak, T. and Ennil Köse., 2008 " Boron removal from aqueous solution by reverse osmosis", Desalination 223 , (1–9).
 - Oh, J.I., Yamamoto, K., K., Kitawaki, H., Nakao, S., Sugawara, T., Rahaman, M.M. and Rahaman, M.H. 2000 " Application of low-pressure nanofiltration coupled with a bicycle pump for the treatment of arsenic-contaminated groundwater", Desalination, 132 : 307-314.
 - Patrick, M., "Membrane Seperation Processes", Elsevier, Amstrdam, 1976.
 - Sourirajan.S, "Reverse Osmosis", Academic, New York, 1970.
 - Spiegler, K., and Kedem, O.,1966, "Thermodynamics of Hyperfiltration (Reverse Osmosis): Criteria for Efficient Membranes", Desalination, 311 .
 - Srisuwan, G. and Thongchai, P.,2002 " Removal of heavy metals from electroplating wastewater by membrane". Songklanakarin J. Sci. Technol, 24(Suppl.) : 965-976.
 - Syed, R.Q. Edward, M.M. and Guang Z., 2000, "Water Works Engineering: Planning, Design, and Operation", Prentice – Hall, Inc., USA.
 - Taha, Y.K., 2000 "Performance of Reverse Osmosis", M.Sc. thesis, Baghdad University.
 - Yip, N.Y., Tiraferri, A., Phillip, W.A., Schiffman, J.D., and Elimelech, M., 2010, "High performance thin-film composite forward osmosis membrane", Environmental Science & Technology, (44), 3812–3818.

NOMENCLATURE

Symbol	Definition	Units
ℓ	Boundary layer thickness	M
ΔP	Transmembrane pressure	Bar
A	Pure water permeability constant	$l/(m^2 \cdot hr \cdot bar)$
B	Osmotic pressure constant	
C	Molar density of solution	$gmol \cdot Cm^{-3}$
CA_1	Solute concentration inlet	p.p.m
$CA_2=C_m$	Solute concentration in the membrane	p.p.m
CA_3	Solute concentration in the product solution	p.p.m
C_f	Feed concentration	Ppm
C_P	Product concentration	Ppm
D_{AB}	Diffusivity of solute in the aqueous feed solution	$M^2 \cdot Sec^{-1}$
D_{AM}	Diffusivity of solute in membrane	$m^2 \cdot Sec^{-1}$
J	Permeation flux	$l/m^2 \cdot h$
K	Constant	
k_1	Mass transfer coefficient	$m \cdot sec^{-1}$
N_A	Solute flux through membrane	$gmol \cdot m^2 \cdot sec^{-1}$
N_B	Solvent flux through membrane	$gmol \cdot m^2 \cdot sec^{-1}$
N_B	Solvent flux through membrane	$gmol \cdot m^2 \cdot sec^{-1}$
N_{Bp}	Solvent Flux using pure water as feed	$gmol \cdot m^2 \cdot sec^{-1}$
P	Applied pressure	Bar
Q_p	Product flow rate	l/h
R	Rejection	
t	Time	H
X_{A1}	Solute mole fraction in the bulk solution.	
X_{A2}	Solute mole fraction in the membrane.	
X_{A3}	Solute mole fraction in the product solution.	
X_{AM}	Mole fraction of solute on the membrane	
Y	Recovery percent	

Greek symbols

Symbol	Definition	Units
δ	Membrane Thickness.	M
π	Osmotic Pressure	Bar

AN E-LEARNING PACKAGE FOR DATA STRUCTURE USING VISUAL BASIC

Yasmin M. Kassim
Ass. Lec. In Nahrain University

ABSTRACT

E-learning comprises all forms of electronically supported teaching and learning. The information and communication system, whether networked or not, serve as specific media to implement the learning process; Computer based learning is one of the applications and processes of E-learning, sometimes abbreviated to CBL, refers to the use of computers as a key component of the educational environment [2]. Through my teaching, I found that there is a need for software learning packages at the lab to help students understand their courses especially in the subjects that need imagination like data structure. This research presents a data structure learning package for array and linear structure. Linear structure covers non-linked structure (stack and queue) and linked structure with their kinds. Through out this project the students can obtain a demonstration of how data structure is represented in memory. Most of the windows consist of three tabs, the first one is the information tab which contains all the information about the structures. The second tab contains all the operations performed on it and there is an ability to display all the operations in one executable program (full program), which receives inputs from the students, the students can enter different inputs according to the choices displayed and produce output after implementing by C++ program. The third tab contains exercises for the students to test their ability in understanding and after completing all the questions the package gives a score depending upon solutions. The package includes pictures and demos (movies) that represent the data structure implemented with 3D Max, finally all the windows are supplied with voice (my voice) to teach the students how to use the package.

الحقيبة التعليمية الالكترونية لمادة هياكل البيانات باستخدام الفيجوال بيسك

الخلاصة

التعليم الالكتروني يشمل جميع نماذج التعليم و التدريس الالكتروني. نظام المعلومات و الاتصالات سواء كان متصلا بشبكة أو غير متصل فهو يخدم كواسطة لتنفيذ عملية التعليم. أحد أنواع التعليم الالكتروني هو التعليم بواسطة الحاسبة، أحيانا يسمى بال (CBL) وهو يشير إلى استعمال الحاسبات كعنصر أساسي في عملية التعليم. من خلال تدريسي لاحظت وجود حاجة لحقيبة تعليمية في المختبر لمساعدة الطلاب لفهم المقررات التعليمية و خاصة في المواضيع التي تحتاج إلى تخيل كمادة هيكلية البيانات. لذلك هذا البحث يقدم حقيبة تعليمية خاصة بهيكلية البيانات و التي تغطي المصفوفة و الهياكل الخطية التي تضم الهياكل الغير متصلة (المكدس و الطابور) و الهياكل المتصلة بأنواعها. من خلال هذه الحقيبة يتمكن الطلاب من الحصول على شرح مفصل عن كيفية تمثيل هياكل البيانات في الذاكرة و ان معظم الواجهات في الحقيبة تتكون من ثلاث واجهات متغيرة، الأولى هي واجهة المعلومات و التي تتضمن جميع المعلومات عن الهيكل، و الثانية تعرض جميع العمليات الخاصة بالهيكل مع وجود إمكانية لعرضها جميعها في برنامج واحد قابل للتنفيذ من خلال الحقيبة بواسطة برنامج ال (C++) حيث يتمكن الطالب من وضع المدخلات الخاصة بتنفيذ البرنامج و المعروضة من خلال اختيارات في الواجهة و بعد التنفيذ تظهر النتائج أيضا في الواجهة و الواجهة الثالثة تحتوي على تمارين للطلاب لمعرفة مدى استيعابه للمادة و بعد إكمال جميع الأسئلة يعرض البرنامج الدرجة التي حصل عليها بالاعتماد على إجابته. كذلك تحتوي الحقيبة على صور و فلم يوضح آلية خزن الهياكل للبيانات مصممة بال (3D MAX)، و أخيرا جميع الواجهات مزودة بالية الصوت (صوت معد هذا البحث) لتعليم الطلبة كيفية استخدام الحقيبة.

Keywords: Learning Package (LP), Learning Package Platform (LPP), Electronic Learning (E-learning).

1. INTRODUCTION

During my teaching in computer and software engineering department, I found that there is a need for a software package that facilitates learning and understanding.

One of the fundamentals in software engineering study is data structure. Data Structure is any programming construction for representing and managing a collection of data. Data management in turns means storing and accessing data in a consistent way for a particular problem. The study of data structures involves two complementary goals. The first goal is to identify and develop useful mathematical entities and operation to identify what classes of problems using these entities and operations can solve. The second goal is to determine representation for those abstract entities and to implement the abstract operation on these concrete representations [9-11].

The learning package is implemented using Visual Basic because of the tools that permit the programmer to design graphical applications [5].

The package covers array (1D, 2D and ND), linear structure (non-linked structure and linked-structure), non-linked structure covered stack and queue (circular queue and double ended queue), linked structure covered linked list, circular linked list, double linked list, linked stack and linked queue. All of these are represented in a beautiful screens contain information, examples and exercises in addition to a movie to represent each of them.

2. LEARNING PACKAGE (LP) FRAMEWORK

This section presents a model of how LP can be integrated with a certain course.

2.1 Design model

The research has developed a design model of how to apply LP in a data structure through five steps as shown in fig. 1.

- A. The platform is chosen according to the course content (here visual basic is chosen).
- B. The design of exercises must reflect the limitations and constraints of the chosen LPP.
- C. Start design and implementation according to the constraints within the course and LPP.
- D. Documentation.
- E. Analysis and Evaluation to learn from success and mistakes.

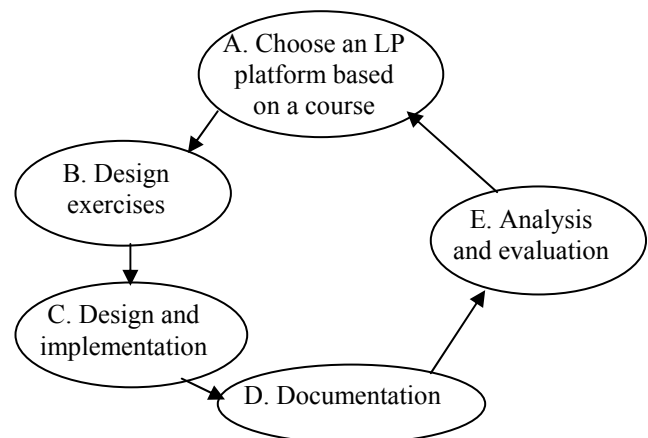


Fig. 1
Model of designing an LP

3. IMPLEMENTATION OF DATA STRUCTURE LEARNING PACKAGE

This section contains a brief illustration of how to use the package, the main screen, and the function of each object. The complete design consists of six (6) forms:

1. Main Window.
2. Chapter 1 (Array).
3. Chapter 2 (Linear Structures).
4. Stack.
5. Queue.
6. Linked Structures.

Each form is supplied with "Menu Bar", "Tool Bar", and a "Status Bar". Voice comments are provided to facilitate the package usage.

3.1 Main Window

It contains the abstract information of the package as shown in fig. 2.

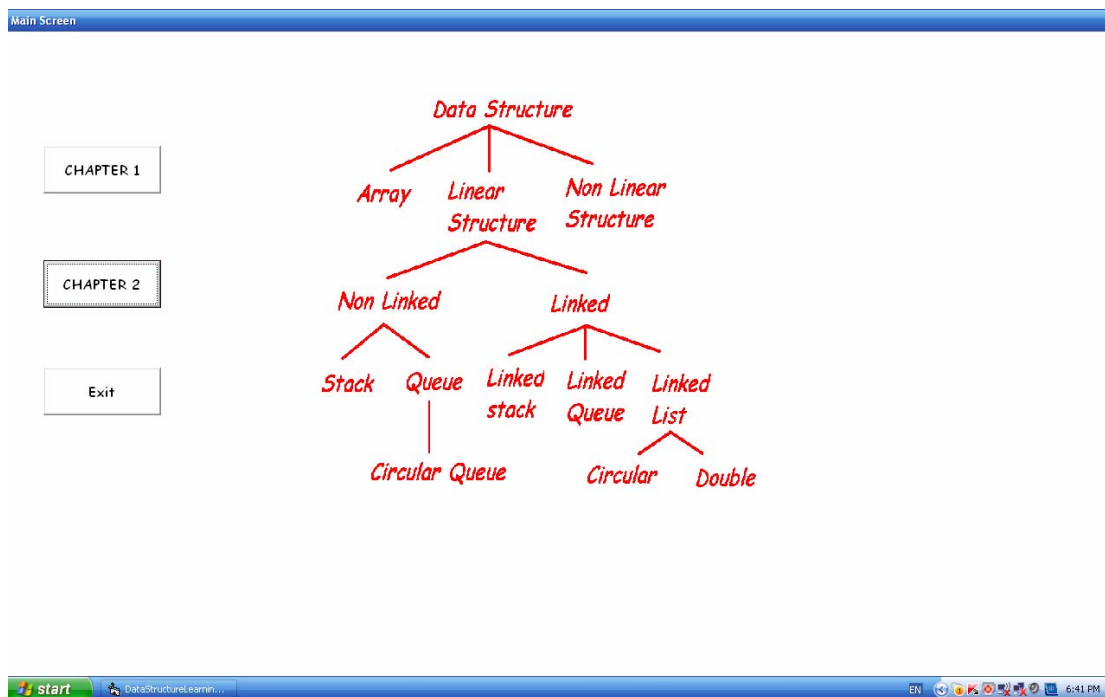


Fig. 2
Main Window

Here the package will begin to branch in to two chapters: Chapter 1 and Chapter 2. When you click on chapter1 a window will appear which contains all the information about the array.

3.2 Chapter1 (Array)

The window contains three tabs and each of them is shown below:

1. Information tab: all the information about array includes one-dimensional array, two-dimensional array and n-dimensional array are presented in the

rich text box and the chosen subject can be selected by an option buttons beside it as shown in fig. 3.

2. Example tab: which contains all the functions implemented on array (Create the array, destroy it, checking if it is empty, return it's length, return the location of a specific element, insert an element, remove an element and print the array), each of these

operations is represented as a button and when you click on this button the corresponding program will appear in the rich text box beside the abstract data type ; also to test all the preceding operations a special button is placed at the bottom of the ADT field , when clicking on it a part of the form will change to make implementing the full program possible, the user may choose a function by writing his choice in the "choice box". If it's required to give input data, it must be written in the

"input box" and when finishing the user must enter 0 to exit then press the run button to execute the program, a message is displayed asking the user to wait for few seconds, the output is given in a textbox after pressing the show result as shown in fig. 4; The choices above include all the operations done on the array and the inputs of the user will be written on a file and this file will be the input for another C++ program; this program will be executed depending upon user input. The output is written to another file displayed by a text box in our package by clicking the show result button. An example is shown in fig. 4, entering an input in the choice textbox such as 55260 which means that the user first chooses a choice number 5 that represents the element insertion, when typing 5, the right textbox beside the choice box will be activated to receive the input to be inserted to the array (here the user inserts number 8), after that the textbox will be deactivated and the cursor returns to the preceding textbox to receive the next choice which is also 5 (here the user inputs number 9), after inserting number 8 and 9 the user now wants to know the length of the array, so he chooses number 2 in the choice textbox then enters number 6 to print the array and 0 for exit after that the user must run the program by clicking on the run button and the output (execution result) will appear on the output textbox below show result.

3. Exercises tab: there are four questions with choices are given to test the user understandability, if the user fails in the current question, he can't return to it, the next button at the right lower corner will move him to the next question, a score is computed after attempting all questions as shown in fig. 5 here for example, the selected question is about the declaration of data structure, the student succeeds in this question by choosing B button, the program displays "correct answer" message to proceed in receiving questions.

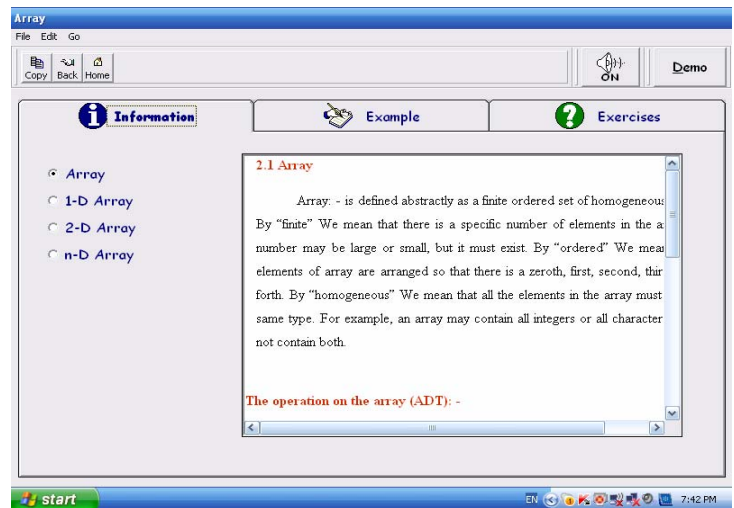


Fig. 3
Array information tab

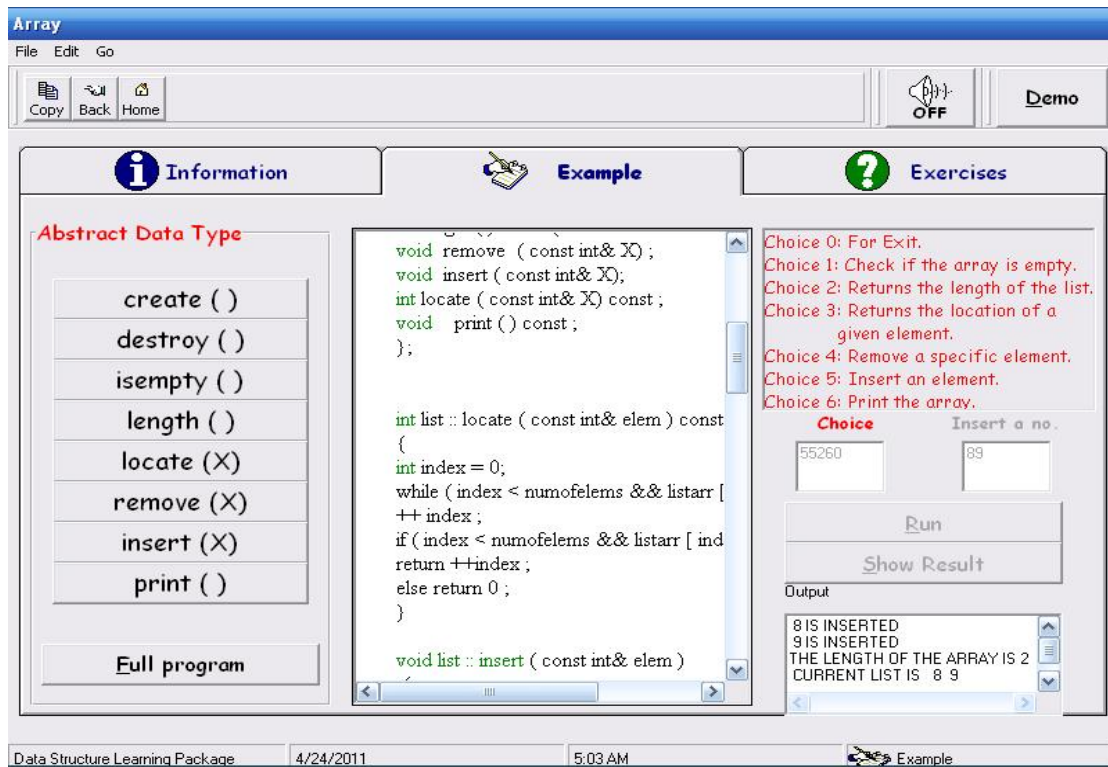


Fig. 4
Array Example tab

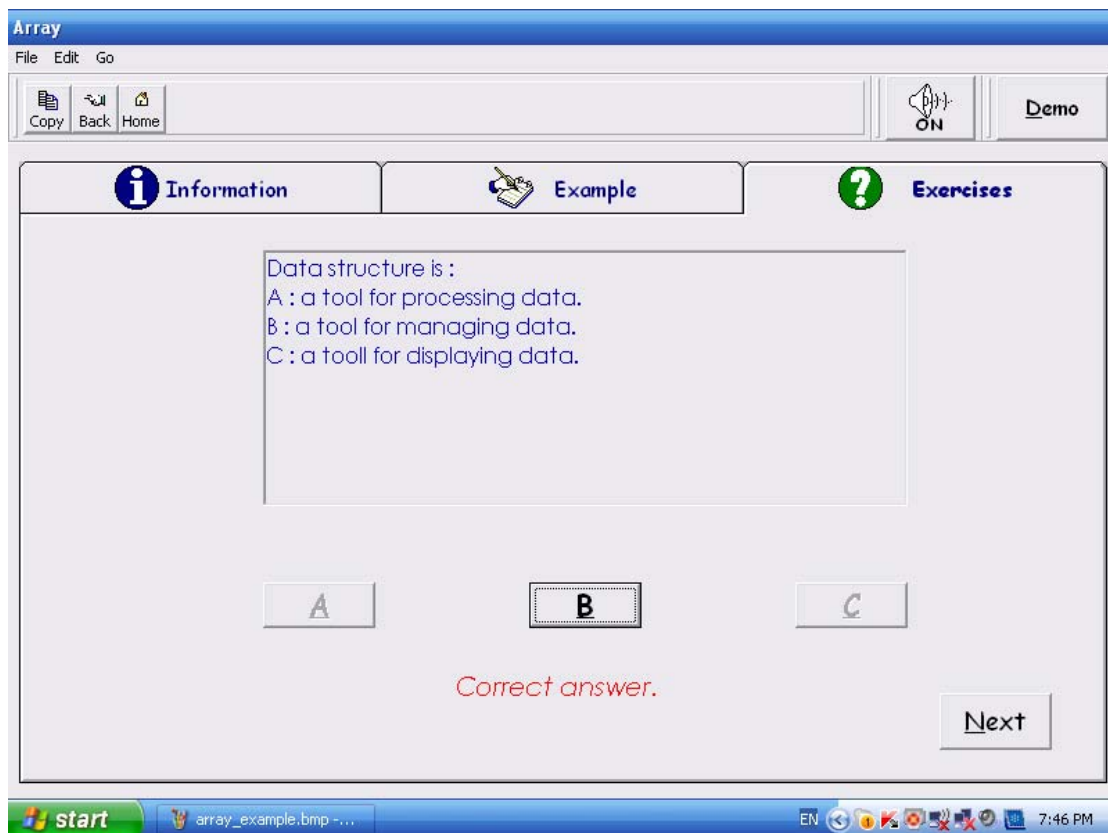


Fig. 5
Array Exercise tab

Also there is a button called Demo, when the user clicks on it, a movie will appear to represent the array types as shown in fig. 6, the first part of the figure shown in blue color is to tell student that 1D array takes a linear place in memory, as for the second part of the same figure below it representing 2D in gray color shows the storage as a set of cells having a rectangular configuration and the third one with yellow color is for representing N-D storage.

The window also has a button showing a speaker icon for controlling the voice related to the package; also the window contains the following buttons:

1. Copy: to copy any desired information to another document.
2. Back: to facilitate translation from screen to another screen .
3. Home: to return to home page.

Also the window contains a menu which has three elements:

1. File: includes the term "about" by clicking it, shows programmer's information and exit to exit from the package.
2. Edit: contains copy command.
3. Go: contains back and home page commands.

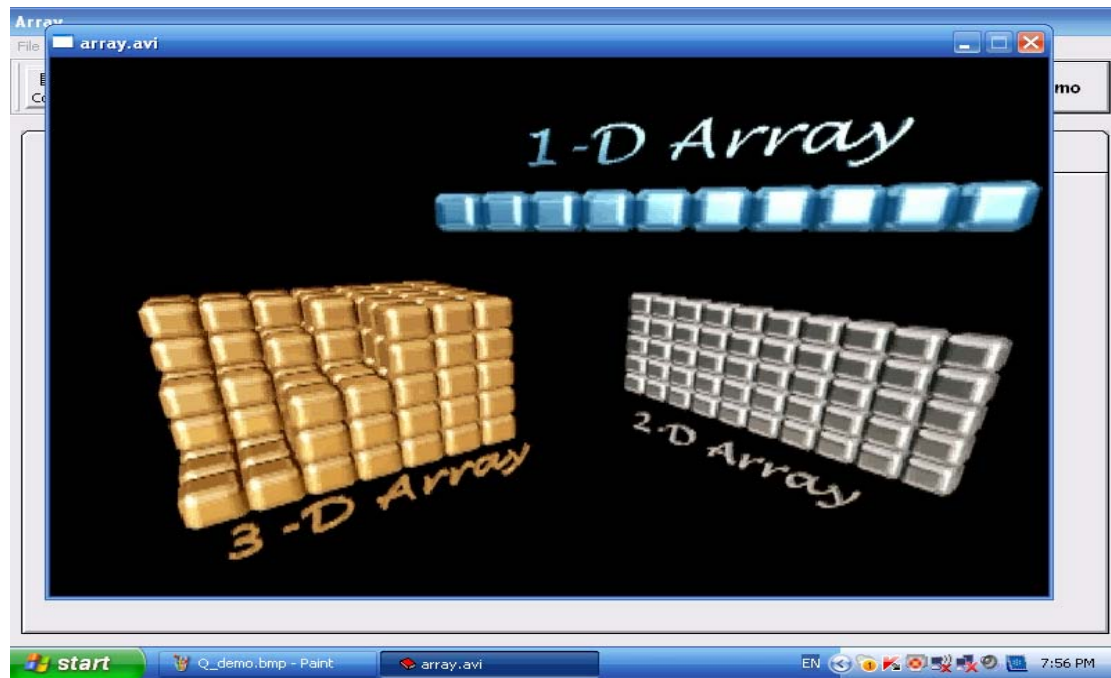


Fig. 6
Array picture from demo

Here we have completed chapter1 which includes the array only, after clicking on back, the package returns to the main window; here there is another button called chapter 2 which contains all the information about linear structure as listed below.

3.3 Chapter2 (Linear Structure)

This screen contains information about linear structure shown in fig. 7. Linear structure consists of non linked structure (Stack and Queue) and linked structure. There is a detailed explanation for each of them in the preceding window. It contains buttons called Stack, Queue and linked structure, when the user click on each of them, the package will go to the window attached to it. Also there is back and exit button to exit from the package.

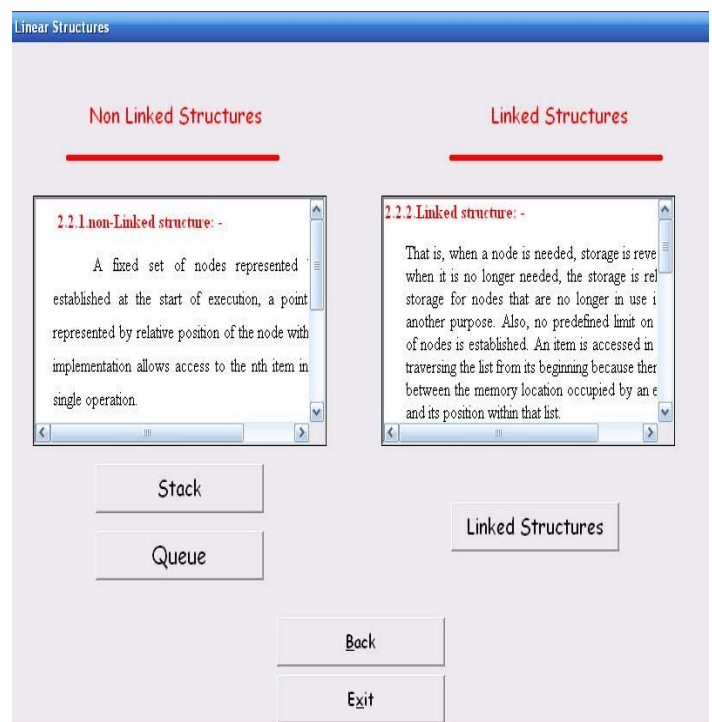


Fig. 7
Linear structure

3.4 Stack

The Stack data structure is a lifo (last-in first-out) structure. It is obtained from a linear list by restricting the insertions and deletions to take place from the same end. This end is called the top. The other end is called a bottom. This declaration and many other information about the stack are displayed in the stack screen in the package as shown in fig. 8.

In fig. 9 the user chooses the full program button so the full program appears in the large text box beside buttons. Here the user for example wants to add two elements into stack, to know the top element of it, he writes 4420 in the choice textbox, 4 (represents push), the second 4 (represents another push), 2 (represents retrieving top element) and 0 (for exit), then after execution the results will appear in the output textbox which is "THE UPPER ELEMENT IS : 2" this is to represent the second element he has inserted which is located on the top of the stack.

in the inverse order and many applications require that form, but if any one wants the same word to show in the same order, he must use the queue to store it.

Fig. 10 shows the solving of 4 questions, 2 of them are true and the other two are false, so his score shows 50% from 100% as shown in exercises result window. Finally in all stack widows there is a demo button (to show movie) when the student clicks on it the demo begins as shown in fig. 11, the demo starts with entering "stack" word characters into the stack one after the other, beginning with S and ending with k accompanied with stack pointer "SP" updating for each character entered, after completing all characters, the characters begin to pull out from the stack in the same way but with the inverse order and this procedure will teach the student that any word stored in the stack will exit

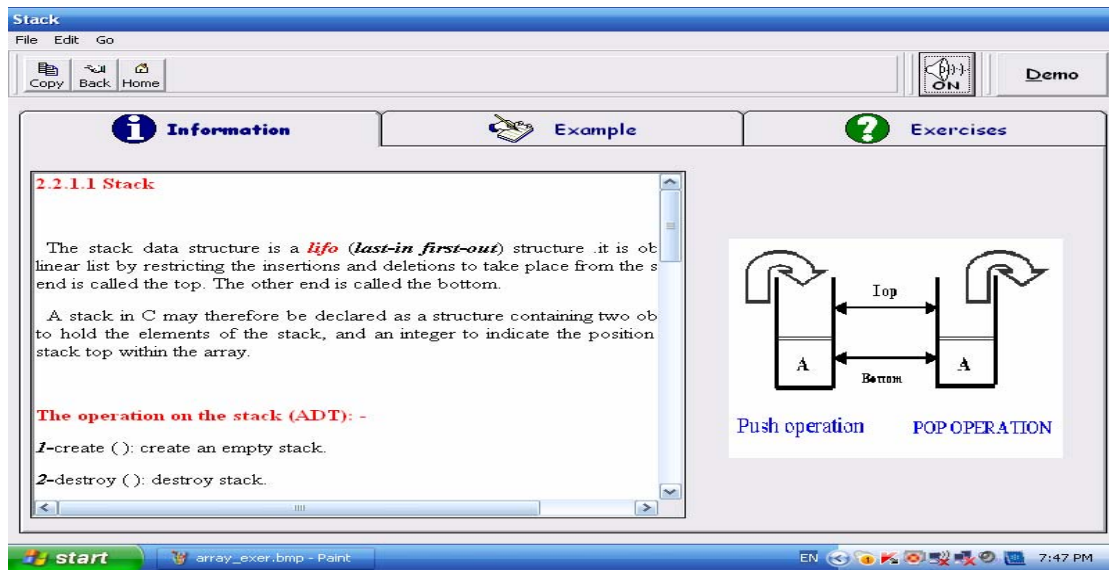


Fig. 8
Stack information tab

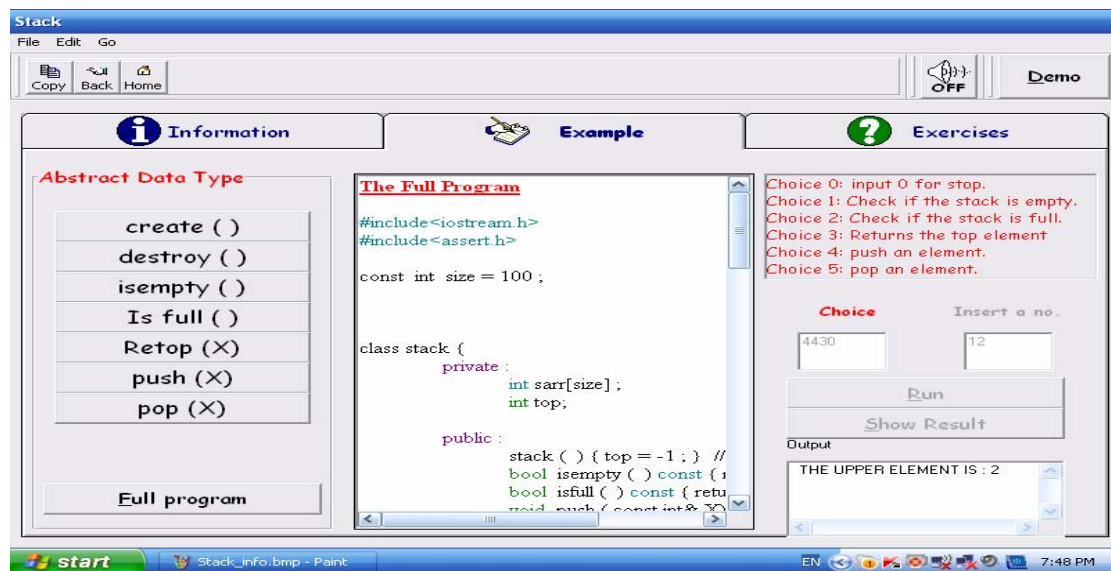


Fig. 9
Stack example tab

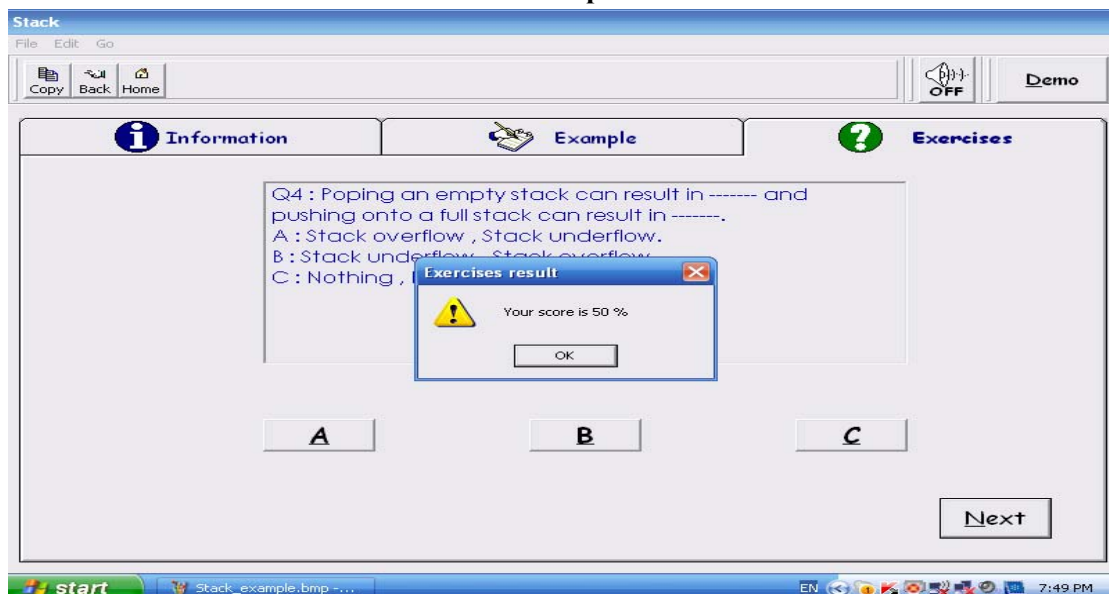


Fig. 10
Stack exercise tab



Fig. 11
Stack's Picture from movie

3.5 Queue

The same window with alternative information is appeared in fig.12, where Queue's information are displayed, this window will tell the student that there are two types of queues, the linear queue and the circular queue including simple description for each of them, functions implemented on the queue are displayed in the example tab as shown in fig. 13. Here the student input 22140 in the text box to implement five operations which are shown below:

- 2 → Insert an element to the queue which is 6.
- 2 → Insert another element to the queue which is 5.
- 1 → Check if the queue is empty.
- 4 → Print the content of the queue
- 0 → End.

After running the program the result is shown in the output textbox.

Also a movie will appear when the user clicks on demo as shown in fig. 14, the demo here shows the students

word into the queue from the left and how the pointers (front and rear) will change from cell to cell after entering each character and when the whole operation is done, the characters begin to exit from the right side of the queue resulting the same word in the same order to make the student understand that any word entered the queue exit in the same order.

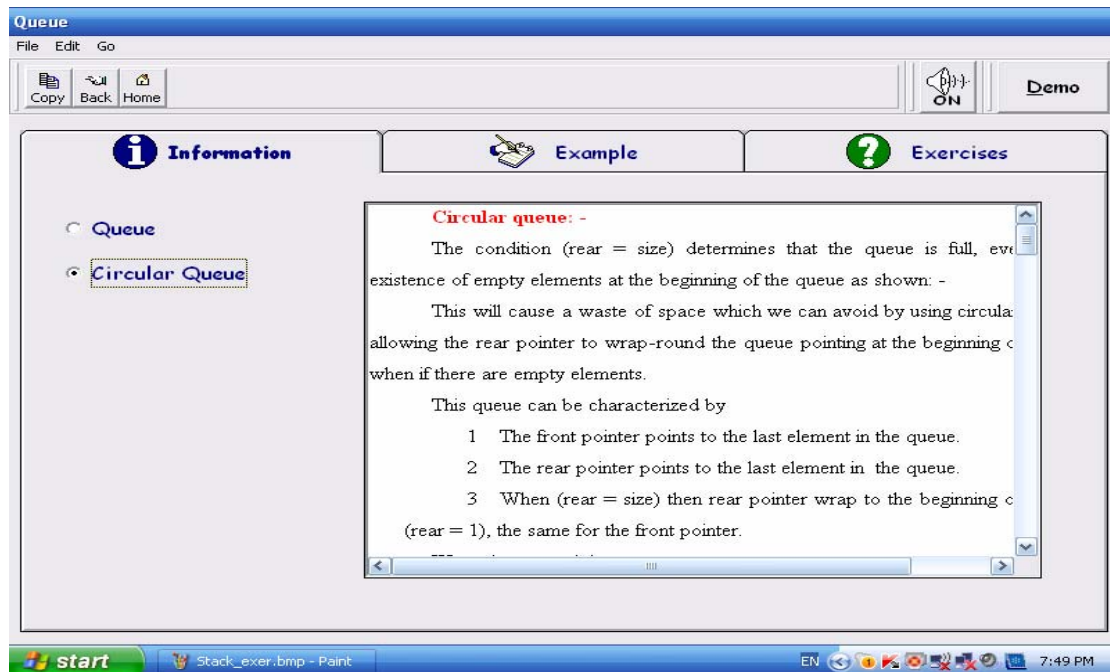


Fig. 12
Queue information tab

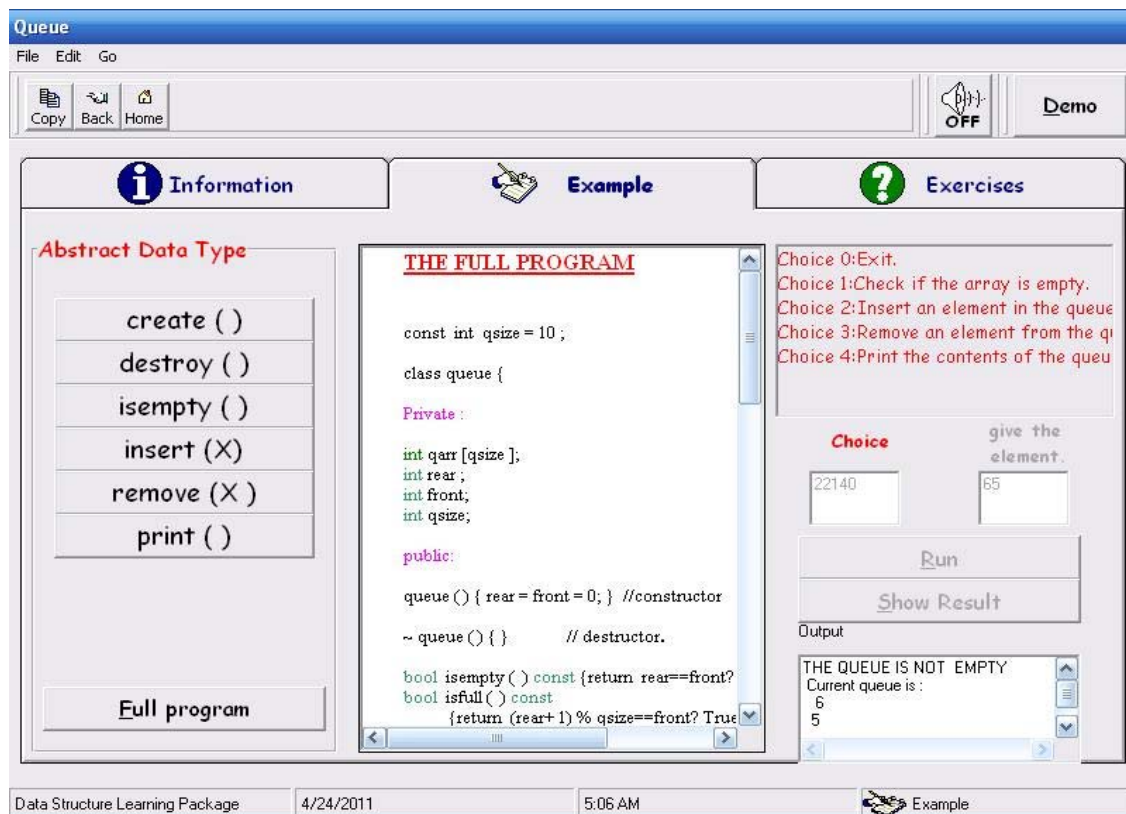


Fig. 13
Queue example tab



Fig. 14
Queue movie picture

3.6 Linked structure

All the details about linked data structure presented in this window include the same as the tabs shown above with alternative information as shown in fig.15 & 16. Fig. 15 shows the students that there are 5 types of linked structure. In fig. 16 there is a picture of train, it is not only a picture but it is a demo which runs after clicking on demo button, the train is chosen because it is very resembling linked structure, each vehicle represents a node and the nodes are linked with each other by pointers like the connection of train vehicles, these vehicles are numbered to show to the students that each node has a pointer, also the demo showing a feature in the linked list which is the head and tail pointers in the first and end vehicles, the demo showing also the addition and deletion operations are

represented similar to exiting one vehicle from the train and leaving it in the desert (representing the deletion of a node) and then after taking a tour the same vehicle will return to the same or another location in the train (representing the addition of a node), this is to show the student that the deletion and addition exist in any index in the linked list and their pointers will be updated according to it's place, this is in contrary to the insertion and deletion of the stack and queue where updating only takes place at the beginning and their end.

Examples and exercises of the linked list are not mentioned because they are in the same form as in array, stack and queue.

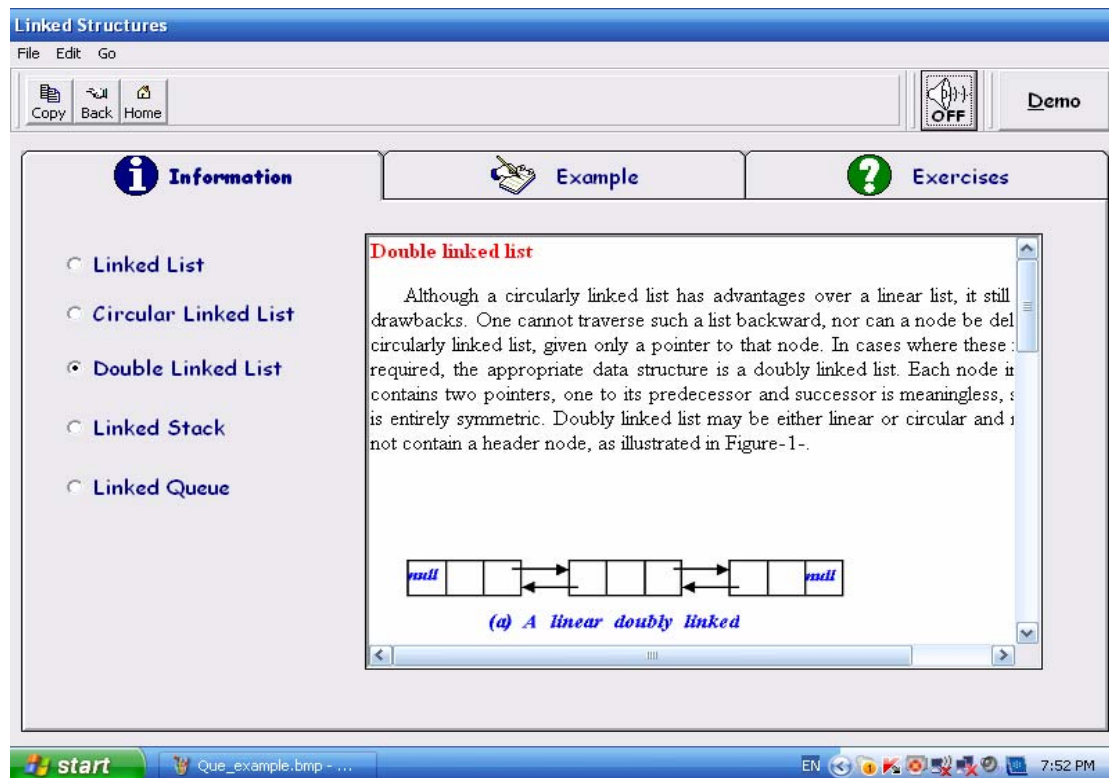


Fig. 15
Linked structure information tab

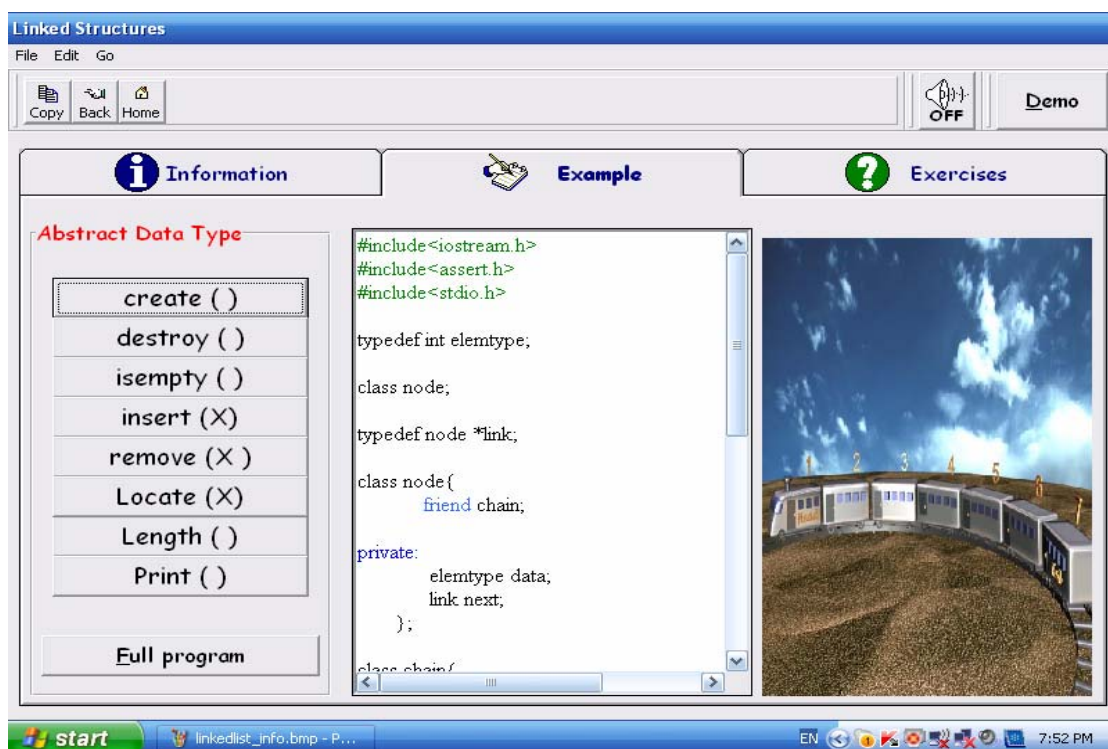


Fig. 16
Linked structure example tab with picture from movie

At this point, the research covered most of the windows. The chosen information in information tap in all the windows is not a copy from one book but it is abstracts from multiple of books further to lectures. These abstracts and lectures were collected, assorted and written by me in word documents and were retrieved by the learning package program. If any student want these information, he/she can take it by copying them by the copy button or by taking the word documents which are available with the package. The examples tap first display each operation alone to help the student to focus in each operation then see all operations in one executable program, also the exercises are chosen to cover all package subjects to ensure that the student completely understands. The reason for focusing on demos and pictures, for the fact that pictures are stored in the brain much more than text.

4. USER ACCEPTANCE TESTING

User Acceptance testing is one of the important test activities in software development. It requires the participation of the end-users. An acceptance test plan was developed to guide the testing process. In order to conduct this testing, 31 users were selected at random to participate in the test. These participants were first given the LP to learn data structure using the system. They were each given a number of questionnaires to answer to indicate their level of satisfaction on LP, fig. 17 and fig. 18 show the user acceptance test results.

Table 1 and figure 17 show that 5 (0.16) and 21 (0.67) students, totally agree and agree that data structure LP is very sufficient for learning in the course. However, 4 (0.12) students are not sure. This could possibly be due to the fact that there were not given enough time to use LP. Only 1 student (0.03) disagrees with the other students' opinion.

Table 1
Student's test1

	Totally agree	agree	Not sure	disagree	Totally not agree
students	5	21	4	1	0

Table 2 and Figure 18 show that 7 (0.22) and 20 (0.64) students, totally agree and agree that they are satisfied with the functions and features provided in our LP, respectively. Only 4 (0.12) students indicated that they are not sure if LP can help to learn data structure. Overall, 27 (0.87) of the students agree that DSLP can assist them in the learning of data structure in an easy and interesting way.

Table 2
Student's test2

	Totally agree	agree	Not sure	disagree	Totally not agree
students	7	20	4	0	0

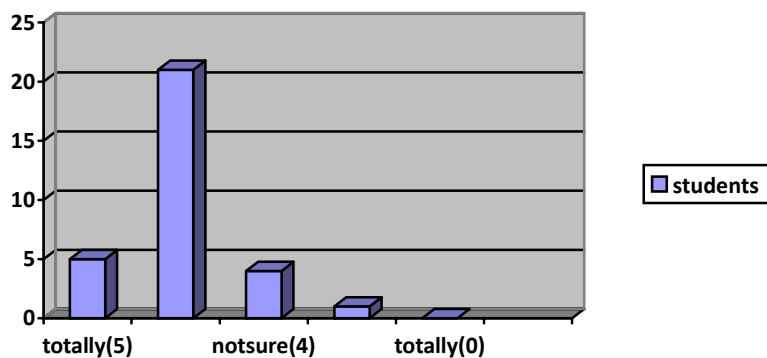


Fig. 17
Student's test1

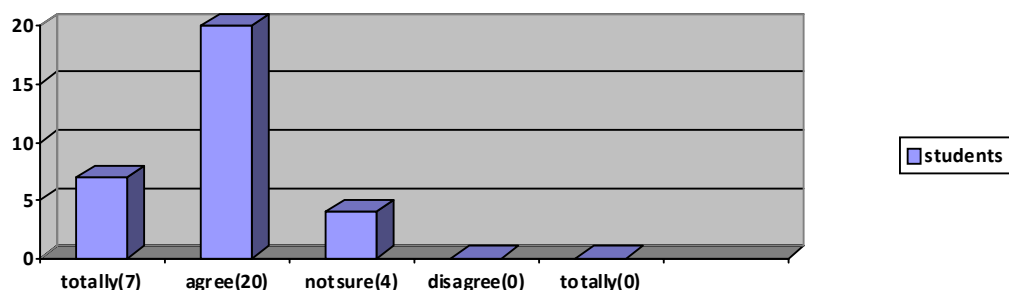


Fig. 18
Student's test2

5. CONCLUSIONS AND FUTURE WORK

This research involves a data structure learning package concerning arrays and linear structure. The package teaches the student through illustrations of how to represent data structure in memory. The package uses many windows showing three taps. The first is the information tap covering the demonstration structure, the second tap includes all operations performed on it which can be displayed in one executable program receiving inputs from students who can enter different inputs according to the choices displayed and output is displayed after C++ program is implemented. The third tap includes exercises for testing the ability of the

students in understanding. The package will give a score for the student after completion of all questions depending on the solutions. Teaching aids are used in the package such as pictures, movies and voices that represent the data structure implemented with 3D max and to teach the students for using the package.

As a future plan:

1. Expanding this project to include non linear structures represented as graphs.
2. Using front page to design it can provide much better facility and flexibility.
3. By using large database, exercises can be selected randomly which gives the package higher quality.
4. More movies that show the mechanism of the ADT in a simple manner.
5. New sections can be used for writing C++ programs by students. This program then will be connected to the C++ compiler for checking it.
6. Some other languages (Pascal, Turbo C, Basic...) can be used to implement data structure.

REFERENCES

- [1] Allen, "Michael Allen's Guide into E-Learning", admin, 2010.
- [2] Bruno R., "Data Structure and algorithms with object oriented design patterns in C++", John Wiley & Sons, 1998.
- [3] Clifford A., "Practical information to data structure and algorithm analysis third edition (C++ version)", Freeteckbooks.com, 2010.
- [4] Daviniahl, "Investigations of E-Learning Patterns", 2011.
- [5] Granville B. and Luca T., "Data structures and algorithms: Annotated Reference with examples", Dotnetslackers, 2008.
- [6] Jane S., "Copyright and e-learning : a guide for practitioners", London Facet, 2010.
- [7] Nigel P. and Eliom M., " E-Learning Perspectives", The MASIL Center, 2010.
- [8] Som N., "E-learning A Guidebook of Principles, Procedures and Practices", CEMCA, 2006.
- [9] Tavangarian D., Leybold M., Nolting K. and Roser M., "Is e_learning the solution for individual learning?", Journal of e_learning, 2004.
- [10] Yedidyah L., Moshe J. and Aaron M., " Data Structures using C and C++", 1998.
- [11] Yahya H. and Mohamed B., "Visual Basic 6", Dar Wael, Jordan, 2001.